TU Delft

Delft University of Technology

Document Version
Final published version

Citation (APA)
Oktiovan, Y. P. (2026). *Advancing the Distinct Element Modelling of Masonry Structures: A Joint Constitutive Model for Cracking, Shearing, and Crushing Under Cyclic and Dynamic Loading*. [Dissertation (TU Delft), Delft University of Technology]. https://doi.org/10.4233/uuid:b11cc807-d655-4e33-82e0-2934cd994b5f

Important note
To cite this publication, please use the final published version (if applicable).
Please check the document version above.

Copyright
In case the licence states “Dutch Copyright Act (Article 25fa)”, this publication was made available Green Open Access via the TU Delft Institutional Repository pursuant to Dutch Copyright Act (Article 25fa, the Taverne amendment). This provision does not affect copyright ownership.
Unless copyright is transferred by contract or statute, it remains with the copyright holder.

Sharing and reuse
Other than for strictly personal use, it is not permitted to download, forward or distribute the text or part of it, without the consent of the author(s) and/or copyright holder(s), unless the work is under an open content license such as Creative Commons.

Takedown policy
Please contact us and provide details if you believe this document breaches copyrights.
We will remove access to the work immediately and investigate your claim.

This work is downloaded from Delft University of Technology.

ADVANCING THE DISTINCT ELEMENT MODELLING OF MASONRY STRUCTURES



A Joint Constitutive Model for Cracking, Shearing, and Crushing under Cyclic and Dynamic Loading

Yopi Prabowo OKTIOVAN

Advancing the Distinct Element Modelling of Masonry Structures

A Joint Constitutive Model for Cracking, Shearing, and Crushing under Cyclic and Dynamic Loading

ADVANCING THE DISTINCT ELEMENT MODELLING OF MASONRY STRUCTURES

A JOINT CONSTITUTIVE MODEL FOR CRACKING, SHEARING, AND CRUSHING UNDER CYCLIC AND DYNAMIC LOADING

Dissertation

for the purpose of obtaining the degree of doctor
at Delft University of Technology
by the authority of the Rector Magnificus,
Prof. dr. ir. H. Bijl,
chair of the Board for Doctorates
to be defended publicly on
Tuesday, 24 November 2026, 15:00

by

Yopi Prabowo OKTIOVAN

This dissertation has been approved by the (co)promotors.
Composition of the doctoral committee:

Rector Magnificus		chairperson
Em. prof. dr. ir.	J. G. Rots	Delft University of Technology, *promotor*
Dr. ing.	F. Messali	Delft University of Technology, *copromotor*

Independent members:

Prof. dr. ir.	M. A. N. Hendriks	Delft University of Technology
Prof. dr.	A. Penna	University of Pavia, Italy
Prof. dr.	V. Sarhosis	University of Leeds, United Kingdom
Prof. dr.	I. E. Bal	University of Groningen, the Netherlands
Dr.	B. Pulatsu	Carleton University, Canada
Prof. dr. ir.	L. J. Sluys	Delft University of Technology, *reserve member*



Keywords: unreinforced masonry, distinct element method, joint constitutive model, multi-surface damage plasticity, explicit integration scheme, cyclic degradation

Printed by: Ipskamp Printing, The Netherlands

Cover by: Sharen Gisella Meitiovan (sketch)
Shania Gabriella Gustiovan (rendering and digitisation)

Copyright © 2026 by Y.P. Oktiovan

ISBN 978-94-6518-484-5

An electronic version of this dissertation is available at:
https://repository.tudelft.nl/.

Lasciate ogne speranza, voi ch'intrate.[1]

Dante Alighieri, *Inferno*, Canto III

[1] 'Abandon all hope, ye who enter here.'

Contents

Summary xiii

Samenvatting xvii

Propositions xxi

Symbols and Nomenclature xxiii

1. Introduction 1
1.1. Background . . . 2
1.2. Problem statement . . . 5
1.3. Research objectives and scope . . . 6
1.3.1. Design criteria . . . 7
1.3.2. Sub-projects division . . . 7
1.4. Thesis outline . . . 8
1.5. Highlights of this research . . . 12

Bibliography of Chapter 1 13

2. Literature Review 17
2.1. Mechanical behaviour and constitutive framework in masonry structures . 18
2.2. Overview of modelling strategies for masonry structures . . . 22
2.2.1. Block-based modelling strategy . . . 24
2.2.2. Continuum-based modelling strategy . . . 29
2.2.3. Geometry-based models . . . 37
2.2.4. Macroelement modelling strategy . . . 39
2.3. Discontinuum modelling strategies for masonry analysis . . . 45
2.3.1. The Distinct Element Method . . . 46
2.3.2. Non-smooth Contact Dynamics . . . 51
2.3.3. Applied Element Method . . . 54
2.3.4. Summary . . . 58
2.4. Knowledge gaps and research focus . . . 59

Bibliography of Chapter 2 63

3. Distinct Element Method for Masonry Structures: Formulation and Practices 83
3.1. Theoretical background of the Distinct Element Method . . . 84
3.1.1. Contact handling scheme in DEM . . . 84
3.1.2. Mechanical formulation and computational scheme in DEM . . . 87

3.2. Dynamic analysis in DEM . . . 90
3.2.1. Mass-proportional Rayleigh damping . . . 91
3.2.2. Stiffness-proportional damping . . . 92
3.2.3. Maxwell damping . . . 93
3.3. Summary and remarks . . . 97

Bibliography of Chapter 3 **99**

4. A New Contact Constitutive Model for Masonry Structures: Masonry Advanced Softening cONtact model (MASON) **101**
4.1. Overview of the adopted modelling strategy . . . 102
4.2. Formulation of the multi-surface plasticity . . . 103
4.3. Damage evolution laws . . . 104
4.4. Inclusion of dilatancy softening and uplift mechanisms . . . 107
4.5. Energy dissipation mechanism . . . 110
4.6. Stress update routine in explicit scheme . . . 113
4.7. Numerical implementation in commercial DEM framework . . . 114
4.8. Bifurcation validation of the contact model . . . 116
4.8.1. The bifurcation problem in softening systems . . . 116
4.8.2. Test geometry and loading protocol . . . 117
4.8.3. Variant A: Uniform tensile strength . . . 118
4.8.4. Variant B: Single seed defect . . . 119
4.8.5. Variant C: Weibull-distributed tensile strength . . . 121
4.8.6. Summary and remarks . . . 123

Bibliography of Chapter 4 **125**

5. Material-level Validation of the MASON Model **129**
5.1. Introduction . . . 130
5.2. Monotonic material characterisation tests . . . 130
5.2.1. Shear-compression test on masonry couplets . . . 132
5.2.2. Four-point bending test on wallettes . . . 135
5.2.3. Uniaxial compression test: simplified micro-model . . . 138
5.2.4. Uniaxial compression test: bonded-block model . . . 140
5.3. Cyclic material characterisation tests . . . 146
5.3.1. Uniaxial cyclic compression tests on masonry wallettes . . . 148
5.3.2. Cyclic shear-compression tests on masonry assemblage . . . 150
5.3.3. Shear-compression test on masonry triplets . . . 151
5.4. Conclusions . . . 154

Bibliography of Chapter 5 **155**

6. Component-level Validation of the MASON Contact Constitutive Model **157**
6.1. Introduction . . . 158
6.2. Component-level validation under monotonic in-plane loading . . . 159
6.2.1. Experimental description and numerical modelling setup . . . 159
6.2.2. Numerical results: global and local behaviours . . . 162

6.2.3. Cross-comparison to other numerical methods . . . 166
6.2.4. Rigid- vs deformable-block configurations . . . 168
6.2.5. Inclusion of dilatancy effects . . . 174
6.2.6. Mesh objectivity . . . 182
6.2.7. Computational timestep objectivity . . . 186
6.3. Component-level validation under cyclic in-plane loading . . . 189
6.3.1. Experimental description . . . 189
6.3.2. Numerical modelling setup . . . 191
6.3.3. Numerical results: global and local behaviours . . . 194
6.3.4. Influence of local numerical damping on energy dissipation . . . 200
6.3.5. Transition of failure mechanism in in-plane loading scenario . . . 203
6.3.6. Sensitivity analysis to imposed peak displacement rate . . . 205
6.3.7. Cross-comparison to other numerical methods . . . 207
6.4. In-plane response of modular steel frame-retrofitted masonry piers . . . 212
6.4.1. Experimental description . . . 213
6.4.2. Numerical modelling setup . . . 215
6.4.3. Numerical result: global and local behaviours . . . 218
6.4.4. Sensitivity analysis on the material parameters . . . 223
6.4.5. Quasi-static cyclic analysis results . . . 230
6.5. Summary and conclusions . . . 233

Bibliography of Chapter 6 **237**

7. Dynamic Validation and Damping Sensitivity **241**
7.1. Introduction . . . 242
7.2. Contact model comparison on the masonry cross-vault . . . 244
7.2.1. Brief description of the SERA cross-vault shake-table experiment . . . 244
7.2.2. Differences between the contact constitutive models . . . 247
7.2.3. Numerical model and input parameters . . . 247
7.2.4. Displacement response comparison . . . 252
7.2.5. Local damage comparison . . . 256
7.2.6. Acceleration response comparison . . . 258
7.2.7. Discussion . . . 262
7.3. Damping model comparison on the masonry cross-vault . . . 263
7.3.1. Damping configurations . . . 264
7.3.2. Selection of the target damping ratio . . . 264
7.3.3. Adopted damping parameters . . . 269
7.3.4. Displacement response comparison . . . 271
7.3.5. Damage progression comparison . . . 271
7.3.6. Acceleration response comparison . . . 273
7.3.7. Discussion . . . 276
7.4. Shake-table tests on masonry gable walls . . . 277
7.4.1. Experimental description . . . 277
7.4.2. Numerical modelling setup . . . 283
7.4.3. Numerical results . . . 285
7.4.4. Comparison to mass-proportional damping on the STIFF specimen . 299

7.4.5. Discussion . . . 301
7.5. Summary and conclusions . . . 302

Bibliography of Chapter 7 **305**

8. Application of the Modelling Strategies at the Building Level **309**
8.1. Introduction . . . 310
8.2. Experimental description . . . 312
8.3. Numerical modelling setup . . . 314
8.4. Monotonic pushover comparison: rigid vs deformable blocks . . . 319
8.5. Quasi-static cyclic analysis with rigid blocks . . . 322
8.5.1. Global responses . . . 322
8.5.2. Local responses . . . 324
8.5.3. Summary of the quasi-static cyclic analysis . . . 326
8.6. Explorative study on the dynamic shake-table performance of the building . 327
8.6.1. Ground-motion input and signal characteristics . . . 327
8.6.2. Peak displacement response evolution . . . 330
8.6.3. Interstorey drift ratio versus intensity measure . . . 332
8.6.4. Damage evolution at each intensity level . . . 340
8.6.5. Global hysteretic responses . . . 341
8.6.6. Remarks on the dynamic performance of the unreinforced building . 344
8.7. Explorative retrofit assessment with the modular steel frame exoskeleton . . 345
8.7.1. Retrofit schemes and design rationale . . . 346
8.7.2. Numerical modelling setup for the retrofitted configurations . . . 348
8.7.3. Pushover calibration result . . . 351
8.7.4. Incremental dynamic analysis results . . . 354
8.7.5. Remarks on the performance of the retrofitted building . . . 361
8.8. Summary and conclusions . . . 362

Bibliography of Chapter 8 **365**

9. Conclusion **369**
9.1. Revisiting the research objectives . . . 370
9.2. Conclusions . . . 372
9.3. Intrinsic limitations of the MASON model . . . 376
9.4. Limitations of the analyses in this work . . . 378
9.5. Recommendations for further study . . . 378

Bibliography of Chapter 9 **383**

A. Normal Force Evaluation in a Nonlinear Interface **387**

B. Appendix B **391**
B.1. Dilatancy sensitivity: TU Eindhoven wall, HIGH pre-compression . . . 391
B.2. Joint compression damage scalar plot at the end of analysis . . . 395
B.3. Spatial maps of damage occurrence probability over all realisations of S-HEA-U wall . . . 396

C. Appendix C **397**
C.1. Displacement comparison between TSCLinear and MASON 398
C.2. Acceleration comparison between TSCLinear and MASON 400
C.3. Damage distributions for the damping ratio parametric sweep 402
C.4. Displacement comparison for the damping model variations 404
C.5. Acceleration comparison for the damping model variations 406
C.6. Per-run hysteretic response of the gable wall specimens 408

D. Appendix D **411**
D.1. Damage state of the unreinforced TUD-BUILD-1 test 412
D.2. Interstorey drift versus intensity measure, unreinforced 414

Acknowledgements **417**

Curriculum Vitæ **421**

List of Publications **423**

Summary

Masonry is among the oldest construction methods devised. The earliest shaped mud bricks recovered to date, found in the upper Tigris region and south-east Anatolia (Asia Minor), predate 7500 BC, and stone and mud-brick construction has been used across civilisations since. This long use has associated masonry with permanence and strength. The association holds under gravitational loading, for which historical masonry structures were proportioned, but it does not extend to horizontal action. Masonry is a composite of units and mortar joints, and the contrast in the properties of its constituents and their geometric arrangement produces a nonlinear and anisotropic mechanical response. Under earthquake loading, and under imposed deformations such as differential settlement, masonry is damaged at its joints and units. The joints crack in tension and slide along the bed joints, while compression crushes the masonry and splits and spalls the units. The assessment of existing masonry structures has gained relevance where loading conditions have changed over time, as in the induced seismicity case affecting the Groningen region in the Netherlands, where the building stock was not designed for seismic demand. Experimental testing of masonry structures is expensive and difficult to generalise across the diversity of the building stock. Numerical modelling provides a complementary route to assessment, provided the model reproduces all the significant mechanisms.

The distinct element method (DEM) represents masonry as an assembly of blocks, with the mortar and the unit-mortar interfaces lumped into zero-thickness interfaces where the constitutive law is evaluated at a series of contact points. This representation reproduces the discontinuous kinematics of the response, namely the opening, sliding, and re-contact of the blocks. The accuracy of the cracking, shear, and crushing then rests on the constitutive model assigned at the contacts. The basic contact model implemented in *3DEC*, the commercial software used in this work, is the Coulomb friction joint model, in which the tensile and shear strengths drop instantaneously at the onset of damage, and the compressive response is linearly elastic. This formulation cannot reproduce the mode-dependent behaviour of masonry. The instantaneous strength drop excludes the progressive softening that accompanies tensile cracking and shear sliding, and the linear-elastic compressive response excludes crushing. More refined contact models have since introduced linear softening in tension and shear, as well as a capped compressive response with linear post-peak softening. These models reproduce the governing mechanisms only approximately, which limits the accuracy of the predicted response. Constitutive models of comparable sophistication are well established in the finite element method, where their ability to predict the nonlinear structural response of masonry has been demonstrated, although the implicit solution limits the tracking of large displacements and collapse that the explicit DEM resolves. Within the explicit DEM, no single contact model offered exponential tensile and shear softening based on the mode-I and mode-II fracture energies, a hardening/softening law in compression

with coupled shear-compression elliptical cap, dilatancy degradation, and nonlinear unloading in compression. The cyclic unloading was the least developed of these: the available models unload along fixed normal and shear stiffnesses that ignore the active failure mode, capturing neither the damage-driven stiffness and strength degradation in tension and shear, with their coupling and the attendant pinching, nor the nonlinear compressive unloading that governs the energy dissipated and the contact transition under cyclic and dynamic loading.

As its first major contribution, this dissertation develops and implements a DEM-tailored contact constitutive model that meets these requirements and validates it from the material and component scale to full structures, under quasi-static monotonic, cyclic, and dynamic loading. The model, named **MASON** (Masonry Advanced Softening cONtact), is formulated within multi-surface plasticity and combines three surfaces: a tension cut-off, a Coulomb friction surface in shear, and an elliptical shear-compression cap. The compressive failure of the masonry composite, which combines mortar crushing with tensile splitting of the units, is represented phenomenologically at the interface by this cap and a hardening/softening law governing the uniaxial compression response. This representation reproduces the compressive crushing of masonry without explicitly discretising the units, recovering the global response at a low computational cost. The tensile and shear strengths soften after the peak according to an exponential law governed by the mode-I and mode-II fracture energies, and the dilatancy associated with shear sliding decays exponentially. Mode-dependent unloading and reloading rules govern the response under cyclic loading. The model is implemented as a user-defined contact constitutive model in *3DEC* 9.0 for both the rigid configuration, in which all deformation is concentrated at the contacts, and the deformable configuration, in which the blocks are meshed and deform internally. The stress update is strictly local to each contact point, which suits the explicit integration of the distinct element method, and the model is compiled as a Windows dynamic library and a Linux shared object for use on high-performance computing clusters.

The constitutive model is verified and validated from the bottom up. The implementation is first verified at the element level against the prescribed constitutive response, then validated at the material scale against couplet, triplet, four-point bending, and uniaxial compression tests, which characterise the tensile bond, shear, flexural bond, and compressive response. On a masonry triplet, the model is also shown to handle the bifurcation that arises in softening systems, where a small seed imperfection resolves the loss of uniqueness and recovers progressive crack propagation. At the component scale, the model is applied to clay shear walls under monotonic lateral loading and to calcium-silicate walls and piers retrofitted with a modular steel frame under cyclic loading. A single set of material parameters, calibrated from the material characterisation tests, adequately predicts the component-scale response and reproduces the governing failure mode across the pre-compression levels examined for both rigid and deformable block configurations. The rigid-block idealisation achieves a comparable peak strength at a fraction of the computational cost, making it the economical choice when the global capacity is the quantity of interest. Pre-peak response metrics are independent of mesh size and timestep within the stable range, whereas post-peak softening remains dependent on the mesh discretisation. Under cyclic loading, the model captures the rocking-to-sliding transition

of slender calcium-silicate walls as drift increases, with residual discrepancies confined to hysteretic pinching and stiffness recovery at large drift. For the steel-frame retrofitted piers, the model captures the initial stiffness and the small-displacement strengthening effect well and provides a conservative, safe-sided estimate of the peak capacity and the deformation-capacity gain.

The validation up to this point concerns quasi-static loading, both monotonic and cyclic. The extension to dynamic loading makes damping a critical modelling choice, and a second methodological contribution concerns its investigation in explicit dynamic analyses. A Maxwell damping formulation is adopted in place of classical Rayleigh damping, and its parameters are automatically identified via a Levenberg–Marquardt routine that yields an approximately uniform damping ratio over a chosen frequency band, without the timestep penalty of stiffness-proportional damping. These choices are examined on the SERA cross-vault shake-table benchmark, a clay-brick cross-vault supported on four piers and tested under a scaled L'Aquila record up to in-plane shear failure of the webs. The contact model is first assessed by comparing MASON with a simpler contact model that uses linear softening in tension, shear, and compression, and an elastic unloading/reloading mechanism across all regimes. The choice of contact model has a limited effect on peak displacement but a clearer effect on acceleration amplitudes and the spatial spread of damage, because the secant unloading in MASON softens the re-contact transition and attenuates the high-frequency content. The sensitivity to damping is examined next across the damping ratio and the damping scheme, comparing mass-proportional damping, Maxwell damping, and the undamped case. On this benchmark, Maxwell damping improves agreement with the experiment compared to mass-proportional damping, with a larger gain in accelerations than in displacements, at a moderate increase in runtime. Because both the damping scheme and the constitutive law shape the high-frequency content of the response, they govern the accelerations far more than the displacements and should be chosen together when accelerations or local damage are of interest. This finding rests on the cross-vault and gable-wall benchmarks. Its extension to in-plane and building-scale dynamic response remains to be verified. Bringing the two together, the MASON-Maxwell combination is applied to full-scale solid clay gable walls tested incrementally up to complete collapse on a dual shake-table under two different diaphragm idealisations. Using a single material parameter set supplemented by a calibrated purlin–wall friction coefficient, the combination reproduces the collapse of both configurations at the experimental peak base acceleration. The overturning mechanism of the flexible-diaphragm configuration is reproduced, whereas in the rigid-diaphragm configuration the model rocks about a higher hinge than the specimen, a mismatch attributed to the spatial variability of the bond strength.

The framework is then extended up to the building scale on TUD-BUILD-1, a two-storey, full-scale calcium-silicate house with reinforced-concrete floors that represents the Groningen terraced-house typology and was tested under quasi-static cyclic loading at TU Delft. Simulating this experiment allows the investigation of how in-plane piers, transverse walls, and floor diaphragms interact. The experimental peak capacity is reproduced well under both deformable- and rigid-block idealisations. The rigid-block model closely matches the envelope and cumulative dissipated work while reducing runtime from days to hours, whereas the deformable-block model is required for retrofit analyses for a

specific practical reason: the beam finite elements representing the steel frame can be coupled only to deformable-block meshes. The quasi-static cyclic simulation recovers the hysteretic envelope, the asymmetry between the two loading directions, the soft-storey mechanism, and the coupled in-plane-to-out-of-plane mechanism at the west corner. An exploratory incremental dynamic analysis places the near-collapse intensity of the unreinforced building at a peak ground acceleration somewhat below 0.5 g under a single record, EQ-NPR, a Groningen-induced seismicity input matched to the 2475-year uniform hazard spectrum for the Ten Boer region of the Netherlands. The dynamic and quasi-static analyses converge on the same final damage state. Collapse is triggered by exhaustion of the in-plane drift capacity in the ground-storey piers, coupled with out-of-plane overturning of the transverse walls. Retrofitting the building with a modular steel-frame exoskeleton raises the near-collapse intensity by roughly a factor of 1.8 and reduces the displacement demand. The collapse sequence is unchanged, but the in-plane mode of the piers shifts from diagonal shear cracking to flexural rocking with toe crushing. The intensities reported at this scale remain conditional on a single ground-motion record and the adopted sequential analysis protocol. They mark the current limit of the framework, pending experimental evidence at the building scale.

The thesis thus contributes MASON, a contact constitutive model for DEM, and an automatically calibrated damping formulation for explicit dynamic analysis. Both are released openly, in the hope that the strategy finds use beyond the engineered clay and calcium-silicate typologies examined here, including the historical and heritage structures that make up much of the vulnerable building stock.

Samenvatting

Metselwerk behoort tot de oudste bouwmethoden die de mens heeft ontwikkeld. De vroegste tot nu toe teruggevonden gevormde leemstenen, aangetroffen in de bovenloop van de Tigris en in zuidoostelijk Anatolië (Klein-Azië), dateren van vóór 7500 v.Chr. Sindsdien is steen- en leemsteenbouw in vele beschavingen toegepast. Door dit langdurige gebruik wordt metselwerk geassocieerd met bestendigheid en sterkte. Die associatie gaat op onder verticale belasting, waarop historische metselwerkconstructies zijn gedimensioneerd, maar niet onder horizontale belasting. Metselwerk is een samengesteld materiaal van stenen en mortelvoegen, en het contrast tussen de eigenschappen van de bestanddelen en hun geometrische rangschikking leidt tot een niet-lineaire en anisotrope mechanische respons. Onder aardbevingsbelasting, en onder opgelegde vervormingen zoals verschilzettingen, raakt metselwerk beschadigd in de voegen en de stenen. De voegen scheuren onder trek en glijden langs de lintvoegen, terwijl druk het metselwerk verbrijzelt en de stenen doet splijten en afschilferen. De beoordeling van bestaande metselwerkconstructies waarvoor de belastingscondities in de loop van de tijd zijn veranderd, wint aan belang, zoals bij de geïnduceerde seismiciteit in Groningen, waar het gebouwenbestand nooit op seismische belasting was ontworpen. Experimenteel onderzoek aan metselwerkconstructies is kostbaar en laat zich moeilijk generaliseren, gezien de grote diversiteit van het gebouwenbestand. Numerieke modellering biedt een aanvullende beoordelingsroute, mits het model alle maatgevende mechanismen reproduceert.

De discrete-elementenmethode (DEM) representeert metselwerk als een samenstel van blokken, waarbij de mortel en de steen-mortelaanhechting worden samengevoegd tot grensvlakken met nuldikte, waar de constitutieve wet op een reeks contactpunten wordt geëvalueerd. Op deze wijze worden het scheuren, het afschuiven en het hernieuwde contact bij ontlasten weergegeven, die het gedrag van metselwerk kenmerken. De nauwkeurigheid waarmee deze mechanismen, met inbegrip van het verbrijzelen, worden weergegeven, berust op het constitutieve model dat aan de contacten wordt toegekend. Het basiscontactmodel in *3DEC*, de in dit werk gebruikte DEM-software, is het Coulomb-voegmodel, waarin de trek- en afschuifsterkte abrupt wegvallen zodra schade begint, en de drukrespons lineair-elastisch is. Deze formulering kan het modusafhankelijke gedrag van metselwerk niet nabootsen. Het ogenblikkelijke sterkteverlies sluit de geleidelijke softening uit die met trekscheuren en afschuiven gepaard gaat, en de lineair-elastische drukrespons sluit verbrijzeling uit. Verfijndere contactmodellen hebben sindsdien lineaire softening in trek en afschuiving ingevoerd, evenals een begrensde drukrespons met lineaire softening na de piek. Deze modellen reproduceren de maatgevende mechanismen slechts bij benadering, wat de nauwkeurigheid van de voorspelde respons beperkt. Constitutieve modellen van vergelijkbare verfijning zijn in de eindige-elementenmethode goed ingeburgerd, waar hun vermogen om de niet-lineaire constructieve respons van metselwerk te voorspellen is aangetoond, al beperkt de impliciete oplossingsprocedure

het volgen van grote verplaatsingen en instorting, iets wat de expliciete DEM wél aankan. Binnen de expliciete DEM bood geen enkel contactmodel de combinatie van exponentiële trek- en afschuifsoftening op basis van de mode-I- en mode-II-breukenergieën, een elliptische afschuif-drukkap, dilatantiedegradatie en niet-lineaire ontlasting onder druk.

Als eerste belangrijke bijdrage ontwikkelt en implementeert dit proefschrift een op DEM toegesneden contact-constitutief model dat aan deze eisen voldoet, en valideert het van de materiaalschaal, via de componentschaal, tot volledige constructies onder quasi-statische monotone, cyclische en dynamische belasting. Het model, **MASON** (Masonry Advanced Softening cONtact) genaamd, is geformuleerd binnen de multi-surface-plasticiteit en combineert drie oppervlakken: een trekafsnijding, een Coulomb-wrijvingsoppervlak in afschuiving en een elliptische afschuif-drukkap. De trek- en afschuifsterkte nemen na de piek af volgens een exponentiële wet die wordt bepaald door de mode-I- en mode-II-breukenergieën, en de dilatantie die met het afschuiven samenhangt dooft exponentieel uit. Modusafhankelijke ontlastings- en herbelastingsregels bepalen de respons bij cyclische belasting. Het model is geïmplementeerd als een door de gebruikers gedefinieerd contact-constitutief model in *3DEC* 9.0, zowel voor de stijve configuratie, waarin alle vervorming in de contacten is geconcentreerd, als voor de vervormbare configuratie, waarin de blokken van een mesh zijn voorzien en inwendig vervormen. De spanningsupdate is strikt lokaal per contactpunt, wat aansluit bij de expliciete integratie van de discrete-elementenmethode, en het model is gecompileerd als een dynamische bibliotheek voor Windows en een gedeeld object voor Linux, voor gebruik op high-performance rekenclusters. Het constitutieve model wordt van onderop geverifieerd en gevalideerd. De implementatie wordt eerst op elementniveau geverifieerd aan de hand van de voorgeschreven constitutieve respons, en vervolgens op materiaalschaal gevalideerd aan de hand van couplet-, triplet-, vierpuntsbuig- en uniaxiale drukproeven, die respectievelijk de trekhechting, het afschuifgedrag, de buighechting en de drukrespons karakteriseren. Op een metselwerk-triplet wordt bovendien aangetoond dat het model bestand is tegen de bifurcatie die in systemen met softening optreedt: een kleine geïntroduceerde imperfectie lost het verlies van uniciteit op en herstelt een progressieve scheurvoortplanting. Vervolgens wordt het model op componentniveau toegepast op baksteen-schuifwanden onder monotone laterale belasting en op kalkzandsteenwanden en met een modulair staalframe versterkte penanten onder cyclische belasting.

Eén enkele set materiaalparameters, gekalibreerd op de materiaalkarakteriseringsproeven, voorspelt de respons op componentschaal adequaat, en het maatgevende bezwijkmechanisme wordt correct gereproduceerd voor verschillende voordrukniveaus, voor zowel de stijve als de vervormbare blokconfiguratie. De stijve-blokidealisering bereikt een vergelijkbare pieksterkte tegen een fractie van de rekenkosten, wat haar tot de economische keuze maakt wanneer de globale capaciteit de grootheid van belang is. Het gedrag vóór de piek is binnen het stabiele bereik onafhankelijk van de meshgrootte en de tijdstapgrootte, terwijl de softening na de piek afhankelijk blijft van de meshdiscretisatie. Onder cyclische belasting geeft het model de overgang van kantelen naar afschuiven van slanke kalkzandsteenwanden bij toenemende zijdelingse verplaatsing (drift) weer, waarbij de resterende afwijkingen minimaal zijn en zich beperken tot de hysteretische insnoering (pinching) en het stijfheidsherstel bij grote drift. Voor de met het staalframe versterkte penanten worden de beginstijfheid en het versterkende effect bij kleine verplaatsingen goed

weergegeven, terwijl de piekcapaciteit en een deel van de winst in vervormingscapaciteit conservatief, aan de veilige kant worden ingeschat.

De validatie tot dusver betreft quasi-statische belasting, zowel monotoon als cyclisch. De uitbreiding naar dynamische belasting maakt demping tot een cruciale modelleringskeuze, en een tweede methodologische bijdrage betreft het onderzoek ervan in expliciete dynamische analyses. Een Maxwell-dempingsformulering wordt gehanteerd in plaats van de klassieke Rayleigh-demping, en de parameters ervan worden automatisch geïdentificeerd met een Levenberg-Marquardt-routine die een nagenoeg uniforme dempingsverhouding over een gekozen frequentieband oplevert, zonder het tijdstapnadeel van stijfheidsproportionele demping. Deze keuzes worden onderzocht op de SERA-kruisgewelfbenchmark, een bakstenen kruisgewelf op vier penanten, op een schudtafel beproefd onder een geschaalde L'Aquila-registratie tot afschuifbezwijken in het vlak van de gewelfschalen. Het contactmodel wordt eerst beoordeeld door MASON te vergelijken met een eenvoudiger contactmodel met lineaire softening in trek, afschuiving en druk, en een elastisch ontlastings- en herbelastingsmechanisme in alle regimes. De keuze van het contactmodel heeft een beperkt effect op de piekverplaatsing, maar een duidelijker effect op de versnellingsamplitudes en op de ruimtelijke spreiding van de schade, doordat de secansontlasting van MASON de overgang bij hernieuwd contact verzacht en de hoogfrequente componenten dempt. Vervolgens wordt de gevoeligheid voor demping onderzocht, over de dempingsverhouding en het dempingsschema, waarbij massaproportionele demping, Maxwell-demping en het ongedempte geval worden vergeleken. Op deze benchmark verbetert Maxwell-demping, vergeleken met massaproportionele demping, de overeenstemming van de voorspelling met het experiment, met een grotere winst voor de versnellingen dan voor de verplaatsingen, tegen een matige toename van de rekentijd. Doordat zowel het dempingsschema als de constitutieve wet de hoogfrequente componenten van de respons bepalen, beïnvloeden zij de versnellingen veel sterker dan de verplaatsingen en moeten zij samen worden gekozen wanneer versnellingen of lokale schade van belang zijn. Deze bevinding berust op de kruisgewelf- en topgevelbenchmarks. De uitbreiding naar dynamische respons in het vlak en op gebouwschaal moet nog worden geverifieerd. Door beide te combineren wordt de MASON-Maxwell-combinatie toegepast op massieve baksteentopgevels op ware grootte, die op een dubbele schudtafel incrementeel zijn beproefd tot volledige instorting onder twee verschillende dakschijfidealiseringen. Met één set materiaalparameters, aangevuld met een gekalibreerde wrijvingscoëfficiënt tussen gording en wand, reproduceert de combinatie de instorting van beide configuraties bij de experimentele piekversnelling van de schudtafel. Het kantelmechanisme van de configuratie met flexibele dakschijf wordt gereproduceerd, terwijl het model in de configuratie met stijve dakschijf om een hoger scharnier roteert dan het proefstuk, een verschil dat wordt toegeschreven aan de ruimtelijke variatie van de hechtsterkte.

Het ontwikkelde DEM-raamwerk wordt vervolgens uitgebreid tot de gebouwschaal met TUD-BUILD-1, een kalkzandstenen woning van twee verdiepingen op ware grootte met gewapend-betonvloeren, die de Groningse rijtjeswoningtypologie vertegenwoordigt en aan de TU Delft onder quasi-statische cyclische belasting is beproefd. De simulatie van dit experiment maakt het mogelijk te onderzoeken hoe de penanten in het vlak, de dwarswanden en de vloerschijven op elkaar inwerken. De experimentele piekcapaciteit

wordt onder zowel de vervormbare- als de stijve-blokidealisering goed gereproduceerd. Het stijve-blokmodel volgt de omhullende en de cumulatief gedissipeerde arbeid nauwkeurig en verkort de rekentijd van dagen tot uren, terwijl het vervormbare-blokmodel om een specifieke praktische reden noodzakelijk is voor de versterkingsanalyses: de balk-eindige-elementen die het staalframe voorstellen, kunnen alleen aan vervormbare-blokmeshes worden gekoppeld. De quasi-statische cyclische simulatie geeft de hysteretische omhullende weer, evenals de asymmetrie tussen de twee belastingsrichtingen, het zwakke-verdiepingsmechanisme en het gekoppelde in-het-vlak-uit-het-vlakmechanisme bij de westhoek. Een verkennende incrementele dynamische analyse plaatst de bijna-bezwijkintensiteit van het onversterkte gebouw bij een piekgrondversnelling iets onder 0.5 g, onder één registratie, EQ-NPR, een invoersignaal voor Groningse geïnduceerde seismiciteit dat is afgestemd op het uniforme dreigingsspectrum met een herhalingstijd van 2475 jaar voor de regio Ten Boer. De dynamische en de quasi-statische analyse komen uit op dezelfde uiteindelijke schadetoestand. Bezwijken wordt ingeleid door uitputting van de driftcapaciteit in het vlak van de penanten op de begane grond, gekoppeld aan kantelen uit het vlak van de dwarswanden. Versterking van het gebouw met een modulair stalen exoskelet verhoogt de bijna-bezwijkintensiteit met een factor van ongeveer 1,8 en verlaagt de gevraagde verplaatsing. De volgorde van bezwijken blijft gelijk, maar het mechanisme van de penanten in het vlak verandert van diagonale afschuifscheuren naar buigend kantelen met teenverbrijzeling. De op deze schaal gerapporteerde intensiteiten blijven afhankelijk van één grondbewegingsregistratie en het gehanteerde sequentiële analyseprotocol. Zij markeren de huidige grens van het raamwerk, in afwachting van experimenteel bewijs op gebouwschaal.

Dit proefschrift levert aldus twee bijdragen: MASON, een contact-constitutief model voor de DEM, en een automatisch gekalibreerde dempingsformulering voor expliciete dynamische analyse. Beide zijn vrij beschikbaar gesteld, in de hoop dat de strategie toepassing vindt buiten de hier onderzochte baksteen- en kalkzandsteentypologieën, waaronder de historische en monumentale constructies die een groot deel van het kwetsbare gebouwenbestand uitmaken.

Propositions

accompanying the dissertation

ADVANCING THE DISTINCT ELEMENT MODELLING OF MASONRY STRUCTURES

A JOINT CONSTITUTIVE MODEL FOR CRACKING, SHEARING, AND CRUSHING UNDER CYCLIC AND DYNAMIC LOADING

by

Yopi Prabowo OKTIOVAN

1. The performance of a Coulomb friction contact model alone is inadequate to represent the complex cyclic mechanisms in masonry structures. (*)
2. A model calibrated only to capacity can be right for the wrong reason: quantitative agreement does not imply a correct failure mechanism. (*)
3. In dynamic masonry simulation, the damping model can govern the response as strongly as the constitutive law, so it must be justified, not adopted by default. (*)
4. Explicit solvers never fail to converge, which means they never warn you when the result is wrong. (*)
5. Simulation tools used without regard for their assumptions and validation limits produce quick answers, not the right ones, and presenting them with unwarranted confidence can mislead public risk perception.
6. A PhD programme cultivates technical rigour but offers little structured preparation for academic politics, despite the latter weighing heavily on a researcher's career trajectory.
7. Status competition is academic noise: it rewards comparison over contribution and steadily erodes collaboration, trust, and the willingness to share work-in-progress.
8. Retrofitting of heritage masonry should leverage the original load-resisting mechanism rather than disrupt it, since that mechanism is itself part of what authenticity preserves.
9. Life, like explicit integration, advances best in small honest steps: move forward without waiting to be certain, correct as you go, and never take a step longer than your leg, *non fare il passo più lungo della gamba.*
10. The yield surface is not "violated". It is "politely ignored" until you implement the correction routine.

(*) *These propositions pertain to this dissertation.*

These propositions are regarded as opposable and defendable, and have been approved as such by the promotors Em. prof. dr. ir. J. G. Rots and Dr. ing. F. Messali.

Symbols and Nomenclature

This dissertation uses the following general notations and nomenclature as much as possible to maintain consistency throughout the document. The notations are introduced, whenever possible, with explanations in the main body for clarity. This is also done for non-generic symbols that are specific to a certain chapter or section. In Chapter 4, tension is taken positive; in the implementation and in Appendix A, closure is positive.

Roman symbols

Symbol	Description
$\mathbf{F}$	Resultant force vector at a node.
$\mathbf{F}^{\ell}$, $\mathbf{F}^{c}$, $\mathbf{F}^{z}$	External load, contact force, and internal element force vectors at a node, respectively.
F_n, $\mathbf{F}_s$	Normal (scalar) and shear (vector) subcontact forces.
$\mathbf{M}$	Global mass matrix.
$\mathbf{I}$	Global moment of inertia matrix.
$\mathbf{u}$	Nodal displacement vector.
$\Delta\mathbf{u}$	Increment of relative subcontact displacement in one timestep.
$\mathbf{u}(t)$	Relative subcontact displacement vector at time t.
u_n, $\boldsymbol{u}_s$	Normal (scalar) and shear (vector) components of the relative joint displacement.
$\mathbf{v}$	Nodal velocity vector.
t, Δt	Time and timestep.
$\mathbf{x}$, $\dot{\mathbf{x}}$, $\ddot{\mathbf{x}}$	Position, velocity, and acceleration vectors of a node or block centroid, respectively.
$\dot{\mathbf{x}}(t \pm \Delta t/2)$	Velocity vector at the half-step times of the central-difference scheme.
m_i	Lumped mass associated with node i.
k_i	Effective nodal stiffness associated with node i.
$k_{\text{tet},i}$	Stiffness contribution of the tetrahedral elements connected to node i.
k_n, k_s	Elastic normal and shear stiffnesses of a joint (subcontact).
k_n^{un}	Tangent stiffness at the onset of compressive unloading, $\gamma_{\text{un}} k_n$.
k_n^{pl}	Tangent stiffness at the end of compressive unloading (plastic displacement).
k_n^{re}	Stiffness of the linear compressive reloading branch.

Symbol	Description
A_c	Tributary contact area associated with a subcontact.
A_{pre}	Area between the pre-peak compressive backbone and the residual level.
P_i	Damping power at node i used in the definition of global (viscous) damping.
$\dot{E}_{k,i}$	Time rate of kinetic energy at node i.
R	User-defined viscosity ratio for global damping.
Δt_{block}	Stable timestep associated with the block discretisation.
E	Young's modulus of masonry, unit, or mortar.
G	Shear modulus of masonry, unit, or mortar.
K	Bulk modulus.
$l_{\max}$	Maximum edge length of the elements connected to a node.
$h_{\min}$	Minimum height of the elements connected to a node.
F_1, F_2, F_3	Yield functions for the tension cut-off, the Coulomb friction line, and the compression cap, respectively.
G_1, G_2, G_3	Plastic potentials associated with F_1, F_2, and F_3, respectively.
$f_t(u_n^t)$	Degraded tensile strength as a function of the normal crack opening u_n^t.
f_t	Peak tensile strength of the joint.
$f_{t,0}$	Initial (peak) tensile strength of the joint; written f_t in the parameter tables.
$f_s(\boldsymbol{u}_s)$	Cohesive shear strength as a function of the shear displacement vector.
c_0	Initial cohesive strength (peak cohesion) in shear.
$f_c(u_n^c)$	Normal compressive stress on the backbone as a function of the compressive normal displacement u_n^c.
f_c	Peak compressive strength of the joint.
f_{cm}	Intermediate post-peak compressive stress $(f_c+f_{cr})/2$ at the transition from quadratic to exponential softening ($\xi = 0.3$).
f_{cr}	Residual compressive strength.
f_c^{un}	Compressive stress at the onset of unloading.
f_{cr}^e	Compressive stress at the lower end of the unloading branch.
f_{cr}^o	Compressive stress at the onset of reloading.
n	Hardening multiplier setting the hardening length $u_{cp} = n f_c / k_n$.
r	Residual strength ratio f_{cr}/f_c.
m	Midpoint strength ratio $(1+r)/2$ of the compressive softening law.
m_W	Shape parameter of the Weibull distribution of subcontact tensile strengths.
L	Compressive softening length, set so that the backbone dissipates G_c exactly.
S	Area above the residual level of the normalised multilinear softening envelope, $0.326\,(1-r)$.

Symbol	Description
m_0, m_1	User-defined coefficients of the plastic-displacement ratio; m_0 sets the offset of an undamaged joint and m_1 its increase with compressive damage.
p	Auxiliary variable of the plastic-displacement ratio in compression.
u_n^t	Tensile normal displacement (crack opening) at the joint.
u_n^c	Compressive normal displacement at the joint.
u_n^{el}	Normal displacement at the elastic compressive stress $\sigma_n^{\mathrm{el}} = 0.2 f_c$, i.e. $\sigma_n^{\mathrm{el}} / k_n$.
u_{cp}	Hardening length from u_n^{el} to the peak, $n f_c / k_n$.
u_p	Normal displacement at peak compressive strength, $u_n^{\mathrm{el}} + u_{cp}$.
u_n^{un}	Normal displacement at the onset of unloading.
u_n^{pl}	Plastic normal displacement at the end of unloading, $\varphi\, u_n^{\mathrm{un}}$.
u_{nr}^o	Normal displacement at the onset of reloading.
u_n^{rev}	Normal displacement at a reversal point on a reload line (partial loop).
u'_{un}, u'_{rec}	Unloading and recovery displacements normalised by u_{cp}.
$\boldsymbol{u}_s$	Shear displacement vector at the joint.
u_s^{el}	Elastic shear displacement at the current shear strength, $\tau_{\max} / k_s$.
$u^{s,p}$	Plastic slip, $\lVert \boldsymbol{u}_s \rVert - \tau_{\max} / k_s$.
$u_{s,\max}$	Plastic slip at which the dilatancy angle reaches zero.
$\Delta u_{\mathrm{dil}}^n$	Dilatant opening increment produced by the plastic slip increment.
$\lVert \boldsymbol{u}_s \rVert$	Euclidean norm of the shear displacement vector.
$d_t(u_n^t)$	Tensile damage scalar as a function of the normal opening.
$d_s(\boldsymbol{u}_s)$	Shear damage scalar as a function of the shear displacement.
$d_c(\xi)$	Compressive damage scalar as a function of the softening coordinate.
$d_{ts}(u_n, \boldsymbol{u}_s)$	Combined tensile–shear damage scalar coupling the degradation of the tensile and cohesive strengths.
G_f^I	Mode-I (tension) fracture energy of the joint.
G_f^{II}	Mode-II (shear) fracture energy of the joint.
G_c	Compressive fracture energy of the joint.
C_{nn}, C_{ss}	Parameters controlling the semi-axes of the elliptical compression cap in the (σ_n, τ) plane.
C_n	Parameter controlling the centre of the compression cap on the normal-stress axis.
$\mathbf{C}$	Global viscous damping matrix.
$\mathbf{K}_t$	Tangent (current) stiffness matrix.
N_ω	Number of sampled frequencies in the Maxwell damping optimisation.
$M_T(\omega)$	Normalised complex modulus of the Maxwell damping system at frequency ω.
$M_r(\omega)$	Complex modulus contribution of the r-th Maxwell branch.
B_1, B_2, B_3	Coefficients of the rational function describing the compressive unloading curve.

Symbol	Description
E_s	Secant stiffness between the onset of unloading and the plastic displacement.
e	Exponent governing the decay of the plastic tangent stiffness with unloading displacement.
E_{tens}, E_{comp}, E_{shear}	Signed work of the subcontact forces in tension, compression, and shear, summed over the joints.
E_{phys}	Cumulative energy dissipated by the joint constitutive law.
W_k	Cumulative work removed by local numerical damping.
E_D, E_{So}	Dissipated energy and secant strain energy of a hysteresis loop.
e_F	Relative deviation of the numerical peak force from the experimental peak force.
J	Weighted objective for the best-fit selection (standardised peak-force and curve-shape errors).
w_F, w_c	Weights of the peak-force and curve-shape terms in J.
M_{SG}, P_{SG}, C_{SG}	Sprague–Geers magnitude, phase, and combined errors.
C_s	Base shear coefficient V_b/W read from the backbone at a given drift.
V_b, W	Base shear and seismic weight of the building.
f'_m	Compressive strength of masonry at the component scale.
f_x	Flexural strength obtained from bending tests.
$E_{\parallel}, E_{\perp}$	In-plane Young's moduli parallel and perpendicular to the bed joints.
$G_{\parallel\perp}$	In-plane shear modulus of the orthotropic masonry.

Greek symbols

Symbol	Description
α	Local damping constant of the DEM nodal damping scheme.
α_ω	Rotational damping coefficient of a rigid block.
α_M	Non-dimensional stiffness factor of a Maxwell damping branch.
α_R	Mass-proportional Rayleigh damping coefficient.
β_R	Stiffness-proportional Rayleigh damping coefficient.
β_d	Damage factor modulating the reloading stiffness as a function of the normalised recovery displacement.
γ_{un}	Multiplier relating the unloading stiffness to the initial normal stiffness.
γ_{pl}	Multiplier controlling the plastic tangent stiffness.
φ	Plastic-displacement ratio $u_n^{\text{pl}}/u_n^{\text{un}}$ in compressive unloading.
$\varphi_{\max}$	Upper bound of the plastic-displacement ratio.
χ	Normalised coordinate along the compressive unloading branch, zero at the onset of unloading.

Symbol	Description
χ_h	Normalised coordinate along the compressive hardening branch.
ξ	Normalised softening coordinate $(u_n^c - u_p)/L$ in compression (Chapter 4); damping ratio of a vibration mode elsewhere.
η_M	Maxwell viscosity parameter.
η	Share of numerical damping in the total energy balance, $W_k/(W_k + E_{\text{phys}})$.
τ	Shear stress (scalar) or magnitude of the shear stress vector at a joint.
$\boldsymbol{\tau}$	Shear stress vector along the joint plane.
$\tau_{\max}$	Current shear strength on the F_2 surface.
τ_M	Maxwell relaxation time.
σ_n	Normal stress at the joint interface.
σ_n^{el}	Elastic compressive stress at the origin of the hardening parabola, $0.2 f_c$.
σ^{rev}	Normal stress at a reversal point on a reload line (partial loop).
$\boldsymbol{\sigma}$	Stress state at a contact.
ϕ_{cv}	Friction angle at constant volume.
ϕ_{res}	Residual friction angle, reached at full combined damage when no dilatancy is assigned.
$\psi(u^{s,p})$	Dilatancy angle as a function of the plastic slip.
ψ_0	Initial dilatancy angle.
δ	Softening gradient controlling the decay of the dilatancy angle.
λ	Scale parameter of the Weibull distribution of subcontact tensile strengths.
ρ	Mass density.
ν	Poisson's ratio.
$\boldsymbol{\theta}$	Rotation vector of a block.
ω	Circular frequency of a vibration mode or loading.
$\boldsymbol{\omega}$	Angular velocity vector of a block.
$\omega_{\max}$	Highest circular frequency of the system, governing the stable timestep.
ω_ζ	Frequency at which a single Maxwell element reaches its peak damping ratio.
ω_r	Centre frequency of the r-th Maxwell branch.
ω_j	j-th sampled frequency in the Maxwell damping optimisation.
ω_{lb}, ω_{ub}	Lower and upper bounds of the frequency band targeted in the Maxwell damping optimisation.
ω_{sec}	Secant circular frequency of the building at a given drift.
$\xi_{\text{MP}}, \xi_{\text{SP}}$	Damping ratio contributions of mass- and stiffness-proportional Rayleigh damping.
ξ_{eq}	Equivalent viscous damping ratio of a hysteresis loop.
ξ_α	Damping ratio imposed by mass-proportional damping at the secant frequency.
$\zeta(\omega)$	Damping ratio of the Maxwell damping system at frequency ω.

Symbol	Description
$\zeta^\star$	Target damping ratio over the specified frequency band.
μ	Friction coefficient relating shear and normal stresses, where used.

Subscripts and superscripts

Index	Meaning
i	Index for blocks, nodes, or contacts.
j	Index for vibration modes or sampled frequencies.
r	Index for Maxwell branches (e.g. ω_r, M_r).
(s)	Quantity of subcontact s.
n	Normal component.
s	Shear component.
t	Tension.
c	Compression; as a superscript on a force, contact (e.g. $\mathbf{F}^c$).
el	Elastic limit (e.g. u_n^{el}, σ_n^{el}).
pl	Plastic (e.g. u_n^{pl}).
p	Peak (e.g. u_p) or plastic slip (e.g. $u^{s,p}$).
cp	Hardening length (e.g. u_{cp}).
cm	Intermediate post-peak quantity (e.g. f_{cm}).
cr	Residual quantity (e.g. f_{cr}).
res	Residual value (e.g. ϕ_{res}).
un	Onset of unloading (e.g. u_n^{un}, f_c^{un}).
re, o	Reloading branch and onset of reloading (e.g. k_n^{re}, u_{nr}^o).
rev	Reversal point of a partial loop (e.g. u_n^{rev}).
rec	Recovery displacement (e.g. u'_{rec}).
dil	Dilatant component (e.g. $\Delta u_{\mathrm{dil}}^n$).
pre	Pre-peak (e.g. A_{pre}).
0	Initial value (e.g. c_0, ψ_0).
max	Maximum value (e.g. $\omega_{\max}$, $\tau_{\max}$).
M	Maxwell damping (e.g. α_M, τ_M, η_M).
R	Rayleigh damping (e.g. α_R, β_R).
W	Weibull distribution (e.g. m_W).
SG	Sprague–Geers error measure.
lb, ub	Lower and upper bounds of a frequency band.
$\parallel$, $\perp$	Parallel and perpendicular to the bed joints.
ℓ	External load (e.g. $\mathbf{F}^\ell$).
z	Internal element force (e.g. $\mathbf{F}^z$).
k	Kinetic (e.g. E_k) or numerical damping (e.g. W_k).
T	Total (e.g. M_T).

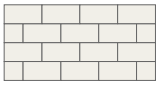
1

Introduction

Dixeruntque alter ad proximum suum: Venite, faciamus lateres, et coquamus eos igni. Habueruntque lateres pro saxis, et bitumen pro caemento. Dixeruntque: Venite, faciamus nobis civitatem et turrim, cuius culmen pertingat ad caelum; et celebremus nomen nostrum, antequam dividamur in universas terras.

Genesis 11:3–4 (Vulgate)[1]

[1] They said, each to his neighbour, "Come, let us make bricks and bake them hard." They had brick for stone, and bitumen for mortar. Then they said, "Come, let us build ourselves a city and a tower with its top in the heavens, and let us make a name for ourselves, lest we be scattered over the whole earth."



1.1. Background

Structural engineers still struggle to assess the seismic vulnerability of existing masonry structures, since available tools often fail to reproduce the failure mechanisms of masonry under strong loading [1]. Many historic city centres are dominated by unreinforced masonry (URM) structures, some of them retrofitted, whose long-term environmental degradation undermines their structural capacity. In regions exposed to seismic action, structures in this degraded condition must withstand cyclic demands that far exceed the original design intent. Under demanding conditions, masonry structures are susceptible to complex failure mechanisms, including cracking, shearing, and crushing at both mortar joints and brick units. These different forms of damage complicate conventional analysis and informed decisions on repair, strengthening or replacement. Examples of earthquake-induced damage are shown in Figure 1.1.



(A) Oyguc, 2025



(B) Brandonisio *et al.*, 2013

Figure 1.1. Examples of earthquake-induced damage in unreinforced masonry structures on (A) a low-rise residential building in Eastern Türkiye [2] and (B) a historical church in L'Aquila [3]

Predictive modelling of URM remains relevant even outside seismic regions. Historic masonry structures are exposed to a range of slow and transient hazards. Climate-induced effects such as thermal and moisture cycles can progressively damage mortar joints [4]. Ground movements caused by tunnelling, mining, or fluid extraction can introduce differential settlements that open new cracks or reopen existing ones [5]. These conditions differ from earthquake loading in timescale and intensity, but they activate the same physical mechanisms in the units and mortar joints, namely cracking, sliding, and localised crushing. Numerical tools able to reproduce these joint-level processes, therefore, find application well beyond the seismic scenario.

Gas extraction has similarly been linked to induced seismicity, a hazard with particular relevance in parts of northern Europe. In the Netherlands, induced seismicity associated with gas extraction in the province of Groningen has affected a large number of primarily masonry constructions and farmsteads [6, 7]. More than 1300 events have been recorded since 1991, mostly of low-to-moderate magnitude, with a few events reaching local magnitudes of up to about M_L 3.6 [8]. Despite their moderate size, these earthquakes have caused widespread damage to the vulnerable masonry building

stock [9]. Furthermore, seismicity has persisted even after gas production from the Groningen field was formally phased out in October 2023, with a significant event of M_L 3.4 near Zeerijp on 14 November 2025 [10]. This recent earthquake illustrates that elevated seismic hazard can persist locally for years after extraction operations end owing to the delayed response of the subsurface.

Seismic actions associated with these earthquakes often impose particularly high demands on so-called short-period structures, i.e., relatively stiff, low-rise buildings that vibrate quickly when shaken, such as typical URM houses. This reflects the fact that the dominant period range of such ground motions often coincides with the fundamental periods of common low-rise building typologies in many regions [11]. When this spectral overlap causes (near-)resonance, even moderate earthquakes can produce significant cyclic deformations and cumulative damage in vulnerable URM structures. These considerations motivate the development of robust mechanical models that represent damage initiation and accumulation under repeated seismic excitation.

From a modelling standpoint, the difficulty arises not only because masonry consists of different materials arranged in a complex pattern, but also because its behaviour can change abruptly as damage develops. Cracks may localise along joints, units may slide, rock, or crush, and parts of a wall may lose and regain contact, leading to drastic shifts in load transfer. Continuum-based modelling approaches (e.g., Figure 1.2A) idealise masonry as an orthotropic continuous medium, in which damage is smeared into deformation, rather than represented as separations between elements. As a result, they often struggle to capture the growth of individual cracks and gaps, particularly when these follow the joint pattern at the contact surface between units and mortar, and the resulting mechanisms such as rocking, sliding, and local crushing of blocks. These

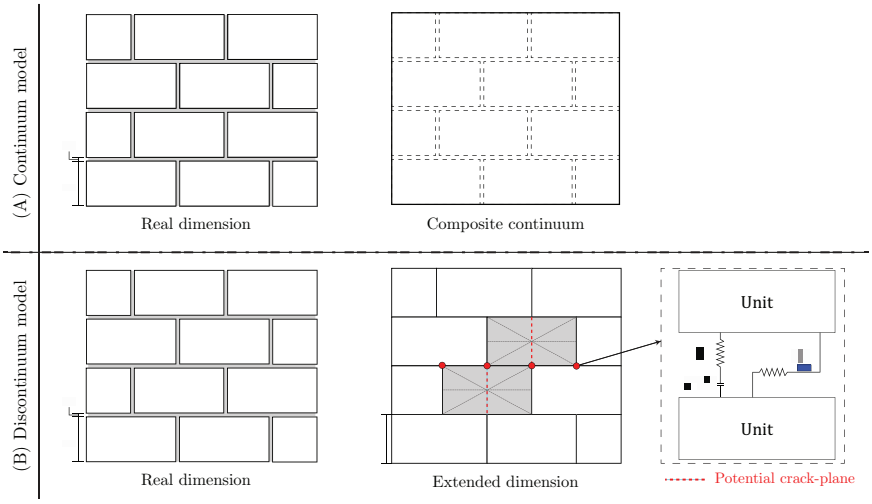


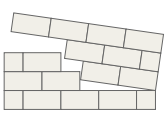
Figure 1.2. Comparison of two modelling strategies: (A) Continuum model with direct approach and (B) Discontinuum model with contact-based mortar representation.

shortcomings are particularly pronounced in the local out-of-plane response (loading perpendicular to the wall plane) of façade and gable walls, where stability is governed by rigid-body rocking, joint opening, and impact between blocks rather than distributed material deformation. Alongside the steady increase in computational power and the development of more efficient numerical algorithms, these shortcomings have motivated alternative strategies that treat masonry as an assembly of discrete units, with mortar joints modelled as zero-thickness interfaces.

To that end, several discontinuum-based approaches have been proposed in the literature, including the Distinct Element Method, the Applied Element Method, and finite-element formulations with interface elements (e.g., Figure 1.2B). These approaches offer a promising alternative to continuum modelling by explicitly representing masonry as an assembly of interacting blocks connected through interfaces. In such models, the evolution from an initially intact configuration to a highly damaged or collapsed state is captured by the progressive failure of the interface (and unit) constitutive response, combined with large relative motions between blocks. This enables a more faithful description of the localised degradation and interaction mechanisms that govern the response and collapse of masonry structures. Consequently, discontinuum-based models have been widely used for the analysis of existing and historical masonry structures such as churches [12–14], towers [15, 16], and bridges [17–19], particularly in the context of seismic assessment and collapse mechanism identification.

Despite these advances, the predictive capacity of discontinuum-based models hinges critically on the constitutive description adopted at joints and contacts, where most inelastic processes occur. Current implementations in commercial software packages, as well as many research-oriented discontinuum formulations for masonry, idealise interface behaviour using relatively simple normal (*perpendicular* to the interface plane) and shear (*parallel* to the interface plane) laws, typically based on a Mohr–Coulomb friction envelope with a tension cut-off. In simple terms, the Mohr–Coulomb model states that a joint starts to slip or crack when the shear stress exceeds a limit that depends on how hard the surfaces are pressed together (normal stress) and on their inherent 'stickiness' (cohesion and friction angle). Although such models are simple and computationally efficient, they may not capture the complex interplay among cracking (tensile failure), shearing (shear failure), and crushing (compressive failure) in masonry joints under realistic loading conditions. Compressive failure, in particular, is composite, involving mortar crushing at the joints and unit splitting within the blocks, and requires a constitutive description that a simple cut-off cannot provide.

To address these limitations, the literature has proposed more sophisticated interface models for discontinuum-based modelling [20–23], particularly for the Distinct Element Method (DEM) used in masonry analyses [24, 25]. These approaches lump the nonlinearities in the interface elements using multi-surface plasticity models, with damage-based formulations that combine tension cut-off with frictional shear and nonlinear compression caps. Other approaches use composite interface–contact models in which interface elements describe tensile and shear failure, while compressive behaviour is treated using contact-mechanics formulations within a block-based finite-element context [26]. These models have expanded the choice of interface laws and reproduce experimental results more accurately.



Yet, when such advanced interface models are embedded in large-scale DEM analyses of realistic masonry structures (such as existing buildings, historical monuments, or building portfolios subjected to induced seismicity), several challenges remain. First, mixed failure modes that combine cracking, shearing, and crushing are often still represented in a simplified manner, raising questions about the robustness of predictions under complex loading paths, including cyclic and repeated seismic events or combined in-plane (loading parallel to the wall plane) and out-of-plane (loading perpendicular to the wall plane) actions. Second, identifying model parameters and transferring them from small-scale tests to full-scale structures is far from straightforward, especially in the presence of softening and localisation, where regularisation issues arise. Third, the computational robustness and efficiency of these constitutive laws within explicit time-integration schemes remain challenging for large discontinuum models with extensive damage, evolving contact networks, and impact events. Addressing these issues is crucial to improving the reliability and applicability of discontinuum-based models for masonry, particularly for seismic assessment and risk mitigation.

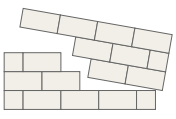
A related methodological aspect concerns the use of damping in DEM. Since DEM relies on explicit dynamic time integration, the representation of damping is a recurring concern in both transient and quasi-static analyses, the latter typically being solved through dynamic relaxation. In practice, viscous damping is often introduced ad hoc. Mass-proportional damping remains popular for its simplicity and minimal impact on the critical timestep, but it tends to overdamp low-frequency modes and underdamp high-frequency modes. Stiffness-proportional or Rayleigh-type damping can provide better control of energy dissipation over a selected frequency range. Yet, they may severely restrict the stable timestep in explicit schemes and can be difficult to calibrate consistently across different structural configurations. Alternative formulations, such as Maxwell-type damping and other frequency-dependent models [27, 28], offer greater flexibility but have not yet been systematically assessed for large masonry assemblies in a distinct-element context. Their applicability under combined cracking, shearing, and crushing mechanisms, therefore, remains an open question, with direct implications for the reliability of seismic predictions. These limitations in both joint constitutive modelling and damping representation motivate the developments undertaken in this dissertation.

1.2. Problem statement

Against this background, the central problem addressed in this dissertation is the lack of a joint constitutive framework for DEM analysis of masonry structures that is at once physically grounded, computationally robust, adequately validated from the material to the structural scale, and compatible with a rational damping description for dynamic analysis.

More specifically, the most advanced existing DEM contact models are those of Lemos [24] and Pulatsu [25]. Although these represent essential advances, there is still no widely adopted, experimentally validated framework that simultaneously:

1. **Reproduces mixed-mode fracture behaviour.**
   It should capture experimentally observed post-peak softening in tension and



shear, including realistic coupling between opening and sliding, consistent with fracture mechanics. The dilatant behaviour of the joints under shear, namely the normal opening induced by shear sliding, and its progressive degradation with accumulated slip, should also be reproduced.

2. **Represents composite compressive failure and its interaction with shear.**
   It should describe the composite nature of compressive failure in masonry, including mortar crushing at the joints, unit splitting, and spalling, as well as the interaction between compressive and shear transfer under high confining stress.

3. **Accounts for cyclic degradation and energy dissipation.**
   It should reproduce stiffness and strength degradation, hysteresis, and energy dissipation under cyclic and seismic loading in a physically sound manner for masonry interfaces.

4. **Is validated from material tests to structural applications.**
   The parameters and predictive performance should be checked systematically against experimental data at unit-mortar joint, component (walls and piers), and structure (full-scale buildings) levels.

5. **Is suitable for large-scale distinct element analyses.**
   The implementation should be robust in explicit time integration, efficient for a large number of blocks and contacts, and able to cope with extensive damage and evolving contact topologies without prohibitive cost.

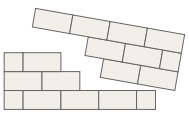
In parallel, frequency-dependent alternatives, such as Maxwell damping [27, 28], are conceptually promising for modelling energy dissipation in large masonry assemblies under dynamic excitation. However, the current understanding and implementation of this type of damping for the dynamic analysis of large masonry assemblies lack systematic validation and comprehensive calibration procedures for structural-level applications. This study seeks to bridge the gap by conducting sensitivity analyses of the predicted responses to these damping models, aiming to establish a more rational and robust description of damping for dynamic analysis.

1.3. Research objectives and scope

Against this background on the capabilities and limitations of DEM for masonry structures, as well as the need for a DEM-based joint constitutive formulation, the overarching research objective of this dissertation is formulated as follows:

> **To develop, implement, and validate a joint constitutive model within a distinct element framework that realistically captures masonry failure mechanisms and cyclic degradation, while remaining efficient for large-scale analyses.**

The proposed joint constitutive formulation is hereafter referred to as the **Masonry Advanced Softening cONtact model (MASON)** for consistency throughout this dissertation.



1.3.1. Design criteria

To make this objective operational, the **MASON contact model** must satisfy a set of design criteria related to accuracy, robustness, and computational performance. In particular, the model should reproduce the **tensile and shear responses** observed in material characterisation tests, and the damage mechanisms associated with tensile separation and shear slip should be distinguishable in the numerical results.

The toughness of masonry, expressed through **fracture energy** and **the shape of the softening branch** for each strength component, should be robust with respect to user input, allowing either fracture-energy regularisation or user-defined piecewise softening functions to be prescribed.

The model should also **capture compressive failure** in material characterisation and structural tests. Mortar crushing should be lumped phenomenologically into a compression cap at the joint interface, with softening to reproduce the post-peak compressive response. Where unit-level mechanisms such as splitting and spalling become relevant, they should be addressed through complementary block-level representations (e.g., deformable or bonded blocks). The interaction between normal and shear stresses under combined shear-compression loading should also be reproduced.

Under cyclic loading, the model should reproduce **stiffness degradation and hysteretic behaviour** when validated against experimental tests on different masonry typologies. It should capture salient cyclic features, including strength degradation, pinching, and progressive loss of energy-dissipation capacity associated with crack opening–closing and frictional sliding. The unloading–reloading stiffness should be differentiated by failure mode, namely elastic in shear, secant in tension, and a nonlinear combination of elastic and secant in compression.

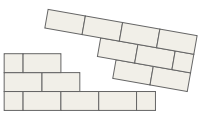
Lastly, the model should maintain **acceptable computational cost** in large-scale DEM simulations. This requires a strictly local update scheme with a bounded number of operations per contact and no global iterations, so the overall cost scales approximately linearly ($\mathcal{O}(N)$) with the number of active contacts, where N denotes the number of contacts or joints.

1.3.2. Sub-projects division

The design criteria mentioned above are addressed through a set of sub-projects, each focusing on a specific aspect of the overall development and validation of the joint constitutive model. The hierarchical breakdown of the research into sub-projects is illustrated in Figure 1.3 and outlined as follows:

SP1 **State-of-the-art review.** Conduct a comprehensive literature review to identify current advances in distinct element modelling of masonry structures and joint constitutive formulations, highlighting the advantages and limitations of existing DEM interface models and damping strategies.

SP2 **Development of the DEM joint constitutive model.** Formulate and implement the Masonry Advanced Softening cONtact model (MASON) for masonry interfaces in DEM to capture tensile, shear, and compressive behaviour, including softening and cyclic degradation.



SP3 **Calibration and validation against experimental evidence.** Calibrate the MASON model using experimental data at the joint and component levels, and validate its performance under monotonic and cyclic loading for different masonry typologies.

SP4 **Dynamic analysis and damping strategies.** Investigate viscous and alternative damping formulations for DEM and evaluate their influence on the dynamic response of masonry assemblies governed by the MASON model, with emphasis on energy dissipation, numerical stability, and consistency.

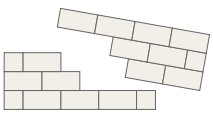
SP5 **Application to engineering-scale masonry structures.** Apply the calibrated MASON model in DEM to representative masonry structures subjected to seismic loading, and assess its predictive capability and numerical robustness in practical engineering problems. This stage evaluates the overall usefulness of the MASON model for the seismic assessment of existing masonry buildings and assesses its compliance with the combined accuracy and efficiency criteria.

The scope of this research is restricted to the development, implementation, and validation of the MASON contact model for masonry interfaces within a Distinct Element Method (DEM) framework. The work focuses on unreinforced and retrofitted masonry typologies commonly found in existing buildings subjected to seismic loading. Model calibration and validation are performed using experimental datasets from the literature at the joint, component, and structural levels. The research also explores the interaction between the MASON model and advanced damping techniques in explicit dynamic analyses. The ultimate aim is to enhance the constitutive modelling capabilities of DEM for masonry by providing a robust contact formulation that supports reliable seismic assessment of existing masonry structures.

1.4. Thesis outline

This dissertation is organised into nine chapters, which together develop, implement, and validate a DEM strategy for masonry structures, from fundamental concepts to building-scale applications. All numerical analyses are performed within the explicit dynamic time-integration scheme inherent to DEM. Quasi-static problems, including the material-level tests (Chapter 5), the component-level analyses (Chapter 6), and the pushover and quasi-static cyclic analyses at the building scale (Chapter 8), are addressed by applying loads slowly enough to render inertial effects negligible. Dynamic analyses, including shake-table simulations (Chapter 7) and the shake-table study on the URM building (Section 8.6), use realistic timescales and explicitly account for the system's inertia.

Chapter 2 presents a comprehensive review of the mechanical behaviour and constitutive modelling of masonry structures. The chapter is primarily linked to SP1. It surveys modelling strategies, with particular emphasis on block-based discontinuum methods, critically discussing their theoretical foundations, constitutive formulations, and applications, and highlighting their main advantages and limitations. The chapter concludes by identifying key knowledge gaps in the constitutive modelling of masonry joints within discontinuum frameworks.



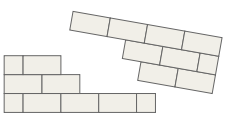
Chapter 3 sets out the methodological backbone of the work by reviewing the formulation and practical aspects of the Distinct Element Method (DEM) for masonry analysis. The chapter mainly addresses SP1, while providing foundational material for SP2 and SP5. The chapter outlines the theoretical background and discusses key issues in dynamic analysis using DEM, including time integration, numerical stability, and the role of damping.

Chapter 4 presents the **Masonry Advanced Softening cONtact model (MASON)** within the DEM framework, introducing a multi-surface plasticity formulation with damage evolution in tension, shear, and compression, including dilatancy and its progressive degradation, and the associated energy dissipation under cyclic loading. The chapter forms the core of SP2 and contributes to SP3 and SP4. The chapter also outlines the stress-update algorithm for explicit integration and the numerical implementation of the model in DEM, providing the basis for subsequent calibration, validation, and dynamic applications.

Chapter 5 addresses material-level validation of the **MASON model** and is mainly associated with SP3. It presents quasi-static monotonic characterisation tests on masonry couplets, triplets, beams, and wallettes (shear–compression, direct shear, four-point bending, and uniaxial compression) modelled using a simplified micro-modelling strategy. Additional focus on uniaxial compression is provided through dedicated analyses employing the bonded-block approach. Quasi-static cyclic tests are then examined, including cyclic direct shear on couplets and uniaxial cyclic compression on wallettes. For each test series, numerical results are compared with experiments on global response and local damage evolution to assess the **MASON model** against the accuracy criteria for strength, toughness, and cyclic degradation.

Chapter 6 extends the validation of the **MASON model** to the component scale, i.e., walls and piers. The chapter contributes to SPs 3 and 4. In this context, bricks are modelled either as perfectly rigid bodies or as deformable blocks with finite stiffness, allowing the influence of unit deformability on wall response to be assessed explicitly. The chapter first examines quasi-static monotonic in-plane tests on masonry walls under shear and compression, investigating rigid versus deformable blocks, the influence of dilatancy, and the objectivity of the mesh and timestep. The chapter then analyses quasi-static cyclic in-plane tests on shear walls, focusing on mechanism transitions, displacement-rate sensitivity, and cross-comparisons with alternative numerical approaches. Finally, the model is also validated for retrofitted masonry piers with modular steel frames, including parameter sensitivity analyses and quasi-static cyclic analyses on deformable blocks, thereby strengthening the link to practical applications.

Chapter 7 investigates the dynamic response of masonry structures with the proposed DEM framework. The chapter is closely related to SP4 and also supports SP5. It first analyses shake-table tests on a masonry cross-vault, comparing the **MASON model** with the Tension–Shear–Compression Linear model [25]. On the same benchmark, mass-proportional damping, Maxwell damping and the undamped case are compared through sensitivity analyses. Particular attention is paid to the interaction between the damping scheme and the joint constitutive law, since the unloading–reloading behaviour at the joints controls the high-frequency content generated at re-contact. The chapter

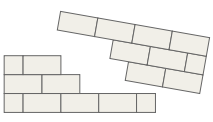


then validates the MASON–Maxwell combination against shake-table tests on full-scale masonry gable walls tested up to collapse.

Chapter 8 applies the MASON-based DEM strategy at building scale and mainly addresses SP5. The case study is TUD-BUILD-1, a full-scale calcium silicate house representative of the Groningen terraced-house typology, tested under quasi-static cyclic loading at TU Delft. Pushover analyses first compare rigid- and deformable-block idealisations with the experimental envelope. A quasi-static cyclic analysis then assesses the hysteretic response and the damage pattern against the test. An exploratory incremental dynamic analysis under an induced-seismicity record estimates the near-collapse intensity of the unreinforced building and of the building retrofitted with a modular steel-frame system. The chapter concludes with an appraisal of what the strategy can and cannot do for real buildings.

Chapter 9 summarises the main conclusions of the dissertation and reflects on the implications for the analysis and assessment of masonry structures, summarising the outcomes of sub-projects SP1 to SP5. The key contributions in constitutive modelling, damping representation, and DEM validation for masonry are highlighted, along with the practical relevance of the findings. The chapter ends with recommendations for future research, including extensions of the constitutive framework, uncertainty quantification of the model parameters and applications to other masonry typologies.

The overall structure of this dissertation and its relation to the five sub-projects are summarised in Figure 1.3. In particular, the building-scale case study in Chapter 8 (SP5) builds directly on the developments and validations of Chapters 5 and 6. The masonry parameters of the building model [29] are taken from material [30] and component [31] tests on the same calcium silicate masonry, supplemented by empirical correlations for the fracture energies. Only the unit crack-plane parameters were adjusted to the global building response; the origin of every parameter is summarised in Table 9.1.



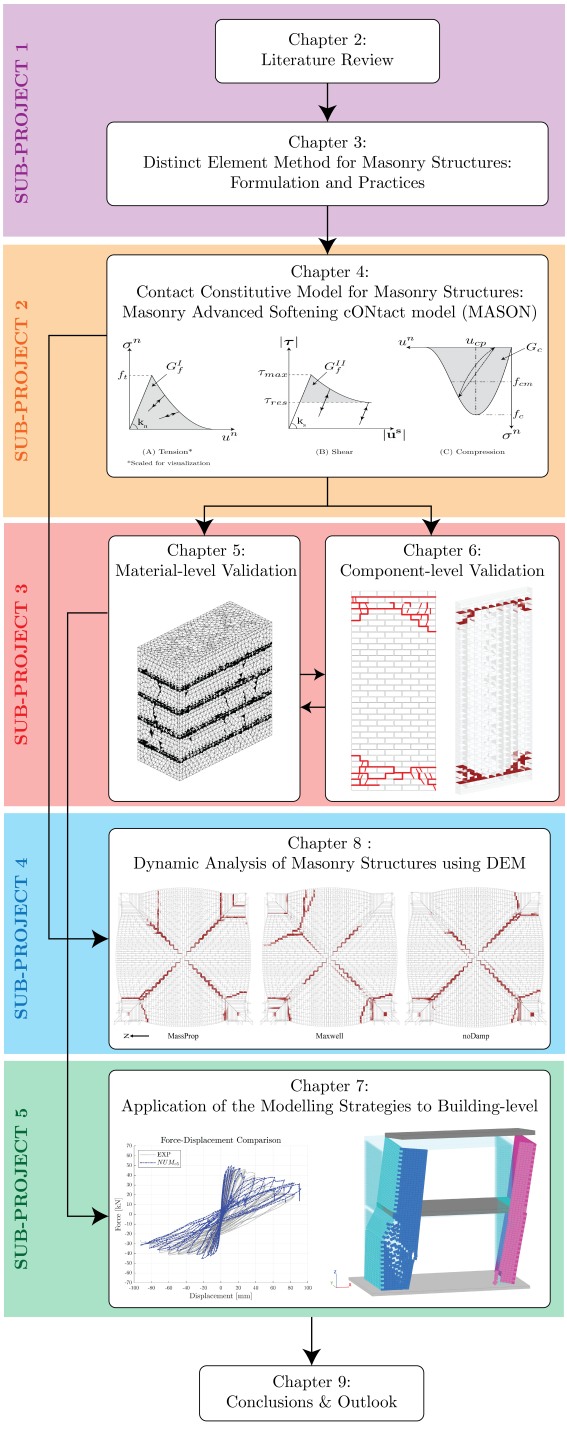
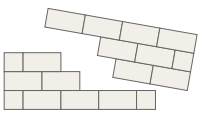
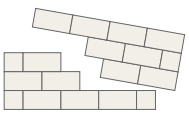


Figure 1.3. Thesis structure and sub-projects.



1.5. Highlights of this research

- A robust joint constitutive model for distinct element modelling of masonry that captures cracking, shearing, and crushing under realistic loading scenarios.
- The dilatant behaviour of joints under shear and its progressive degradation are integrated into the constitutive framework and validated against experimental data.
- An energy-dissipation mechanism under cyclic loading, including transitions between failure mechanisms.
- Systematic calibration against interface and material tests, and validation on masonry walls under monotonic and cyclic loading, with cross-comparisons to alternative numerical approaches.
- Assessment of mass-proportional, Maxwell, and undamped in explicit dynamic analysis, with sensitivity analyses on the damping parameters.
- Application of the developed DEM model at building scale, including a case study on a full-scale masonry building representative of the Groningen stock, tested under induced-seismicity-type motions, with assessment of seismic performance and retrofitting options.



Bibliography of Chapter 1

[1] A. M. D'Altri, V. Sarhosis, G. Milani, J. Rots, S. Cattari, S. Lagomarsino, E. Sacco, A. Tralli, G. Castellazzi and S. de Miranda. 'Modeling Strategies for the Computational Analysis of Unreinforced Masonry Structures: Review and Classification'. In: *Archives of Computational Methods in Engineering* 27.4 (2020), pp. 1153–1185. ISSN: 1134-3060. DOI: 10.1007/s11831-019-09351-x.

[2] R. Oyguc. 'Seismic Behavior and Vulnerability of Masonry Dwellings in Eastern Türkiye: A Comprehensive Analysis'. In: *Applied Sciences* 15.10 (2025), p. 5490. DOI: 10.3390/app15105490.

[3] G. Brandonisio, G. Lucibello, E. Mele and A. De Luca. 'Damage and performance evaluation of masonry churches in the 2009 L'Aquila earthquake'. In: *Engineering Failure Analysis* 34 (2013), pp. 693–714. DOI: 10.1016/j.engfailanal.2013.01.021.

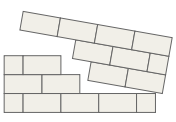
[4] E. Sesana, A. S. Gagnon, C. Ciantelli, J. Cassar and J. J. Hughes. 'Climate change impacts on cultural heritage: A literature review'. In: *WIREs Climate Change* 12.4 (2021), e710. DOI: 10.1002/wcc.710.

[5] A. Prosperi, M. Longo, P. A. Korswagen, M. Korff and J. G. Rots. 'Sensitivity modelling with objective damage assessment of unreinforced masonry façades undergoing different subsidence settlement patterns'. In: *Engineering Structures* 286 (2023), p. 116113. DOI: 10.1016/j.engstruct.2023.116113.

[6] Nederlandse Aardolie Maatschappij (NAM). *Technical Addendum to the Winningsplan Groningen 2013 — Subsidence, Induced Earthquakes and Seismic Hazard Analysis in the Groningen Field*. Technical Report. Assen, The Netherlands: NAM, 2013.

[7] Nederlandse Aardolie Maatschappij (NAM). *Production, Subsidence, Induced Earthquakes and Seismic Hazard and Risk Assessment in the Groningen Field: Technical Addendum to the Winningsplan Groningen 2016*. Technical Report. Commonly cited as the 2016 NAM Technical Addendum. Assen, The Netherlands: NAM, 2016.

[8] M. Ntinalexis, P. P. Kruiver, J. J. Bommer, E. Ruigrok, A. Rodriguez-Marek, B. Edwards, R. Pinho, J. Spetzler, E. Obando Hernandez, M. Pefkos, M. Bahrampouri, E. P. van Onselen, B. Dost and J. van Elk. 'A database of ground motion recordings, site profiles, and amplification factors from the Groningen gas field in the Netherlands'. In: *Earthquake Spectra* 39 (2023), pp. 687–701. DOI: 10.1177/87552930221140926.



[9] I. E. Bal, E. Smyrou and E. Bulder. 'Liability and Damage Claim Issues in Induced Earthquakes: Case of Groningen'. In: *SECED 2019 Conference: Earthquake Risk and Engineering Towards a Resilient World*. Conference paper. Greenwich, London, UK, 9th–10th Sept. 2019.

[10] KNMI. *Aardbeving van 3,4 in Groningse Zeerijp*. KNMI Nieuwsbericht (in Dutch). 14th Nov. 2025. URL: https://www.knmi.nl/over-het-knmi/nieuws/aardbeving-van-3-4-in-groningse-zeerijp.

[11] H. Crowley, R. Pinho, J. van Elk and J. Uilenreef. 'Probabilistic damage assessment of buildings due to induced seismicity'. In: *Bulletin of Earthquake Engineering* 17 (2019), pp. 4495–4516. DOI: 10.1007/s10518-018-0462-1.

[12] G. Lancioni, S. Lenci and Q. Piattoni. 'Dynamics and failure mechanisms of ancient masonry churches subjected to seismic actions by using the NSCD method: The case of the medieval church of S. Maria in Portuno'. In: *Engineering Structures* 56 (2013), pp. 1527–1546. DOI: 10.1016/j.engstruct.2013.07.027.

[13] N. Mendes, S. Zanotti and J. V. Lemos. 'Seismic Performance of Historical Buildings Based on Discrete Element Method: An Adobe Church'. In: *Journal of Earthquake Engineering* 24.8 (Aug. 2020), pp. 1270–1289. ISSN: 13632469. DOI: 10.1080/13632469.2018.1463879. URL: https://www.tandfonline.com/doi/abs/10.1080/13632469.2018.1463879.

[14] L. Diana, G. Vaiano, A. Formisano, L. Scandolo, S. Podestà and P. Lestuzzi. 'The Seismic Vulnerability Assessment of Heritage Buildings: A Holistic Methodology for Masonry Churches'. In: *International Journal of Architectural Heritage* 18.6 (2024), pp. 994–1022. DOI: 10.1080/15583058.2023.2203097.

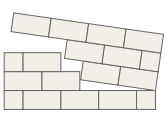
[15] A. Ferrante, D. Loverdos, F. Clementi, G. Milani, A. Formisano, S. Lenci and V. Sarhosis. 'Discontinuous approaches for nonlinear dynamic analyses of an ancient masonry tower'. In: *Engineering Structures* 230 (2021), p. 111626. ISSN: 0141-0296. DOI: 10.1016/j.engstruct.2020.111626.

[16] P. Meriggi, G. De Felice, S. De Santis, F. Gobbin, A. Mordanova and B. Pantò. 'Distinct Element Modelling of Masonry Walls under Out-Of-Plane Seismic Loading'. In: *International Journal of Architectural Heritage* 13.7 (2019), pp. 1110–1123. ISSN: 1558-3066. DOI: 10.1080/15583058.2019.1615152. URL: https://www.tandfonline.com/action/journalInformation?journalCode=uarc20.

[17] A. Rafiee, M. Vinches and C. Bohatier. 'Modelling and analysis of the Nimes arena and the Arles aqueduct subjected to a seismic loading, using the Non-Smooth Contact Dynamics method'. In: *Engineering Structures* 30.12 (2008), pp. 3457–3467. DOI: 10.1016/j.engstruct.2008.05.018.

[18] A. Furiosi *et al.* 'Seismic Fragility Assessment of a Multi-Span Masonry Arch Bridge Using a Discontinuum Modeling Approach'. In: *Earthquake Engineering & Structural Dynamics* (2025). DOI: 10.1002/eqe.70029.

[19] E. Farneti, F. Ávila, N. Cavalagli and F. Ubertini. 'Collapse analysis of a masonry arch bridge using the Applied Element Method'. In: *Engineering Research Express* 6.3 (2024), p. 035109. DOI: 10.1088/2631-8695/ad6ad8.



[20] B. R. Hamid Lotfi and P. Benson Shing. 'Interface Model Applied to Fracture of Masonry Structures'. In: *Journal of Structural Engineering* 120.1 (Jan. 1994), pp. 63–80. ISSN: 0733-9445. DOI: 10.1061/(ASCE)0733-9445(1994)120:1(63).

[21] P. B. Lourenço and J. G. Rots. 'Multisurface Interface Model for Analysis of Masonry Structures'. In: *Journal of Engineering Mechanics* 123.7 (July 1997), pp. 660–668. ISSN: 0733-9399. DOI: 10.1061/(ASCE)0733-9399(1997)123:7(660).

[22] L. Macorini and B. A. Izzuddin. 'A non-linear interface element for 3D mesoscale analysis of brick-masonry structures'. In: *International Journal for Numerical Methods in Engineering* 85.12 (Mar. 2011), pp. 1584–1608. ISSN: 00295981. DOI: 10.1002/nme.3046.

[23] Y. Nie, A. Sheikh, P. Visintin and M. Griffith. 'A robust computational strategy for failure prediction of masonry structures using an improved multi-surface damage-plastic based interface model'. In: *International Journal for Numerical Methods in Engineering* 124.11 (June 2023), pp. 2498–2528. ISSN: 10970207. DOI: 10.1002/NME.7218.

[24] J. V. Lemos and V. Sarhosis. 'Discrete Element Bonded-Block Models for Detailed Analysis of Masonry'. In: *Infrastructures* 7.3 (Feb. 2022), p. 31. ISSN: 2412-3811. DOI: 10.3390/infrastructures7030031.

[25] B. Pulatsu. 'Coupled elasto-softening contact models in DEM to predict the in-plane response of masonry walls'. In: *Computational Particle Mechanics* 10 (2023), pp. 1759–1770. ISSN: 2196-4378. DOI: 10.1007/s40571-023-00586-x.

[26] A. M. D'Altri, F. Messali, J. Rots, G. Castellazzi and S. de Miranda. 'A damaging block-based model for the analysis of the cyclic behaviour of full-scale masonry structures'. In: *Engineering Fracture Mechanics* 209 (Mar. 2019), pp. 423–448. ISSN: 00137944. DOI: 10.1016/j.engfracmech.2018.11.046.

[27] E. M. Dawson and Z. Cheng. 'Maxwell Damping: An Alternative to Rayleigh Damping'. In: *Geo-Extreme 2021*. Geo-Extreme 2021. ASCE, 2021, pp. 34–45. DOI: 10.1061/9780784483701.004.

[28] J. V. Lemos, E. Dawson and Z. Cheng. 'Application of Maxwell damping in the dynamic analysis of masonry structures with discrete elements'. In: *International Journal of Masonry Research and Innovation* 7.6 (2022), pp. 663–686. ISSN: 2056-9459. DOI: 10.1504/ijmri.2021.10043266.

[29] R. Esposito, F. Messali, G. J. P. Ravenshorst, H. R. Schipper and J. G. Rots. 'Seismic assessment of a lab-tested two-storey unreinforced masonry Dutch terraced house'. In: *Bulletin of Earthquake Engineering* 17.8 (2019), pp. 4601–4623. DOI: 10.1007/s10518-019-00572-w. URL: https://doi.org/10.1007/s10518-019-00572-w.

[30] R. Esposito, F. Messali and J. G. Rots. *Tests for the Characterization of Replicated Masonry and Wall Ties*. 2016. URL: http://resolver.tudelft.nl/uuid:a0923cf9-0ccd-48a1-9ce1-082aa66e97af.



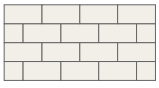
[31] F. Messali, R. Esposito, G. Ravenshorst and J. Rots. 'Experimental investigation of the in-plane cyclic behaviour of calcium silicate brick masonry walls'. In: *Bulletin of Earthquake Engineering* 18.8 (2020), pp. 3963–3994. DOI: 10.1007/s10518-020-00835-x.



2

Literature Review

Masonry is a heterogeneous assemblage whose response is governed by nonlinear joint behaviour and damage processes that localise to cracking, shearing, and crushing. While masonry construction has historically been prevalent, rigorous experimental characterisation and performance assessment have emerged only relatively recently. In parallel, developments in computational mechanics have produced a broad family of modelling strategies, commonly distinguished by their representation of the masonry assemblage. This chapter provides a state-of-the-art review of modelling strategies in masonry, with a focused treatment of contact-based block approaches (also referred to as discontinuum-based modelling). Section 2.1 starts with the mechanical behaviour and constitutive framework in masonry structures. Section 2.2 provides an overview of general modelling strategies for masonry structures, ranging from homogenised continua and damage-plasticity formulations to micro/meso-modelling and explicit block-based approaches, and highlights their domains of applicability and principal limitations. Section 2.3 narrows the scope to contact-based discontinuum formulations, with emphasis on DEM: its theoretical underpinnings, modelling assumptions, and representative applications in masonry analysis. Section 2.4 identifies knowledge gaps in current DEM practices for masonry and outlines the research focus of this dissertation. These gaps motivate the development of the Masonry Advanced Softening cONtact model (MASON), presented in Chapter 4.



2.1. Mechanical behaviour and constitutive framework in masonry structures

Masonry is among the oldest and most widely used structural systems, consisting of discrete units (bricks, blocks, or stones) bonded by mortar joints and optimised historically for compression-dominated load paths, conferring exceptional capacity to resist gravitational loads. Its mechanical behaviour depends strongly on the geometry (bond pattern, arching, confinement), construction quality, and the mechanical contrast between relatively stiff units and weaker, more compliant mortar joints. At the material (joint) level, masonry exhibits pronounced nonlinearity, anisotropy, and rate-dependence, with failure modes including joint cracking, sliding, crushing, and unit splitting (Figure 2.1). It is important to note that the failure modes presented in Figure 2.1A and Figure 2.1D relate to the failure modes at the interface level, while Figure 2.1E relates to the failure of the masonry constituents (units and mortar layers). The remaining two modes are composite mechanisms: Figure 2.1B (compressive failure) involves unit splitting, spalling, and cracking together with mortar crushing at the joints, while Figure 2.1C (diagonal cracking) propagates through both units and interfaces.

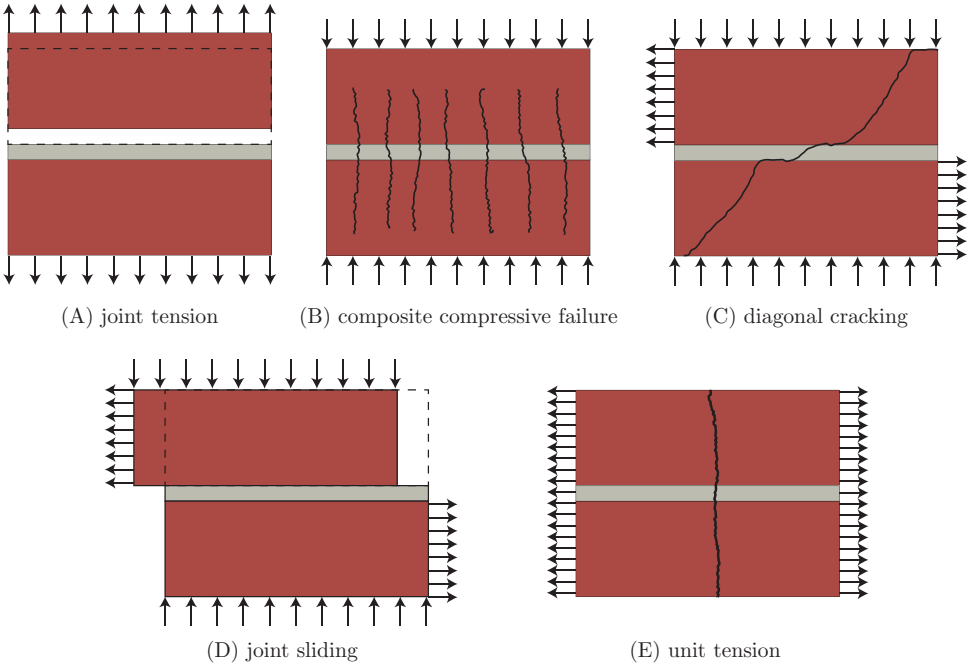


Figure 2.1. Typical joint-level failures observed in the masonry couplets. Adapted from [1]

At the wall pier scale (Figure 2.2), the in-plane response is governed by the interplay of axial force N, shear force V, wall aspect ratio (defined as the height-to-length ratio of the wall), boundary restraint (clamped-clamped or cantilever), and the joint parameters (f_t, c, μ, fracture energies) and the masonry parameters such as f_c and the corresponding

fracture energies. Four archetypal failure mechanisms are distinguished in Figure 2.2 and can be interpreted in terms of the mean shear stress τ_m and the average normal stress σ_n.

For low levels of pre-compression, σ_0(A), failure is governed by **shear-sliding** (SS, Figure 2.2A). As the axial load increases to σ_0(B), the response transitions to a **shear friction** mechanism (SF, Figure 2.2B), where a stepped sliding path develops through alternating bed and head joint failures. In this regime, shear resistance is enhanced by frictional interlock and dilatancy, and the corresponding increase in capacity is represented by an effective cohesion τ_0^* in the shear–friction branch of the failure envelope [2, 3].

For intermediate pre-compression levels, σ_0(C), the wall fails in **diagonal tension** (DT, Figure 2.2C). Distributed cracks form at an angle of approximately 45° to the horizontal when the principal tensile stress in the panel exceeds the tensile strength, f_t, a failure mode typical of relatively strong mortar or confined panels and associated with a sudden loss of shear capacity. Finally, for high pre-compression approaching the masonry compressive strength f_c, the response is dominated by a **toe crushing-rocking** mechanism (TC-R, Figure 2.2D). For cantilever walls, crushing initiates at the compressed toe, while uplift occurs at the opposite edge; the global capacity is governed by a combination of flexural rocking and local compressive failure. For walls with restrained rotation at the top (double-clamped), pure rocking is suppressed, and the high-axial response transitions to toe crushing at the diagonally opposite corners without uplift.

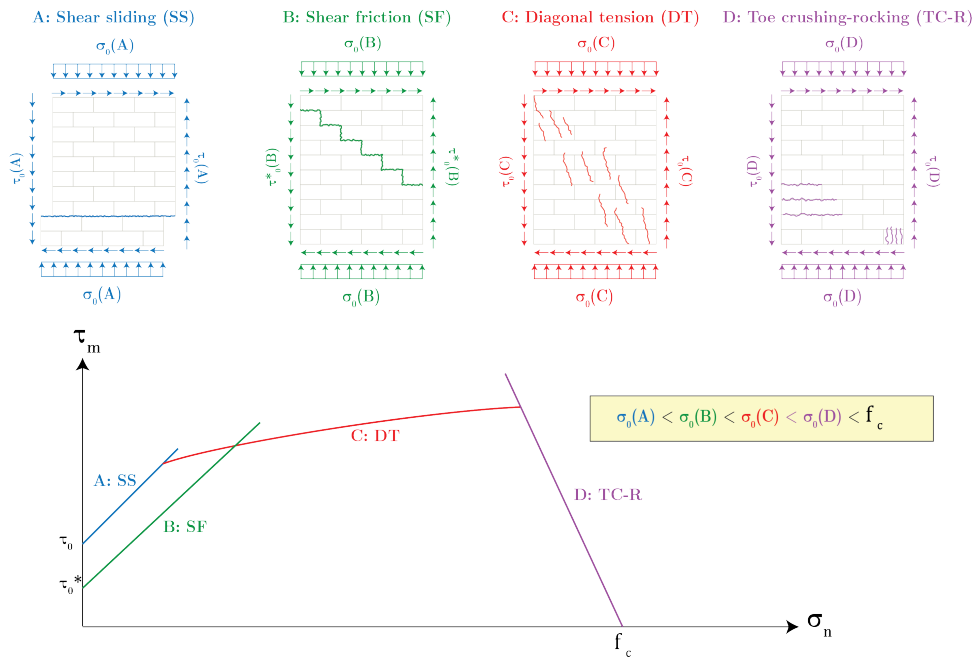
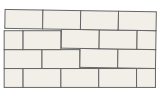


Figure 2.2. Typical component-level failure of URM walls subjected to compression and in-plane loads, adapted from [4]



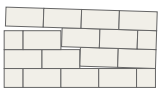
The stress states are schematically summarised in the (σ_n, τ_m) plane at the lower part of Figure 2.2. The sequence illustrates how increasing axial compression drives a transition from sliding-dominated to tension-dominated, and ultimately to compression failure, at the component scale.

From the depiction of the failure mechanisms of URM structures at both the material and component levels, it is clear that the response of masonry is governed not only by the properties of its constituents but also by the integrity and properties of the interfaces. Both constituents are quasi-brittle, exhibiting low tensile capacity with softening and limited compressive ductility culminating in compaction/crushing, which together control crack initiation, interfacial slip, and post-peak degradation. Masonry is intrinsically anisotropic, with orthotropy inherited from its layered fabric of bed and head joints and from the bond pattern. At the macroscale, this manifests as elastic properties such as direction-dependent elastic moduli ($E_{\parallel}, E_{\perp}$), shear modulus $G_{\parallel\perp}$, and Poisson's ratios, as well as inelastic properties such as tensile, shear, and compression capacities. The material is best idealised as orthotropic, with two in-plane directions aligned with the bed and head joints and one out-of-plane direction.

Experimental characterisation that captures these complexities is essential for accurate modelling, yet its reliability and scalability across the material and component levels remain challenging. In laboratory settings, the Young's modulus E and Poisson's ratio ν of masonry are commonly obtained from prism compression tests run per ASTM C1314 [5] (originally intended for compressive strength), with axial and lateral deformations instrumented to derive secant or tangent moduli from the stress–strain curve. EN 1052-1 [6] also prescribes compressive testing of masonry to identify E. The shear modulus G is commonly estimated from diagonal compression tests (ASTM E519 [7]) or from EN shear tests with complementary kinematic measurements. EN 1996-1 [8] recommends a fixed ratio of $G = 0.4E$ for preliminary design, a value also supported by experimental investigations [9]. However, subsequent studies have shown that this simplification overlooks the pronounced anisotropy and variability of masonry stiffness. Wilding *et al.* [10] reported G/E ratios in the range of 0.30–0.40 for solid-block masonry (including solid calcium silicate units) and 0.20–0.25 for hollow or vertically perforated blocks, typically at or below the EN 1996 value.

In situ characterisation in the heritage conservation context often poses challenges due to greater variability compared to laboratory testing in controlled environments [11]. Several non-destructive testing (NDT) methods have been proposed to estimate the elastic properties of masonry in existing structures [12]. ASTM C1197 [13] formalises the double flat-jack method that provides a minimally destructive route to estimate deformability (secant E). With regard to the dynamic moduli for units, ASTM E1876 [14] outlines a resonant frequency method to derive dynamic E and G from natural frequencies, which are typically higher than dynamic moduli due to strain-rate effects and microcrack closure. Beyond these techniques, semi-destructive "core-testing" methods have recently been proposed to extract cylindrical masonry specimens and assess their nonlinear compressive response, thereby offering a practical compromise between invasiveness and the ability to directly obtain elastic, strength, and post-peak properties from existing structures [15].

The tensile strength f_t of masonry is difficult to measure directly due to the challenges



in applying pure tension and the relatively brittle behaviour of the constituents. At small strains, the response is quasi-linear and orthotropic, but once cracking nucleates, the behaviour is dominated by cohesive fracture along interfaces or through units, with rapid stiffness degradation and pronounced size effects. Direct tensile testing of masonry prisms is experimentally challenging due to gripping issues and stress concentrations, resulting in high variability in results [16]. Consequently, indirect methods such as bending tests, Brazilian splitting tests, and bond-wrench tests are commonly used. Flexural testing of wallettes/prisms about axes parallel and perpendicular to the bed joints is standardised in EN 1052-2 [17], while the bond wrench test is described in EN 1052-5 [18]. The flexural strength f_x obtained from bending tests is converted to uniaxial tensile strength f_t using empirical relations [19, 20]. At the constitutive level, the tensile response is often defined using a Rankine tension cut-off with exponential/multi-linear softening in orthotropic directions, embedded in damage-plasticity frameworks to capture stiffness degradation and irreversible strains. In models with interface elements, tensile behaviour is often coupled with shear cohesive laws and dilation, which requires calibration against the fracture energy G_f obtained from experiments [20] or empirical equations from the Model Code 90 [21].

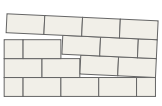
The shear behaviour of masonry is governed by the frictional and cohesive properties of the mortar joints, which are influenced by factors such as mortar composition, joint thickness, and curing conditions [20, 22, 23]. The shear strength is dependent on the normal stress acting on the joint, typically described by the Coulomb friction with cohesion c and friction angle ϕ, formulated in Equation (2.1) at the unit-mortar interface level.

$$\tau = c + \sigma_n \tan(\phi) \tag{2.1}$$

where τ is the shear strength and σ_n is the normal stress on the joint. This captures the peak envelope under constant normal stress σ_n. After peak, the shear response typically softens to a residual branch due to damage and slip, which can be modelled using cohesive laws with fracture energy $G_{f,II}$ to describe the post-peak behaviour. The dilatant behaviour of the mortar joint, described as the conjugate normal opening induced by shear load, depends on the joint roughness, interlocking effects, and confinement level. This is typically expressed by a non-associative dilation angle ψ that decays with plastic shear slip. For models employing continuum elements, a range of plasticity and damage formulations is used to capture shear yielding and degradation. Common isotropic choices include non-associative Drucker-Prager and Mohr-Coulomb plasticity models with hardening/softening. To capture the inherent anisotropy of masonry, orthotropic formulations have been proposed, notably the Rankine-Hill plasticity model developed for masonry by Lourenço *et al.* [24] and orthotropic continuum damage models [25, 26].

Shear-compression tests on masonry triplets under varying normal loads, as outlined in EN 1052-3 [27], are commonly used to derive these parameters. Although not a pure sliding test, the diagonal compression test (ASTM E519 [7]) is also used to estimate shear strength parameters, as discussed in Calderini *et al.* [28].

Finally, the compression behaviour of masonry is typically identified as a composite response, in contrast to the distinct behaviours in tension and shear. The Young's modulus E and compressive strength f_c are commonly derived from uniaxial compression tests



on masonry prisms per ASTM C1314 [5] or EN 1052-1 [6]. Typical behaviour of the compressive response is quasi-linear up to approximately 30-40% of f_c, followed by nonlinear hardening and eventual softening due to microcracking and crushing. The failure mechanisms involved under compression include unit splitting due to Poisson effects, mortar joint crushing, and combined toe crushing under eccentric loading.

Ample experimental tests have been conducted to characterise the compressive behaviour of masonry, particularly on the peak load [29–32] and the behaviour under cyclic loading [33–36], and much less on the post-peak compressive behaviour. The conclusions from these studies indicate that the unloading/reloading paths exhibit stiffness degradation and hysteresis due to microcrack opening/closure and progressive joint damage. This led to the analytical formulation of damage-plasticity models for masonry under compression [33, 37–39] considering a nonlinear unloading/reloading mechanism accounting for the irreversible strains and stiffness degradation.

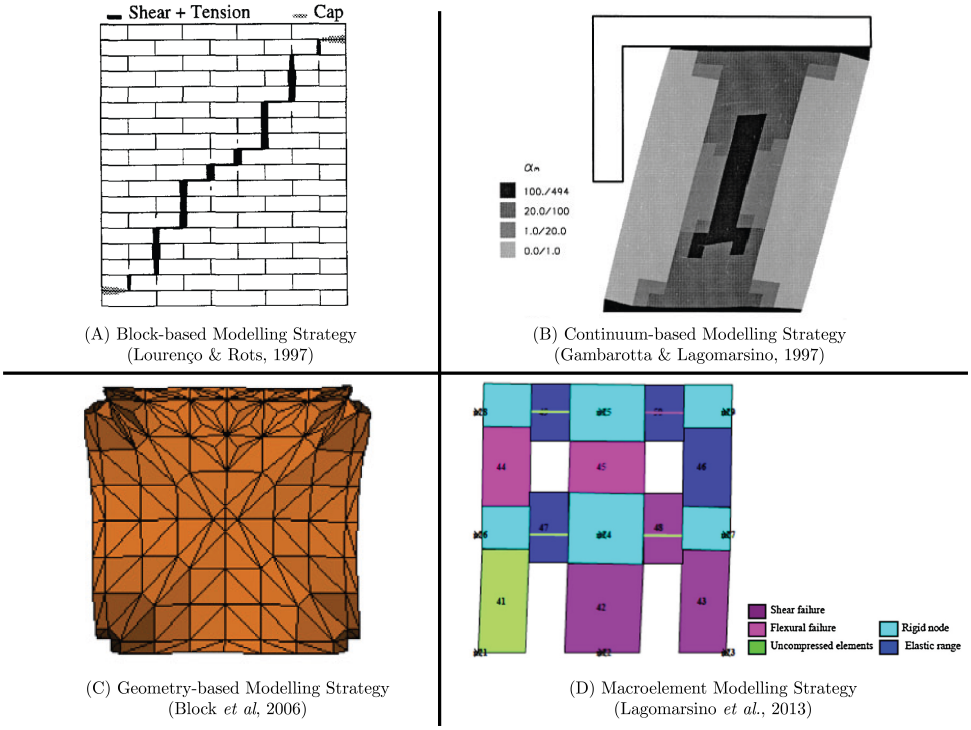
2.2. Overview of modelling strategies for masonry structures

Unreinforced masonry (URM) structures, ranging from ancient monuments to residential housing, pose unique challenges for numerical modelling due to their intrinsically heterogeneous and discontinuous nature. As masonry is a composite system comprising brick units and mortar joints, the performance of masonry structures is significantly influenced by the interaction between these components. This composite nature, combined with the brittle characteristics of the constituent materials, renders their mechanical response highly complex, especially under extreme conditions such as earthquakes. In the early years, dating back to the 19th century, the structural analysis of masonry constructions was primarily based on empirical methods and simplified analytical models. These analytical models relied on the concept of graphic statics pioneered by Karl Culmann, which provided a graphical method for analysing the equilibrium of structures [40]. Jacques Heyman later extended these ideas, introducing the concept of limit analysis for masonry structures [41] based on the assumptions that masonry has no tensile strength, that compressive strength is effectively infinite, and that sliding between blocks does not occur. This approach provides an intuitive yet rigorous means of identifying admissible thrust lines and predicting possible collapse mechanisms, but it lacks an understanding of complex behaviour under extraordinary actions. Consequently, the development of robust modelling strategies to address these extraordinary actions in masonry structures has been an active research focus in computational mechanics and heritage conservation domains.

With the rise of computational power, the 20th century witnessed a shift towards numerical methods for masonry analysis. These numerical methods were classified by the level of detail they provide in representing the masonry structure [42], which divides them into three main categories: macro-modelling, simplified micro-modelling, and detailed micro-modelling. D'Altri et al. [1] recently provided a comprehensive review of the state-of-the-art in computational modelling strategies for masonry structures, offering a systematic framework that organises the approaches into four main categories:

- **Block-based models** represent masonry structures as assemblies of discrete blocks, capturing the geometric and mechanical properties of individual units and their





(A) Block-based Modelling Strategy (Lourenço & Rots, 1997)

(B) Continuum-based Modelling Strategy (Gambarotta & Lagomarsino, 1997)

(C) Geometry-based Modelling Strategy (Block *et al*, 2006)

(D) Macroelement Modelling Strategy (Lagomarsino *et al.*, 2013)

Figure 2.3. Schematic representation of the main modelling strategies for masonry structures.

interactions, e.g., the interface model by Lourenço and Rots [43] (Figure 2.3A).

- **Continuum-based models** treat masonry as a continuous medium, employing continuum mechanics principles to describe the overall behaviour of the structure, e.g., the homogenised continuum damage model by Gambarotta and Lagomarsino [44] (Figure 2.3B).
- **Geometry-based models** refine the approach by Heyman, focusing on the geometric configuration of masonry structures to analyse their stability and load-bearing capacity either through static or kinematic theorems, e.g., the static limit analysis by Milani [45] (Figure 2.3C).
- **Macroelement models** idealise masonry structures as assemblies of simplified structural components, typically piers and spandrels, whose constitutive models are tailored to reproduce the global structural response of these elements, rather than the detailed micro-mechanical behaviour of the masonry material, e.g., the macroelement model by Lagomarsino *et al.* [46] (Figure 2.3D). These macroelements are conceptually distinct from the macro-blocks employed in block-based discontinuum approaches, which use larger discrete blocks that retain explicit interactions between units.



Each category represents a different compromise between computational efficiency, geometric fidelity (i.e., the level of explicit representation of units and joints), and material representation, thereby serving specific applications in structural analysis and safety assessment. This section provides an overview of these modelling strategies, highlighting their respective advantages and limitations.

2.2.1. Block-based modelling strategy

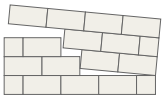
Block-based (or discontinuum) strategies treat masonry as an assembly of distinct units whose individual rigid body motions and mutual interactions are resolved explicitly. Mortar joints are not smeared: they are represented (i) by zero-thickness interfaces embedded between adjacent blocks [43, 47–49], (ii) by contact formulations with cohesive–frictional behaviour at discrete interaction points [50, 51], or (iii) by finite-thickness joint elements that carry their own constitutive response [52, 53]. Typically, for the cases of (i) and (ii), the dimensions of the block units are expanded to account for the thickness of the mortar joints.

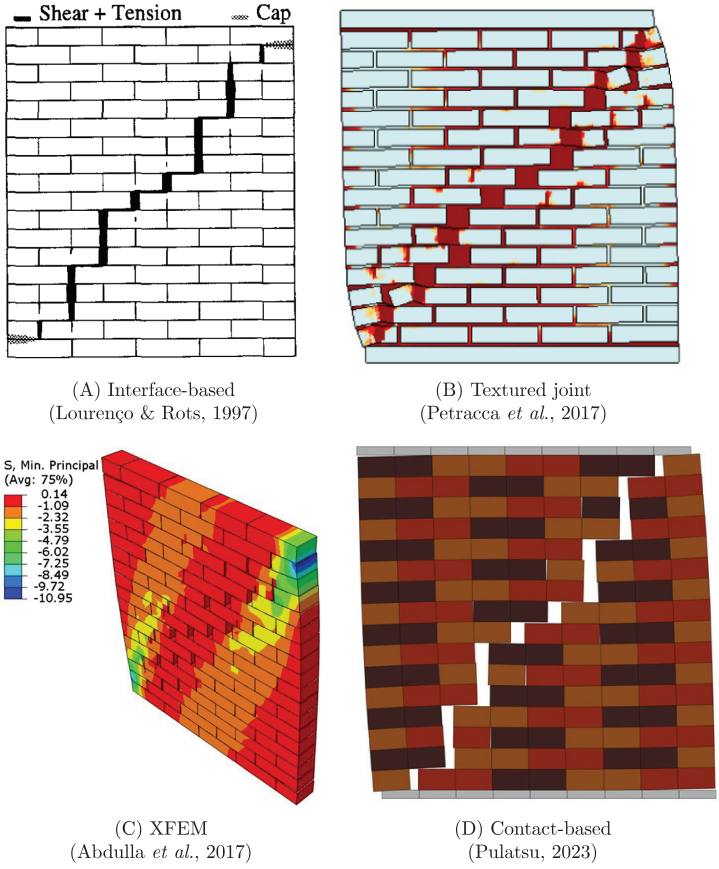
In all three variants, the interaction between adjacent units is ultimately governed by traction-separation behaviour at the unit-mortar discontinuity. In the interface-based (i) and contact-based (ii) formulations, the units are extended (blown-up) to occupy the mortar volume, and the discontinuity is represented as a zero-thickness joint with normal and tangential stiffness (k_n, k_s) adapted to account for the deformability of the omitted mortar layer [42]. In variant (i), the joint is treated as an interface element with a finite element discretisation. In variant (ii), it is treated as a contact between discrete bodies following standard contact mechanics with active-set updates to detect transitions between stick-slip and open-closed states. In both cases, the joint normal and tangential reactions evolve with opening/closure and sliding, with a tension cut-off, softening in mode-I, a frictional law in mode-II, and a compressive cap to model mortar crushing.

Finite-thickness joint elements (iii), likewise, rely on an interface/contact description at the unit-mortar boundaries, but additionally resolve the deformability of the mortar layer itself (normal and shear compliance, dilatancy). This explicit representation of the mortar volume modifies the definition of the joint elastic parameters, which are now linked directly to the mortar stiffness and thickness. The representation enables the inclusion of additional failure modes within the mortar layer in the nonlinear regime, beyond those captured by a pure interface law [52, 53]. At the same time, the definition of the blocks is also altered, as they are now directly associated with the masonry units themselves. The block elastic modulus E_{block} is taken at its measured value from unit characterisation tests, and the unit-mortar interface stiffness k_n is then calibrated to reproduce the overall masonry response.

The blocks themselves may be idealised as rigid or deformable, depending on the target phenomena and scale. Rigid-block formulations, common in discrete element frameworks, prioritise discontinuity kinematics and large rotations at low cost [51], whereas deformable-block formulations (e.g., finite elements with embedded interfaces) capture intra-block stress redistribution and bending of units at a higher computational expense [48]. In both cases, interface parameters are calibrated against masonry triplet, shear–compression, or wedge-splitting tests [43].

In the interface- and contact-based formulations, the composite compressive failure of





(A) Interface-based (Lourenço & Rots, 1997)

(B) Textured joint (Petracca *et al.*, 2017)

(C) XFEM (Abdulla *et al.*, 2017)

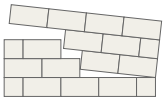
(D) Contact-based (Pulatsu, 2023)

Figure 2.4. Examples of block-based modelling strategies for masonry structures validating the same experimental test by Vermeltfoort *et al.*. [54]

masonry, including mortar crushing, unit splitting, and spalling, is typically lumped into a phenomenological compression cap at the joint interface. The cap represents the combined unit-mortar response as a single surface in stress space, with softening parameters calibrated against experimental compression tests on masonry assemblies.

A more refined approach captures unit splitting explicitly without remeshing bricks into multiple solids by introducing a predefined potential crack plane at (or near) mid-length of the block, following Lotfi and Shing's work [47]. This internal plane is a zero-thickness cohesive interface governed by a mixed-mode traction–separation law. It remains inactive until a tensile or mixed-mode criterion is met, then softens with fracture-energy control, and reverts to frictional contact under compression. This extension has proven effective for out-of-plane bending of wythes and in-plane tension across head joints at modest additional cost relative to a joint-only discontinuum representation.

A more general representation assigns a nonlinear continuum constitutive law to the



masonry units (see, e.g., D'Altri *et al.* [55]), so that splitting and crushing arise from the bulk material response instead of from a predefined crack plane or a lumped interface description. This approach, however, entails a higher computational cost and stricter requirements on mesh refinement and parameter calibration.

Block-based modelling strategies for masonry can be grouped into five classes: (a) zero-thickness interface micromodels, (b) finite-thickness ("textured") joint models, (c) embedded-discontinuity formulations based on XFEM, (d) contact-based approaches, and (e) rigid-block limit analysis models. Figure 2.4 shows four representative block-based modelling strategies for masonry structures and their characteristic responses under the same experimental test by Vermeltfoort *et al.* [54], where a masonry wall panel was subjected to constant compression (at 0.3 MPa) and monotonic shear load. Because the Vermeltfoort tests are deformation-controlled and governed by mixed-mode softening, rigid-block models, which yield only ultimate collapse multipliers under rigid, perfectly plastic assumptions, are poorly suited to reproducing the observed load path and degradation; hence, they are rarely applied to this dataset. Overall, all four approaches recover the characteristic stepped-diagonal shear failure mode observed in the experiments [54], with varying degrees of accuracy for peak load, post-peak response, and damage localisations.

Interface-based models

Interface-based discontinuum models for masonry idealise the assemblage as linear-elastic units connected by zero-thickness interfaces, at which all nonlinear behaviour is concentrated. These interfaces are placed at unit–mortar contacts and, when unit splitting is permitted, at internal potential crack planes between sub-blocks. Within this class of models, the zero-thickness interface formulation by Lourenço and Rots [43] (Figure 2.4A) marked an important improvement after the early applications by Page [56] and Lotfi and Shing [47], introducing a multi-surface damage–plasticity law that localises the nonlinear response entirely at the unit–mortar and unit–unit interfaces. The corresponding constitutive description combines a tensile cut-off, a frictional sliding law, and a compressive cap in a unified interface framework. The compression cap closes the yield surface in the high-compression regime, limiting increases in shear strength under confinement and phenomenologically representing composite compressive failure at elevated normal stresses, typically with softening governed by a compressive fracture energy or crushing parameter. In its original multi-surface formulation by Lourenço and Rots [43], this framework is plasticity-based with elastic unloading and reloading, and therefore does not reproduce cyclic stiffness degradation or hysteretic energy dissipation.

Oliveira and Lourenço [39] extended this interface framework to cyclic loading by introducing secant unloading in tension, nonlinear unloading in compression, and elastic unloading in shear, with paths governed by accumulated plastic strain at the interface level. Van Zijl [57] further refined the multi-surface formulation by adding a dilatancy coefficient to better capture the volumetric uplift during shear sliding. The results showed that a zero dilation angle is a conservative assumption that may underestimate the shear capacity of masonry walls, depending on the boundary conditions.

Chaimoon and Attard [58] developed a simplified micromodelling framework for walls subjected to combined shear and compression, in which brick units are



meshed with constant-strain triangular elements with side nodes to host joint kinematics, while mortar joints and potential unit–unit contacts are represented by zero-thickness interfaces. Macorini and Izzuddin [48] propose a block-based modelling strategy in a 3D arrangement, accounting for the brick arrangement in-plane and through-thickness of the wall panel. Brick units are 3D solids, and unit–mortar interfaces are represented by 16-node zero-thickness interfaces with co-rotational kinematics and a multi-surface elastoplastic law. The approach captures both material and geometric nonlinearities, enabling the simulation of in-plane and out-of-plane responses, as well as damage-induced anisotropy.

A recent development on interface-based models is by Nie *et al.* [49], which was also formulated using the multi-surface damage-plasticity concept. The plasticity stage employs a smooth hyperbolic surface for tension-shear and a compression cap with hardening for shear-compression behaviour, integrated into the effective stress space via an implicit return-mapping scheme. Numerical robustness is enhanced by separating plasticity and damage updates and using an adaptive sub-stepping scheme.

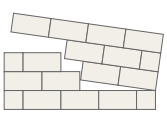
Textured joint models

Also considered within the block-based modelling strategy is the approach of Ali and Page [59], who proposed a modelling strategy using nonlinear elements in an FEM framework. In this approach, the unit-mortar bond is not represented by an additional interface with independent kinematics. Instead, the bed joints are modelled by special link elements whose normal-shear strength envelope, calibrated from tests, governs bond failure, so that tensile and shear degradation of the joint effectively captures loss of adhesion between brick and mortar. Ali and Page [59] developed an early FEM micro-model in which units and mortar layers are discretised separately with nonlinear continuum elements. A stress-based failure criterion triggers damage initiation and propagation, while post-peak behaviour is captured via a smeared-crack formulation.

Petracca *et al.* [52] (Figure 2.4B) adopted a similar approach, where the unit blocks are modelled as deformable finite elements, and the mortar joints are represented by finite-thickness joint elements with their own constitutive response. The proposed micro-model meshes both bricks and mortar joints with continuum elements and employs a tension–compression damage formulation, refined to accurately capture nonlinear shear behaviour and to regulate dilatancy. Serpieri *et al.* [53] developed a textured model formulated within a multiplane cohesive-zone framework that accounts for mixed-mode decohesion, sliding, and finite dilatancy due to asperity interlocking.

Extended-FEM models

Another approach, following the block-based modelling strategy, was proposed by Abdulla *et al.* [60] (Figure 2.4C), where a combination of a constitutive model for the masonry joints and the extended finite element method (XFEM) for the masonry units was used to model the masonry wall panel. The XFEM was used to capture crack initiation and propagation in the masonry units without *a priori* definition of the crack location. This concentrates nonlinearity where it physically occurs, yielding realistic strength, diagonal failure patterns, and post-peak decay with modest computational cost. The use of XFEM in the masonry structure analysis focused on masonry-infilled RC



frames, where the interaction between the frame and the masonry infill is critical to capture the overall structural response, see [61, 62]. XFEM is used to simulate cracking and compressive failure in the brick units, while the mortar joints and interactions between the RC frame and masonry are modelled using interface elements.

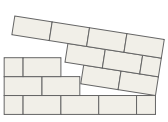
Contact-based models

Contact-based approaches form one family within the broader *discontinuum*-based modelling strategies. They have gained traction in masonry because they offer robust performance under conditions involving large displacements, block separation, and sliding. Within these approaches, discontinuities are modelled explicitly between discrete blocks, and interactions are enforced through contact laws (penalty, complementarity, or set-valued formulations). This distinguishes them from FEM-based discontinuum approaches, in which discontinuities are represented through cohesive interface elements embedded within a continuum framework (e.g., LS-DYNA implementations with cohesive surface contacts [63, 64]).

Three prominent families are commonly distinguished: the Distinct Element Method (DEM), which adopts soft-contact (penalty or augmented-Lagrangian) laws with normal/tangential springs and is typically advanced by explicit time integration [65]; Non-Smooth Contact Dynamics (NSCD), which uses hard-contact set-valued laws and an implicit time-stepping scheme that solves a complementarity problem for contact impulses [66]; and the Applied Element Method [67, 68], which is a rigid body model with springs connecting adjacent elements to represent both material deformability and joint behaviour, solved via an implicit time integration scheme.

Despite differences in enforcement and kinematics, these methods share a workflow of explicit block tessellation, contact detection/update, and interface traction laws in the normal and tangential directions. Contemporary formulations often enrich frictional contact with cohesive–damage or elastoplastic behaviour and fracture-energy regularisation, enabling mixed-mode softening and credible post-peak response.

Two representative applications illustrate the range. First, a coupled tension-shear and compression–shear contact law proposed by Pulatsu [50] with rigid blocks and a few embedded crack planes can reproduce the Vermeltfoort wall's force–displacement curve and stepped diagonal failure while retaining efficiency (Figure 2.4D). Second, a bonded-block DEM by Lemos and Sarhosis [51], in which mortar joints and intra-unit cracking are represented by a dense network of initially bonded discontinuities governed by cohesive–frictional softening, allows crack paths to develop through multiple potential planes within each unit, albeit at a higher computational cost. Notably, the simpler approach by Lotfi and Shing [47] with a single predefined plane at mid-length remains empirically well supported, since the majority of unit cracks in masonry walls typically localise near the brick mid-length. These examples illustrate the central trade-off between kinematic richness and crack-path freedom on one side, and computational expense on the other. A detailed methodological overview of the discontinuum strategies follows in Section 2.3.



Rigid-block limit analysis models

Rigid-block limit-analysis models treat masonry as an assemblage of undeformable blocks linked by unilateral/frictional interfaces and assess ultimate capacity via the static and kinematic theorems of plasticity. Under Heyman-type assumptions (infinite compressive strength, no tension, and sliding either precluded or bounded by Coulomb friction), collapse is obtained by solving for an admissible thrust field (lower bound) or a compatible mechanism (upper bound) that minimises the load factor subject to equilibrium and joint yield constraints.

The assumptions given by Heyman are translated into rigid-block models as Rigid Block Equilibrium (RBE) [69]. In this approach, the limiting load factor is maximised subject to the equilibrium equations of each block and the frictional constraints at the interfaces. The method was first developed without frictional constraints and later extended to account for Coulomb friction at the interfaces. The RBE method was then refined by Whiting *et al.* [70], who reformulated the equilibrium equations as a quadratic programming problem, which streamlines the implementation for the design, analysis, and optimisation of masonry structures. However, RBE struggles with complex assemblies due to its reliance on force-based equilibrium equations.

Kao *et al.* [71] addressed this issue by introducing Coupled Rigid Analysis (CRA), where both force- and displacement-based equilibrium equations are employed in a penalty formulation of a nonlinear programming problem. Iannuzzo *et al.* [72] address the limitations of RBE through the energy-based formulations, termed Piecewise Rigid Displacement (PRD). In PRD, the static and kinematic theorems are unified through a dual linear programming formulation, where the minimum of the complementary energy is discretised to find admissible internal stress states that are compatible with the deformed shape obtained through the primal problem. The rigid-block limit-analysis approach was also implemented with non-associative Coulomb friction at the interfaces by Gilbert *et al.* [73], in which the problem was cast as a sequence of linear programs via a piecewise-linear yield surface. Further applications of this method can be seen in [74–76].

As summarised in Table 2.1, block-based modelling strategies offer a powerful framework for simulating the complex behaviour of masonry structures by explicitly representing the material's discrete nature. These approaches effectively capture the initiation and propagation of cracks, the interaction between masonry units and mortar joints, and the overall structural response under various loading conditions. In compression, however, the response is often treated in a homogenised sense at the masonry scale, so that the constitutive parameters are calibrated for the composite assemblage rather than for the individual constituents, which reinforces the need for reliable experimental characterisation of masonry as a whole. At the same time, block-based models present challenges, including the need for detailed material characterisation, computational intensity for large-scale structures, and sensitivity to mesh discretisation and interface parameter calibration.

2.2.2. Continuum-based modelling strategy

Continuum-based modelling strategies treat masonry as a homogeneous deformable medium, employing principles of continuum mechanics to describe the overall behaviour of the structure. Damage and inelastic processes are represented as smeared strains

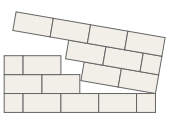
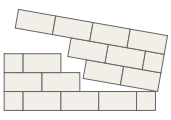


Table 2.1. Summary of the advantages and limitations of block-based modelling strategies for masonry structures

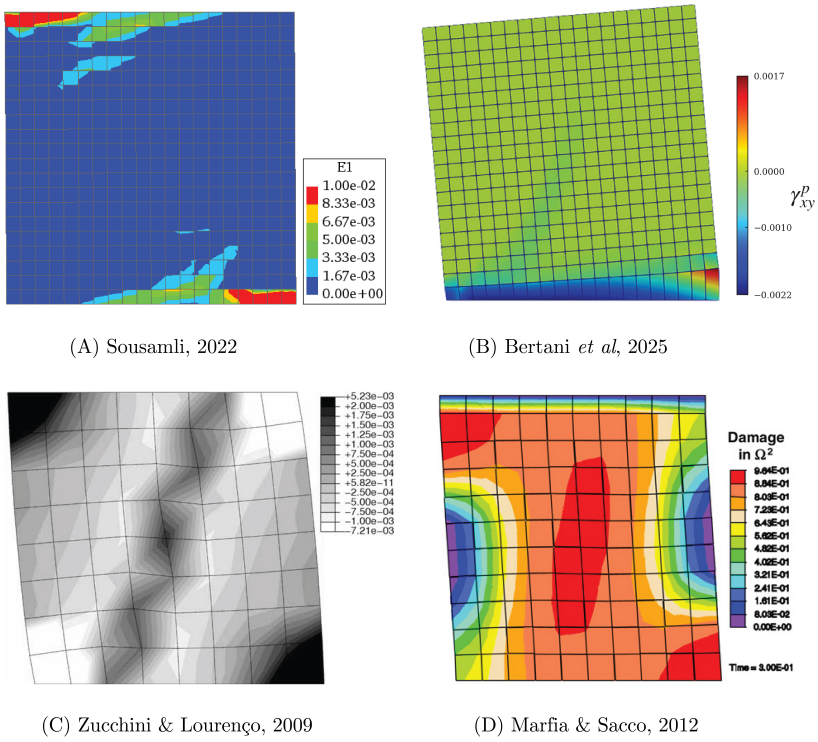
Advantages	Limitations
+ Explicit resolution of brick units and mortar joints; discontinuities are captured directly.	– High computational cost for large or 3D models with many blocks and joints.
+ Material parameters can be identified from standard small-scale tests (e.g., triplet, wedge-splitting, compression).	– Joint–unit interaction laws are often uncertain and require calibration and sensitivity analysis.
+ Failure modes such as rocking, sliding, separation, crushing, and unit splitting emerge with minimal post-processing and interpretation.	– Results can be sensitive to mesh/discretisation, contact enforcement, and softening parameter calibration.
+ Masonry anisotropy is represented through directional joint properties and contact/interface laws.	– Model set-up is labour-intensive (geometry discretisation, contact definitions, parameter assignment).
+ Well-suited to simulating failure mechanisms, large displacements/rotations, and post-peak behaviour.	– Dynamic/cyclic analyses require careful damping and time-integration choices to avoid numerical artefacts and ensure stability.

within the elements, with crack opening and joint sliding captured implicitly through the constitutive response of the continuum. This modelling strategy is particularly advantageous compared to the block-based strategy in terms of computational efficiency, as it avoids the need to explicitly model individual blocks and joints, making it suitable for large-scale structures, parametric studies, and assessments where global response (e.g., capacity curves, drift limits) is of primary interest rather than unit-by-unit failure kinematics. However, continuum-based models may struggle to define appropriate constitutive laws that consistently capture the heterogeneous nature of masonry constituents (e.g., orthotropic behaviour, micro-cracking, and anisotropy arising from the arrangement of bricks and mortar joints).

To that end, the mechanical complexities of masonry can be addressed through direct approaches, in which constitutive laws are calibrated to phenomenologically reproduce the overall behaviour of masonry, or through homogenisation techniques that derive effective material properties at the structural level from the micromechanical characteristics of masonry constituents. The homogenisation process often relies on



refined micro-models to simulate the behaviour of representative volume elements (RVEs) of masonry, from which effective properties are extracted for use in macro-scale continuum models. Figure 2.5 illustrates how continuum formulations reproduce the Vermeltfoort *et al.* [54] failure mode under $\sigma_0 = 0.3$ MPa without explicitly modelling individual units and joints. Figure 2.5A–B exemplify direct macro-constitutive approaches, whereas Figure 2.5C–D depict homogenisation-based continua.



(A) Sousamli, 2022 (B) Bertani *et al*, 2025

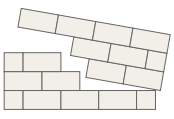
(C) Zucchini & Lourenço, 2009 (D) Marfia & Sacco, 2012

Figure 2.5. Examples of continuum-based modelling strategies for masonry structures validating the same experimental test by Vermeltfoort *et al.* [54]: (A) and (B) for the direct approaches, (C) and (D) for the homogenised approaches.

Direct approaches

Direct continuum models are a sub-family of continuum modelling strategies in which the constitutive behaviour of masonry is defined at the macro-scale without explicit reference to the material's microstructure. These models derive their material parameters through material-level calibration rather than homogenisation techniques.

One of the first families of direct approaches is the assumption of masonry as a no-tension material, pioneered by Maier and Nappi [77], which was then followed by other implementations within the FEM framework (see, among others, [78–81]). This simplification follows the assumption of Heyman [41] that the masonry constituents are



incapable of carrying tensile stress but infinitely strong in compression. This assumption is conservative but valuable for the preliminary assessment of masonry structures, particularly for the compression-dominated typologies such as arches and vaults.

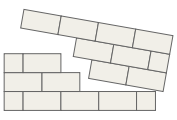
Since the post-peak behaviour is key to the vulnerability assessment of real-world case studies or scenarios, the development of more sophisticated direct approaches has focused on continuum nonlinear constitutive laws based on fracture mechanics (smeared-crack approaches), plasticity theories, damage mechanics, or combined damage-plasticity frameworks. Several frameworks that were initially proposed for the numerical analysis of concrete structures have been adapted to model masonry structures, given the similarities in their quasi-brittle behaviour [82–85].

The problem with these smeared crack and damage-plasticity models is that they often assume initially isotropic behaviour, limiting the ability to capture the anisotropic and heterogeneous nature of masonry due to the arrangement of bricks and mortar joints. Their strain-softening response further requires regularisation, typically through a crack band (or crush band) approach [86] in which a characteristic length is linked to the element size, so that mesh-objective energy dissipation depends on careful control of mesh refinement. The predicted crack patterns may also exhibit mesh-directional bias, with cracks tending to align with the mesh axes.

This problem was addressed by Lotfi and Shing [87], who evaluated the smeared crack models with fixed and (coaxial and non-coaxial) rotating crack assumptions. Their findings showed that the flexural response of masonry panels can be accurately reproduced with the smeared crack models, while the brittle shear-dominated behaviour was overestimated due to the limitation of the smeared crack model, where crack opening is modelled by the displacement field of the continuum, leading to the diagonal crack that has to be associated with the diagonal compressive strain, which results in increased shear resistance after cracking.

A major step toward representing masonry's inherent orthotropy was the anisotropic plasticity model of Lourenço *et al.* [88], which couples a Rankine tensile surface with a Hill-type compressive criterion. The framework reproduced mixed-mode cracking and shear–compression interactions in validation studies [24, 88], though it tended to overpredict capacity in crushing-dominated regimes —- underscoring the need for a more nuanced treatment of compressive inelasticity and localisation. Expanding on this research, Pelà et al. [26, 89] proposed an orthotropic damage formulation that maps anisotropic field tensors to an auxiliary isotropic space for constitutive updates, subsequently returning the response to the physical configuration. This mapping maintains direction-dependent stiffness and strength and supports efficient integration schemes, providing a flexible alternative to exclusively plastic orthotropy in continuum modelling of masonry.

A parallel family in continuum modelling is provided by the total strain-based crack models originally developed by Feenstra and de Borst [90, 91] for concrete. These models express the constitutive response directly as a function of the total strain, with damage activated when the strain in the relevant direction exceeds a softening threshold. Two variants are commonly distinguished. In the fixed crack version, the crack orientation is set at the moment of crack initiation and remains fixed thereafter. In the rotating-crack version, the crack direction co-rotates with the principal strain directions, avoiding the



need for shear retention factors at the cost of losing memory of the initial crack direction and producing a non-physical response under cyclic or non-proportional loading. Both variants are implemented in commercial FEM packages such as DIANA FEA [92].

For masonry, the total strain framework has been extended by Sousamli *et al.* [93] (Figure 2.5A) through a total-strain rotating crack (TSRC) formulation targeting the cyclic nonlinear response of unreinforced brick masonry. The formulation incorporates orthotropic behaviour, an internal iterative algorithm for shear failure, and unloading-reloading branches that depend on the cracking angle at onset, with secant unloading adopted for flexure-induced cracks and elastic unloading for shear- or compression-induced cracks. These features address two well-known limitations of the basic rotating-crack approach for masonry, namely the misestimation of hysteretic behaviour and the diffusion of cracks across multiple elements.

The most recent development in the use of direct approaches in continuum-based modelling strategies is the work of Bertani *et al.* [94] (Figure 2.5B), where a plastic-damage constitutive model for masonry is proposed. In this work, a single-surface multi-failure strength domain that encloses seven mechanisms (crushing, joint-horizontal/vertical/diagonal, and mixed joint-unit failures) is implemented in an elasto-plastic framework. Failure-mode weights obtained via a smooth RealSoftMax intersection identify the active mechanism(s) at each Gauss point, while ad-hoc non-associated flow rules compute the corresponding plastic-strain increments.

Homogenised approach

The continuum models for masonry structures based on homogenised and multiscale approaches constitute a class of modelling strategies in which mechanical properties and the heterogeneous nature of the masonry constituents are addressed at the cell level (representative volume element, RVE) to derive effective material properties for use in structural-scale continuum models. This approach yields a structural-level continuum that averages the microstructural behaviour of the masonry via homogenisation techniques. Selecting the appropriate RVE is crucial, as it should represent the masonry's microstructure and capture the essential features of the brick-and-mortar arrangement.

To this end, there are three main families of homogenisation techniques commonly used in masonry analysis:

(i) *A priori* homogenisation approaches, where mechanical properties of the masonry constituents are first derived through a homogenisation process, and then introduced to the structural-level continuum model.

(ii) Step-by-step multi-scale approaches, where the structural-level continuum model is coupled with a micro-scale RVE model that resolves the microstructural behaviour of masonry constituents at each integration point.

(iii) Adaptive multi-scale approaches, where the material-scale model is inserted adaptively, and resolved only in regions where microstructural effects are significant (e.g., high stress gradients, crack propagation zones).

In both step-by-step (ii) and adaptive (iii) multi-scale approaches, the micro-scale nonlinear response under tension, shear, and compression, as well as cyclic degradation

and hysteretic energy dissipation, is captured through the constitutive laws assigned to the bricks and joints within the RVE. These laws typically combine interface or contact formulations with softening cohesive laws and damage or damage-plasticity descriptions for cyclic behaviour. Because the macro response depends on the loading history at each integration point, history variables (damage indicators, plastic strains, kinematic variables) must be stored at the RVE level for every macro-scale integration point, making cyclic analyses substantially more memory- and CPU-intensive than monotonic ones. This computational cost is the principal practical limitation of multi-scale approaches for masonry under seismic loading.

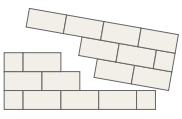
In the *a priori* homogenisation approaches, the effective properties of masonry are derived from the microstructural characteristics of the RVE, which are then used to define the constitutive behaviour of the structural-level continuum model. The derivation of the homogenised constitutive laws is typically based on analytical closed-form solutions, semi-analytical methods, or within the framework of a generalised Cosserat continuum theory. Pietruszczak and Niu [95] pioneered the development of three-dimensional mathematical formulations for describing the averaged properties of masonry structures through homogenisation. Anthoine [96] further contributed by heuristically deriving the in-plane characteristics of masonry through a homogenisation process for periodic media before applying it to masonry walls under shear loading. Further development of the homogenised elastic properties for masonry structures can be found in [97–101].

Zucchini and Lourenço [102] proposed a micromechanical homogenisation scheme for stretcher-bond masonry that introduces additional internal deformation mechanisms representative of the staggered unit-mortar arrangement. The periodic unit cell is idealised through simple kinematic assumptions, yielding the macroscopic orthotropic elastic stiffness as an explicit function of the constituent properties. The periodic unit cell is idealised using simple but judicious kinematic assumptions and is used to derive the macroscopic orthotropic elastic stiffness as an explicit function of the constituent properties.

Regarding the step-by-step multi-scale approaches, the structural-level continuum model is coupled with a micro-scale RVE model that resolves the microstructural behaviour of masonry constituents at each integration point. The approaches included in this category differ based on the configuration of masonry (periodic or nonperiodic), chosen macro-scale continuum model (classical Cauchy or generalised Cosserat), constitutive model for the brick units (linear or nonlinear), and the mortar joints (interface or finite-thickness joint elements), and the modelling technique used to derive the effective properties at the material level.

One of the first multi-scale models was the work of Gambarotta and Lagomarsino [44], who used the interface model for mortar joints [103] with damage and friction capabilities in the first step and applied the homogenisation technique to formulate the continuum damage model. This model was then improved by Calderini and Lagomarsino [104] by incorporating a more refined damage model that accounts for the specific behaviour of old masonry materials, using energy-based evolution laws for the damage model and a non-associated flow rule for the Coulomb friction.

Zucchini and Lourenço [105] (Figure 2.5C) later extended this scheme to the nonlinear range. They replaced the quarter cell under normal load of their earlier work with a



full periodic cell, and coupled its elastic deformation mechanisms with damage and plasticity to describe post-peak softening.

Sacco [106] proposed a homogenisation process based on the Transformation Field Analysis (TFA). The procedure is sequential: masonry units are modelled as linearly elastic, while mortar joints follow a nonlinear law that explicitly couples damage and friction. The finite-element framework then assembles the macroscopic response by superposition. A key advantage of the TFA formulation is efficiency: micromechanical FE analyses are required only once to determine the overall elastic moduli and associated localisation tensors, after which the nonlinear evolution is tracked at the macroscale. Marfia and Sacco [107] further extended the method to nonuniform eigenstrain and nonlinear block behaviour (Figure 2.5D).

Despite their advantages, first-order computational homogenisation (FE^2) methods have two significant drawbacks. First, they enforce uniform macroscopic fields within each RVE, an assumption that fails in regions with strong deformation gradients (e.g., near boundaries or during localisation). Second, once softening is incorporated into the constitutive law, the classical Cauchy continuum, lacking an intrinsic length scale, renders the boundary-value problem ill-posed, leading to spurious localisation and mesh-dependent results.

The problems were tackled by Massart *et al.* [108] using an enhanced multi-scale model that utilised a nonlocal, isotropic damage model for both the units and the mortar joints. The localisation of macroscopic damage was addressed using a finite-width damage band model within the macroscopic description. The enhanced model allows for the consideration of localised damage at the material (microscopic) level. The problems were also addressed by using Cosserat continuum models at the structural scale, as demonstrated by several authors [109–113].

The adaptive multi-scale approach is also used to tackle the aforementioned limitations [114–117]. In these approaches, the structure is modelled with a first-order homogenised continuum until an indicator of damage initiation or propagation is met. The flagged subdomain is then replaced by an explicit heterogeneous, material-scale description (e.g., due to damage), enabling accurate capture of highly localised deformation while avoiding the mesh dependence inherent to first-order formulations.

As summarised in Table 2.2, continuum models idealise masonry as a homogeneous deformable medium, enabling efficient finite element analyses that can scale to large structures, support broad parametric studies, and leverage mature nonlinear solution procedures. Their flexibility accommodates anisotropy (via homogenised RVE-based properties), enables mesh-objective softening, and allows practical calibration against global responses or modal data, provided suitable regularisation (nonlocal/gradient or crack-band) is applied. However, these benefits are accompanied by notable limitations: damage and cracks are typically smeared into bands and therefore require careful interpretation; classical Cauchy continua become ill-posed without appropriate regularisation (nonlocal/gradient or crack-band), and the definition of crack width is non-trivial; enriched kinematics (such as layered, Cosserat, or higher-order continua) are often necessary to capture out-of-plane mechanisms, wythe-to-wythe delamination, and unit rocking. Ultimately, the choice between modelling strategies should balance physical realism, computational efficiency, and the intended engineering application.

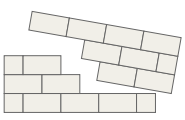
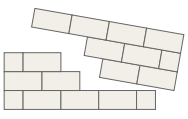


Table 2.2. Summary of the advantages and limitations of continuum modelling strategies for masonry structures

Advantages	Limitations
+ Computationally efficient for large-scale analyses, parametric studies, and performance-based assessments.	– Few higher-order continuum models demonstrate robust performance under cyclic or non-proportional loading, partly due to the complexity of carrying history variables across nested scales.
+ Robust element libraries and mature nonlinear solution procedures are widely available in most FE platforms.	– Joint failure (opening/sliding), unit rocking, and block interlocking are represented indirectly; crack paths are "smeared", which requires further interpretation.
+ Nonlocal/gradient or crack-band formulations can readily enforce mesh-objective softening and localisation.	– The definition of crack width in smeared-crack formulations is non-trivial and strongly mesh-dependent. Crack-band regularisation is typically required to obtain mesh-objective estimates.
+ Anisotropic properties can be derived from RVEs, transferring micro-calibrated behaviour to the structural scale while retaining macro efficiency.	– Material characterisation typically relies on larger-scale tests (e.g., wallet compression, diagonal compression) to calibrate homogenised continuum parameters.
+ Parameter calibration against global response measures (e.g., force-displacement, modal properties) is tractable and relatively stable.	– Capturing through-thickness delamination or wythe-to-wythe interaction may require enriched kinematics.
	– FE^2/on-the-fly homogenisation improves fidelity but can approach the cost of discontinuum models unless surrogate RVEs or reduced bases are used.



2.2.3. Geometry-based models

The geometry-based modelling strategy is a category that assesses structural equilibrium using simplified lower-bound solutions based on static or kinematic theorems. This category idealises masonry as an assemblage of rigid bodies with unilateral (no-tension) interactions. In their classical form, these approaches are rooted in Heyman's rigid no-tension framework (RNT) [41] and evaluate stability by enforcing equilibrium and compatibility of compression-only states in masonry constituents. The only essential inputs are the structural geometry and the applied actions (typically self-weight, with optional live or horizontal loads). Structural assessment is then performed through graphic statics (thrust line or network constructions) or kinematic limit analysis.

In geometry-based models, the feasibility of purely static assessment rests on Heyman's Safe Theorem [41]: *if there exists a compression-only stress state (equivalently, a thrust line in 2D or a thrust network in 3D) that is in equilibrium with the applied loads, and which remains everywhere within the masonry thickness, and neither sliding nor crushing can occur, then collapse cannot take place for that load level.* This provides a sufficient (lower-bound) condition on the collapse load under the Heyman idealisation. Under this idealisation, the following assumptions are adopted:

(i) compressive strength of masonry is infinite

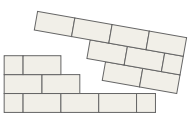
(ii) masonry has no tensile strength

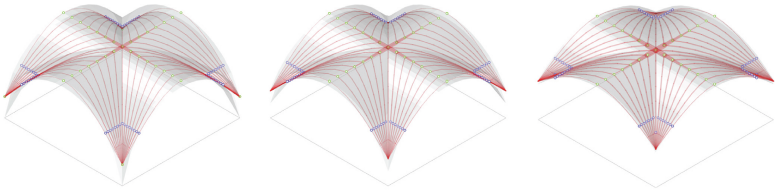
(iii) no sliding can occur between elements of the masonry structure

These hypotheses align well with historic masonry structures: service stress levels typically lie far below compressive strength *(i)*, weathered or weak mortars render interfaces effectively no-tension *(ii)*, and traditional stereotomy, interlocking, and buttressing are expressly arranged to mobilise compression and suppress sliding *(iii)*. Within this setting, verifying that a thrust line/network remains within the thickness becomes a geometric check that provides a rigorous lower bound on safety, without recourse to material constitutive parameters beyond the no-tension/no-sliding idealisation. However, drawing and finding the appropriate thrust line (or thrust network) for complex, non-prismatic or three-dimensional masonry geometries is not trivial and often requires numerical assistance. Modern implementations translate the geometric problem into an optimisation or limit-analysis formulation (e.g., thrust-network or kinematic limit analysis), enabling automated searches for admissible compression fields that satisfy equilibrium, boundary conditions and the within-thickness requirement [41, 118]. Examples of these implementations are shown in Figure 2.6.

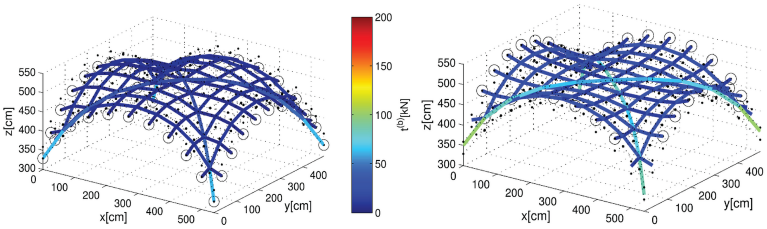
Algebraic formulations for form-finding and automated drawing of force diagrams were proposed by Van Mele and Block [119], which were then extended by Maia Avelino *et al.* [120] with a user-friendly interactive modification to the force diagrams. This formulation has been coupled with optimisation algorithms to find specific solutions that satisfy the geometric constraints of the masonry structure, as demonstrated by Marmo and Rosati [121] and Nanayakkara *et al.* [122].

In order to address 3D problems such as vaulted systems, the thrust line method needs to be extended to the thrust network method. O'Dwyer [123] pioneered the development

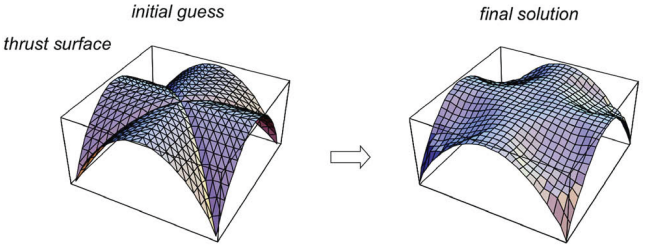




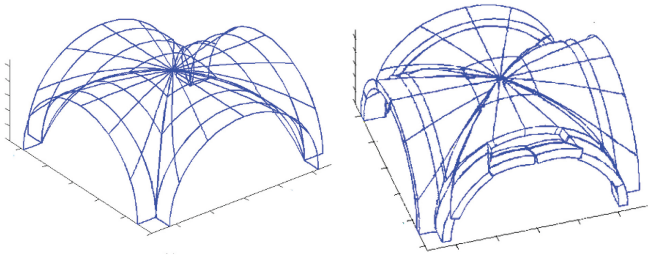
(A) Maia Avelino, 2021



(B) Marmo & Rosati, 2017



(C) Fraternali, 2009



(D) Chiozi *et al.*, 2017

Figure 2.6. Geometry-based models for masonry analysis

of the thrust network method for the analysis of vaulted systems, which was then extended by Block and Ochsendorf [124] with the introduction of a graphical method to generate the thrust network for complex vaulted geometries, termed the Thrust Network Analysis (TNA). The TNA method, based on the principles of graphic statics and thrust lines, finds possible funicular solutions for vaulted systems under self-weight loading by constructing a network of compressive forces that satisfy equilibrium and remain within the geometry of the vault. This has been the basis for several implementations of the thrust network method for vaulted systems, such as in the work of Block [125], Rippmann

et al. [126], and Maia Avelino *et al.* [127] (Figure 2.6A). This approach was also extended by Nodargi and Bisegna [128], who formulated the problem as a linear program in which the vertical positions of discrete thrust nodes are expressed in terms of bending moments along the edges of a planar network.

Block and Lachauer [129] reformulated the method as a single coupled optimisation problem, with a fixed-form diagram and independent edges. Marmo and Rosati [121] (Figure 2.6B) later revisited the TNA formulation, discarded the dual grid, and extended it to structures subjected to horizontal forces.

Fraternali *et al.* [130, 131] proposed a membrane-based approach where the admissible state under the Heyman idealisation is found in the compressive membranes within the structural geometry. In this context, a masonry vault is defined as a membrane structure that can carry only compressive forces, and the equilibrium is solved considering the potential stress (Airy) functions to describe the stress distribution within the membrane (Figure 2.6C). The stress within the membrane is related to the curvature of the Airy function, and the no-tension constraint is ensured by enforcing the positivity of the Airy function's Laplacian. Different approaches have been proposed to solve the second-order differential equation within the membrane, see [131–133].

Kinematic limit analysis is another geometry-based approach for masonry structures, in which the collapse load is estimated by considering possible failure mechanisms. Milani [45] proposed a discontinuous limit analysis with a sequential linear programming (UBS-LP) mesh adaptation sequence to estimate the actual failure mechanism of masonry structures. Chiozzi *et al.* [134] proposed a genetic algorithm for the limit analysis of masonry vaults, where a non-uniform rational B-spline (NURBS) mesh is idealised as a rigid body and adjusted using the genetic algorithm to find the collapse load and failure mechanism of the vault (Figure 2.6D).

As summarised in Table 2.3, geometry-based models provide rigorous lower-bound verification under the Heyman idealisation, leveraging as-built geometry to establish funicular equilibrium states at very low computational cost with minimal reliance on material calibration. These methods are therefore suitable for preliminary stability assessments of arches, vaults, and domes, particularly in heritage contexts where uncertainty is high, and interventions should be targeted and reversible. However, since these methods do not deliver stiffness, deformation, or vibration predictions and their validity degrades with the presence of tensile cracking, frictional sliding, crushing, or load paths strongly altered by horizontal actions, they are best viewed as complementary tools within a broader structural analysis framework, which requires more detailed continuum or discontinuum models for performance-based assessments.

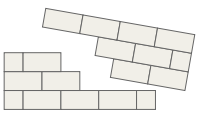
2.2.4. Macroelement modelling strategy

Macroelement modelling provides a meso-scale idealisation that bridges detailed discontinuum formulations and simplified continuum or purely geometry-based approaches. The macroelements discussed here are structural-element formulations with internal degrees of freedom and phenomenological constitutive laws, separate from the macro-blocks used in the block-based discontinuum modelling (Section 2.2.1), which retain explicit contact mechanics between discrete bodies. In this method, masonry walls are partitioned into vertical piers and horizontal spandrels at openings, with each

Table 2.3. Summary of the advantages and limitations of geometry–based modelling strategies for masonry structures

Advantages	Limitations
+ Direct geometry-to-stability workflow with minimal material input.	– Validity rests on ideal assumptions (no tension, no sliding, no crushing). High compressive stresses or low friction invalidate the safe bound.
+ Rigorous lower-bound (safe) check via admissible thrust lines/networks.	– Provides no stiffness, deflection, vibration, or serviceability information essential for performance-based assessments.
+ Very low computational cost. Scalable to large or complex geometries.	– Joint opening/rocking/sliding and unit interlock are represented only indirectly.
+ Minimal material input—-robust when properties are uncertain. Results hinge primarily on geometry and boundary conditions.	– Sensitive to geometry, thickness, supports, and load distribution. Modelling uncertainties can significantly affect results.
+ Mechanism-oriented insight that guides targeted, reversible conservation measures (e.g., ties, added buttresses).	– Out-of-plane instability and multi-wythe interaction require dedicated 3D checks.
+ Naturally extends to 3D funicular analysis (thrust-network analysis) for ribbed, groin, and composite vault geometries.	– Few geometry-based formulations explicitly account for horizontal actions (e.g., seismic or wind), which can substantially modify the thrust path and equilibrium of vaulted structures.

macroelement condensing the collective response of many units and joints into a small set of parameters and nonlinear laws. This discretisation, assembled through equilibrium and compatibility at nodal interfaces, is expressly tailored to building-scale analyses of masonry structures with pier-spandrel topology, while remaining computationally efficient. It preserves the primary geometric drivers of behaviour (panel slenderness, opening layout, wall thickness, and boundary conditions). The approach is less directly applicable to other large-scale masonry typologies such as arch bridges, quay walls, or gravity retaining structures, which lack the pier-spandrel decomposition and typically require alternative idealisations.



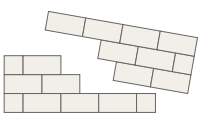
The discretisation of masonry buildings into piers and spandrels needs to be defined *a priori*, typically based on geometric features (openings, wall intersections) and expected failure modes. Piers are masonry components that resist vertical loads and bending moments, while spandrels are horizontal elements that transfer loads between piers and resist lateral forces. This identification might be trivial in regular masonry buildings, but it can be challenging in complex geometries or irregular layouts. In addition, the discretisation must remain compatible with both in-plane and out-of-plane failure mechanisms, which may interact and localise differently along the wall's height and thickness. This further complicates the definition of the representative macroelements. Examples of macroelement modelling strategies are shown in Figure 2.7.

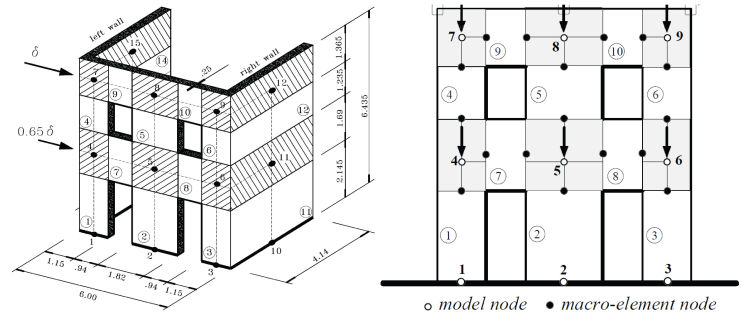
The most common approach is to idealise the piers and spandrels as beam or frame elements (termed the Equivalent Frame Model, EFM) (Figure 2.7A-B), in which the nonlinear behaviour of each macroelement is defined by moment-curvature and axial force-deformation relationships derived from experimental tests or detailed micro-models. A more recent approach is to use spring-based macroelements (Figure 2.7C-D), in which nonlinear behaviour is captured by a series of springs representing the macroelement's axial, shear, and bending responses.

The first EFM model with regard to the analysis of masonry structures was proposed by Tomaževič [135] with the so-called POR method. This program considers the storey failure mechanism based on piers with diagonal shear failure after earthquake loading. The method assumes rigid spandrels, limiting its applicability to masonry buildings with strong piers and weak spandrels. Brencich *et al.* [136] (Figure 2.7A) proposed a 3D macroelement model for seismic analysis of masonry buildings that assembles shear walls (modelled as piers and spandrels) and flexible diaphragms into a reduced, nonlinear system solved via an incremental–iterative scheme. The macroelement comprises two-node beam elements that concentrate axial/bending effects in elastic end layers and inelastic behaviour in a central panel governed by coupled frictional sliding and a damage variable to capture stiffness degradation, peak strength, and post-peak softening under monotonic and cyclic loads. The approach enforces compatibility at wall edges and diaphragm connections, allowing transitions between overturning and shear mechanisms and reproducing hysteretic energy dissipation.

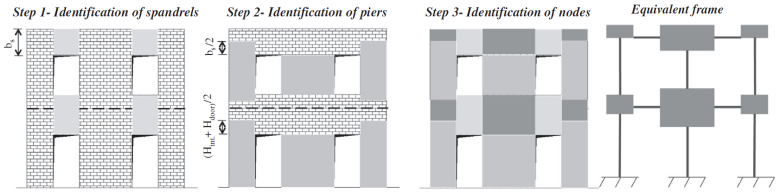
Addessi *et al.* [137] advanced the EFM framework by proposing a force-based macroelement model for in-plane, monotonic analysis of masonry panels and walls with openings. The element is a two-node Timoshenko beam with a central flexible part governed by a no-tension nonlinear elastic constitutive law, and a lumped nonlinear shear hinge to capture diagonal-shear or sliding failures. The work is extended in Addessi *et al.* [138], where the nonlinear elastic central part is replaced with plastic hinges at both ends of the beam element, endowed with elastic-plastic evolution (Kuhn-Tucker consistency), and implemented in a displacement-based global solver for building-scale analysis.

Another influential work in the field of EFM is by Lagomarsino *et al.* [46] (Figure 2.7B), in which the software TREMURI is presented. In this work, walls are discretised into piers and spandrels modelled as nonlinear beam elements with lumped plasticity, adopting bilinear elastic-perfectly plastic laws with strength cut-off and drift-based ultimate limits to capture flexural and shear mechanisms. The software assembles the members into

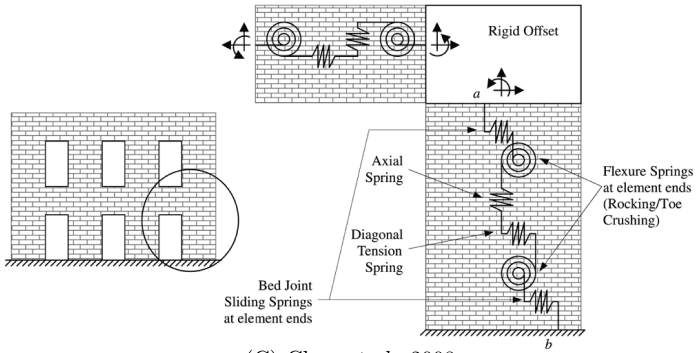




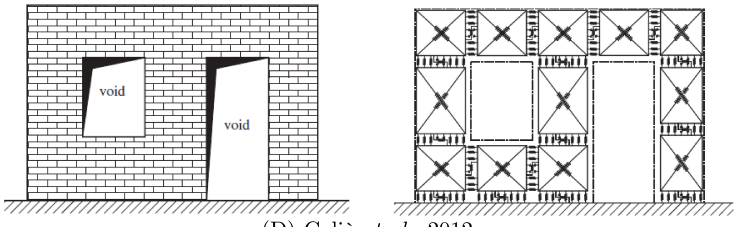
(A) Brencich *et al.*, 1998



(B) Lagomarsino *et al.*, 2013



(C) Chen *et al.*, 2008



(D) Caliò *et al.*, 2012

Figure 2.7. Examples of macroelement modelling strategies for masonry structures: (A) and (B) Equivalent Frame Model (EFM), (C) and (D) Spring-based macroelement models

full 3D models that also account for floor/roof diaphragm connectivity and mixed masonry-RC components, enabling computationally robust pushover analyses. The software was refined in Cattari and Lagomarsino [139] to include nonlinear constitutive laws through a piecewise-linear approach. This refinement allows for a more accurate representation of the inelastic behaviour of masonry structures under seismic loading.

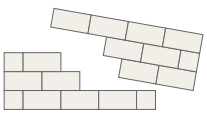
A more recent contribution in the field of EFM macroelement models is the work of Vanin *et al.* [140], where a three-node 3D macroelement is proposed and implemented in the OpenSees framework. This work unifies the in-plane and out-of-plane response of masonry within a single element at a modest computational cost. It enforces equilibrium at three flexural sections and lumps the shear response in a mid-height interface whose strength is coupled to the axial load. The shear behaviour is defined using either the cohesive/frictional interface model by Alfano and Sacco [141] or the shear model by Gambarotta and Lagomarsino [103] used in Penna *et al.* [142].

Spring-based macroelement models idealise the pier or spandrel as a series of springs that represent the axial, shear, and bending responses of the macroelement. Chen *et al.* [143] (Figure 2.7C) proposed a macroelement model that assembles nonlinear springs (one axial, one shear, and two rotational) in series to capture axial load effects, bed-joint sliding, diagonal tension, rocking and toe-crushing. Two shear springs were added to pier elements at the top and bottom of the element to simulate shear sliding.

Gambarotta and Lagomarsino [144] and Brencich and Lagomarsino [145] developed a two-node element to simulate the in-plane cyclic mechanism of a masonry panel with separate springs for shear and coupled axial-flexural behaviour. Penna *et al.* [142] formalise the TREMURI two-node macroelement for cyclic in-plane analysis of masonry panels, condensing the wall behaviour into end interfaces in series with a central shear panel to reproduce flexure/rocking and shear sliding mechanisms. The model also incorporates nonlinear behaviour when rocking governs to account for finite compressive strength.

Caliò *et al.* [146] (Figure 2.7D) proposed a macroelement with piers and spandrels idealised through equivalent discrete elements made of nonlinear springs for in-plane analysis of masonry buildings. The panel element is discretised into four edges connected by hinges and two diagonal nonlinear springs. This has been used in several works [147–149] to simulate the masonry material and structural responses.

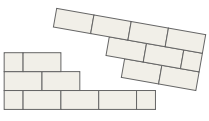
In summary, equivalent-frame macroelement model idealisation offers a pragmatic compromise between geometric parsimony and behavioural fidelity at the building scale. As summarised in Table 2.4, the principal strengths lie in the computational efficiency, accuracy in global behaviour prediction, mechanism-oriented constitutive laws, and transparent parameterisation. These are the attributes that make it suitable for nonlinear static and dynamic assessments of walls with three-dimensional assemblies. However, these benefits come with limitations: results depend on the chosen pier/spandrel partition and node constraints; local phenomena (joint-level sliding paths, crack patterns, stress concentrations) are not resolved; out-of-plane mechanisms are often neglected or require separate elements; constitutive choices for cyclic degradation and pinching may need calibration against detailed tests or micro-models; and serviceability outputs (stiffness, floor drifts under moderate loading, vibration) and local damage states are less reliable than global strength/ductility predictions. Consequently, while macroelements



are an effective workhorse for code-oriented evaluation and scenario analyses, cases dominated by localised shear transfer, complex spandrel arching, or stability under softening may warrant complementary block-based or continuum checks.

Table 2.4. Summary of the advantages and limitations of macroelement modelling strategies for masonry structures

Advantages	Limitations
+ Predicts the strength and ductility of in-plane mechanisms in individual components (piers and spandrels).	– Results depend on the chosen equivalent-frame partition (pier/spandrel definition, rigid offsets, node constraints)
+ Meso–scale discretisation (piers-spandrels) captures dominant in-plane mechanism with minimal parameter set.	– Structural components (pier and spandrels) need to be defined *a priori*, which can be challenging in complex geometries.
+ Computationally efficient for building-scale nonlinear static and dynamic analyses.	– Limited resolution of local phenomena such as joint-level sliding paths, crack patterns/spacing, stress concentrations, and multi-wythe/leaf interaction.
+ Openings and storey-to-storey connectivity are represented directly through the pier–spandrel partition.	– Out-of-plane mechanisms and the interaction with in-plane are often neglected or require separate/add-on elements.
+ Parameters map transparently to measurable or code-calibrated quantities (axial stress, shear strength, drift limits), aiding calibration and interpretation.	– Constitutive choices for cyclic degradation and pinching are model-specific and may require calibration against detailed tests or micro-models.
+ Can include axial-shear-flexure interaction, $P-\Delta$ effects, and foundation flexibility with modest extensions	– Requires idealised representation of openings and storey-to-storey connectivity, and its extension to full 3D frames with diaphragm constraints and mixed masonry—RC components is often non-trivial and relies on significant modelling assumptions.

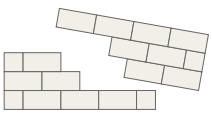


2.3. Discontinuum modelling strategies for masonry analysis

Although continuum and macroelement formulations implemented in commercial FEM platforms remain the de facto choice for practitioners owing to familiar workflows, robust solvers, and modest computational demand, their predictive envelope is intrinsically narrow. Continuum models rely on homogenised constitutive laws and smeared damage formulations that are effective for regular, wall-type geometries under predominantly in-plane actions. Still, they struggle to resolve discontinuous interface kinematics such as unit rocking, joint opening–closure, frictional sliding, re-contact, and the resulting localised crack patterns. Macroelement idealisations (e.g., pier–spandrel assemblages) further compress structural behaviour into a small set of lumped degrees of freedom. While efficient from a computational point of view, these templates presuppose a modular, largely orthogonal discretisation and therefore represent irregular stereotomy, complex openings, or three-dimensional discontinuities only through ad hoc partitioning and heavy calibration. As a result, out-of-plane instability, panel overturning, and other local mechanisms that govern URM collapse are often misrepresented or overlooked. Purely geometry-based (limit) approaches offer rigorous lower- or upper-bound assessments of capacity under compression-dominated states, but, by design, they do not capture post-peak evolution, cyclic degradation, or path-dependent dynamics. They provide collapse multipliers and admissible stress/resultant fields at incipient mechanism formation, not the subsequent softening response, re-contact events, or inertia-driven failure sequences that frequently arise in URM structures under seismic or transient loading.

These limitations collectively motivate the adoption of block-based strategies, in which interface behaviour and mechanism formation are modelled explicitly. Block-based modelling spans both interface-element formulations within finite-element frameworks (treated earlier in Section 2.2.1 as part of block-based micro-modelling) and contact-based discontinuum formulations. The present section focuses on the latter, which models masonry as an assembly of discrete blocks interacting according to contact laws. These methods, which are rooted in the distinct-element framework, perform automatic detection of evolving contacts and naturally accommodate large displacements, finite rotations, opening/closure, sliding, and separation with possible re-impact as the calculation progresses [150]. By construction, this class excludes interface-based or “textured” FEM approaches that prescribe a fixed set of potential interfaces and typically enforce contact with master–slave constraints. In addition to failing to track the rigid-body motion of individual blocks or the formation of new contacts away from predefined surfaces, such formulations often suffer from numerical stability and convergence pathologies under implicit time integration. These limitations motivate the adoption of discontinuum block-based models when the target phenomena are governed by interface kinematics and mechanism formation rather than by smeared continuum damage.

As explained in Section 2.2.1, the discontinuum modelling strategy is grouped into three main categories: (i) the Distinct Element Method (DEM), (ii) the Non-smooth Contact Dynamics Method (NSCD), (iii) the Applied Element Method (AEM). Each of these methods has its own formulation and practices, which are discussed in the following sections. Due to the disproportionate amount of work on the methods



mentioned above, methods that share the same core principles but are much less employed, such as Discontinuous Deformation Analysis (DDA) [151] and Combined Finite-Discrete Element Method (FDEM) [152], are not discussed in detail herein, but readers are referred to the work of Lemos and Bagi [153].

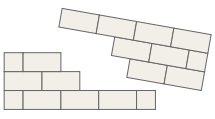
2.3.1. The Distinct Element Method

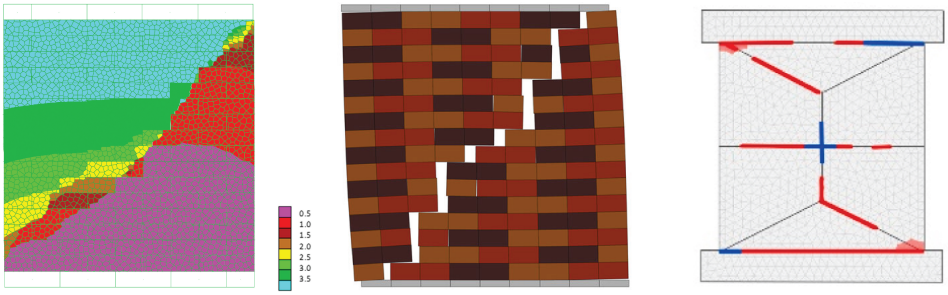
In DEM, the interaction between discrete assemblies is governed by contact/interface laws based on the *soft* contact approach, defined as a function of contact stiffness over the relative displacements/velocities between the blocks in contact. Contact interpenetration between elements is deliberately admitted to represent localised compressive deformation at the joint, namely asperity deformation in dry joints, or the compaction of mortar in the case of mortared masonry, lumped into a zero-thickness interface. This compliance is not a physical violation of impenetrability but rather a faithful representation of the compressive deformation lumped into the interface, and it also enables stable explicit time integration [150]. The finite compression force corresponds to the force required to compress the lumped mortar (or the contacting surfaces) by a given amount of interpenetration.

In the DEM proposed by Cundall [65], the core of the DEM formulations lies in an explicit time-marching integration scheme that accounts for both translational and rotational degrees of freedom. The interaction between discrete bodies is computed based on the contact constitutive laws correlating the contact forces to the relative displacements/velocities at the contact points. The explicit scheme is robust and suitable for modelling large displacements and collapse scenarios, but it is conditionally stable and requires small timesteps to maintain accuracy. In representing masonry with DEM, blocks can be defined as rigid or deformable bodies with expanded dimensions, while the mortar joints are modelled as zero-thickness interfaces formed at contact points, with constitutive laws that capture normal and tangential behaviour, including friction, cohesion, and potential damage or softening.

Figure 2.8 underscores the versatility of DEM by showing three different modelling approaches to simulate the same wall test subjected to in-plane lateral load and compression at varying levels of detail yet within the same DEM framework. In Figure 2.8A, the particle/irregular-block DEM through Voronoi or polyhedral tessellation treats the masonry units as a granular assembly with bonded contacts [51]. This approach allows cracks, fragmentation, and complex failure patterns to emerge naturally, without predefined joint paths. In Figure 2.8B, the classical unit-by-unit rigid-block DEM is used, where the masonry units are defined as rigid blocks with expanded dimensions and a potential crack plane at mid-length for the unit-splitting mechanism [50]. In Figure 2.8C, the deformable-block DEM is adopted with homogenised macro–blocks connected by discrete interfaces that are determined *a priori* following the possible crack paths [154]. Despite these modelling choices, all three share DEM's core strengths: evolving contact detection, large displacements and rotations, and failure mechanisms governed by the interface.

A coherent understanding of URM demands models that are credible across scales, from the micro-scale of unit-joint interactions to the macro-scale of wall and building responses. Key works on relevant applications of DEM, from material characterisation





(A) Lemos & Sarhosis, 2022 (B) Pulatsu, 2023 (C) Malomo & Dejong, 2021

Figure 2.8. Examples of Distinct Element Method (DEM) models for masonry structures. (A) and (B) validated the experimental wall test by Vermeltfoort *et al.* [54]

tests to complex monuments and buildings, are critically discussed herein. At the material level, Chen *et al.* [155] (Figure 2.9A) used DEM to simulate brick and mortar block tests, as well as shear tests on triplets and Brazilian tests on masonry prisms. Bricks are modelled as deformable blocks with Mohr-Coulomb plasticity and strain softening, while mortar joints are discretised as elastic Voronoi blocks with weakened interfaces to represent pre-existing micro-cracks. Similarly, Sarhosis and Lemos [156] used DEM to simulate the compressive behaviour of masonry assemblages, in which units and mortar joints are randomly generated using Voronoi tessellation. The authors concluded that while the results satisfactorily capture the overall compressive response, a systematic calibration procedure for the micro-mechanical parameters and their effects on the macroscopic response is still needed.

Pulatsu *et al.* [157] used DEM to simulate material characterisation tests, employing the same Voronoi tessellation approach for the brick units and the mortar layer. The authors used a polynomial softening contact law for the contact planes between the Voronoi particles to represent the fracture process in both bricks and mortar. The model was validated against experimental results from shear-compression tests on couplets [20] using Voronoi tessellation of the mortar layer. The authors also used the Voronoi tessellation on the brick units to simulate the fracture process in masonry prisms under direct tension [158], and on the walls subjected to a four-point bending test [159]. Readers are also referred to other authors who performed material characterisation tests in addition to the component-level validations; see [160, 161].

At the component level (walls, spandrels, piers), DEM often reproduces the global in-plane and out-of-plane response of masonry, but discrepancies in local failure mechanisms remain. Lemos and Sarhosis [51] employed Voronoi-tessellated DEM to match the in-plane response of walls under lateral load and constant axial compression, with load–displacement curves and cracking consistent with Vermeltfoort *et al.* [54] (Figure 2.8A). Using 2D rigid-block DEM with zero-thickness brittle joints, the authors captured the failure mode but overpredicted peak strength by ≈20 %.

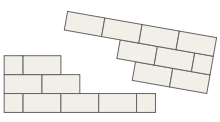
Pulatsu *et al.* [162] validated the same experimental test using a 3D deformable-block DEM with a linear softening contact law for the unit-mortar interfaces. The authors

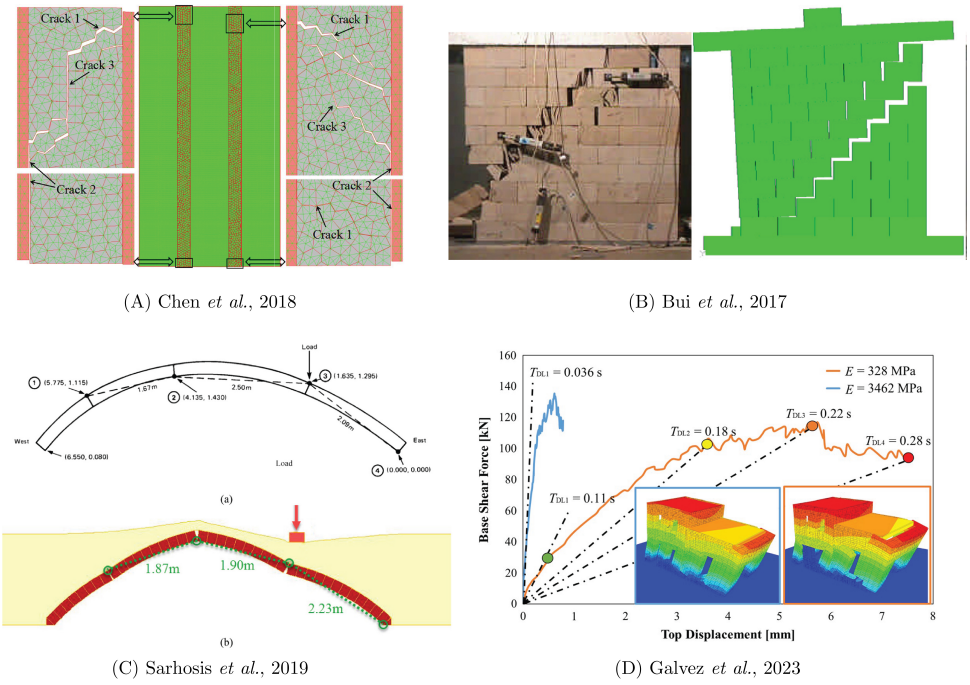
further extended the approach by adding potential crack planes in the units to capture the unit-splitting mechanism observed in the experiments. Bui *et al.* [163] (Figure 2.9B) used DEM to validate a regular stone wall with dry joints subjected to pre-compression and in-plane lateral load. The model captured the diagonal shear failure mechanism but overestimated the observed peak capacity. Pulatsu [50] highlighted the importance of the compression cap in limiting the shear-compression behaviour of URM walls under in-plane loading (Figure 2.8B). The author used a rigid-block DEM with a potential crack plane at the brick's mid-length, while the mortar joints were represented by a linear softening contact law with a compression cap. The proposed elasto-softening contact model was also used in the Monte-Carlo simulation by Pulatsu *et al.* [164] to assess the sensitivity of the prediction results to changes in micro-mechanical parameters.

Validating in-plane quasi-static cyclic loading of URM walls is necessary yet challenging due to the complex hysteretic behaviour, which involves stiffness degradation, strength deterioration, and pinching effects. The main issue remains the lack of robust contact models that capture the cyclic behaviour of masonry joints. Pulatsu *et al.* [165] used a rigid-block DEM with potential crack planes at the mid-length of the units and a contact model with compression cut-off to simulate the cyclic response of URM walls under in-plane loading. Malomo *et al.* [166] used a macro-DEM (M-DEM) approach with Mohr-Coulomb plasticity and strain softening blocks based on the work of Feenstra and de Borst [167] (Figure 2.8C). This approach has also been used to validate the experimental cyclic response of retrofitted and unretrofitted URM walls [161]

With regard to the out-of-plane response of masonry walls, Malomo *et al.* [154] used deformable-block DEM with Mohr-Coulomb plasticity and strain softening coupled with discrete interfaces defined *a priori* to represent the mortar joints and potential crack planes in the units. De Felice [168] investigated the dependence of the out-of-plane seismic capacity of URM walls on real masonry sections based on surveys of historical buildings using a 2D rigid-block DEM with Mohr-Coulomb contact models. Al-Shawa *et al.* [169] studied the out-of-plane seismic behaviour of a rocking wall using a single rigid block with an inclined base. Galvez *et al.* [170] used DEM to investigate the damping phenomena in rocking masonry walls, highlighting how different allocations of viscous damping affect predicted energy dissipation and kinematics. The study indicates that stiffness-proportional damping is preferable for rocking URM walls, whereas mass-proportional damping can spuriously increase energy loss due to impact forces.

DEM has also been used to investigate the structural and seismic behaviour of compression-dominated masonry arches and vaults. In comparison with geometry-based Heyman-type models, DEM retains similar advantages, such as limited material input and flexible geometric representation, and is simulated in a conditionally stable explicit integration scheme, but it overcomes the intrinsic limitation of neglecting shear sliding by explicitly resolving joint opening, closing, rocking, and sliding mechanisms, albeit at a higher computational cost. De Lorenzis *et al.* [171] used a 2D rigid-block DEM to study the dynamic response of URM arches subjected to impulse base motions. The study concluded that Heyman's no-sliding assumption holds for typical URM arches, whose joint friction angle exceeds that required to prevent sliding. The authors also highlighted that mass-proportional damping can lead to unwanted joint vibrations and early collapses. Sarhosis *et al.* [172] (Figure 2.9C) highlighted that the load-carrying





(A) Chen *et al.*, 2018 (B) Bui *et al.*, 2017

(C) Sarhosis *et al.*, 2019 (D) Galvez *et al.*, 2023

Figure 2.9. Examples of DEM applications from material level to building-level

capacity of the arch decreases with increasing skew angles of the arches, a similar finding as pointed out by Forgács *et al.* [173].

Regarding the use of DEM for masonry vaulted structures, McInerney and DeJong [174] studied masonry groin vault and arch models with varied geometries subjected to horizontal and vertical support displacements. The authors found that the collapse mechanism and displacement capacity of the groin vault can be approximated through 2D arch models for most geometries, except for low-rise vaults where three-dimensional effects dominate. Lengyel [175] analysed barrel and cross vaults under self-weight and horizontal support displacement. The author concluded that the vault curvature (semi-circular or pointed) and large displacements at the supports can cause shear failures in both vault geometries. Bianchini [176] used DEM to replicate the experimental shake-table test on both retrofitted and unretrofitted masonry cross-vault specimens, and compared the prediction results to continuum FEM based on the total strain rotating crack model [177]. The author concluded that calibrating the joint stiffness in the DEM model is crucial for obtaining an accurate prediction of the vault's nonlinear response. Other applications to vaulted structures can be found in [178–180].

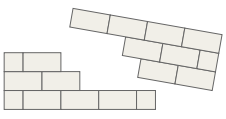
DEM has also been used to investigate the response of URM arch bridges under static and dynamic loading, with or without backfill elements. To this end, Sarhosis *et al.* [181] compared different representations of backfill elements (single elasto-plastic continuum, elastic Voronoi-packed blocks, and elasto-plastic Voronoi blocks) through comparison

to experimental static loading tests on a masonry arch bridge. The authors concluded that considering backfill elements as elasto-plastic Voronoi blocks can provide a more accurate prediction of the arch bridge response, as the randomness of the Voronoi patterns minimises the mesh effects that can occur due to the backfill's nonlinear behaviour. This approach, termed the mixed discrete-continuum approach, has been utilised in other works [182–184].

Building on insights from component-level studies and arched systems, the DEM framework has proved effective for historical monuments and geometrically complex URM buildings, capturing intricate damage patterns and collapse mechanisms, and extending to realistic post-collapse debris simulations. Azevedo *et al.* [185] first used the 2D DEM model on a bell tower in San Giorgio in Trignano and the Lisbon aqueduct, both subjected to seismic excitations. The computational investigation showed good qualitative agreement with the post-earthquake reconnaissance of the actual structures. de Felice *et al.* [186] proposed an assessment framework for the seismic capacity of collapse mechanisms of URM church façades, where the actual pattern gained from surveys of the wall face is replicated using rigid-block DEM. The authors compared the numerical prediction with the rigid-block model based on Housner's theory and found that the DEM model yields a more conservative estimate of the overturning capacity under pulse-based motion.

Schiavoni *et al.* [187] compared the use of discontinuous modelling strategies in DEM and NSCD against the continuum model with Concrete Damaged Plasticity (CDP) for the seismic assessment of the Santa Maria Annunziata church in Camerino, Italy, under the central Italy 2016 seismic sequence. All three approaches consistently identified the belfries and their connections to the main nave as the most vulnerable zones. The authors reported that the discontinuous techniques (DEM and NSCD) provided a more precise delineation of the emergence and progression of structural cracks than the continuum model, while the choice of interface law within DEM (smooth vs non-smooth contact) had only a minor influence on the predicted response. Similar conclusions on the descriptive power of discontinuum approaches for masonry aggregates have been reported by the same group [188]. Other applications of DEM to historical monuments can be found in [189–193].

DEM has not yet been employed extensively for the seismic assessment of full URM buildings, likely due to its high computational cost and the challenges of calibrating micro-mechanical parameters in large-scale models. Notable exceptions are presented herein. Ulrich *et al.* [194] conducted DEM pushover analyses of 3D aggregate URM buildings. The authors validated a quasi-static experiment using force-controlled loading by progressively increasing the load multiplier until failure occurred. Post-failure, the structure is subjected to a constant load multiplier corresponding to the critical load multiplier at failure until collapse is imminent. Galvez *et al.* [195] (Figure 2.9D) simulated a shake-table experiment [196] of interacting stone masonry buildings using 3D rigid-block DEM. The model showed remarkable accuracy in predicting base shear, crack patterns, and failure mechanisms at the experimental stage. The ultimate displacement capacity at near collapse was underestimated due to the lack of mortar compressive behaviour in the contact model. Malomo and DeJong [197] used a macro-DEM model to simulate the same experiment. The prediction model underestimated the floor



displacements but provided a satisfactory match for the overall base shear, due to the interlocking macro-blocks, which overestimated the building's lateral stiffness. The post-diction model addressed this by adding corner elements and increasing the system's deformability, thereby improving the accuracy of floor-displacement predictions.

2.3.2. Non-smooth Contact Dynamics

The Non-smooth Contact Dynamics (NSCD) method is another discontinuum modelling strategy that shares similarities with DEM in representing discrete assemblies and their interactions. Initially developed by Jean [66] and Moreau [198] for rock mechanics and simulation of granular materials, NSCD has been adapted for various engineering applications, including structural and seismic analysis of masonry structures. In contrast to DEM, NSCD employs a *hard* contact approach that enforces impenetrability between contacting bodies, preventing interpenetration. This is due to three conditions: (i) The elements in NSCD are confined in an R^n space where the boundary is made up of pieces of hypersurfaces and not smooth manifolds (non-smoothness in space); (ii) collisions between elements are expected to induce velocity jumps (non-smoothness in time); and (iii) contact forces attributed to the non-interpenetration constraints are governed by irregular constitutive laws (non-smoothness in constitutive law).

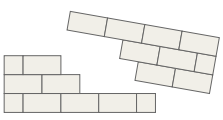
The discrete assemblies in NSCD can be modelled as rigid or deformable bodies, similar to DEM. The contact detection algorithm identifies potential contacts between bodies, and the contact law is formulated based on Signorini's impenetrability condition, which states that the normal contact force is non-negative and acts only when there is no gap between the bodies in contact. The tangential contact behaviour is governed by Coulomb's friction law, which relates the tangential force to the normal force through a friction coefficient. This condition makes NSCD suitable for simulating damaged or dry-joint URM structures where joint opening/closure and frictional sliding dominate the response. The NSCD method uses an incremental-iterative solution procedure due to the non-smooth nature of dynamic contacts.

Contacts are first detected using a geometric search algorithm, and contact forces are computed by solving a complementarity problem that enforces impenetrability and frictional constraints. Then, the positions and velocities of the discrete assemblies are updated using the incremental-iterative solution procedure. During this update, three conditions are checked at each contact point before proceeding to the next timestep:

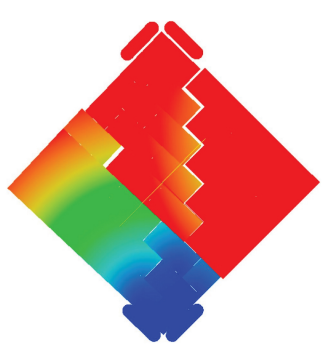
1. The gap at the new step is computed without interaction. If the gap is positive, the blocks are not in contact, and the contact force is zero. If the gap is zero or negative, the contact constraint is evaluated in the next check.

2. The normal contact force needed to prevent interpenetration is computed. If this force is non-negative (compressive), the contact is maintained, and the friction condition is checked through the Coulomb law. If it is negative (tensile), the contact cannot hold the blocks together, so the force is set to zero and the blocks separate.

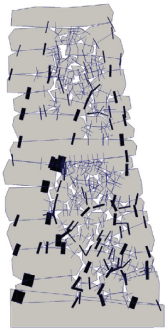
3. If the Coulomb condition is violated, the blocks slide, and the tangential relative velocity becomes non-zero. The tangential force is then set so that it does not exceed the product of the normal force and the friction coefficient.



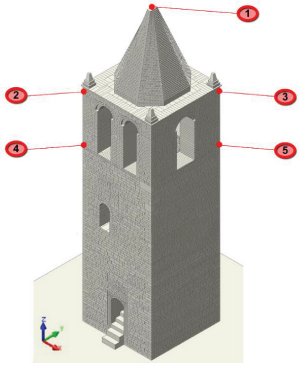
These conditions are defined by the shock law in NSCD [199] and must be satisfied at each contact point before proceeding to the next timestep. The nonlinear Gauss-Seidel method is implemented to solve the contact resolution problem before the implicit solver is used to update the positions and velocities. NSCD has been applied to various masonry structures, ranging from material-level characterisation to component-level validation and complete building-scale analyses, with examples shown in Figure 2.10. These examples illustrate the diverse applications of NSCD in capturing the complex behaviour of masonry structures under various loading conditions.



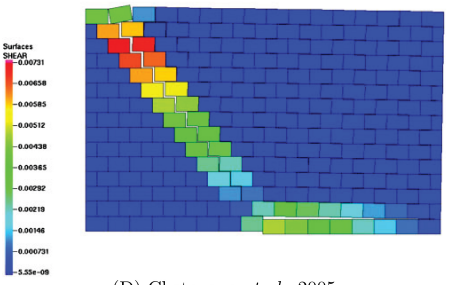
(A) Bisoffi-Sauve *et al.*, 2019



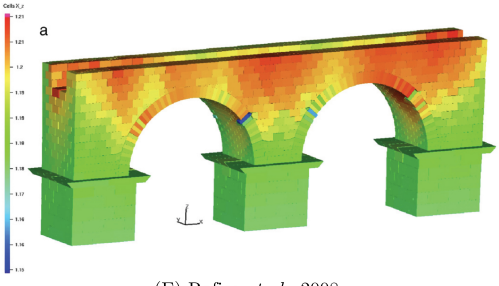
(B) Dubois *et al.*, 2018



(C) Ferrante *et al.*, 2021



(D) Chetouane *et al.*, 2005



(E) Rafiee *et al.*, 2008

Figure 2.10. Examples of NSCD applications from material level to building-level

At the material characterisation level, Bisoffi-Sauve *et al.* [200] (Figure 2.10A) are one of the few that validate material characterisation tests of masonry components using NSCD. In their work, a fracture mechanics-based cohesive contact law is implemented to replace the default Coulomb condition in NSCD. A mixed-mode formulation is proposed to couple the tensile and shear behaviour of the mortar joints. Validated against a diagonal compression test on a masonry prism, direct tensile, and triplet tests, the model showed good agreement in global behaviour and failure kinematics but required further improvement in the friction-cohesion coupling.

At the component (wall) level, validations of NSCD for in-plane mechanisms of URM walls remain limited. Bouckaert *et al.* [201] used NSCD to simulate the pushover response of URM walls under in-plane lateral load, exploring force-controlled loading protocols

and comparing results to experimental data and DEM-based simulations. Both NSCD and DEM reproduced the peak load multiplier and the overall force–displacement envelope with good agreement. Differences between the two methods arose in local peaks triggered by sudden block detachment, which were detected at slightly different instants due to differences in contact enforcement and time-stepping strategies.

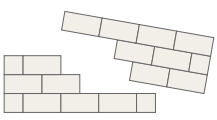
At the out-of-plane component level, Isfeld and Shrive [202] employed NSCD to simulate a historical rubble stone masonry wall of the Prince of Wales Fort in Manitoba, Canada. The wall was subjected to one-way bending actions with varying tangential-to-normal cohesion ratios to represent the mortar condition. The authors concluded that the out-of-plane capacity of the wall is highly dependent on the mortar condition, with higher cohesion leading to increased capacity and altered failure mechanisms, but highlighted that experimental observations are needed to validate the numerical findings.

Dubois *et al.* [203] analysed the cross-section of a 1.5m retaining wall in Largentière, France, subjected to out-of-plane loading (Figure 2.10B). The authors intended the analysis to demonstrate the capabilities of NSCD in simulating historical URM structures. The model captured a faithful description of wall overturning under out-of-plane actions, including stick-slip at the base, contact-force redistribution at the joints, and impact-driven damping. Other work on the out-of-plane response of URM walls using NSCD can be found in [204].

Chetouane *et al.* [205] (Figure 2.10D) employed NSCD to study the response of stone masonry walls under quasi-static settlement loading and dynamic in-plane loading. The observed model parameters are the construction history (equilibrium calculated after construction or through the sequential addition of blocks), the presence of mortar joints, and block deformability. They concluded that construction history can inflate block-wise stress invariants (≈ 58% on average), a continuum FEM neglecting joints overestimates layer-wise stress by 2.4x relative to the discrete jointed model, and rigid-block NSCD is ≈3x faster but can misrepresent local stress partitions, since the absence of block deformability shifts all compliance to the joints and removes the within-block stress variation, motivating a mixed rigid/deformable strategy.

NSCD was also implemented for the numerical simulations of vaulted structures, leveraging the dry contact assumption that is often valid for compression-dominated arches and vaults. Rafiee *et al.* [206] tested the NSCD framework on a historical aqueduct bridge in Arles, France (Figure 2.10E). The aqueduct bridge was tested under artificial sinusoidal vibrations and real recorded seismic excitation in both horizontal and vertical directions. The numerical analysis showed that the bridge was able to withstand the artificial vertical vibrations but failed under the horizontal seismic excitation, in line with the experimental observations. Similar works on the application of NSCD to arches can be found in Beatini *et al.* [207]. In this work, the authors varied the friction angles of the arches and studied their influence when the arches are subjected to gravity and quasi-static vertical point loads. The authors concluded that the optimal angle of 38° yields collapse capacity and mechanisms that match those of conventional thrust-line models. Other work related to vaulted structures can be found in [208, 209].

Schiavoni *et al.* [187] gave a quantitative comparison between DEM and NSCD against continuum FEM based on Concrete Damaged Plasticity (CDP) for the seismic assessment



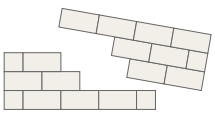
of the Santa Maria Annunziata church in Camerino, Italy. For NSCD, the default dry friction contact was used. Both models predicted comparable failure mechanisms, with cracks localised at the front bell towers. Further comparisons on the effect of stereotomy were done by Schiavoni *et al.* [188]. The authors showed that DEM and NSCD were comparable in predicting the seismic response of multi-wythe stone-masonry churches, with both methods capturing the complex interaction between masonry units and mortar joints, consistent with the post-earthquake reconnaissance. The authors also showed that modelling complexity can create an accuracy-computational time trade-off, since the simplified model could not replicate the localised crushing and debris formation observed at the site.

Ferrante *et al.* [193] (Figure 2.10C) did a similar comparison between DEM and NSCD on a multi-leaf URM tower with varying stereotomy on the bricks and stones. The authors tested three different levels of detail: an as-built with ≈30,000 blocks, a simplified single-wythe model with ≈20,000 blocks, and a rough model with ≈1000 blocks. The authors reached the same conclusions as Schiavoni *et al.* [188]. Both DEM and NSCD yielded comparable results, but the rough model provided the most idealised damage pattern and failure mechanism. NSCD produced displacement histories and damage onset that were broadly comparable to the DEM results. However, in the coarsest geometrical discretisation, the predicted response reduced to a highly idealised global rocking-overturning mechanism of the shaft, with damage localised in a few cracking zones and a clean separation of the upper portion of the tower. This contrasts with the more fragmented cracking patterns captured by the refined multi-leaf models and in situ observations.

2.3.3. Applied Element Method

Originally proposed by Tagel-Din and Meguro [210], AEM is a discontinuum strategy tailored to structural systems that transition from continuous to discrete states. Similar to DEM and NSCD, which treat masonry as an assembly of discrete parts, AEM represents each unit as a rigid element whose interfaces are populated with distributed pairs of normal and shear springs. These zero-thickness interface springs deliver tractions and relative deformations over tributary areas, enabling the capture of both continuum-like behaviour under small deformations and discrete mechanism formation under large displacements. The Poisson effect and shear retention are considered through the arrangement of normal and shear springs along the interfaces. Unlike DEM/NSCD, where contact points are typically generated by local triangulation and activated only upon geometric contact, AEM prescribes an a priori regular distribution of spring–contact points along element edges (Figure 2.11A). Mechanisms such as damage, softening, opening, and sliding are then captured through the constitutive behaviour of these interface springs, as shown in Figure 2.11B.

In order to form the general stiffness matrix, the element location and the springs are first defined in the global coordinate system. The stiffness matrix components corresponding to each degree of freedom are defined by assuming a unit displacement in the respective direction and determining the forces acting at the element's centroid. The global stiffness matrix is then assembled by summing the contributions from all elements and their associated springs. Consequently, since the degrees of freedom of each element



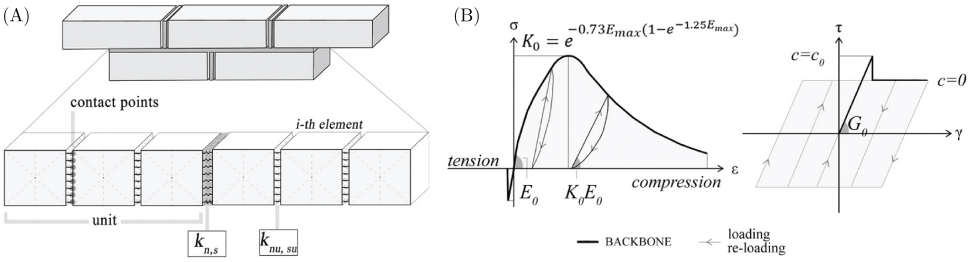


Figure 2.11. (A) Schematic of Applied Element Method (AEM) representation of masonry structures and (B) material constitutive model for the unit-mortar interfaces. Image taken from [211]

comprise three translations and three rotations defined at the element centroids, the number of springs does not influence the size of the global stiffness matrix. The spring count instead affects the accuracy of the interface behaviour representation [67]. The global system is advanced through implicit time integration, allowing larger timesteps at the cost of solving a global system at each step.

The number of springs along the interfaces also affects the rotational stiffness of the elements, since rotation is resisted primarily by the shear springs acting together with the normal springs. For small elements, the relative rotation between adjacent elements is limited, and the error introduced by the discrete spring representation is typically negligible. For larger elements, however, Meguro and Tagel-Din [67] showed that, for a generic element edge, more than 10 springs are required along that edge to limit the discrepancy between the numerical and analytical rotational stiffness to less than 1 %.

Cracking is detected through a maximum principal tensile stress criterion (Rankine-type) reconstructed from the local normal and shear spring forces, providing a mixed-mode indicator that combines tensile and shear contributions at the inter-element interface. The global stress tensor is not used directly due to the discrete nature of the method. Once the principal stress at a spring exceeds the tensile resistance, the normal and shear spring forces at that spring are redistributed in the next increment, while frictional transfer under compression is retained. These redistributed forces are transferred to the element centroid as force and moment, and applied to the structure in the next increment. This criterion operates at the interface level, and classical AEM with rigid elements does not directly resolve the tensile failure within the blocks, such as the transverse tensile stresses that drive unit splitting in compression struts; capturing such mechanisms requires subdividing the units into multiple elements connected by additional springs (Figure 2.11).

The AEM framework uses an implicit incremental-iterative integration scheme based on the Newmark-beta method to solve the equilibrium equations. The global force matrix is equated to the sum of the centroid force vectors and the residual force carried from the previous increment [212].

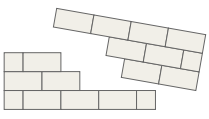
From a constitutive standpoint, AEM assigns nonlinear laws to the normal and shear springs along element interfaces, including tension softening, compression nonlinearity, and frictional sliding with degradation. These spring models, initially developed for

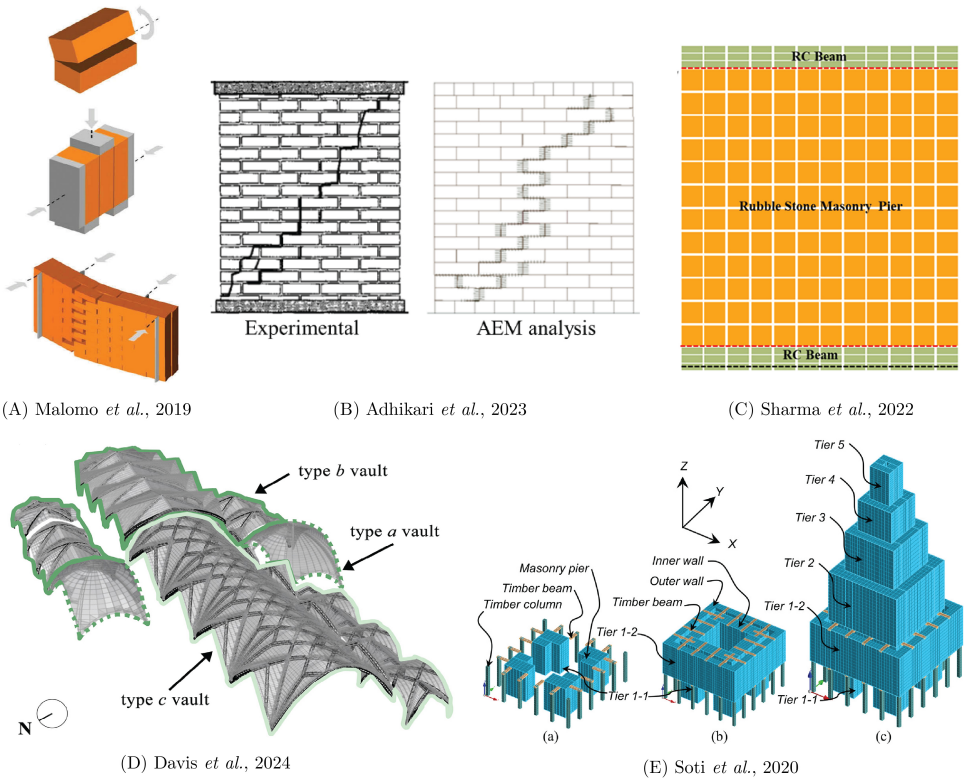
reinforced concrete and other structural materials, can be adapted to reproduce the quasi-brittle response of masonry joints [210]. The Maekawa compression model [213] is adopted as the constitutive law assigned to the normal springs under compressive loading (Figure 2.11B). The tangent stiffness of each spring is computed from its strain history and current loading/unloading phase. Under uniaxial tension, a brittle law is employed, neglecting post-peak softening behaviour for simplicity. The Coulomb friction criterion governs shear-compression behaviour, as in DEM. Because the spring represents uniaxial normal and shear responses between rigid elements, the compressive law captures the response along the inter-element direction but does not resolve stress variations within the element. Energy is dissipated through the hysteretic behaviour of the springs and through impacts between elements during collisions. Because hysteresis acts only once the springs are damaged, AEM dynamic analyses typically add viscous or Rayleigh damping to represent dissipation in the elastic range.

AEM has been applied to various masonry structures, ranging from material-level characterisation to component-level validation and full building-scale analyses, with examples shown in Figure 2.12. On the material characterisation level, Malomo *et al.* [214] conducted a series of validations on material characterisation tests for masonry couplets, triplets, and wallettes using AEM (Figure 2.12A). The validations showed that AEM can adequately capture the tensile resistance, shear bond, and flexural resistance of the masonry assemblages, including the localised out-of-plane failure mechanisms in the wallettes. The same strategy was used in Malomo *et al.* [215] on the material characterisation tests of calcium silicate and clay bricks. Adhikari and D'Ayala [216] used AEM to simulate the uniaxial compression test of a stone masonry assemblage from Nepal. The model captured fracture within the units by further discretising the units into smaller rigid elements connected by interface springs that act as the potential crack plane.

At the component (wall) level, Pandey and Meguro [217] first used AEM to simulate the masonry wall test by Vermeltfoort *et al.* [54] with an opening and pre-compression level of 0.3 MPa. Using rigid blocks and the Mohr-Coulomb contact law with exponential softening in compression and tension for the unit-mortar interfaces, the model captured the overall lateral load-displacement response and failure mechanism reasonably well, with a smooth transition from debonding and friction sliding to the loss of shear resistance due to the formation of diagonal tension cracks. The solid wall experiment with the pre-compression of 0.3 MPa was validated in Mayorca and Meguro [218]. The comparison showed that the model could capture the diagonal cracks observed in the experiment, but the authors did not report the load-displacement behaviour. This experiment was revisited by Adhikari *et al.* [219] (Figure 2.12B), where the experimental test was used before the application to a full-scale school building subjected to seismic loading. The authors used AEM to validate the in-plane monotonic response of the Vermeltfoort wall with and without opening, subjected to a pre-compression level of 0.3 MPa. The model neglects the potential crack plane at the brick's mid-length to save computational time. Consequently, the crack pattern shown in Figure 2.12B only shows the diagonal shear cracks without the unit-splitting mechanism observed in the experiment.

With regard to the cyclic performance of AEM on URM walls subjected to in-plane





(A) Malomo *et al.*, 2019 (B) Adhikari *et al.*, 2023 (C) Sharma *et al.*, 2022

(D) Davis *et al.*, 2024 (E) Soti *et al.*, 2020

Figure 2.12. Examples of masonry structures analysed using the AEM framework

loading, Adhikari and D'Ayala [216] simulated the cyclic response of a stone masonry wall with mud mortar joints subjected to cyclic in-plane loading. Similar to [219], the validation is used as the basis for application to the seismic performance of masonry buildings in Nepal. The reported model captured the initial stiffness, peak load, and ductility relatively well, but overestimated the hysteretic energy dissipation. Malomo *et al.* [220] used iterative calibration to match the masonry elastic properties (Young's and shear moduli of mortar) to enhance the modelling results of cyclic in-plane loading of calcium silicate masonry walls. Morandini *et al.* [221] calibrated the AEM model against the cyclic quasi-static tests on URM piers and a full-scale URM building façade with regular openings, capturing the influence of openings on the seismic response and satisfactorily simulating the damage and hysteretic response of the URM piers. Sharma *et al.* [222] (Figure 2.12C) used AEM with continuum-like discretisation to simulate the cyclic in-plane loading of rubble stone masonry walls, capturing the initial stiffness, peak load, and hysteretic response with good agreement.

There has been limited application of AEM for the case of arched structures, mainly due to the limitation of the geometrical modelling of curved structures in the commercial AEM software package Extreme Loading for Structures [223]. Davis *et al.* [224] worked on

this issue by building the geometries from point clouds, which were then transformed into quad-meshed rigid-block assemblages (Figure 2.12D). The authors simulated the seismic response of two historic churches in the UK, capturing the complex damage and collapse mechanisms observed during post-earthquake reconnaissance.

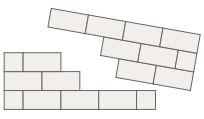
Applications of AEM to historical monuments remain limited relative to DEM and NSCD. Soti *et al.* [225] (Figure 2.12E) compared AEM against conventional FEM for seismic assessment of a historical pagoda in Nepal, employing a continuum-like meso-scale representation of URM combined with detailed timber column and beam elements. The AEM predictions showed reasonable agreement with FEM-derived response envelopes and modal characteristics. Diana *et al.* [226] used AEM to simulate the vulnerability assessment of historical churches in Italy and Switzerland in three phases: selecting the most vulnerable churches, applying kinematic methods to estimate the probability of out-of-plane failure, and performing AEM simulations to assess out-of-plane damage.

On the contrary, AEM was used extensively for the seismic assessment of full URM buildings, likely due to the computational efficiency and the robust representation of both continuum and discontinuum behaviour. Notable examples include Malomo *et al.* [214, 215] who used AEM as a validation against shake-table tests on full-scale building specimens with clay or calcium silicate bricks. The model simplifies the timber floor diaphragms as a roughly discretised membrane element with an equivalent shear modulus to simulate the in-plane diaphragm stiffness. Calò *et al.* [227] revisited the simplified approach by Malomo *et al.* [214] and showed that the modelling simplifications did not compromise the in-plane displacement response, but they did limit the accuracy of the predicted damage patterns and out-of-plane failure mechanisms.

Karbassi and Nollet [228] used AEM for performance-based earthquake engineering (PBEE) assessment of URM buildings, integrating AEM simulations with probabilistic seismic demand to derive fragility functions for various performance levels. Adhikari and D'Ayala [216] similarly used AEM to form the fragility curves for residential houses with stone masonry walls in Nepal, giving a qualitative correlation between the observed damage and the predicted damage states from the fragility curves. This concept was also used in their later work on school buildings [219]. Other works on URM buildings can be seen in Khattak *et al.* [229] and Domaneschi *et al.* [230].

2.3.4. Summary

The three discontinuum modelling strategies discussed above, DEM, NSCD, and AEM, offer distinct approaches to modelling the complex behaviour of masonry structures, each with its own strengths and limitations. DEM is particularly effective for capturing large deformations, joint interactions, and post-collapse behaviour, making it suitable for detailed analyses of masonry components and structures. NSCD excels at simulating contact dynamics and frictional interactions, providing robust solutions for structures in which joint behaviour is critical, e.g., dry-jointed URMs. AEM offers a versatile framework that bridges continuum and discontinuum behaviour, enabling efficient simulations of both small and large deformations in masonry structures using an implicit integration scheme. Each method has been successfully applied at various levels of masonry structures, from material characterisation to full building analyses, demonstrating its



capabilities to capture the complex responses of URM structures under different loading conditions. Cyclic loading capability also differs across the three methods. AEM was developed with cyclic behaviour as a primary target and natively supports hysteretic response through its spring constitutive laws. In DEM, cyclic capability depends on the contact constitutive model adopted; classical elastic-unloading laws cannot capture cyclic stiffness degradation under load reversals, whereas damage-plasticity contact models can. NSCD provides cyclic capability primarily through frictional and impact dissipation, with cyclic stiffness degradation requiring additional constitutive extensions. The three methods also differ in their time integration schemes. DEM uses explicit time integration, while NSCD and AEM use implicit schemes. This distinction has practical implications for problems with many simultaneous contact state changes, such as those encountered in seismic analyses near collapse, and is developed further in Section 2.4. However, challenges remain in computational efficiency, parameter calibration, and the accurate representation of the full spectrum of masonry behaviour, particularly in large-scale applications. The three methods are summarised in Table 2.5.

2.4. Knowledge gaps and research focus

The review shows that DEM, NSCD and AEM each have distinct strengths for masonry. AEM models large assemblies efficiently through interface springs with relatively rich constitutive laws, which suits structural-scale seismic analysis. NSCD treats unilateral contact and friction rigorously and is well suited to large displacements, impacts and rocking. DEM combines explicit block kinematics with soft-contact laws at the joints. It can therefore represent opening, sliding and rocking at the joints, and follow damage through to collapse.

This thesis adopts DEM as its discontinuum strategy, mainly because of its explicit time integration. Each timestep is computed directly from the state of the previous one, and stability is governed by the CFL condition rather than by iterative convergence. DEM therefore remains stable through post-peak softening, frictional rearrangement, and re-contact, which dominate masonry response near collapse. NSCD and AEM, by contrast, use implicit time-stepping. Like implicit FEM, they can fail to converge when many contacts change state within one step. The explicit framework also allows damping to be applied at the global, block and contact levels. In return, it requires careful control of the timestep and of the damping parameters, the latter addressed in Chapter 7.

Several challenges nevertheless remain for DEM. They concern the joint constitutive model, the control of numerical dissipation in dynamic analysis, and validation beyond the component scale. The following knowledge gaps are identified.

G1 Post-peak tensile–shear softening laws.
Existing DEM interface models ([50, 165]) rely on simple linear softening that cannot reproduce the exponential curved softening shapes and mixed-mode coupling seen experimentally. A piecewise-linear or exponential softening, consistent with mode-I/II fracture energies and with an ultimate displacement beyond the linear cut-off, is needed to capture the observed tail response and maintain energy consistency.

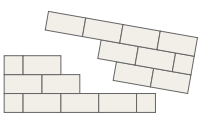
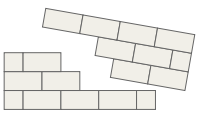


Table 2.5. Comparison of discontinuum modelling strategies for masonry structures

Criterion	DEM	NSCD	AEM
Contact Type	Soft-contact with interpenetration allowed	Hard contact with zero interpenetration	No contact; replaced with normal/shear spring pairs.
Body Discretisation	Rigid or deformable blocks	Rigid or deformable blocks	Rigid blocks with interface springs.
Time Integration Scheme	Explicit time-marching scheme	Implicit time integration scheme	Implicit incremental-iterative scheme.
Contact Detection	Common-plane search	Common-plane search	Predefined regular distribution of springs along interfaces.
Constitutive description	Joint-based Mohr–Coulomb with tension cut-off and mixed-mode fracture; nonlinear softening laws with prescribed fracture energies in normal and shear and compression cut-off in more advanced models	Non-smooth Signorini impenetrability condition with Coulomb friction; nonlinearity introduced via state transitions	Nonlinear spring laws based on Maekawa-type compression, brittle tension, and Mohr–Coulomb shear–compression, including softening, shear retention, and fracture-energy-based degradation.
Key Calibrations	Normal/shear joint stiffnesses, tensile and compressive strengths, cohesion, friction angle, mode-I/II fracture energies for advanced constitutive models, and (for dynamic analyses) contact damping parameters	Friction coefficients and, where adopted, cohesive strength parameters, together with numerical controls such as solver tolerances and stabilisation or dissipation parameters in the contact algorithm	Normal/shear spring stiffnesses, interface tensile and shear capacities, parameters of the compression and shear–tension softening laws (including fracture energies), and, in dynamic applications, the adopted viscous or Rayleigh damping to match the target damping ratios.

G2 Pressure-dependent compressive failure.
Current DEM joint models prioritise tension and shear, while underrepresenting crushing and confinement effects. A cap-type yield surface (normal-stress dependent strength with shear coupling), together with a modest dilatancy law, is required to represent mortar crushing, bed-joint compaction, and the transition from shear to compression-dominated failure.

G3 Cyclic degradation and energy dissipation.
Existing DEM models often lack robust cyclic degradation laws that capture deterioration in stiffness and strength under repeated loading, as well as realistic energy dissipation mechanisms. Incorporating hysteretic behaviour and damage

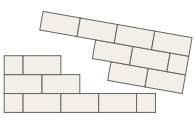


accumulation into the joint constitutive model is essential for accurate predictions of seismic response.

G4 Validation across scales.
Building-scale DEM studies exist [194, 195, 197], but they use simple joint laws and rarely trace their parameters from material tests through component tests to the building. Full-scale tests on buildings with floor diaphragms are needed to show whether a joint law calibrated on small specimens carries over to the global response.

G5 Damping modelling and parameter identification in dynamic DEM analyses.
In most DEM applications, damping is introduced through ad hoc Rayleigh coefficients or viscous contact laws, with limited guidance on how to identify these parameters for large masonry assemblies and over a broad frequency range. A systematic strategy is needed to calibrate and validate damping models against experimental data and to quantify how key seismic response measures, e.g., peak drifts, residual displacements, and collapse times, vary with damping formulations and parameter choices.

To address these gaps, the thesis develops an energy-consistent joint constitutive model for DEM analysis of URM structures. The model couples tensile and shear softening through the mode-I and mode-II fracture energies (G1). It adds a pressure-dependent compression cap with softening (G2), together with cyclic degradation and energy dissipation in each failure mode (G3). The model is calibrated on material characterisation tests and validated on walls under monotonic and cyclic in-plane loading. It is then applied to a full-scale URM building with floor diaphragms (G4). In parallel, the thesis identifies Maxwell damping parameters through optimisation and compares damping schemes against shake-table tests (G5).



Chapter 2

Bibliography of Chapter 2

[1] A. M. D'Altri, V. Sarhosis, G. Milani, J. Rots, S. Cattari, S. Lagomarsino, E. Sacco, A. Tralli, G. Castellazzi and S. de Miranda. 'Modeling Strategies for the Computational Analysis of Unreinforced Masonry Structures: Review and Classification'. In: *Archives of Computational Methods in Engineering* 27.4 (2020), pp. 1153–1185. ISSN: 1134-3060. DOI: 10.1007/s11831-019-09351-x.

[2] W. Mann and H. Müller. 'Failure of shear-stressed masonry: An enlarged theory, tests and application to shear walls'. In: *Proceedings of the British Ceramic Society* 30 (1982), pp. 223–235.

[3] G. Magenes and G. M. Calvi. 'In-plane seismic response of brick masonry walls'. In: *Earthquake Engineering & Structural Dynamics* 26.11 (1997), pp. 1091–1112. DOI: 10.1002/(SICI)1096-9845(199711)26:11<1091::AID-EQE693>3.0.CO;2-6.

[4] A. K. Thomoglou, M. A. Karabini, D. V. Achillopoulou, T. C. Rousakis and C. E. Chalioris. 'Failure Mode Prediction of Unreinforced Masonry (URM) Walls Retrofitted with Cementitious Textile Reinforced Mortar (TRM)'. In: *Fibers* 11.6 (2023), p. 53. DOI: 10.3390/fib11060053. URL: https://doi.org/10.3390/fib11060053.

[5] *Test Method for Compressive Strength of Masonry Prisms*. Tech. rep. ASTM C1314-23a. West Conshohocken, PA, 2023. URL: https://www.astm.org/c1314-23a.html.

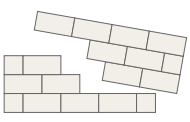
[6] *Methods of Test for Masonry — Part 1: Determination of Compressive Strength*. Tech. rep. EN 1052-1:1998. Brussels, 1998.

[7] *techreport Test Method for Diagonal Tension (Shear) in Masonry Assemblages*. Tech. rep. ASTM E519/E519M-22. West Conshohocken, PA, 2022. URL: https://www.astm.org/e0519_e0519m-21.html.

[8] *Eurocode 6: Design of masonry structures — Part 1-1: General rules for reinforced and unreinforced masonry structures*. Tech. rep. EN 1996-1-1:2005 + A1:2012. Consolidated version incorporating Amendment A1:2012. Brussels, 2013.

[9] F. Messali, R. Esposito, G. Ravenshorst and J. Rots. 'Experimental investigation of the in-plane cyclic behaviour of calcium silicate brick masonry walls'. In: *Bulletin of Earthquake Engineering* 18.8 (2020), pp. 3963–3994. DOI: 10.1007/s10518-020-00835-x.

[10] B. V. Wilding, M. Godio and K. Beyer. 'The ratio of shear to elastic modulus of in-plane loaded masonry'. In: *Materials and Structures* 53.2 (2020), p. 40. DOI: 10.1617/s11527-020-01464-1.



[11] A. Borri, G. Castori, M. Corradi and E. Speranzini. 'Shear behavior of unreinforced and reinforced masonry panels subjected to in situ diagonal compression tests'. In: *Construction and Building Materials* 25.12 (2011), pp. 4403–4414. DOI: 10.1016/j.conbuildmat.2011.01.009.

[12] D. M. McCann and M. C. Forde. 'Review of NDT methods in the assessment of concrete and masonry structures'. In: *NDT & E International* 34.2 (2001), pp. 71–84. DOI: 10.1016/S0963-8695(00)00032-3.

[13] *techreport Test Method for In Situ Measurement of Masonry Deformability Properties Using the Flatjack Method*. Tech. rep. ASTM C1197-22. West Conshohocken, PA, 2022. URL: https://www.astm.org/c1197-22.html.

[14] *techreport Test Method for Dynamic Young's Modulus, Shear Modulus, and Poisson's Ratio by Impulse Excitation of Vibration*. Tech. rep. ASTM E1876-22. West Conshohocken, PA, 2022. URL: https://www.astm.org/e1876-22.html.

[15] S. Jafari, J. G. Rots and R. Esposito. 'Core testing method to assess nonlinear behavior of brick masonry under compression: A comparative experimental study'. In: *Construction and Building Materials* 218 (Sept. 2019), pp. 193–205. ISSN: 0950-0618. DOI: 10.1016/J.CONBUILDMAT.2019.04.188.

[16] S. Peng, T. Parent, Z. M. Sbartaï and S. Morel. 'Experimental characterisation of masonry unit–mortar interface under uniaxial cyclic tension'. In: *Engineering Fracture Mechanics* 274 (2022), p. 108790. DOI: 10.1016/j.engfracmech.2022.108790.

[17] *Methods of test for masonry — Part 2: Determination of flexural strength*. Tech. rep. EN 1052-2:2016. Incorporates corrigendum EN 1052-2:2016/AC:2017. Brussels, 2016.

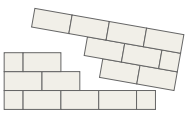
[18] *Methods of test for masonry — Part 5: Determination of bond strength by the bond wrench method*. Tech. rep. EN 1052-5:2005. Brussels, 2005.

[19] S. Jafari, J. G. Rots and R. Esposito. 'A correlation study to support material characterisation of typical Dutch masonry structures'. In: *Journal of Building Engineering* 45 (Jan. 2022). ISSN: 23527102. DOI: 10.1016/j.jobe.2021.103450.

[20] R. van der Pluijm. 'Out-of-Plane Bending of Masonry: Behaviour and Strength'. PhD thesis. Eindhoven, The Netherlands: Technische Universiteit Eindhoven, 1999, p. 259. ISBN: 90-6814-099-X. DOI: 10.6100/IR528212. URL: https://research.tue.nl/files/1570536/528212.pdf.

[21] Comité Euro-International du Béton (CEB). *CEB-FIP Model Code 1990: Final Draft*. CEB Bulletin d'Information Nos. 213/214. Lausanne, Switzerland, 1991.

[22] R. Lumantarna, D. T. Biggs and J. M. Ingham. 'Compressive, Flexural Bond, and Shear Bond Strengths of In Situ New Zealand Unreinforced Clay Brick Masonry Constructed Using Lime Mortar between the 1880s and 1940s'. In: *Journal of Materials in Civil Engineering* 26.4 (2014), pp. 559–566. DOI: 10.1061/(ASCE)MT.1943-5533.0000685.



[23] G. Andreotti, F. Graziotti and G. Magenes. 'Detailed micro-modelling of the direct shear tests of brick masonry specimens: The role of dilatancy'. In: *Engineering Structures* 168 (Aug. 2018), pp. 929–949. ISSN: 0141-0296. DOI: 10.1016/J.ENGSTRUCT.2018.05.019.

[24] P. B. Lourenço, J. G. Rots and J. Blaauwendraad. 'Continuum Model for Masonry: Parameter Estimation and Validation'. In: *Journal of Structural Engineering* 124.6 (1998), pp. 642–652. ISSN: 0733-9445. DOI: 10.1061/(ASCE)0733-9445(1998)124:6(642).

[25] L. Berto, A. Saetta, R. Scotta and R. Vitaliani. 'An orthotropic damage model for masonry structures'. In: *International Journal for Numerical Methods in Engineering* 55.2 (Sept. 2002), pp. 127–157. ISSN: 1097-0207. DOI: 10.1002/NME.495. URL: https://onlinelibrary.wiley.com/doi/full/10.1002/nme.495%20https://onlinelibrary.wiley.com/doi/abs/10.1002/nme.495%20https://onlinelibrary.wiley.com/doi/10.1002/nme.495.

[26] L. Pelà, M. Cervera and P. Roca. 'Continuum Damage Model for Orthotropic Materials: Application to Masonry'. In: *Computer Methods in Applied Mechanics and Engineering* 200.9–12 (2011), pp. 917–930. ISSN: 0045-7825. DOI: 10.1016/j.cma.2010.11.010.

[27] *Methods of test for masonry — Part 3: Determination of initial shear strength*. Tech. rep. EN 1052-3:2002 + A1:2007. Amends and supersedes EN 1052-3:2002. Brussels, 2007.

[28] C. Calderini, S. Cattari and S. Lagomarsino. 'The use of the diagonal compression test to identify the shear mechanical parameters of masonry'. In: *Construction and Building Materials* 24.5 (2010), pp. 677–685. DOI: 10.1016/j.conbuildmat.2009.11.001.

[29] J. Garzón-Roca, C. Obrer Marco and J. M. Adam. 'Compressive strength of masonry made of clay bricks and cement mortar: Estimation based on Neural Networks and Fuzzy Logic'. In: *Engineering Structures* 48 (2013), pp. 21–27. DOI: 10.1016/j.engstruct.2012.09.029.

[30] W. Mann. 'Statistical evaluation of tests on masonry by potential functions'. In: *Proceedings of the Sixth International Brick Masonry Conference*. 1982.

[31] H. B. Kaushik, D. C. Rai and S. K. Jain. 'Stress–strain characteristics of clay brick masonry under uniaxial compression'. In: *Journal of Materials in Civil Engineering* 19.9 (2007), pp. 728–739. DOI: 10.1061/(ASCE)0899-1561(2007)19:9(728).

[32] A. T. Vermeltfoort. 'Brick-mortar interaction in masonry under compression'. PhD thesis. Eindhoven, The Netherlands: Eindhoven University of Technology, Built Environment, 2005. ISBN: 90-6814-582-7. DOI: 10.6100/IR589402.

[33] K. Naraine and S. Sinha. 'Cyclic Behavior of Brick Masonry under Biaxial Compression'. In: *Journal of Structural Engineering* 117.5 (May 1991), pp. 1336–1355. ISSN: 0733-9445. DOI: 10.1061/(ASCE)0733-9445(1991)117:5(1336). URL: https://ascelibrary.org/doi/abs/10.1061/%28ASCE%290733-9445%281991%29117%3A5%281336%29%20https://ascelibrary.org/doi/10.1061/%28ASCE%290733-9445%281991%29117%3A5%281336%29.

[34] D. V. Oliveira, P. B. Lourenço and P. Roca. 'Cyclic behaviour of stone and brick masonry under uniaxial compressive loading'. In: *Materials and Structures* 39.2 (2006), pp. 247–257. DOI: 10.1617/s11527-005-9050-3.

[35] J. Segura, L. Pelà and P. Roca. 'Monotonic and cyclic testing of clay brick and lime mortar masonry in compression'. In: *Construction and Building Materials* 193 (Dec. 2018), pp. 453–466. ISSN: 0950-0618. DOI: 10.1016/J.CONBUILDMAT.2018.10.198.

[36] N. Mojsilović. 'Masonry subjected to semi-cyclic compression: Inelastic response modelling'. In: *Construction and Building Materials* 263 (Dec. 2020), p. 120147. ISSN: 0950-0618. DOI: 10.1016/J.CONBUILDMAT.2020.120147.

[37] F. J. Crisafulli. 'Seismic Behaviour of Reinforced Concrete Structures with Masonry Infills'. Ph.D. thesis. Christchurch, New Zealand: University of Canterbury, Department of Civil Engineering, 1997, p. 404.

[38] L. Facconi, F. Minelli and F. J. Vecchio. 'Predicting Uniaxial Cyclic Compressive Behavior of Brick Masonry: New Analytical Model'. In: *Journal of Structural Engineering* 144.2 (Feb. 2018). ISSN: 0733-9445. DOI: 10.1061/(asce)st.1943-541x.0001961.

[39] D. V. Oliveira and P. B. Lourenço. 'Implementation and validation of a constitutive model for the cyclic behaviour of interface elements'. In: *Computers & Structures* 82.17-19 (July 2004), pp. 1451–1461. ISSN: 0045-7949. DOI: 10.1016/J.COMPSTRUC.2004.03.041.

[40] K. Culmann. *Die graphische Statik*. Vol. 1. 2nd revised edition, with 210 woodcuts in text and 17 plates. Zürich: Meyer & Zeller (A. Reimann), 1875, xxx, 2 l., [3]–644.

[41] J. Heyman. 'The stone skeleton'. In: *International Journal of Solids and Structures* 2.2 (1966), pp. 249–279. DOI: 10.1016/0020-7683(66)90018-7.

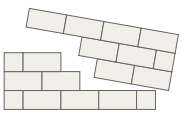
[42] P. Lourenco. 'Computational strategies for masonry structures'. PhD thesis. Delft, Netherlands: Delft University of Technology, 1996.

[43] P. B. Lourenço and J. G. Rots. 'Multisurface Interface Model for Analysis of Masonry Structures'. In: *Journal of Engineering Mechanics* 123.7 (July 1997), pp. 660–668. ISSN: 0733-9399. DOI: 10.1061/(ASCE)0733-9399(1997)123:7(660).

[44] L. Gambarotta and S. Lagomarsino. 'Damage models for the seismic response of brick masonry shear walls. Part II: The continuum model and its applications'. In: *Earthquake Engineering & Structural Dynamics* 26.4 (Apr. 1997), pp. 441–462. DOI: 10.1002/(SICI)1096-9845(199704)26:4<441::AID-EQE651>3.0.CO;2-0.

[45] G. Milani. 'Upper bound sequential linear programming mesh adaptation scheme for collapse analysis of masonry vaults'. In: *Advances in Engineering Software* 79 (2015), pp. 91–110. DOI: 10.1016/j.advengsoft.2014.09.004.

[46] S. Lagomarsino, A. Penna, A. Galasco and S. Cattari. 'TREMURI program: An equivalent frame model for the nonlinear seismic analysis of masonry buildings'. In: *Engineering Structures* 56 (Nov. 2013), pp. 1787–1799. ISSN: 0141-0296. DOI: 10.1016/J.ENGSTRUCT.2013.08.002.



[47] B. R. Hamid Lotfi and P. Benson Shing. 'Interface Model Applied to Fracture of Masonry Structures'. In: *Journal of Structural Engineering* 120.1 (Jan. 1994), pp. 63–80. ISSN: 0733-9445. DOI: 10.1061/(ASCE)0733-9445(1994)120:1(63).

[48] L. Macorini and B. A. Izzuddin. 'A non-linear interface element for 3D mesoscale analysis of brick-masonry structures'. In: *International Journal for Numerical Methods in Engineering* 85.12 (Mar. 2011), pp. 1584–1608. ISSN: 00295981. DOI: 10.1002/nme.3046.

[49] Y. Nie, A. Sheikh, P. Visintin and M. Griffith. 'A robust computational strategy for failure prediction of masonry structures using an improved multi-surface damage-plastic based interface model'. In: *International Journal for Numerical Methods in Engineering* 124.11 (June 2023), pp. 2498–2528. ISSN: 10970207. DOI: 10.1002/NME.7218.

[50] B. Pulatsu. 'Coupled elasto-softening contact models in DEM to predict the in-plane response of masonry walls'. In: *Computational Particle Mechanics* 10 (2023), pp. 1759–1770. ISSN: 2196-4378. DOI: 10.1007/s40571-023-00586-x.

[51] J. V. Lemos and V. Sarhosis. 'Discrete Element Bonded-Block Models for Detailed Analysis of Masonry'. In: *Infrastructures* 7.3 (Feb. 2022), p. 31. ISSN: 2412-3811. DOI: 10.3390/infrastructures7030031.

[52] M. Petracca, L. Pelà, R. Rossi, S. Zaghi, G. Camata and E. Spacone. 'Micro-scale continuous and discrete numerical models for nonlinear analysis of masonry shear walls'. In: *Construction and Building Materials* 149 (2017), pp. 296–314. ISSN: 0950-0618. DOI: 10.1016/j.conbuildmat.2017.05.130.

[53] R. Serpieri, M. Albarella and E. Sacco. 'A 3D microstructured cohesive–frictional interface model and its rational calibration for the analysis of masonry panels'. In: *International Journal of Solids and Structures* 122–123 (2017), pp. 110–127. ISSN: 0020-7683. DOI: 10.1016/j.ijsolstr.2017.06.006.

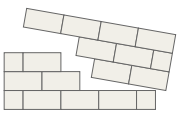
[54] A. T. Vermeltfoort, T. M. J. Raijmakers and H. J. M. Janssen. 'Shear Tests on Masonry Walls'. In: *Proceedings of the 6th North American Masonry Conference*. Ed. by A. A. Hamid and H. G. Harris. Philadelphia, Pennsylvania, USA: Technomic Publishing Co., June 1993, pp. 1183–1193.

[55] A. M. D'Altri, F. Messali, J. Rots, G. Castellazzi and S. de Miranda. 'A damaging block-based model for the analysis of the cyclic behaviour of full-scale masonry structures'. In: *Engineering Fracture Mechanics* 209 (Mar. 2019), pp. 423–448. ISSN: 00137944. DOI: 10.1016/j.engfracmech.2018.11.046.

[56] A. W. Page. 'Finite Element Model for Masonry'. In: *Journal of the Structural Division* 104.ST8 (Aug. 1978), pp. 1267–1285. DOI: 10.1061/JSDEAG.0004969.

[57] G. van Zijl. 'Modeling Masonry Shear-Compression: Role of Dilatancy Highlighted'. In: *Journal of Engineering Mechanics* 130.11 (Nov. 2004), pp. 1289–1296. ISSN: 0733-9399. DOI: 10.1061/(asce)0733-9399(2004)130:11(1289).

[58] K. Chaimoon and M. M. Attard. 'Modeling of unreinforced masonry walls under shear and compression'. In: *Engineering Structures* 29.9 (Sept. 2007), pp. 2056–2068. ISSN: 0141-0296. DOI: 10.1016/J.ENGSTRUCT.2006.10.019.



[59] S. S. Ali and A. W. Page. 'Finite Element Model for Masonry Subjected to Concentrated Loads'. In: *Journal of Structural Engineering* 114.8 (1988), pp. 1761–1784. ISSN: 0733-9445. DOI: 10.1061/(ASCE)0733-9445(1988)114:8(1761).

[60] K. F. Abdulla, L. S. Cunningham and M. Gillie. 'Simulating masonry wall behaviour using a simplified micro-model approach'. In: *Engineering Structures* 151 (Nov. 2017), pp. 349–365. ISSN: 0141-0296. DOI: 10.1016/j.engstruct.2017.08.021.

[61] C. Zhai, X. Wang, J. Kong, S. Li and L. Xie. 'Numerical Simulation of Masonry-Infilled RC Frames Using XFEM'. In: *Journal of Structural Engineering* 143.10 (2017), p. 04017144. DOI: 10.1061/(ASCE)ST.1943-541X.0001886.

[62] B. Liu, C. Liu, X. Wang, J. Kong and Z. Chang. 'Numerical Modeling Technique of Damage Behavior of Masonry-Infilled RC Frames'. In: *Applied Sciences* 13.3 (2023), p. 1521. DOI: 10.3390/app13031521.

[63] C. Avanes, C. Fusco, M. Mooneghi, Y. Huang, M. Palmieri and R. Sturt. 'LS-DYNA numerical simulation of unreinforced masonry terraced house tested dynamically'. In: *Proceedings of the 16th European Conference on Earthquake Engineering (16ECEE)*. Thessaloniki, Greece, June 2018.

[64] M. Malaspina, D. Bond, J. Dennis, M. Palmieri, G. Montalbini and R. Sturt. 'LS-DYNA numerical simulation of masonry gables out-of-plane response tested dynamically'. In: *Proceedings of the 10th ECCOMAS Thematic Conference on Computational Methods in Structural Dynamics and Earthquake Engineering (COMPDYN 2025)*. Ed. by M. Papadrakakis and M. Fragiadakis. Rhodes Island, Greece: Eccomas Proceedia, 2025, pp. 5059–5068. DOI: 10.7712/120125.12794.25324.

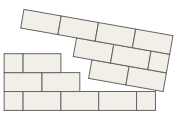
[65] P. A. Cundall. 'Formulation of a three-dimensional distinct element model—Part I. A scheme to detect and represent contacts in a system composed of many polyhedral blocks'. In: *International Journal of Rock Mechanics and Mining Sciences & Geomechanics Abstracts* 25.3 (June 1988), pp. 107–116. ISSN: 0148-9062. DOI: 10.1016/0148-9062(88)92293-0.

[66] M. Jean. 'The non-smooth contact dynamics method'. In: *Computer Methods in Applied Mechanics and Engineering* 177.3–4 (1999), pp. 235–257. ISSN: 0045-7825. DOI: 10.1016/S0045-7825(98)00383-1.

[67] K. Meguro and H. Tagel-Din. 'Applied element simulation of RC structures under cyclic loading'. In: *Journal of Structural Engineering* 127.11 (2001), pp. 1295–1305. DOI: 10.1061/(ASCE)0733-9445(2001)127:11(1295).

[68] K. Meguro and H. Tagel-Din. 'Applied element method used for large displacement structural analysis'. In: *Journal of Natural Disaster Science* 24.1 (2002), pp. 25–34.

[69] R. K. Livesley. 'Limit analysis of structures formed from rigid blocks'. In: *International Journal for Numerical Methods in Engineering* 12.12 (1978), pp. 1853–1871. ISSN: 0029-5981. DOI: 10.1002/nme.1620121207.



[70] E. Whiting, J. Ochsendorf and F. Durand. 'Procedural modeling of structurally-sound masonry buildings'. In: *ACM Transactions on Graphics* 28.5 (Dec. 2009), 112:1–112:9. ISSN: 0730-0301. DOI: 10.1145/1618452.1618458.

[71] G. T.-C. Kao, A. Iannuzzo, B. Thomaszewski, S. Coros, T. V. Mele and P. Block. 'Coupled Rigid-Block Analysis: Stability-Aware Design of Complex Discrete-Element Assemblies'. In: *Computer-Aided Design* 146 (2022), p. 103216. ISSN: 0010-4485. DOI: 10.1016/j.cad.2022.103216.

[72] A. Iannuzzo, T. Van Mele and P. Block. 'Piecewise rigid displacement (PRD) method: A limit analysis-based approach to detect mechanisms and internal forces through two dual energy criteria'. In: *Mechanics Research Communications* 107 (2020), p. 103557. ISSN: 0093-6413. DOI: 10.1016/j.mechrescom.2020.103557.

[73] M. Gilbert, C. Casapulla and H. M. Ahmed. 'Limit analysis of masonry block structures with non-associative frictional joints using linear programming'. In: *Computers & Structures* 84.13–14 (2006), pp. 873–887. ISSN: 0045-7949. DOI: 10.1016/j.compstruc.2006.02.005.

[74] C. Casapulla, E. Mousavian and M. Zarghani. 'A digital tool to design structurally feasible semi-circular masonry arches composed of interlocking blocks'. In: *Computers & Structures* 221 (2019), pp. 111–126. ISSN: 0045-7949. DOI: 10.1016/j.compstruc.2019.05.001.

[75] F. Portioli, C. Casapulla, M. Gilbert and L. Cascini. 'Limit analysis of 3D masonry block structures with non-associative frictional joints using cone programming'. In: *Computers & Structures* 143 (2014), pp. 108–121. ISSN: 0045-7949. DOI: 10.1016/j.compstruc.2014.07.010.

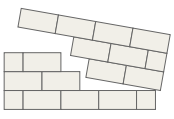
[76] C. C. Smith and M. Gilbert. 'Application of discontinuity layout optimization to plane plasticity problems'. In: *Proceedings of the Royal Society A: Mathematical, Physical and Engineering Sciences* 463.2086 (2007), pp. 2461–2484. DOI: 10.1098/rspa.2006.1788.

[77] G. Maier and A. Nappi. 'A Theory of No-Tension Discretized Structural Systems'. In: *Engineering Structures* 12.4 (1990), pp. 227–234. ISSN: 0141-0296. DOI: 10.1016/0141-0296(90)90021-J.

[78] M. Angelillo. 'A finite element approach to the study of no-tension structures'. In: *Finite Elements in Analysis and Design* 17.1 (1994), pp. 57–73. DOI: 10.1016/0168-874X(94)90020-5.

[79] G. Alfano, L. Rosati and N. Valoroso. 'A numerical strategy for finite element analysis of no-tension materials'. In: *International Journal for Numerical Methods in Engineering* 48.3 (2000), pp. 317–350. DOI: 10.1002/(SICI)1097-0207(20000530)48:3<317::AID-NME868>3.0.CO;2-C.

[80] M. Cuomo and G. Ventura. 'A complementary energy formulation of no-tension masonry-like solids'. In: *Computer Methods in Applied Mechanics and Engineering* 189.1 (2000), pp. 313–339. DOI: 10.1016/S0045-7825(99)00298-4.



[81] M. Bruggi and A. Taliercio. 'Analysis of no-tension structures under monotonic loading through an energy-based method'. In: *Computers & Structures* 159 (2015), pp. 14–25. DOI: 10.1016/j.compstruc.2015.07.002.

[82] A. Hillerborg, M. Modéer and P.-E. Petersson. 'Analysis of crack formation and crack growth in concrete by means of fracture mechanics and finite elements'. In: *Cement and Concrete Research* 6.6 (1976), pp. 773–782. ISSN: 0008-8846. DOI: 10.1016/0008-8846(76)90007-7.

[83] J. Lubliner, J. Oliver, S. Oller and E. Oñate. 'A Plastic-Damage Model for Concrete'. In: *International Journal of Solids and Structures* 25.3 (1989), pp. 299–326. ISSN: 0020-7683. DOI: 10.1016/0020-7683(89)90050-4.

[84] J. G. Rots and R. de Borst. 'Analysis of Mixed-Mode Fracture in Concrete'. In: *Journal of Engineering Mechanics* 113.11 (1987), pp. 1739–1758. ISSN: 0733-9399. DOI: 10.1061/(ASCE)0733-9399(1987)113:11(1739).

[85] J.-W. Lee and G. L. Fenves. 'Plastic-Damage Model for Cyclic Loading of Concrete Structures'. In: *Journal of Engineering Mechanics* 124.8 (Aug. 1998), pp. 892–900. ISSN: 0733-9399. DOI: 10.1061/(ASCE)0733-9399(1998)124:8(892).

[86] Z. P. Bažant and B. H. Oh. 'Crack band theory for fracture of concrete'. In: *Matériaux et Construction* 16.3 (1983), pp. 155–177. DOI: 10.1007/BF02486267.

[87] H. R. Lotfi and P. B. Shing. 'An appraisal of smeared crack models for masonry shear wall analysis'. In: *Computers & Structures* 41.3 (1991), pp. 413–425. ISSN: 0045-7949. DOI: 10.1016/0045-7949(91)90134-8.

[88] P. B. Lourenço, R. de Borst and J. G. Rots. 'A Plane Stress Softening Plasticity Model for Orthotropic Materials'. In: *International Journal for Numerical Methods in Engineering* 40.21 (1997), pp. 4033–4057. ISSN: 0029-5981. DOI: 10.1002/(SICI)1097-0207(19971115)40:21<4033::AID-NME248>3.0.CO;2-0.

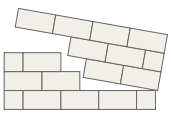
[89] L. Pelà, M. Cervera and P. Roca. 'An Orthotropic Damage Model for the Analysis of Masonry Structures'. In: *Construction and Building Materials* 41 (2013), pp. 957–967. ISSN: 0950-0618. DOI: 10.1016/j.conbuildmat.2012.07.014.

[90] P. H. Feenstra. 'Computational aspects of biaxial stress in plain and reinforced concrete'. PhD thesis. Delft, The Netherlands: Delft University of Technology, 1993.

[91] P. H. Feenstra and R. de Borst. 'A composite plasticity model for concrete'. In: *International Journal of Solids and Structures* 33.5 (1996), pp. 707–730. DOI: 10.1016/0020-7683(95)00060-N.

[92] DIANA FEA bv. *DIANA Finite Element Analysis - User's Manual*. Delft, The Netherlands, 2024. URL: https://dianafea.com/.

[93] M. Sousamli. 'Orthotropic Cyclic Continuum Constitutive Model for Masonry Structures and Comparative Studies'. Doctoral thesis. Delft, The Netherlands: Delft University of Technology, May 2024, p. 214. ISBN: 978-94-6384-584-7. DOI: 10.4233/uuid:34614723-9a3c-42c8-b70c-e4ac1dca5e8c. URL: https://doi.org/10.4233/uuid:34614723-9a3c-42c8-b70c-e4ac1dca5e8c.



[94] G. Bertani, L. Patruno, A. M. D'Altri, G. Castellazzi, M. Cervera and S. de Miranda. 'A Continuum Model for In-Plane Analysis of Masonry: An Approach Based on Failure Mode Classification'. In: *Meccanica* 60.7 (2025), pp. 1983–1999. DOI: 10.1007/s11012-024-01864-5.

[95] S. Pietruszczak and X. Niu. 'A Mathematical Description of Macroscopic Behaviour of Brick Masonry'. In: *International Journal of Solids and Structures* 29.5 (1992), pp. 531–546. ISSN: 0020-7683. DOI: 10.1016/0020-7683(92)90052-U.

[96] A. Anthoine. 'Derivation of the In-Plane Elastic Characteristics of Masonry through Homogenization Theory'. In: *International Journal of Solids and Structures* 32.2 (1995), pp. 137–163. DOI: 10.1016/0020-7683(94)00140-R.

[97] R. Masiani and P. Trovalusci. 'Cosserat and Cauchy materials as continuum models of brick masonry'. In: *Meccanica* 31.4 (Aug. 1996), pp. 421–432. ISSN: 0025-6455. DOI: 10.1007/BF00429930.

[98] I. Stefanou, J. Sulem and I. Vardoulakis. 'Three-dimensional Cosserat homogenization of masonry structures: Elasticity'. In: *Acta Geotechnica* 3.1 (2008), pp. 71–83. DOI: 10.1007/s11440-007-0051-y.

[99] A. Cecchi and K. Sab. 'A multi-parameter homogenization study for modeling elastic masonry'. In: *European Journal of Mechanics - A/Solids* 21.2 (2002), pp. 249–268. DOI: 10.1016/S0997-7538(01)01195-0.

[100] A. Drougkas, P. Roca and C. Molins. 'Analytical micro-modeling of masonry periodic unit cells – elastic properties'. In: *International Journal of Solids and Structures* 69–70 (2015), pp. 169–188. ISSN: 0020-7683. DOI: 10.1016/j.ijsolstr.2015.04.039.

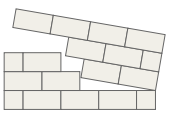
[101] M. Mistler, A. Anthoine and C. Butenweg. 'In-plane and out-of-plane homogenisation of masonry'. In: *Computers & Structures* 85.17–18 (2007), pp. 1321–1330. ISSN: 0045-7949. DOI: 10.1016/j.compstruc.2006.08.087.

[102] A. Zucchini and P. B. Lourenço. 'A micro-mechanical model for the homogenisation of masonry'. In: *International Journal of Solids and Structures* 39.12 (2002), pp. 3233–3255. ISSN: 0020-7683. DOI: 10.1016/S0020-7683(02)00230-5.

[103] L. Gambarotta and S. Lagomarsino. 'Damage models for the seismic response of brick masonry shear walls. Part I: The mortar joint model and its applications'. In: *Earthquake Engineering & Structural Dynamics* 26.4 (1997), pp. 423–439. DOI: 10.1002/(SICI)1096-9845(199704)26:4<423::AID-EQE650>3.0.CO;2-J.

[104] C. Calderini and S. Lagomarsino. 'A Micromechanical Inelastic Model for Historical Masonry'. In: *Journal of Earthquake Engineering* 10.4 (July 2006), pp. 453–479. DOI: 10.1080/13632460609350605.

[105] A. Zucchini and P. B. Lourenço. 'A micro-mechanical homogenisation model for masonry: Application to shear walls'. In: *International Journal of Solids and Structures* 46.3–4 (2009), pp. 871–886. ISSN: 0020-7683. DOI: 10.1016/j.ijsolstr.2008.09.034.



[106] E. Sacco. 'A nonlinear homogenization procedure for periodic masonry'. In: *European Journal of Mechanics - A/Solids* 28.2 (2009), pp. 209–222. ISSN: 0997-7538. DOI: 10.1016/j.euromechsol.2008.06.005.

[107] S. Marfia and E. Sacco. 'Multiscale Damage Contact–Friction Model for Periodic Masonry Walls'. In: *Computer Methods in Applied Mechanics and Engineering* 205–208 (2012), pp. 189–203. ISSN: 0045-7825. DOI: 10.1016/j.cma.2010.12.024.

[108] T. J. Massart, R. H. J. Peerlings and M. G. D. Geers. 'An enhanced multi-scale approach for masonry wall computations with localization of damage'. In: *International Journal for Numerical Methods in Engineering* 69.5 (2007), pp. 1022–1059. DOI: 10.1002/nme.1799.

[109] D. Addessi, S. Marfia, E. Sacco and J. Toti. 'Modeling Approaches for Masonry Structures'. In: *The Open Civil Engineering Journal* 8 (2014), pp. 288–300. ISSN: 1874-1495. DOI: 10.2174/1874149501408010288.

[110] G. Salerno and G. de Felice. 'Continuum modeling of periodic brickwork'. In: *International Journal of Solids and Structures* 46.5 (2009), pp. 1251–1267. ISSN: 0020-7683. DOI: 10.1016/j.ijsolstr.2008.10.034.

[111] S. Casolo. 'Macroscopic modelling of structured materials: Relationship between orthotropic Cosserat continuum and rigid elements'. In: *International Journal of Solids and Structures* 43.3–4 (2006), pp. 475–496. ISSN: 0020-7683. DOI: 10.1016/j.ijsolstr.2005.03.037.

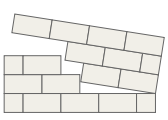
[112] D. Addessi, E. Sacco and A. Paolone. 'Cosserat model for periodic masonry deduced by nonlinear homogenization'. In: *European Journal of Mechanics - A/Solids* 29.4 (2010), pp. 724–737. ISSN: 0997-7538. DOI: 10.1016/j.euromechsol.2010.03.001.

[113] M. L. D. Bellis and D. Addessi. 'A Cosserat Based Multi-Scale Model for Masonry Structures'. In: *International Journal for Multiscale Computational Engineering* 9.5 (2011), pp. 543–563. DOI: 10.1615/IntJMultCompEng.2011002758.

[114] L. Leonetti, F. Greco, P. Trovalusci, R. Luciano and R. Masiani. 'A multiscale damage analysis of periodic composites using a couple-stress/Cauchy multidomain model: Application to masonry structures'. In: *Composites Part B: Engineering* 141 (2018), pp. 50–59. DOI: 10.1016/j.compositesb.2017.12.025.

[115] S. Brasile, R. Casciaro and G. Formica. 'Multilevel approach for brick masonry walls – Part II: On the use of equivalent continua'. In: *Computer Methods in Applied Mechanics and Engineering* 196.49–52 (2007), pp. 4801–4810. DOI: 10.1016/j.cma.2007.06.020.

[116] E. Reccia, L. Leonetti, P. Trovalusci and A. Cecchi. 'A multiscale/multi-domain model for the failure analysis of masonry walls: A validation with a combined FEM/DEM approach'. In: *International Journal for Multiscale Computational Engineering* 16.4 (2018), pp. 325–343. DOI: 10.1615/IntJMultCompEng.2018026988.



[117] O. Lloberas-Valls, D. J. Rixen, A. Simone and L. J. Sluys. 'Multiscale domain decomposition analysis of quasi-brittle heterogeneous materials'. In: *International Journal for Numerical Methods in Engineering* 89.11 (2012), pp. 1337–1366. DOI: 10.1002/nme.3286.

[118] P. Block, T. Ciblac and J. A. Ochsendorf. 'Real-time limit analysis of vaulted masonry buildings'. In: *Computers & Structures* 84.29–30 (2006), pp. 1841–1852. ISSN: 0045-7949. DOI: 10.1016/j.compstruc.2006.08.002.

[119] T. Van Mele and P. Block. 'Algebraic graph statics'. In: *Computer-Aided Design* 53 (2014), pp. 104–116. ISSN: 0010-4485. DOI: 10.1016/j.cad.2014.04.004.

[120] R. M. Avelino, J. Lee, T. V. Mele and P. Block. 'An interactive implementation of algebraic graphic statics for geometry-based teaching and design of structures'. In: *Proceedings of the International fib Symposium on the Conceptual Design of Structures*. Ed. by C. Fivet, P. D'Acunto and M. F. Ruiz. Vol. 55. fib Symposium Proceedings. Attisholz-Areal, Switzerland, Sept. 2021, pp. 447–454. DOI: 10.35789/fib.PROC.0055.2021.CDSymp.P054.

[121] F. Marmo. 'ArchLab: a MATLAB tool for the Thrust Line Analysis of masonry arches'. In: *Curved and Layered Structures* 8.1 (2021), pp. 26–35. DOI: 10.1515/cls-2021-0003.

[122] K. I. U. Nanayakkara, A. C. Liew and M. Gilbert. 'Application of thrust layout optimization to masonry structures'. In: *Proceedings of the Royal Society A: Mathematical, Physical and Engineering Sciences* 479.2273 (2023), p. 20230053. DOI: 10.1098/rspa.2023.0053.

[123] D. O'Dwyer. 'Funicular analysis of masonry vaults'. In: *Computers & Structures* 73.1–5 (1999), pp. 187–197. ISSN: 0045-7949. DOI: 10.1016/S0045-7949(98)00279-X.

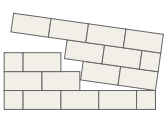
[124] P. Block and J. Ochsendorf. 'Thrust Network Analysis: A New Methodology for Three-Dimensional Equilibrium'. In: *Journal of the International Association for Shell and Spatial Structures* 48.3 (2007), pp. 167–173.

[125] P. Block. 'Thrust Network Analysis: Exploring Three-Dimensional Equilibrium'. Ph.D. thesis. Cambridge, MA: Massachusetts Institute of Technology, 2009. URL: https://dspace.mit.edu/handle/1721.1/49539.

[126] M. Rippmann, L. Lachauer and P. Block. 'Interactive Vault Design'. In: *International Journal of Space Structures* 27.4 (2012), pp. 219–230. DOI: 10.1260/0266-3511.27.4.219.

[127] R. M. Avelino, A. Iannuzzo, T. Van Mele and P. Block. 'Assessing the safety of vaulted masonry structures using thrust network analysis'. In: *Computers & Structures* 257 (2021), p. 106647. ISSN: 0045-7949. DOI: 10.1016/j.compstruc.2021.106647.

[128] N. A. Nodargi and P. Bisegna. 'Generalized thrust network analysis for the safety assessment of vaulted masonry structures'. In: *Engineering Structures* 270 (2022), p. 114878. ISSN: 0141-0296. DOI: 10.1016/j.engstruct.2022.114878.



[129] P. Block and L. Lachauer. 'Three-dimensional funicular analysis of masonry vaults'. In: *Mechanics Research Communications* 56 (2014), pp. 53–60. DOI: 10.1016/j.mechrescom.2013.11.010.

[130] F. Fraternali, M. Angelillo and A. Fortunato. 'A lumped stress method for plane elastic problems and the discrete–continuum approximation'. In: *International Journal of Solids and Structures* 39.25 (2002), pp. 6211–6240. ISSN: 0020-7683. DOI: 10.1016/S0020-7683(02)00472-9.

[131] F. Fraternali. 'A thrust network approach to the equilibrium problem of unreinforced masonry vaults via polyhedral stress functions'. In: *Mechanics Research Communications* 37.2 (Mar. 2010), pp. 198–204. ISSN: 0093-6413. DOI: 10.1016/J.MECHRESCOM.2009.12.010.

[132] M. Angelillo, E. Babilio and A. Fortunato. 'Singular stress fields for masonry-like vaults'. In: *Continuum Mechanics and Thermodynamics* 25.2–4 (2013), pp. 423–441. DOI: 10.1007/s00161-012-0270-9.

[133] A. Fraddosio, N. Lepore and M. D. Piccioni. 'Lower Bound Limit Analysis of Masonry Vaults Under General Load Conditions'. In: *Structural Analysis of Historical Constructions: An Interdisciplinary Approach*. Ed. by R. Aguilar, D. Torrealva, S. Moreira, M. A. Pando and L. F. Ramos. Vol. 18. RILEM Bookseries. Cham: Springer, 2019, pp. 1090–1098. ISBN: 978-3-319-99440-6. DOI: 10.1007/978-3-319-99441-3_118.

[134] A. Chiozzi, G. Milani and A. Tralli. 'A Genetic Algorithm NURBS-based new approach for fast kinematic limit analysis of masonry vaults'. In: *Computers & Structures* 182 (Apr. 2017), pp. 187–204. ISSN: 0045-7949. DOI: 10.1016/J.COMPSTRUC.2016.11.003.

[135] M. Tomaževič. *The Computer Program POR*. Tech. rep. Report (in Slovenian). Ljubljana, Slovenia: ZRMK — Institute for Testing, Research in Materials and Structures, 1978.

[136] A. Brencich, L. Gambarotta and S. Lagomarsino. 'A macroelement approach to the three-dimensional seismic analysis of masonry buildings'. In: *Proceedings of the 11th European Conference on Earthquake Engineering (11ECEE)*. Paris, France: A. A. Balkema, 1998, Paper 602.

[137] D. Addessi, A. Mastrandrea and E. Sacco. 'An equilibrated macro-element for nonlinear analysis of masonry structures'. In: *Engineering Structures* 70 (2014), pp. 82–93. ISSN: 0141-0296. DOI: 10.1016/j.engstruct.2014.03.034.

[138] D. Addessi, D. Liberatore and R. Masiani. 'Force-Based Beam Finite Element (FE) for the Pushover Analysis of Masonry Buildings'. In: *International Journal of Architectural Heritage* 9.3 (2015), pp. 231–243. DOI: 10.1080/15583058.2013.768309.

[139] S. Cattari and S. Lagomarsino. 'Masonry Structures'. In: *Developments in the Field of Displacement-Based Seismic Assessment*. Ed. by T. Sullivan and G. M. Calvi. Pavia, Italy: IUSS Press and EUCENTRE, 2013, pp. 151–200. ISBN: 978-88-6198-090-7.



[140] F. Vanin, A. Penna and K. Beyer. 'Equivalent-Frame Modeling of Two Shaking Table Tests of Masonry Buildings Accounting for Their Out-Of-Plane Response'. In: *Frontiers in Built Environment* 6 (Apr. 2020), p. 519374. ISSN: 22973362. DOI: 10.3389/FBUIL.2020.00042/BIBTEX.

[141] G. Alfano and E. Sacco. 'Combining interface damage and friction in a cohesive-zone model'. In: *International Journal for Numerical Methods in Engineering* 68.5 (Oct. 2006), pp. 542–582. ISSN: 1097-0207. DOI: 10.1002/NME.1728. URL: https://onlinelibrary.wiley.com/doi/full/10.1002/nme.1728%20https://onlinelibrary.wiley.com/doi/abs/10.1002/nme.1728%20https://onlinelibrary.wiley.com/doi/10.1002/nme.1728.

[142] A. Penna, S. Lagomarsino and A. Galasco. 'A nonlinear macroelement model for the seismic analysis of masonry buildings'. In: *Earthquake Engineering & Structural Dynamics* 43.2 (2014), pp. 159–179. DOI: 10.1002/eqe.2335.

[143] S.-Y. Chen, F. L. Moon and T. Yi. 'A macroelement for the nonlinear analysis of in-plane unreinforced masonry piers'. In: *Engineering Structures* 30.8 (2008), pp. 2242–2252. DOI: 10.1016/j.engstruct.2007.12.001.

[144] L. Gambarotta and S. Lagomarsino. 'On the dynamic response of masonry panels'. In: *Masonry Mechanics Between Theory and Practice: Proceedings of the National Conference.* Ed. by L. Gambarotta. Bologna: Pitagora Editrice, 18th–20th Sept. 1996, pp. 451–462.

[145] A. Brencich and S. Lagomarsino. 'A macroelement dynamic model for masonry shear walls'. In: *Computer Methods in Structural Masonry IV*. Ed. by G. N. Pande and J. Middleton. London: E & FN Spon (Taylor & Francis), 1998, pp. 67–75.

[146] I. Caliò, M. Marletta and B. Pantò. 'A new discrete element model for the evaluation of the seismic behaviour of unreinforced masonry buildings'. In: *Engineering Structures* 40 (2012), pp. 327–338. DOI: 10.1016/j.engstruct.2012.02.039.

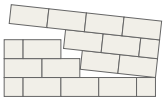
[147] B. Pantò, F. Cannizzaro, S. Caddemi and I. Caliò. '3D macro-element modelling approach for seismic assessment of historical masonry churches'. In: *Advances in Engineering Software* 97 (2016), pp. 40–59. DOI: 10.1016/j.advengsoft.2016.02.009.

[148] B. Pantò, I. Caliò and P. B. Lourenço. 'A 3D discrete macro-element for modelling the out-of-plane behaviour of infilled frame structures'. In: *Engineering Structures* 175 (2018), pp. 371–385. DOI: 10.1016/j.engstruct.2018.08.022.

[149] I. Caliò and B. Pantò. 'A macro-element modelling approach of infilled frame structures'. In: *Computers & Structures* 143 (2014), pp. 91–107. DOI: 10.1016/j.compstruc.2014.07.008.

[150] P. A. Cundall and R. D. Hart. 'Numerical modelling of discontinua'. In: *Engineering Computations* 9.2 (1992), pp. 101–113. ISSN: 0264-4401. DOI: 10.1108/eb023851.

[151] G.-H. Shi. 'Discontinuous Deformation Analysis: A New Numerical Model for the Statics and Dynamics of Block Systems'. In: *Engineering Computations* 9.2 (1992), pp. 157–168. ISSN: 0264-4401. DOI: 10.1108/eb023888.



[152] A. A. Munjiza. *The Combined Finite–Discrete Element Method*. Hoboken: Wiley, 2004.

[153] J. V. Lemos and K. Bagi. 'Discrete Element Modeling'. In: *Discrete Computational Mechanics of Masonry Structures*. Ed. by K. Bagi and M. Angelillo. CISM International Centre for Mechanical Sciences. Cham: Springer, 2023, pp. 189–232. ISBN: 978-3-031-32475-8. DOI: 10.1007/978-3-031-32476-5_5.

[154] D. Malomo and M. J. DeJong. 'M-DEM simulation of seismic pounding between adjacent masonry structures'. In: *Bulletin of Earthquake Engineering* 22.12 (Sept. 2022), pp. 6067–6092. ISSN: 15731456. DOI: 10.1007/S10518-022-01545-2/FIGURES/12. URL: https://link.springer.com/article/10.1007/s10518-022-01545-2.

[155] W. Chen, H. Konietzky, C. Liu, H. Fu and J. Zhang. 'Prediction of Brickwork Failure Using Discrete-Element Method'. In: *Journal of Materials in Civil Engineering* 30.9 (Sept. 2018), p. 06018012. DOI: 10.1061/(ASCE)MT.1943-5533.0002431.

[156] V. Sarhosis and J. V. Lemos. 'A detailed micro-modelling approach for the structural analysis of masonry assemblages'. In: *Computers & Structures* 206 (Aug. 2018), pp. 66–81. ISSN: 00457949. DOI: 10.1016/j.compstruc.2018.06.003.

[157] B. Pulatsu, E. Erdogmus, P. B. Lourenço, J. V. Lemos and J. Hazzard. 'Discontinuum analysis of the fracture mechanism in masonry prisms and wallettes via discrete element method'. In: *Meccanica* 55.3 (Mar. 2020), pp. 505–523. ISSN: 15729648. DOI: 10.1007/s11012-020-01133-1.

[158] H. P. Backes. 'Tensile Strength of Masonry'. In: *Proceedings of the 7th International Brick Masonry Conference*. Melbourne, Australia, 1985, pp. 779–790.

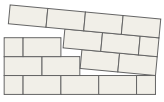
[159] C. R. Willis. 'Design of Unreinforced Masonry Walls for Out-of-Plane Loading'. Ph.D. thesis. Adelaide, Australia: The University of Adelaide, School of Civil and Environmental Engineering, 2004. URL: https://digital.library.adelaide.edu.au/bitstream/2440/22133/2/02whole.pdf.

[160] M. Godio, I. Stefanou and K. Sab. 'Effects of the dilatancy of joints and of the size of the building blocks on the mechanical behavior of masonry structures'. In: *Meccanica* 53.7 (2018), pp. 1629–1643. DOI: 10.1007/s11012-017-0688-z.

[161] N. Damiani, M. J. DeJong, L. Albanesi, A. Penna and P. Morandi. 'Distinct element modeling of the in-plane response of a steel-framed retrofit solution for URM structures'. In: *Earthquake Engineering & Structural Dynamics* 52.10 (2023), pp. 3030–3052. ISSN: 1096-9845. DOI: https://doi.org/10.1002/eqe.3910.

[162] B. Pulatsu, E. Erdogmus, P. B. Lourenço, J. V. Lemos and K. Tuncay. 'Simulation of the in-plane structural behavior of unreinforced masonry walls and buildings using DEM'. In: *Structures* 27 (2020), pp. 2274–2287. DOI: 10.1016/j.istruc.2020.08.026.

[163] T. T. Bui, A. Limam, V. Sarhosis and M. Hjiaj. 'Discrete element modelling of the in-plane and out-of-plane behaviour of dry-joint masonry wall constructions'. In: *Engineering Structures* 136 (Apr. 2017), pp. 277–294. ISSN: 18737323. DOI: 10.1016/J.ENGSTRUCT.2017.01.020.



[164] B. Pulatsu, S. Gonen, F. Parisi, E. Erdogmus, K. Tuncay, M. F. Funari and P. B. Lourenço. 'Probabilistic approach to assess URM walls with openings using discrete rigid block analysis (D-RBA)'. In: *Journal of Building Engineering* 61 (Dec. 2022), p. 105269. ISSN: 2352-7102. DOI: 10.1016/J.JOBE.2022.105269.

[165] B. Pulatsu, R. Wilson, J. V. Lemos and N. Mojsilović. 'Exploring the Cyclic Behaviour of URM Walls with and without Damp-Proof Course (DPC) Membranes through Discrete Element Method'. In: *Infrastructures 2024, Vol. 9, Page 11* 9.1 (Jan. 2024), p. 11. ISSN: 2412-3811. DOI: 10.3390/INFRASTRUCTURES9010011. URL: https://www.mdpi.com/2412-3811/9/1/11/htm%20https://www.mdpi.com/2412-3811/9/1/11.

[166] D. Malomo and M. J. DeJong. 'A Macro-Distinct Element Model (M-DEM) for simulating the in-plane cyclic behavior of URM structures'. In: *Engineering Structures* 227 (2020), p. 111428. DOI: 10.1016/j.engstruct.2020.111428.

[167] P. H. Feenstra and R. de Borst. 'A composite plasticity model for concrete'. In: *International Journal of Solids and Structures* 33.5 (1996), pp. 707–730. DOI: 10.1016/0020-7683(95)00060-N.

[168] G. de Felice. 'Out-of-Plane Seismic Capacity of Masonry Depending on Wall Section Morphology'. In: *International Journal of Architectural Heritage* 5.4–5 (2011), pp. 466–482. DOI: 10.1080/15583058.2010.530339.

[169] O. Al Shawa, G. de Felice, A. Mauro and L. Sorrentino. 'Out-of-plane seismic behaviour of rocking masonry walls'. In: *Earthquake Engineering & Structural Dynamics* 41.5 (2012), pp. 949–968. DOI: 10.1002/eqe.1168.

[170] F. Galvez, L. Sorrentino, D. Dizhur and J. M. Ingham. 'Damping considerations for rocking block dynamics using the discrete element method'. In: *Earthquake Engineering & Structural Dynamics* 51.4 (2022), pp. 935–957. DOI: 10.1002/eqe.3598.

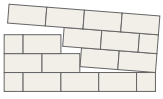
[171] L. De Lorenzis, M. J. DeJong and J. A. Ochsendorf. 'Failure of masonry arches under impulse base motion'. In: *Earthquake Engineering & Structural Dynamics* 36.14 (2007), pp. 2119–2136. DOI: 10.1002/eqe.719.

[172] V. Sarhosis, D. V. Oliveira, J. V. Lemos and P. B. Lourenco. 'The effect of skew angle on the mechanical behaviour of masonry arches'. In: *Mechanics Research Communications* 61 (Oct. 2014), pp. 53–59. ISSN: 0093-6413. DOI: 10.1016/J.MECHRESCOM.2014.07.008.

[173] T. Forgács, V. Sarhosis and K. Bagi. 'Minimum thickness of semi-circular skewed masonry arches'. In: *Engineering Structures* 140 (2017), pp. 317–336. DOI: 10.1016/j.engstruct.2017.02.036.

[174] J. McInerney and M. J. DeJong. 'Discrete Element Modeling of Groin Vault Displacement Capacity'. In: *International Journal of Architectural Heritage* 9.8 (2015), pp. 1037–1049. DOI: 10.1080/15583058.2014.923953.

[175] G. Lengyel. 'Discrete element analysis of gothic masonry vaults for self-weight and horizontal support displacement'. In: *Engineering Structures* 148 (2017), pp. 195–209. DOI: 10.1016/j.engstruct.2017.06.014.



[176] N. Bianchini, N. Mendes, P. B. Lourenço and C. Calderini. 'Modelling of the Dynamic Response of a Full-Scale Masonry Groin Vault: Unstrengthened and Strengthened with Textile-Reinforced Mortar (TRM)'. In: *International Journal of Architectural Heritage* 18.12 (2024), pp. 2042–2066. DOI: 10.1080/15583058.2024.2320857.

[177] R. G. Selby and F. J. Vecchio. 'A constitutive model for analysis of reinforced concrete solids'. In: *Canadian Journal of Civil Engineering* 24.3 (1997), pp. 460–470. DOI: 10.1139/l96-135.

[178] V. Paris, A. Pizzigoni and S. Adriaenssens. 'Statics of self-balancing masonry domes constructed with a cross-herringbone spiraling pattern'. In: *Engineering Structures* 215 (July 2020), p. 110440. ISSN: 0141-0296. DOI: 10.1016/j.engstruct.2020.110440.

[179] J. Simon and K. Bagi. 'Discrete Element Analysis of the Minimum Thickness of Oval Masonry Domes'. In: *International Journal of Architectural Heritage* 10.4 (2016), pp. 457–475. DOI: 10.1080/15583058.2014.996921.

[180] S. Chen and K. Bagi. 'DEM Analysis of Masonry Open Vaults with Square Bays'. In: *International Journal of Architectural Heritage* (2024), pp. 1–19. DOI: 10.1080/15583058.2024.2394687.

[181] V. Sarhosis, T. Forgács and J. V. Lemos. 'A discrete approach for modelling backfill material in masonry arch bridges'. In: *Computers & Structures* 224 (2019), p. 106108. ISSN: 0045-7949. DOI: 10.1016/j.compstruc.2019.106108.

[182] B. Pulatsu, E. Erdogmus and P. B. Lourenço. 'Comparison of in-plane and out-of-plane failure modes of masonry arch bridges using discontinuum analysis'. In: *Engineering Structures* 178 (2019), pp. 24–36. DOI: 10.1016/j.engstruct.2018.10.016.

[183] A. Furiosi *et al.* 'Seismic Fragility Assessment of a Multi-Span Masonry Arch Bridge Using a Discontinuum Modeling Approach'. In: *Earthquake Engineering & Structural Dynamics* (2025). DOI: 10.1002/eqe.70029.

[184] J.-C. Quezada-Guajardo, É. Vincens, R. Mouterde and J.-C. Morel. '3D failure of a scale-down dry stone retaining wall: A DEM modelling'. In: *Engineering Structures* 117 (2016), pp. 506–517. DOI: 10.1016/j.engstruct.2016.03.020.

[185] J. Azevedo, G. Sincraian and J. V. Lemos. 'Seismic Behavior of Blocky Masonry Structures'. In: *Earthquake Spectra* 16.2 (2000), pp. 337–365. DOI: 10.1193/1.1586116.

[186] G. de Felice, R. Fugger and F. Gobbin. 'Overturning of the façade in single-nave churches under seismic loading'. In: *Bulletin of Earthquake Engineering* 20.2 (2022), pp. 941–962. DOI: 10.1007/s10518-021-01243-5.

[187] M. Schiavoni, E. Giordano, F. Roscini and F. Clementi. 'Numerical modeling of a majestic masonry structure: A comparison of advanced techniques'. In: *Engineering Failure Analysis* 149 (2023), p. 107293. ISSN: 1350-6307. DOI: 10.1016/j.engfailanal.2023.107293.



[188] M. Schiavoni, E. Giordano, F. Roscini and F. Clementi. 'Advanced numerical insights for an effective seismic assessment of historical masonry aggregates'. In: *Engineering Structures* 285 (June 2023), p. 115997. ISSN: 0141-0296. DOI: 10.1016/J.ENGSTRUCT.2023.115997.

[189] E. Çaktı, Ö. Saygılı, J. V. Lemos and C. S. Oliveira. 'Discrete element modeling of a scaled masonry structure and its validation'. In: *Engineering Structures* 126 (2016), pp. 224–236. DOI: 10.1016/j.engstruct.2016.07.044.

[190] A. Mehrotra and M. J. DeJong. 'The Performance of Slender Monuments during the 2015 Gorkha, Nepal, Earthquake'. In: *Earthquake Spectra* 33.1_suppl (2017), S321–S343. DOI: 10.1193/120616EQS223M.

[191] R. Yanez Chura, P. Meriggi, C. Choueiri and G. de Felice. 'Seismic assessment of churches through integration of digital survey, texture recognition and distinct element modelling'. In: *Journal of Building Engineering* 98 (2024), p. 111375. DOI: 10.1016/j.jobe.2024.111375.

[192] P. Meriggi, G. De Felice, S. De Santis, F. Gobbin, A. Mordanova and B. Pantò. 'Distinct Element Modelling of Masonry Walls under Out-Of-Plane Seismic Loading'. In: *International Journal of Architectural Heritage* 13.7 (2019), pp. 1110–1123. ISSN: 1558-3066. DOI: 10.1080/15583058.2019.1615152. URL: https://www.tandfonline.com/action/journalInformation?journalCode=uarc20.

[193] A. Ferrante, D. Loverdos, F. Clementi, G. Milani, A. Formisano, S. Lenci and V. Sarhosis. 'Discontinuous approaches for nonlinear dynamic analyses of an ancient masonry tower'. In: *Engineering Structures* 230 (2021), p. 111626. ISSN: 0141-0296. DOI: 10.1016/j.engstruct.2020.111626.

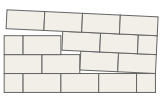
[194] T. Ulrich, C. Negulescu and A. Ducellier. 'Using the discrete element method to assess the seismic vulnerability of aggregated masonry buildings'. In: *Bulletin of Earthquake Engineering* 13.10 (2015), pp. 3135–3150. DOI: 10.1007/s10518-015-9754-x.

[195] F. Galvez, D. Dizhur and J. M. Ingham. 'Adjacent interacting masonry structures: shake table test blind prediction discrete element method simulation'. In: *Bulletin of Earthquake Engineering* 22.12 (Sept. 2023), pp. 6037–6063. ISSN: 15731456. DOI: 10.1007/S10518-023-01640-Y/FIGURES/16. URL: https://link.springer.com/article/10.1007/s10518-023-01640-y.

[196] I. Tomić, A. Penna, M. J. DeJong *et al.* 'Shake-table testing of a stone masonry building aggregate: overview of blind prediction study'. In: *Bulletin of Earthquake Engineering* 22 (2024), pp. 5993–6035. DOI: 10.1007/s10518-022-01582-x.

[197] D. Malomo and M. J. DeJong. 'M-DEM simulation of seismic pounding between adjacent masonry structures'. In: *Bulletin of Earthquake Engineering* 22.12 (2022), pp. 6067–6092. DOI: 10.1007/s10518-022-01545-2.

[198] J.-J. Moreau. 'Unilateral Contact and Dry Friction in Finite Freedom Dynamics'. In: *Nonsmooth Mechanics and Applications*. Ed. by J.-J. Moreau and P. D. Panagiotopoulos. Vol. 302. CISM International Centre for Mechanical Sciences. Springer-Verlag Wien, 1988, pp. 1–82. DOI: 10.1007/978-3-7091-2624-0_1.



[199] T. Unger and J. Kertész. 'The Contact Dynamics Method for Granular Media'. In: *AIP Conference Proceedings*. Vol. 661. 1. Melville, NY: American Institute of Physics, 2003, pp. 116–138. DOI: 10.1063/1.1571300.

[200] M. Bisoffi-Sauvé, S. Morel and F. Dubois. 'Modelling mixed mode fracture of mortar joints in masonry buildings'. In: *Engineering Structures* 182 (2019), pp. 316–330. DOI: 10.1016/j.engstruct.2018.11.064.

[201] I. Bouckaert, M. Godio and J. Pacheco de Almeida. 'A Strategy for Generating Pushover Curves of Block Assemblies Including Post-peak Branch Using the Discrete Element Method'. In: *Proceedings of the 3rd European Conference on Earthquake Engineering & Seismology (3ECEES)*. 4–9 September 2022. Bucharest, Romania, 2022. URL: https://urn.kb.se/resolve?urn=urn:nbn:se:ri:diva-60142.

[202] A. Isfeld and N. Shrive. 'Discrete Element Modeling of Stone Masonry Walls with Varying Core Conditions: Prince of Wales Fort Case Study'. In: *International Journal of Architectural Heritage* 9.5 (2015), pp. 564–580. DOI: 10.1080/15583058.2013.819135.

[203] F. Dubois, V. Acary and M. Jean. 'The Contact Dynamics method: A nonsmooth story'. In: *Comptes Rendus Mécanique* 346.3 (2018), pp. 247–262. DOI: 10.1016/j.crme.2017.12.009.

[204] P. Taforel, F. Dubois and S. Pagano. 'Evaluation of Numerical Uncertainties on the Modeling of Dry Masonry Structures Submitted to Out-of-Plane Loading, Using the NSCD Method in Comparison with Experimental Test'. In: *Proceedings of the European Congress on Computational Methods in Applied Sciences and Engineering (ECCOMAS 2012)*. Full text available online. Vienna, Austria, 2013. URL: https://www.researchgate.net/publication/281991603.

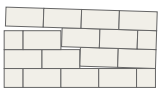
[205] B. Chetouane, F. Dubois, M. Vinches and C. Bohatier. 'NSCD discrete element method for modelling masonry structures'. In: *International Journal for Numerical Methods in Engineering* 64.1 (2005), pp. 65–94. DOI: 10.1002/nme.1358.

[206] A. Rafiee, M. Vinches and C. Bohatier. 'Modelling and analysis of the Nimes arena and the Arles aqueduct subjected to a seismic loading, using the Non-Smooth Contact Dynamics method'. In: *Engineering Structures* 30.12 (2008), pp. 3457–3467. DOI: 10.1016/j.engstruct.2008.05.018.

[207] V. Beatini, G. Royer-Carfagni and A. Tasora. 'Modeling the shear failure of segmental arches'. In: *International Journal of Solids and Structures* 158 (2019), pp. 21–39. DOI: 10.1016/j.ijsolstr.2018.08.023.

[208] G. Lancioni, D. Gentilucci, E. Quagliarini and S. Lenci. 'Seismic vulnerability of ancient stone arches by using a numerical model based on the Non-Smooth Contact Dynamics method'. In: *Engineering Structures* 119 (July 2016), pp. 110–121. DOI: 10.1016/j.engstruct.2016.04.001.

[209] A. Ferrante, F. Dubois and P. Morenon. 'Comparison of Continuous and Discrete Modeling Strategies for the Structural Assessment of a Masonry Vault Under Dynamic Seismic Loading'. In: *International Journal of Architectural Heritage* 18.12 (2024), pp. 1873–1885. DOI: 10.1080/15583058.2024.2377297.



[210] H. Tagel-Din and K. Meguro. 'Applied Element Method for simulation of nonlinear materials: theory and application for RC structures'. In: *Structural Engineering / Earthquake Engineering* 17.2 (2000), pp. 137–148.

[211] D. Malomo and B. Pulatsu. 'Discontinuum models for the structural and seismic assessment of unreinforced masonry structures: a critical appraisal'. In: *Structures* 62 (Apr. 2024), p. 106108. ISSN: 2352-0124. DOI: 10.1016/J.ISTRUC.2024.106108.

[212] H. Tagel-Din. 'A New Efficient Method for Nonlinear, Large Deformation and Collapse Analysis of Structures'. Ph.D. thesis. Tokyo, Japan: University of Tokyo, 1998.

[213] H. Okamura and K. Maekawa. *Nonlinear Analysis and Constitutive Models of Reinforced Concrete*. Tokyo: Gihodo Co., Ltd., 1991.

[214] D. Malomo, R. Pinho and A. Penna. 'Applied Element Modelling of the Dynamic Response of a Full-scale Clay Brick Masonry Building Specimen with Flexible Diaphragms'. In: *International Journal of Architectural Heritage* 14.10 (2020), pp. 1484–1501. DOI: 10.1080/15583058.2019.1616004.

[215] D. Malomo, R. Pinho and A. Penna. 'Numerical modelling of the out-of-plane response of full-scale brick masonry prototypes subjected to incremental dynamic shake-table tests'. In: *Engineering Structures* 209 (Apr. 2020), p. 110298. ISSN: 0141-0296. DOI: 10.1016/J.ENGSTRUCT.2020.110298.

[216] R. K. Adhikari and D. D'Ayala. '2015 Nepal earthquake: seismic performance and post-earthquake reconstruction of stone in mud mortar masonry buildings'. In: *Bulletin of Earthquake Engineering* 18.8 (2020), pp. 3863–3896. DOI: 10.1007/s10518-020-00834-y.

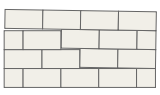
[217] B. H. Pandey and K. Meguro. 'Simulation of brick masonry wall behavior under in-plane lateral loading using the Applied Element Method'. In: *Proceedings of the 13th World Conference on Earthquake Engineering (13WCEE)*. IAEE. Vancouver, Canada, Aug. 2004.

[218] P. Mayorca and K. Meguro. 'Modeling Masonry Structures using the Applied Element Method'. In: *Seisan Kenkyu* 55.6 (Nov. 2003), pp. 581–584. DOI: 10.11188/seisankenkyu.55.581.

[219] R. K. Adhikari, A. Parammal Vatteri and D. D'Ayala. 'Seismic Performance Assessment of Low-Rise Unreinforced and Confined Brick Masonry School Buildings Using the Applied Element Method'. In: *Buildings* 13.1 (2023), p. 159. DOI: 10.3390/buildings13010159.

[220] D. Malomo, R. Pinho and A. Penna. 'Using the applied element method for modelling calcium silicate brick masonry subjected to in-plane cyclic loading'. In: *Earthquake Engineering & Structural Dynamics* 47.7 (2018), pp. 1610–1630. DOI: 10.1002/eqe.3032.

[221] C. Morandini, D. Malomo and A. Penna. 'Equivalent frame discretisation for URM façades with irregular opening layouts'. In: *Bulletin of Earthquake Engineering* 20.5 (2022), pp. 2589–2618. DOI: 10.1007/s10518-022-01315-0.



[222] S. Sharma, A. Marasca, M. Ponte and R. Bento. 'Modelling the in-plane cyclic behaviour of typical Portuguese rubble stone masonry using the applied element method'. In: *Structures* 46 (2022), pp. 1224–1242. DOI: 10.1016/j.istruc.2022.10.107.

[223] Applied Science International, LLC. *Extreme Loading for Structures (ELS)*. Computer software. 2018.

[224] L. Davis, M. Cogliano, C. Casotto, G. Grecchi, S. Ozcebe, C. Tsioli and D. Malomo. 'Pragmatic seismic collapse meso-scale analysis of old Dutch masonry churches'. In: *Earthquake Engineering and Structural Dynamics* 53 (2023), pp. 622–645. ISSN: 10969845. DOI: 10.1002/EQE.4037.

[225] R. Soti, L. Abdulrahman, A. R. Barbosa, R. L. Wood, M. E. Mohammadi and M. J. Olsen. 'Case study: Post-earthquake model updating of a heritage pagoda masonry temple using AEM and FEM'. In: *Engineering Structures* 206 (2020), p. 109950. DOI: 10.1016/j.engstruct.2019.109950.

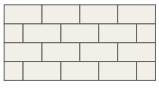
[226] L. Diana, G. Vaiano, A. Formisano, L. Scandolo, S. Podestà and P. Lestuzzi. 'The Seismic Vulnerability Assessment of Heritage Buildings: A Holistic Methodology for Masonry Churches'. In: *International Journal of Architectural Heritage* 18.6 (2024), pp. 994–1022. DOI: 10.1080/15583058.2023.2203097.

[227] M. Calò, D. Malomo, G. Gabbianelli and R. Pinho. 'Shake-table response simulation of a URM building specimen using discrete micro-models with varying degrees of detail'. In: *Bulletin of Earthquake Engineering* 19.14 (Nov. 2021), pp. 5953–5976. ISSN: 15731456. DOI: 10.1007/s10518-021-01202-0.

[228] A. Karbassi and M. J. Nollet. 'Performance-Based Seismic Vulnerability Evaluation of Masonry Buildings Using Applied Element Method in a Nonlinear Dynamic-Based Analytical Procedure'. In: *Earthquake Spectra* 29.2 (2013), pp. 399–426. DOI: 10.1193/1.4000148.

[229] N. Khattak, H. Derakhshan, D. P. Thambiratnam, D. Malomo and N. J. Perera. 'Modelling the in-plane/out-of-plane interaction of brick and stone masonry structures using Applied Element Method'. In: *Journal of Building Engineering* 76 (2023), p. 107175. DOI: 10.1016/j.jobe.2023.107175.

[230] M. Domaneschi, G. P. Cimellaro and G. Scutiero. 'A simplified method to assess generation of seismic debris for masonry structures'. In: *Engineering Structures* 186 (2019), pp. 306–320. DOI: 10.1016/j.engstruct.2019.01.092.

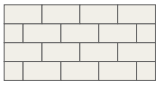


3

Distinct Element Method for Masonry Structures: Formulation and Practices

Building on the state-of-the-art review of the modelling strategies for masonry structures in Chapter 2, this chapter introduces the Distinct Element Method (DEM) framework adopted in this dissertation for masonry analysis, with emphasis on its formulation and practical use. The DEM approach is particularly suited for modelling the discrete nature of masonry, capturing the interactions between individual units and mortar joints, since the governing response is dominated by discontinuities rather than by smooth continuum deformation. Section 3.1 delves into the theoretical underpinnings of DEM, discussing the explicit time-marching integration scheme that accounts for both translational and rotational degrees of freedom. The use of rigid- and deformable-block configurations is explored, highlighting their respective advantages and limitations in simulating masonry behaviour. Section 3.2 focuses on dynamic analysis within the DEM framework, addressing the challenges of simulating the complex interactions and failure mechanisms inherent in masonry structures under dynamic loading. Section 3.3 summarises the key insights and establishes connections to subsequent chapters, setting the stage for further exploration of DEM applications in masonry analysis.

Parts of this chapter have been published in *Computers & Structures* (2024), doi: 10.1016/j.compstruc.2024.107499.



3.1. Theoretical background of the Distinct Element Method

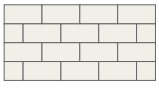
The core of the Distinct Element Method (DEM) formulation is an explicit time-marching integration scheme that accounts for both translational and rotational degrees of freedom. The schematic comparison between explicit and implicit time integration schemes in the presence of evolving nonlinearity is illustrated in Figure 3.1. Red curves denote the numerical trajectory while blue curves represent the reference (analytical or experimental) response. Figure 3.1A shows a typical explicit update with a timestep adjusted to the implicit timestep size Δt in Figure 3.1C. In Figure 3.1A, the explicit update advances without iteration within each timestep, relying solely on information from the previous timestep. However, the time increment cannot be too large, since the method becomes unstable and the error accumulates rapidly, causing the numerical solution to deviate significantly from the reference response, as illustrated by Points B to E in Figure 3.1A.

In contrast, the implicit scheme in Figure 3.1C iteratively refines the solution within each timestep until convergence is achieved at each point of interest. Here, *convergence* is understood in the usual numerical sense, i.e., when the residual (or incremental correction) falls below a prescribed tolerance. This iterative process allows for larger timesteps, enhancing stability and accuracy, as evidenced by the close alignment with the reference solution from Point D to E in Figure 3.1C. The relatively converged solution using an explicit scheme can only be achieved by significantly reducing the timestep, as illustrated in Figure 3.1B, where it systematically recovers the reference response as the simulation progresses. Figure 3.1D illustrates the implicit scheme using truncated iterations or heavy regularisation. Despite the relatively large timestep, incomplete convergence within each increment degrades the solution accuracy and can produce an overshooting response similar to that observed with the explicit scheme.

In DEM for masonry analysis, explicit time-marching schemes are often preferred because the problem is dominated by non-smooth events such as widespread contact creation and loss, transient impacts, frictional sliding, joint opening/closure, and block fragmentation. Explicit updates advance block translations and rotations without any global solving of simultaneous equations; hence, accuracy is not dependent on regularising contacts or smoothing the discontinuities to achieve convergence. Inevitably, the trade-off is the stability-limited timestep, as accuracy hinges on Δt, which must be controlled by the highest eigenfrequency of the system.

3.1.1. Contact handling scheme in DEM

In DEM, the interaction between discrete blocks is managed through a contact detection and handling scheme. Contacts are detected through the "common-plane" (CP) concept [1], which is essentially a plane in which the maximum overlap between the two blocks is minimised, as illustrated in Figure 3.2. It is important to note that the illustration is presented in two dimensions for simplicity, but the same logic applies in the three-dimensional context. Furthermore, rigid translation without any rotation is assumed for the blue block in Figure 3.2B for the sake of simplicity. This implies that equal velocity is imposed on the nodal points of the blue block. In reality, incremental rotation can occur, causing the unit normal to the CP for each subcontact to vary.



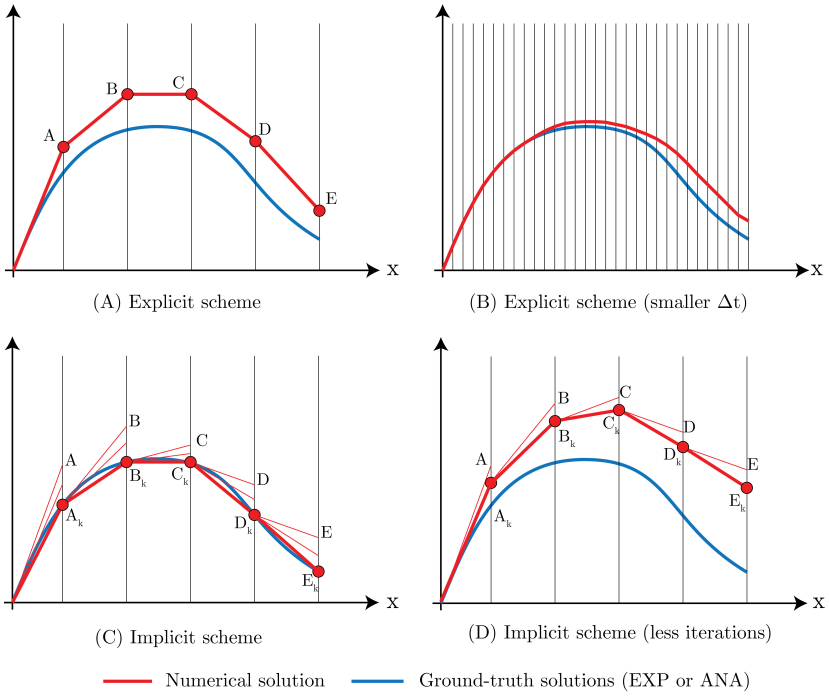


Figure 3.1. Comparison between explicit and implicit time integration schemes

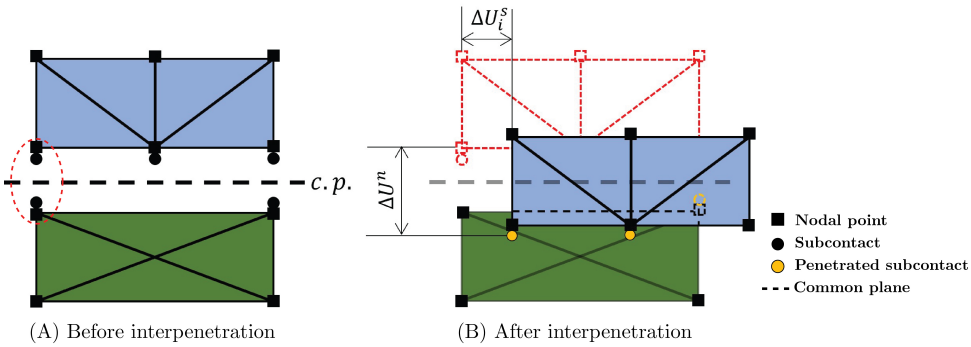


Figure 3.2. Common-plane concept for contact detection between two blocks. Adapted from [2]

Once the gap between the block and the CP, measured along the normal, is less than the specified tolerance, the blocks are assumed to be in contact. The contact points (termed subcontacts) are then defined on both blocks (the black circles in Figure 3.2A and Figure 3.2B). The subcontacts comprise normal and shear springs that relate the relative displacements to the subcontact forces. For the case of Figure 3.2A, the subcontacts are

created for each node on the contacting faces. If the blue and green blocks move with nodal velocities $\mathbf{v}_b$ and $\mathbf{v}_g$, evaluated at the half step $t + \Delta t/2$, the relative velocity at each subcontact is computed as:

$$\mathbf{v} = \mathbf{v}_b - \mathbf{v}_g \tag{3.1}$$

If the green block is stationary (as in Figure 3.2B), the opposing velocity $\mathbf{v}_g$ is zero. The relative displacement increment at the subcontact in the blue block $\Delta\mathbf{u}$ over the timestep Δt is then calculated as:

$$\Delta\mathbf{u} = \mathbf{v}(t + \Delta t/2)\,\Delta t \quad \text{where} \quad \mathbf{u}(t + \Delta t) = \mathbf{u}(t) + \Delta\mathbf{u} \tag{3.2}$$

where Δt is the timestep, $\mathbf{v}(t + \Delta t/2)$ is the relative velocity at the subcontact at the half step, and $\mathbf{u}(t)$ and $\mathbf{u}(t + \Delta t)$ are the relative subcontact displacements at times t and $t + \Delta t$, respectively. This displacement increment along the CP is then resolved into normal and shear components (Δu_n and $\Delta\mathbf{u_s}$, respectively) as follows:

$$\Delta u_n = \Delta\mathbf{u} \cdot \mathbf{n}, \qquad \Delta\mathbf{u_s} = \Delta\mathbf{u} - \big(\Delta\mathbf{u} \cdot \mathbf{n}\big)\mathbf{n}. \tag{3.3}$$

where $\mathbf{n}$ is the unit normal from the blue block to the green block, denoting the vector components in the global coordinate system. With this definition, a closing displacement gives $\Delta u_n > 0$ and, through Equation (3.4), a compressive normal force increment; in this chapter, as in the implementation, closure and compression are therefore taken positive. Chapter 4 instead takes tension positive, following the usual convention for interface yield functions. The subcontact forces in normal and shear are then defined in Equations (3.4) and (3.5), respectively, in the linear elastic law.

$$F_n = F_n + \Delta F_n \quad \text{where} \quad \Delta F_n = k_n A_c \Delta u_n \tag{3.4}$$

$$\mathbf{F}_s = \mathbf{F}_s + \Delta\mathbf{F}_s \quad \text{where} \quad \Delta\mathbf{F}_s = k_s A_c \Delta\mathbf{u_s} \tag{3.5}$$

where k_n and k_s are the normal and shear stiffness of the subcontact, respectively, and A_c is the contact area associated with the subcontact. A_c is defined as 1/3 of the triangular faces' areas where the subcontact lies. This area is halved for face-to-face contact or coinciding blocks, since the subcontacts are defined at the vertices of both blocks that occupy the same position in space (see the circled region in Figure 3.2A). The contact force vector for each subcontact is then expressed as:

$$\mathbf{F}^c = F_n\mathbf{n} + \mathbf{F}_s \tag{3.6}$$

For rigid blocks, the resultant subcontact forces and moments are applied directly to the block as lumped quantities. When blocks are modelled as deformable, however, these interaction forces must be transferred to the underlying finite-element mesh. In this case, each subcontact force is added directly to the nodes. For face-to-face contacts, as in Figure 3.3, the subcontact force is distributed to the three nodes of the triangular face using an area-weighted distribution.

$$\mathbf{F}^\alpha = \mathbf{F}^\alpha \pm \mathbf{F}^c W_\alpha \quad \mathbf{F}^\beta = \mathbf{F}^\beta \pm \mathbf{F}^c W_\beta \quad \mathbf{F}^\gamma = \mathbf{F}^\gamma \pm \mathbf{F}^c W_\gamma \tag{3.7}$$



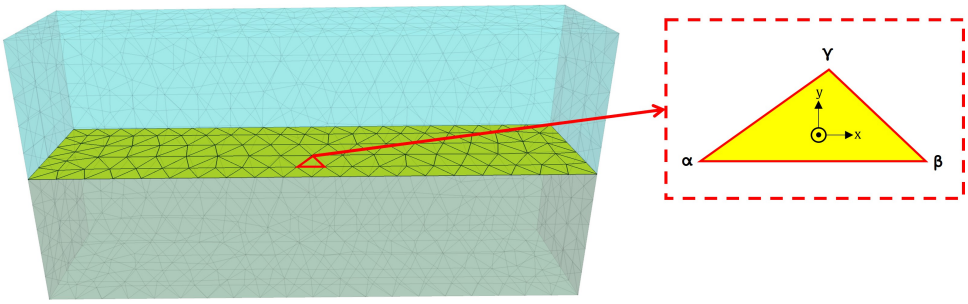


Figure 3.3. Local coordinates of contacting faces between two blocks

where $\mathbf{F}^{\alpha}$, $\mathbf{F}^{\beta}$, and $\mathbf{F}^{\gamma}$ are the nodal force vectors at nodes α, β, and γ, respectively (Figure 3.3), and W_{α}, W_{β}, and W_{γ} are the area-weighted coefficients defined as follows for vertex α. The formulations for β and γ are calculated by circular permutation of the subscripts.

$$W_{\alpha} = \frac{Y_{\gamma}X_{\beta} - Y_{\beta}X_{\gamma}}{(X_{\alpha} - X_{\gamma})(Y_{\beta} - Y_{\gamma}) - (Y_{\alpha} - Y_{\gamma})(X_{\beta} - X_{\gamma})} \tag{3.8}$$

where X and Y are the local coordinates of the contacting face as illustrated in Figure 3.3.

3.1.2. Mechanical formulation and computational scheme in DEM

Rigid block formulation

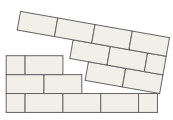
The mechanical formulation in DEM is grounded in Newtonian mechanics, where the motion of discrete blocks is governed by Newton's second law. However, the implementation differs between rigid and deformable blocks. For rigid blocks, the equations of motion are expressed as Equation (3.9) for a single block in three-dimensional space. Note that the translational and rotational motions are calculated at the block's centre of mass.

$$m\ddot{\mathbf{x}} + c\dot{\mathbf{x}} = \mathbf{F} + m\mathbf{g}, \quad \dot{\boldsymbol{\omega}}_i + \alpha_R \boldsymbol{\omega}_i = \frac{M_i}{I_i}, \qquad i = 1,2,3. \tag{3.9}$$

where the force/torques ($\mathbf{F}$, M_i) arise from a combination of external forces and the contact forces, m is the block mass, c is the damping coefficient, defined as $c = \alpha_R m$ with α_R being the mass-proportional Rayleigh coefficient, $\mathbf{g}$ is the gravitational acceleration vector, I_i is the moment of inertia about axis i, $\boldsymbol{\omega}_i$ is the angular velocity component about axis i, and α_{ω} is the rotational damping coefficient.

The equations of motion in Equation (3.9) are advanced with a staggered central-difference scheme: translational and angular velocities are stored at half steps and positions/orientations at integer steps. Translational and rotational velocities are defined at time t in terms of values at mid-intervals:

$$\dot{\mathbf{x}}(t) = \frac{\dot{\mathbf{x}}(t + \Delta t/2) + \dot{\mathbf{x}}(t - \Delta t/2)}{2}, \quad \boldsymbol{\omega}_i(t) = \frac{\boldsymbol{\omega}_i(t + \Delta t/2) + \boldsymbol{\omega}_i(t - \Delta t/2)}{2} \tag{3.10}$$



Consequently, the accelerations are calculated as:

$$\ddot{\mathbf{x}}(t) = \frac{\dot{\mathbf{x}}(t+\Delta t/2) - \dot{\mathbf{x}}(t-\Delta t/2)}{\Delta t}, \quad \dot{\boldsymbol{\omega}}_i(t) = \frac{\boldsymbol{\omega}_i(t+\Delta t/2) - \boldsymbol{\omega}_i(t-\Delta t/2)}{\Delta t} \tag{3.11}$$

Equations (3.10) and (3.11) are then substituted into Equation (3.9) to obtain the update equations for translational and angular velocities at mid-intervals, $\dot{\mathbf{x}}(t+\Delta t/2)$, $\boldsymbol{\omega}_i(t+\Delta t/2)$, respectively. Increments of the translational and rotational displacements are then computed as Equation (3.12).

$$\Delta\mathbf{x} = \dot{\mathbf{x}}(t+\Delta t/2)\Delta t, \quad \Delta\boldsymbol{\theta}_i = \boldsymbol{\omega}_i(t+\Delta t/2)\Delta t \tag{3.12}$$

which updates the block's position and orientation as expressed in Equation (3.13).

$$\mathbf{x}(t+\Delta t) = \mathbf{x}(t) + \Delta\mathbf{x}, \quad \boldsymbol{\theta}_i(t+\Delta t) = \boldsymbol{\theta}_i(t) + \Delta\boldsymbol{\theta}_i \tag{3.13}$$

The new positions of the block vertices (nodes) are then computationally derived from the updated block position and orientation.

$$\mathbf{x}^v(t+\Delta t) = \mathbf{x}^v(t) + \Delta\mathbf{x} + \Delta\boldsymbol{\theta} \times \left[\mathbf{x}^v(t+\Delta t/2) - \mathbf{x}(t+\Delta t/2)\right] \tag{3.14}$$

where the mid-step positions are taken as $\mathbf{x}(t+\Delta t/2) = \mathbf{x}(t) + \frac{1}{2}\Delta\mathbf{x}$ and likewise for $\mathbf{x}^v$.

Deformable block formulation

In the case of deformable blocks, the equations of motion are formulated in a nodal-based approach, where each block is discretised into nodes connected by elements. The equations of motion for deformable blocks are expressed in Equation (3.15).

$$m\ddot{\mathbf{u}} = \mathbf{F} + m\mathbf{g} \tag{3.15}$$

where $\mathbf{u}$ is the nodal displacement vector, m is the mass lumped at the node, $\mathbf{g}$ is the gravitational acceleration vector, and $\mathbf{F}$ is the resultant force acting on the node. This resultant comprises the internal forces from the deformable block, the contact forces from neighbouring blocks and the external loads, as given in Equation (3.16). The resultant forces include contact forces from neighbouring blocks, body forces, and external loads, as defined in Equation (3.16).

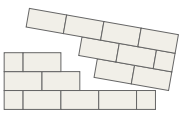
$$\mathbf{F} = \mathbf{F}^z + \mathbf{F}^c + \mathbf{F}^\ell \tag{3.16}$$

where $\mathbf{F}^z$ is the internal force from the constant strain elements adjacent to the node, $\mathbf{F}^c$ is the contact force vector and $\mathbf{F}^\ell$ is the externally applied load vector. The internal force is obtained from the element stresses as:

$$\mathbf{F}^z = \int_c \boldsymbol{\sigma}\,\mathbf{n}\,\mathrm{d}S \tag{3.17}$$

where $\boldsymbol{\sigma}$ is the stress tensor of the adjacent elements, c is the surface that bisects the elements connected to the node and encloses it, and $\mathbf{n}$ is the outward unit normal to c.

If the block is in equilibrium or steady-state flow, the internal forces balance the external forces, resulting in $\mathbf{F} = 0$. Otherwise, the nodes accelerate according to the



finite-difference form of the equations of motion in Equation (3.15), using a similar explicit time-marching scheme as for rigid blocks in Equation (3.10). This is presented in Equation (3.18).

$$\dot{\mathbf{u}}(t+\Delta t/2) = \dot{\mathbf{u}}(t-\Delta t/2) + \frac{\Delta t}{m}\left((\mathbf{F}-\mathbf{F}^d)+m\mathbf{g}\right) \tag{3.18}$$

where $\mathbf{F}^d$ is the damping force vector, defined as $\mathbf{F}^d = \alpha|\mathbf{F}|\text{sgn}(\dot{\mathbf{u}}^{t-\Delta t/2})$. This damping force is proportional to the magnitude of the resultant force $\mathbf{F}$, with α being the non-dimensional damping constant, set to 0.8 by default.

This formulation, referred to as local damping [3], converges quickly to quasi-static solutions without significantly affecting the dynamic response. This scheme is similar to the dynamic relaxation scheme introduced by Otter *et al.* [4]. Alternatively, global damping can also be applied, where a viscosity constant is continuously adjusted so that the power absorbed by the damping force is proportional to the rate of change of the kinetic energy in the model [5].

$$R = \frac{\Sigma_i P_i}{\Sigma_i \dot{E_{ki}}} \tag{3.19}$$

where R is the user-defined viscosity ratio, P_i is the damping power at node i and $\dot{E_{ki}}$ is the rate of change of kinetic energy at node i. Both P and $\dot{E_{ki}}$ are summed over all nodes.

After updating the nodal velocities, the nodal displacements are incremented as in Equation (3.2). The nodal displacement increment then updates the subcontact forces, adjusted according to the assigned contact law. The flowchart in Figure 3.4 summarises the overall computational scheme for DEM. The solution procedure at one node described above is repeated for all nodes in the model at each timestep until either equilibrium or failure is reached. In the context of the explicit scheme, failure is defined as the condition where the evaluated node cannot find a steady-state flow because it accelerates to infinity.

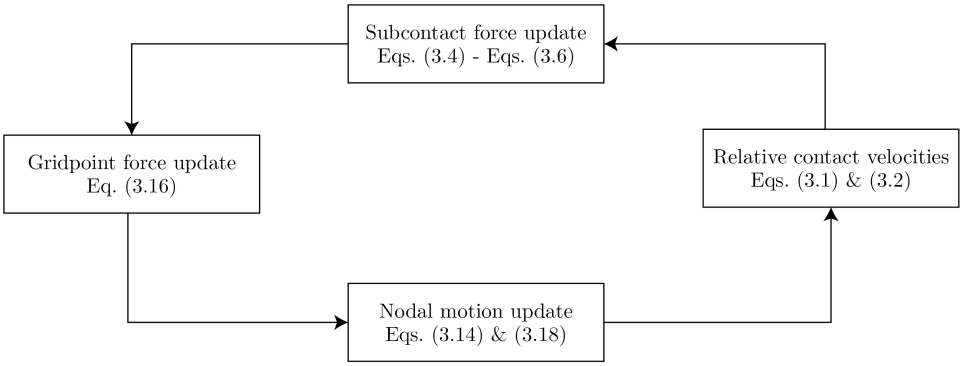


Figure 3.4. Calculation cycle in DEM [6]

Stable timestep calculation

The numerical procedure in DEM is already implemented in a commercial three-dimensional distinct element code, called 3DEC [6]. It is important to highlight that the explicit time marching integration scheme used for DEM is conditionally stable, as is typical for other methods based on explicit integration [7]. The timestep required to achieve stability when calculating internal block deformation for deformable blocks or rigid-body motion for rigid blocks is determined by the Courant-Friedrichs-Lewy (CFL) condition [8].

$$\Delta t_{block} = 2\min\left(\sqrt{\frac{m_i}{k_i}}\right) \tag{3.20}$$

where m_i is the mass associated with node i, and k_i is the equivalent stiffness at node i, calculated as the sum of the stiffnesses of all elements connected to node i.

The mass-to-stiffness ratio relates to the system's highest eigenfrequency: $\omega_{max} \approx \sqrt{k_i/m_i}$. The equivalent nodal stiffness k_i combines the stiffness of the contacts at the block boundary, $k_{\mathrm{n},i}$ (zero if the node does not lie on a contact), and the stiffness contributions from the elements connected to the node $k_{\mathrm{tet},i}$, as expressed in Equation (3.21).

$$k_{\mathrm{tet},i} = \frac{8}{3}(K + \frac{4}{3}G)\frac{l_{max}^2}{h_{min}} \tag{3.21}$$

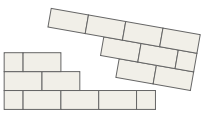
where K and G are the block's bulk and shear moduli, respectively, l_{max} is the maximum edge length of the elements connected to node i, and h_{min} is the minimum height of those elements.

Equation (3.21) is neglected for the rigid-block formulation, considering that the internal deformation is not calculated. The stable timestep in Equation (3.20) gives a conservative estimate based on an upper bound of the highest eigenfrequency [9]. This estimate has been shown to be sufficiently stable even for complex nonlinear systems [10, 11].

3.2. Dynamic analysis in DEM

The explicit scheme used in DEM allows for the direct simulation of transient events, such as impacts and rapid loading changes, without the need for iterative convergence procedures, making it suitable for investigation and behaviour prediction of complex structures subjected to dynamic loads [12–14]. This is crucial for capturing the dynamic response of masonry structures, which often involve sudden changes in contact conditions, such as joint opening and closing, block fragmentation, and frictional sliding.

For dynamic analysis in DEM, the damping in the numerical simulation should approximately reproduce the energy losses observed in real masonry structures during dynamic events. This is typically achieved through a "natural" damping mechanism, which is mainly hysteretic (frequency-independent). However, as pointed out by Galvez *et al.* [15] and De Lorenzis *et al.* [16], the inherent hysteretic damping is difficult to control since the precise nature of the hysteretic behaviour is often unknown in complex



loading-unloading scenarios, and ratcheting (i.e., a progressive accumulation of plastic strain under cyclic loading) can occur in the contacts, increasing path-dependencies.

To this end, viscous damping in the form of the Rayleigh damping formulation is typically used to control high-frequency content while preserving the low-frequency (rigid-body) response. In its classical form, a viscous damping matrix is constructed as in Equation (3.22)

$$\mathbf{C} = \alpha_R \mathbf{M} + \beta_R \mathbf{K}_t, \tag{3.22}$$

where α_R and β_R are the mass-proportional (MP) and stiffness-proportional (SP) Rayleigh coefficients, respectively, and $\mathbf{K}_t$ is the current (elastic/tangent) stiffness used for the deformable blocks. The resulting nodal damping force is shown in Equation (3.23)

$$\mathbf{F}^d = \mathbf{C}\dot{\mathbf{u}}. \tag{3.23}$$

The critical damping ratio ζ at any given angular frequency ω can be obtained as presented in Equation (3.24).

$$\zeta = \frac{1}{2}\left(\frac{\alpha_R}{\omega} + \beta_R \omega\right) \tag{3.24}$$

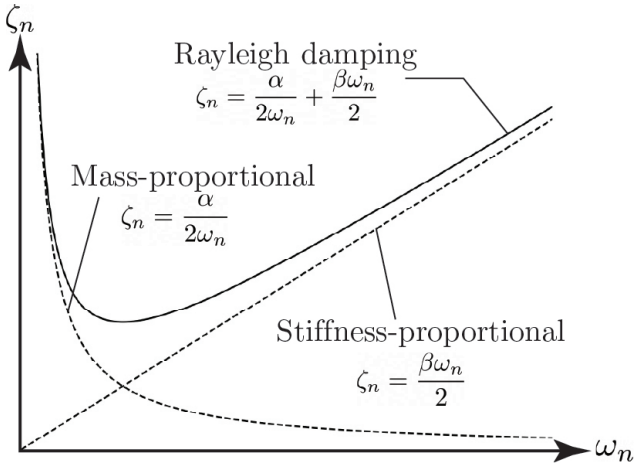


Figure 3.5. Rayleigh damping and its components plotted over angular frequency

The plot of the variation of the damping ratio ζ with respect to angular frequency ω is illustrated in Figure 3.5. The MP damping component dominates the low-frequency range, while the SP damping component becomes significant at higher frequencies.

3.2.1. Mass-proportional Rayleigh damping

Mass-proportional (MP) damping is the first term in the Rayleigh expression of Equation (3.22), obtained by setting $\beta_R = 0$ so that $\mathbf{C} = \alpha_R \mathbf{M}$. It produces uncoupled nodal viscous forces proportional to velocity and lumped mass:

$$\mathbf{F}^d_{\mathrm{MP}} = \alpha_R \mathbf{M}\dot{\mathbf{u}} \tag{3.25}$$

Substituting Equation (3.25) into the explicit update of Equation (3.18) gives, for node i,

$$\dot{u}_i^{t+\Delta t/2} = \dot{u}_i^{t-\Delta t/2} + \frac{\Delta t}{m_i}\left(F_i - \alpha_R m_i \dot{u}_i^{t-\Delta t/2} + m_i g_i\right). \tag{3.26}$$

For mode j of angular frequency ω_j, the critical damping ratio contribution from MP damping is obtained by adjusting Equation (3.24)

$$\zeta_j^{\mathrm{MP}} = \frac{\alpha_R}{2\omega_j}, \tag{3.27}$$

showing that MP damping predominantly affects low-frequency (rigid-body) modes and diminishes as ω_j increases. This results in plausible damping ratios for higher-frequency modes, but overdamped low-frequency modes, which can artificially suppress rigid-body motions and affect the overall dynamic response of the structure [15].

3.2.2. Stiffness-proportional damping

Stiffness-proportional (SP) damping is the second term in the Rayleigh expression of Equation (3.22), obtained by setting $\alpha_R = 0$ so that $\mathbf{C} = \beta_R \mathbf{K}_t$. It produces nodal viscous forces proportional to velocity and the current stiffness:

$$\mathbf{F}^d_{\mathrm{SP}} = \beta_R \mathbf{K}_t \dot{\mathbf{u}}. \tag{3.28}$$

Substituting Equation (3.28) into the explicit velocity update (Equation (3.18)) gives, for node i,

$$\dot{u}_i^{t+\Delta t/2} = \dot{u}_i^{t-\Delta t/2} + \frac{\Delta t}{m_i}\left(F_i - \beta_R (K_t \dot{u})_i + m_i g_i\right). \tag{3.29}$$

For a vibration mode j of angular frequency ω_j, the SP contribution to the critical damping ratio follows from Equation (3.24) with $\alpha_R = 0$:

$$\zeta_j^{\mathrm{SP}} = \frac{\beta_R \omega_j}{2}, \tag{3.30}$$

Hence, SP damping grows linearly with frequency and is negligible for the low (rigid-body) modes that often govern masonry rocking, while efficiently removing spurious high-frequency content generated by rapid contact state changes.

As shown in Figure 3.5, MP damping yields a high damping ratio at lower frequencies, while SP damping provides an increasing damping ratio at higher frequencies. Several researchers working on the dynamic analysis of DEM have used only the MP component for masonry structures [14, 17–19], mainly to avoid the additional stiffness-proportional damping that would further reduce the critical timestep in explicit integration and increase computational cost. In many cases, they have matched numerical predictions to experimentally observed values while ignoring that low-frequency modes are overdamped and high-frequency modes are underdamped. The damaged dominant

frequency could fall within the low-frequency range of MP damping, thereby artificially restricting the dynamic response.

On the other hand, because of an explicit time-marching scheme, SP damping is also discouraged because it imposes an additional restriction on the CFL condition for a stable timestep [6]. With the SP damping considered, the stable timestep in Equation (3.20) is modified to Equation (3.31) [9].

$$\Delta t = \frac{2}{\omega_{max}} \left(\sqrt{1+\zeta_{max}^2} - \zeta_{max} \right) \tag{3.31}$$

where ζ_{max} is the maximum damping ratio in the system, typically occurring at the highest frequency ω_{max}. As the damping ratio increases linearly with the given frequency for SP damping, Equation (3.31) causes a significant reduction in the stable timestep, leading to increased computational cost up to one or two orders of magnitude [20]. The computational effort due to the timestep limitation could be reduced by using simple models, such as masonry arches or idealised rocking blocks, or by resorting to rigid-block formulations. In these cases, the reduced number of degrees of freedom and the absence of deformable-block dynamics permit larger stable timesteps, while still capturing the essential features of the collapse mechanisms. However, in complex models such as cross-vaults or domes or in deformable-block formulations with many degrees of freedom, the timestep reduction induced by the SP component can become prohibitive.

3.2.3. Maxwell damping

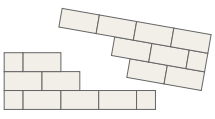
Given this limitation, several researchers have proposed alternative damping formulations to reduce overdamping of rigid-body modes in the MP component and the severe timestep restrictions imposed by the SP component. This alternative uses springs and dashpots placed in series to dissipate the energy, known as Maxwell damping. Dawson & Cheng [21] implemented a Maxwell damping formulation in an explicit FEM for geotechnical seismic analysis. Lemos *et al.* [22] extended the work to numerically simulate rigid blocks in DEM and applied it to the dynamic analysis of masonry arches [20].

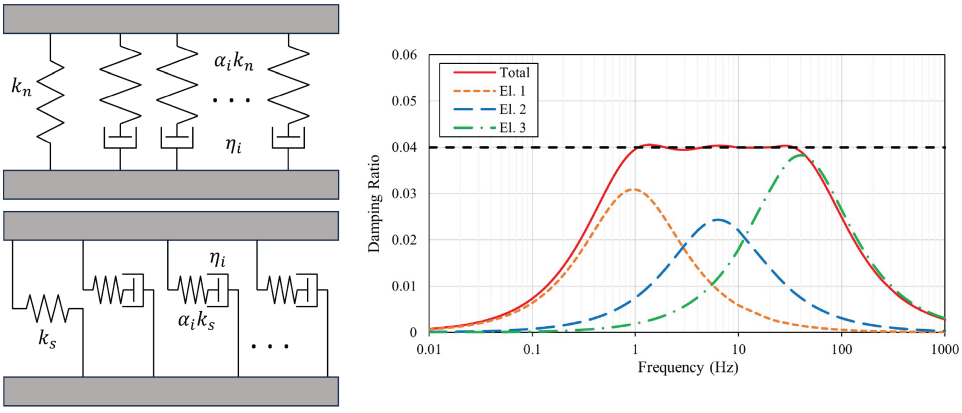
Formulation for a single Maxwell element

The Maxwell damping concept is based on the Standard Linear Solid (SLS) model, which consists of two parallel systems: a Maxwell "arm" with a spring and a dashpot in series, and another system comprising a single spring (Figure 3.6A). Under the linear elastic law, the stress due to the constitutive model σ_j depends on the elastic stiffness and the joint relative displacement. Meanwhile, the Maxwell element stress is described by the standard viscoelastic equation, where the joint displacement rate $\dot{u}$ relates the Maxwell element stress σ^m to its rate $\dot{\sigma^m}$. The relation is defined in Equation (3.32).

$$\dot{u} = \frac{\dot{\sigma^m}}{\alpha_M \cdot k} + \frac{\sigma^m}{\eta_M} \tag{3.32}$$

where α_M is the non-dimensional factor that defines the Maxwell spring as a fraction of the joint stiffness k, and the viscosity parameter η_M relates the joint stress to the joint displacement rate.





(A) Maxwell elements (B) Maxwell damping ratio vs frequency

Figure 3.6. Implementation of Maxwell damping element in DEM

The differential equation in Equation (3.32) is solved in the frequency domain using the phasor method. A steady-state harmonic response is assumed, as given in Equation (3.33), where only the real parts are physically meaningful. Because of the viscous dashpot, stress and displacement are not in phase.

$$u = u_0 \exp(i\omega t) \quad \text{and} \quad \sigma^m = \sigma_0^m \exp(i\omega t) \tag{3.33}$$

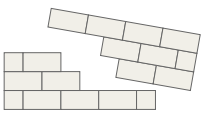
where ω is the angular frequency, and u_0 and σ_0^m are the complex amplitudes of the displacement and the Maxwell stress, respectively. Substituting Equation (3.33) into Equation (3.32) relates the two amplitudes through the complex modulus $k\overline{M}$, as expressed in Equation (3.34).

$$\sigma_0^m = k\overline{M}u_0 \quad \text{where} \quad \overline{M} = \frac{\alpha_M \tau_M^2 \omega^2}{1+\tau_M^2\omega^2} + i\frac{\alpha_M \tau_M \omega}{1+\tau_M^2\omega^2} \tag{3.34}$$

where $\tau_M = \eta_M / k_M$ is the relaxation time and $k_M = \alpha_M k$ is the stiffness of the Maxwell spring. Since the SLS model comprises the Maxwell element and the elastic spring in parallel, the system stiffness is the sum of the two stiffnesses, and the normalised complex modulus is given by Equation (3.35).

$$\overline{M_T} = 1 + \overline{M} = 1 + \frac{\alpha_M \tau_M^2 \omega^2}{1+\tau_M^2\omega^2} + i\frac{\alpha_M \tau_M \omega}{1+\tau_M^2\omega^2} \tag{3.35}$$

The critical damping ratio for the SLS model is defined as half the ratio of the imaginary to the real terms of the complex modulus ([21]), as presented in Equation (3.36). The critical damping ratio reaches the maximum value ζ_{max} at the frequency ω_{max}, as expressed in Equation (3.37).



$$\zeta = \frac{\mathrm{Im}(\overline{M_T})}{2\mathrm{Re}(\overline{M_T})} = \frac{\alpha_M \tau_M \omega}{2\left[1+(\tau_M\omega)^2(1+\alpha_M)\right]} \tag{3.36}$$

where

$$\zeta_{max} = \frac{\alpha_M}{4\sqrt{1+\alpha_M}} \quad \text{at} \quad \omega_{max} = \frac{1}{\tau_M\sqrt{1+\alpha_M}} \tag{3.37}$$

The spring in the Maxwell element increases the overall stiffness of the joint, which is represented by the absolute value of the complex modulus, as shown in Equation (3.38).

$$|\overline{M_T}| = \sqrt{1+\alpha_M(2+\alpha_M)\frac{\tau_M^2\omega^2}{1+\tau_M^2\omega^2}} \quad \text{where} \quad |\overline{M_T}|_{max} = 1+\alpha_M \tag{3.38}$$

At low excitation frequencies ($\omega \to 0$), the dashpots do not resist (their stress tends to zero), so the effective stiffness is that of the main elastic springs alone. At high frequencies ($\omega \to \infty$), the dashpots behave as rigid links (no dashpot deformation), and the effective stiffness tends to the sum of the main spring and all Maxwell-branch springs. At intermediate frequencies, the dashpots deform and carry stress, dissipating energy and yielding a non-zero damping ratio $\zeta(\omega)$.

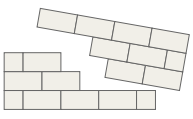
Generalised Maxwell damping formulation

In general, the Maxwell damping scheme comprises multiple Maxwell elements stacked in parallel along with the joint stiffness. These elements are subjected to the same joint displacements, and the contact stress is calculated as the sum of the joint stress and all of the Maxwell element stresses. Although the formulation can be extended to multiple Maxwell elements, Lemos *et al.* [20] and Dawson & Cheng [21] show that three Maxwell elements are sufficient to provide uniform damping over a range of frequencies. The damping ratio and the complex modulus for multiple Maxwell elements are then calculated as in Equation (3.39) (Figure 3.6B).

$$\zeta_n = \frac{\mathrm{Im}(\overline{M_{T_n}})}{2\mathrm{Re}(\overline{M_{T_n}})} \quad \text{where} \quad \overline{M_{T_n}} = 1+\sum_i^n (\overline{M})_i \tag{3.39}$$

Similar to the SLS model with a single Maxwell element, the magnitude of the total complex modulus in Equation (3.39) imposes an increase in the joint stiffness due to the presence of the Maxwell elements. The increase in the system's response frequency is proportional to the square root of the total modulus factor ([20]).

The stiffness increase also causes a reduction of the timestep in the explicit solver ([20]), as presented in Equation (3.40). The term in parentheses is the reduction of the timestep imposed by the Maxwell damping scheme, with the sum of the α_M parameters representing the stiffness increase. The reduction due to Maxwell damping is smaller than Equation (3.31).



$$\Delta t < \frac{2}{\omega_{max}} \left(\frac{1}{\sqrt{1 + \sum_i^n \alpha_{M_i}}} \right) \tag{3.40}$$

The Maxwell damping elements are deactivated at the onset of tensile and shear failure, similar to the procedure used in SP damping, as the SP β component is implemented directly into the joint model.

Optimisation of the Maxwell damping parameters

While centre frequencies and damping ratios can be tuned by trial-and-error (heuristic approaches), as in prior uses of Maxwell damping, e.g., [20–22], the problem is reformulated by solving a nonlinear least-squares optimisation problem that targets an approximately constant damping ratio $\zeta^\star$ over a specified frequency range $[\omega_{lb}, \omega_{ub}]$. To that end, a set of $N_\omega = 500$ logarithmically spaced evaluation frequencies is sampled within the prescribed band:

$$\omega_j = \omega_{\text{lb}} \left(\frac{\omega_{\text{ub}}}{\omega_{\text{lb}}} \right)^{\frac{j-1}{N_\omega - 1}}, \quad j = 1, \ldots, N_\omega, \tag{3.41}$$

and the Maxwell parameters are identified by minimising Equation (3.42).

$$\min_{\boldsymbol{\alpha}_M, \boldsymbol{\tau}_M} \sum_{j=1}^{N_\omega} \left[\zeta^\star - \zeta\left(\omega_j; \boldsymbol{\alpha}_M, \boldsymbol{\tau}_M\right) \right]^2 \tag{3.42}$$

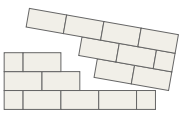
where $\boldsymbol{\alpha}_M = \{\alpha_{M_1}, \alpha_{M_2}, \alpha_{M_3}\}$ and $\boldsymbol{\tau}_M = \{\tau_{M_1}, \tau_{M_2}, \tau_{M_3}\}$ collect the stiffness ratios and relaxation times of the three Maxwell branches. Each branch is placed by its peak frequency ω_r, from which the relaxation time follows through Equation (3.36) as $\tau_{M_r} = 1/(\omega_r \sqrt{1 + \alpha_{M_r}})$. The outer branches are pinned to the band limits and only the middle branch is free, as given in Equation (3.43).

$$\omega_1 = \omega_{\text{lb}}, \qquad \omega_{\text{lb}} \le \omega_2 \le \omega_{\text{ub}}, \qquad \omega_3 = \omega_{\text{ub}} \tag{3.43}$$

The ordering $\omega_1 \le \omega_2 \le \omega_3$ therefore holds at every iterate without an explicit constraint, and ω_2 is initialised at the geometric mean $\sqrt{\omega_{\text{lb}}\,\omega_{\text{ub}}}$. Frequencies outside $[\omega_{\text{lb}}, \omega_{\text{ub}}]$ are not sampled and do not enter the objective. The input parameters for the optimisation algorithm are thus constrained to the target damping ratio $\zeta^\star$, and the frequency band $[\omega_{\text{lb}}, \omega_{\text{ub}}]$. The initial guess for the damping parameters at each Maxwell element is arbitrarily defined.

The objective in Equation (3.42) is solved as a nonlinear least-squares problem with the Levenberg–Marquardt (LM) algorithm. Unless stated otherwise, equal weights are used, a gradient (infinity-norm) tolerance of 10^{-9} is adopted, and the maximum number of iterations is set to 200. Initial values place ω_r uniformly on the log scale in $[\omega_{\text{lb}}, \omega_{\text{ub}}]$. Up to three small random restarts are allowed, and the best solution is retained.

The fitted damping curve is compared against the parameters reported by Lemos & Sarhosis [20]. For this comparison, the frequency band is set to 1 Hz to 40 Hz and the target damping ratio set to 5 %, matching [20], while the initial guesses of the damping



ratios for the three Maxwell branches are randomised. Figure 3.7 plots $\zeta(\omega)$ for the initial guess (green), the LM-converged fit (red), and the reference parameters from [20] (blue). In this case, convergence is achieved in 8 LM iterations, and the fitted parameters reproduce the nearly uniform target damping within the specified band with high accuracy. The same optimisation setup (band, grid, solver, and mappings) is used in all subsequent numerical analyses.

The Maxwell damping is assigned per contact point (and per internal tetrahedral link for deformable blocks), with three parallel Maxwell branches at each contact. Consequently, the formulation is mesh-agnostic, as refining the discretisation only changes the number of contacts, not the damping law at a contact. The parameter identification in Equation (3.42) is also independent of mesh size and contact count. It fits dimensionless branch fractions and branch centre frequencies/relaxation times to produce an approximately constant $\zeta(\omega)$ over a prescribed band, and it applies the resulting three-branch set uniformly to all contacts. If a change in discretisation alters the model's resolvable frequency band (through $\omega_{\max}$ or numerical dispersion), the same optimisation is re-run with the updated $[\omega_{\text{lb}}, \omega_{\text{ub}}]$.

3.3. Summary and remarks

This chapter establishes the theoretical framework for the Distinct Element Method (DEM) as applied to masonry structures, covering key aspects such as time integration schemes, contact mechanics, and damping strategies. It highlights the advantages of an explicit time-marching integration scheme for handling non-smooth, contact-dominated problems typical in masonry analysis, where mortar layers are idealised as zero-thickness interfaces. The chapter details a common-plane approach for contact detection and force

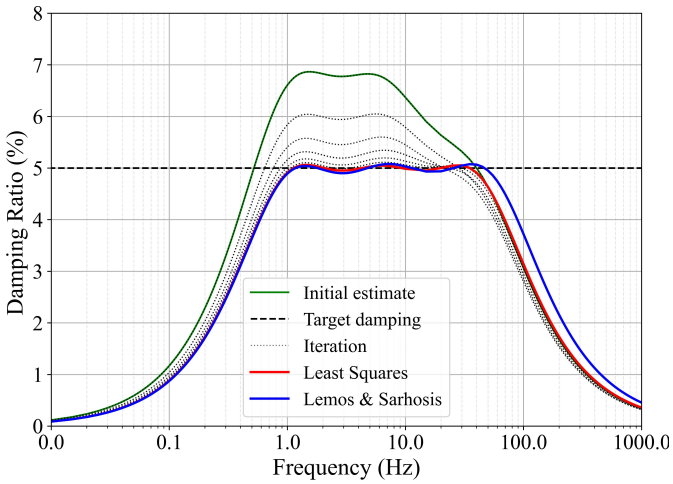


Figure 3.7. Comparison of the Levenberg-Marquardt predicted Maxwell damping parameters against those reported by Lemos *et al.* [20]

transfer, along with mechanical formulations for both rigid and deformable blocks.

The chapter discusses dynamic analysis considerations, focusing on damping mechanisms to control energy dissipation during transient events. The two components of classical Rayleigh damping, mass-proportional and stiffness-proportional, are examined separately, highlighting their respective limitations, namely overdamping of low-frequency modes in the former and stringent timestep restrictions in explicit schemes when the latter is included. To address these challenges, a Maxwell damping formulation is introduced, providing a more uniform damping profile over a specified frequency band with milder impacts on timestep stability. Finally, a practical optimisation procedure based on the Levenberg–Marquardt algorithm is presented to identify Maxwell damping parameters that achieve target damping ratios within desired frequency ranges, thereby avoiding ad hoc or heuristic tuning.

In the following chapters, the modelling choices and algorithms introduced here, contact laws, explicit integration, stability control, and damping strategies, are used directly in the numerical studies that follow. Specifically, the contact detection and mechanical formulations described in Section 3.1 are omitted from the chapter where the development of the contact constitutive model for the analysis of masonry structures is presented (Chapter 4). Then, the dynamic analysis with the damping formulation described in Section 3.2 is revisited in Chapter 7 to validate the proposed contact constitutive model for experimental masonry structures subjected to dynamic loads.



Bibliography of Chapter 3

[1] P. A. Cundall. 'Formulation of a three-dimensional distinct element model—Part I. A scheme to detect and represent contacts in a system composed of many polyhedral blocks'. In: *International Journal of Rock Mechanics and Mining Sciences & Geomechanics Abstracts* 25.3 (June 1988), pp. 107–116. ISSN: 0148-9062. DOI: 10.1016/0148-9062(88)92293-0.

[2] Y. P. Oktiovan, F. Messali, B. Pulatsu, J. V. Lemos and J. G. Rots. 'A contact-based constitutive model for the numerical analysis of masonry structures using the distinct element method'. In: *Computers & Structures* 303 (2024), p. 107499. ISSN: 0045-7949. DOI: 10.1016/J.COMPSTRUC.2024.107499.

[3] P. Cundall and C. Detournay. 'Dynamic relaxation applied to continuum and discontinuum numerical models in geomechanics'. In: *Rock Mechanics and Engineering* (Apr. 2017), pp. 45–90. DOI: 10.1201/B20402-2.

[4] J. R. Otter. 'Dynamic relaxation compared with other iterative finite difference methods'. In: *Nuclear Engineering and Design* 3.1 (Jan. 1966), pp. 183–185. ISSN: 0029-5493. DOI: 10.1016/0029-5493(66)90157-9.

[5] P. Cundall. 'Adaptive Density-Scaling for Time-Explicit Calculations'. In: *Proceedings of the 4th International Conference on Numerical Methods in Geomechanics (Edmonton, 1982)* (1982).

[6] Itasca Consulting Group Inc. *3DEC - Three Dimensional Distinct Element Code Ver. 9.1*. Minneapolis, 2024.

[7] G. Noh and K. J. Bathe. 'An explicit time integration scheme for the analysis of wave propagations'. In: *Computers & Structures* 129 (Dec. 2013), pp. 178–193. ISSN: 0045-7949. DOI: 10.1016/J.COMPSTRUC.2013.06.007.

[8] R. Courant, K. Friedrichs and H. Lewy. 'Über die partiellen Differenzengleichungen der mathematischen Physik'. In: *Mathematische Annalen* 100 (1928), pp. 32–74. DOI: 10.1007/BF01448839.

[9] T. Belytschko. 'An overview of semidiscretization and time integration procedures'. In: *Computational methods for transient analysis*. Ed. by T. Belytschko and T. Hughes. New York: Elsevier Science Publisher, 1983, pp. 1–65.

[10] P. Smolinski, S. Sleith and T. Belytschko. 'Stability of an explicit multi-time step integration algorithm for linear structural dynamics equations'. In: *Computational Mechanics* 18 (1996), pp. 236–244.

[11] P. Smolinski. 'Stability analysis of a multi-time step explicit integration method'. In: *Computer Methods in Applied Mechanics and Engineering* 95.3 (Mar. 1992), pp. 291–300. ISSN: 0045-7825. DOI: 10.1016/0045-7825(92)90188-P.



[12] A. Mehrotra and M. DeJong. 'The Performance of Slender Monuments during the 2015 Gorkha, Nepal, Earthquake'. In: (2017). DOI: 10.17863/CAM.21431. URL: https://www.repository.cam.ac.uk/handle/1810/274305.

[13] J. V. Lemos and V. Sarhosis. 'Discrete Element Bonded-Block Models for Detailed Analysis of Masonry'. In: *Infrastructures* 7.3 (Feb. 2022), p. 31. ISSN: 2412-3811. DOI: 10.3390/infrastructures7030031.

[14] J. Kim, F. Lorenzoni, M. Salvalaggio and M. R. Valluzzi. 'Seismic vulnerability assessment of free-standing massive masonry columns by the 3D Discrete Element Method'. In: *Engineering Structures* 246 (2021), p. 113004. ISSN: 0141-0296. DOI: 10.1016/j.engstruct.2021.113004.

[15] F. Galvez, L. Sorrentino, D. Dizhur and J. M. Ingham. 'Damping considerations for rocking block dynamics using the discrete element method'. In: *Earthquake Engineering & Structural Dynamics* 51.4 (2022), pp. 935–957. DOI: 10.1002/eqe.3598.

[16] L. De Lorenzis, M. J. DeJong and J. A. Ochsendorf. 'Failure of masonry arches under impulse base motion'. In: *Earthquake Engineering & Structural Dynamics* 36.14 (2007), pp. 2119–2136. DOI: 10.1002/eqe.719.

[17] N. Bianchini, N. Mendes, P. B. Lourenço and C. Calderini. 'Modelling of the Dynamic Response of a Full-Scale Masonry Groin Vault: Unstrengthened and Strengthened with Textile-Reinforced Mortar (TRM)'. In: *International Journal of Architectural Heritage* 18.12 (2024), pp. 2042–2066. DOI: 10.1080/15583058.2024.2320857.

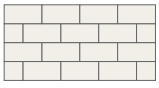
[18] F. Masi, I. Stefanou, V. Maffi-Berthier and P. Vannucci. 'A Discrete Element Method based-approach for arched masonry structures under blast loads'. In: *Engineering Structures* 216 (Aug. 2020), p. 110721. ISSN: 0141-0296. DOI: 10.1016/J.ENGSTRUCT.2020.110721.

[19] F. Peña, F. Prieto, P. B. Lourenço, A. Campos Costa and J. V. Lemos. 'On the dynamics of rocking motion of single rigid-block structures'. In: *Earthquake Engineering & Structural Dynamics* 36.15 (Dec. 2007), pp. 2383–2399. ISSN: 1096-9845. DOI: 10.1002/EQE.739.

[20] J. Lemos and V. Sarhosis. 'Dynamic analysis of masonry arches using Maxwell damping'. In: *Structures* 49 (2023), pp. 583–592. DOI: 10.1016/j.istruc.2023.01.139.

[21] E. M. Dawson and Z. Cheng. 'Maxwell Damping: An Alternative to Rayleigh Damping'. In: *Geo-Extreme 2021*. Geo-Extreme 2021. ASCE, 2021, pp. 34–45. DOI: 10.1061/9780784483701.004.

[22] J. V. Lemos, E. Dawson and Z. Cheng. 'Application of Maxwell damping in the dynamic analysis of masonry structures with discrete elements'. In: *International Journal of Masonry Research and Innovation* 7.6 (2022), pp. 663–686. ISSN: 2056-9459. DOI: 10.1504/ijmri.2021.10043266.



4

A New Contact Constitutive Model for Masonry Structures: Masonry Advanced Softening cONtact model (MASON)

*Following the DEM formulation and dynamic considerations established in Chapter 3, this chapter presents the **Masonry Advanced Softening cONtact model (MASON)**, a novel constitutive model developed to simulate the mechanical behaviour of masonry structures using the Distinct Element Method (DEM). The formulation captures the interactions between masonry units and mortar joints, accounting for cracking, shearing, and crushing phenomena. A comprehensive overview of the adopted contact mechanics is provided in Section 4.1, followed by the formulation of the multi-surface plasticity framework in Section 4.2. Damage evolution laws are detailed in Section 4.3, while Section 4.4 discusses dilatancy softening and uplift mechanisms. Hysteretic contact laws and cyclic degradation rules are presented in Section 4.5, and the stress update routine for explicit time integration is outlined in Section 4.6. The implementation in 3DEC is described in Section 4.7, providing the computational basis for the calibration and validation studies in the subsequent chapters. The chapter closes with Section 4.8, which verifies the contact model on a masonry triplet test and examines how uniform, single-seed defect, and Weibull-distributed tensile strength assignments resolve the loss of uniqueness under softening.*

Parts of this chapter have been adapted from two papers published in *Computers & Structures*, 10.1016/j.compstruc.2024.107499 and in *Computers & Structures*, 10.1016/j.compstruc.2025.108094.

4.1. Overview of the adopted modelling strategy

This chapter presents the theoretical formulation of a joint constitutive model for unreinforced masonry (URM) structures within the Distinct Element Method (DEM) framework. The joint constitutive formulation developed in this dissertation is hereafter termed the **Masonry Advanced Softening cONtact model (MASON)**, and it governs the contact response of masonry interfaces in tension, shear, and compression under monotonic and cyclic loading. The modelling strategy integrates contact mechanics with a multi-surface plasticity framework, damage evolution, dilatancy softening and uplift, cyclic degradation, and an explicit stress update to capture the nonlinear behaviour of URM joints under monotonic and cyclic loading. The adopted strategy represents masonry units as rigid or deformable blocks with extended dimensions to account for mortar-joint thickness, thereby modelling masonry structures as assemblies of discrete blocks.

In the deformable-block configuration, the blocks are modelled as a linear-elastic continuum, while the mortar joints are represented as a set of cohesive-frictional contact points distributed along the interfaces between the blocks. Meanwhile, in the rigid-block configuration, the masonry units are treated as rigid bodies, so their internal deformation is not represented explicitly. The elastic and inelastic deformability of the assemblage is therefore lumped in the interfaces. In this setting, the mortar joints are again discretised as cohesive-frictional contact points distributed along the block boundaries, and the global response arises from rigid-body motions of the units, together with joint opening, sliding, and crushing, all governed by the contact constitutive law.

Figure 4.1 illustrates the discretisation strategy for masonry structures using DEM in two-dimensional space. To capture unit splitting under tension-dominated states, a potential crack plane is introduced at the brick mid-length, shown as the dashed red line in Figure 4.1. This interface is modelled as a zero-thickness cohesive–frictional contact with the same kinematics as external joints, but with independent history variables.

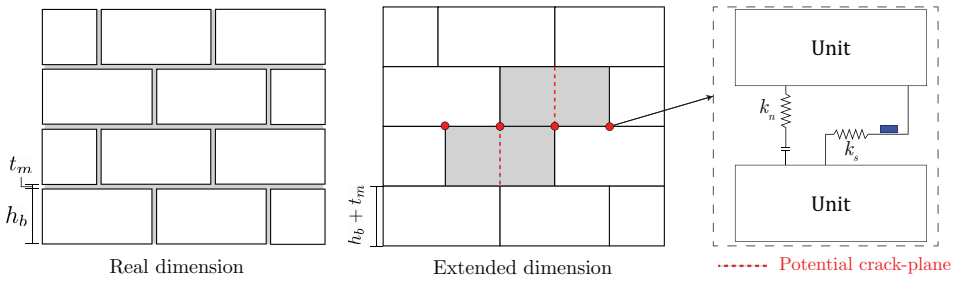
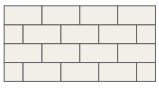


Figure 4.1. Discretisation strategy for masonry structures using the Distinct Element Method (DEM).

When masonry units are modelled as rigid blocks, the block's Young's modulus does not enter the stiffness and strength calculations of the contact points. The overall elastic compliance of the assemblage is lumped at the interfaces (k_n and k_s in Figure 4.1), which govern the initial stiffness and are first estimated via homogenisation and then

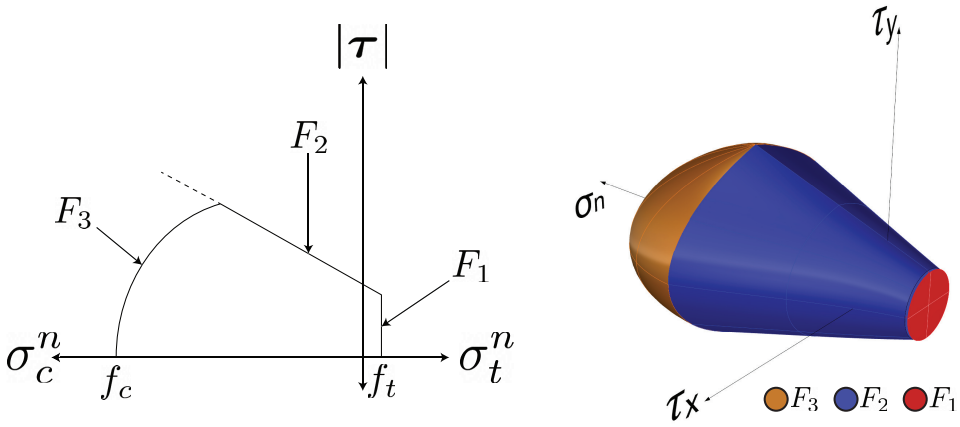


recalibrated to match the experimental tests. When masonry units are modelled as deformable blocks, the block's Young's modulus is used in the stiffness calculations of the contact points, while the joint stiffness is only used to capture the shear slip and opening behaviour.

The explanation of the constitutive model is structured into three stages: a definition of the plastic yield functions in Section 4.2, damage evolution laws in Section 4.3, and the inclusion of dilatancy softening and uplift mechanism in Section 4.4. Energy dissipation mechanisms in the form of hysteretic contact laws and cyclic degradation rules are presented in Section 4.5, followed by the stress update routine for explicit time integration in Section 4.6. Finally, the numerical implementation of the model within 3DEC, the commercial DEM code in which the model is implemented, is described in Section 4.7. In this chapter, the terms *joint* and *contact* are used interchangeably to denote the interface law assigned to masonry joints within the DEM framework.

4.2. Formulation of the multi-surface plasticity

The present model uses the multi-surface plasticity concept as illustrated in Figure 4.2. The yield functions are mathematically defined in Equations (4.1) to (4.3).



(A) Two-dimensional yield surface (B) Three-dimensional representation

Figure 4.2. Schematic illustration of the multi-surface plasticity model for masonry joints in the normal-shear stress space.

$$F_1 = \sigma_n - f_t(u_n^t) \tag{4.1}$$

$$F_2 = \|\boldsymbol{\tau}\| - \left(f_s(\mathbf{u_s}) - \sigma_n \tan\left(\phi_{cv} + \psi(\mathbf{u_s})\right)\right) \tag{4.2}$$

$$F_3 = C_{nn}\sigma_n^2 + C_{ss}\|\boldsymbol{\tau}\|^2 + C_n\sigma_n - [f_c(u_c^n)]^2 \tag{4.3}$$

where u_n^c and u_n^t are the relative normal subcontact displacements in compression and tension, respectively, σ_n is the normal stress, $\boldsymbol{\tau}$ is the shear stress vector, ϕ_{cv} is the friction

angle at constant volume, $f_t(u_t^n)$ is the tensile strength that reduces according to the tensile normal displacement u_t^n, $f_s(\mathbf{u^s})$ is the cohesive strength that decays depending on the shear displacement vector $\mathbf{u^s}$, $\psi(\mathbf{u}^s)$ is the dilatancy angle corresponding to the shear displacement vector, $f_c(u_c^n)$ is the compressive strength that evolves under the compressive normal displacement u_c^n, C_{nn} and C_{ss} are the parameters that control the semi-axes of the ellipse in Figure 4.2, and C_n is the centre of the ellipse.

In this framework, multi-surface plasticity is adopted to represent, within a single contact formulation, the different inelastic mechanisms that can occur at masonry joints under combined normal and shear loading. Each yield function F_i defines a different failure mechanism: mode-I cracking in tension (F_1), frictional slip with cohesion and friction (with dilatancy) in shear (F_2), and compressive crushing with confinement-dependent strength cap (F_3). The overall response is then governed by the active set of yield surfaces, such that, depending on the stress state and loading history, one or more mechanisms may be simultaneously mobilised. Plastic flow is determined from the corresponding plastic potential G_i together with standard loading-unloading (Kuhn-Tucker) conditions. This multi-surface structure is essential to capture the experimentally observed transition from tensile cracking to frictional sliding and, at higher confinement, to compressive failure of the masonry assemblage, while allowing each mechanism to exhibit its own evolution of strength and stiffness.

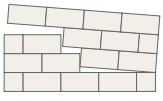
The yield functions F_1 and F_2 match those used in the Coulomb-slip contact model. The elliptical yield surface F_3 is the compression cap adopted from Lourenço and Rots [1]. An associated flow rule is assumed for the tensile cut-off and compression cap regions, in which the plastic potentials G_1 and G_3 are equal to F_1 and F_3, respectively. Meanwhile, a non-associated flow rule is used for the F_2 yield surface to address the role of dilatancy at the onset of damage in the mortar joints [2–5]. The mathematical expression of the plastic potential G_2 is defined in Equation (4.4).

$$G_2 = \|\boldsymbol{\tau}\| + \sigma_n \tan\psi(\mathbf{u_s}) - f_s(\mathbf{u_s}) \tag{4.4}$$

In this way, the tensile and compressive mechanisms are treated according to the normality rule, which simplifies the algorithmic treatment of cracking and crushing and preserves the symmetry between the yield and potential surfaces in the F_1 and F_3 domains, while the shear mechanism is governed by an independent dilatant response through G_2. The choice of G_2 ensures that the direction of plastic flow in shear is governed by the mobilised dilatancy angle $\psi(\mathbf{u_s})$. This decoupling between strength and dilatancy is essential for reproducing the experimentally observed volumetric behaviour of the mortar joints, in which the shear capacity is sustained primarily through the constant-volume friction angle ϕ_{cv} while the accompanying normal uplift remains small. An associated flow rule would couple shear strength and normal opening through the same angle, overpredicting the uplift relative to the shear resistance reported in shear-compression tests of mortared masonry.

4.3. Damage evolution laws

The separation of the damage parameters is essential in the contact constitutive model, since the masonry interfaces behave differently under different modes of deformation, as



indicated in Figure 2.1. The strength degradation of the contact points during material softening is controlled by three damage scalars corresponding to tensile (d_t), shear (d_s), and compressive damage (d_c). In the MASON model, the tensile and shear softening are defined by an exponential softening law in which the decay with respect to crack opening (mode-I) or inelastic slip (mode-II) is governed by the respective fracture energies G_f^I and G_f^{II}, as expressed in Equations (4.5) and (4.7) and shown in Figure 4.3A and Figure 4.3B. The parameters of the exponential curves are chosen so that the area under the traction-separation law matches these fracture energies. This ensures mesh-objective energy dissipation and allows direct calibration from experimental data.

$$f_t(u_t^n) = \left[1 - d_t(u_t^n)\right] f_{t,0}, \qquad d_t(u_t^n) = 1 - \exp\left[-\frac{f_{t,0}}{G_f^I}\left\langle u_t^n - \frac{f_{t,0}}{k_n}\right\rangle_+\right] \tag{4.5}$$

$$\tau(\mathbf{u}^s) = f_s(\mathbf{u}^s) - \sigma^n \tan\left(\phi_{cv} + \psi_0\right) \tag{4.6}$$

where $d_t(u_t^n)$ is the tensile damage scalar, $f_{t,0}$ and f_t are the initial and softened tensile strengths, G_f^I is the mode-I fracture energy, and $\tau(\mathbf{u}^s)$ is the shear strength on the F_2 surface evaluated at the initial dilatancy ψ_0. The exponential softening law for shear strength is applied to the cohesive strength, defined in Equation (4.7).

$$f_s(\mathbf{u}^s) = \left[1 - d_s(\mathbf{u}^s)\right] f_s, \qquad d_s(\mathbf{u}^s) = 1 - \exp\left[-\frac{f_s}{G_f^{II}}\left\langle \|\mathbf{u}^s\| - u_{el}^s\right\rangle_+\right] \tag{4.7}$$

where f_s is the softened cohesive strength, $d_s(\mathbf{u}^s)$ is the shear damage scalar, G_f^{II} is the mode-II fracture energy, and u_{el}^s is the elastic shear displacement, defined by Equation (4.8).

$$u_{el}^s = \frac{\tau_{max}}{k_s} = \frac{f_s - \sigma^n \tan\left(\phi_{cv} + \psi_0\right)}{k_s} \tag{4.8}$$

where f_s is the peak cohesive strength, and ψ_0 is the initial dilatancy angle. It is important to note that the default implementation assumes a fixed dilatancy value. The dilatancy

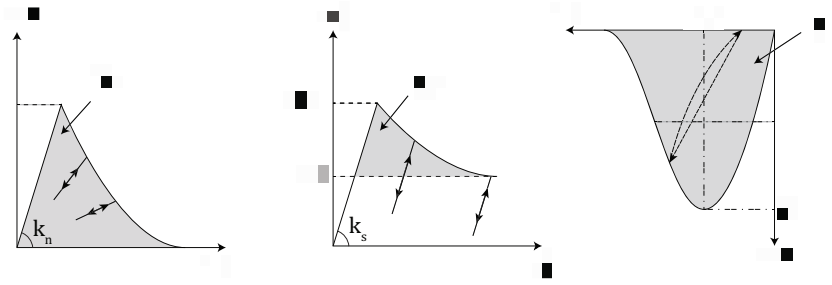


Figure 4.3. Damage evolution under each failure regime

softening effect is discussed in the Section 4.4. To couple the post-peak softening in tension and shear, following [6–8], a combined damage scalar d_{ts} is introduced in Equation (4.9), replacing the tensile d_t and shear d_s damage scalars in Equations (4.5) and (4.7), respectively. This scalar governs the degradation of strength and of the normal unloading stiffness (Section 4.5). It does not imply an isotropic degradation of the contact stiffness, since the shear stiffness follows a separate rule. To prevent round-off accumulation error, both $f_t(u_t^n)$ and $f_s(u^s)$ are bounded below by 1×10^{-12} according to the precision limit of the user-defined model in 3DEC [9].

$$d_{ts}(u_t^n, \mathbf{u^s}) = d_t(u_t^n) + d_s(\mathbf{u^s}) - d_t(u_t^n) d_s(\mathbf{u^s}) \tag{4.9}$$

The uniaxial compressive behaviour of the joint constitutive model is governed by the hardening/softening law introduced by Lourenço and Rots [1]. The hardening branch is the parabolic function in Equation (4.10), which starts at the elastic stress $\sigma_{el}^n = 0.2 f_c$ and reaches the compressive strength f_c at the peak displacement u_p:

$$f_c(u_c^n) = \sigma_{el}^n + (f_c - \sigma_{el}^n)\sqrt{2\chi_h - \chi_h^2}, \qquad \chi_h = \frac{u_c^n - u_{el}^n}{u_{cp}}, \qquad 0 \le \chi_h \le 1 \tag{4.10}$$

where $u_{el}^n = \sigma_{el}^n / k_n$ is the normal displacement at the elastic stress, $u_{cp} = n f_c / k_n$ is the hardening length from u_{el}^n to the peak, and $u_p = u_{el}^n + u_{cp}$ is the displacement at compressive strength. The user-supplied multiplier n scales the hardening length relative to f_c / k_n, the displacement that the initial normal stiffness alone would predict at peak strength.

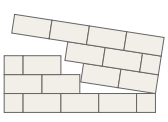
The parabola has a vertical tangent at u_{el}^n and therefore lies above the elastic line $\sigma = k_n u_c^n$ over the first part of the hardening range. The backbone is taken as the lower of the two, so the elastic branch governs until it meets the parabola, at about $0.37 f_c$ for $n = 7.5$ and $0.60 f_c$ for $n = 3$. The elastic stress σ_{el}^n thus fixes the origin of the parabola rather than the end of the linear response.

The multiplier n allows the model to represent masonry that remains ductile well beyond the elastic displacement at peak strength, as reported by Jafari et al. [10]. The softening phase is defined by a compressive damage scalar d_c in Equation (4.11), which reduces strength from the peak f_c to the residual f_{cr}.

$$f_c(u_c^n) = [1 - d_c(\xi)]\, f_c, \qquad \xi = \frac{u_c^n - u_p}{L}, \qquad u_p = u_{el}^n + u_{cp} \tag{4.11}$$

where u_p is the displacement at compressive strength defined with Equation (4.10) and L is the softening length of Equation (4.13), so that ξ runs from 0 at the peak to 1 at the residual strength $f_{cr} = r f_c$. The damage follows the smooth law of Equation (4.12), quadratic from the peak to the intermediate stress $f_{cm} = (f_c + f_{cr})/2$ at $\xi = 0.3$ and exponential from there to f_{cr}, with $r = f_{cr}/f_c$ and $m = (1 + r)/2$.

$$1 - d_c(\xi) = \begin{cases} 1 - (1 - m)\left(\dfrac{\xi}{0.3}\right)^2, & 0 \le \xi \le 0.3 \\ r + (m - r)\exp\left(-\dfrac{\xi - 0.3}{0.15}\right), & 0.3 < \xi \le 1 \end{cases} \tag{4.12}$$



The two branches are continuous in value and slope at $\xi = 0.3$. In the implementation, the envelope is multilinear, i.e., Equation (4.12) is sampled at eight knots, $\xi = 0$, 0.1, 0.2, 0.3, 0.4, 0.55, 0.75 and 1, and interpolated linearly between them, with the last knot placed exactly on the residual.

The softening length L is not a material input. It is set so that the area between the envelope and the residual level, pre-peak part included, equals the compressive fracture energy G_c,

$$L = \frac{G_c - A_{\text{pre}}}{f_c\, S}, \qquad S = \sum_{i=1}^{7} \tfrac{1}{2}\,(\xi_{i+1} - \xi_i)\,[s_i + s_{i+1} - 2r] = 0.326\,(1 - r) \tag{4.13}$$

where A_{pre} is the area above the residual between the origin and u_p, evaluated in closed form from the elastic line and Equation (4.10), and S is the area above r of the multilinear envelope, with ξ_i the eight knots listed above and $s_i = 1 - d_c(\xi_i)$ their values from Equation (4.12), the last knot being set to r. G_c is therefore dissipated exactly, independently of k_n and of the hardening ratio n. When $G_c \le A_{\text{pre}}$, the prescribed energy is already stored before the peak and the response drops to the residual at u_p.

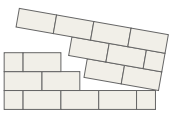
Figure 4.4 shows the resulting backbone for the calcium-silicate parameters of Chapter 5. The pre-peak branch follows the elastic line until it meets the hardening curve at $0.37 f_c$ for $n = 7.5$ (inset), since the parabola in Equation (4.10) starts at $0.2 f_c$ with a vertical tangent and lies above the elastic line until then. The multilinear envelope closely follows the smooth law, and the shaded area above f_{cr} equals $G_c = 15$ N/mm.

4.4. Inclusion of dilatancy softening and uplift mechanisms

Experimental tests on masonry couplets [2, 3, 5, 11, 12] have shown that the dilatancy angle decreases with continued shear slip and, in some cases, vanishes. The normal displacement induced by dilation therefore stops increasing and approaches a constant value. Several researchers have proposed numerical modelling strategies to address the dilatancy effect observed in mortar joints using an interface constitutive model. Lourenço and Rots [1] and Giambanco et al. [13] included the dilatancy effect via a non-associative flow rule, with a dilatancy angle decoupled from the friction angle. This dilatancy angle also decreased with increasing normal pressure for Lourenço and Rots [1], whereas Giambanco et al. [13] attributed the decrease to the loss of cohesive strength. Van Zijl [2] extended the approach of Lourenço and Rots [1] to account for the volumetric increase that caused masonry units to uplift under shear load. Andreotti et al. [5] proposed a data-driven strategy to calibrate the dilatancy angle using experimental data. The dilatancy angle was coupled to the friction angle, and the decrease was related to plastic shear and normal displacements observed in the experiments.

As shown in Equation (4.2), the Coulomb friction line F_2 departs from the formulation of Oktiovan et al. [14] by adopting the shear-strength definition of Andreotti et al. [5], in which the friction coefficient is expressed as the sum of a constant-volume friction angle, ϕ_{cv}, and a dilatancy angle, ψ, that decays with accumulated plastic slip.

Several authors [3, 5, 6, 11] describe ϕ_{cv} as reflecting the surface roughness governing sliding resistance, while ψ controls the joint opening or inclination of the sliding surface as shear slip develops. Furthermore, as the shear displacement increases, the



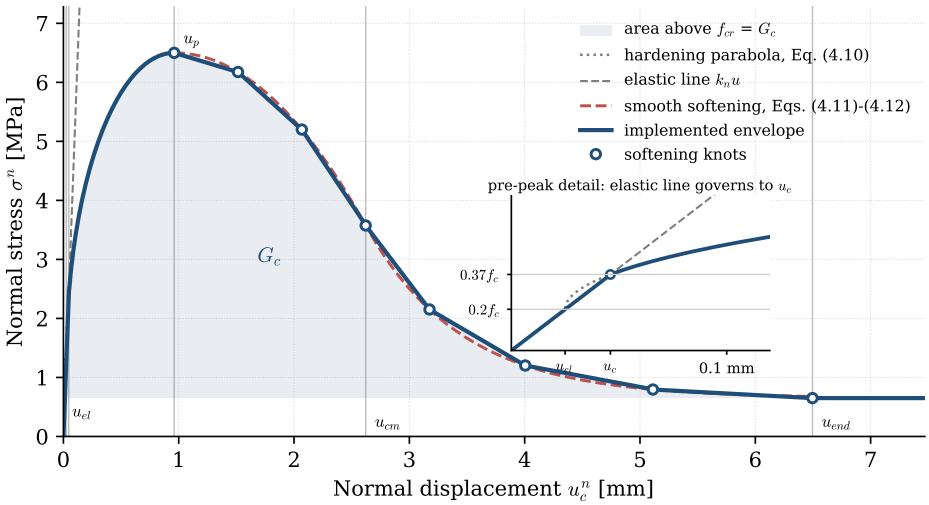


Figure 4.4. Compressive backbone as implemented. The pre-peak branch follows the elastic line until it meets the hardening parabola of Equation (4.10) at u_c (inset). The softening envelope is multilinear, sampled at eight knots from the smooth law of Equation (4.12) (dashed), with the softening length L set by Equation (4.13) so that the shaded area above f_{cr} equals G_c. Parameters: $f_c = 6.5$ MPa, $f_{cr} = 0.1 f_c$, $k_n = 52.1$ GPa/m, $n = 7.5$, $G_c = 15$ N/mm.

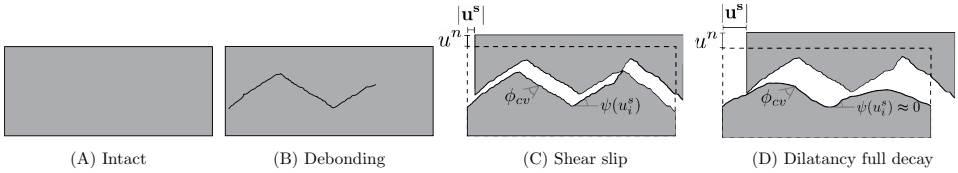
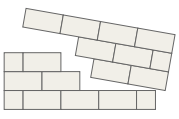


Figure 4.5. Phases of the mortar joints when subjected to shear load [5]

uplift/dilatant displacement reaches a relatively constant value, which is interpreted as the smoothed bed-joint due to the fully decayed dilatancy angle (Figure 4.5D) [2].

The above behaviour is illustrated in Figure 4.5. At the initial state (Figure 4.5A), the shear stress is defined as given in Equation (4.6), where the friction angle at constant volume ϕ_{cv} is added to the initial dilatancy angle ψ. As the crack through the joint develops (Figure 4.5B), the cohesion and the dilatancy angle soften. This differs from the previous formulation defined by the authors [14] and the typical interface-based constitutive model for masonry that considers dilatant behaviour [1, 2, 8, 15, 16]. While the cohesive strength softens according to the combined damage scalar d_{ts} (Equation (4.9)), the dilatancy angle decays with the accumulated plastic slip, reaching zero at the slip $u_{s,max}$, as expressed in Equation (4.14) [17].



$$\tan\psi(u^{s,p}) = \begin{cases} \tan\psi_0 \left(1 - \dfrac{u^{s,p}}{u_{s,max}}\right) \exp\left(-\delta\, u^{s,p}\right), & u^{s,p} \le u_{s,max} \\ 0, & u^{s,p} > u_{s,max} \end{cases} \tag{4.14}$$

where ψ_0 is the initial dilatancy angle, δ is the softening gradient [2], $u_{s,max}$ is the plastic slip at zero dilation, and $u^{s,p} = \|\mathbf{u}^s\| - \tau_{max}/k_s$ is the plastic slip, obtained as the total shear displacement minus the elastic shear displacement at the current shear strength τ_{max}. If the plastic slip exceeds $u_{s,max}$, the decay is capped at zero to prevent negative dilation, which would correspond to spurious joint closure under continued shear.

Plastic slip initiates as soon as the shear traction reaches the Coulomb friction line in Figure 4.2, after which shear damage accumulates (Figure 4.5C). After the onset, the slip evolves while the cohesive strength softens and the dilatant part of Equation (4.2) decays according to Equation (4.14). When cohesion has fully degraded ($f_s \to 0$) and $\psi \approx 0$, the residual shear strength is purely frictional. The mathematical definition in Equation (4.6) shows that at large slips, the tangential response tends to the frictional branch. The physical representation of the dilatancy softening is shown in Figure 4.5D, which shows that the surface of asperities softens as shear slip progresses [5, 17, 18].

To represent the uplift in the normal direction, a dilatant opening increment Δu^n_{dil} is computed from the plastic slip increment $\Delta u^{s,p}$ of the current step and the current dilatancy angle, as given in Equation (4.15).

$$\Delta u^n_{dil} = \Delta u^{s,p} \tan\psi(u^{s,p}) \tag{4.15}$$

Since the normal displacement of the subcontact is kinematically prescribed by the block motion in the explicit scheme, the dilatant opening cannot be imposed directly. Its effect is instead introduced as a correction to the normal force obtained from Equation (3.4), given in Equation (4.16) with tension positive.

$$F^n := F^n - k_n A_c \Delta u^n_{dil} \tag{4.16}$$

The correction applies only when F_2 is active, so elastic shear displacement produces no uplift. The cap at $u_{s,max}$ is already contained in Equation (4.14), since $\tan\psi$ vanishes beyond that slip.

During unloading in shear, the yield condition is inactive, so only elastic closure occurs. The accumulated plastic offset and current dilation angle are retained (i.e., no healing), matching the partial recovery observed in experimental tests. Although the shear strength in Equation (4.6) combines friction and dilation throughout the loading history, the uplift correction in the normal direction (Equation (4.15)) depends only on the dilatant component. As shown in Figure 4.5C and Figure 4.5D, only the dilatant behaviour of the mortar layer causes the roughness of the asperity surface that mobilises uplift movement. Furthermore, the uplift-correction framework used here follows the established formulation of Van Zijl [2] and Andreotti et al. [5]. The contribution of the MASON model lies in the exponential dilatancy decay law and its consistent integration into the DEM framework.

The MASON formulation adopts a different decomposition of the cohesion–friction interaction from the damage-weighted coupling, such as that proposed by Cera *et al.* [19],

in which the frictional contribution grows from zero at the intact interface to its full Coulomb value at complete decohesion through the function $f_d(d) = d^p$. In MASON, the friction angle in Equation (4.2) takes its full value $\phi_{cv} + \psi_0$ at the onset of yielding on F_2, and the cohesion-to-friction transition emerges from the independent softening of the cohesive strength f_s in Equation (4.7) and the dilatancy angle ψ in Equation (4.14). When no dilatancy is assigned ($\psi_0 = 0$), the firciton angle instaed softens from ϕ_{cv} to a residual value ϕ_{res} in proportion to the combined damage $\phi = \phi_{res} + (\phi_{cv} - \phi_{res})(1 - d_{ts})$. This choice is consistent with the explicit time-marching scheme adopted in this dissertation, in which yield-surface activation does not require a smooth tangent modulus and avoids the additional state variable required to track a separate damaged area alongside the plastic slip already in use. Incorporating a damage-activated frictional mobilisation similar to the work of Cera *et al.* [19], which gives a smooth transition between cohesive and frictional regimes within an implicit finite element framework, is noted as a future extension.

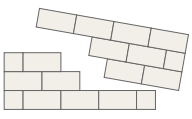
4.5. Energy dissipation mechanism

The joint constitutive model incorporates an enhanced energy-dissipation framework to capture damage accumulation under cyclic loading. Dissipation activates in a fracture–mode–dependent manner through controlled stiffness degradation. In tension, unloading follows a secant rule (see Figure 4.3A): the unloading stiffness is the secant from the origin to the current point on the degraded tensile envelope, so the apparent joint stiffness decreases as the normal opening increases. The degradation rate of this unloading stiffness is governed by the combined tensile–shear damage scalar (Equation (4.9)), as expressed in Equation (4.17).

$$k_n^{unl} = (1 - d_{ts}) \frac{f_{t,0}}{u_t^n} \tag{4.17}$$

Elastic unloading is adopted in the shear regime (Figure 4.3B), where the initial shear stiffness k_s is retained irrespective of the accumulated damage. The secant degradation in Equation (4.17) applies only to the tensile branch, where the contact opens, and the load path is a cohesive bond degraded by both mode-I and mode-II damage. By contrast, shear stiffness governs a contact that closes under compression, where shear is transferred by friction and interlock between crack faces rather than by bond. Tensile damage removes the bond, but not this contact, and its effect on shear transfer is already captured by the softening of the cohesive strength (Equation (4.7)), which reduces the shear strength to its frictional residual. Retaining k_s therefore affects the elastic deformation in the stick state but not the shear capacity. This assumption is consistent with earlier interface and contact formulations for masonry [7, 15, 20] and is supported by the cyclic direct shear tests of Atkinson et al. [18], in which fully debonded joints unload along a branch close to the initial stiffness.

The unloading mechanism used in the compression regime follows the nonlinear unloading/reloading formulation defined by Facconi et al. [21], as illustrated in Figure 4.6. Experimental results on uniaxial compression tests of masonry walletes [21–25] showed that the masonry composite unloads in a nonlinear manner with irreversible strain (or



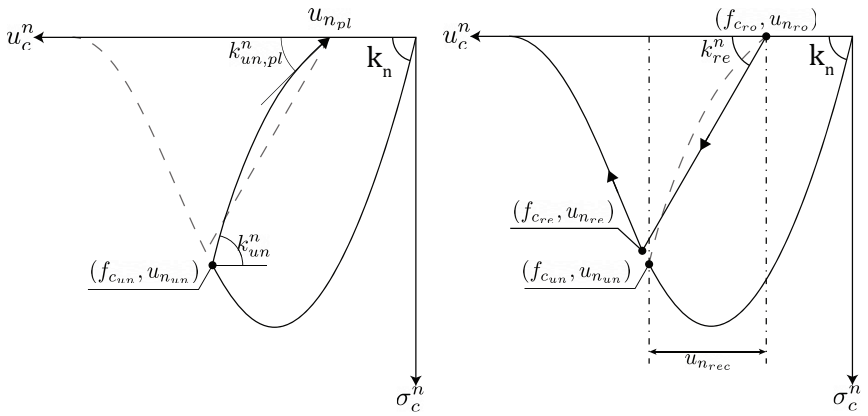
deformation) and stiffness degradation to account for energy dissipation.

Leveraging the robustness of the explicit time marching integration scheme, a nonlinear unloading branch is proposed, as shown in Figure 4.6A. The unloading branch reaches a normal plastic displacement $u_{n_{pl}}$ at zero compressive stress, which defines the irrecoverable deformation of the masonry assemblage due to loading and unloading sequences. The plastic displacement is expressed as a fraction φ of the displacement at the onset of unloading, $u_{n_{un}}$, in Equation (4.18).

$$u_{n_{pl}} = \varphi\, u_{n_{un}}, \qquad \varphi = \frac{\varphi_{\max}\, p}{\varphi_{\max} + p}, \qquad p = (m_0 + m_1 d_c)\left(0.235\, u'_{n_{un}} + 0.25\right) \tag{4.18}$$

where $u'_{n_{un}} = u_{n_{un}} / u_{cp}$ is the unloading displacement normalised by the hardening length u_{cp} (Figure 4.3C). The linear term in p is adapted from the plastic displacement relation of Facconi et al. [21], rewritten in terms of displacement under a small-displacement assumption. The multiplier $m_0 + m_1 d_c$ scales this term and replaces the separate post-peak branch of the original relation. Its coefficients are user-defined: m_0 sets the plastic offset of an undamaged joint, and m_1 increases it as compressive damage accumulates. With $m_0 = 1$ and $d_c = 0$, the linear term retains the coefficients of the original relation. The default values are $m_0 = 1.0$ and $m_1 = 2.5$; analyses that use other values state them in their parameter tables. The cap $\varphi_{max} = 0.97$ equals the plastic ratio reached by the original relation at the peak and ensures that $u_{n_{pl}}$ remains below $u_{n_{un}}$ at all damage levels. The unloading branch is then defined between $u_{n_{un}}$ and $u_{n_{pl}}$ by the general formulation in Equation (4.19).

$$\sigma_c^n = f_{c_{un}} - \left(f_{c_{un}} - f_{c_{re}}\right) \frac{B_1 \chi + \chi^2}{1 + B_2 \chi + B_3 \chi^2}, \qquad \chi = \frac{u_c^n - u_{n_{un}}}{u_{n_{pl}} - u_{n_{un}}} \tag{4.19}$$



(A) Unloading (B) Reloading

Figure 4.6. Nonlinear unloading mechanism for the compressive behaviour of masonry assemblage [21]

where σ_c^n is the compressive stress during unloading, χ is the normalised position along the branch, equal to zero at the onset of unloading and to one at the plastic displacement, $f_{c_{un}}$ is the stress at the onset of unloading, $f_{c_{re}}$ is the stress at the end of the branch (zero for complete unloading to $u_{n_{pl}}$), and B_1, B_2 and B_3 are the shape parameters of Equation (4.20).

$$B_1 = \frac{k_{un}^n}{E_s}; \quad B_2 = B_1 - B_3; \quad B_3 = 2 - \frac{k_{pl}^n}{E_s}(1 + B_1); \tag{4.20}$$

where $E_s = f_{c_{un}}/(u_{n_{un}} - u_{n_{pl}})$, the secant stiffness between the onset of unloading and the plastic displacement (from Equation (4.18)), k_{un}^n and k_{pl}^n are the unloading and plastic tangent stiffnesses (Figure 4.6A), respectively. Both values are defined according to Equation (4.21).

$$k_{un}^n = \gamma_{un} k_n; \quad k_{pl}^n = \frac{\gamma_{pl} k_n}{\left(1 + \frac{u_{n_{un}}}{u_{cp}}\right)^e} \tag{4.21}$$

where $\gamma_{un} = 1.5$, $\gamma_{pl} = 0.15$, and $e = 2$, empirically defined according to the suggestions provided by Facconi et al. [21], where e defines the nonlinear curve close to the plastic displacement and the point of inflection between $k_{n_{un}}$ and $k_{n_{pl}}$. Those variables were determined from the best fit of the unloading curves of a uniaxial compression test on masonry walletes gathered from the literature.

The reloading branch (Figure 4.6B) starts when compressive displacement increases after either complete (when the compressive stress reaches zero) or partial unloading [21]. Due to damage accumulated during the cyclic loading sequence, the reloading curve typically intersects the envelope curve at a displacement larger than the displacement level during the unloading onset [26]. With that in mind, the linear reloading mechanism is adopted in this model, deviating from the nonlinear representation defined by Facconi et al. [21], to simplify the formulation. Furthermore, several authors [26–28] have shown that the linear representation of the reloading sequence is adequate to simulate a masonry assemblage's energy dissipation mechanism under uniaxial cyclic compression. The linear reloading compressive stress is defined in Equation (4.22).

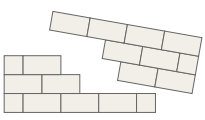
$$\sigma_c^n = f_{c_{ro}} + k_{re}^n (u_c^n - u_{n_{ro}}) \tag{4.22}$$

where $f_{c_{ro}}$ and $u_{n_{ro}}$ are the compressive stress and displacement at the onset of reloading, and k_{re}^n is the reloading stiffness, defined in Equation (4.23).

$$k_{re}^n = \frac{\beta_d f_{c_{un}} - f_{c_{ro}}}{u_{n_{un}} - u_{n_{ro}}} \tag{4.23}$$

where

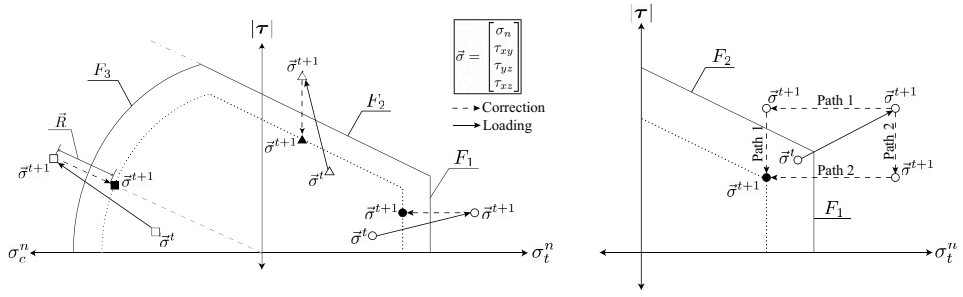
$$\beta_d = \begin{cases} \dfrac{1}{1 + 0.2(u'_{n_{rec}})^{0.5}} & \text{for} \quad u_{n_{un}} < u_{cp} \\ \dfrac{1}{1 + 0.45(u'_{n_{rec}})^{0.2}} & \text{for} \quad u_{n_{un}} \geq u_{cp} \end{cases} \tag{4.24}$$



is the damage factor correlated to the normalised recovery displacement $u_{n_{rec}} = \frac{u_{n_{un}} - u_{n_{ro}}}{u_{cp}}$, as illustrated in Figure 4.6B. The coefficients following the normalised recovery displacement are calibrated with acceptable accuracy based on the experimental data gathered in the literature [21–23, 29, 30].

4.6. Stress update routine in explicit scheme

Proper handling of the force (or stress) update when the stress state violates a yield surface is essential to maintain the stability of the explicit time-marching integration scheme. In contrast to implicit solvers, which typically employ return-mapping or substepping algorithms for stress correction [8, 31–33], the stress update in the present explicit formulation remains relatively straightforward. The adopted update procedure, applied whenever one of the failure surfaces is violated, is illustrated schematically in Figure 4.7A.



(A) Correction algorithm (B) Corner handling

Figure 4.7. Stress update on the interface once the failure surface is violated

From time t to $t + \Delta t$, the stress state progresses either linearly through the increments in Equations (3.4) and (3.5), or through hardening for the normal compressive stress in Equation (4.10). When F_1 is violated at time $t + \Delta t$ (circle marker in Figure 4.7A), only the normal stress component σ^n of the stress state $\vec{\sigma}$ is corrected to the current tensile strength, which is weakened through Equation (4.5). This is because damage in mode-I fracture reduces the normal capacity, while shear components are unaffected at the instant of pure tensile failure. This avoids introducing artificial shear when the joint opens. The normal traction is thus limited to the softened tensile strength and vanishes only when the crack is fully developed. The shear capacity of a partially opened joint remains bounded by F_2. For $0 < \sigma^n < f_t(u_t^n)$, this gives $|\tau| \leq f_s(\mathbf{u}^s) - \sigma^n \tan(\phi_{cv} + \psi)$. This residual cohesive capacity is physically consistent, since the crack is not yet fully formed. As the opening progresses, d_{ts} drives the tensile and cohesive strengths to zero together (Equations (4.5) and (4.7)). A fully developed tensile crack therefore sustains neither normal nor shear traction. The loss of shear transfer across a tensile crack is enforced through the coupled softening of the yield surfaces, evaluated at every timestep, not through a reduction of k_s. This force correction occurs at the same timestep $t + \Delta t$ at which the failure surface is violated.

When F_2 is violated (triangle marker in Figure 4.7A), the shear stress components are projected onto the friction line at the current normal stress through Equation (4.25). This accounts for the tangential component of plastic flow along the non-associated potential G_2. The normal stress is not modified by this projection. The dilatant component of the plastic flow, governed by the term $\sigma^n \tan\psi$ in G_2, is applied separately through the dilatancy update in Equations (4.15) and (4.16), which computes the dilatant opening $\Delta u^n_{dil} = \Delta u^{s,p} \tan\psi(u^{s,p})$ from the plastic slip increment and adjusts the normal force accordingly. The two operations together approximate the non-associated flow along G_2 as a sequence of explicit corrections.

$$\boldsymbol{\tau}^{\mathbf{s}} = \boldsymbol{\tau}^{\mathbf{s}} \frac{\boldsymbol{\tau}^{\mathbf{s}}(d_{ts})}{\|\boldsymbol{\tau}^{\mathbf{s}}\|} \tag{4.25}$$

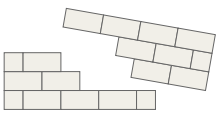
When the compression or shear-compression mode in F_3 is violated, as illustrated by the square marker in Figure 4.7A, both the normal and shear stresses are corrected through a radial return from the origin to the weakened cap. This is done by taking the radius from the point of origin (zero normal and shear stress), and correcting the stress state $\vec{\sigma}$ proportionally to the weakened cap of Equation (4.3), whose size is set by the current compressive strength from Equation (4.12). The correction amount is the radius difference between the violated stress state and the stress state at the weakened yield surface, termed $\vec{R}$ in Figure 4.7A, which has the same structure as $\vec{\sigma}$. The correction for F_3 is formally defined as follows.

$$\left(\vec{\sigma}^{\,t+1}\right)_1 := \left(\vec{\sigma}^{\,t+1}\right)_1 - \left(\vec{R}\right)_1, \qquad \left(\vec{\sigma}^{\,t+1}\right)_{2:4} := \left(\vec{\sigma}^{\,t+1}\right)_{2:4} \frac{\left(\vec{R}\right)_{2:4}}{\left|\left(\vec{\sigma}^{\,t+1}\right)_{2:4}\right|} \tag{4.26}$$

This choice yields a unique, path-independent correction that drives the yield function to zero in a single step and captures the coupled nature of shear-compression failure. As pointed out by Nie et al. [8], problems with multi-surface plasticity models arise when the updated stress is located close to a corner, i.e., the intersection between F_1 and F_2 and between F_2 and F_3 in the case of Figure 4.7A. This approach implements a general solution [34], as illustrated in Figure 4.7B when both tensile cut-off F_1 and Coulomb friction line F_2 are violated. Two sequential stress correction paths converge at the intersection of $F_1 \cap F_2$ and are evaluated as alternative candidates. Path 1 first corrects the tension condition, then corrects the shear stress to satisfy the F_2 line. Path 2 first reduces the shear stress on F_2, then applies the secondary correction to meet F_1. Each path yields a candidate at the corner of the intersection. The active path is determined by the trigger order; the surface violated first in the current increment is selected as the candidate. This tie-break rule yields a unique update, preserves non-negative dissipation, and prevents oscillation between surfaces in subsequent steps.

4.7. Numerical implementation in commercial DEM framework

The joint constitutive model for analysing masonry structures using DEM is implemented in *3DEC* [9]. The numerical treatment of loading, unloading and reloading in the

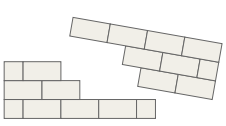


normal direction is given in Appendix A. In an explicit time-marching scheme, contact displacement increments fluctuate from step to step, particularly at re-contact, under local perturbations, or when damping is insufficient. A cyclic constitutive law formulated in terms of displacement increments can read these fluctuations as loading and unloading events. In compression, this results in artificial damage accumulation, or loops that dissipate no energy because the force simply retraces the loading curve. The tensile branch is unaffected, since the force is recomputed from the current opening at every step and damage depends only on the largest opening reached. The shear branch is also unaffected, since unloading is elastic and damage grows only with plastic slip. Three measures in the compressive branch address the problem.

First, branch selection is based on displacement history rather than force. A contact is on the backbone only when it is closing and has reached the largest closure recorded for that contact; every other state is unloading or reloading inside the envelope. Second, a reversal within a narrow band below the current peak, of width $\min(0.015\,u_{\text{hist,comp}},\, 0.10\,(u_{\text{hist,comp}} - u_{n_{pl}}))$, unloads elastically at the initial stiffness and does not open a hysteresis loop. This band filters the oscillations of the explicit scheme without affecting genuine reversals, whose amplitude exceeds it by orders of magnitude. Third, a reversal that starts from a reloading line opens an inner loop anchored at the reversal point. The inner unloading curve is the outer curve shifted to pass through the anchor, and the inner reloading line returns to the anchor, so that nested reversals under dynamic loading dissipate energy without force jumps. All three apply only to compressive unloading and reloading; the backbone, tensile branch, and shear branch remain unchanged.

The compressive unloading and reloading rules assume that unloading starts from the envelope. Under cyclic and dynamic loading, a joint may also reverse while it is still reloading, before it has returned to the envelope. For this case, the implementation follows the partial-loop rules of Facconi et al. [21]. When unloading starts from a point on a reload line, that point is stored as a reversal point $(u_{n_{rev}}, \sigma_{rev})$, together with the start of the reload line on which it lies. The new unloading curve is the outer unloading curve of Equation (4.19), shifted so that it passes through both ends of that reload line. Below the start of the line, the shift decreases linearly to zero at the plastic displacement $u_{n_{pl}}$, so the curve still ends there. Because the outer curve is convex, the shifted curve lies below the reload line, and every partial loop is traversed clockwise and dissipates energy. On reloading, the joint follows a straight line from the bottom of the partial loop back to the reversal point. Beyond it, the joint continues on the original reload line until it meets the envelope. Only one reversal point is stored, and it is replaced only by a reversal at a larger closure, so that small oscillations do not accumulate spurious history. Finally, a joint that has yielded in compression and then separates keeps its plastic displacement: on re-contact it carries compression only once the closure exceeds $u_{n_{pl}}$. These rules are listed in Algorithm 4.

The history variables of the model are the largest tensile opening $u_{\text{hist,ten}}$, the largest closure $u_{\text{hist,comp}}$ with its stress f_{peak}, the end point of the last unloading branch (u^n_{ro}, f_{cro}), the inner-loop anchor, and the plastic shear displacement. The damage scalars d_t, d_s, and d_c are evaluated from these variables at every step, so the strength and normal unloading stiffness depend on the maximum deformation reached, not the



current loading direction. The compressive history is retained when a contact separates fully, since it represents plastic compaction of the joint; on re-contact, the compressive stiffness restarts at its initial value, and the reloading branch resumes from the recorded unloading point. The shear response unloads and reloads elastically at the initial shear stiffness, as discussed in Section 4.5.

4.8. Bifurcation validation of the contact model

Following the formulation and numerical implementation of the MASON contact model in previous sections, a fundamental verification step is required. When softening constitutive models are applied to symmetric structures, multiple equilibrium paths may coexist once two or more material points reach their strength simultaneously. This loss of uniqueness, referred to as *bifurcation*, has been a central challenge in the nonlinear finite-element analysis of quasi-brittle materials [35, 36]. The present section examines how the MASON contact model handles bifurcation in a masonry triplet test, progressing from a theoretically perfect (uniform) strength assignment to a statistically heterogeneous one.

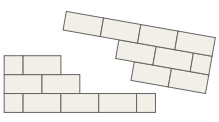
4.8.1. The bifurcation problem in softening systems

The understanding of bifurcation in tensile softening has evolved significantly over the last few decades, shifting from identifying structural effects to developing robust algorithmic circumventions. Rots and de Borst [35, 37] analysed the direct tension test on notched plain concrete specimens by Hordijk [38] using finite elements and identified a bifurcation in the equilibrium path. They found that the descending branch of the load-displacement curve is often dominated by asymmetric crack propagation rather than uniform material softening. They showed that even a slight material imperfection is sufficient to trigger a limit problem where the crack propagates from one notch while the opposite side unloads [37].

This non-symmetric path is characterised by a sudden shift in the softening branch, which they identified as a structural effect arising from the transition from one active notch to another [37]. Furthermore, they highlighted *snap-back* behaviour, in which both load and displacement decrease, noting that indirect displacement control is essential for capturing the post-peak response without numerical path discontinuities.

Rots *et al.* [36] revisited these findings and showed that incremental-iterative Newton techniques struggle to follow the physically meaningful, non-symmetric equilibrium branch in the presence of bifurcations. Imperfections must be added to the model, and the load steps must be kept small enough to avoid overshooting the local material perturbation, often combined with arc-length control. As an alternative, Rots and Invernizzi [39] proposed *Sequentially Linear Analysis* (SLA), in which the load is scaled so that only one integration point changes its constitutive status per analysis cycle. Because no two points reach the failure threshold in the same cycle, the system of equations never becomes ill-conditioned, and the non-symmetric mode in the direct tension tests is recovered without manually imposed imperfections.

Drawing on the notch-test findings [35, 36], the present section applies the same reasoning to a masonry triplet pulled in uniaxial tension using the MASON contact



model. The triplet contains two discrete joint planes in series rather than a continuum cross-section, but the underlying numerical pathology is identical: simultaneously reaching the failure criterion at multiple subcontacts. Three strength assignments are compared to examine how this problem can be resolved: a uniform field, a deterministic single-seed defect, and a Weibull-distributed field. No experimental data are available for this particular test configuration. The exercise is intended solely to verify the contact model's robustness under conditions known to produce bifurcations in continuum formulations.

4.8.2. Test geometry and loading protocol

The specimen consists of three deformable masonry units stacked vertically and connected by two horizontal bed joints (Figure 4.8). The geometry measures $200 \times 100 \times 180$ mm, with joints at $z = 60$ mm (bottom) and $z = 120$ mm (top). Each bed joint is discretised into a set of subcontacts governed by the MASON constitutive law formulated in the previous sections. The blocks are meshed with an edge length of 15 mm, and assigned linear-elastic material properties ($E_b = 15$ GPa, $\nu = 0.2$, $\rho = 2000\,\mathrm{kg/m^3}$).

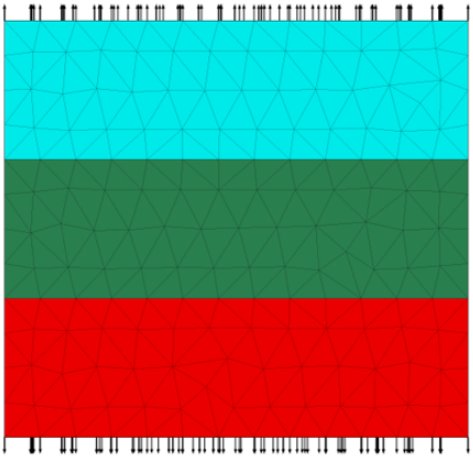


Figure 4.8. DEM model for the bifurcation test where the top and bottom blocks are subjected to displacement-controlled tensile load

Loading is applied as a symmetric, displacement-controlled, uniaxial tension where the top face of the upper block is pulled up at a constant velocity of $1 \times 10^{-4}\,\mathrm{m\,s^{-1}}$, while the bottom face of the lower block is pulled down at the same rate, as indicated by the black arrows in Figure 4.8. The symmetric arrangement is adopted to preserve the symmetry of the boundary condition in the explicit time-marching scheme, so that the centre of mass of the assemblage remains stationary and the inertial loading transmitted through both joints is identical by construction. A configuration with a fixed bottom face and a single pulled top face would yield equivalent results in the quasi-static limit, since the relative opening at each joint is the only kinematic quantity entering the constitutive law.

Two history records are tracked throughout each simulation: the spatial average of normal stress and relative normal displacement across all subcontacts on the bottom interface (hereafter the "bottom" curve), and the corresponding spatial average across all subcontacts on the top interface (the "top" curve). For Variant B, an additional history records the local stress and displacement at the seeded subcontact, isolating the response of the imperfection from the surrounding averaged interface. The contact parameters common to all three variants are listed in Table 4.1.

Table 4.1. Contact properties assigned to the bed joints in the triplet test.

Parameter	Symbol	Value
Normal stiffness	k_n	150×10^9 Pa/m
Shear stiffness	k_s	70×10^9 Pa/m
Friction angle	ϕ_{cv}	31.0°
Residual friction	ϕ_{res}	21.8°
Cohesion	f_s	1.5 MPa
Compressive strength	f_c	15 MPa
Mode I fracture energy	G_f^{I}	10 N/m
Mode II fracture energy	G_f^{II}	50 N/m
Nominal tensile strength	f_t (baseline)	1.0 MPa

Three variants of the model are considered, differing only in the tensile strength assignment:

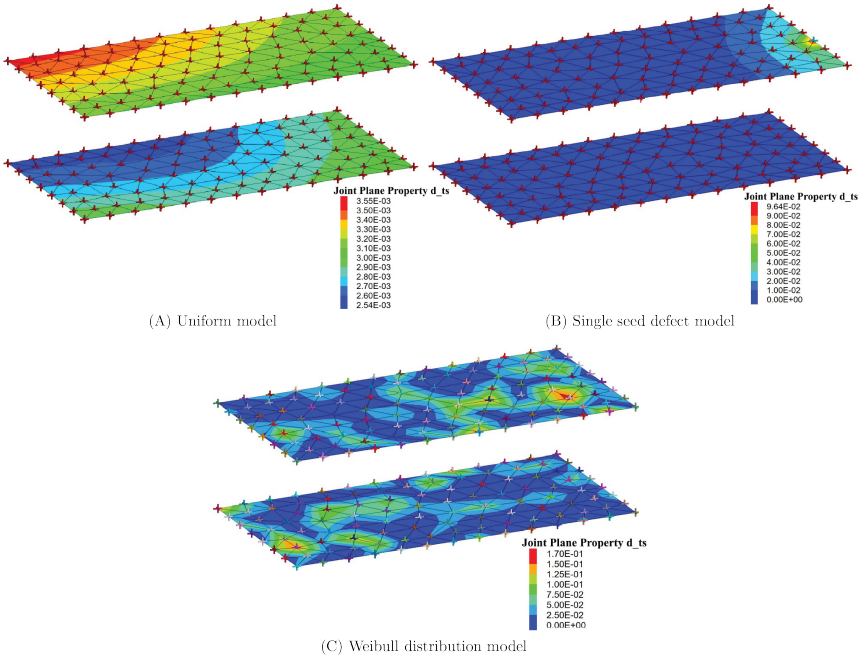
A. **Uniform**: all subcontacts on both interfaces are assigned $f_t = 1.0$ MPa.

B. **Single seed defect**: all subcontacts are assigned $f_t = 1.0$ MPa except for one subcontact at the edge of the top interface, which is reduced to $f_t = 0.8$ MPa.

C. **Weibull**: the tensile strength of each subcontact is drawn independently from a two-parameter Weibull distribution [40] with shape parameter $m_W = 5$ and scale parameter $\lambda = 1.08$ MPa. No spatial correlation is imposed between adjacent draws.

4.8.3. Variant A: Uniform tensile strength

With a uniform strength assignment, both interfaces load in exact symmetry and reach $f_t = 1.0$ MPa at effectively the same point in the loading history. At the bifurcation point, the explicit solver's floating-point round-off error (of the order of 10^{-15} MPa) triggers one subcontact to violate the tensile cut-off marginally before the others. The resulting stress redistribution propagates failure to neighbouring subcontacts over subsequent timesteps, but the propagation order is determined by floating-point noise rather than by physical stress concentration. The nucleation site shifts with changes in mesh sequence or solver precision, and the damage field at the onset of softening is effectively uniform across the plane, as shown in Figure 4.9A. At this stage, d_{ts} ranges from 2.54×10^{-3} to 3.55×10^{-3}, a spread of about 1×10^{-3}. The colour variation visible in the contour plot is an artefact of the narrow bandwidth and does not represent a meaningful spatial gradient.



(A) Uniform model (B) Single seed defect model

(C) Weibull distribution model

Figure 4.9. Combined joint damage scalar d_{ts} for all three variants at the onset of softening. The colour variation visible in the contour plot is an artefact of the narrow bandwidth and does not represent a meaningful spatial gradient.

One interface is directed into the softening branch while the other unloads elastically, reproducing the non-symmetric path described by Rots *et al.* [36]. The selection of the softening interface is governed entirely by floating-point noise, since the two joint planes are identical in their material assignment and boundary conditions. In Figure 4.10A, the top interface happens to be the one that enters softening while the bottom interface unloads elastically, but this assignment is a feature of the specific numerical realisation shown and would not necessarily be preserved under a change of mesh sequence or solver precision.

The structurally meaningful observation is that one interface softens and the other unloads, not that the softening occurs at a particular position in the assemblage. However, within the softening interface, the absence of any physically meaningful heterogeneity means that the intra-plane failure process is non-physical. There is no identifiable nucleation point, and no progressive redistribution among neighbouring subcontacts.

4.8.4. Variant B: Single seed defect

In this variant, a single subcontact at the edge of the top interface is assigned a reduced tensile strength of $f_t = 0.8\,\text{MPa}$, while all remaining subcontacts retain $f_t = 1.0\,\text{MPa}$. The 20 % strength reduction in the seeded subcontact is an arbitrary choice constrained by

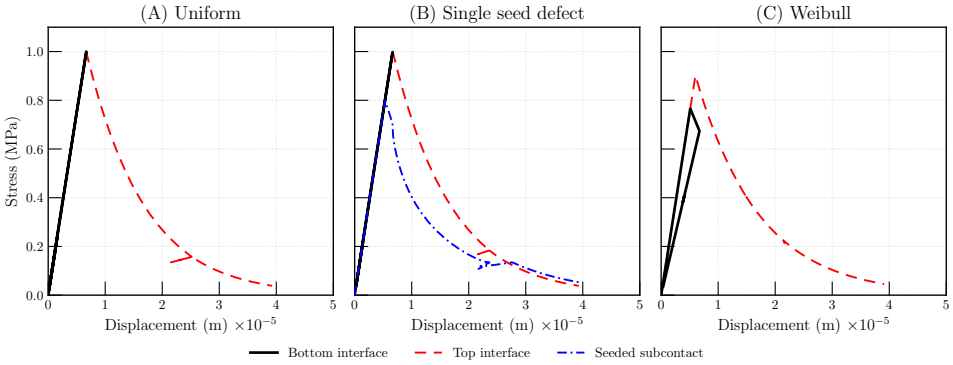


Figure 4.10. Stress–displacement histories at the bottom interface (black, solid) and the top interface (red, dashed) for each variant, as well as the seeded subcontact (blue, dashdot) for the single seed defect.

two practical requirements. The reduction is large enough to produce a clearly visible separation between the stress-displacement response of the seeded subcontact and the interface-averaged response, and small enough for the surrounding subcontacts to retain control over the global peak of the interface. The purpose of this configuration is to introduce a controlled imperfection whose effect can be isolated from the statistical complexity of a full random field, following the approach used in Rots and de Borst [35] in their analysis of bifurcation in concrete fracture.

Inter-plane localisation

The seeded subcontact reaches its reduced capacity before the rest of the interface, failing first. This unambiguously resolves the inter-plane bifurcation, as the top interface is selected as the failure plane by a physically meaningful strength deficit rather than by floating-point round-off noise. The stress–displacement histories in Figure 4.10B confirm the response, where the top interface accumulates displacement as it enters the softening regime, while the bottom interface unloads elastically and its relative displacement remains small.

Intra-plane progressive failure

The damage field at the onset of softening in Figure 4.9B shows a clear gradient in the damage scalar d_{ts} across the top interface. Damage is highest near the edge where the seed defect was placed ($d_{ts} \approx 9.6 \times 10^{-2}$) and diminishes towards the opposite side of the interface, where subcontacts remain intact ($d_{ts} = 0$). The bottom interface retains $d_{ts} = 0$.

This gradient confirms that the failure process within the top interface is *progressive* as the crack nucleates at the seeded subcontact and propagates inward as the stress redistribution from each newly failed subcontact overloads its immediate neighbour. The single seed defect is therefore sufficient to resolve not only the inter-plane bifurcation, but also the intra-plane simultaneous-failure behaviour. This outcome is possible

because the stress redistribution following the failure of the seed subcontact is spatially non-uniform: the stress concentration decays with distance from the failed contact, so that the nearest neighbours exceed $f_t = 1.0$ MPa while more distant subcontacts do not.

The stress–displacement history of the seeded subcontact itself (Figure 4.10B, blue dash-dot line) provides further detail. The seeded contact peaks at its reduced capacity of 0.8 MPa and begins softening, while the interface-averaged stress (red dashed line) continues rising towards 1.0 MPa, confirming that a single weak point among many does not govern the global peak. The softening rate of the seeded contact changes abruptly at the instant the surrounding subcontacts reach their own tensile capacity and begin to crack. At that point, the seeded subcontact is no longer the only source of compliance on the interface, and the global redistribution alters the local unloading path. As the crack propagates further and the entire interface enters the softening regime, the seeded-contact curve gradually reconverges with the interface-averaged softening curve, indicating that the local and global energy dissipation rates have stabilised.

4.8.5. Variant C: Weibull-distributed tensile strength

In the third variant, the tensile strength assigned to each subcontact is drawn independently from a two-parameter Weibull distribution [40]:

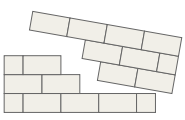
$$P(f_t \leq x) = 1 - \exp\left[-\left(\frac{x}{\lambda}\right)^{m_W}\right], \tag{4.27}$$

where $\lambda = 1.08$ MPa is the scale parameter and $m_W = 5$ is the shape parameter governing the degree of scatter. The resulting probability density function is shown in Figure 4.11. The shaded area in the lower tail of the distribution highlights the population of subcontacts with assigned strength substantially below the nominal value. These weakest subcontacts fail well before the interface-averaged stress reaches the baseline strength and serve as natural nucleation sites for cracking. The presence and spatial arrangement of this weak tail population govern where the crack initiates and how it propagates across the interface. Each subcontact receives an independent realisation, producing a spatially heterogeneous strength field across both interfaces.

The same distribution governs every subcontact regardless of its position on the interface, and no spatial correlation is imposed between adjacent draws. Two subcontacts at any separation distance are therefore equally likely to carry different strengths, and the spatial pattern of weak and strong points emerges solely from the random sampling process. The strength field is a realisation of a spatially uncorrelated, identically distributed random process across both joint planes.

Inter-plane localisation

The global peak stress is approximately 0.95 MPa, below the nominal 1.0 MPa. This reduction follows from the Weibull lower tail: the structural tensile capacity of the interface is governed not by the mean strength but by the weakest cluster of subcontacts that can initiate a through-going crack. This effect is most pronounced in uniformly loaded systems such as the present triplet test. In more complex structural problems, where the stress distribution is heterogeneous and only a fraction of the subcontacts



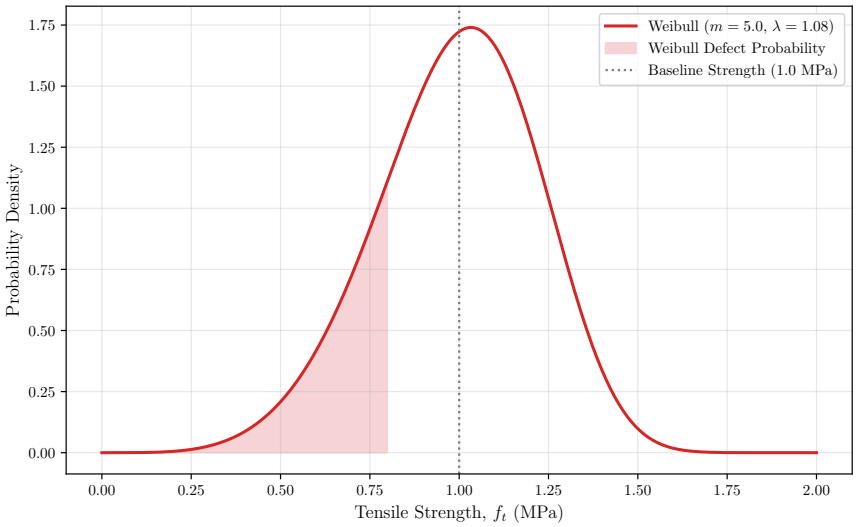


Figure 4.11. Probability density function of the Weibull distribution used in Variant C ($m_W = 5$, $\lambda = 1.08$ MPa).

carry the peak stress, the probability that a weak cluster coincides with the most-loaded region is reduced, and the apparent strength reduction is correspondingly smaller.

The interface that contains this cluster localises as the failure plane. Because the two interfaces are statistically equivalent under the independent and identically distributed strength field, the inter-plane selection is itself a random outcome. A different realisation of the random field would assign the weakest cluster to the bottom interface with equal probability and would localise failure at that interface instead. The result reported here, therefore, captures a single sample from a probabilistic ensemble, and a quantitative characterisation of this variant would require a Monte Carlo study across multiple realisations. This limitation is acknowledged among the open items in Section 4.8.6. Unlike the uniform variant, the selection is driven by a quantifiable strength deficit, and unlike the seed-defect variant, it is not prescribed but emerges from the random field.

The damage field at the onset of softening (Figure 4.9C) shows that the failing interface exhibits a patchy d_{ts} distribution (up to 1.7×10^{-1}) concentrated at the subcontacts with the lowest assigned strength, while large portions of the interface remain undamaged ($d_{ts} = 0$). This pattern is consistent with crack nucleation at the weakest cluster followed by progressive propagation.

Intra-plane progressive failure

Because no two subcontacts share the same tensile strength, their failure events are naturally staggered in the loading history. The stress–displacement curves (Figure 4.10C) confirm this sequential behaviour. The failing interface (red curve) loads to approximately 0.95 MPa and then enters a softening branch with increasing displacement, while the

passive interface (black curve) loads to approximately 0.8 MPa, then unloads (first gradually as the failing top interface reaches its maximum capacity, then sharply), recovering its stored elastic displacement. At the failing interface, the post-peak response is smoother than would be expected from a single abrupt plane failure because the sequential activation of subcontacts distributes energy dissipation over a range of displacement increments rather than concentrating it in a single step.

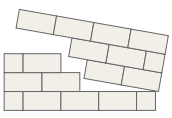
4.8.6. Summary and remarks

The triplet test presented in this section verified the behaviour of the MASON contact model under conditions known to produce bifurcations in continuum formulations. Three variants were compared. The **uniform** variant confirmed that the model correctly selects the non-symmetric equilibrium path at the inter-plane level, but the intra-plane failure process is non-physical, as all subcontacts fail in a near-simultaneous sequence governed by numerical noise. The **single seed defect** demonstrated that a deterministic imperfection on a single subcontact (here 20 %) is sufficient to produce progressive crack propagation from the seeded edge inward, resolving both the inter-plane and intra-plane problems. This outcome was obtained for a single defect magnitude, chosen within the limits discussed in Section 4.8.4; its sensitivity to the magnitude of the imperfection was not examined. The **Weibull** variant achieved the same progressive failure behaviour through a statistical mechanism, with the nucleation site emerging from the random field rather than being prescribed. The Weibull approach is therefore the preferred strategy for general structural analysis, as it does not require prior knowledge of where the crack will initiate. Several aspects of this verification exercise remain open and are noted here for completeness:

1. **Single realisation.** The Weibull variant reported above uses a single random-field realisation. The observed progressive failure character may depend on the specific spatial arrangement of weak and strong subcontacts. A Monte Carlo study across multiple realisations would be needed to confirm that the sequential failure mode is a robust outcome of Weibull heterogeneity rather than a feature of a single favourable draw.

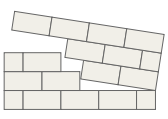
2. **Sensitivity to the shape parameter m.** The Weibull shape parameter $m = 5$ used in this test controls the degree of scatter. A low m produces wide scatter and a pronounced reduction in apparent structural strength, while a high m drives the distribution towards a deterministic limit and progressively recovers the simultaneous-failure behaviour of the uniform case. A parametric study over a representative range of m is needed to establish the sensitivity of the peak load and the failure-front morphology.

3. **Dynamic transients in the explicit solver.** The explicit time-marching scheme used in 3DEC can produce stress-wave reflections that transiently perturb the stress field. In the uniform variant, a small stress perturbation was observed on the elastically unloading interface shortly after bifurcation. Whether this perturbation belongs to the quasi-static non-symmetric equilibrium path (as described by Rots *et al.* [36]) or is a dynamic transient has not been conclusively determined.



Repeating the test with increased mechanical damping or a quasi-static solver would clarify this.

4. **Extension to mixed-mode loading.** The present test is restricted to pure Mode I (uniaxial tension). Combined normal-and-shear loading (Mode I+ Mode II) would activate the F_2 yield surface (Equation (4.2)) and the dilatancy mechanism (Section 4.4), and would test whether the sequential failure character is preserved when shear redistribution is also active. The material-level validation tests on couplets and triplets presented in Chapter 6 address this loading regime and provide partial evidence that the progressive failure behaviour carries over to mixed-mode conditions.



Bibliography of Chapter 4

[1] P. B. Lourenço and J. G. Rots. 'Multisurface Interface Model for Analysis of Masonry Structures'. In: *Journal of Engineering Mechanics* 123.7 (July 1997), pp. 660–668. ISSN: 0733-9399. DOI: 10.1061/(ASCE)0733-9399(1997)123:7(660).

[2] G. van Zijl. 'Modeling Masonry Shear-Compression: Role of Dilatancy Highlighted'. In: *Journal of Engineering Mechanics* 130.11 (Nov. 2004), pp. 1289–1296. ISSN: 0733-9399. DOI: 10.1061/(asce)0733-9399(2004)130:11(1289).

[3] K. Chaimoon. 'Numerical simulation of fracture in unreinforced masonry'. PhD thesis. Sydney: University of New South Wales, 2007. DOI: 10.26190/UNSWORKS/17488.

[4] M. Godio, I. Stefanou and K. Sab. 'Effects of the dilatancy of joints and of the size of the building blocks on the mechanical behavior of masonry structures'. In: *Meccanica* 53.7 (2018), pp. 1629–1643. DOI: 10.1007/s11012-017-0688-z.

[5] G. Andreotti, F. Graziotti and G. Magenes. 'Detailed micro-modelling of the direct shear tests of brick masonry specimens: The role of dilatancy'. In: *Engineering Structures* 168 (Aug. 2018), pp. 929–949. ISSN: 0141-0296. DOI: 10.1016/J.ENGSTRUCT.2018.05.019.

[6] P. Lourenco. 'Computational strategies for masonry structures'. PhD thesis. Delft, Netherlands: Delft University of Technology, 1996.

[7] B. Pulatsu. 'Coupled elasto-softening contact models in DEM to predict the in-plane response of masonry walls'. In: *Computational Particle Mechanics* 10 (2023), pp. 1759–1770. ISSN: 2196-4378. DOI: 10.1007/s40571-023-00586-x.

[8] Y. Nie, A. Sheikh, P. Visintin and M. Griffith. 'A robust computational strategy for failure prediction of masonry structures using an improved multi-surface damage-plastic based interface model'. In: *International Journal for Numerical Methods in Engineering* 124.11 (June 2023), pp. 2498–2528. ISSN: 10970207. DOI: 10.1002/NME.7218.

[9] Itasca Consulting Group Inc. *3DEC - Three Dimensional Distinct Element Code Ver. 9.1*. Software. Minneapolis, 2023.

[10] S. Jafari. 'Material characterisation of existing masonry: A strategy to determine strength, stiffness and toughness properties for structural analysis'. PhD thesis. Delft: Delft University of Technology, 2021, pp. 1–272. DOI: https://doi.org/10.4233/uuid:3bcbbc72-0212-44e9-ac86-2fdc54ec5987.

[11] R. Pluijm, van der. 'Out-of-plane bending of masonry : behaviour and strength'. English. Phd Thesis. Eindhoven,Netherlands: Technische Universiteit Eindhoven, 1999. ISBN: 90-6814-099-X. DOI: 10.6100/IR528212.

[12] Y. Li and B. Zeng. 'Modeling of masonry structures using a new 3D cohesive interface material model considering dilatancy softening'. In: *Engineering Structures* 277 (Feb. 2023), p. 115466. ISSN: 0141-0296. DOI: 10.1016/J.ENGSTRUCT.2022.115466.

[13] G. Giambanco, S. Rizzo and R. Spallino. 'Numerical analysis of masonry structures via interface models'. In: *Computer Methods in Applied Mechanics and Engineering* 190.49-50 (Oct. 2001), pp. 6493–6511. ISSN: 0045-7825. DOI: 10.1016/S0045-7825(01)00225-0.

[14] Y. P. Oktiovan, F. Messali, B. Pulatsu, J. V. Lemos and J. G. Rots. 'A contact-based constitutive model for the numerical analysis of masonry structures using the distinct element method'. In: *Computers & Structures* 303 (2024), p. 107499. ISSN: 0045-7949. DOI: 10.1016/J.COMPSTRUC.2024.107499.

[15] A. J. Aref and K. M. Dolatshahi. 'A three-dimensional cyclic meso-scale numerical procedure for simulation of unreinforced masonry structures'. In: *Computers and Structures* 120 (2013), pp. 9–23. ISSN: 00457949. DOI: 10.1016/j.compstruc.2013.01.012.

[16] A. M. D'Altri, F. Messali, J. Rots, G. Castellazzi and S. de Miranda. 'A damaging block-based model for the analysis of the cyclic behaviour of full-scale masonry structures'. In: *Engineering Fracture Mechanics* 209 (Mar. 2019), pp. 423–448. ISSN: 00137944. DOI: 10.1016/j.engfracmech.2018.11.046.

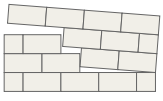
[17] S. Sharma, F. Graziotti and G. Magenes. 'Torsional shear strength of unreinforced brick masonry bed joints'. In: *Construction and Building Materials* 275 (Mar. 2021), p. 122053. ISSN: 0950-0618. DOI: 10.1016/J.CONBUILDMAT.2020.122053.

[18] R. H. Atkinson, B. P. Amadei, S. Saeb and S. Sture. 'Response of Masonry Bed Joints in Direct Shear'. In: *Journal of Structural Engineering* 115.9 (Sept. 1989), pp. 2276–2296. ISSN: 0733-9445. DOI: 10.1061/(ASCE)0733-9445(1989)115:9(2276). URL: https://ascelibrary.org/doi/abs/10.1061/%28ASCE%290733-9445%281989%29115%3A9%282276%29%20https://ascelibrary.org/doi/10.1061/%28ASCE%290733-9445%281989%29115%3A9%282276%29.

[19] G. Cera, J. G. Rots, A. T. Slobbe and F. Messali. 'Modelling interface damage in masonry structures under cyclic loading conditions with cohesive fracture and regularized friction'. In: *Computers and Structures* 322 (2026), p. 108116. ISSN: 0045-7949. DOI: 10.1016/j.compstruc.2026.108116.

[20] D. V. Oliveira and P. B. Lourenço. 'Implementation and validation of a constitutive model for the cyclic behaviour of interface elements'. In: *Computers & Structures* 82.17-19 (July 2004), pp. 1451–1461. ISSN: 0045-7949. DOI: 10.1016/J.COMPSTRUC.2004.03.041.

[21] L. Facconi, F. Minelli and F. J. Vecchio. 'Predicting Uniaxial Cyclic Compressive Behavior of Brick Masonry: New Analytical Model'. In: *Journal of Structural Engineering* 144.2 (Feb. 2018). ISSN: 0733-9445. DOI: 10.1061/(asce)st.1943-541x.0001961.



[22] M. Ispir and A. Ilki. 'Behavior of Historical Unreinforced Brick Masonry Walls under Monotonic and Cyclic Compression'. In: *Arabian Journal for Science and Engineering* 38.8 (Aug. 2013), pp. 1993–2007. ISSN: 21914281. DOI: 10.1007/S13369-013-0567-4/METRICS. URL: https://link.springer.com/article/10.1007/s13369-013-0567-4.

[23] K. Naraine and S. Sinha. 'Cyclic Behavior of Brick Masonry under Biaxial Compression'. In: *Journal of Structural Engineering* 117.5 (May 1991), pp. 1336–1355. ISSN: 0733-9445. DOI: 10.1061/(ASCE)0733-9445(1991)117:5(1336). URL: https://ascelibrary.org/doi/abs/10.1061/%28ASCE%290733-9445%281991%29117%3A5%281336%29%20https://ascelibrary.org/doi/10.1061/%28ASCE%290733-9445%281991%29117%3A5%281336%29.

[24] N. Mojsilović. 'Masonry subjected to semi-cyclic compression: Inelastic response modelling'. In: *Construction and Building Materials* 263 (Dec. 2020), p. 120147. ISSN: 0950-0618. DOI: 10.1016/J.CONBUILDMAT.2020.120147.

[25] J. Segura, L. Pelà and P. Roca. 'Monotonic and cyclic testing of clay brick and lime mortar masonry in compression'. In: *Construction and Building Materials* 193 (Dec. 2018), pp. 453–466. ISSN: 0950-0618. DOI: 10.1016/J.CONBUILDMAT.2018.10.198.

[26] Crisafulli, F.J. 'Seismic behaviour of reinforced concrete structures with masonry infills'. PhD thesis. Christchurch, New Zealand: University of Canterbury, Civil Engineering, 1997. DOI: 10.26021/1979.

[27] J. B. Mander, M. J. N. Priestley and R. Park. 'Theoretical Stress-Strain Model for Confined Concrete'. In: *Journal of Structural Engineering* 114.8 (Aug. 1988), pp. 1804–1826. ISSN: 0733-9445. DOI: 10.1061/(ASCE)0733-9445(1988)114:8(1804). URL: https://ascelibrary.org/doi/abs/10.1061/%28ASCE%290733-9445%281988%29114%3A8%281804%29%20https://ascelibrary.org/doi/10.1061/%28ASCE%290733-9445%281988%29114%3A8%281804%29.

[28] J. Eibl, E. Keintzel and V. Vratsanouu. 'Determination of earthquake duration dependent behaviour factors for unreinforced brick masonry panels by nonlinear time history calculations'. In: *Proc. 11th World Conf. on Earthquake Engineering*. Elsevier. Amsterdam, Netherlands: Proc. 11th World Conf. on Earthquake Engineering, 1996, pp. 1–8.

[29] K. Naraine and S. Sinha. 'Loading and Unloading Stress-Strain Curves for Brick Masonry'. In: *Journal of Structural Engineering* 115.10 (Oct. 1989), pp. 2631–2644. ISSN: 0733-9445. DOI: 10.1061/(ASCE)0733-9445(1989)115:10(2631). URL: https://ascelibrary.org/doi/abs/10.1061/%28ASCE%290733-9445%281989%29115%3A10%282631%29%20https://ascelibrary.org/doi/10.1061/%28ASCE%290733-9445%281989%29115%3A10%282631%29.

[30] I. Galman. 'Ściany z ceramicznej cegły pełnej cyklicznie ściskane w swej płaszczyźnie lub zginane prostopadle do płaszczyzny'. in Polish. PhD thesis. Gliwice, Poland: Silesian University of Technology, 2012.



[31] J. Lee, H. J. Bong and M. G. Lee. 'Return mapping with a line search method for integrating stress of the distortional hardening law with differential softening'. In: *Computers & Structures* 257 (Dec. 2021), p. 106652. ISSN: 0045-7949. DOI: 10.1016/J.COMPSTRUC.2021.106652.

[32] S. W. Sloan. 'Substepping schemes for the numerical integration of elastoplastic stress–strain relations'. In: *International Journal for Numerical Methods in Engineering* 24.5 (May 1987), pp. 893–911. DOI: 10.1002/NME.1620240505.

[33] Z. Xie, M. Sousamli, F. Messali and J. G. Rots. 'A sub-stepping iterative constitutive model for cyclic cracking-crushing-shearing in masonry interface elements'. In: *Computers & Structures* 257 (Dec. 2021), p. 106654. ISSN: 0045-7949. DOI: 10.1016/J.COMPSTRUC.2021.106654.

[34] J. C. Simo and T. J. R. Hughes. *Computational Inelasticity*. 1st ed. Vol. 1. Springer Science & Business Media, 1998. DOI: 10.1007/B98904.

[35] J. G. Rots and R. De Borst. 'Analysis of concrete fracture in "direct" tension'. In: *International Journal of Solids and Structures* 25.12 (1989), pp. 1381–1394. DOI: 10.1016/0020-7683(89)90107-8.

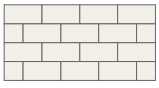
[36] J. G. Rots, S. Invernizzi, B. Belletti and M. A. N. Hendriks. 'Circumventing bifurcations in structural softening'. In: *Computational Modeling Workshop on Concrete, Masonry and Fiber-reinforced Composites*. Delft, The Netherlands, 2009, pp. 49–52.

[37] J. G. Rots and R. de Borst. 'Analysis of Mixed-Mode Fracture in Concrete'. In: *Journal of Engineering Mechanics* 113.11 (1987), pp. 1739–1758. ISSN: 0733-9399. DOI: 10.1061/(ASCE)0733-9399(1987)113:11(1739).

[38] D. A. Hordijk. 'Local approach to fatigue of concrete'. PhD thesis. Delft University of Technology, 1991.

[39] J. G. Rots and S. Invernizzi. 'Regularized sequentially linear saw-tooth softening model'. In: *International Journal for Numerical and Analytical Methods in Geomechanics* 28.7–8 (2004), pp. 821–856. DOI: 10.1002/nag.371.

[40] W. Weibull. 'A statistical distribution function of wide applicability'. In: *Journal of Applied Mechanics* 18.3 (1951), pp. 293–297.



5

Material-level Validation of the MASON Model

This chapter builds directly on Chapter 4, which introduced the MASON contact model developed within the Distinct Element Method framework. Here, the model is calibrated and validated at the material scale through a consistent set of material characterisation tests and their DEM counterparts. First, monotonic material characterisation tests are described in Section 5.2, covering shear-compression response on masonry couplets, flexural behaviour from four-point bending tests on wallettes, and compressive response from uniaxial compression. For this last case, simulations using both a simplified micro-model and a bonded-block idealisation are considered. Validation of cyclic characterisation tests is provided in Section 5.3, where the load-reversal effects and damage accumulation are evaluated using cyclic shear-compression tests on a masonry assemblage and uniaxial cyclic compression tests on wallettes, and shear-compression tests on masonry triplets. Collectively, these sections establish the necessary material-scale evidence base required before extending the model to component-scale and structural-scale studies in Chapters 6 and 8, respectively.

Contents

5.1. Introduction . . . 130
5.2. Monotonic material characterisation tests . . . 130
5.2.1. Shear-compression test on masonry couplets . . . 132
5.2.2. Four-point bending test on wallettes . . . 135
5.2.3. Uniaxial compression test: simplified micro-model . . . 138
5.2.4. Uniaxial compression test: bonded-block model . . . 140
5.3. Cyclic material characterisation tests . . . 146
5.3.1. Uniaxial cyclic compression tests on masonry wallettes . . . 148

Parts of this chapter have been adapted from the published paper in *Computers & Structures*, 10.1016/j.compstruc.2024.107499. and in *Computers & Structures*, 10.1016/j.compstruc.2025.108094"

5.3.2. Cyclic shear-compression tests on masonry assemblage 150
5.3.3. Shear-compression test on masonry triplets 151
5.4. Conclusions 154

5.1. Introduction

This chapter calibrates and validates the MASON contact model introduced in Chapter 4 at the material scale. The objective is to establish quantitative reliability before moving to component- and building-scale analyses. In a distinct element formulation, structural response emerges from local contact laws. Model reliability, therefore, depends on reproducing the joint and masonry mechanisms that control strength, deformation, and energy dissipation at the structural scale.

The validation targets three requirements. First, the model must capture initial stiffness and peak resistance under monotonic loading. Second, it must reproduce post-peak softening and the associated fracture-energy dissipation. Third, it must represent cyclic effects. These include hysteresis shape, energy dissipation, stiffness degradation, residual deformation, and damage accumulation under load reversals.

The chapter follows a structured test hierarchy. Monotonic characterisation is addressed first. Shear–compression tests on couplets constrain the normal–shear coupling and the mobilisation of frictional strength. Four-point bending tests on wallettes interrogate tensile cracking and mixed-mode separation. Uniaxial compression is then assessed in two numerical idealisations, namely the simplified micro-model and the bonded-block model. This is used to verify that the constitutive ingredients governing crushing and confinement effects remain consistent when the masonry assembly is represented with different levels of discretisation.

Cyclic characterisation is then used to evaluate aspects that monotonic response alone cannot reliably infer, namely stiffness degradation, energy dissipation, hysteresis shape, residual offsets, and the accumulation of irreversible deformation and damage under repeated loading. Cyclic direct shear tests on assemblages and uniaxial cyclic compression tests on wallettes are selected because they activate the load-reversal physics central to the MASON formulation. They also capture progressive degradation of unloading and reloading stiffness and exhibit asymmetric opening and closure responses. Across all benchmarks, model performance is assessed not only by matching peak capacities but also by reproducing deformation demand, softening rate, hysteretic energy dissipation, and key qualitative features of the observed failure modes.

5.2. Monotonic material characterisation tests

This section presents a set of material characterisation tests to demonstrate the MASON model's ability to reproduce masonry response in tension, shear, compression, and mixed-mode loading. To this end, three experimental datasets are considered. Shear–compression tests on masonry couplets are taken from Van der Pluijm [1]. Uniaxial compression tests are taken from Oliveira [2]. Finally, the campaign by Esposito *et al.* [3] is used to validate the simplified micro-model for four-point bending and uniaxial compression.



Deformable blocks are adopted in the monotonic characterisation tests to ensure that the simulated response is governed by the contact constitutive law, rather than by kinematic artefacts of rigid-body block motion. This choice is motivated by both physics and identification considerations.

First, the monotonic benchmarks are used to calibrate stiffness, peak strength, and post-peak softening. With rigid blocks, deformation can only occur through relative motion at contacts. This tends to concentrate strains into a few interfaces, which can bias the pre-peak stiffness and trigger premature localisation.

Second, several tests develop non-uniform stress states along the interface (e.g., shear–compression couplets and pre-compressed triplets). Deformable blocks allow stress redistribution within the units and more realistic pressure gradients at the joint. This improves the representation of friction mobilisation, dilatancy effects, and the transition from sticking to sliding.

Third, post-peak behaviour is sensitive to local bearing and progressive contact engagement. Deformable units can represent these effects and avoid unrealistically abrupt force drops that may arise from discrete contact opening/closure with rigid blocks. Overall, deformable blocks improve parameter identifiability. They reduce artefacts due to idealisation and make the calibration more transferable to later component- and structural-scale applications.

Finally, the main drawback of deformable blocks is computational cost: intra-unit deformability increases the number of degrees of freedom and reduces the stable explicit timestep, thereby increasing runtime. This is acceptable for the relatively small benchmarks in this chapter, but becomes prohibitive at component- and building-scale, where rigid blocks are typically adopted for efficiency when the response is governed primarily by joint nonlinearity and when explicit modelling of retrofit structural elements is not required.

Since the experimentally obtained elastic properties are valid for the actual dimensions of the mortar joints and units, homogenisation is required to relate the elastic properties of the extended unit with zero-thickness unit-mortar interfaces [4]. This can be achieved by assuming the same elastic properties for the extended and actual unit dimensions and that both configurations undergo the same elongation. The normal and shear stiffnesses are then obtained as defined in Equation (5.1) [4].

$$k_n = \frac{E_b E_m}{t_m(E_b - E_m)} \quad and \quad k_s = \frac{G_b G_m}{t_m(G_b - G_m)} \tag{5.1}$$

where E_b and E_m are the brick and mortar Young's Moduli, respectively, G_b and G_m are the brick and mortar shear moduli, respectively, and t_m is the thickness of the mortar joints. The material properties used in the material-level validation are given in Table 5.1.

The material properties were obtained directly from the corresponding material tests: the Van der Pluijm test [1] for the SC (Shear-compression) case and the experimental campaign by Esposito et al.[3] for the FPB (Four-point bending), CV (Vertical compression), and CH (Horizontal compression) cases. Specifically, for the SC test, the mortar Young's Modulus was calibrated to reproduce the experimentally observed stress-displacement response.

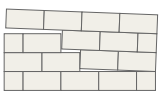


Table 5.1. Material properties used in the validation cases

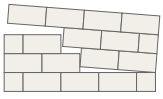
Material parameters	Unit	Value			
		SC[a]	FPB[a]	CV[a]	CH[a]
Unit properties					
E_b	GPa	16.7		4.8	
ρ	$\mathrm{kg\,m^{-3}}$	2300		1800	
$f_{s,b}$	MPa	-	3.1		3.0
$f_{t,b}$	MPa	-	1.55		1.5
ϕ_p	°	-		36.87	
Interface properties					
E_m	GPa	1.37[b]	1.2[b]		2.5
k_n	$\mathrm{GPa\,m^{-1}}$	150	160[c]		521[c]
k_s	$\mathrm{GPa\,m^{-1}}$	70	70[c]		227[c]
f_{sp}	MPa	1.0	0.15		0.11
f_t	MPa	0.3	0.11		0.1
f_c	MPa	-	-	5.93	7.55
G_f^I	$\mathrm{N\,m^{-1}}$	18.8	2.4		8.1
G_f^{II}	$\mathrm{N\,m^{-1}}$	188	24		81.03
G_c	$\mathrm{N\,m^{-1}}$	-	-	15000	31500
n[d]	[-]	-	-	68.5	85
f_{sr}	MPa	0.1	$0.1 f_{sp}$		$0.1 f_{sp}$
ϕ_p	°	45	29.64		23.27
ϕ_r	°	35	28.37		23.27

[a] SC: Shear-compression, FPB: Four-point bending, CV: Vertical compression, CH: Horizontal compression tests
[b] Calibrated such that the global numerical response matched the experimental response
[c] Derived values from eq. (5.1), with $t_m = 10$ mm and $\nu = 0.15$ for unit and mortar
[d] Hardening multiplier setting the hardening length $u_{cp} = n f_c / k_n$ (eq. (4.10))

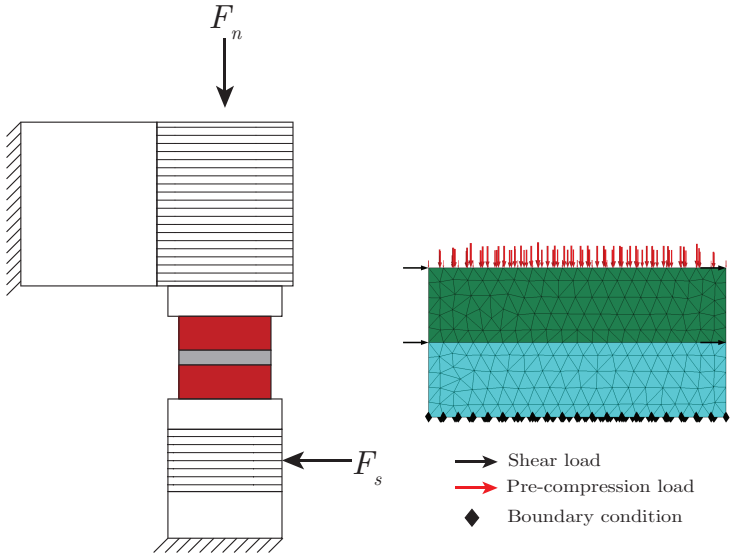
5.2.1. Shear-compression test on masonry couplets

The shear-compression tests on masonry couplets reported by Van der Pluijm [1] are employed as the first benchmark to calibrate and assess the normal–shear coupling of the MASON model. This test configuration is suitable as it isolates the response of a single bed joint subjected to combined shear and compressive loading, while limiting the complexity of geometric boundary conditions.

The shear-compression test was performed on clay brick masonry couplets with unit dimensions of $210 \times 80 \times 100$ mm ($L \times H \times W$) and the mortar joint thickness of 10 mm. In the experimental setup (Figure 5.1A), a prescribed normal force F_n is applied to the upper unit to generate a uniform pre-compression at the bed joint, while shear is induced by imposing a horizontal displacement on the upper unit. Three different



levels of pre-compression stresses were considered in the experiment: 0.1, 0.5, and 1.0 MPa. The remaining boundaries are restrained to prevent rigid-body motion, thereby localising deformation primarily at the joint interface. By varying the level of applied pre-compression, the test probes the mobilisation of frictional resistance and the transition from cohesion-dominated to friction-dominated behaviour.



(A) Experimental Setup (B) Numerical model

Figure 5.1. Shear-compression test on masonry couplets: (A) experimental setup of Van der Pluijm [1] and (B) corresponding numerical model with loading and boundary conditions

Meanwhile, the corresponding numerical model in Figure 5.1B reproduces the experimental loading and boundary conditions within the distinct element framework. Both masonry units are modelled as deformable blocks, and the bed joint is explicitly represented by the MASON constitutive formulation, which governs normal compliance, shear resistance, and post-peak degradation. Pre-compression is applied as a distributed vertical load on the top surface of the upper unit, while shear loading is imposed through controlled lateral displacement or force at the boundary of the upper unit. The nodes of the bottom block are fixed in all directions. The system is first brought to equilibrium under gravitational load, and then the pre-compression stress is applied to the top surface of the top block. Then, a lateral velocity of 2.5 mm s^{-1} is applied until the displacement reaches 3.0 mm.

Figure 5.2 compares the experimental and numerical shear stress–displacement responses of masonry couplets under three levels of applied pre-compression. The results demonstrate that the MASON model reproduces the key features of the shear–compression response across the investigated confinement range, including peak

strength mobilisation, post-peak softening, and residual shear resistance.

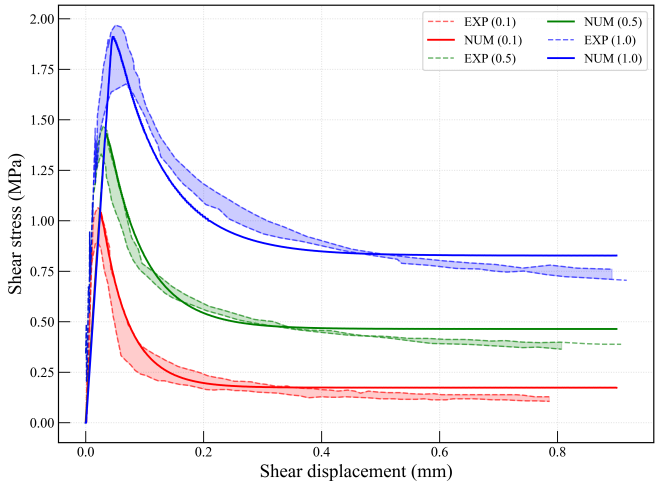


Figure 5.2. Comparison of experimental and numerical responses of the couplet test [1]

For all pre-compression levels, the numerical simulations capture the initially stiff elastic response, followed by a rapid mobilisation of shear resistance and a distinct peak. The peak shear stress increases systematically with increasing normal stress, reflecting the correct activation of frictional resistance and confirming that the normal–shear coupling embedded in the constitutive formulation is physically consistent. The predicted peak values show close agreement with the experimental envelopes, with only minor deviations at low confinement, where experimental scatter is more pronounced.

Post-peak behaviour shows a clear transition from brittle softening at low pre-compression to a more gradual degradation at higher confinement. This trend, observed experimentally, is reproduced by the numerical model and reflects the combined effects of reduced dilatancy and enhanced frictional sliding under increasing normal stress. At large shear displacements, the simulations converge towards stable residual shear stresses that scale with the applied pre-compression, in line with experimental observations.

Table 5.2 quantifies the agreement between the experimental and numerical peak and residual shear stresses for the couplet test. Peak shear stress τ_p is defined as the maximum value of the shear stress-displacement curve, while residual shear stress τ_r is evaluated as the mean shear stress over the final 10 % of the displacement range. Experimental reference values correspond to the mean of the reported lower and upper bounds.

Peak shear stress is reproduced with good accuracy for all pre-compression levels, with relative errors below 7 %, and typically below 5 %, confirming a consistent calibration of the normal-shear coupling. Residual shear stress is systematically overpredicted, particularly at low confinement, where the error approaches 43 %, but this discrepancy decreases with increasing normal stress, reducing to approximately 12 %

Table 5.2. Quantitative comparison between EXP and NUM.

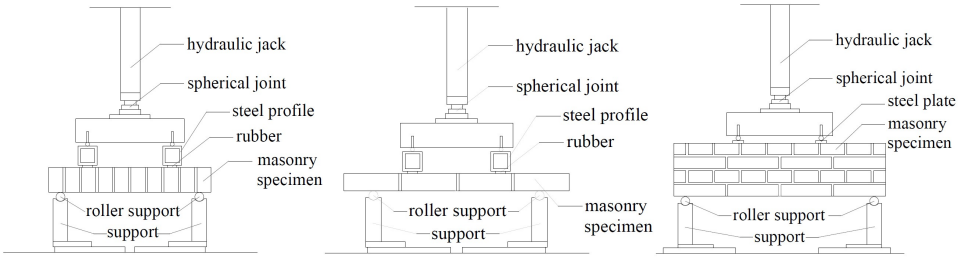
Case	τ_p^{EXP} (MPa)	τ_p^{NUM} (MPa)	$\Delta\tau_p$ (MPa)	$\Delta\tau_p$ (%)	τ_r^{EXP} (MPa)	τ_r^{NUM} (MPa)	$\Delta\tau_r$ (%)
0.1	0.976	1.040	0.064	6.53	0.121	0.173	42.98
0.5	1.400	1.430	0.030	2.14	0.385	0.464	20.66
1.0	1.823	1.910	0.087	4.78	0.741	0.828	11.66

at $\sigma_n = 1.0$ MPa. Overall, the results confirm that the MASON contact model captures confinement-dependent joint behaviour at the material level, providing a reliable basis for subsequent validation under cyclic loading and more complex stress states.

5.2.2. Four-point bending test on wallettes

Four-point bending tests are widely employed to characterise the flexural behaviour of quasi-brittle materials, including concrete and masonry, as they provide direct insight into flexural strength and fracture energy under bending [5]. The experimental benchmarks considered in this study are taken from the testing campaign reported by Esposito *et al.* [3], including four-point bending tests on masonry wallettes constructed with both calcium silicate and clay bricks. In the present validation, only the calcium silicate specimens are considered.

The four-point bending test configuration adopted in the experimental campaign is shown in Figure 5.3. Flexural properties of masonry are commonly evaluated using two standardised four-point bending configurations [6]: (i) tests with the bending moment vector parallel to the bed joints (OOP1, Figure 5.3A), and (ii) tests with the moment vector orthogonal to the bed joints (OOP2, Figure 5.3B). In addition, a non-standard four-point bending configuration with the bending moment vector orthogonal to the wall plane (IP, Figure 5.3C) is considered to enable a direct comparison between in-plane and out-of-plane vertical flexural strength of the masonry wallettes.



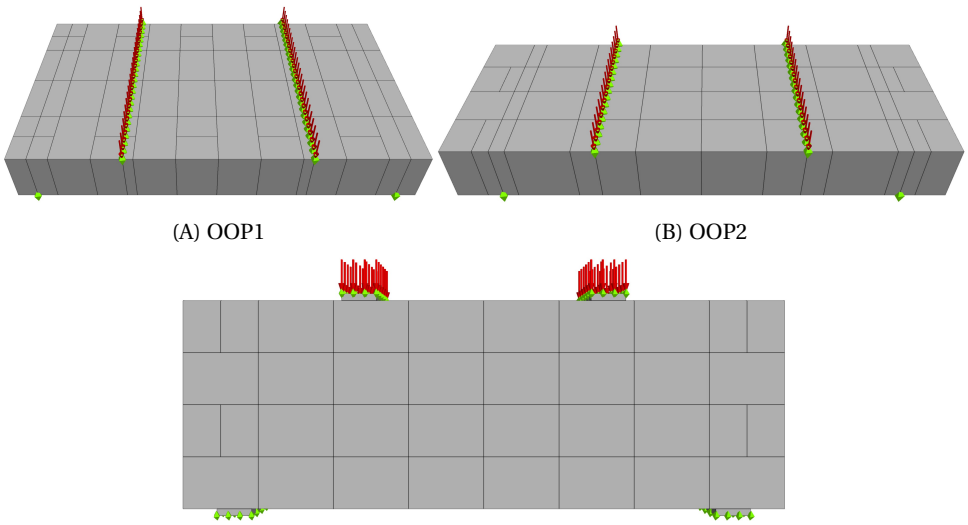
(A) OOP1 (B) OOP2 (C) IP

Figure 5.3. Experimental set-ups for the four-point bending tests [3]

The wall specimen comprises 2 × 10 courses of 210 × 70 × 100 mm^3 (L × H × W) calcium silicate bricks for the OOP1 test, while the OOP2 and IP tests comprise 4 × 4

courses of bricks. The distance between the loading points was set at 360 mm, and the distance between the roller supports was set at 720 mm.

The model configuration for the four-point bending tests is shown in Figure 5.4. The displacement-controlled load is applied as a line load for OOP1 and OOP2, as shown in Figures 5.4A and 5.4B, respectively. In order to conduct the IP test (Figure 5.4C), it is necessary to ensure that the loading plate remains orthogonal to the plane of the masonry wall. Therefore, the load is applied through a plate modelled via rigid blocks. Similarly, for the boundary conditions, the roller supports are directly applied to the nodal points in the OOP1 and OOP2 models, whereas the supports in the IP model are defined by rigid blocks representing the steel roller supports in the experiment. The linear elastic law is applied to the contact points between the masonry blocks and the loading and support plates.



(A) OOP1 (B) OOP2

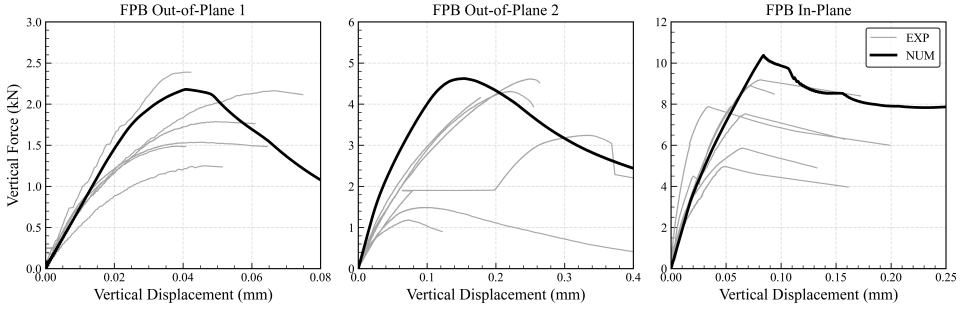
(C) IP

Figure 5.4. Model setup for the four-point bending tests in 3DEC [7]

The material properties for the four-point bending tests are presented in Table 5.1. The same properties are applied to all tests to maintain consistency. The displacement in the experiment is obtained from linear interpolation of the vertical Linear Variable Differential Transformers (LVDTs), while the displacement in the numerical simulation is obtained by averaging the nodal points in the mid-span of each model. The force in the numerical simulation is tracked by defining a subroutine in the *3DEC* software, using the FISH function, an executable programming language developed by ITASCA.

The force-displacement curves of all four-point bending tests are presented in Figure 5.5. The material characterisation tests were run six times for each configuration to enable a statistical assessment. Readers are referred to the report by Esposito et al. [3] for full details of the individual test results. The numerical model reasonably predicted the global behaviour of the experimental specimens, despite adopting a single, fixed set

of material properties across all repeats. By contrast, the experimental curves exhibit substantial scatter, indicating marked variability in strength and deformation capacity between nominally identical specimens.



(A) OOP1 (B) OOP2 (C) IP

Figure 5.5. Force-displacement comparison of the four-point bending tests

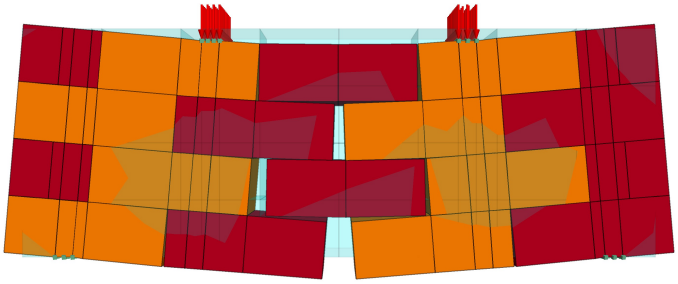
The numerical post-peak response for the IP case was also in good agreement with the experimentally observed behaviour. The stable post-peak response for the IP case was due to the interlocking mechanism of the masonry units at the onset of failure, which provided stability to the specimens before complete collapse was observed. On the other hand, the experimental post-peak response for the OOP1 and OOP2 cases cannot be compared, as the tests were conducted so that the gravity effect was not retained at the onset of damage. This caused the immediate collapse of the experimental specimens soon after the peak load was achieved, as shown by the interruption of the experimental curves in Figures 5.5A and 5.5B.

It is also clear from the force-displacement curve in Figure 5.5 that the same experimental tests conducted multiple times would produce a scattered global response. To demonstrate the effect of material variability when compared against a deterministic numerical model, a comparison is drawn between the experimentally observed crack pattern and the numerically predicted deformed shape, presented in Figure 5.6. The experimental photos in Figures 5.6A and 5.6B correspond to the upper- and lower-bound results for the in-plane bending force-displacement tests shown in Figure 5.5C, respectively. The experimental crack pattern exhibited the same crack initiation (from the bottom-most section of the mid-span) but different crack propagation for the same loading protocols and materials from the same batch, i.e., supposedly the same material properties. The crack found in the upper-bound test (Figure 5.6A) propagated to the left side of the mid-span region, while the lower-bound (Figure 5.6B) propagated to the right.

The numerical model predicted the crack initiation at the bottom-most section of the mid-span region in Figure 5.6C. However, in contrast with the experimentally observed crack pattern, the crack propagation was symmetric and localised only in the mid-span region of the model. Such different crack propagation within the same material properties and loading protocols could be attributed to the spatial variability of the material properties, as reported by several researchers [8–10]. Nevertheless, despite the



(A) TUD EXP MAT14b (B) TUD EXP MAT14a



(C) NUM FPB IP (Def. factor:100)

Figure 5.6. Comparison of experimental crack pattern and numerical deformed shape (magnified 100 times)

material variability observed in the experimental specimens, the numerical model could still predict the peak load and stiffness, as well as the post-peak behaviour in some cases, with relatively high accuracy.

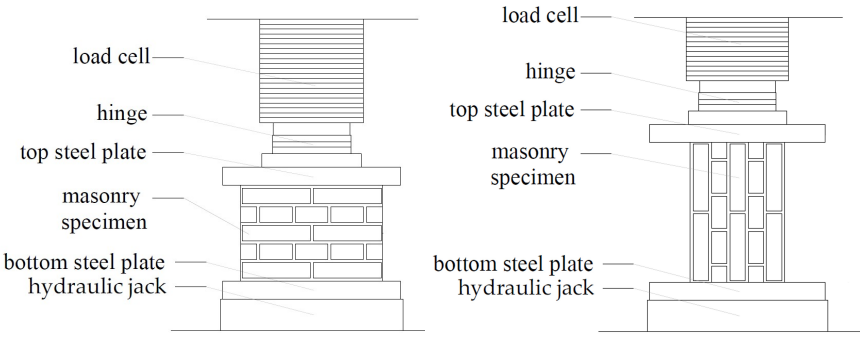
5.2.3. Uniaxial compression test: simplified micro-model

In the uniaxial compression tests, the masonry prism is modelled using a simplified micro-model in which masonry units are represented explicitly with expanded dimensions, while the mortar joints are idealised as zero-thickness interfaces governed by the MASON model. This modelling strategy balances physical fidelity and computational efficiency for monotonic compression, where the global response is governed primarily by joint closure, confinement effects, and progressive damage accumulation rather than by detailed stress gradients within the mortar.

The MASON contact model performance is validated using the same series of experiments conducted by Esposito *et al.* [3] on calcium silicate bricks. The compression test is conducted in accordance with the standard EN 1052-1:1998 [11]. The masonry prism comprises 2 × 6 courses (L × H) of brick units with a 10 mm layer of mortar joints.

The experimental setup is presented in Figure 5.7. There are two configurations

considered in the test: a "vertical" configuration (Figure 5.7A) where the load was perpendicular to the bed joints, which is in line with the European standard, and a "horizontal" configuration (Figure 5.7B) where the compression load was parallel to the bed joints. The latter was used to observe the orthotropic behaviour of the masonry prism. The numerical modelling for this test is straightforward: a displacement-controlled compressive load is applied at the bottom of the model via a rigid loading plate, with support at the top. The plate-unit interfaces use an elastic contact with $k_n = k_s = 10^{13}\,\mathrm{Pa\,m^{-1}}$ and no slip or separation criterion. The high stiffness avoids artificial compliance in the plate, and the absence of slip fully restrains the interface in shear. This choice matters because restraint at the plates confines the end courses, raising apparent strength and producing the hourglass failure pattern typical of prism tests, whereas a frictionless plate would remove this confinement and promote splitting over the full height. The fully restrained condition is adopted because it matches the experimental test, in which the loaded faces were capped with gypsum and bore directly on the steel plates [3], so the ends were level and effectively bonded. The measured prism strength therefore includes the same restraint as the model, and it is used as input in Table 5.1 without correction. The plate parameters were not calibrated, and the gypsum layer compliance is not modelled, since the pre-peak strain is taken from the LVDTs on the specimen in both the experiment and the model.



(A) Vertical configuration (B) Horizontal configuration

Figure 5.7. Compressive test setup on masonry prism [3]

The material properties considered for this test are presented in Table 5.1. The hardening multiplier n is set to 68.5 and 85 for the vertical and horizontal tests, respectively. The reason for such high values is that calcium silicate wallettes typically exhibit a higher secant elastic modulus, evaluated at 30% of the compressive strength, than clay masonry, but their response is followed by a longer hardening before the peak compressive strength is reached [3, 5].

The axial strain in the pre-peak phase was taken from the set of LVDTs attached to the specimen. Because the LVDTs detached and the specimen rotated near the peak, the post-peak strain in the experiment came from the hydraulic jack readings, and the stress-strain relationship was derived accordingly. In the numerical model, the pre-peak strain was taken from the displacement at the LVDT measurement locations, and the

post-peak strain from the displacement at the loading plate.

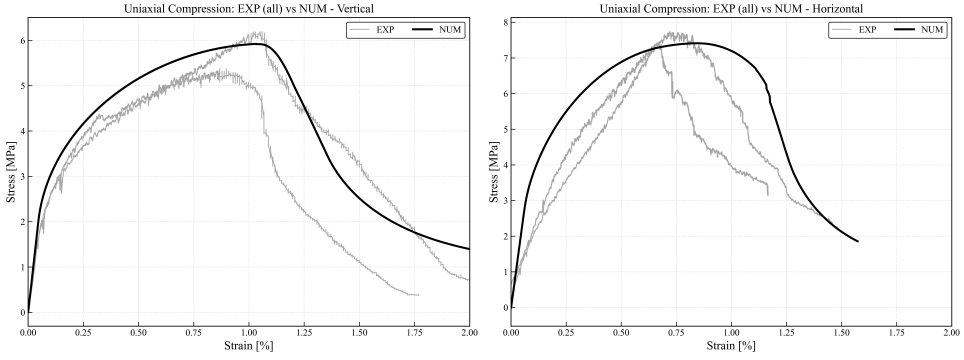
The comparison of the stress-strain diagram between the numerical model and the averaged result from the series of compression tests for each configuration is presented in Figure 5.8. The predicted peak compressive strengths agree well with the experimentally observed responses. However, the hardening and softening curves for each test configuration could still be improved by calibrating the peak ratio parameter according to the averaged experimental responses.

Within the simplified micro-model, crushing damage under uniaxial compression is represented through the evolution of the compressive contact damage scalar d_c, which governs stiffness degradation and strength reduction in the normal compressive contact response. As presented in Figure 5.9, the accumulation of compressive damage is localised primarily along the horizontal bed joints for the vertical configuration (Figure 5.9A) and the head joints for the horizontal configuration (Figure 5.9B), followed by crack splitting at the respective orthogonal joints. These regions, highlighted in red, correspond to contact planes experiencing sustained high normal stress and progressive compaction, while intact contact planes remain predominantly undamaged and are shown in blue.

Although intra-unit cracking is not modelled explicitly, the spatial distribution of the compressive damage variable provides a physically meaningful representation of experimentally observed crushing mechanisms, confirming the suitability of the simplified micro-model for capturing compression-induced degradation at the material level.

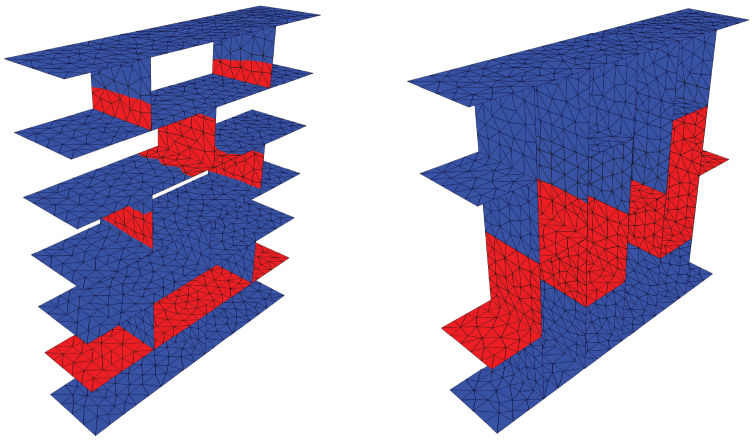
5.2.4. Uniaxial compression test: bonded-block model

In addition to the simplified micro-model, a bonded-block representation is adopted to examine the influence of internal unit discretisation on the predicted uniaxial compressive response. In this approach, the masonry assemblage is first meshed at the continuum level by discretising both brick units and mortar layers with a tetrahedral finite-element mesh. The resulting tetrahedral elements are then exported as individual



(A) Vertical configuration (B) Horizontal configuration

Figure 5.8. Stress-strain comparison of the direct compression test



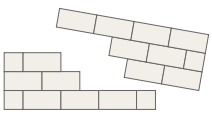
(A) Vertical (B) Horizontal

Figure 5.9. Distribution of joint damage in the simplified micro-model under uniaxial compression. Blue regions indicate intact contact planes, while red regions denote damaged contacts associated with joint closure and crushing under axial loading.

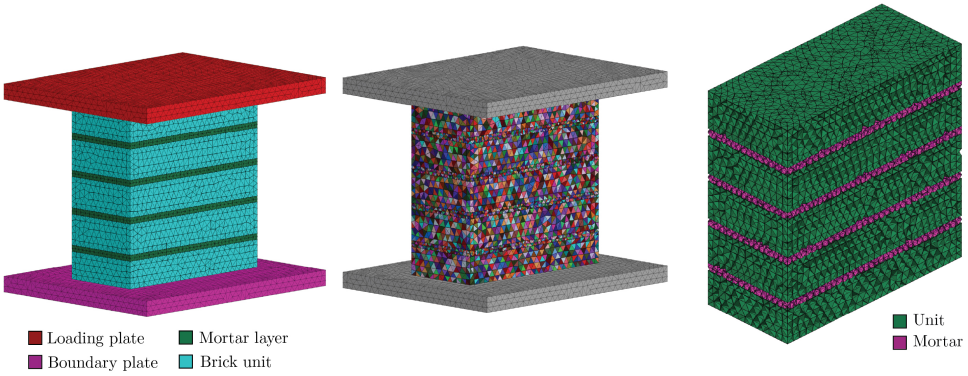
discrete blocks, whose nodal coordinates define the block geometry, thereby generating an internal tessellation of the masonry units and joints.

This bonded-block idealisation enables stress redistribution, tensile splitting, and progressive cracking to develop explicitly within the masonry units and mortar layers under compressive loading, allowing macroscopic crushing and cracking mechanisms to emerge from the degradation of internal bonds rather than being imposed phenomenologically. The joint strength and fracture parameters were obtained from the characterisation tests or from empirical correlations; the few that were calibrated are identified in the parameter tables. The normal and shear stiffnesses and the hardening factor n depend on the block idealisation: they are derived from the constituent moduli for deformable blocks and, in the cyclic analyses with rigid blocks, calibrated to the measured initial stiffness, since the joint must then also carry the deformation of the units. On this basis, the material-scale parameters provide a defensible starting point for the component-level validation in the next chapter. The increased modelling fidelity, however, comes at the expense of substantially more degrees of freedom and contact interactions, leading to significantly higher computational costs that are often prohibitive for large-scale or parametric analyses.

The experimental benchmark used for the uniaxial compression validation consists of a masonry prism test under monotonic axial loading conducted by Oliveira [12]. In this experiment, the clay bricks are cut into smaller rectangular sections with dimensions $120 \times 40 \times 40$ mm, and five courses of bricks are compressed between two rigid plates under displacement-controlled axial loading. As illustrated in Figure 5.10, this three-dimensional discretisation enables stress redistribution, cracking, and



crushing to develop throughout the specimen volume, providing a physically consistent representation of the experimental loading and failure mechanisms.



(A) Meshed compression setup (B) Discretised bonded-block model (C) Contact discretisation

Figure 5.10. Bonded-block modelling strategy for the uniaxial compression tests, illustrating the meshing of the masonry prism, the resulting bonded-block discretisation, and the corresponding contact representation between units and mortar layers.

The masonry prism is first discretised by meshing the brick units (with the original dimensions, unlike the expanded ones in the simplified micro-model), the mortar layers, and the loading and boundary plates using a constant-strain tetrahedral mesh (Figure 5.10A). The tetrahedral elements are subsequently exported into individual discrete blocks to form the bonded-block representation (Figure 5.10B), in which adjacent blocks belonging to the same material phase are connected by bonded contacts. The resulting contact discretisation (Figure 5.10C) distinguishes explicitly between unit-unit interaction and mortar layers, while the unit-mortar interfaces are governed by the MASON contact model. This modelling workflow enables the natural development of internal stress redistribution and progressive damage within the masonry assemblage under compressive loading, while remaining consistent with the experimental boundary conditions.

The bonded-block discretisation is defined by the average edge length of the tetrahedral mesh used to generate the discrete blocks. A coarser average edge length of 2.5 mm is adopted for the brick units to ensure computational efficiency while allowing internal stress redistribution and cracking to develop under compression. This results in a total of 55 404 tetrahedral blocks representing the brick units. Meanwhile, the mortar layers are discretised with a finer average edge length of 1 mm to accurately resolve the thin joint geometry and associated stress concentrations. This average edge length yields a total of 42 998 tetrahedral blocks in the mortar layers. This differentiated meshing strategy ensures that the contact behaviour at the bed joints is captured with sufficient resolution without introducing unnecessary computational cost [13].

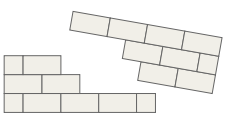
Table 5.3 summarises the material and contact parameters adopted for the numerical

simulation of the uniaxial compression test. The loading and boundary plates are assigned linear-elastic properties with high normal and shear stiffness to ensure uniform stress transfer and minimise artificial compliance at the masonry-plate interfaces. The tetrahedral blocks are modelled as deformable blocks with their elastic and strength properties selected to remain stiffer than the mortar joints, so that the global response is governed primarily by the joint behaviour.

Figure 5.11 compares the experimental and numerical responses of the masonry prism under uniaxial compression, together with the associated failure mechanisms. The stress-strain response (Figure 5.11D) shows that the bonded-block model with the MASON contact formulation reproduces both the compressive strength and the post-peak softening behaviour within the experimental envelope. The experimental failure pattern (Figure 5.11A, then simplified into Figure 5.11B) is characterised by vertical splitting and hourglass-shaped cracking, typical of compressive failure in quasi-brittle masonry. This mechanism is consistently reproduced by the numerical model, as evidenced by the corresponding bonded-block damage distribution at the end of analysis in Figure 5.11C. The damage distribution is visualised through the combined

Table 5.3. Material and contact properties adopted for the uniaxial compression simulations.

Component	Parameter	Symbol	Value	Unit
Loading plates	Density	ρ_{st}	7780	$\mathrm{kg\,m^{-3}}$
	Young's modulus	E_{st}	200	GPa
	Normal stiffness	k_n^{st}	1.0×10^{13}	$\mathrm{Pa\,m^{-1}}$
	Shear stiffness	k_s^{st}	1.0×10^{13}	$\mathrm{Pa\,m^{-1}}$
Masonry units	Density	ρ_b	2000	$\mathrm{kg\,m^{-3}}$
	Young's modulus	E_b	100	GPa
	Poisson ratio	ν_b	0.20	–
	Tensile strength	$f_{t,b}$	2.5	MPa
	Cohesion	c_b	4.0	MPa
	Normal stiffness	k_n^b	1.0×10^{13}	$\mathrm{Pa\,m^{-1}}$
	Shear stiffness	k_s^b	4.17×10^{12}	$\mathrm{Pa\,m^{-1}}$
Bed-joint contacts	Density	ρ_m	2000	$\mathrm{kg\,m^{-3}}$
	Young's modulus	E_m	20.95	GPa
	Normal stiffness	k_n	6.96×10^{11}	$\mathrm{Pa\,m^{-1}}$
	Shear stiffness	k_s	3.48×10^{11}	$\mathrm{Pa\,m^{-1}}$
	Tensile strength	f_t	0.15	MPa
	Cohesion	c	0.30	MPa
	Residual cohesion	c_r	0.03	MPa
	Residual tensile strength	$f_{t,r}$	0.0	MPa
	Friction angle	ϕ	20	°
	Residual friction angle	ϕ_r	20	°
	Compressive strength	f_c	6.55	MPa
	Fracture energy (compression)	G_c	31.5	$\mathrm{kN\,m^{-1}}$



tensile-shear damage scalar d_{ts}. Damage initially develops in a distributed manner along the bed joints, followed by localisation and the formation of dominant vertical cracking paths that govern the post-peak response.

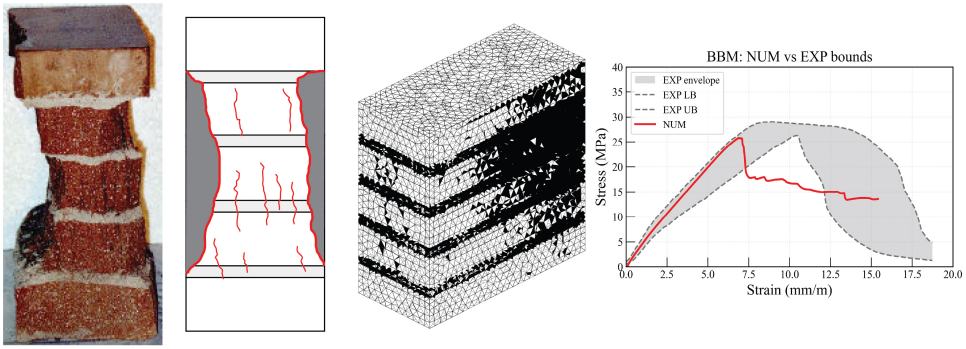


Figure 5.11. Uniaxial compression of masonry prisms: (A) Experimental specimen after failure [12]; (B) Simplified representation of the experimentally observed failure pattern, highlighting vertical splitting and crushing localisation; (C) Numerical failure mechanism at the end of analysis; (D) The comparison between numerical stress–strain response and experimental bounds.

Figure 5.12 shows the progression of subcontact damage in the bonded-block model represented through the combined tensile-shear damage scalar, d_{ts}. Four distinct phases are identified: dispersed damage at the mortar joints close to 95 % of the peak strength, the onset of failure at the peak compressive stress, the drop of more than 80 % of the peak strength corresponding to the formation of a primary crack, and finally the development of secondary crack formation pre-failure. These points are chosen to highlight the transition from distributed damage to localisation and eventual global failure.

The corresponding damage patterns, shown through perspective views and longitudinal and transverse cuts extracted at the specimen's centroid, provide insight into the internal evolution of the failure mechanisms. At the pre-peak level in Point 1, damage remains diffuse and is primarily confined to the bed joints, reflecting progressive joint closure and compaction. At the peak stress in Point 2, damage begins to localise along preferential load paths, indicating the onset of vertical splitting.

During the post-peak softening phase in Point 3, the longitudinal and transverse cuts reveal the rapid development of continuous cracking and crushing bands throughout the specimen core, which are not apparent from the external surface alone. Notably, the drop of more than 80 percent of the peak stress occurs almost instantaneously once primary vertical splitting has formed at multiple locations within the specimen. This indicates a transition from distributed damage to a localisation-dominated failure regime.

In the pre-failure stage in Point 4, defined here as the onset of unstable degradation immediately preceding the final residual branch, the previously formed damage bands link up into dominant vertical fracture zones that span a large portion of the specimen height. At this stage, the longitudinal and transverse cuts indicate the development

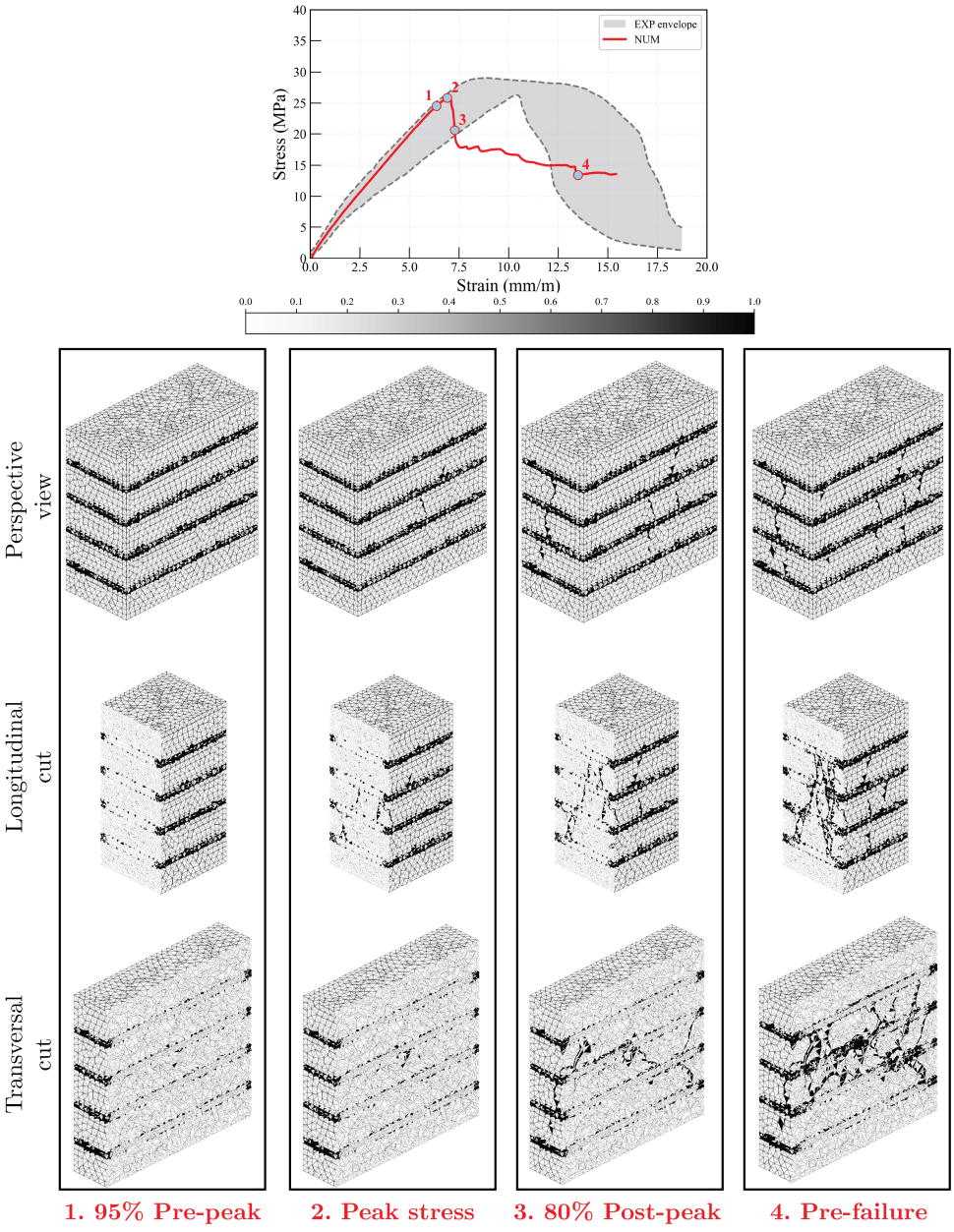


Figure 5.12. Progressive evolution of combined damage scalar d_{ts} in the bonded-block uniaxial compression simulation.

of secondary cracking that branches from the principal splitting planes, progressively

degrading load transfer and confinement within the masonry core. The activation of these secondary cracking mechanisms coincides with the pronounced stress reduction observed at a strain of approximately 13.5 mm m^{-1}, marking the transition towards unstable failure.

Overall, the MASON contact model reproduces the experimental stress-strain response of masonry prisms under uniaxial compression with good accuracy, capturing both the peak strength and the characteristic post-peak softening. The associated damage evolution provides a consistent mechanical interpretation of this response, linking stiffness degradation and strength loss to the transition from distributed joint compaction to primary vertical splitting, and subsequently to secondary cracking. Note that the bonded-block simulation was computationally demanding. Using an AWS remote instance of *hpc6id.32xlarge* with 64 3.5 GHz cores and 1024 GiB of memory, the complete analysis required approximately two weeks of wall-clock time. This highlights both the fidelity of the modelling approach and the substantial computational cost associated with high-resolution three-dimensional bonded-block discretisations.

5.3. Cyclic material characterisation tests

While monotonic characterisation tests establish the elastic response, peak strength, and post-peak softening of masonry joints, they are insufficient to fully assess the behaviour of masonry under cyclic loading. Cyclic loading tests activate additional mechanisms, including stiffness degradation, hysteretic energy dissipation, residual deformation, and progressive damage accumulation, which govern the response of masonry under seismic and repeated loading conditions.

In contrast to the analyses conducted for validation against monotonic tests, the cyclic analyses are conducted using a rigid-block formulation. This modelling choice reflects that interface-level phenomena, such as frictional sliding, opening/closure, and damage evolution, dominate the cyclic response. The elastic deformation within the masonry units plays a secondary role, allowing a more efficient and numerically stable evaluation of the load-reversal effects.

To this end, the cyclic direct shear test on masonry assemblage by Atkinson *et al.* [14], the masonry triplet test by Andreotti *et al.* [15], and the cyclic uniaxial compression test on masonry prism by Esposito *et al.* [3] are selected as the validation cases. The tests by Esposito *et al.* [3] and Andreotti *et al.* [15] were conducted on calcium silicate masonry samples, while Atkinson *et al.* [14] conducted the test on clay brick samples. Table 5.4 summarises the material properties used as input parameters in the selected material characterisation tests.

The parameters include normal and shear stiffnesses, strength characteristics in tension, shear, and compression regimes, the corresponding fracture energies, and the dilatancy-related values governing the mechanical response of the masonry components. Due to the rigid-block formulation, where the deformability of the units is neglected and their Young's modulus is not explicitly defined, the initial normal k_n and shear k_s stiffnesses must be calibrated to the initial stiffness of the experiments. Therefore, the initial stiffnesses are first defined through the homogenised equation by Lourenço [4] (Equation (5.1)), which are then calibrated to match the experimental values. For the

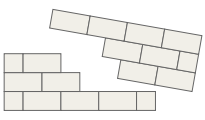
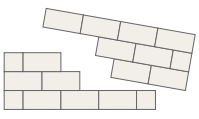


Table 5.4. Material properties of the material characterisation tests and the input parameters of their numerical models

Material parameters	Symbol	Unit	Cyclic compression[1]		Cyclic shear-I[2]		Cyclic shear-II[3]
			Vertical	Horizontal	Old	New	
Experimental parameters							
Density	ρ	$kg\,m^{-3}$	1800	1800	1800	2300	1800
Peak cohesion	f_{sp}	MPa	0.22	0.22	0.20	0.16	0.11
Residual cohesion	f_{sr}	MPa	0.022	0.022	0.02	0.016	0.011
Friction at constant volume	ϕ_{cv}	°	25.0	25.0	36.0	34.79	30.0
Initial dilatancy angle	ψ_0	°	–	–	0.0	0.0	20.0
Compressive strength	f_c	MPa	6.5	7.45	–	–	–
Compressive fracture energy	G_c	$N\,mm^{-1}$	15.0	31.5	–	–	–
Numerical model parameters							
Normal stiffness	k_n	$N\,mm^{-3}$	52.1	52.1	45.8	45.8	32.0
Shear stiffness	k_s	$N\,mm^{-3}$	22.7	22.7	19.7	19.7	32.0
Tensile strength[4]	f_t	MPa	0.11	0.11	0.10	0.10	0.11
Hardening factor[4]	n	–	7.5	5.0	3.0	3.0	3.0
Zero dilation displacement	$u^s_{\max}$	mm	–	–	–	–	3.0
Dilatancy softening gradient	δ	–	–	–	–	–	2.0
Mode-I fracture energy	G^I_f	$N\,mm^{-1}$	0.0086	0.0086	0.012	0.094	0.0086
Mode-II fracture energy	G^{II}_f	$N\,mm^{-1}$	0.086	0.086	0.12	0.94	0.086
Cap parameters	C_n, C_{nn}, C_{ss}	–	0.0, 1.0, 12.0				

[1] Cyclic uniaxial compression test by Esposito et al. [3].
[2] Cyclic shear-compression test by Atkinson et al. [14].
[3] Shear-compression triplet test by Andreotti et al. [15].
[4] Based on the recommendations by Jafari et al. [5].
–: not applicable to this test, or not a parameter of its model.



calcium silicate masonry of Esposito et al. [3], this gives $k_n = 52.1\,\text{GPa/m}$, one tenth of the value derived from Equation (5.1) for the deformable-block models of Table 5.1, because the joint of a rigid-block model must also carry the elastic deformation of the units. The cohesion is taken as $f_{sp} = 2.0 f_t$ from an empirical correlation [5], whereas in the monotonic analyses of Table 5.1 it was calibrated to the measured response. The friction angle has no effect on the uniaxial compression response and is listed only for completeness. The hardening factor n is reduced from 68.5 and 85 to 7.5 and 5.0 for the same reason, since the hardening length $u_{cp} = n f_c / k_n$ scales with the inverse of k_n.

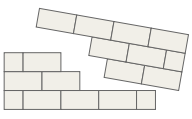
The peak cohesion f_{sp} and the friction angle at constant volume ϕ_{cv} were obtained from direct-shear and couplet tests using the relation $\tau = f_{sp} + \sigma_n \tan\phi_{cv}$ for the shear cases. The residual cohesion f_{sr} was read from the large-slip plateau. The initial dilatancy angle ψ_0 is taken from the peak dilation observed in the triplet test by Andreotti et al. [15]. The other parameters related to dilatancy softening ($u_{s,\max}$ and δ) are refined based on experimental findings. The tensile strength f_t was taken from the companion splitting and bond tests and was then recalibrated to align the simulated peak load with the average measured response of the test cases. The recalibration uses the empirical relations summarised by Jafari et al. [5]. The mode-I G_f^I and mode-II G_f^{II} fracture energies are taken from the empirical equation set by CEB-FIP Model Code 90 [16]. The compressive strength f_t and the fracture energy G_c for the cyclic compression tests were taken from the experimentally reported values in Esposito et al. [3] The hardening factor n for compressive strength was defined according to the recommendations of Jafari et al. [5]. This tailored parameter set provides a robust foundation for accurately simulating and validating the mechanical behaviour of masonry under cyclic loading.

Figure 5.13 presents the geometries and the loading configurations of the selected material characterisation tests, with the extended dimensions of the brick units. The extended dimensions account for the thickness of the mortar layers while maintaining the actual height and width of the experimental specimens. The vertical and horizontal compression tests (Figure 5.13A and Figure 5.13B, respectively) also included the locations of the LVDTs used to record the axial strain. The axial strain in the numerical model is calculated from the relative displacement between the two vertical LVDTs on the front and back sides of the specimen.

5.3.1. Uniaxial cyclic compression tests on masonry wallettes

Similar to the monotonic tests considered in Section 5.2.3, there are two configurations considered in the uniaxial compression test: a vertical configuration, where the compression load is orthogonal to the bed joints, and a horizontal configuration, where the compression load is orthogonal to the head joints. Following the experimental protocol, a displacement-controlled load is applied at the base of the model using a rigid plate, with stresses recorded at the top of the prisms. [3] Due to the brittle post-peak response, the experimental cyclic unloading/reloading scheme was performed only during the pre-peak phase. The unloading/reloading scheme was conducted three times at the 25 %, 50 %, and 75 % of the peak compressive stress.

The comparison of the uniaxial cyclic compression test on the vertical and horizontal prisms is presented in Figure 5.14. Two results were reported because the cyclic loading experiment was conducted twice to highlight variability in the mechanical response.



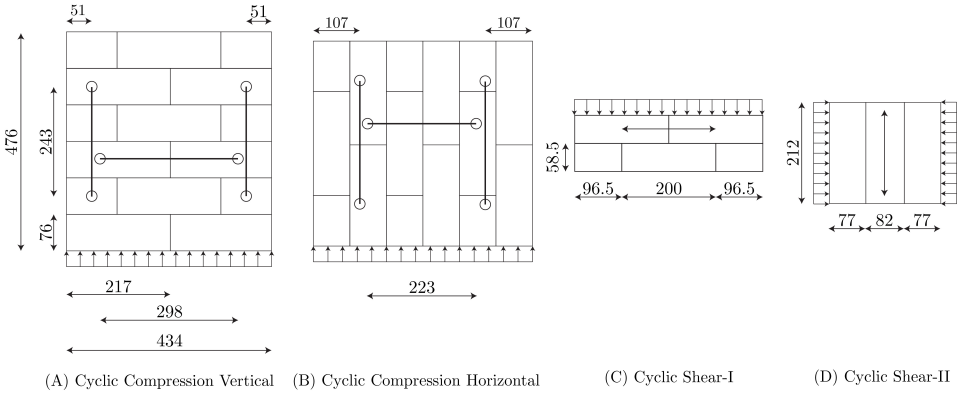


Figure 5.13. Illustration of the validated material characterisation tests with extended brick dimensions

Despite being cast from the same batch, the specimens exhibited different responses, indicating non-negligible experimental variability or inherent material heterogeneity. However, the model was tuned to one specific specimen, TUD-MAT-11G for the vertical case, and TUD-MAT-11K for the horizontal case.

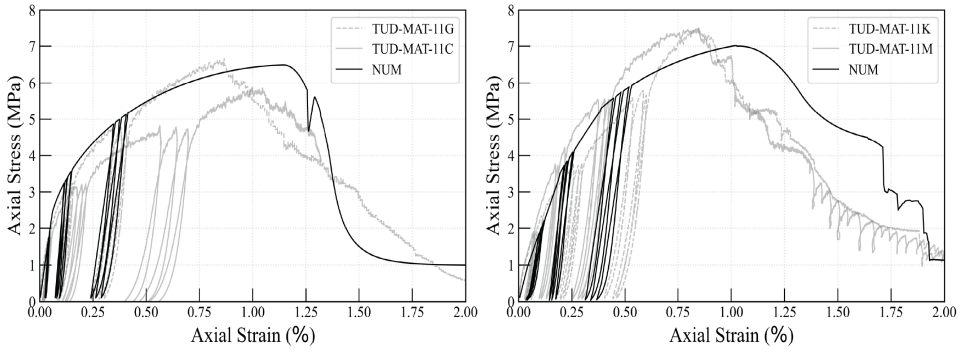


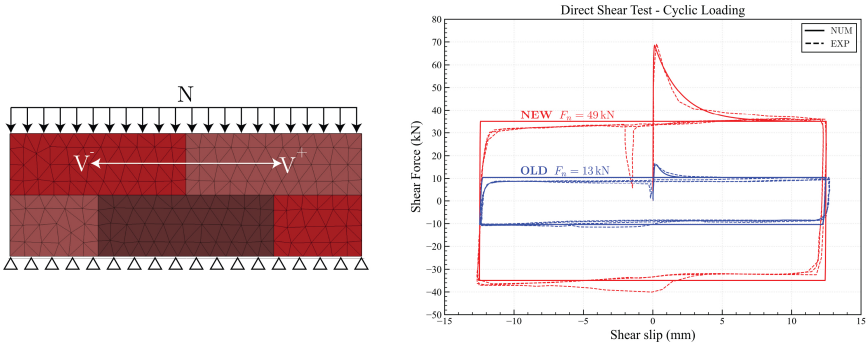
Figure 5.14. Uniaxial compression test results comparison

By employing the nonlinear unloading scheme in Equation (4.19), the model effectively captured the energy dissipation observed during unloading and reloading in both vertical and horizontal prism tests. It reproduced key hysteretic behaviours such as stiffness degradation and residual strains, demonstrating its ability to simulate the cyclic compressive response of masonry-like materials with directional consistency. Furthermore, the behaviour in which the reloading strain exceeded the unloading onset was also evident in both vertical and horizontal cases, consistently simulated by the proposed joint constitutive model.

5.3.2. Cyclic shear-compression tests on masonry assemblage

Atkinson *et al.* [14] performed cyclic direct-shear tests on masonry assemblages built with reclaimed late-19th-century clay bricks and a lime-rich mortar (cement-to-water ratio of 0.51), with bed joint thickness of 7 and 13 mm, and modern clay bricks with a richer mortar (cement-to-water ratio of 0.83) and an approximately 7 mm joint. The old-brick series was tested under 13 kN of pre-compression, and the modern-brick series under 49 kN of pre-compression. In each test, the loading plate was sheared up to 12 mm, unloaded, and then reloaded in the opposite direction.

Accordingly, the simulation is represented with two interface parameter sets (OLD and NEW) in Table 5.4. The OLD set uses lower interface stiffness and cohesive capacity to reflect the weaker lime-rich mortar, aged units, and (for part of the campaign) the thicker joint reported in the experimental programme, whereas the NEW set corresponds to the modern and stronger materials. The applied normal force is prescribed according to the test (13 kN for OLD, 49 kN for NEW), so that differences in response reflect both material quality and confinement. The DEM model and the boundary conditions are shown in Figure 5.15A, where the bottom units are fixed, and pre-compression is applied directly to the top units, along with the cyclic shear load.



(A) DEM model

(B) Shear force vs displacement

Figure 5.15. The DEM model with the boundary conditions and the comparison to experimental results

The cyclic shear responses in Figure 5.15B are characterised by predominantly frictional hysteresis loops with a near-rectangular shape, indicating that, once sliding is mobilised, the response is governed by a stable residual shear resistance with limited stiffness recovery upon load reversal. This is particularly evident for the old assemblage at $F_n = 13$kN, where both experiment and simulation rapidly transition from an initial elastic branch to a plateau response around the residual level. The MASON contact model reproduces the early mobilisation of shear resistance and the subsequent steady sliding regime, while maintaining comparable loop width and residual offset, which together reflect the energy dissipated per cycle and the accumulation of irreversible slip.

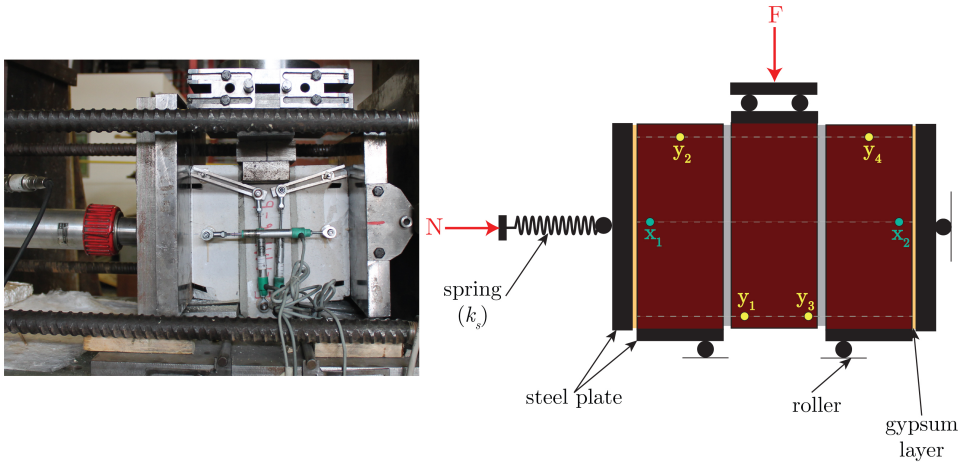
For the higher confinement level ($F_n = 49$kN), the experiment shows a higher shear capacity with a transient peak near load reversal, followed by softening towards a lower

residual plateau. This response is consistent with progressive loss of joint interlock and strength under repeated sliding, where cyclic abrasion at the interface degrades the load-carrying mechanisms and drives the response towards a friction-dominated residual level. Overall, the numerically predicted responses closely reproduce the experimental behaviour, accurately capturing key features such as the initial stiffness, peak shear strength, post-peak mode-II softening, the elastic unloading/reloading branch typical of shear, and the residual strength plateau under both normal stress conditions.

5.3.3. Shear-compression test on masonry triplets

The dilatant behaviour of masonry joints subjected to combined shear and compressive loads was experimentally investigated by Andreotti et al. [15]. The test setup adopted in their study is illustrated in Figure 5.16A. The test was conducted on calcium silicate brick specimens with dimensions 212 × 102 × 72 mm and mortar layers with thickness 10 mm. The pre-compression force actuator was controlled through a spring with a stiffness of 1070 N mm^{-1} to regulate and maintain the desired pre-compression level (N). The shear force is applied through a vertical jack, and the rotation of the whole triplet is not restricted. The triplet was subjected to three time windows, defined by the sequential application of the shear load, with increasing pre-compression level at each window. In each window, the shear force is characterised by loading and complete unloading to a zero shear force condition. Time window zero refers to the shear test of a pristine triplet, while the subsequent time windows are done to find the residual shear strength corresponding to the constant volume phase. Readers are referred to Andreotti et al. [15] for further details pertaining to the experimental procedure.

The numerical model follows the configuration and procedure of the experimental tests as closely as possible, illustrated in Figure 5.16B. In the experiments, the axial load



(A) Experimental setup

(B) Modelling sketch

Figure 5.16. Experimental setup [15] and the boundary conditions of the DEM model

was held within three time windows by a spring-regulated actuator (force-controlled target with finite actuator stiffness), not by an unconstrained constant-force device. This keeps the prescribed pre-compression while allowing the normal force to react to specimen dilation. In the model, this is reproduced by a simple servo/spring control, where, given a target displacement set at each time window, the model calculates the relative displacement between the triplet's volumetric expansion and the target displacement and transfers that as an applied force to the steel plate, allowing the normal pre-compression force to be adjusted according to the volumetric expansion. This is formally expressed as:

$$F(t) = K_{act}\left[u_{cmd}(t) - u_{spec}(t)\right] \tag{5.2}$$

where K_{act} is the actuator stiffness, set at $1070\,\mathrm{N\,mm^{-1}}$, $u_{cmd}(t)$ is the commanded actuator displacement (target) and $u_{spec}(t)$ is the measured specimen-side displacement at the actuator interface.

Leveraging the conditional stability of the explicit solver, the simulation of the triplet test is done sequentially from one time window to another using the same material properties and boundary conditions from the previous window, consistent with the experimental procedure. The shear displacement ($u_{s,rel}$) and the volumetric expansion ($u_{n,rel}$) are calculated according to Equations (5.3) and (5.4), respectively, averaged on the front and back side of the specimen [15].

$$u_{s,rel} = \frac{(y_1 - y_2) + (y_3 - y_4)}{2} \tag{5.3}$$

$$u_{n,rel} = x_2 - x_1 \tag{5.4}$$

The responses from the MASON model (shown in solid lines) are compared to the experimental data (dashed lines) of the triplet test in Figure 5.17. In time window 0 (displayed in blue), the numerical model exhibited the exponential softening response where the shear stress decayed to a residual value of 0.2 MPa (Figure 5.17A), while the normal stress initially increased due to volumetric expansion but stayed constant at the same level as the experimental test (Figure 5.17B).

The gradual decline of the experimental shear stress is explained by the sequential failure of the mortar joints: cracking initiated in the left-hand joint of Figure 5.16A and subsequently propagated to the right-hand joint, progressively diminishing the overall shear-carrying capacity. By contrast, the numerical model is nominally symmetric and assigns the identical properties to both joints, with no explicit imperfections. Damage therefore develops more evenly, and the cyclic response remains near-symmetric.

The volumetric expansion (Figure 5.17C) was also in good agreement with the experimental observation, where the exponential volumetric expansion due to the normal displacement correction in Equation (4.15) is evident in the numerical response. From the comparison of the dilatancy coefficient in Figure 5.17D, the experimental results showed that the coefficient dropped to zero beyond the shear displacement of 3.0 mm, which was consistently modelled by the exponential decay function in Equation (4.14).

At time window 1 (displayed in red), the shear stress, normal stress and dilatancy coefficient were in good agreement with the experimental data. The numerical volumetric expansion, however, was larger and more variable than the measured one. It arose from

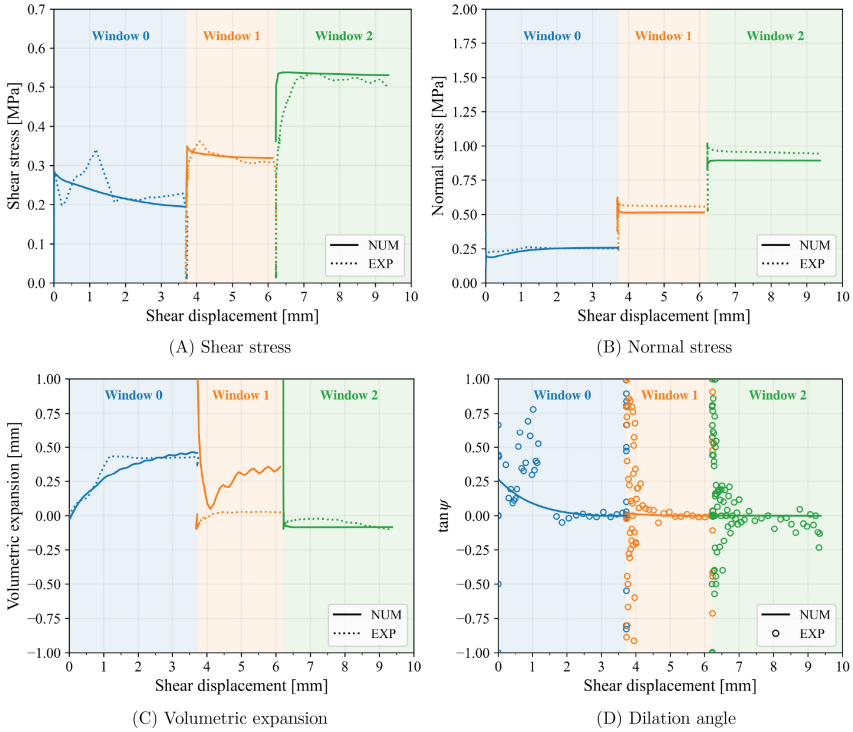


Figure 5.17. Validation of the modelling strategy to a triplet test on multiple time windows [15]

the specimen's ability to rotate freely: when the pre-compression is increased abruptly, this unconstrained rotation interacts with the sudden confinement and triggers a rapid dilative response. At time window 2 (displayed in orange), the normal stress was elevated to 0.9 MPa, resulting in the shear stress of approximately 0.55 MPa. It is important to note that, at this point, the cohesive contribution is nearly zero because the interface has accumulated sufficient damage and slip in the preceding cycles to exhaust cohesion, and the shear resistance is governed primarily by friction under the increased normal compression. Thereafter, the joint again evolves towards a stable, slightly dilatant state, with the dilatancy coefficient fluctuating about zero as the asperities are fully smoothed.

Overall, the MASON model reproduced the main features of the dilatancy behaviour. Across all windows, the numerical solution closely matches the measured trends, capturing stress jumps, the progressive reduction in dilatancy, and the ultimate approach to steady-state shear and volumetric responses, lending confidence to the implemented constitutive formulation. The benchmarks were chosen to span the representative failure modes (cracking, shearing and crushing) as well as mixed-mode combinations and transitions between them, so that the assessment probed the model across the full spectrum of observed responses.

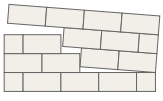
More broadly, the MASON contact model is inherently multi-scale. It supports a

mechanistic interpretation of local joint phenomena, such as unit splitting, mixed-mode damage evolution, and dilatancy, while remaining computationally viable for component- and building-scale simulations in which these mechanisms govern global stiffness, strength, and energy dissipation. This provides a consistent pathway from material characterisation and calibration to structural performance assessment within a single constitutive framework.

5.4. Conclusions

This chapter validated the MASON model at the material scale against a broad set of monotonic and cyclic masonry characterisation tests, using the block-based modelling strategies consistent with the intended DEM application. Across shear–compression, bending, and uniaxial compression benchmarks, the model reproduced key response quantities targeted by the design criteria: initial stiffness, peak resistance, post-peak softening governed by fracture energy, and the transition between tensile cracking, frictional sliding, and compressive crushing under mixed-mode loading. Beyond global force–displacement agreement, the simulations produced stable, mechanically consistent localisation patterns that support the interpretation of experimental failure mechanisms.

Under cyclic loading, the model captured the dominant hysteretic features observed experimentally, including progressive stiffness degradation and the evolution of energy dissipation under repeated reversals Overall, the results show that a parameter set identified from material tests can be transferred across loading configurations and idealisations, used to investigate local material behaviours and provide a defensible basis for the component-level validation presented in the next chapter.



Bibliography of Chapter 5

[1] R. Pluijm, van der. 'Out-of-plane bending of masonry : behaviour and strength'. English. Phd Thesis. Eindhoven,Netherlands: Technische Universiteit Eindhoven, 1999. ISBN: 90-6814-099-X. DOI: 10.6100/IR528212.

[2] D. V. Oliveira, P. B. Lourenço and P. Roca. 'Cyclic behaviour of stone and brick masonry under uniaxial compressive loading'. In: *Materials and Structures* 39.2 (2006), pp. 247–257. DOI: 10.1617/s11527-005-9050-3.

[3] R. Esposito, F. Messali and J. G. Rots. *Tests for the Characterization of Replicated Masonry and Wall Ties*. 2016. URL: http://resolver.tudelft.nl/uuid:a0923cf9-0ccd-48a1-9ce1-082aa66e97af.

[4] P. Lourenco. 'Computational strategies for masonry structures'. PhD thesis. Delft, Netherlands: Delft University of Technology, 1996.

[5] S. Jafari, J. G. Rots and R. Esposito. 'A correlation study to support material characterisation of typical Dutch masonry structures'. In: *Journal of Building Engineering* 45 (Jan. 2022). ISSN: 23527102. DOI: 10.1016/j.jobe.2021.103450.

[6] EN 1052-1. *Method of test masonry – Part 1: Determination of compressive strength*. Tech. rep. Nederlands Normalisatie-instituut, 1999.

[7] Itasca Consulting Group Inc. *3DEC - Three Dimensional Distinct Element Code Ver. 9.1*. Minneapolis, 2024.

[8] S. Gonen, B. Pulatsu, E. Erdogmus, P. B. Lourenço and S. Soyoz. 'Effects of spatial variability and correlation in stochastic discontinuum analysis of unreinforced masonry walls'. In: *Construction and Building Materials* 337 (June 2022), p. 127511. ISSN: 0950-0618. DOI: 10.1016/J.CONBUILDMAT.2022.127511.

[9] D. Müller, V. Förster and C.-A. Graubner. 'Influence of material spatial variability on required safety factors for masonry walls in compression'. In: *Mauerwerk* 21.4 (Aug. 2017), pp. 209–222. ISSN: 1437-1022. DOI: 10.1002/DAMA.201700004.

[10] B. Pulatsu, S. Gonen, F. Parisi, E. Erdogmus, K. Tuncay, M. F. Funari and P. B. Lourenço. 'Probabilistic approach to assess URM walls with openings using discrete rigid block analysis (D-RBA)'. In: *Journal of Building Engineering* 61 (Dec. 2022), p. 105269. ISSN: 2352-7102. DOI: 10.1016/J.JOBE.2022.105269.

[11] *Methods of Test for Masonry — Part 1: Determination of Compressive Strength*. Tech. rep. EN 1052-1:1998. Brussels, 1998.

[12] D. V. d. C. Oliveira. 'Experimental and Numerical Analysis of Blocky Masonry Structures under Cyclic Loading'. Ph.D. dissertation. Braga, Portugal: Universidade do Minho, 2003.

[13] R. Wilson, M. Pouragha, S. Acikgoz and B. Pulatsu. 'A DEM-based modelling framework to investigate fracture processes in masonry'. In: *Computational Particle Mechanics* 12 (2025), pp. 3057–3076. DOI: 10.1007/s40571-025-00951-y.

[14] R. H. Atkinson, B. P. Amadei, S. Saeb and S. Sture. 'Response of Masonry Bed Joints in Direct Shear'. In: *Journal of Structural Engineering* 115.9 (Sept. 1989), pp. 2276–2296. ISSN: 0733-9445. DOI: 10.1061/(ASCE)0733-9445(1989)115:9(2276). URL: https://ascelibrary.org/doi/abs/10.1061/%28ASCE%290733-9445%281989%29115%3A9%282276%29%20https://ascelibrary.org/doi/10.1061/%28ASCE%290733-9445%281989%29115%3A9%282276%29.

[15] G. Andreotti, F. Graziotti and G. Magenes. 'Detailed micro-modelling of the direct shear tests of brick masonry specimens: The role of dilatancy'. In: *Engineering Structures* 168 (Aug. 2018), pp. 929–949. ISSN: 0141-0296. DOI: 10.1016/J.ENGSTRUCT.2018.05.019.

[16] Comité Euro-International du Béton (CEB). *CEB-FIP Model Code 1990*. Bulletin d'information No. 213/214. Lausanne, Switzerland: Thomas Telford, 1993.



6

Component-level Validation of the MASON Contact Constitutive Model

This chapter evaluates the MASON contact model at the component (walls and piers) level, building on the material-level calibration and validation reported in Chapter 5. At this scale, the global response emerges from the interaction of many joints, blocks, and boundary conditions. The selected experimental benchmark and the adopted modelling idealisations are introduced first. The validation is organised around the monotonic (Section 6.2) and cyclic (Section 6.3) component responses, followed by masonry piers retrofitted with a modular steel frame (Section 6.4). For the retrofitted configuration, the MASON contact model is compared with commonly used distinct-element formulations that represent unit failure through Mohr–Coulomb plasticity. All component-level analyses are quasi-static, including the retrofitted configurations. The dynamic response is not addressed at this scale and is examined in Chapter 7. The chapter closes by synthesising the component-level evidence and defining the modelling settings that are carried forward to building-scale applications.

Contents

6.1. Introduction 158
6.2. Component-level validation under monotonic in-plane loading 159
6.2.1. Experimental description and numerical modelling setup 159
6.2.2. Numerical results: global and local behaviours 162
6.2.3. Cross-comparison to other numerical methods 166
6.2.4. Rigid- vs deformable-block configurations 168

Parts of this chapter have been adapted from the published paper in *Computers & Structures*, 10.1016/j.compstruc.2024.107499 and in *Computers & Structures*, 10.1016/j.compstruc.2025.108094.



6.2.5. Inclusion of dilatancy effects . . . 174
6.2.6. Mesh objectivity . . . 182
6.2.7. Computational timestep objectivity . . . 186
6.3. Component-level validation under cyclic in-plane loading . . . 189
6.3.1. Experimental description . . . 189
6.3.2. Numerical modelling setup . . . 191
6.3.3. Numerical results: global and local behaviours . . . 194
6.3.4. Influence of local numerical damping on energy dissipation . . . 200
6.3.5. Transition of failure mechanism in in-plane loading scenario . . . 203
6.3.6. Sensitivity analysis to imposed peak displacement rate . . . 205
6.3.7. Cross-comparison to other numerical methods . . . 207
6.4. In-plane response of modular steel frame-retrofitted masonry piers . . . 212
6.4.1. Experimental description . . . 213
6.4.2. Numerical modelling setup . . . 215
6.4.3. Numerical result: global and local behaviours . . . 218
6.4.4. Sensitivity analysis on the material parameters . . . 223
6.4.5. Quasi-static cyclic analysis results . . . 230
6.5. Summary and conclusions . . . 233

6.1. Introduction

This chapter evaluates the proposed Masonry Advanced Softening cONtact (MASON) constitutive model at the component scale, comprising masonry piers and walls, where the macroscopic response arises from the combined interaction of joints, blocks, and boundary conditions and not from the behaviour of individual interfaces (see Figure 2.2). The objective is to examine the model predictive capability beyond load-displacement capacity, with emphasis on whether the simulations reproduce the governing failure mechanisms and their spatial evolution at the pier level under in-plane actions. Particular attention is given to localisation patterns, sliding- and cracking-dominated responses, and damage accumulation under cyclic loading to assess whether the material-level calibration consistently transfers to structural components representative of engineering practice.

After the model has been properly validated for both monotonic and cyclic loading protocols, the MASON model is used to evaluate component-level behaviour under retrofit interventions. Specifically, the simulations examine how external strengthening systems modify load transfer, stiffness, and deformation capacity, and whether they shift the governing failure mode within the masonry from brittle localisation to more distributed and controllable collapse. This stage, therefore, assesses not only the resulting capacity gains but also the consistency of the predicted damage patterns and the interface activity.

For the monotonic loading sequence, the MASON model is validated against the widely cited clay-brick masonry wall experiments by Vermeltfoort *et al.* [1] These tests provide a well-documented benchmark for in-plane shear behaviour under imposed pre-compression, capturing the evolution of stiffness and strength up to peak load and the subsequent formation of the governing failure mechanism. For the cyclic loading

sequence, the MASON model is validated against four single-wythe calcium silicate (CS) masonry walls tested by Messali *et al.* [2] under pre-compression and quasi-static in-plane cyclic loading. Finally, retrofitted masonry piers are validated against the experimental campaign reported by Albanesi et al. [3], complemented by a systematic sensitivity study on the unreinforced configuration quantifying the influence of the material parameters on the global and local responses of the piers.

The monotonic validation is reported in Section 6.2 and includes the rigid vs deformable comparison (Section 6.2.4), the dilatancy parametric study (Section 6.2.5), and the mesh and timestep objectivity assessments (Sections 6.2.6 and 6.2.7, respectively). The cyclic validation in Section 6.3 covers the global and local responses (Section 6.3.3), the algorithmic damping share (Section 6.3.4), the rocking-to-sliding transition (Section 6.3.5), and velocity sensitivity (Section 6.3.6). The retrofit benchmark in Section 6.4 includes a 300-realisation sensitivity analysis (Section 6.4.4) and a quasi-static cyclic verification of the best-fit parameter set (Section 6.4.5), aside from the monotonic validation of the experimental campaign (Section 6.4.3).

6.2. Component-level validation under monotonic in-plane loading

This section presents the component-level monotonic validation of the MASON contact constitutive model against the clay-brick masonry wall experiments by Vermeltfoort *et al.* [1]. The experimental study reported a series of tests on masonry walls with dimensions 990 × 1080 × 98 mm (L × H × t) subjected to restrained vertical deformations under displacement-controlled, monotonically increasing in-plane lateral loading. The campaign comprised both solid walls and walls with openings; only the solid specimens are considered in this validation. This selection isolates the in-plane shear-compression response of the homogeneous panel and the joint and unit failure mechanisms that the MASON contact model is intended to reproduce. Openings introduce geometric stress concentrations and combined pier and spandrel actions, which would confound the assessment of the constitutive model with configuration-dependent effects.

In this validation, masonry units are modelled as deformable blocks, so their elastic deformation influences the assemblage's pre-localisation response. This approach affects both the overall elastic stiffness and the internal stress distribution, which in turn determine the initiation and location of damage at the unit-mortar interfaces. In parallel, an equivalent rigid-block configuration is analysed in Section 6.2.4 to isolate the role of block deformability at the unit-mortar interfaces and potential crack planes. The potential contribution of dilatancy at the component scale is examined in Section 6.2.5. Finally, the rigid-block idealisation is employed for targeted parametric studies of the computational settings, namely the mesh discretisation density (Section 6.2.6) and the mechanical timestep (Section 6.2.7), given its lower computational cost.

6.2.1. Experimental description and numerical modelling setup

Each wall comprised 18 courses of solid clay bricks with dimensions 204 × 98 × 50 mm (L × W × H). The bottom- and top-most courses were clamped to steel beams, in which



a vertical compression load and a monotonic displacement-controlled lateral load were applied to the top steel beam. The actual dimensions of the steel beams are not represented in the model, and each beam is idealised as a block with the same length and width as the wall and a height of 50 mm. This simplification does not capture the actual beam stiffness, which may influence the computed response. Three levels of vertical pre-compression were considered, namely 0.3 MPa (LOW), 1.21 MPa (MID), and 2.12 MPa (HIGH), selected to span the range from low to moderately high axial stress representative of typical loading conditions in low-rise unreinforced masonry buildings. The experimentally observed damage pattern at the end of each test is shown in Figure 6.1.

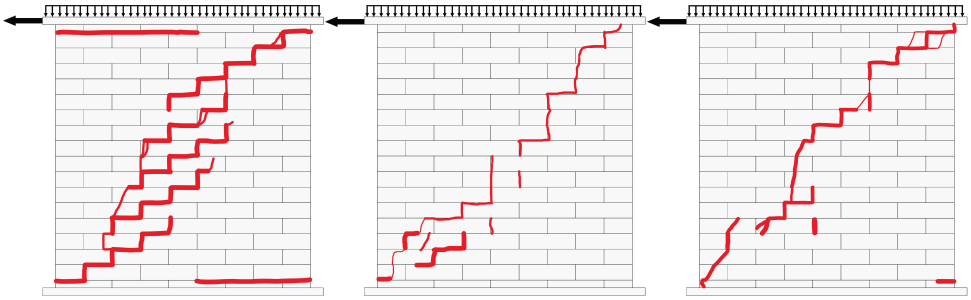


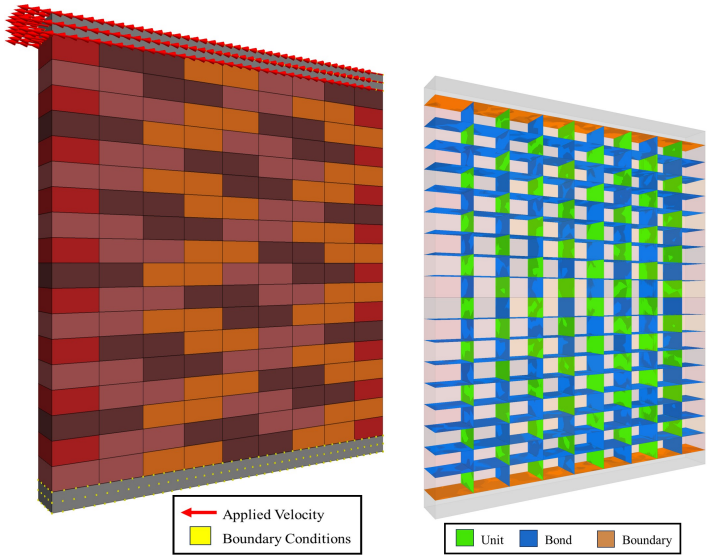
Figure 6.1. Damage pattern of the shear-compression masonry wall test [1]

The crack patterns indicate a clear confinement-dependent change in localisation. In the LOW pre-compression case (Figure 6.1A), diagonal cracking is localised at the mortar joints, with only limited crack penetration into the brick units. At MID pre-compression (Figure 6.1B), cracking through the bricks becomes more pronounced, indicating increased engagement of the units in the failure mechanism. In the HIGH pre-compression case (Figure 6.1C), diagonal cracking is more widespread, with more cracks propagating through the brick units and a broader damaged zone.

The numerical model geometry and the corresponding joint-plane discretisation are shown in Figures 6.2A and 6.2B, respectively. Each masonry unit is represented by two deformable half-bricks separated by a potential crack plane located at mid-length. The unit-mortar bond is represented by zero-thickness contact interfaces governed by the MASON contact model and positioned at the mortar joint locations. Because the mortar layer is reduced to a zero-thickness interface, each masonry unit is expanded by the mortar joint thickness, so that the modelled unit dimensions exceed the nominal brick dimensions and the overall bond pattern and assemblage geometry remain consistent with the experiment. The support and loading plates are represented by blocks assigned the Young's modulus of steel, 210 GPa, and are coupled to the masonry assemblage through linear-elastic contact planes (the orange surfaces in Figure 6.2B).

A double-clamped boundary condition is imposed to replicate the experimental setup, with the top block free to translate only laterally. The vertical displacement of the top block is released upon application of the axial stress to establish the target





(A) Model geometry (B) Joint geometry

Figure 6.2. Brick discretisation of the solid URM wall experiment

pre-compression, and is subsequently restrained during the displacement-controlled lateral loading. Contact-point material properties are adopted from primary literature and from studies that have previously employed the same experimental campaign as the validation benchmark (see [4–10]). The resulting input parameter sets, specified for each pre-compression level, are summarised in Table 6.1. The reported stiffnesses correspond to the deformable-block configuration. In the rigid-block configuration, the contact stiffnesses are reduced by a factor of 0.7 to lump the block deformability into the interface, and this configuration is examined in Section 6.2.4.

The peak ratio n (the ratio of peak compressive stress to the stress at the onset of compressive hardening, governing the shape of the compressive cap) is set to 2.0, based on the recommendation from the material characterisation test on solid clay bricks conducted by Jafari [11]. The fracture energies adopted for the unit-mortar interface are derived from the companion material characterisation tests reported alongside the wall experiments, ensuring consistency between the component benchmark and the model calibration. The system is first brought to equilibrium under the gravity load, followed by the application of the pre-compression load as distributed loads on the top surface of the upper boundary block. Once the equilibrium is achieved again, the top block vertical displacement is fixed, and the lateral load is applied as a velocity with a constant rate of $1\,\mathrm{mm\,s^{-1}}$ in the deformable-block model. The rigid-block models of Section 6.2.4 use $5\,\mathrm{mm\,s^{-1}}$.

Table 6.1. Material properties as input parameters to the numerical model

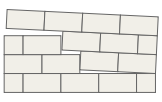
Masonry unit properties						
E_b, ν	$k_{n,b}$, $k_{s,b}$	$f_{t,b}$	$f_{sp,b}$, $f_{sr,b}$	$\phi_{p,b}$	$G^b_{f,I}$, $G^b_{f,II}$	ρ
(GPa,[-])	(GPa m^{-1})	(MPa)	(MPa)	(°)	(N m^{-1})	(kg m^{-3})
16.7, 0.15	820, 360	2.0	2.8, 0.0	45	80, 500	1800
Interface properties - σ_n = 0.30 MPa (LOW)						
k_n, k_s	f_t, f_{cp}	f_{sp}, f_{sr}	ϕ_p, ϕ_r	G_c, n	$G_{f,I}$, $G_{f,II}$	C_n, C_{nn}, C_{ss}
(GPa m^{-1})	(MPa)	(MPa)	(°)	(N m^{-1},[-])	(N m^{-1})	([-])
82, 36	0.25, 10.5	0.35, 0.0	35, 35	5000, 2.0	18, 125	0.0, 1.0, 9.0
Interface properties - σ_n = 1.21 MPa (MID)						
k_n, k_s	f_t, f_{cp}	f_{sp}, f_{sr}	ϕ_p, ϕ_r	G_c, n	$G_{f,I}$, $G_{f,II}$	C_n, C_{nn}, C_{ss}
(GPa m^{-1})	(MPa)	(MPa)	(°)	(N m^{-1},[-])	(N m^{-1})	([-])
110, 50	0.16, 11.5	0.22, 0.0	35, 35	5000, 2.0	18, 50	0.0, 1.0, 9.0
Interface properties - σ_n = 2.12 MPa (HIGH)						
k_n, k_s	f_t, f_{cp}	f_{sp}, f_{sr}	ϕ_p, ϕ_r	G_c, n	$G_{f,I}$, $G_{f,II}$	C_n, C_{nn}, C_{ss}
(GPa m^{-1})	(MPa)	(MPa)	(°)	(N m^{-1},[-])	(N m^{-1})	([-])
82, 36	0.16, 11.5	0.22, 0.0	35, 35	5000, 2.0	18, 50	0.0, 1.0, 9.0

A zero dilatancy angle is adopted in all simulations.
The differences in the peak tensile strength f_t, the cohesion f_{sp}, and the mode-II fracture energy $G_{f,II}$ between the pre-compression levels follow the wall-specific values reported by Lourenço and Rots [5].

6.2.2. Numerical results: global and local behaviours

The force-displacement responses of the numerical simulations ("NUM") and the experiments ("EXP") for each pre-compression level are compared in Figure 6.3. The LOW pre-compression case was tested twice, and the experimental envelope therefore appears as a bounded response range. Across the investigated range of confinement levels, the numerical model reproduces the principal global trends with good agreement.

For the LOW pre-compression level, σ_n = 0.30 MPa (blue curve in Figure 6.3), the experimental response is comparatively ductile and remains stable up to a horizontal displacement of approximately 2.5 mm, after which the load-carrying capacity decreases gradually. In the corresponding numerical simulation, a short-lived reduction in shear resistance occurs at around 1.0 mm. This transient drop is associated with the rapid opening of the developing diagonal crack, which propagates primarily along the mortar joints and activates the potential crack plane within the brick units [12]. The combined shear-tension damage scalar d_{ts} (Equation (4.9)) aggregates the tensile and shear damage accumulated at a contact into a single isotropic measure, bounded between zero for the



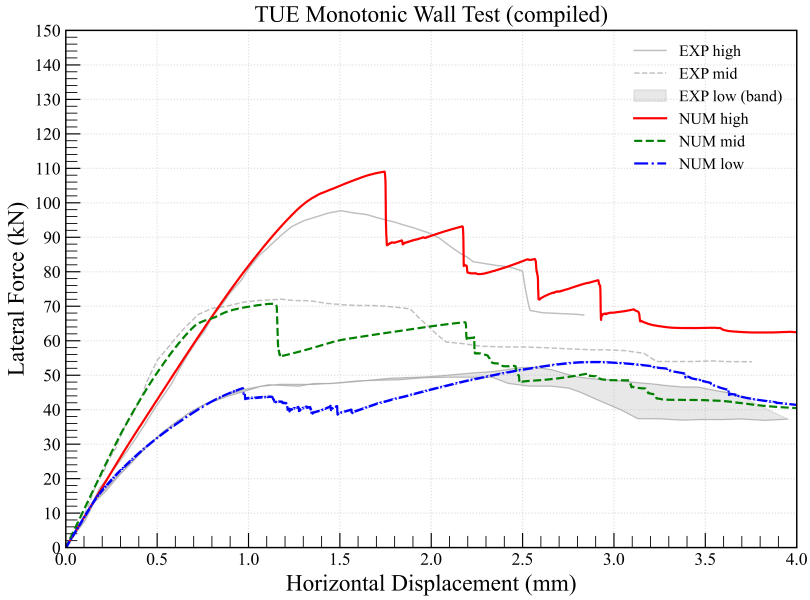


Figure 6.3. Force-displacement response comparison at each pre-compression level

intact state and unity at full softening of the governing mode. Its evolution in Figure 6.4 corroborates this mechanism and indicates full development of the diagonal crack at about 2.0 mm.

Since compressive damage remains limited during this stage, the model partially recovers shear capacity as displacement increases. This recovery arises from the boundary conditions of the test, in which the top beam is clamped and prevented from rotating or translating vertically. As damage localises and the cracked bed joints open, the kinematic constraint at the top boundary increases the vertical reaction, which in turn raises the axial stress acting on the wall. The in-plane lateral resistance of the wall is governed by two mechanisms, both dependent on this axial stress. In rocking, a bed joint cracks at the tensile edge and the pier rotates about its compressed toe, with the vertical load supplying the stabilising moment that limits the lateral force. In shear-friction, sliding along a bed joint is resisted by a Coulomb law whose residual strength, once cohesion is lost, is the frictional product of the vertical load and the friction coefficient. The self-induced compression force therefore raises the lateral capacity through both mechanisms and produces the observed post-peak rise in horizontal force. Subsequent toe crushing initiates at around 3.0 mm after which the response enters a progressive softening regime, and the capacity declines gradually.

For the MID pre-compression model with σ_n = 1.21 MPa (green curve in Figure 6.3), the experimental response remains stable up to approximately 1.0 mm of lateral displacement, after which opening of the unit-mortar interfaces initiates within the diagonal strut. Compared with the LOW case, a larger contribution from cracking through potential crack planes in the brick units is observed, resulting in a more abrupt loss

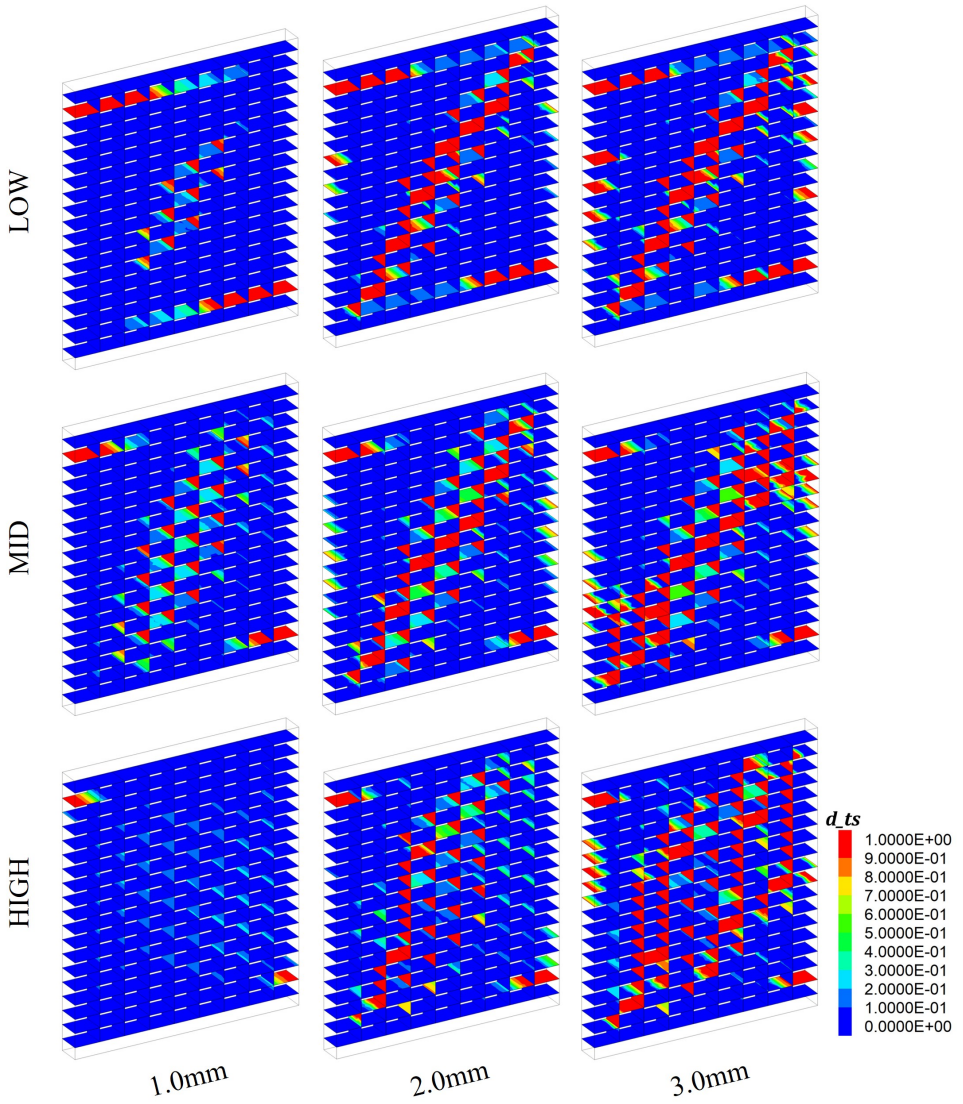


Figure 6.4. Damage progression in combined tension and shear (d_{ts}) when lateral displacement is 1.0 mm, 2.0 mm, and 3.0 mm (left to right)

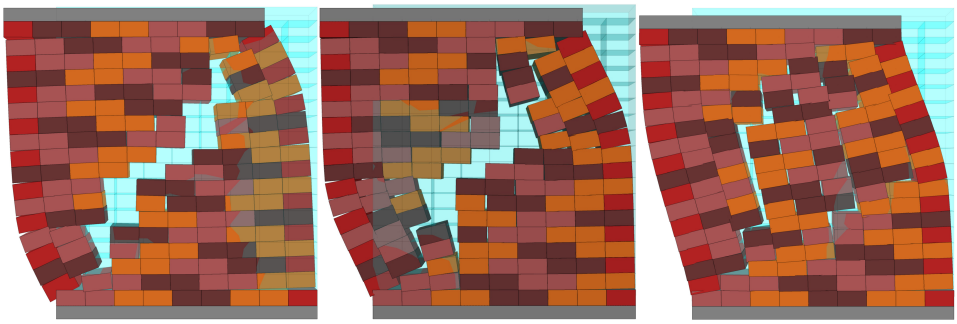
of load-carrying capacity as displacement approaches 2.0 mm. Despite the increased incidence of unit cracking, the damage remains predominantly confined to a single diagonal strut, as evidenced by the combined shear-tension damage scalar d_{ts} in Figure 6.4.

Under HIGH pre-compression with σ_n = 2.12 MPa (red curve in Figure 6.3), the wall attains a higher peak shear capacity of 110 kN. This peak is followed by a rapid

reduction in resistance, resulting from the formation and opening of a diagonal crack that propagates along the mortar joints and through the brick units. As splitting develops within the units, subcontact forces are redistributed to neighbouring blocks as they bear against one another. This redistribution increases the local normal forces, and, consequently, the mobilised frictional resistance, which explains the partial recovery of capacity observed after the initial drop in Figure 6.3. The recovery persists until further splitting events occur, which trigger a subsequent reduction in shear capacity. This pattern continues until compressive toe crushing becomes dominant, beyond 3.0 mm. The damage progression and formation of the diagonal cracks for the high pre-compression model are also well-represented by the tension-shear damage parameter d_{ts} plot in Figure 6.4, where the diagonal cracks formed between 1.0 mm and 2.0 mm, which included both the openings of the mortar joints and the potential crack surfaces on the brick units and progressed until the full formation of the diagonal cracks at the horizontal displacement of 3.0 mm.

Unlike the behaviour observed during the experiment, where inclined cracks could occur across any part of the units and with any inclination, the cracks in the numerical model were constrained to occur at the mid-length of the brick units through the vertical potential crack surfaces, which produced the stepwise numerical force-displacement curve and explains its discrepancy with the smooth decline of the experimental force-displacement curve in Figure 6.3. This stepwise behaviour persisted until the crushing damage at the compressed toes was observed at the horizontal displacement of 3.0 mm. An alternative solution to alleviate this behaviour is to refine the potential crack surfaces into multiple planes, resulting in smoother crack representations through the brick units.

The crack pattern at the end of the analysis (at the horizontal displacement of 4.0 mm) at each pre-compression level is shown in Figure 6.5, magnified 50 times. The collapse mechanisms are consistent with those observed during the experiments (Figure 6.1). It is also evident that contact interpenetration between blocks was observed at the compressed toes within the diagonal cracks of the models in Figure 6.5, indicating that compressive crushing occurred and localised within those regions.



(A) LOW (B) MID (C) HIGH

Figure 6.5. Crack pattern of the model at the end of the analysis (Def factor: 50)

6.2.3. Cross-comparison to other numerical methods

The force-displacement curve for the MASON contact model shown in Figure 6.3 is also compared against the results from numerical approaches proposed by other researchers. The comparison was only drawn to the selected numerical methods within the block-based modelling strategy. Figure 6.6 shows the predictions made by the proposed model, the experimental results, and the numerical results reported by Pulatsu [6] and Pulatsu & Tuncay [12], Nie et al. [9], and Lourenço & Rots [5]. Nie et al. [9] did not report a comparison to the intermediate pre-compression stress (σ_n = 1.21 MPa). Hence, the comparison for the MID model is restricted to the results reported by Pulatsu and Tuncay [12] and Lourenço and Rots [5].

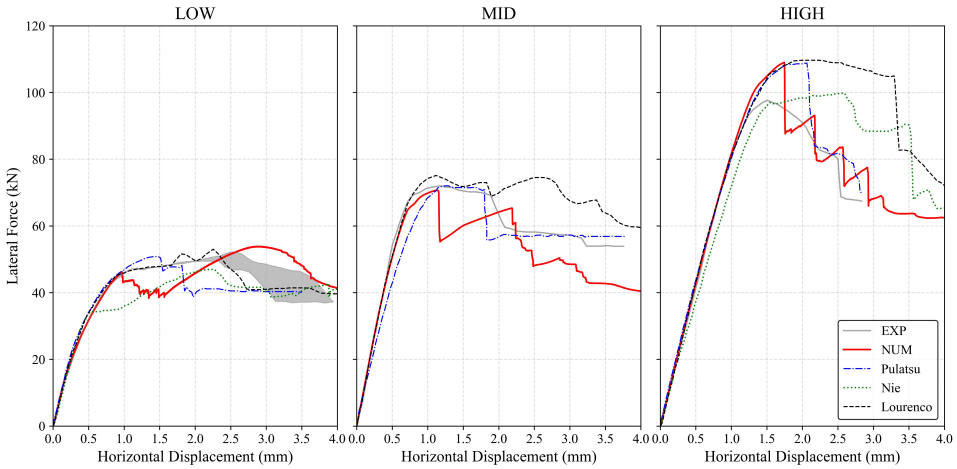


Figure 6.6. Comparison of force-displacement response to other approaches in the literature

It is evident on each pre-compression level that the responses from the proposed numerical model fall within the range of those reported by the other researchers [5, 6, 9, 12]. The only exception is the test with low pre-compression, for which the model proposed by Nie et al. [9] predicts a premature stiffness reduction, followed by hardening before the final capacity drop due to toe crushing.

Nie et al. [9], Lourenço and Rots [5] and the proposed model share an exponential softening law for tension and shear, but differ in the implementation of the hardening and softening law in compression. These differences are apparent in the global behaviour of the wall models. They could be attributed to the different modelling schemes (interface against contact models) and numerical implementations (implicit against explicit). Differences in the material input parameters may also contribute.

Meanwhile, the difference between the results of the proposed model and those reported by Pulatsu and Tuncay [12] could be attributed to the definition of the constitutive model and to the one-way coupling between shear and compression, since both models were developed within the DEM framework.

Table 6.2. Comparison of peak load, displacement, and dissipated energy predictions

				EXP	NUM	Pulatsu [6, 12]	Nie et al. [9]	Lourenço & Rots [5]
LOW[a]	Peak Load	kN		52.23	53.83 (-3.06)	50.82 (2.70)	46.98 (10.06)	53.04 (-1.55)
	Peak Disp.	mm		2.49	2.91 (-16.47)	1.41 (43.31)	2.16 (13.40)	2.25 (9.81)
	Diss. Energy[b]	kN	mm	158.9	155.8 (1.99)	139.2 (12.44)	138.1 (13.10)	151.0 (4.97)
MID[a]	Peak Load	kN		72.03	70.70 (1.85)	72.05 (-0.01)	- (N/A)	75.15 (-4.32)
	Peak Disp.	mm		1.18	1.12 (4.89)	1.26 (-6.79)	- (N/A)	1.13 (4.24)
	Diss. Energy[b]	kN	mm	216.3	194.0 (10.28)	210.1 (2.85)	- (N/A)	235.9 (-9.06)
HIGH[a]	Peak Load	kN		97.69	109.02 (-11.59)	108.80 (-11.40)	99.89 (-2.24)	109.69 (-12.28)
	Peak Disp.	mm		1.51	1.74 (-15.62)	2.06 (-36.99)	2.58 (-71.77)	2.22 (-47.62)
	Diss. Energy[b]	kN	mm	199.9	206.8 (-3.47)	213.9 (-7.00)	208.9 (-4.51)	228.8 (-14.43)

[a] Values in brackets represent the percentage of relative error to experimental values; the LOW case is referenced to the experimental upper bound
[b] Dissipated energy calculated until the displacement at the end of the experiment

The differences in the prediction of peak load, corresponding displacement, and dissipated energy on all compared approaches are quantified in Table 6.2. The dissipated energy, used to quantify modelling accuracy in terms of pre-peak stiffness and post-peak strength degradations, was calculated as the area under the force-displacement curve. For a fair comparison, the energy calculated for each numerical method was limited until the displacement corresponding to the end of the experiment.

Table 6.2 shows that the accuracy of the peak load prediction does not vary monotonically with the applied pre-compression stress for any of the four numerical methods considered. The MASON model and that of Pulatsu [6, 12] exhibit a

non-monotonic pattern, with the relative error reduced at the MID configuration (1.85 % and −0.01 %, respectively) and amplified at both LOW (−2.89 % and 2.70 %) and HIGH (−11.58 % and −11.40 %). The Lourenço and Rots [5] model behaves differently, with the relative error growing monotonically more negative as pre-compression increases, from −1.55 % at LOW to −4.32 % at MID and −12.28 % at HIGH, indicating a progressive underprediction of the peak load at higher axial stress.

These fluctuations could be influenced by many factors, including the inherent variability of wall material properties relative to the values used in the numerical models, and the representation of potential crack surfaces in the brick units. In the LOW model, splitting through the brick units was minimal, as the failure mode was governed by a localised stair-stepped diagonal crack. The response of the brick units did not significantly affect the peak load prediction of the URM wall.

As pre-compression increased, the failure mode remained governed by the stair-stepped diagonal crack in the MID model. Again, the peak load prediction was still unaffected by the mechanical behaviour of the brick units. In contrast, in the HIGH model, the peak load prediction was governed by cracking through both brick units and unit-mortar interfaces, with the former being predominant. Since this local failure is forced to occur at mid-length in the brick units and is associated with brittle post-peak strength degradation, its occurrence reduces the accuracy of numerical predictions, as seen with the HIGH model.

Overall, the MASON contact model can predict experimental responses within 20 % of the experimental values. The predicted responses from the proposed strategy also agreed with those from the other numerical approaches.

6.2.4. Rigid- vs deformable-block configurations

This subsection compares the rigid- and deformable-block configurations adopted for the Vermeltfoort *et al.* [1] benchmark. The joint-network layout, the block geometry, and the strength and softening parameters of the contact constitutive model are identical between the two configurations. The elastic parameters differ because each idealisation distributes the elastic deformability of the masonry differently. In the deformable-block configuration, the blocks are assigned a finite Young's modulus of 16.7 GPa and the bed joints the stiffnesses reported in Table 6.1. In the rigid-block configuration, the blocks do not deform, and the contact stiffnesses are reduced by a factor of 0.7 to lump the block deformability into the interface. The objective is to quantify how block deformability affects global stiffness, peak capacity, and damage localisation, and to assess whether a rigid-block idealisation remains an adequate approximation. In the rigid-block configuration, each unit retains only its six rigid-body degrees of freedom and carries no internal discretisation. The number of equations of motion integrated at each timestep is therefore lower than in the deformable-block configuration, and a reduced computational cost is expected. The rigid-block configuration is adopted on this basis for the subsequent sensitivity analyses of the computational settings and dilatancy effects.

The equivalent vertical Young's modulus of the masonry implied by the tabulated parameters is recovered through a one-dimensional series combination of the unit and



bed-joint compliances over a repeating cell of height $t_b + t_m$,

$$E_{mas} = \frac{t_b + t_m}{\frac{t_b}{E_b} + \frac{1}{k_n}}, \tag{6.1}$$

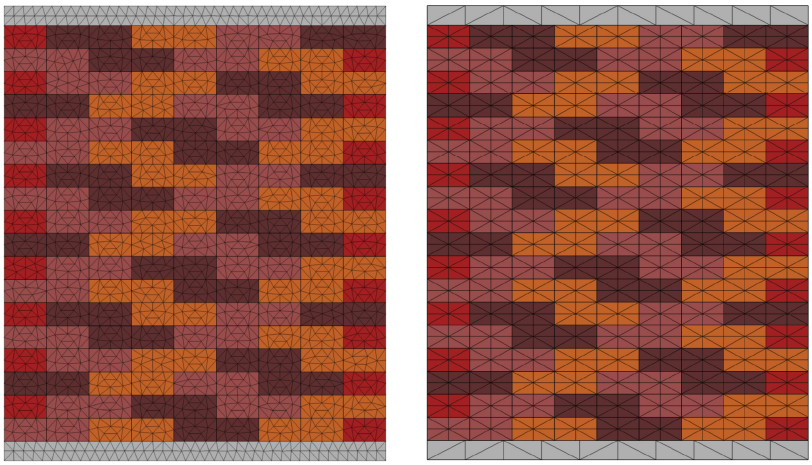
in which $t_b = 50\,\text{mm}$ and $t_m = 10\,\text{mm}$ denote the brick height and the mortar joint thickness, $E_b = 16.7\,\text{GPa}$ the brick Young's modulus, and k_n the bed-joint normal stiffness. For the deformable-block configuration in Section 6.2.2, with $k_n = 8.2 \times 10^{10}\,\text{N m}^{-3}$, Equation (6.1) yields $E_{mas} = 3.95\,\text{GPa}$. For the rigid-block configuration considered in this subsection, the units carry no compliance, so $E_b \to \infty$ and the relation reduces to $E_{mas} = (t_b + t_m)\,k_n$. With the reduced bed-joint stiffness $k_n = 5.74 \times 10^{10}\,\text{N m}^{-3}$, this gives $E_{mas} = 3.44\,\text{GPa}$. The reduced stiffness is 0.7 times the deformable-block value (Section 6.2.2), so the rigid-block configuration is more compliant and a small offset in initial stiffness between the two configurations is expected. The overall wall height follows $18 \times 50\,\text{mm} + 18 \times 10\,\text{mm} = 1080\,\text{mm}$.

Figure 6.7 compares the discretisation adopted for the deformable- and rigid-block configurations. In the deformable model (Figure 6.7A), the masonry units are discretised into tetrahedral elements using an average target edge length of 0.025 m, providing a relatively fine internal discretisation to represent unit compliance. In the rigid model (Figure 6.7B), the unit faces are subdivided using the radial-8 default, in which each face receives a central vertex and mid-edge vertices, yielding nine contact points per face. The contact-point density on rigid blocks can also be set directly through a target edge length, and its effect on the response is examined in Section 6.2.6. The radial-8 subdivision is retained as the baseline for this comparison, and the mesh-objectivity study confirms that the peak capacity is insensitive to further refinement of the contact-point density. The boundary (loading and support) blocks are discretised more coarsely, with an average edge length of 0.1 m, which is sufficient to represent the contact interfaces without unnecessarily increasing the computational cost.

The resulting model sizes and the associated mechanical timesteps for both discretisations are reported in Table 6.3, providing a direct basis for interpreting the differences in computational cost and numerical stability between the two configurations. While both configurations contain the same number of blocks, the deformable-block configuration introduces substantially more vertices and tetrahedral elements to represent unit deformability, since the tetrahedral mesh fills the entire block volume. This increases the number of degrees of freedom and reduces the stable mechanical timestep (Equations (3.20) and (3.21)).

By contrast, the rigid-block model eliminates internal discretisation of the block (removing Equation (3.21)), markedly lowering the discretisation density and permitting a larger timestep. This increases computational efficiency and makes the model suitable for sensitivity studies that aim to isolate the influence of numerical settings instead of material compliance. The 0.7 reduction is applied to the stiffnesses of both the unit-mortar interfaces and the internal potential crack planes, with the resulting values summarised in Table 6.4.

In the rigid-block formulation, boundary conditions are imposed directly on the blocks rather than on nodal degrees of freedom, as is required in the deformable-block model.



(A) Deformable model (B) Rigid model

Figure 6.7. Mesh discretisation for the deformable and rigid models.

Table 6.3. Comparison of deformable- and rigid-block model discretisation and computational timestep

Quantity	**Deformable model**	**Rigid model**
Number of blocks	164	164
Number of vertices	15448	4316
Number of tetrahedral elements	46123	0
Mechanical timestep	1.68862×10^{-6}	7.71861×10^{-6}

Table 6.4. Normal and shear stiffnesses adopted for the rigid-block configuration

Interface type	k_n (GPa m^{-1})	k_s (GPa m^{-1})
Unit–mortar interfaces	$0.70 \times 82 = 57.4$	$0.70 \times 36 = 25.2$
Potential crack planes	$0.70 \times 820 = 574$	$0.70 \times 360 = 252$

The loading protocol is otherwise identical, except for the loading rate of 5 mm s^{-1}: the model is first brought to equilibrium under self-weight, after which the target pre-compression is applied as a uniform surface load on the top beam. Monotonic in-plane lateral load is then applied to the top block under displacement control until a horizontal displacement of 4.0 mm is reached.

Figure 6.8 shows that both idealisations reproduce the overall confinement-dependent increase in strength and the subsequent post-peak degradation, while exhibiting systematic differences in stiffness and softening characteristics. For the LOW

pre-compression model, the rigid-block model underestimates the peak resistance and exhibits a more pronounced reduction in post-peak capacity than the deformable-block simulation. For the MID case, the rigid model overpredicts the peak load more than the deformable model, whereas for the HIGH case it captures the peak load more closely. In both cases, it alters the sequence and amplitude of the step-like capacity drops associated with crack opening along the potential crack plane and force redistribution. Across the three pre-compression levels, the deformable-block configuration follows the experimental envelopes more consistently, notably in the post-peak branch, where the rigid-block model peaks early at low pre-compression and hardens after the peak at high pre-compression. The rigid-block configuration predicts the peak load within about 8% at all levels (Table 6.5) and is therefore sufficiently representative for the subsequent sensitivity analyses of numerical settings.

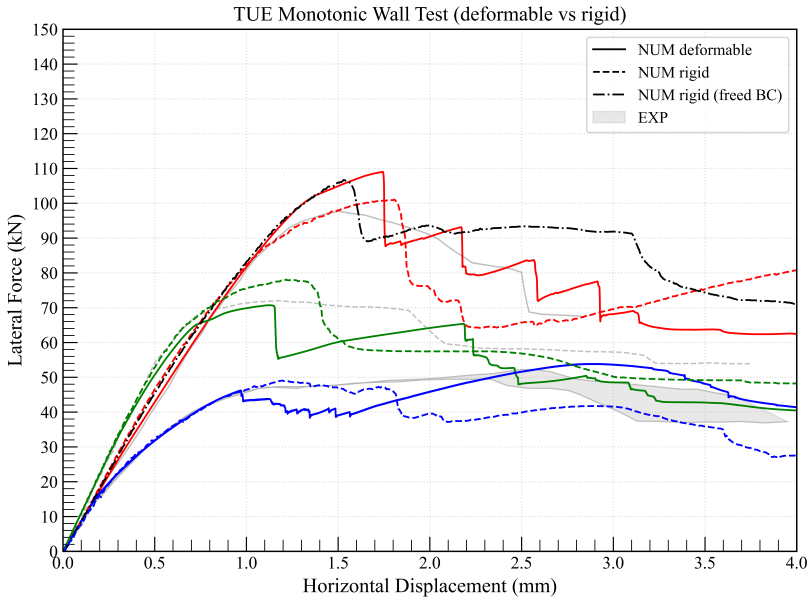


Figure 6.8. TU Eindhoven monotonic shear-wall force–displacement response: deformable vs rigid numerical models compared with experimental envelopes.

Table 6.5 compares the peak load, displacement at peak, and dissipated energy up to 4.0 mm. In the HIGH case, both configurations overestimate the dissipated energy by approximately 40 %, with the rigid model predicting the peak resistance more accurately than the deformable model, with relative errors to EXP of 3.4 % and 11.6 %, respectively, although at a later peak displacement. For the MID case, agreement is strongest overall for both models. The deformable model is within ±6 % for all three metrics, while the rigid model slightly overpredicts the peak load (+8.4 %) but matches the energy closely at +0.8 %. For the LOW case (referenced to the EXP upper bound), the deformable model remains close in peak load and energy, overpredicting them by 3.1 % and 6.8 %, respectively. The rigid model underpredicts both by about 6 % and peaks markedly earlier,

followed by faster softening (Figure 6.8). This is consistent with an earlier localisation of damage in the rigid model, where the absence of unit compliance concentrates the deformation at the joints.

The rigid HIGH configuration develops post-peak hardening between approximately 2.5 mm and 4.0 mm, with the residual force rising from 65 kN to 80 kN. This response is reproduced by neither the deformable HIGH configuration nor the experimental envelope, both of which exhibit monotonic post-peak softening. The hardening is attributed to the kinematic over-constraint at the clamped top boundary. As deformation accumulates, the restrained vertical displacement raises the axial stress acting on the wall, following the mechanism described for the LOW case. In the HIGH configuration, this self-induced compression suppresses the localisation of compressive contact stress required to activate the compression cap, so the lateral capacity does not drop. The deformable HIGH configuration is less affected, since the elastic compliance of the units accommodates part of the kinematic incompatibility internally.

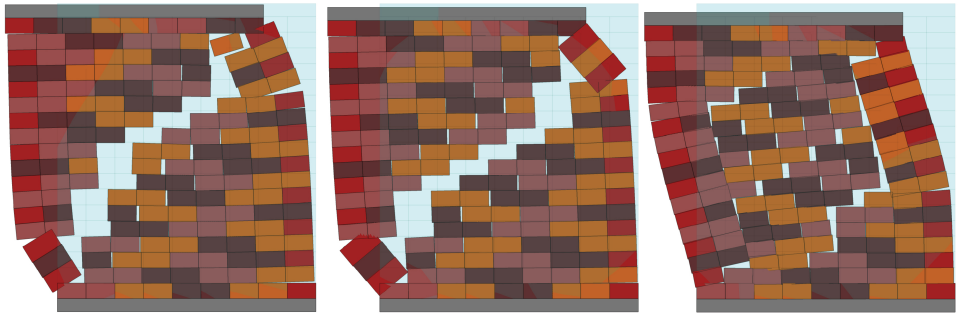
Table 6.5. Summary metrics up to 4 mm for the TUE monotonic wall tests.

	NUM deformable vs EXP			**NUM rigid vs EXP**		
Level	**Peak load**	**Peak disp.**	**Diss. energy**	**Peak load**	**Peak disp.**	**Diss. energy**
	(kN)	(mm)	(kN mm)	(kN)	(mm)	(kN mm)
LOW	53.832 (-3.058)	2.910 (-16.476)	169.804 (-6.839)	49.054 (6.089)	1.195 (52.144)	149.273 (6.080)
MID	70.697 (1.859)	1.122 (4.899)	203.981 (5.684)	78.056 (-8.357)	1.215 (-2.978)	217.915 (-0.759)
HIGH	109.022 (-11.592)	1.743 (-15.704)	283.105 (-41.590)	101.052 (-3.433)	1.808 (-20.027)	279.333 (-39.704)

Values are reported as *value* with the *relative error (%)* on a new line in parentheses, referenced to the experimental curve (EXP – NUM)/EXP × 100%; the LOW case is compared against the EXP upper bound.

A direct comparison with the corresponding deformed configurations for the deformable model in Figure 6.5 and the rigid model in Figure 6.9 highlights that both configurations reproduce the same governing kinematics across the three confinement levels, namely the formation of a dominant diagonal mechanism accompanied by local opening and sliding along the joints and the potential crack planes. Compared with the deformable-block results, the rigid-block model exhibits a more segmented deformation field, characterised by sharper discontinuities and a more pronounced block rotation at the compressed toes (bottom-left corner).

Beyond the similarities in the predicted mechanisms, the principal advantage of the rigid-block configuration is its computational efficiency. On the same hardware (a 4.00 GHz AMD Ryzen 9 processor with 32 GB of memory) and with a plotting interval of 100 steps, the rigid model, run at a loading velocity of 5.0 mm s^{-1}, reaches 4.0 mm lateral displacement in approximately 3 minutes on average. The deformable-block model, run at 1.0 mm s^{-1}, requires approximately 27 hours to reach the same displacement. The loading rates differ, so the ratio of about 540 includes a factor of up to five that stems from the rate alone. This substantial reduction in wall-clock time motivates adopting the



(A) LOW (B) MID (C) HIGH

Figure 6.9. Deformed shape of the rigid model at 4.0 mm for all cases (Def factor: 50)

rigid-block formulation for subsequent sensitivity analyses.

Across the three pre-compression levels considered, the rigid- and deformable-block configurations reproduce the same local failure mechanisms and yield comparable predictions of peak lateral capacity at LOW and MID pre-compression. At HIGH pre-compression, the two configurations diverge in the post-peak regime due to the interaction between rigid-block kinematics and the clamped top boundary condition. This divergence is confined to the global force response and does not extend to the spatial damage pattern, which remains comparable between the two configurations across all three levels.

The principal limitation of the rigid-block idealisation is the absence of unit-scale elastic compressibility. Under vertical load, a deformable unit expands laterally through the Poisson effect, whereas a rigid unit cannot. In the rigid configuration, the lateral strain developed under vertical load therefore originates entirely from interface compliance, with its magnitude governed by the ratio k_s/k_n. This contribution is small relative to the global in-plane wall behaviour, which is governed by interface opening and sliding, and the rigid-block configuration reproduces such response with sufficient fidelity. Where confinement-driven lateral strain, normal-shear coupling at the unit-mortar interface, or stress redistribution within the units affects damage initiation or propagation, the deformable-block configuration is required.

On this basis, the rigid-block configuration is adopted for the parametric studies of computational settings reported in the subsequent sections, where the response remains within the regime of equivalence between the two formulations. The recalibration of contact stiffnesses to compensate for unit compliance is geometry- and stress-state-dependent and requires verification when transferred across specimens.

The numerical-convergence studies in Sections 6.2.6 and 6.2.7, namely the mesh discretisation density and the mechanical timestep, are conducted on the rigid HIGH configuration with the clamped top boundary adopted in the validation. They investigate discretisation error and yield conclusions independent of the boundary configuration. The dilatancy study in Section 6.2.5 is instead conducted on the rigid LOW configuration, where the clamped boundary does not contribute appreciably to the post-peak regime,

so that the constitutive contribution of dilatancy is isolated. The corresponding variation at HIGH pre-compression is reported in Appendix B.1. There, a part of the measured sensitivity is attributable to boundary-induced amplification and not to the constitutive contribution alone. This limitation is acknowledged and identified as a target for further investigation under a released top boundary configuration.

6.2.5. Inclusion of dilatancy effects

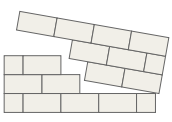
Building on the rigid-block configuration established in the previous subsection, this subsection investigates the influence of dilatancy on the monotonic wall response through a parameter variation of the dilation angle ψ over the range 0° to 30°. The study is performed for the LOW pre-compression configuration ($\sigma_n = 0.30\,\text{MPa}$), where the response is governed by joint-dominated diagonal cracking and the kinematic interaction with the clamped top boundary identified in the previous section does not contribute appreciably to the post-peak regime. This configuration isolates the constitutive contribution of dilatancy at the unit-mortar interface from the boundary contribution that affects the rigid-block response at higher confinement. The corresponding parameter variation at HIGH pre-compression is reported in Appendix B.1, where the boundary-amplified term to the dilatancy sensitivity is identified as a constraint on the transferability of calibrated ψ values to other confinement levels and boundary configurations.

The parameter variation serves a dual purpose. It characterises the sensitivity of the model response to the dilatancy treatment across the parameter range, and it identifies the configurations that produce the closest agreement with the experimental envelope as a basis for the recommended ψ values reported at the end of the section. To capture phenomenological behaviours observed across different masonry typologies, two bounding assumptions are considered:

1. **Lower-bound assumption**. The lower-bound setting represents a mechanically coupled interpretation of dilatancy, typically observed in regular brick masonry [13]. In this approach, ϕ and ψ are varied while keeping $\phi + \psi$ constant, which is interpreted here as a proxy for the mobilised peak shear resistance angle of the mortar joint. The target value $\phi + \psi = 35°$ is set to preserve the peak-level shear capacity implied by the baseline calibration, while isolating the role of dilation on the post-peak response. This constraint reflects the physical reality of smooth, planar bed joints where, as dilatancy forces units to ride over surface asperities, the effective frictional contact area is reduced.

2. **Upper-bound assumption**. Conversely, the upper-bound setting reflects the conventional geotechnical interpretation for granular materials, which is often applicable to rubble stone masonry. The friction angle is held constant at $\phi = 35°$ while ψ is increased sequentially, so that the peak mobilised shear resistance increases with dilatancy. This represents an interlocking-dominated response, in which dilation increases apparent strength through kinematic constraints, while the intrinsic frictional parameter is assumed to remain unchanged.

The two formulations span a range of physical interpretations rather than a numerical



envelope. Their resulting response curves characterise the sensitivity of peak capacity, post-peak softening, and damage localisation to the assumed dilatancy behaviour and bracket the response of masonry typologies for which the appropriate interpretation lies between the two limiting cases. The parameter relationships are illustrated in Figure 6.10, and the corresponding numerical values are summarised in Table 6.6.

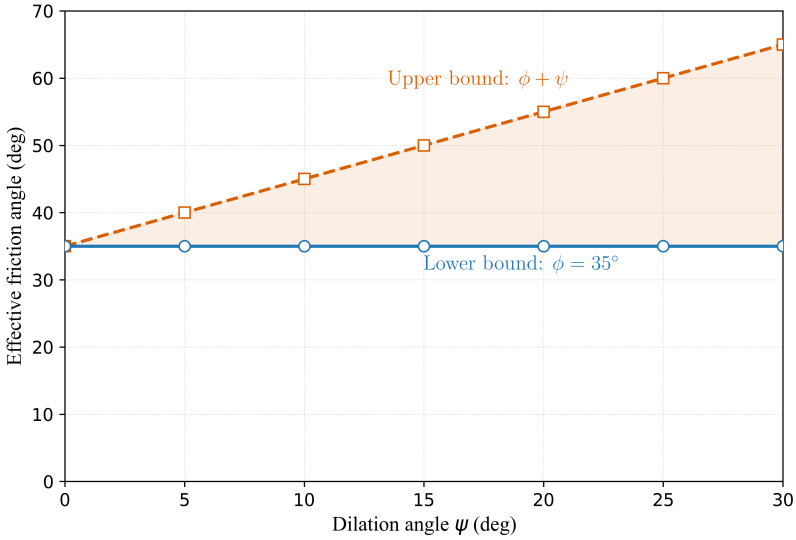


Figure 6.10. Lower- and upper-bound dilatancy parameter variation.

Table 6.6. Dilatancy sensitivity ranges for lower- and upper-bound assumptions

Model bound	**Friction angle, ϕ (°)**	**Dilation angle, ψ (°)**	$\phi + \psi$ (°)
Lower bound ($\phi + \psi = 35°$)	$35 \rightarrow 5$	$0 \rightarrow 30$	$35 \rightarrow 35$
Upper bound ($\phi = 35°$)	$35 \rightarrow 35$	$0 \rightarrow 30$	$35 \rightarrow 65$

The upper-bound assumption remains physically motivated, as experimental and micro-modelling studies on masonry bed joints indicate that the apparent peak shear contribution can be interpreted as a combined term $\phi + \psi$ (or $\phi_{cv} + \psi$ where ϕ_{cv} is the friction contribution at constant volume), with reported peak values reaching approximately 55° before dilatancy decays with accumulated slip [13, 14].

The lower-bound formulation is reported first, followed by the upper-bound formulation. For each formulation, the horizontal force-displacement and the vertical force–lateral displacement responses are reported. The best-fit configuration in each formulation is identified by the relative peak-force error and the normalised root-mean-square error (NRMSE) computed on the horizontal force-displacement curve.

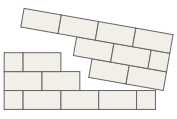
Lower-bound dilatancy parameter variation results

Figure 6.11A shows the horizontal force-displacement response under the lower-bound formulation across the parameter range. The pre-peak branch is reproduced consistently across all values of ψ, and the peak force at approximately 50 kN is preserved because the constraint $\phi + \psi = 35°$ holds the peak shear capacity constant across the range. The post-peak branch exhibits a sharp bifurcation at $\psi \approx 6.5°$ that separates two qualitatively different responses. For $\psi < 6.5°$, the post-peak branch retains a residual capacity in the range 30 kN to 45 kN, oscillating around the experimental envelope through a sequence of stick-slip events along multiple bed and head joints. For $\psi > 6.5°$, the post-peak branch collapses to residual values in the range 10 kN to 25 kN, well below the experimental envelope, and remains at this level through the subsequent loading.

The best match to the experimental envelope is obtained at $\psi = 1°$, with a peak error of 6.5% and a normalised RMSE of 18 % across the displacement range. The NRMSE value indicates that ψ controls a smaller fraction of the post-peak variance than the cohesion, the elastic stiffness, or the loading-rate effects identified at the end of this section, and that the post-peak gap should be addressed through one of these calibration parameters, not through the dilatancy angle. This calibration outcome indicates that the dilatancy contribution at the unit-mortar interface for the LOW specimen is essentially negligible, with the peak shear capacity well-described by friction alone at $\phi \approx 35°$ and the post-peak tail by the residual frictional resistance at the same angle. The threshold at $\phi \approx 28.5°$ falls within the friction angle range reported for unit-mortar interfaces in clay brick masonry, which spans approximately 25° to 35° [13, 14]. The lower-bound formulation, therefore, checks both end-member behaviours of unit-mortar interface friction within the physically representative range, with the distributed mechanism representative of higher-friction interfaces and the single-block sliding mode representative of lower-friction interfaces. The current specimen sits in the high-friction regime, consistent with the calibration outcome at $\psi = 1°$.

Figure 6.11B reports the corresponding vertical response. The pre-peak branch is again reproduced consistently across the parameter range, with the numerical normal force climbing from the initial pre-compression value to approximately 60 kN at peak displacement. The post-peak branch follows the bifurcation observed in the FD response. For $\psi < 6.5°$, the vertical force continues to climb steadily under the sustained distributed mechanism, reaching values close to or within the experimental envelope at the end of the analysis. For $\psi > 6.5°$, the vertical force deviates onto a separate trajectory that remains systematically below the envelope, reflecting the loss of distributed dilatant uplift contribution once the wall localises to single-block sliding and the dilatancy decay parameter $u^{s,max}$ rapidly attenuates the uplift contribution along the single active sliding plane.

The bifurcation reflects a transition between two competing failure mechanisms, as shown in Figure 6.12 for six representative values of ψ. Below the 6.5° threshold (Figure 6.12A-C), the residual frictional capacity along the bed joints, governed by ϕ alone once the dilatancy contribution has decayed through the $u^{s,max}$ parameter, remains sufficient to sustain a distributed diagonal stair-step mechanism. The shear forces redistribute along multiple bed and head joints, with friction at each interface providing distributed resistance and the head joints opening in tension at the stair-step corners.



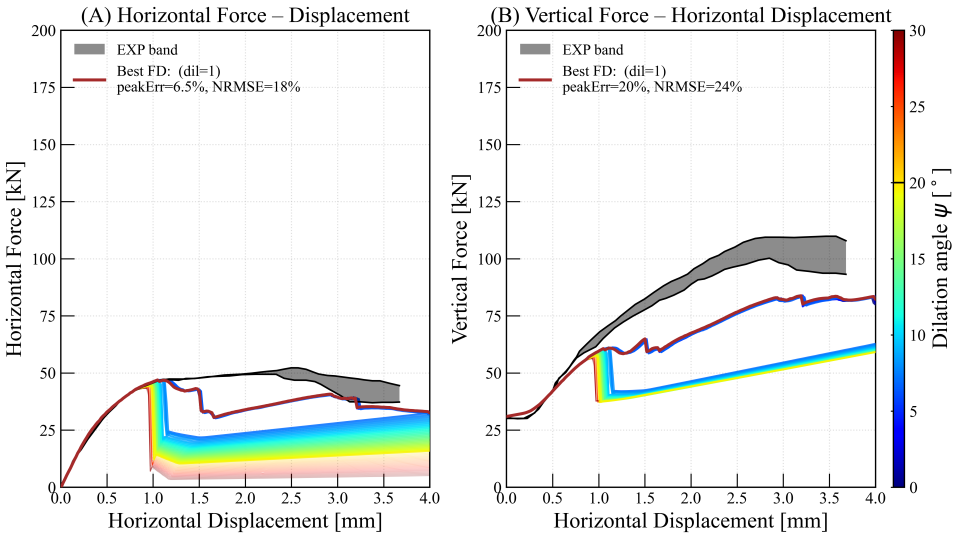


Figure 6.11. Horizontal force (A) and vertical force (B) against horizontal displacement for the LOW specimen under the lower-bound dilatancy parameter variation. The coloured curves show the numerical sweep of the dilation angle ψ from 0° to 30° (colourbar), the grey region denotes the experimental envelope, and the dark red curve is the best-fitting case ($\psi = 1°$), with the peak-load error and NRMSE relative to the experiment annotated in each panel.

Above the threshold (Figure 6.12D-F), the residual friction along any single bed joint becomes too low to support the distributed mechanism, and slip localises at the bed joint with the lowest local resistance. The masonry above the sliding plane translates rigidly as a single block, with the residual capacity governed solely by the residual friction angle applied to a single active sliding interface. The threshold at $\psi \approx 6.5°$ corresponds to a residual friction angle of approximately $\phi = 28.5°$, below which the localised single-block sliding path becomes more easily mobilised than the distributed diagonal mechanism.

The lower-bound formulation reproduces the experimental response within the regime where the distributed diagonal mechanism remains active, and produces a qualitatively different single-block sliding response above the threshold that does not match the experimental damage pattern. The implication for parameter selection is that the lower-bound formulation should be operated at ψ values below the threshold when the experimental response is governed by a distributed diagonal mechanism, and that the threshold itself depends on the wall geometry, the relative strength of bed and head joints, and the pre-compression level.

Upper-bound dilatancy parameter variation results

Figure 6.13A shows the horizontal force-displacement response under the upper-bound formulation across the parameter range. The pre-peak branch is reproduced consistently

across all values of ψ up to displacements of approximately 0.5 mm, beyond which the curves separate progressively. The peak force grows monotonically with ψ because the friction angle is held constant at $\phi = 35°$ and the dilatancy contributes additively to the peak shear capacity through the effective angle $\tan(\phi + \psi)$. At $\psi = 0°$, the peak force coincides with the corresponding lower-bound value at approximately 50 kN, since the two formulations are identical at this end of the parameter range. At $\psi = 30°$, the peak reaches approximately 130 kN, well above the experimental envelope. The post-peak branch retains capacity across the parameter range without a mechanism transition, with the residual values scaling proportionally with the peak strength.

The best match to the experimental envelope is obtained at $\psi = 1°$, with a peak error of 9.8% and a normalised RMSE of 9.8% across the displacement range. This calibration outcome is consistent with the lower-bound calibration, which identified the same value of ψ as the best match, at a different friction angle ($\phi = 34°$ for lower-bound, $\phi = 35°$ for upper-bound). The convergence of both formulations on $\psi = 1°$ confirms that the dilatancy contribution at the unit-mortar interface for the LOW specimen is essentially negligible, with the peak shear capacity well-described by friction alone at $\phi \approx 35°$ in either formulation. For $\psi \geq 1°$, the upper-bound peak force exceeds the experimental envelope, and for $\psi > 25°$ the overshoot becomes substantial, with a peak force more than 1.6 times the experimental value, with the formulation implying a level of

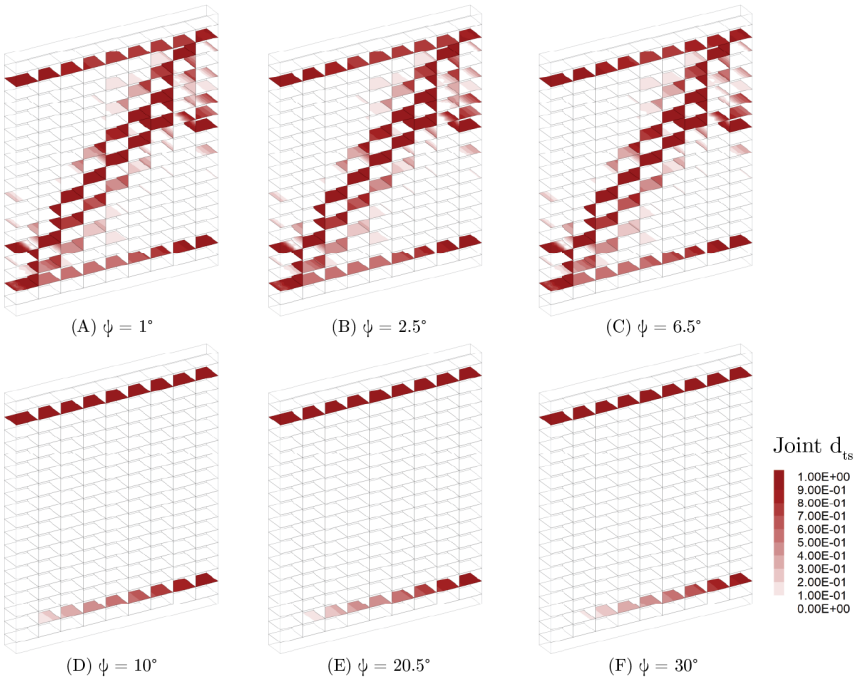


Figure 6.12. Joint shear-tension damage field d_{ts} at the end of the analysis for the lower-bound formulation for the LOW specimen.

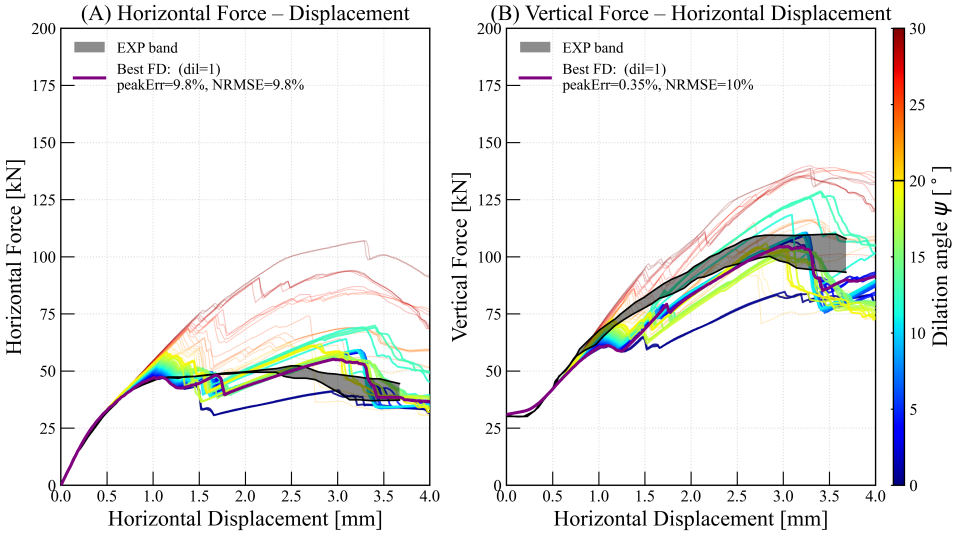


Figure 6.13. Horizontal force (A) and vertical force (B) against horizontal displacement for the LOW specimen under the upper-bound dilatancy parameter variation. The coloured curves show the numerical sweep of the dilation angle ψ from 0° to 30° (colourbar), the grey region denotes the experimental envelope, and the purple curve is the best-fitting case ($\psi = 1°$), with the peak-load error and NRMSE relative to the experiment annotated in each panel.

unit-mortar interface interlocking that is not consistent with the experimental response of the LOW specimen.

Figure 6.13B reports the corresponding vertical response. The numerical vertical force climbs from the initial pre-compression value across all ψ values, with the magnitude of the climb growing monotonically with ψ. At $\psi = 1°$, the vertical force reaches approximately 90 kN at the end of the analysis, just below the experimental envelope, with a peak error of 0.35% and a normalised RMSE of 10% over the displacement range. At $\psi = 30°$, the vertical force reaches approximately 135 kN, well above the envelope. The vertical force trajectory remains smooth across the full parameter range without the bifurcation observed in the lower-bound formulation, again reflecting the constant residual friction angle that maintains the distributed dilatant uplift contribution throughout the analysis. The combined vertical force and horizontal force growths confirm that the dilatant and frictional contributions operate in parallel rather than in a trade-off, which is the defining feature of the upper-bound formulation relative to the lower-bound counterpart.

The failure mechanism in the upper-bound formulation, illustrated in Figure 6.14 for six representative values of ψ, retains the distributed diagonal stair-step pattern across the parameter range, compared with the bifurcation observed in the lower-bound formulation. From $\psi = 1°$ to $\psi = 10°$ (Figure 6.14A-D), the damage localises along a clean stair-stepped diagonal band connecting the loaded corner to the opposite support

through a sequence of bed-joint sliding and head-joint opening events, consistent with the experimental observation. At $\psi = 20.5°$ and $\psi = 30°$ (Figure 6.14E-F), the diagonal stair-step pattern is preserved, but the damage progressively shifts towards unit splitting along the diagonal load path, with activated potential crack planes within the masonry units. This shift reflects the upper-bound formulation, which imposes an effective friction angle $\phi + \psi$ that mobilises shear stresses sufficient to engage the unit body in tension. This behaviour distinguishes the upper-bound response from the lower-bound bifurcation that collapses to a localised single-block sliding mode above the threshold.

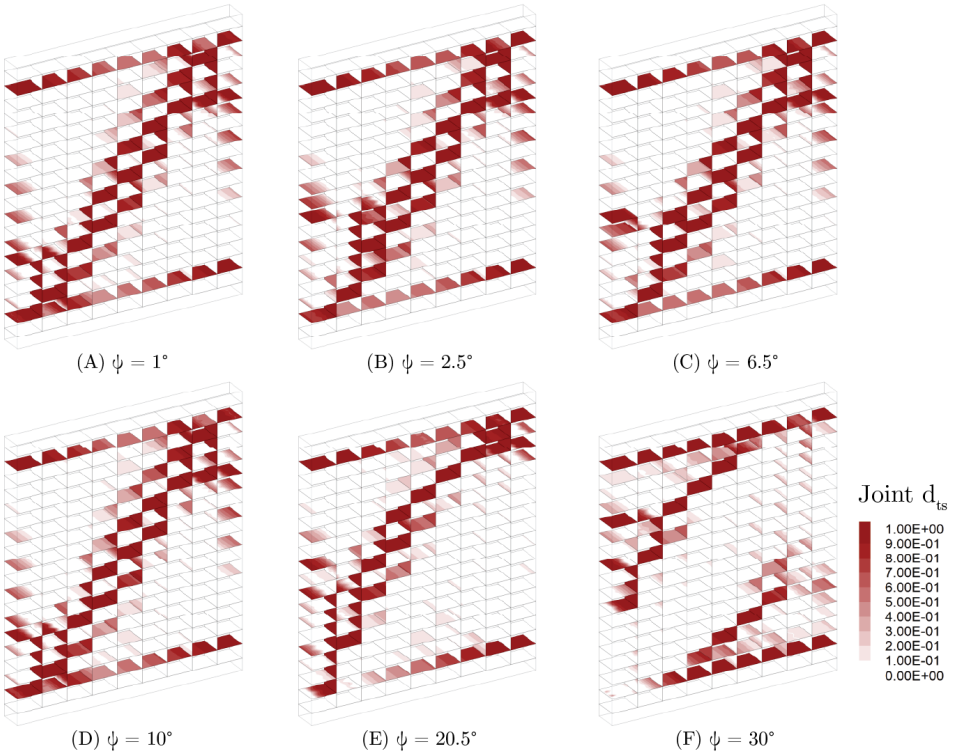


Figure 6.14. Joint shear-tension damage field d_{ts} at the end of the analysis for the upper-bound dilatancy parameter variation.

Comparison of prediction metrics towards experimental values

Figure 6.15 summarises the parameter variation through three normalised metrics: the peak-force $F_{\text{peak}}/F_{\text{peak,EXP}}$, the displacement-at-peak ratio $d(F_{\text{peak}})/d(F_{\text{peak,EXP}})$, and the dissipated work ratio $W_{0\to4}/(W_{0\to4})_{\text{EXP}}$, where $W_{0\to4}$ denotes the work dissipated over the lateral displacement range from zero to four millimetres. At $\psi = 0$, both formulations coincide and underestimate the peak force by approximately 8 % and the dissipated work by approximately 12 % relative to the experimental values.

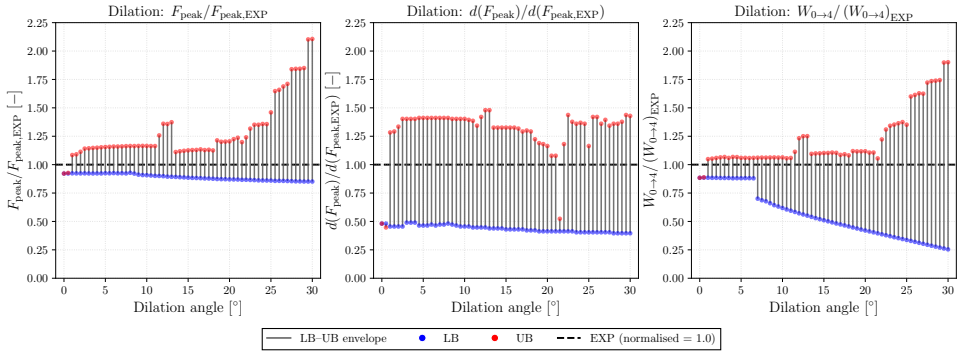


Figure 6.15. Candlestick summary of the LOW pre-compression dilatancy parameter variation. Left panel: peak force ratio $F_{peak}/F_{peak,EXP}$. Centre panel: displacement at peak ratio $d(F_{peak})/d(F_{peak,EXP})$. Right panel: dissipated work ratio $W_{0\to4}/(W_{0\to4})_{EXP}$

The peak-force ratio diverges as ψ increases. The lower-bound formulation remains within the range 0.85 to 0.92 across the parameter range, declining slightly because the residual friction reduction offsets the additional dilatancy contribution at peak (Figure 6.11A). The upper-bound formulation grows monotonically from 0.92 at $\psi = 0°$ to approximately 2.1 at $\psi = 30°$, exceeding the experimental envelope for $\psi > 2°$ (Figure 6.13A). The displacement-at-peak ratio is essentially independent of ψ in both formulations, with the lower-bound formulation maintaining a value close to 0.45 and the upper-bound formulation staying around 1.35. The dissipated-work ratio provides the clearest discrimination between the two formulations. The upper-bound formulation tracks the experimental value within 10 % for $\psi < 10°$ and exceeds it monotonically thereafter, reaching 1.9 at $\psi = 30°$. The lower-bound formulation tracks the experimental value within 15 % for $\psi < 6.5°$ and drops sharply beyond this threshold, reaching 0.25 at $\psi = 30°$. The slope change at $\psi \approx 6.5°$ in the lower-bound formulation is consistent with the bifurcation identified in the F-D response and the corresponding mechanism transition from distributed diagonal cracking to single-block sliding.

Discussion

The convergence of both formulations on $\psi = 1°$ as the closest match to the experimental envelope, with peak-force errors of 6.5% and 9.8% for the lower-bound and upper-bound formulations, respectively, indicates that the dilatancy contribution at the unit-mortar interface for this specimen typology is essentially negligible. The wall response is well-described by friction alone at $\phi \approx 35°$ across both parameter coupling assumptions, and the dilatancy angle is assigned a minimal value and not calibrated to match an apparent dilatant uplift in the experimental vertical force response.

This outcome reconfirms earlier conclusions drawn at the structural scale. Lourenço [15] adopted a low or zero dilatancy angle in the analysis of masonry walls, and van Zijl [16] showed that the dilatant response decays with shear slip and confinement,

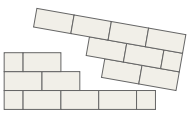
so that its contribution vanishes at the deformation levels reached in pier and wall behaviour. Obtained here for an independent specimen typology and through two coupling formulations, the present result supports the same position, that a near-zero dilatancy angle is adequate at the pier scale.

The two formulations characterise complementary aspects of the dilatancy parametrisation. The lower-bound formulation tests post-peak mechanism stability through the trade-off between ϕ and ψ, while the upper-bound formulation tests the peak strength contribution of dilatancy at constant ϕ. The bracketing of the response between the two formulations serves as an investigation into the coupling of the two parameters, and the convergence on $\psi = 1°$ indicates that the choice of coupling is irrelevant when the dilatancy contribution itself is small.

The displacement-at-peak offset, which is persistent in both formulations, is not addressed by the parameter variation reported here. Cohesion, elastic stiffness, or loading rate are candidate calibration parameters for further investigation. A practical implication of these findings concerns the calibration of the dilatancy parameter when direct shear characterisation of the unit-mortar interface reports only peak strength without a residual branch. In this case, the friction and dilation angles derived from the test should be interpreted as peak values and not extrapolated into the post-peak regime. The residual response should instead be calibrated separately, either by prescribing a conservative residual friction angle and a dilatancy decay towards zero with accumulated slip, or by matching the post-peak force-displacement degradation to a component-level benchmark such as the one reported here. Either approach prevents the model from spuriously sustaining capacity after damage localisation.

6.2.6. Mesh objectivity

This subsection examines the mesh objectivity of the MASON contact model by performing a discretisation sensitivity study for the HIGH pre-compression case (σ_n =2.12 MPa). The HIGH configuration is selected because the experimental response activates a mixed failure mode in which a stair-stepped crack occurs with splitting through the bricks and localised compressive damage at the loaded toe, thereby providing a more demanding test for the discretisation than the joint-dominated regime observed at LOW pre-compression. The assessment is conducted using the rigid-block idealisation, as shown in the preceding comparison, which retains the governing local mechanisms while exhibiting only weak sensitivity to block deformability and offers substantially superior computational efficiency. The objective is to verify that the predicted force-displacement response and damage localisation are not unduly dependent on the adopted density of contact-point discretisation. The contact-point discretisation is controlled by the target edge length specified for the triangulation of each block face. Each face is subdivided into triangular sub-facets whose edges do not exceed the specified length, and the vertices of the sub-facets define the contact points used by the contact formulation. Because the triangulation is unstructured, the realised edge lengths vary across a face, so the specified value acts as an upper bound rather than a uniform spacing. This target edge length was varied over the range 0.005 m to 0.15 m in 60 linearly spaced increments, to evaluate the sensitivity of the force-displacement response and damage localisation to the contact-point density.



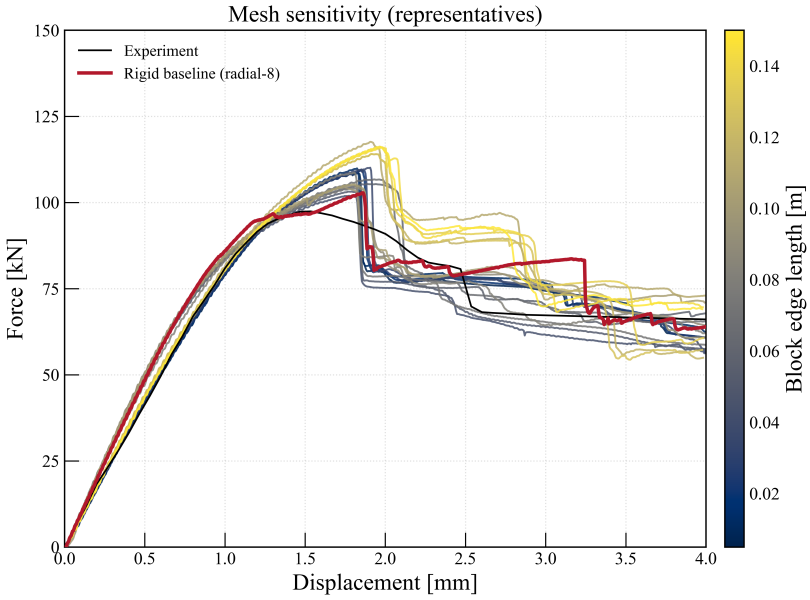


Figure 6.16. Force-displacement responses of the parametric study on mesh sensitivity with rigid-block model

Figure 6.16 summarises the mesh objectivity assessment for the rigid model with the HIGH pre-compression case. Twenty representative force-displacement responses, sampled from the 60 edge-length variations and coloured by block edge length, are shown together with the experimental curve and the radial-8 rigid baseline. Up to the peak load, the global response is weakly sensitive to the contact-point density. The representative responses remain closely grouped along the pre-peak branch and follow the experimental curve, with the radial-8 baseline coinciding within this group. The peak load is reproduced within a narrow range that lies slightly above the experimental value, with the radial-8 baseline near its lower edge and close to the experimental peak. The mesh sensitivity manifests after the peak. The onset displacement and magnitude of the step-like capacity drop, and the level of the subsequent residual, show greater scatter across the edge-length variations. This scatter originates from the discrete failure process, in which each step-like drop corresponds to crack opening and the redistribution of force among the contact points. The order in which individual subcontacts fail and shed load depends on the contact-point layout, so a change in edge length reorders these events and shifts the post-peak branch without altering the overall capacity. The scatter carries a mild systematic component, with the coarser discretisations sustaining marginally higher post-peak force.

Figure 6.17 complements the force-displacement comparison by visualising the joint-plane damage scalar (d_{ts}) at the end of the monotonic loading for six representative average mesh edge lengths. Across the full range $\bar{h} = 0.005$–0.150 m, the dominant failure mechanism is stable as the damage localises into a stepped diagonal band that traverses

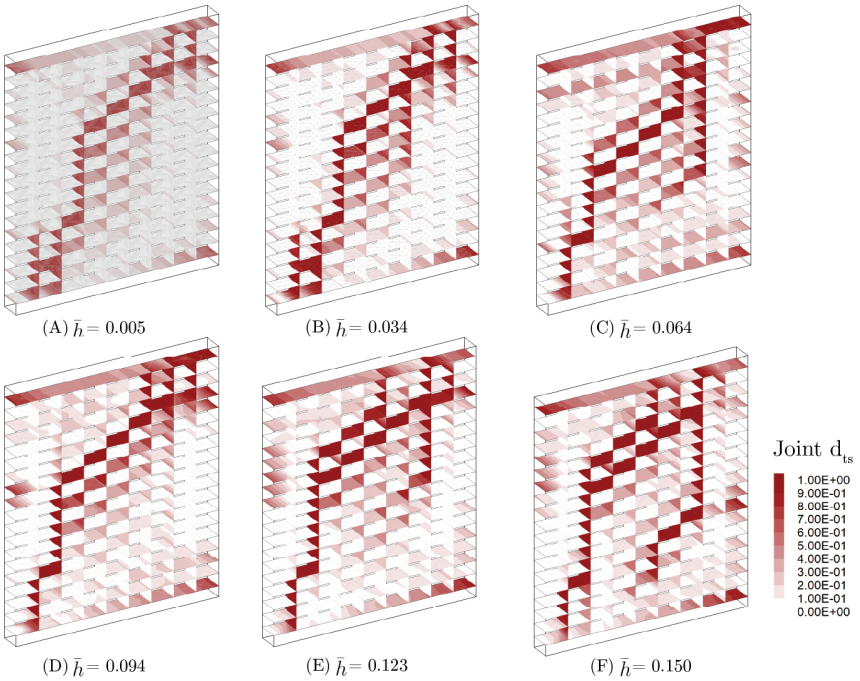


Figure 6.17. Combined shear-tension damage field d_{ts} at the end of the analysis for the HIGH case with mesh size variation ($\bar{h}$ =0.005 m to 0.15 m)

the wall panel and connects to boundary regions, consistent with shear sliding and opening along the bed and head joints. The mesh size primarily affects the spatial resolution of the damage localisation and does not alter the governing failure mode or the position of the main diagonal crack band.

Re-expressing the mesh parametric analysis in terms of normalised scalar response measures gives a clearer view of the mesh objectivity. Figure 6.18 reports the initial secant stiffness K_0, the peak force F_{peak}, and the dissipated work $W_{0\to4}$ across the parameter range. The initial secant stiffness is computed at a lateral displacement of 0.1 mm, which lies within the linear-elastic regime and avoids deviations due to the onset of tensile damage that would alter the apparent slope. Across the full range of average edge lengths, the numerical K_0 predictions fall within ±15% of the experimental baseline. The scatter shows no systematic trend with the discretisation density, which identifies it as realisation noise associated with the contact-point layout.

The peak force F_{peak} exhibits a similarly tight clustering around the experimental value across the parameter range. The dissipated work $W_{0\to4}$, by contrast, shows the greatest and most systematic sensitivity, with a consistent increase from fine to coarse discretisation, showing that energy-related quantities are more affected by how the discretisation regularises post-peak cracking and load redistribution. These results suggest that the mesh discretisation can be selected primarily for computational

efficiency when the objective is to match K_0 and F_{peak}. The energy dissipation and residual softening characteristics are comparatively less mesh-objective and require further calibration. These characteristics are path-dependent quantities assembled from the sequence of discrete cracking and sliding events at the individual contact points. The contact-point layout fixes the order and location of these events, and a change in average edge length reorders them, which shifts the softening path and the integrated work while leaving the capacity unchanged.

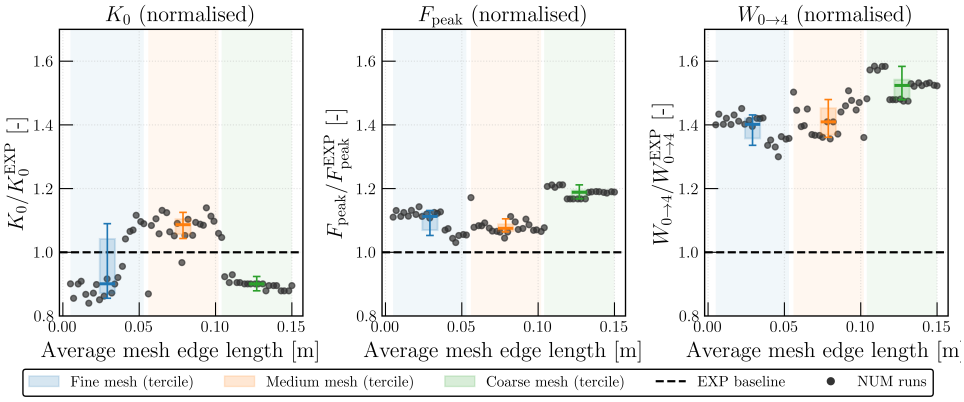


Figure 6.18. Mesh sensitivity metrics

The influence of the contact-point density on the explicit time integration is examined in Figure 6.19. The left panel reports the critical timestep for the undamaged state at the start of the analysis and for the damaged state at the end. At the start, the timestep is independent of the average edge length, with a spread of 0.19 % across the range. This is consistent with the per-area contact formulation, under which the integrated contact stiffness acting on a block is independent of the number of subcontacts into which the joint is divided, so the critical timestep does not change as the contact points are refined. At the end of analysis, the timestep is on average 10.9 % larger, with a spread of 4.48 %. The increase is caused by the softening of the contacts, which reduces the stiffness and lengthens the stable timestep. The spread is wider because the timestep is now set by the contacts that have softened least, and both the residual stiffness of the contacts and their location in the wall depend on the damage pattern, which slightly differs between contact-point layouts. The timestep therefore does not decrease under refinement, and the number of integration steps required to complete the analysis is constant across the discretisation range.

The right panel reports the total kernel time normalised to its value at the coarsest discretisation ($\bar{h} = 0.150\,\text{m}$), for which the absolute kernel time is 0.217 h. The cost rises non-linearly as the mesh is refined. Refinement below $\bar{h} \approx 0.02\,\text{m}$ produces a disproportionate increase, with the finest discretisation reaching 7.13 times the cost of the coarsest and $\bar{h} = 0.007\,\text{m}$ reaching 2.68 times. For discretisations above $\bar{h} \approx 0.04\,\text{m}$ the normalised kernel time approaches unity, indicating diminishing reductions from further coarsening. Since the timestep is invariant under refinement, the cost increase is

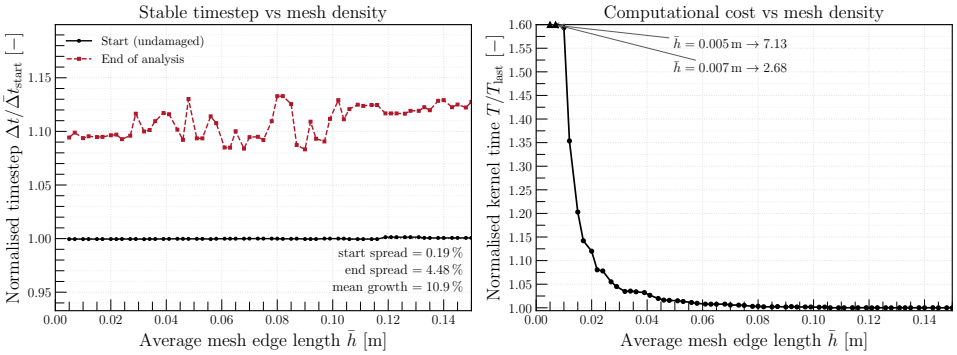


Figure 6.19. Influence of the contact-point density on the explicit time integration. Left: critical timestep Δt normalised to the mean undamaged value $\overline{\Delta t}_{\text{start}}$, for the undamaged state at the start of the analysis and the damaged state at the end. Right: total kernel time T normalised to its value at the coarsest discretisation T_{last} ($\bar{h} = 0.150\,\text{m}$).

attributable to the number of subcontacts processed at each step, which grows with the contact-point density, and not to a reduction in the timestep.

Overall, the mesh sensitivity analysis confirms that the MASON contact model is mesh-objective for the global capacity measures in this benchmark. Global pre-peak metrics such as secant stiffness and peak force are weakly mesh-dependent across the tested range, as shown in Figure 6.16. The clearest discretisation effect is on the dissipated work $W_{0\rightarrow 4}$ and, by implication, on how damage localises and redistributes post-peak (Figure 6.17). Mesh density influences how the model expends work more than it influences the peak resistance it develops. Therefore, for subsequent parametric studies, a mid-range mesh (medium tercile: $\bar{h} \in [0.05\,\text{m}, 0.1\,\text{m}]$) can be justified as a computational cost-accuracy compromise, while post-peak ductility and energy dissipation remain more mesh-dependent and should therefore be interpreted cautiously.

6.2.7. Computational timestep objectivity

Leveraging the rigid-block configuration and the HIGH pre-compression benchmark, this subsection assesses the timestep objectivity of the MASON contact model. The stable explicit timestep is first estimated from the Courant–Friedrichs–Lewy (CFL) condition (see Equation (3.20)), yielding $\Delta t_{\text{crit}} = 7.72 \times 10^{-6}\,\text{s}$ for the benchmark model (Table 6.3). A 20-point linearly spaced parametric analysis is then conducted by varying Δt between 10 % and 100 % of Δt_{crit}. The aim is to verify that reducing the timestep below the CFL-based limit does not introduce systematic changes in the predicted response, since numerical stability is already guaranteed by the CFL criterion.

To minimise confounding numerical effects, the timestep parametric analysis is conducted under deliberately conservative settings for the remaining computational controls. In particular, the contact-point density is refined to an average edge length of $\bar{h} = 0.01\,\text{m}$ and the imposed lateral loading rate is reduced to $1\,\text{mm}\,\text{s}^{-1}$, in contrast to the

rigid-block baseline of Section 6.2.4 (radial-8 subdivision and 5 mm s^{-1}). These choices ensure that any observed variation in the force-displacement response can be attributed primarily to the prescribed timestep, not to discretisation density or rate-dependent numerical effects.

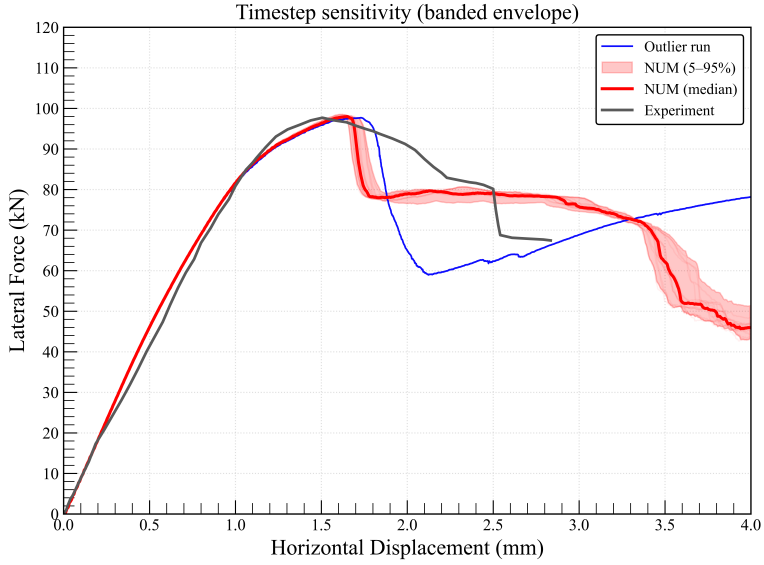


Figure 6.20. Force-displacement curves with the NUM 5 % to 90 % envelope and median overlaid with the experiment.

Figure 6.20 summarises the timestep sensitivity parametric analysis through the force-displacement curve and the 5% to 90% percentile envelope across the 20 sampled timesteps, benchmarked against the experimental force-displacement response of the HIGH specimen, with the single outlier omitted. Across the considered range of Δt (expressed as a fraction of Δt_{crit}), the pre-peak branch and peak strength remain tightly clustered as the median curve tracks the experimental backbone up to the onset of peak softening, and the 5% to 90% band stays narrow in this regime. The dominant timestep sensitivity manifests primarily in the post-peak response. An outlier follows the group up to (and slightly beyond) the peak, but then deviates from the envelope immediately after the peak by undergoing an abrupt strength drop, followed by steady stiffness recovery (re-hardening) beyond 2.25 mm displacement.

Figure 6.20 and the corresponding joint-plane damage fields in Figure 6.21 jointly indicate that the governing failure mechanism is largely timestep-objective over the investigated range. From Δt_{crit} down to 40%Δt_{crit} (Figure 6.21A to Figure 6.21D), the damage topology is essentially unchanged, where a dominant diagonal cracking band develops across the panel, accompanied by localised participation of the bed joints in the lower-left compressed toe, consistent with the narrow pre-peak envelope in Figure 6.20. Further timestep reduction to 20 % and 15 %Δt_{crit} (Figure 6.21E to Figure 6.21F) does not introduce a spurious change in failure mechanism. Instead, it primarily increases the

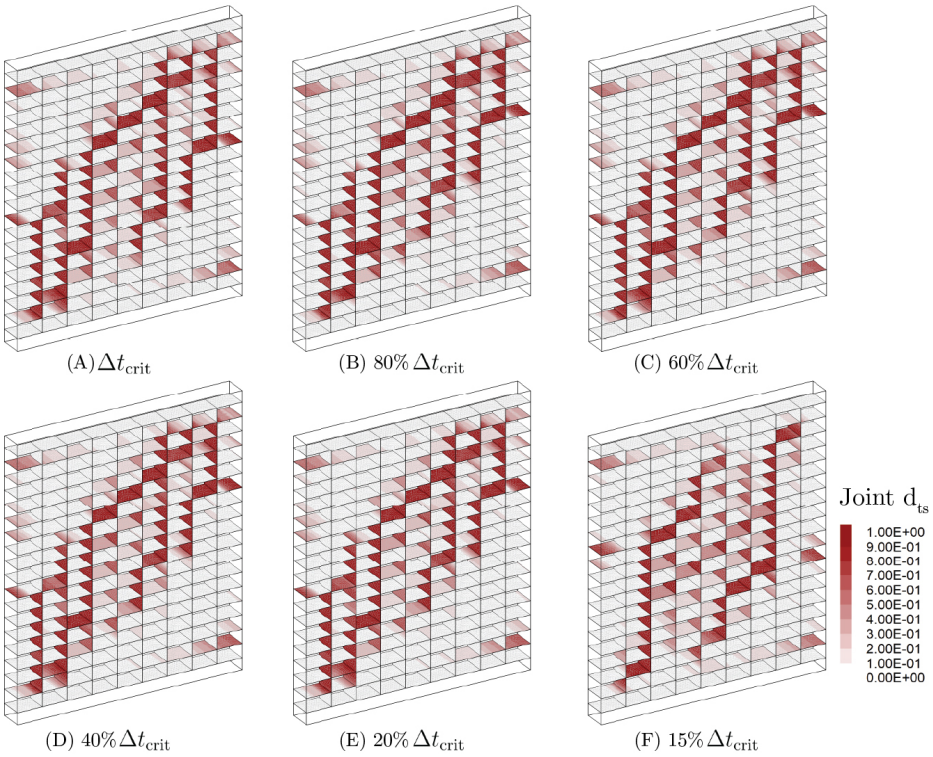


Figure 6.21. Combined shear-tension damage field d_{ts} at the end of analysis for the HIGH case with timestep parametric analysis.

dispersion of moderate joint damage and slightly perturbs the continuity/intensity of the diagonal crack band.

Across the timestep configurations considered, a single run at $\Delta t = 15\% \Delta t_{crit}$ is identified as an outlier and is excluded from the percentile band reported in Figure 6.20. The pre-peak and peak responses agree closely with the band, while the post-peak branch exhibits a sharper capacity drop followed by a gradual recovery that is not reproduced at any neighbouring timestep. A possible explanation is that the explicit DEM scheme at this reduced timestep resolves contact opening and closing, stick-slip transitions, and recontact events with a different temporal ordering than for larger timesteps. In the post-peak regime, where the response is governed by non-smooth friction-damage evolution, small changes in event sequencing can shift the locations at which damage and sliding concentrate. This produces a slightly different failure mechanism and a divergent softening-hardening branch in the force-displacement curve (Figure 6.20). The divergent run is excluded from the percentile band reported in Figure 6.20 on the basis of this single observation, and the consistency of the result across repeated runs has not been verified within the present study. This represents a limitation of the sensitivity assessment at the lower end of the timestep range and is identified as a target for further

investigation.

Overall, the timestep variation indicates an effectively objective global response when Δt is kept close to the stability limit, as reflected by the clustered pre-peak curves and the consistent diagonal damage pattern. The most pronounced deviation occurs at $15\,\%\Delta t_{\text{crit}}$ and is attributed to numerical effects. Reducing Δt resolves contact opening and closing and stick-slip transitions more finely, which can perturb post-peak event sequencing and localisation. In addition, fixing Δt to a single conservative value prevents the timestep from increasing as contacts soften, thereby sustaining high-frequency contact chatter and allowing small differences in contact states to accumulate and influence the force–displacement response.

6.3. Component-level validation under cyclic in-plane loading

In this section, the MASON contact model is validated using four single-wythe calcium silicate (CS) masonry walls subjected to compression and cyclic in-plane lateral load, as part of the experimental campaign conducted by Messali *et al.* [2]. For this validation, a rigid-block idealisation is adopted to enable an efficient exploration of cyclic response while retaining the key discontinuum mechanisms governed by the joint behaviour. The test matrix was designed to isolate the effects of boundary restraint and aspect ratio. Two wall geometries, squat and slender, were evaluated under both cantilever and double-clamped end conditions, yielding four representative specimens. The assessment draws on both global responses (force–displacement hysteresis and energy dissipated per cycle) and local responses, specifically the evolution of crack patterns.

6.3.1. Experimental description

The experimental configuration of the reference case is summarised in Figure 6.22. A constant vertical pre-compression was imposed as a uniform pressure via four actuators acting on the top steel beam, whereas the in-plane cyclic action was applied in displacement control by a single actuator at the wall top. To suppress sliding and premature tensile cracking at the steel-masonry interface, the uppermost and lowermost beams were restrained by a dedicated steel frame, as shown in the A-A' section in Figure 6.22B. The test programme comprised two restraint configurations, cantilever and double-clamped, with distinct control strategies for the vertical actuators. In the cantilever tests, the vertical load was kept constant in each actuator pair (V_E and V_W in Figure 6.22A) such that the measured forces on the east and west sides remained balanced (i.e., $V_E = V_W$). This ensures symmetric pre-compression at the top steel beam.

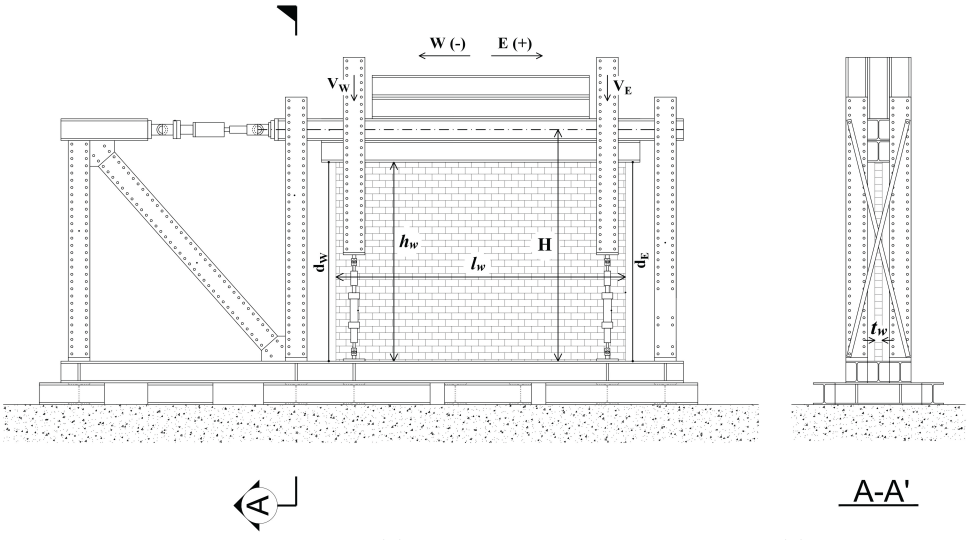
In the double-clamped tests, the vertical actuators were operated under a mixed force-displacement scheme. This control mode continuously adjusted the actuator commands so that the resultant vertical load along the wall remained constant ($V_E + V_W = \text{const.}$) and the top beam was prevented from tilting by enforcing equal vertical displacements at its ends. For the double-clamped walls, the inflection point (i.e., the point at zero bending moment) was assumed at mid-height. Although this assumption does not hold throughout the entire loading history, the inflection-point heights measured at the peak displacement of each cycle are close to mid-height on average for both the slender and squat walls [2].

Table 6.7 summarises the geometry, boundary conditions, pre-compression, and observed failure modes of the four representative specimens. The effective height h_{w0} that defines the shear ratio h_{w0}/l_w is listed for each specimen, equal to half the wall height for the double-clamped specimens and to the height of the load application point for the cantilever specimens. The slender rocking-dominated walls and the squat shear-dominated walls together provide a targeted set for examining the cyclic performance of the MASON contact model across the response regimes.

Table 6.7. Geometrical properties of validated wall specimens (Messali et al. [2])

Specimen name	Dimensions [m] $l_w \times h_w \times t_w$	Effective height h_{w0} [m]	Shear ratio	Boundary conditions	σ_n [MPa]	Failure mode
TUD-COMP-0a	1.1 × 2.76 × 0.102	1.38	1.25	Double clamped	0.70	Rocking–sliding
TUD-COMP-1	1.1 × 2.76 × 0.102	3.19	2.90	Cantilever	0.70	Rocking
TUD-COMP-4	4.0 × 2.76 × 0.102	1.38	0.35	Double clamped	0.50	Diagonal shear
TUD-COMP-6	4.0 × 2.76 × 0.102	3.19	0.80	Cantilever	0.50	Diagonal shear + crushing

A single, consistent set of material parameters was adopted for all validated specimens and is reported in Table 6.8. The unit-level elastic properties (Young's modulus, Poisson's ratio, and density), together with the mortar and masonry compressive strengths, were taken from the material characterisation tests performed prior to the quasi-static wall tests (see Esposito *et al.* [17]). Each calcium silicate unit had nominal dimensions



(A) Front-view (B) Cross-section View

Figure 6.22. Experimental setup of the in-plane test on CS masonry wall [2]

of 210 × 71 × 102 mm (L x H x t), giving a unit height $h_{\text{brick}} = 71$ mm and a thickness equal to the 102 mm wall thickness. The bed and head joints were 10 mm thick (h_{joint}). Parameters not measured in the campaign, such as the compression peak ratio n, were estimated from the empirical relations of Jafari *et al.* [18], providing the basis for its value. The normal and shear interface stiffnesses follow the homogenised expression in Equation (5.1), evaluated with the Young's moduli of the unit and the mortar. The rigid blocks carry no deformation, so these stiffnesses are then adjusted to lump the compliance of the units into the joints, since the global stiffness would otherwise be overestimated. Subsequent validation is therefore assessed using response features that are not directly targeted during fitting, including hysteresis pinching, cycle-by-cycle energy dissipation, and crack-pattern evolution.

6.3.2. Numerical modelling setup

The brick discretisation adopted in the representative models, namely the slender, double-clamped specimen TUD-COMP-0a and the squat, cantilever specimen TUD-COMP-6, is shown in Figure 6.23A and Figure 6.23B, respectively. The colouring of the brick units is provided for visualisation only and does not imply any spatial variation of material properties. Consistent with the experimental arrangements, both the top and bottom beams are clamped in the double-clamped configuration (grey elements), whereas only the bottom beam is clamped in the cantilever configuration. In all cases, the assemblage is free to translate vertically such that the prescribed pre-compression is maintained throughout the loading protocol. In the numerical model, loads and supports are applied via stiff auxiliary blocks that are perfectly connected to the masonry units, thereby minimising interface compliance. Masonry units are modelled as rigid blocks with potential crack planes at mid-length to enable intra-unit discontinuities when required by the simulated failure mechanism.

For the walls with cantilever configuration (TUD-COMP-1 and TUD-COMP-6), the in-plane rotation of the top block is freed, and the block height is extended up to the point where zero moment is observed according to the wall shear ratio reported in Table 6.7. This ensures the applied in-plane load imposes the correct moment at the wall base. For the walls with a double-clamped configuration (TUD-COMP-0a and TUD-COMP-4), the in-plane rotation of the top block is fixed, and its height is set to that of the bottom block, since the location of the applied load is irrelevant in this configuration.

The model is first brought to equilibrium under gravity, and the pre-compression load is then applied via surface forces on the top surface of the top beam. The equilibrium under an explicit integration scheme is quantified by the ratio of the residual out-of-balance force components to the total forces applied at each node. In this validation, the equilibrium is assumed to be reached when that ratio is less than 1×10^{-5}. Local numerical damping is used throughout the simulations, with the damping factor α set to 0.8 by default.

To minimise the inertial overshoot during load reversal, the cyclic load is applied as a sequence of load pulses. The cosine-plateau-cosine velocity history is mathematically defined in Equation (6.2), which concentrates the entire prescribed displacement u_{apv}, within the time span of $t_{\text{tot}} = 2t_a + t_b$.

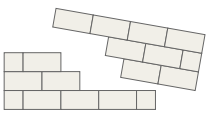
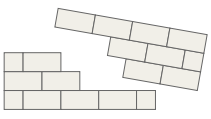


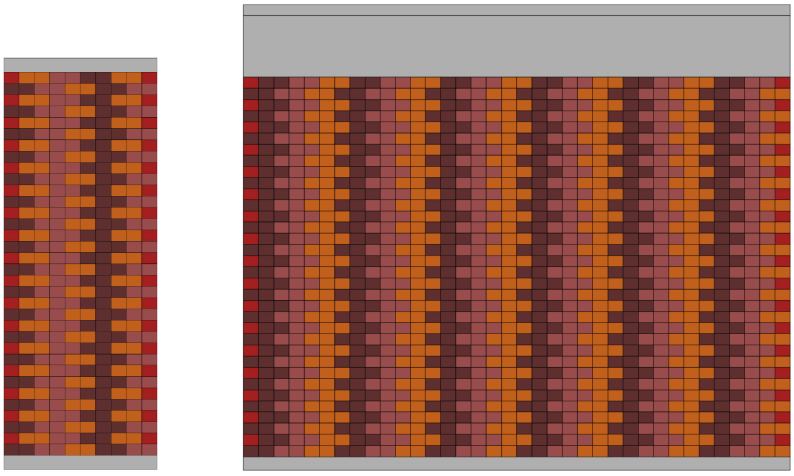
Table 6.8. Material properties of the calcium silicate masonry walls

Properties	Symbol	Unit	Value	
Unit properties				
Density	ρ	$\mathrm{kg\,m^{-3}}$	1800	
Interface properties			Bed joint	Head joint
Masonry modulus of elasticity[a]	E	MPa	3170	3170
Mortar modulus of elasticity[b]	E_m	MPa	1970	
Normal stiffness[c]	k^n	$\mathrm{GPa\,m^{-1}}$	52.2	52.2
Shear stiffness[c]	k^s	$\mathrm{GPa\,m^{-1}}$	22.5	22.5
Tensile strength[c]	f_t	MPa	0.105	0.035
Cohesive strength[c]	c_0	MPa	0.14	0.014
Friction angle[a]	ϕ_{cv}	[°]	25	
Mode-I fracture energy[a]	G_I	$\mathrm{N\,m^{-1}}$	8.38	3.88
Mode-II fracture energy[a]	G_{II}	$\mathrm{N\,m^{-1}}$	83.8	38.8
Compressive strength[a]	f_c	MPa	5.93	7.0
Compressive fracture energy[a]	G_c	$\mathrm{N\,m^{-1}}$	15 000	31 500
Peak ratio[c]	n	[-]	7.5	
Cap parameters	C_n, C_{nn}, C_{ss}	[-]	0.0,1.0,12.0	

[a] Values obtained from material characterisation tests in Esposito, et al. [17]
[b] Values derived from equations reported in Jafari et al. [11]
[c] Evidence-backed input parameters

$$V(t) = \begin{cases} \dfrac{v_{\max}}{2}\left[1-\cos\left(\dfrac{\pi t}{t_a}\right)\right], & 0 \le t < t_a, \\ v_{\max}, & t_a \le t < t_a + t_b, \\ \dfrac{v_{\max}}{2}\left[1+\cos\left(\pi(t-t_a-t_b)/t_a\right)\right], & t_a + t_b \le t < t_{tot}, \\ 0, & t \ge t_{tot} \end{cases} \tag{6.2}$$





(A) TUD-COMP-0a (B) TUD-COMP-6

Figure 6.23. Representative model of the CS wall in *3DEC*

where $t_a = 0.5 d_d$, $t_b = d_d * \kappa$, κ is the dimensionless parameter that defines how long the constant-velocity plateau should last compared to the cosine ramp up and down, and d_d is the ramp duration correlated to the prescribed displacement u_{apv}, maximum velocity v_{max}, and plateau factor κ, as defined in Equation (6.3). In the main analyses, the applied loading velocity is set to 2.5 mm s^{-1} and the plateau factor to 20 %. The sensitivity to the loading velocity is examined in Section 6.3.6.

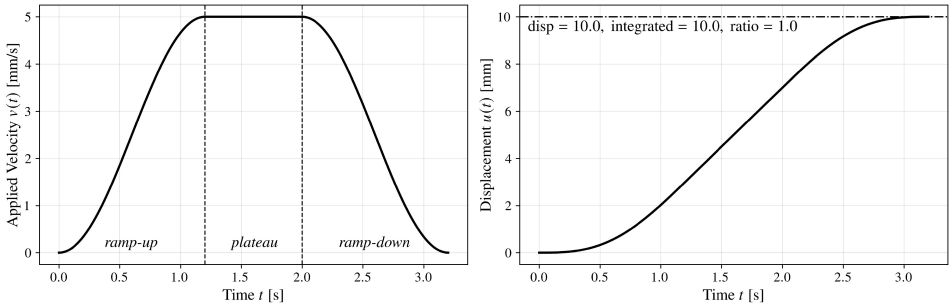
$$d_d = \frac{u_{apv}}{v_{max}(0.5+\kappa)} \tag{6.3}$$

For illustration, the impulse velocity in Equation (6.2) is shown in Figure 6.24 for a target displacement of 10 mm, a maximum velocity of 5 mm s^{-1} and a mechanical timestep of 1×10^{-6} s. Figure 6.24A shows the imposed velocity $v(t)$: a half-cosine ramp-up, a constant velocity plateau set at 5 mm s^{-1}, and a half-cosine ramp-down to zero (dashed lines mark the transitions). The displacement in Figure 6.24B is obtained as the time integral of the prescribed velocity,

$$u_{tar} = \int_0^{2t_a+t_b} v(t)\,\mathrm{d}t = v_{max}(t_a + t_b), \tag{6.4}$$

where u_{tar} is the target prescribed displacement. It can be seen that the resulting displacement in u_{tar} matches the target prescribed displacement of 10 mm.

This profile is suitable for cyclic loading in the explicit scheme. The smooth ramps at each reversal limit the artificial stress waves and dynamic amplification that an abruptly applied velocity would generate, while the constant-velocity plateau between them efficiently advances the displacement. The plateau velocity is set low enough that the kinetic energy remains negligible relative to the system's internal energy, so the analysis



(A) Velocity profile with v_{max} = 5 mm/s (B) Prescribed displacement results

Figure 6.24. Imposed actuator velocity profile $v(t)$ with v_{max} of 5 mm s^{-1} and the resulting displacement.

remains quasi-static, and the recorded hysteresis reflects the masonry nonlinearity rather than inertial effects.

6.3.3. Numerical results: global and local behaviours

This subsection assesses the MASON contact model against the component-scale experimental campaign by comparing global response and local damage development under cyclic loading. The evaluation examines how well the simulations reproduce the measured force-deformation response and the progression of the degradation phenomenon, with particular attention to stiffness and strength evolution and the resulting energy dissipation across the investigated wall typologies.

Global response – Force-displacement curve and hysteresis performance

The lateral force-wall drift responses of the four specimens predicted by the MASON contact model are compared with the experimental measurements in Figure 6.25. For the slender cases, the TUD-COMP-0a (Figure 6.25A) model predicted a symmetric response between the positive and negative loading cycles, reproducing the peak resistance of 28 kN and the softened post-peak trend. At wall drifts exceeding ±0.5%, the numerical loops become more pinched than the experimental hysteresis.

For TUD-COMP-1 (Figure 6.25B), the model overpredicts the peak lateral force, reaching 12.5 kN relative to 10 kN in the experiment, corresponding to a 25 % overestimation. The simulated hysteresis also shows stronger pinching. This behaviour is consistent with a response that remains rocking-dominated for longer, while the onset of sliding and shear-compression mechanisms is delayed relative to the tests, thereby diminishing re-closure forces and accentuating hysteresis pinching. It should also be noted that a single interface parameter set is adopted for all four walls, avoiding specimen-specific calibration at the expense of scatter in peak strength and loop shape, particularly for the TUD-COMP-1 model. Furthermore, Messali *et al.* [2] similarly reported difficulties in reproducing TUD-COMP-1 in preliminary numerical studies, highlighting the sensitivity of this configuration.

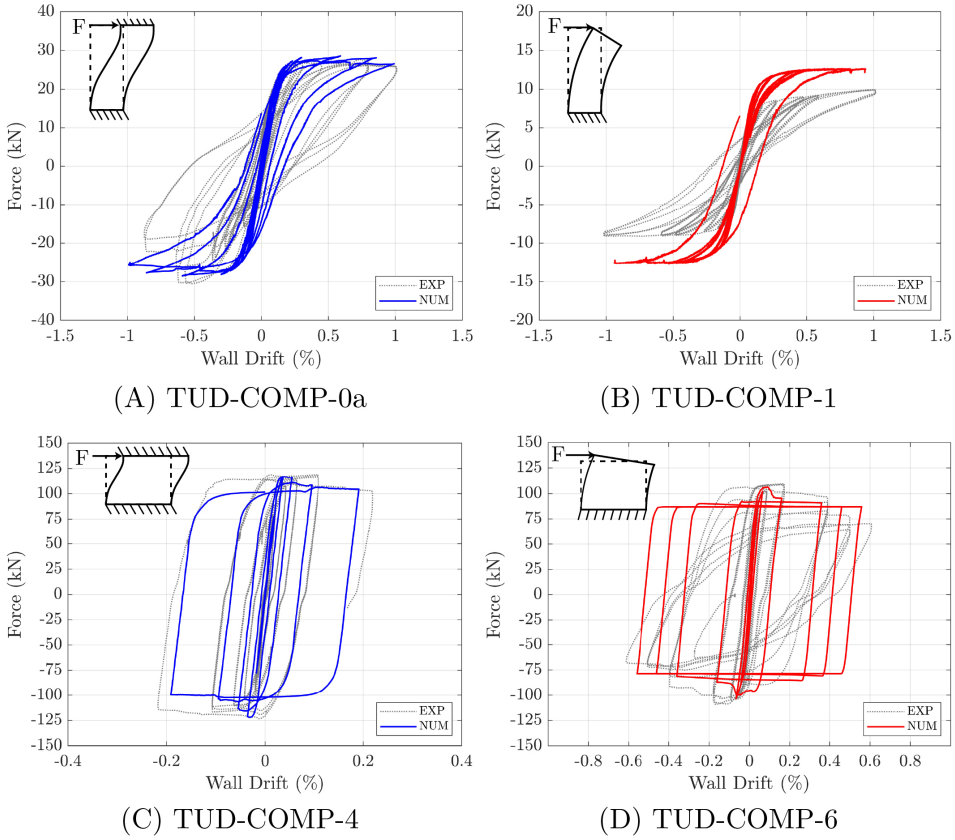


Figure 6.25. Cyclic force-displacement response of the four validated calcium silicate masonry specimens. (A) TUD-COMP-0a, slender double-clamped wall ($h_w/l_w = 2.51$); (B) TUD-COMP-1, slender cantilever wall ($h_w/l_w = 2.51$); (C) TUD-COMP-4, squat double-clamped wall ($h_w/l_w = 0.69$); (D) TUD-COMP-6, squat cantilever wall ($h_w/l_w = 0.69$). Each panel plots the horizontal force against the wall drift and compares the experimental response (EXP, grey dotted; Messali *et al.* [2]) with the numerical prediction (NUM, solid). The inset shows the boundary condition and the direction of the applied load F.

Despite these differences, both slender specimens exhibit early-cycle rocking, evidenced by the near-complete return to the origin in the initial cycles and thus negligible residual drift. With increasing imposed displacement, horizontal sliding along the bed-joint interface becomes progressively mobilised, producing larger residual deformations that are captured by the simulations.

For the squat specimens, the comparison also clarifies how well the model captures the shear-governed cyclic response at increasing drift demand. In TUD-COMP-4 (Figure 6.25C), the double-clamped boundary condition promotes a pronounced

shear-compression load path, and the simulation reflects this through the close agreement in initial stiffness and peak strength. The slightly steeper post-peak drop indicates that the numerical formulation mobilised a faster reduction in shear transfer mechanism after damage localisation than the experimentally observed response, suggesting a more abrupt loss of cohesion and frictional resistance once the governing damage zone forms.

For the cantilever squat wall TUD-COMP-6 (Figure 6.25D), the experiments revealed multiple diagonal cracks and a more distributed pattern of shear damage. The model reproduces the peak capacity with reasonable accuracy, but the hysteresis loops are more plastified than in the tests. This response is consistent with repeated sliding along the damaged interfaces and sustained mobilisation of the frictional resistance. In the model, the loops recover with reduced stiffness at each reversal because a larger fraction of the damaged contacts remains closed and in frictional sliding rather than opening and reclosing. The resisting force is therefore sustained near the reversal, so the pinching observed in the test is underrepresented.

Overall, both squat configurations exhibit the expected features of shear-dominated cyclic behaviour in the simulations, including larger loops, progressive degradation at larger drifts, and an approximately symmetric response between loading directions. Together with the slender-wall results, these findings support the robustness of the proposed interface-shear formulation across aspect ratios and boundary conditions, while indicating that the remaining differences concern the rate of post-peak degradation and the extent of stiffness recovery during load reversals.

Figure 6.26 presents the cycle-by-cycle dissipated energy from the experiments (orange) and the corresponding numerical predictions (blue) for the four benchmark walls. Only cycles that display a clear hysteretic loop in the experimental response are included. For the slender specimens, TUD-COMP-0a and TUD-COMP-1 (Figure 6.26A and Figure 6.26B, respectively), the dissipated energy remains low, staying below 1 kN m, which is consistent with a response dominated by rocking and with sliding confined to the later loading cycles. The simulations capture the increase in dissipated energy with drift, with a slight overestimation in the final two cycles, in line with the differences in loop shape observed in the force-drift curves (Figure 6.25A and Figure 6.25B).

A markedly different response is obtained for the squat specimens. For TUD-COMP-4 (Figure 6.26C), the onset of diagonal cracking is accompanied by a pronounced increase in dissipated energy, reaching approximately 1.8 kN m in the final cycle. The simulation reproduces both the magnitude and the progression of this increase, with cycle-by-cycle values closely aligned to the experimental measurements and only a minor overestimation in the last cycle. An even stronger effect is observed in TUD-COMP-6 (Figure 6.26D), where shear-dominated response combined with crushing along the wall diagonals produces a peak dissipation of about 7 kN m at cycle 9, followed by a modest reduction as degradation develops. The model captures the rapid build-up and subsequent decline, but underpredicts the single cycle with maximum dissipation, consistent with the abrupt unloading evident in the corresponding force-drift response (Figure 6.25D).

Overall, the results indicate that the MASON contact model reproduces the experimentally observed global hysteretic response across the range of wall aspect

ratios investigated. The simulations capture the stepwise evolution of strength and the progressive increase in dissipated energy as damage accumulates and localises. While cycle-level differences persist, the numerical backbones and degradation patterns remain broadly consistent with the measurements, supporting the use of the model for system-level assessment of masonry wall response under cyclic loading.

Local response – Crack patterns

Figure 6.27 compares the experimentally mapped cracks at the end of the test with the numerically predicted joint tensile–shear damage scalar d_{ts} (Equation (4.9)) for the slender specimens. For TUD-COMP-0a (Figure 6.27A), the experiment developed symmetric rocking hinges at the top and bottom corners, expressed as stepped cracking along the bed and head joints. The simulation reproduces this mechanism, with d_{ts} concentrating in stepwise bands at the same corners, consistent with uplift-induced tensile damage as the compression toe shifts during cyclic loading. Complete degradation of the top and bottom bed joints is also predicted in association with hinge formation.

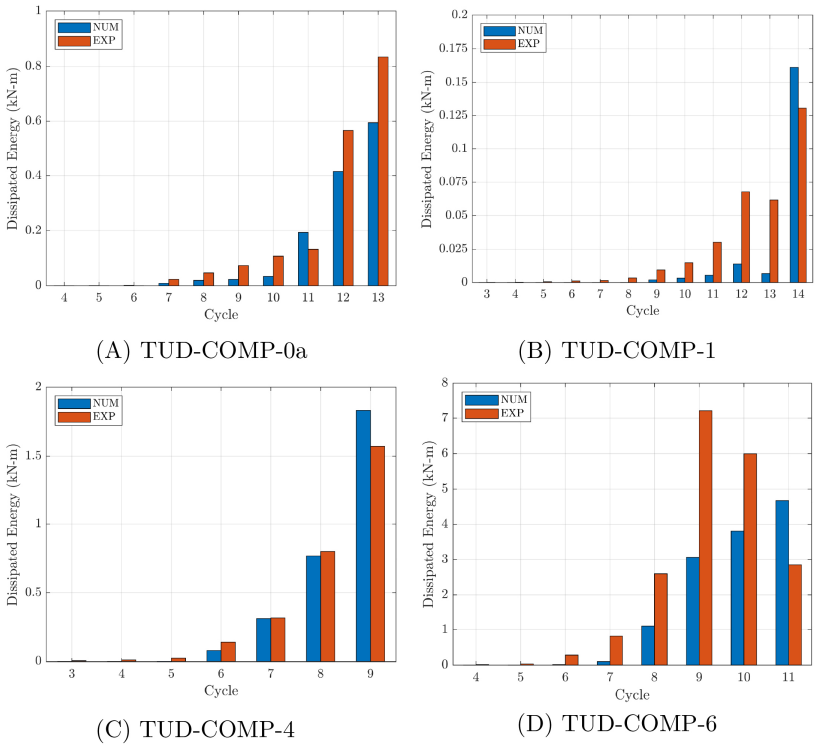


Figure 6.26. Dissipated energy for the four specimens of Figure 6.25, with the same aspect ratios and boundary conditions. Each panel compares the dissipated energy from the experiment (EXP) and the numerical model (NUM) at each loading cycle. Experimental data from Messali *et al.* [2].

The compressive damage field, reported separately in Appendix B.2 for completeness because the present figure is restricted to tensile-shear damage for visual clarity, indicates localised toe crushing at the corners (Figure B.5A) consistent with the high contact stresses developed at the rocking hinges.

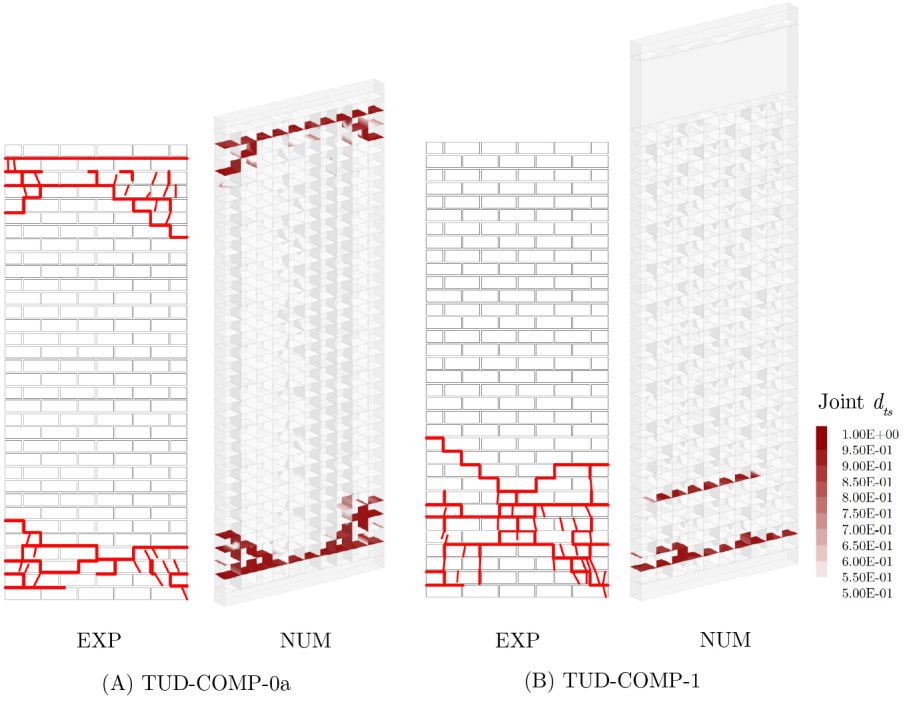
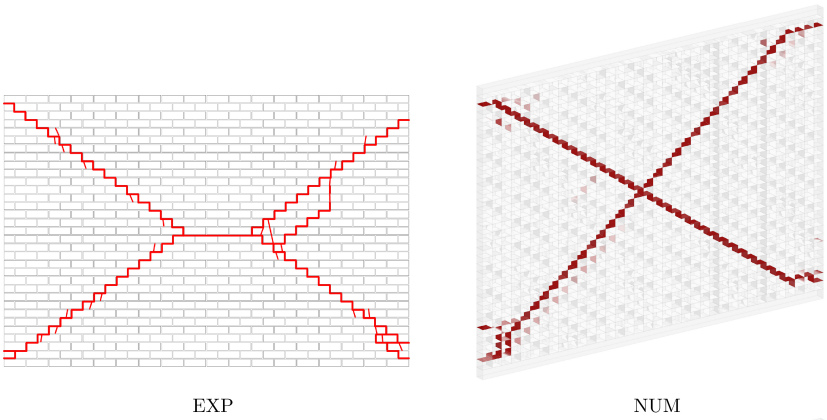


Figure 6.27. The comparison of the experimental crack pattern to the combined d_{ts} damage scalar for the slender wall cases

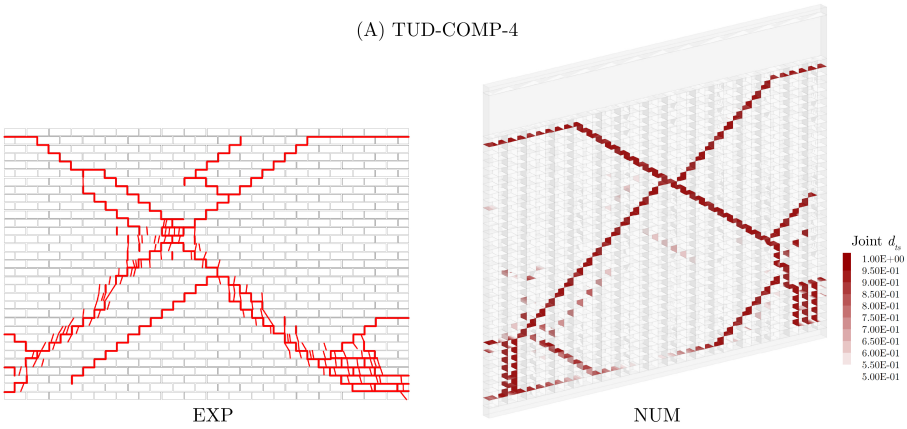
For the cantilever specimen TUD-COMP-1 (Figure 6.27B), the experiment showed a fan-shaped crack network extending from the base towards mid-height, indicating a shift from predominantly rocking to a combined rocking-sliding response as the axial load became increasingly concentrated on the compression side. The simulation reproduces the formation of a horizontal slip line along the first bed joint and its subsequent stepped tension into the next course. The model predicts fewer head-joint fractures, a difference attributed to the homogenised mechanical properties applied to the model. Despite these details, the governing mechanism is captured: a base-sliding interface accompanied by splitting within brick units and diagonal cracking concentrated near the wall corners.

The crack pattern comparison for the squat wall specimens is shown in Figure 6.28. In TUD-COMP-4 (Figure 6.28A), the experiment developed a characteristic shear mechanism, with two diagonal cracks connecting opposite corners and intersecting near mid-height. The simulation closely reproduces this arrangement, with both diagonals originating from the same corners and converging at mid-height. Local splitting of brick

units is also captured near the lower-left corner.



(A) TUD-COMP-4



(B) TUD-COMP-6

Figure 6.28. The comparison of the experimental crack pattern to the combined d_{ts} damage scalar for the squat wall cases

For the cantilever squat wall TUD-COMP-6, the experimental crack pattern (Figure 6.28B) shows multiple diagonal cracks and a distributed pattern of shear damage, accompanied by local crushing at the base and minor compression splitting along the secondary diagonal crack. The model reproduces the diagonal shear cracking through the tensile-shear damage d_{ts} and the toe crushing through the compression damage d_c, which concentrates at the base corners (Figure B.5B). It does not reproduce the compression splitting along the secondary diagonal, where the model develops only d_{ts}. This follows from the rigid-block idealisation, under which damage is confined to the joints and the units' splitting is idealised into potential crack planes, so the compressive damage localises at the bed-joint toes rather than along the diagonal. The hysteretic consequences of this difference, namely the more plastified loops and the underrepresented pinching, are discussed for Figure 6.25D above. The diagonal

compression splitting that the model omits would degrade the strut, which is consistent with the fuller loops of the numerical response.

Across the range of aspect ratios and boundary conditions considered, the MASON contact model reproduces the experimentally observed damage mechanisms with consistent fidelity. Residual discrepancies, including smoother crack paths and reduced stepwise localisation, are attributed to the homogenised mechanical properties adopted in the wall idealisation. Overall, the results support the robustness of the approach for representing damage development in unreinforced masonry walls under cyclic in-plane loading, spanning both rocking- and shear-governed responses.

6.3.4. Influence of local numerical damping on energy dissipation

This section examines the influence of local numerical damping on the energy dissipation response of the benchmark specimen TUD-COMP-0a, with the aim of confirming that the predicted behaviour is controlled by physical dissipation mechanisms instead of by algorithmic stabilisation. Because numerical damping in explicit DEM analyses is inherently problem-dependent, this verification is required to support the interpretation of the mechanical response.

Let $S(t)$ denote the set of active subcontacts considered in the energy accounting, excluding subcontacts between the boundary blocks and the masonry units. All energy quantities are reported in joules. The joint model accumulates the signed work of the mean subcontact force over each timestep; the separation into dissipated and stored energy is made in post-processing from the model-level histories. For each subcontact in $s \in S(t)$, the joint constitutive model evaluates incremental work contributions associated with normal and tangential relative motions across the interface. These terms correspond to the mechanical work of the contact reactions and are accumulated during the explicit time integration.

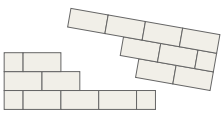
The normal tensile and compressive components are defined as:

$$E^{(s)}_{tens}(t) = \int_0^t \langle F^{(s)}_n \rangle_+ \, \mathrm{d}u^{(s)}_n, \qquad E^{(s)}_{comp}(t) = \int_0^t \langle -F^{(s)}_n \rangle_+ \, \mathrm{d}u^{(s)}_n, \tag{6.5}$$

where $F^{(s)}_n = T^{(s)}_n A^{(s)}_c$ is the normal force on subcontact s, positive in tension, $A^{(s)}_c$ its tributary area, and $\mathrm{d}u^{(s)}_n$ the normal displacement increment, positive in opening. The shear work is

$$E^{(s)}_{shear}(t) = \int_0^t \mathbf{F}^{(s)}_s \cdot \mathrm{d}\mathbf{u}^{(s)}_s, \tag{6.6}$$

where $\mathbf{F}^{(s)}_s = \mathbf{T}^{(s)}_s A^{(s)}_c$ is the shear force vector. In the implementation, the integrals are evaluated with the mean force over each timestep, and the normal work of a step is assigned to the tensile or compressive component according to the sign of that mean force. The joint model then returns the instantaneous energy components as:



$$E_{\text{tens}}(t) = \sum_{s \in \mathscr{S}(t)} E^{(s)}_{\text{tens}}(t), \tag{6.7}$$

$$E_{\text{comp}}(t) = \sum_{s \in \mathscr{S}(t)} E^{(s)}_{\text{comp}}(t), \tag{6.8}$$

$$E_{\text{shear}}(t) = \sum_{s \in \mathscr{S}(t)} E^{(s)}_{\text{shear}}(t), \tag{6.9}$$

After successive cycle peaks t_n of the loading protocol, the dissipated energy for each component is estimated as:

$$E^{\text{diss}}_{\text{tens}}(t_N) = \sum_{n=1}^{N} \left| E_{\text{tens}}(t_n) - E_{\text{tens}}(t_{n-1}) \right|, \tag{6.10}$$

$$E^{\text{diss}}_{\text{comp}}(t_N) = \sum_{n=1}^{N} \left| E_{\text{comp}}(t_n) - E_{\text{comp}}(t_{n-1}) \right|, \tag{6.11}$$

$$E^{\text{diss}}_{\text{shear}}(t_N) = \sum_{n=1}^{N} \left| E_{\text{shear}}(t_n) - E_{\text{shear}}(t_{n-1}) \right|. \tag{6.12}$$

The elastic energy stored in the joints is nearly equal at successive peaks of the symmetric protocol, so each increment approximates the energy dissipated over the half cycle; the absolute value removes the small residual of opposite sign. The components are then combined into the cumulative physical dissipation $E_{\text{phys}}(t_N)$:

$$E_{\text{phys}}(t_N) = E^{\text{diss}}_{\text{tens}}(t_N) + E^{\text{diss}}_{\text{comp}}(t_N) + E^{\text{diss}}_{\text{shear}}(t_N) \tag{6.13}$$

Meanwhile, the cumulative work removed by local numerical damping, denoted by W_k, is evaluated at the block level from the unbalanced forces and translational velocities. At each timestep t_n, the incremental numerical damping work is computed as:

$$\Delta W_k(t_n) = \alpha \, \Delta t \sum_{b \in \mathscr{B}} \left(|F^{(b)}_{u,x}||v^{(b)}_x| + |F^{(b)}_{u,y}||v^{(b)}_y| + |F^{(b)}_{u,z}||v^{(b)}_z| \right), \tag{6.14}$$

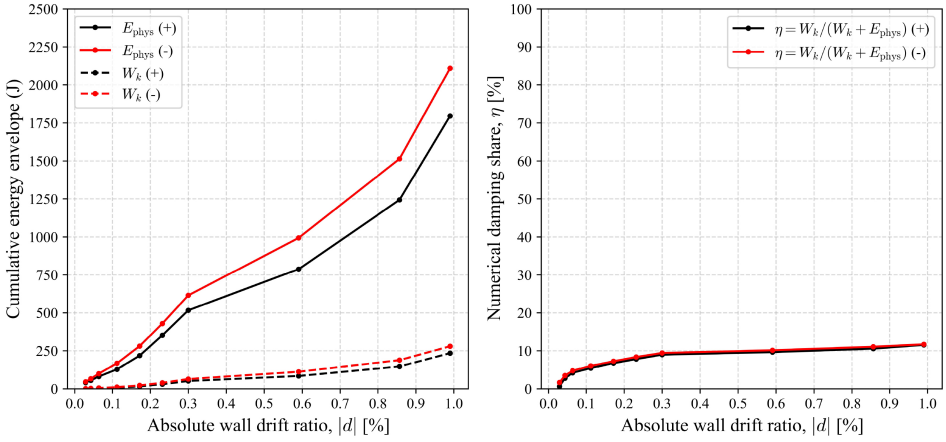
where α is the local damping coefficient (Equation (3.18)), Δt is the mechanical timestep, $\boldsymbol{F}^{(b)}_u = (F^{(b)}_{u,x}, F^{(b)}_{u,y}, F^{(b)}_{u,z})$ is the unbalanced force of block b, $\boldsymbol{v}^{(b)} = (v^{(b)}_x, v^{(b)}_y, v^{(b)}_z)$ is the block translational velocity, and $\mathscr{B}$ denotes the set of blocks excluding boundary blocks. The cumulative numerical damping work is then obtained as:

$$W_k(t_N) = \sum_{n=1}^{N} \Delta W_k(t_n). \tag{6.15}$$

Figure 6.29 compares the cumulative physical dissipation E_{phys} and the cumulative work removed by local numerical damping W_k, evaluated at cycle-peak drift levels in negative and positive loading directions for the benchmark case TUD-COMP-0a. The slender geometry of TUD-COMP-0a develops a rocking mechanism with comparatively smooth oscillation around the corner hinges, so the high-frequency content in the

response is limited and the W_k/E_{phys} ratio reported here represents a lower bound on the numerical damping share that would be observed in shear-dominated specimens, where stick-slip transitions and re-contact events along the bed joints generate higher-frequency content under the same α value. The local damping coefficient α is set to 0.8 by default for this analysis. Figure 6.29A shows the corresponding energy envelopes for both loading directions, while Figure 6.29B reports the numerical damping share:

$$\eta = \frac{W_k}{W_k + E_{\text{phys}}} \tag{6.16}$$



(A) Cumulative energy (B) Numerical damping contribution

Figure 6.29. Energy-based assessment of numerical damping for the benchmark case of TUD-COMP-0a

The energy envelopes show a pronounced separation between physical dissipation and numerical damping across the full drift range. Physical dissipation (red lines in Figure 6.29A) increases sharply with increasing deformation, consistent with the accumulation of joint-level cracking, sliding, and compressive damage. By comparison, the numerical damping contribution (black lines in Figure 6.29A) grows more slowly and is markedly lower. At the maximum drift of 1.0 %, E_{phys} exceeds 2000 J, whereas W_k remains on the order of 250 J in both loading directions.

The damping share η plot in Figure 6.29B provides consistent evidence. After a modest rise at small drift levels, where both physical dissipation and damping are limited, the ratio becomes approximately stationary with increasing deformation and remains below about 10 % to 12 % over the full analysis. Notably, η does not increase at later stages, even as the response approaches mechanism formation, indicating that numerical damping does not become progressively more influential as damage accumulates.

The similarity between the positive and negative loading cycles further indicates that the damping contribution is essentially symmetric and does not introduce a systematic directional bias in the cyclic response. Overall, local numerical damping remains a

secondary component of the total energy balance in this benchmark case, and the global response is primarily governed by constitutive dissipation within the joint model rather than by algorithmic energy removal.

The relative magnitude of numerical damping is nevertheless problem-dependent and may vary with geometry, loading protocol, and material parameter set. An energy-balance check is therefore recommended for each subsequent analysis to verify that the damping share remains a secondary component of total dissipation. This dependence on numerical damping is a property of the explicit time-integration scheme rather than the Distinct Element Method itself, and is shared with explicit finite element analysis. It is the counterpart of the robustness of the explicit scheme for the softening and contact behaviour modelled here, which implicit solvers can struggle to converge for, and the energy-balance check is the routine means of keeping its contribution secondary. The default value of $\alpha = 0.8$ is retained as the starting point, with a reduction warranted when the check shows that the numerical damping share dominates the total dissipation.

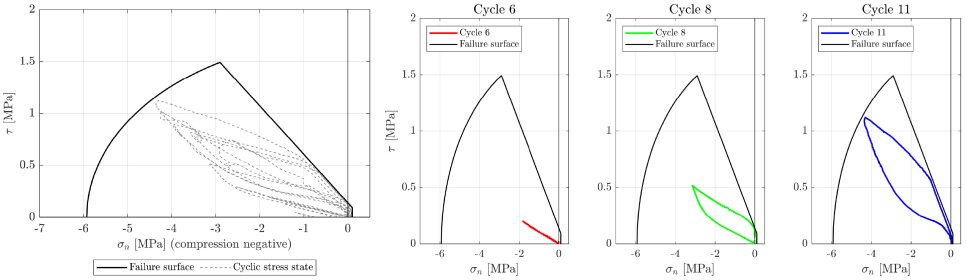
6.3.5. Transition of failure mechanism in in-plane loading scenario

This section examines the development of the failure mechanism in specimen TUD-COMP-0a under double-clamped boundary conditions, focusing on the transition from flexure-dominated rocking to friction-controlled sliding and the associated redistribution of stresses and localisation of damage. Although TUD-COMP-1 also exhibits a coupled rocking-sliding response, the discussion is restricted to TUD-COMP-0a to isolate the influence of double clamping and to facilitate a focused interpretation of the governing mechanics.

Figure 6.30A shows this evolution by reporting the normal-shear stress trajectories at the compressed toe at the bottom-right corner. Up to the 10th loading cycle, the shear yield surface F_2 is not activated, and the only limit reached is the tensile cut-off F_1, which is not discernible at the scale of the compressed-toe stresses. F_2 is activated in the final loading cycle, as described below. Between the 4th and 7th loading cycles (represented by cycle 6 in Figure 6.30B), the stress paths remain well within the yield envelope and form small closed loops associated with repeated loading and unloading while one toe is in compression and the opposite toe lifts off. Because the stress state does not approach the shear envelope in this phase, shear transfer remains limited, and the response is dominated by rocking, with the wall re-closing towards the original hinge region at each load reversal.

Between the 8th and 10th loading cycles (represented by cycle 8 in Figure 6.30B), stepwise cracking develops within the pier, which increases the shear demand at the compressed toes. The corresponding stress trajectories translate upward towards the compression cap, with the normal compressive stress rising to approximately 3.5 MPa to 4.0 MPa. Sliding remains inactive at this stage, as shown by unloading paths that return close to the origin. This interpretation is consistent with the global response in Figure 6.25A and the energy trends in Figure 6.26A, which show only limited dissipation over cycles 8 to 10.

During the final loading cycles (cycle 11 in Figure 6.30B), the averaged normal-shear stress state at the joint plane approaches the compression cap and, upon unloading, intersects the Coulomb friction line. The plotted stress states represent averages over



(A) Cyclic stress state (B) Stress state at selected cycles

Figure 6.30. Evolution of the stress state at the compressed toe (bottom-right corner) of the TUD-COMP-0a model in the shear–normal stress plane, with compression taken negative. The normal and shear stresses are averaged over the toe contact plane. (A) Full cyclic stress path (dashed) against the failure surface (solid), which combines the tension cut-off, the Coulomb friction branch, and the compression cap. (B) Stress paths at cycles 6, 8, and 11, showing the path expanding with increasing amplitude and increasingly engaging the failure surface.

the contact points at the bottom-right corner of the joint. Consequently, yielding in Figure 6.30A and Figure 6.30B occurs before the average stress state visibly reaches the compression cap line. At this stage, the entire length of the bed-joint segment along the compressed toe yields in shear, which enables slip to propagate continuously along the interface. Concurrently, local crushing initiates at the compressed toe. As a result, the rocking mechanism becomes subordinate to friction-controlled sliding, which shifts the hinge location and produces the residual drift observed in Figure 6.25A.

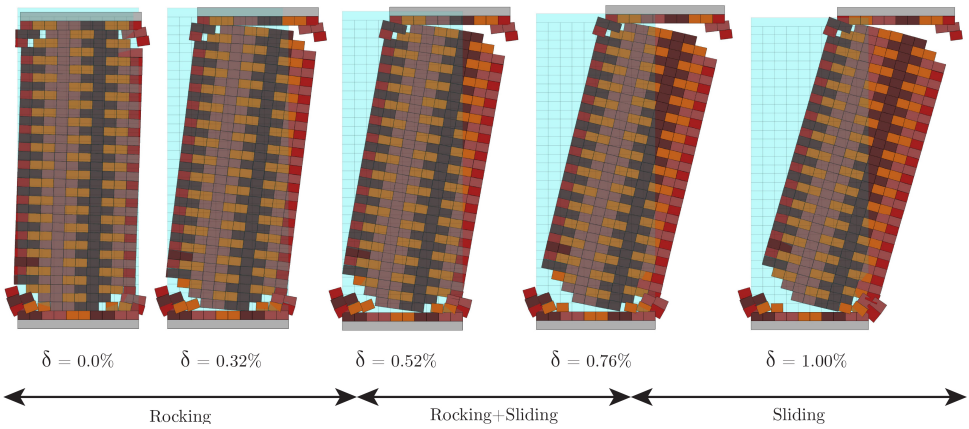


Figure 6.31. Deformed shapes of TUD-COMP-0a at the last positive loading cycle from 0% to 1% drift (Magnified 30x)

Figure 6.31 presents the sequential deformed shapes (magnified 30 times) of specimen TUD-COMP-0a as wall drift, δ, increases from 0 % to 1 % during the final loading cycle. For drifts up to 0.5 %, the pier exhibits near-rigid body behaviour, rocking about one toe as the opposite toe lifts off, while slip along the bed-joint remains negligible.

Once δ exceeds this threshold, the pier begins to translate with respect to the loading toes. By 0.8 % to 1.0 % drift, the response becomes sliding-dominated: the entire bed-joint has yielded in shear, local crushing appears at the compressed toe, and rocking plays only a secondary role. These observations demonstrate that the multi-surface failure surface employed in the MASON contact model can reproduce the drift-dependent transition from the rocking mechanism at lower drift to the sliding mechanism at higher drift.

6.3.6. Sensitivity analysis to imposed peak displacement rate

To assess the influence of the imposed displacement rate on the global response and to verify the quasi-static validity of the constitutive model, a velocity sensitivity study was conducted on specimen TUD-COMP-0a. Five peak loading velocities were considered: $v = 0.5,\ 1.0,\ 2.5,\ 5.0$, and $10.0\ \mathrm{mm\,s^{-1}}$, with $v = 2.5\,\mathrm{mm\,s^{-1}}$ taken as the reference case adopted in the main analyses. Boundary conditions, material properties, and the cyclic protocol remained unchanged. Because the imposed motion follows the cosine–plateau–cosine history defined in Equations (6.2) and (6.3), variations in $v_{\max}$ directly modify the ramp durations ($t_a,\ t_b$) and, as a result, the total actuation time (t_{tot}). Therefore, higher loading velocities result in proportionally shorter actuation times to reach the same prescribed displacement.

The imposed velocities serve as numerical drivers for dynamic relaxation rather than representing experimental actuation rates. Quasi-static solutions are obtained by employing sufficiently small kinetic-energy ratios and residual-force tolerances during the analyses. Within these checks, reducing the velocity to $0.5\,\mathrm{mm\,s^{-1}}$ only marginally affects peak and envelope stiffness but significantly increases runtime. In contrast, higher velocities risk introducing spurious inertial effects. The value $10\,\mathrm{mm\,s^{-1}}$ is used solely as an upper-bound driver to limit runtime, not as a physical rate.

Figure 6.32 compares the force–drift hysteresis at different velocities with the experimental benchmark, and Figure 6.33 presents the corresponding dissipated energy per cycle. Overall, the sensitivity study confirms that the global response is only weakly dependent on the imposed velocity within the quasi-static range. Peak strengths remain nearly unchanged, drift levels at maximum force are consistent, and the primary differences occur in the shape of the hysteresis loops and the magnitude of dissipated energy. These observations suggest that the residual discrepancies arise from velocity-dependent artefacts of the explicit solver.

At the lowest velocities ($0.5\,\mathrm{mm\,s^{-1}}$ to $1.0\,\mathrm{mm\,s^{-1}}$), the hysteresis loops appear less pinched, and the dissipated energy at $0.5\,\mathrm{mm\,s^{-1}}$ aligns closely with the experimental results, especially during the largest cycles. For intermediate velocities ($2.5\,\mathrm{mm\,s^{-1}}$ to $5.0\,\mathrm{mm\,s^{-1}}$), the global hysteresis response is well captured, though the energy dissipated per cycle is slightly underestimated at the largest drift levels. At the highest velocity ($10.0\,\mathrm{mm\,s^{-1}}$), the loops widen and energy dissipation is artificially amplified due to dynamic effects that are not represented by the quasi-static constitutive laws. The cycle-by-cycle energy analysis in Figure 6.33 confirms this ordering. Overall, the

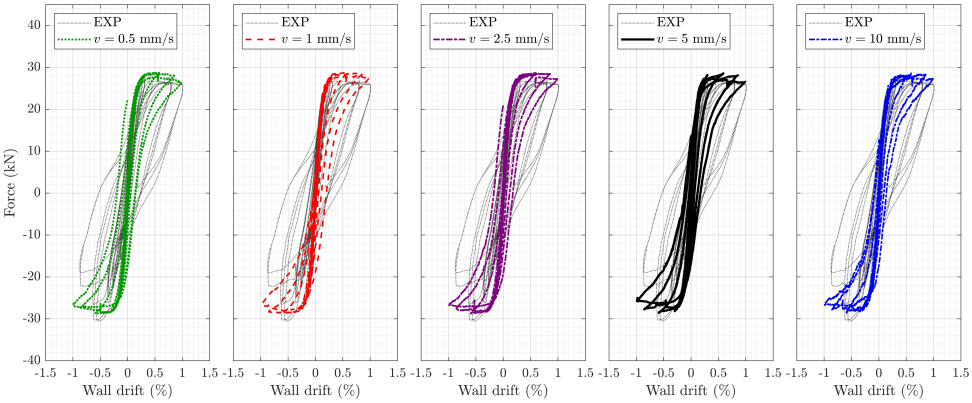


Figure 6.32. Force–drift hysteresis of specimen TUD-COMP-0a under different loading velocities compared with experimental results.

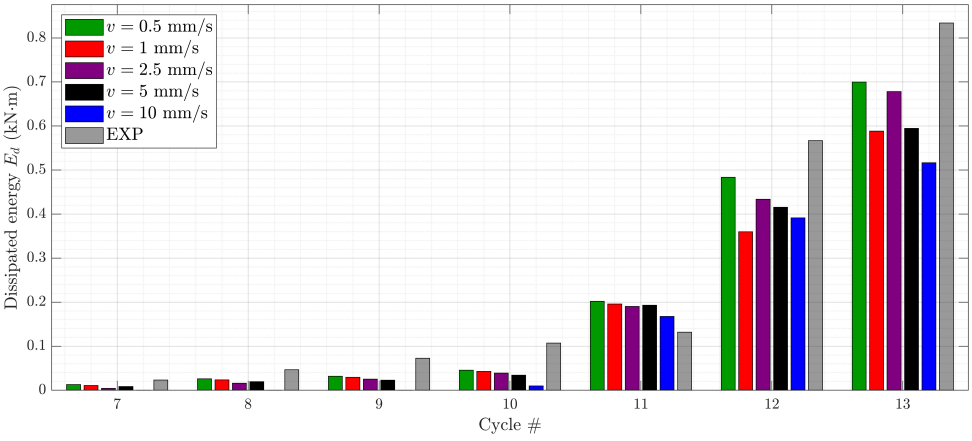


Figure 6.33. Cycle-by-cycle dissipated energy of specimen TUD-COMP-0a under different loading velocities compared with experimental results.

differences across the velocity range are minor, with the lowest velocity providing the closest match to the experimental dissipated energy at the largest drift levels. The velocity of 2.5 mm s^{-1}, adopted in the main analyses, therefore represents a balance between accuracy and computational cost, while the lowest velocity remains the recommended choice when the highest accuracy is required.

Table 6.9 presents the quantitative outcomes. Across the full range of velocities, the predicted peak loads are overestimated by 3 % to 4 % in the positive direction and underestimated by 6 % to 7 % in the negative direction, which iss acceptable for the purpose of this study. Utilising identical computational resources (3.5 GHz Intel Xeon CPU, four cores and 32 GB of memory), the required computational time spans more than an order of magnitude, from approximately 185 hours at 0.5 mm s^{-1} to 10 hours at

$10\,\mathrm{mm\,s^{-1}}$, which highlights the balance between computational accuracy and efficiency.

Table 6.9. Velocity sensitivity results for specimen TUD-COMP-0a.

v [$\mathrm{mm\,s^{-1}}$]	F_{pos} [kN]	F_{neg} [kN]	$\mathrm{Drift}_{\mathrm{pos}}$ [%]	$\mathrm{Drift}_{\mathrm{neg}}$ [%]	Time [h]
0.5	28.74 (−3.8%)	−28.70 (+6.1%)	0.590 (+19.7%)	−0.591 (−13.5%)	185
1.0	28.76 (−3.9%)	−28.64 (+6.3%)	0.591 (+19.7%)	−0.590 (−13.5%)	86
2.5	28.71 (−3.7%)	−28.69 (+6.2%)	0.591 (+19.7%)	−0.590 (−13.5%)	32
5.0	28.60 (−3.3%)	−28.57 (+6.6%)	0.590 (+19.7%)	−0.591 (−13.5%)	26
10.0	28.60 (−3.3%)	−28.57 (+6.6%)	0.591 (+19.7%)	−0.590 (−13.5%)	10

Values in brackets are relative errors (EXP − NUM)/EXP × 100 %, evaluated on the magnitudes, so a negative value denotes an overestimate.
EXP values: $F_{\mathrm{pos,EXP}} = 27.69\,\mathrm{kN}$, $F_{\mathrm{neg,EXP}} = -30.58\,\mathrm{kN}$, $\delta_{\mathrm{pos,EXP}} = 0.736\,\%$, $\delta_{\mathrm{neg,EXP}} = -0.520\,\%$.

These findings indicate that employing intermediate velocities in the range of $2.5\,\mathrm{mm\,s^{-1}}$ to $5.0\,\mathrm{mm\,s^{-1}}$ represents a pragmatic balance, offering satisfactory reproduction of the global hysteresis response and cycle-by-cycle energy evolution while keeping computational requirements manageable. These observations are specific to the component scale, and no single loading velocity transfers across models. The governing requirement is that the kinetic-energy ratio remain small and that the actuation time be long relative to the system's fundamental period, as verified in each analysis. Larger and more flexible structures, such as full buildings, have a longer fundamental period and a greater mass, so meeting the same requirement generally calls for a lower velocity or a longer actuation time, set by the same energy check rather than by reusing the component-scale value.

All simulations in this study are conducted under quasi-static (dynamic-relaxation) conditions, employing slow loading with local numerical damping. Under these conditions, the global response reflects the constitutive behaviour of the interfaces rather than inertia, so the material model can be assessed in isolation from dynamic effects, while the explicit scheme robustly handles softening and contact evolution. The extension to fully dynamic analyses by incorporating physical time histories, reduced numerical damping, and explicit rate effects, will be systematically addressed in the next chapter.

6.3.7. Cross-comparison to other numerical methods

In this subsection, the MASON contact model is benchmarked against alternative numerical models, with the benchmark set by the availability of each specimen. The squat configurations TUD-COMP-4 and TUD-COMP-6 are compared with interface-based models from the literature that were validated in the same experimental programme. The slender configurations TUD-COMP-0a and TUD-COMP-1 have no such published benchmark, so they are compared against additional 3DEC analyses run with the TSCLinear model [6]. For the double-clamped and squat configuration (TUD-COMP-4), the comparison is made with the work of Sousamli [19], who adopted the Plasticity-based

Combined Cracking, Crushing, and Shearing (PCCCS) interface model of Lourenço and Rots [5]. For the cantilever-squat configuration (TUD-COMP-6), the reference model is the Damaging Block-based (D-BB) approach proposed by D'Altri et al. [20], in which blocks interact through damaging interfaces. The PCCCS formulation was implemented in DIANA FEA (v10.4), whereas the D-BB model was implemented as a user-defined constitutive law in Abaqus/Standard; both studies used implicit solution schemes. The results for these reference models are reproduced from the respective publications [19, 20] and were not recomputed by the present author.

Since no computational simulations currently reported for the slender configurations TUD-COMP-0a and TUD-COMP-1, the comparative assessment is instead conducted against additional numerical simulations performed by the authors in *3DEC*, adopting the joint constitutive formulation proposed by Pulatsu [6]. This formulation, denoted here as the Tension-Shear-Compression (TSC) joint model, is grounded in a multi-surface damaged plasticity framework, with compressive failure governed by a compression cut-off criterion [21]. This differs from the compressive cap yield surface employed in the present study, which is intended to represent confinement-dependent yielding and enables a more progressive transition under increasing compressive stress.

In addition, the TSC model assumes linear softening in tension, shear, and compression, whereas the present work adopts damage evolution laws to describe post-peak degradation. These constitutive differences are anticipated to affect stress redistribution and the emergence of failure mechanisms in the simulations. They should therefore be explicitly accounted for when interpreting the comparative trends between the two modelling approaches.

The parameter sets adopted for the cross-comparison are summarised in Table 6.10. Properties are grouped by constitutive formulation, and distinctions between head and bed joints are reported whenever this level of detail is available. For the TSC model, the material properties are identical with those listed in Table 6.8, with the exception of the peak ratio n, since the TSC formulation represents compressive post-peak behaviour through a linear softening law.

The D-BB model [20] requires additional tensile and shear interface characteristics to describe post-peak softening and damage evolution. By contrast, the PCCCS model [5, 19] introduces fracture-energy parameters to control post-peak softening in tensile, shear, and compression regimes.

Brick unit properties are also included in Table 6.10, since both PCCCS and D-BB approaches employ deformable-block discretisations. In the TSC simulations, unit splitting is represented through a potential crack plane at the brick mid-length. Additionally, the D-BB model assigns a continuum plastic-damage constitutive law to masonry units to capture both compressive and tensile failure within bricks.

Figures 6.34A and 6.34B show the force-drift responses of specimens TUD-COMP-0a and TUD-COMP-1, respectively, as obtained with the Tension-Shear-Compression (TSC) joint model proposed by Pulatsu [6]. In general, the simulations reproduce the experimental trends with reasonable fidelity, particularly in the initial linear regime.

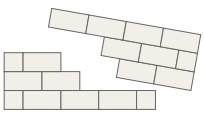
Deviations become apparent once the response enters the non-linear range, particularly beyond a drift level of approximately 0.1 %. Although the TSC model reproduces the initial stiffness and peak strength with reasonable accuracy, it

Table 6.10. Material properties for the cross-validation of the proposed modelling strategy

Properties	Symbol	Unit	TSC[1]		PCCCS		D-BB
			Head joint	Bed joint	Head joint	Bed joint	-
Normal stiffness	k^n	GPa m^{-1}	52.17	52.17	10.44	121.2	75
Shear stiffness	k^s	GPa m^{-1}	22.49	22.49	16.36	39.31	7.5
Tensile strength	f_t	MPa	0.035	0.105	0.003	0.105	0.12
Cohesion	c_0	MPa	0.014	0.14	0.14	0.14	0.11
Friction coefficient	μ	[-]	0.466	0.466	0.43	0.43	0.55
Mode-I fracture energy	G_I	N m^{-1}	3.88	8.38	0.007	7.75	-
Mode-II fracture energy	G_{II}	N m^{-1}	38.8	83.8	100	3000	-
Compressive strength	f_c	MPa	7.0	5.93	7.55	5.93	-
Compressive fracture energy	G_c	N mm^{-1}	31.5	15	34	15	-
Additional parameters							
Ultimate separation	u_k	m	-	-	-	-	0.001
Ultimate slip	δ_k	m	-	-	-	-	0.001
Tension brittleness	ζ	[-]	-	-	-	-	8.0
Shear brittleness	ξ	[-]	-	-	-	-	4.0
Cap shear parameter	C_s	[-]	12		5		-
Brick unit properties							
Young's modulus	E_b	MPa	-	-	8990		4800
Poisson's ratio	ν	[-]	-	-	0.14		0.14
Compressive strength	f_{c_b}	MPa	-	-	-	-	6.8
Tensile strength	f_{t_b}	MPa	1.0	1.0	-	-	1.5

[1] Same material properties as the MASON model (Table 6.8), applied to TUD-COMP-0a and TUD-COMP-1

underestimates the energy dissipated in the subsequent cycles. A relevant difference between the two formulations is the treatment of compression. The TSC model limits compression with a cut-off, whereas the present model uses a compression cap that

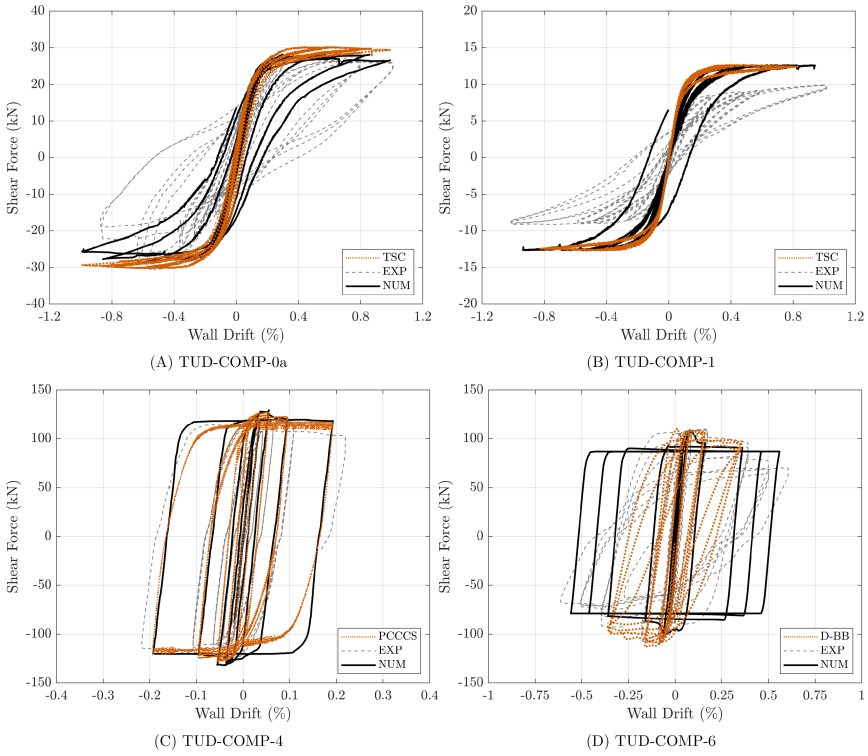


couples shear and compression and yields progressively. This difference is consistent with the larger cyclic dissipation of the present model, although it is one of several formulation differences and is not isolated by the comparison.

For specimen TUD-COMP-0a (Figure 6.34A), the TSC model predicts a marginally higher peak load of approximately 30 kN, compared with 28 kN obtained with the MASON contact model. Additionally, the TSC response shows limited energy dissipation, as indicated by the weak hysteresis development from cycle to cycle. Distinct loop opening is primarily observed only in the final loading cycle, where a non-negligible residual drift suggests the onset of inelastic deformation.

A comparable trend is observed for TUD-COMP-1 (Figure 6.34B). Both the TSC model and the MASON contact model predict a peak load of approximately 12.5 kN, indicating a similar ability to capture the specimen's strength. In the cyclic regime, however, the TSC simulations again exhibited a limited hysteretic response and consequently underrepresented the cumulative energy dissipation over the loading history. Compared to TUD-COMP-0a, where some inelasticity becomes apparent during the final cycle, the TSC response for TUD-COMP-1 shows no pronounced loop opening at any stage of the imposed cyclic loading.

The differences in hysteretic response primarily stem from the interaction between



(A) TUD-COMP-0a (B) TUD-COMP-1

(C) TUD-COMP-4 (D) TUD-COMP-6

Figure 6.34. Cross-comparison of validated wall specimens

shear strength and compression. The MASON contact model employs an evolving compression-capacity surface that accounts for confinement effects and promotes the gradual, spatially distributed development of shear yielding. This facilitates progressive inelastic deformation and reproduces the experimentally observed energy dissipation. By contrast, the TSC formulation relies on a compression cut-off, which introduces a more abrupt compressive limit and weakens the coupling between axial stress and shear response. Although this simplification can be computationally attractive, it tends to delay the onset of shear sliding and suppress damage accumulation, thereby reducing hysteresis. Consequently, for identical masonry compressive strengths, a compression-cap formulation is expected to trigger shear failure earlier than a cut-off criterion, particularly in hybrid rocking-shear regimes where sliding localises at the highly compressed toes. Reproducing the experimental response with a compression cut-off formulation would therefore be expected to require reducing the masonry compressive strength below its measured value as a calibration adjustment, since the model otherwise delays the onset of shear sliding and underestimates the hysteretic dissipation. The MASON formulation avoids this offset because the compressive cap activates progressively through the damage scalar d_c, allowing the experimental compressive strength to remain the input parameter without artificial reduction.

Figure 6.34C and Figure 6.34D present the force-drift responses of specimens TUD-COMP-4 and TUD-COMP-6, respectively, comparing MASON contact model predictions with corresponding reference simulations and experimental results (EXP). Overall, the MASON contact model shows trends broadly consistent with the alternative modelling strategies reported in the literature. For TUD-COMP-4 (Figure 6.34C), the MASON contact model agrees closely with both the experimental response and the PCCCS reference simulation. In the study [19], the loading protocol was repeated three times within each drift cycle, leveraging the stable pre-peak behaviour and the larger time increments permitted by the implicit solver to obtain repeatable hysteresis. Relative to PCCCS, the MASON contact model predicts marginally wider loops in the final cycle, yet both numerical responses remain within the experimental scatter. Accurate peak-load prediction and reproduction of cycle-to-cycle pinching indicate that the model captures joint opening and closure, interface friction, and post-peak softening with high fidelity. Sousamli [19] further noted that, while PCCCS reproduces shear-dominated cases such as TUD-COMP-4 well, its predictive quality decreases for specimens governed by hybrid rocking-shear mechanisms. A contributing factor is the elastic unloading and reloading after the tensile strength has softened, which does not carry the degraded tensile state through load reversal. This is problematic at the transition between tension and compression, where the crack closing and reopening can recover spurious stiffness rather than following the softened envelope [22]. This concerns the normal response of an opening crack, where the cohesive bond is the load path. It does not extend to the shear response of a closed joint. For that case, MASON retains the initial stiffness (Section 4.5).

For TUD-COMP-6 (Figure 6.34D), the proposed model matches both the experimental response and the D-BB reference prediction reasonably well up to a drift of 0.27 %. Beyond this level, the D-BB simulation reported by D'Altri *et al.* [20] fails to converge, which was attributed to severe localisation of damage at the compressed toe. By contrast, the MASON contact model remains numerically stable and completes the full loading

protocol. It predicts slightly larger hysteresis loops and a more gradual post-peak strength decay than observed experimentally, but it preserves the overall cyclic trend and the progressive development of damage. These results indicate that the MASON contact model provides a robust and numerically stable basis for simulating cyclic masonry response across a range of boundary conditions and governing failure modes.

Direct runtime benchmarking against external FEM or DEM studies is not undertaken in this subsection, as published validations typically provide response curves and qualitative failure descriptions, not comparable computational-cost metrics. When runtimes are reported, they are inherently confounded by differences in hardware, discretisation and pre-processing workflows, solver tolerances, and contact regularisation choices, which preclude a like-for-like comparison. Accordingly, the efficiency discussion remains qualitative and is based on the absence of non-linear equilibrium iterations and on the numerical robustness of the explicit integration scheme under softening and evolving contact conditions. Quantitative timing assessments are most informative within a controlled and standardised computational environment, which is not pursued in this dissertation.

6.4. In-plane response of modular steel frame-retrofitted masonry piers

This section evaluates the performance of the MASON contact model for retrofitted masonry piers strengthened with a modular steel-frame system, using the Resisto 5.9 benchmark as a representative case. The experimental reference derives from the 2020 EUCENTRE and University of Pavia campaign reported by Albanesi *et al.* [3], where quasi-static in-plane cyclic tests were conducted on unreinforced and retrofitted wall panels under axial compression, providing both the force-displacement envelope and the observed damage patterns. Building on the experimental programme, Damiani *et al.* [23] adopted a simplified micro-modelling approach within the DEM framework to interpret the observed response. In their formulation, the masonry assemblage is discretised into hexahedral units with non-linear material behaviour, whereas the mortar layer is represented by zero-thickness interfaces that govern the relative kinematics between neighbouring blocks. The retrofit system is represented by beam elements and connector components that idealise the stiffness of the steel frame, the non-linear response of the anchorage, and the interaction with the masonry assemblage.

This reference modelling strategy therefore provides a useful point of comparison, as it distributes inelasticity across both unit behaviour and interface kinematics, whereas the MASON contact model prioritises a lumped non-linear description at the joint level. In this context, the objective is not only to assess whether MASON reproduces the measured global and local responses, but also to examine the modelling assumption that key non-linearities can be concentrated at interfaces through shear-compression coupling, hardening, and softening laws, while the units remain predominantly elastic. At the global level, the comparison focuses on the force-displacement response, including initial stiffness, peak resistance, cycle-to-cycle pinching, and post-peak degradation. At the local level, the assessment considers the predicted localisation pattern and the governing sequence of mechanisms. The numerical comparison is further used to

highlight the consequence on the structural response of two modelling philosophies, i.e. the concentration of non-linearities at the interfaces in MASON versus the distributed representation of unit failure through non-linear block behaviour in the Damiani *et al.* [23] model (hereafter termed the reference model). Finally, a targeted sensitivity analysis of material parameters is performed to quantify how key material parameters in the MASON formulation influence both global response metrics and local damage development.

6.4.1. Experimental description

The experimental campaign on the retrofitting system was conducted in 2020 at the EUCENTRE facilities in Italy. The geometry of the tested panel, together with the modular steel-frame layout and the anchorage locations adopted in the experiments, is shown in Figure 6.35. The corresponding unreinforced configuration shares the same masonry geometry and boundary conditions and is therefore omitted for brevity.

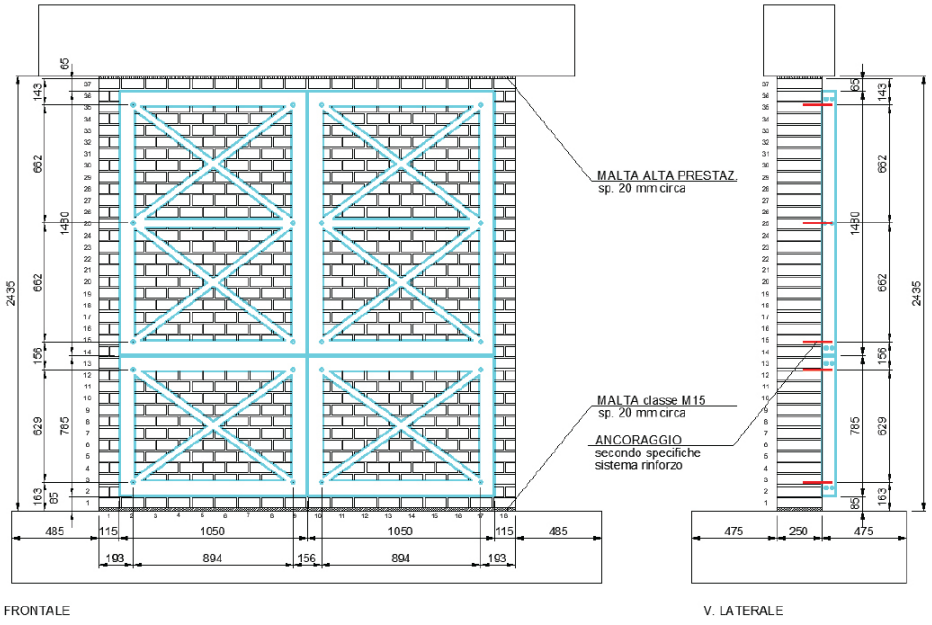


Figure 6.35. Nominal dimension of the retrofitted test wall (Unreinforced specimen is not shown for reasons of brevity) [3]

The experimental campaign investigated the seismic response of the retrofit solution referred to as Resisto 5.9, in which modular steel frames are assembled using 12 mm diameter class 8.8 bolts and anchored to the masonry through chemically bonded threaded bars. The frame members are fabricated from plate sections with nominal strength of $f_y = 250\,\text{MPa}$ and $f_u = 330\,\text{MPa}$. The system was tested on a

2.33 m × 0.25 m × 2.435 m header-bond wall panel (termed S-HEA-U and S-HEA-R for unreinforced and retrofitted specimens, respectively) subjected to a constant axial compressive load and quasi-static in-plane shear loading. The experimental programme further examined the influence of key test parameters governing the wall response, including geometric slenderness, applied vertical pre-compression, and boundary conditions. Further details of the test configuration, loading protocol, and instrumentation are reported by Albanesi *et al.* [3].

Table 6.11 reports the material parameter set for the S-HEA-U/R adopted by the reference model [23], with several key values anchored to the companion characterisation tests [24]. The data imply a joint-governed onset of nonlinearity, since the joint tensile strength is set relatively low ($f_{t_{mo}} = 0.05$ MPa), while shear capacity is predominantly controlled by friction ($c = 0.15$ MPa, $\phi = 31.38°$) and therefore strongly dependent on the compressive normal stress.

Table 6.11. Experimental and empirical material properties of S-HEA-U/R [23]

	E_m	G_m	fc_m	ρ_m	E_b	fc_b	f_{t_b}	G_c	Gt_b
Masonry & Units	[MPa]	[MPa]	[MPa]	[kg m^{-3}]	[MPa]	[MPa]	[MPa]	[N/m]	[N/m]
	4265[a,b]	1706[a]	7.03[a]	1300[a]	7207	19.22[a]	1.79	11248	60
	E_{mo}	G_{mo}	k_n	k_s	c	ϕ	$f_{t_{mo}}$	G_s	G_{t_j}
Joints	[MPa]	[MPa]	[GPa m^{-1}]	[GPa m^{-1}]	[MPa]	[°]	[MPa]	[N/m]	[N/m]
	1259	504	126	50	0.15[a]	31.38[a]	0.05[a]	50	10

[a] Values obtained through accompanying material characterisation tests [24]
[b] Evaluated in the direction perpendicular to bed joints as secant value between 10 % and 30 % of $f_{c,m}$

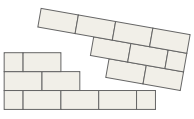
In the reference modelling strategy, the post-peak response is regularised through fracture energy terms that are not measured experimentally, but estimated from empirical relations, namely:

$$G_c = 1600 f_{c,m} \quad [\mathrm{Nm}^{-1}], \tag{6.17}$$

$$G_{t_j} = 25 (2 f_{t_{mo}})^{0.7} \quad [\mathrm{Nm}^{-1}], \tag{6.18}$$

$$G_s = 10 G_{t_j} \quad [\mathrm{Nm}^{-1}], \tag{6.19}$$

for fracture energy in compression, tension, and shear, respectively. The same material parameter set in Table 6.11 is adopted for the MASON contact model to ensure a consistent basis for comparison, with the additional introduction of the peak ratio n, which is calibrated from the material-scale validation to control the post-peak evolution of the interface response.



The failure pattern at the end of the experiment for both unreinforced (S-HEA-U) and the retrofitted (S-HEA-R) cases is shown in Figure 6.36A and Figure 6.36B, respectively. In both cases, the failure mechanism was governed by shear, characterised by diagonal cracks extending from one corner to the other. The cracks were mainly found at the mortar joints, and crushing of the brick units was observed at the compressed toe regions. The ultimate capacity for S-HEA-U, defined as the point where the shear capacity drops 20 % below the peak or the maximum observed drift ratio is reached, occurs at a drift $\theta = 0.14\,\%$ (about 3.4 mm). Meanwhile, the S-HEA-R specimen achieved the ultimate capacity at θ equals 0.57 %. The retrofit system increased the displacement capacity and the initial stiffness of the wall [3].



(A) Unreinforced (S-HEA-U) (B) Retrofitted (S-HEA-R)

Figure 6.36. Experimental crack pattern at the end of the loading sequence [24]

6.4.2. Numerical modelling setup

The overall numerical idealisation follows the modelling setup of the reference study [23] to enable a controlled comparison. In that study, the masonry assemblage is discretised into *deformable* hexahedral blocks with non-linear unit behaviour, defined by finite strengths in tension, compression, and shear, while the mortar layer is represented by zero-thickness interfaces governing the relative kinematics between adjacent units. Because the units are non-linear in the reference study, an explicit potential crack plane within each unit is not required, since the unit constitutive law itself accommodates the intra-unit damage evolution. In the present work, the units are represented as linear elastic *deformable* blocks, and the potential crack plane within each unit is therefore introduced explicitly as an internal interface, with the same constitutive law as the bed and head joints, to allow tensile and shear damage to localise at the unit centre under

combined loading. The same specimen geometry, boundary conditions, and retrofit representation are adopted, including linear-elastic beam elements representing the steel frame and non-linear links at the anchorage locations governed by the calibrated force-displacement law. The adjacent modular frames were connected through rigid links, consistent with the reference idealisation.

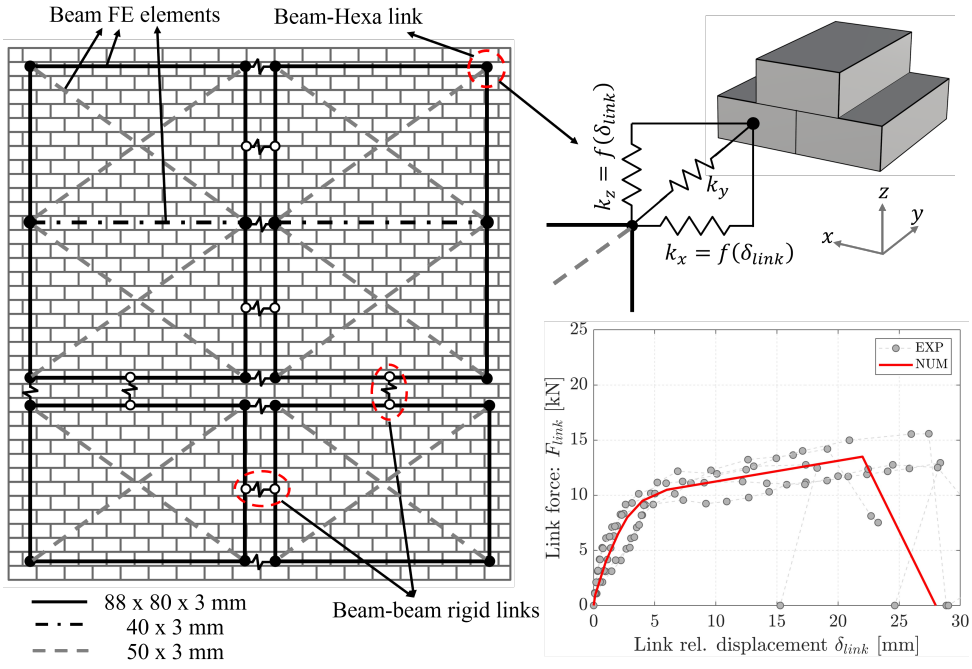


Figure 6.37. Retrofit system modelling strategy: layout and anchor shear behaviour [23]

The L-shaped 88 mm × 80 mm × 3 mm frame is stiffened by diagonal and horizontal braces with dimensions of 40 mm × 3 mm and 50 mm × 3 mm, respectively. This interaction is represented through the structural link, in which a shear-yield deformable behaviour is assigned to the three translational degrees of freedom of the link, while the rotational degrees of freedom are left free. The bilinear force-displacement rule is implemented for the link translation along the out-of-plane Y-direction, with elastic stiffness of 25 kN mm^{-1} and yielding force of 11 kN. Meanwhile, the structural link force-displacement rule along the X and Z directions is calibrated to the shear tests performed on the retrofit-to-masonry anchors [3], as shown in Figure 6.37.

Figure 6.38 compares the mesh discretisation strategies used in the reference model [23] and in the present MASON implementation. A coarse mesh was used for the majority of the brick units, with an aspect ratio of 2 × 1 × 1, given as the proportion of the edge lengths along the three axes, so that the longest edge is twice the shortest. This aspect ratio is defined as the ratio of the shortest to the longest edge. Meanwhile, a critical area within each corner of the wall panel defined by one-third of the diagonal line

was refined to simulate the unit-splitting and crushing behaviour at the toes (Figure 6.38). This corner area is refined with an aspect ratio of 8 × 1 × 4 (R) to resolve the localised compression demand.

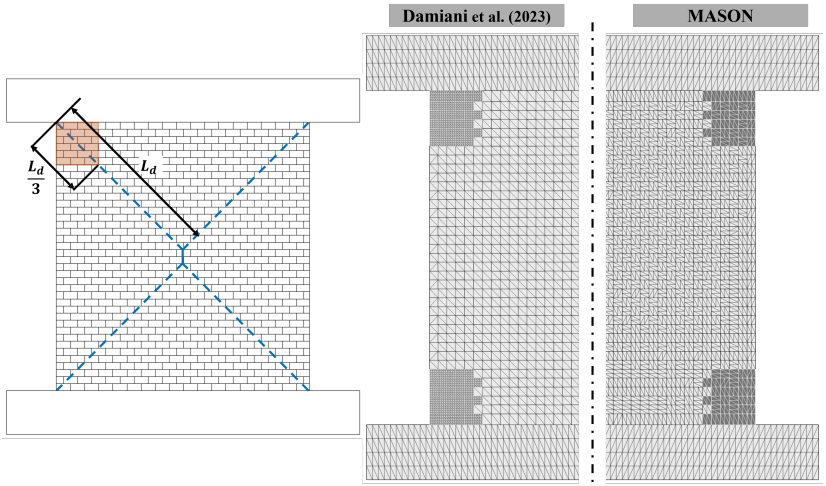


Figure 6.38. Mesh comparison between reference study [23] and the MASON contact model

Meanwhile, in the MASON model, the same corner region is not refined, since compressive localisation and unit splitting are represented by the potential crack plane at the unit's mid-length and by the interface formulation via the compression-cap failure surface. This choice relaxes the explicit stability constraint, as summarised in Table 6.12: the smallest hexahedral volume increases by approximately a factor of four relative to the reference discretisation (Table 6.12), resulting in a larger stable mechanical timestep (4.0×10^{-6} s against 3.4×10^{-6} s). Although the total number of blocks and hexahedral elements increases because brick units are split to enable the unit-splitting kinematics, the parallel processing capabilities of *3DEC* [25] reduce the associated computational overhead and support the net gain in the timestep size.

Table 6.12. Mesh properties of the compared modelling approaches

Model	Number of Blocks	Number of Hex. Elements	Smallest mesh volume	Stable timestep [s]
Damiani et al. [23]	686	39 120	1.01×10^{-5}	3.4×10^{-6}
MASON	1334	59 280	4.06×10^{-5}	4.0×10^{-6}

The masonry panel is connected to a reinforced-concrete (RC) foundation and loading

beam, which were represented by linear-elastic hexahedral elements with an aspect ratio of $1 \times 4 \times 75$ (R). To reproduce the double-clamped boundary condition of the experimental setup, the nodes of the RC blocks are restrained in all translational degrees of freedom. The prescribed overburden stress σ_n is applied at the loading beam by assigning an equivalent density such that the resulting gravitational load matched the target pre-compression force. Lateral in-plane loading is imposed by prescribing an incremental velocity on the loading beam, producing a total displacement of 1.0 mm over 0.135 s. The velocities are subsequently set to zero, and the model is brought to static equilibrium, defined by a global force-imbalance ratio below 1×10^{-5} [23].

6.4.3. Numerical result: global and local behaviours

This subsection presents the numerical results at both the global and local levels for the Resisto 5.9 S-HEA-U/R benchmark, with a focus on how the retrofit alters stiffness, strength, and damage localisation relative to the unreinforced configuration. The discussion is structured to first verify the adopted parameter set through material-scale benchmarks, and then to assess the component-scale response under monotonic pushover and quasi-static cyclic loading.

Material-scale validation results

Prior to the component-scale assessment, the two modelling approaches are first benchmarked at the material scale to confirm their ability to reproduce the companion wallette and triplet responses, thereby enabling subsequent differences at the pier level to be attributed to constitutive modelling choices. Figure 6.39 summarises the material-scale benchmarks used to align the two numerical approaches prior to the component-level assessment.

The upper row compares the masonry wallette response in compression, showing that both simulations reproduce the pre-peak stiffness and the peak stress level within the experimental scatter, while the differences become more pronounced in the hardening process in the MASON model and the post-peak regime due to the respective regularisations. The MASON prediction remains closer to the experimental trend, primarily because the peak ratio n provides direct control over the strain (or displacement) at peak stress and therefore over the onset of post-peak degradation.

The lower row presents the triplet shear response under constant normal stress, which provides the primary constraint on interface sliding and post-peak degradation. Here, the MASON model captures the peak shear resistance and the overall decay trend, while exhibiting a more pronounced stick-slip damage progression in the softening branch. This material-scale agreement confirms that the parameter set reported in Table 6.11 is sufficiently representative of the observed small-scale response, thereby providing a defensible basis for transferring the same parameters to the component-level simulations.

Pushover analysis results – global behaviour

Figure 6.40 compares the monotonic pushover response of the unreinforced (S-HEA-U) and retrofitted (S-HEA-R) panels against the experimental cyclic backbone. Using the

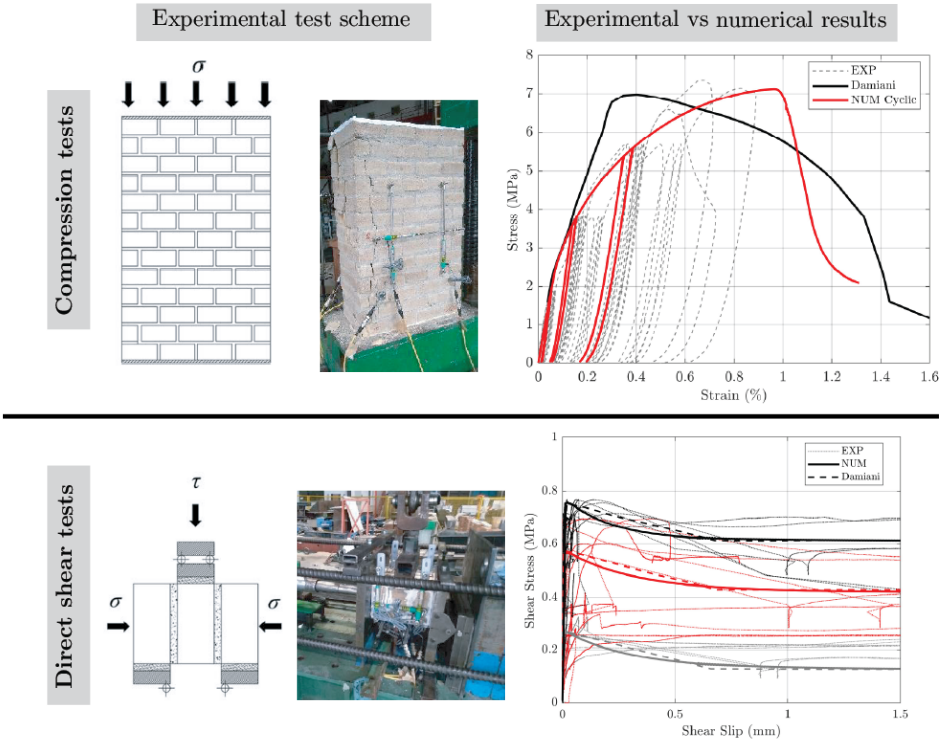
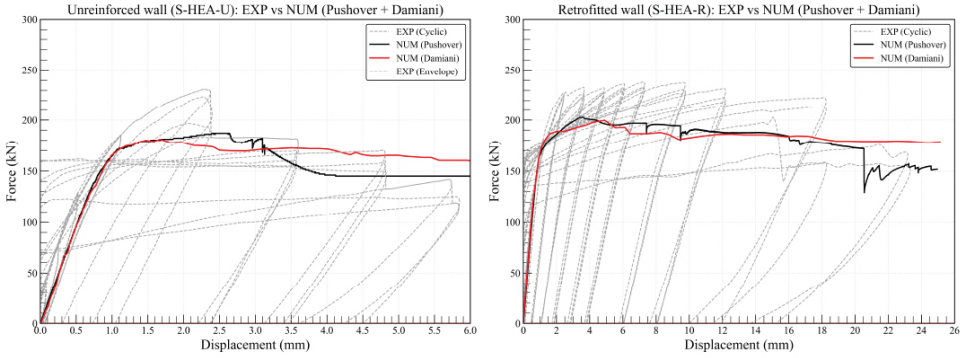


Figure 6.39. Comparison of the two modelling strategies against experimental tests on small masonry samples

same material parameters reported in the reference study, the MASON contact model predicts an initial stiffness and peak shear capacity comparable to those of the reference model, with the post-peak response captured with acceptable accuracy. However, both models underestimate the experimental peak capacity by approximately 19 % to 22 %.

Differences between the two modelling strategies are clearer at the post-peak regime, where the MASON contact model predicted a more pronounced softening and stepwise strength drops due to the unit-splitting constrained at the potential crack plane, whereas the reference model shows a smoother and more sustained residual capacity over the same displacement range.

For the retrofitted wall (Figure 6.40B), the same tendency to underpredict the peak force is apparent, even though both models reproduce the expected retrofit effect of increased resistance at small displacements compared to the unreinforced wall in Figure 6.40A. The MASON model predicts the early peak and subsequent softening more closely to the cyclic response, while the reference model tends to maintain a higher plateau at larger displacements, indicating a more persistent contribution of the retrofit load path once mobilised. The remaining discrepancies in peak strength



(A) Unreinforced (S-HEA-U) (B) Retrofitted (S-HEA-R)

Figure 6.40. The Experimental and numerical envelope comparison of the reference study [23] and the MASON contact modelling strategy for (A) Unreinforced and (B) Retrofitted specimens

and post-peak evolution are consistent with sensitivity to the assumed toe-crushing behaviour, the homogeneity of the adopted material parameters, and the representation of steel frame-to-wall load transfer via the non-linear link law.

Table 6.13 quantifies the pushover agreement using three scalar backbone metrics, namely the peak force $F_{\max}$, the displacement at peak $u(F_{\max})$, and the initial stiffness K_0, and confirms the trend observed qualitatively in Figure 6.40. For both the unreinforced and retrofitted panels, the peak resistance $F_{\max}$ is underestimated by both numerical approaches, by about 19 % to 22 % for the unreinforced case and 14 % to 16 % for the retrofitted case. This is consistent with the adoption of spatially homogeneous material properties and the absence of specimen-specific strength variability. In contrast, the initial stiffness K_0, calculated up to 20 % of $F_{\max}$, is reproduced closely, with errors of at most 4.2 % for the MASON model and 6.7 % for the reference model, indicating that the global elastic compliance of the wall and boundary system is captured adequately.

The largest discrepancies concern the displacement at peak, $u(F_{\max})$, particularly for the retrofitted configuration, where the MASON model predicts the peak at a substantially smaller displacement (3.61 mm against 7.31 mm, an underestimate of 50.7 %), while the reference model also underpredicts the peak displacement (33 %). The diagnostic value of this metric is limited by the plateau-like behaviour of the experimental force-displacement curve near the peak, where small variations in the recorded force can shift the identified peak location across a wide displacement range without necessarily reflecting a corresponding difference in the underlying response. Subject to this caveat, both models mobilise the governing nonlinear mechanism earlier than the experiment, consistent with sensitivity to the representation of frame-to-wall load transfer through the nonlinear links. Overall, the metrics suggest that the principal gap lies not in elastic stiffness but in peak strength and in the deformation scale at which peak capacity is reached.

Table 6.13. Comparison to experiment using three scalar backbone metrics. Errors (in %), defined as (EXP – NUM)/EXP × 100, are shown in parentheses beneath each value, so that a positive value denotes an underestimate.

	Unreinforced (U)			**Retrofitted (R)**		
Model name	F_{max} [kN]	$u(F_{max})$ [mm]	K_0 [kN mm^{-1}]	F_{max} [kN]	$u(F_{max})$ [mm]	K_0 [kN mm^{-1}]
MASON	187.00	2.39	193.39	202.75	3.61	195.55
	(-19.06)	(4.07)	(-1.76)	(-14.31)	(-50.70)	(-4.17)
Damiani [23]	180.98	1.67	190.75	199.62	4.90	217.81
	(-21.66)	(-27.31)	(-3.10)	(-15.64)	(-32.95)	(6.73)
EXP [3]	231.03	2.30	196.86	236.62	7.31	204.06
	(–)	(–)	(–)	(–)	(–)	(–)

Pushover analysis results – local behaviour

The in-plane failure mechanisms predicted by both models at the largest displacement of the experimental envelope (8 mm) are shown in Figure 6.41. Both models predicted the development of the diagonal failure mechanism characterised by the joint opening along the masonry joint (represented in red), consistent with the experimental finding in Figure 6.36A. However, differences arise in how damage progression and unit failure are represented. In the reference model (Figure 6.41A), damage localises in the compressed toe regions at the top-left and bottom-right corners, but it is distributed within the deformable masonry units, leading to a more smeared representation of unit failure. This behaviour reflects the effectiveness of the refined mesh in the compressed toe regions, which allowed the model to simulate crushing and the stress redistribution following diagonal cracking.

In contrast, the MASON model (Figure 6.41B) showed a similar overall failure mechanism, but minimal unit splitting. Since the shear-compression interaction was lumped at the interfaces, damage that was previously smeared through the units in the reference model becomes localised along the bed joints. This results in extended joint opening at the compressed toes (represented in green in Figure 6.41B) and an earlier capacity drop at 3 mm displacement at Figure 6.40A, coinciding with the connection of the diagonal crack from corner to corner.

Figure 6.42 compares the predicted in-plane failure mechanism of the retrofitted model between the reference model and the MASON model observed at 25 mm displacement. Compared to the experimental observation in Figure 6.36B at the same displacement level, the failure mechanism is qualitatively consistent. The reference model (Figure 6.42A) exhibited a distinct diagonal crack pattern extending from corner to

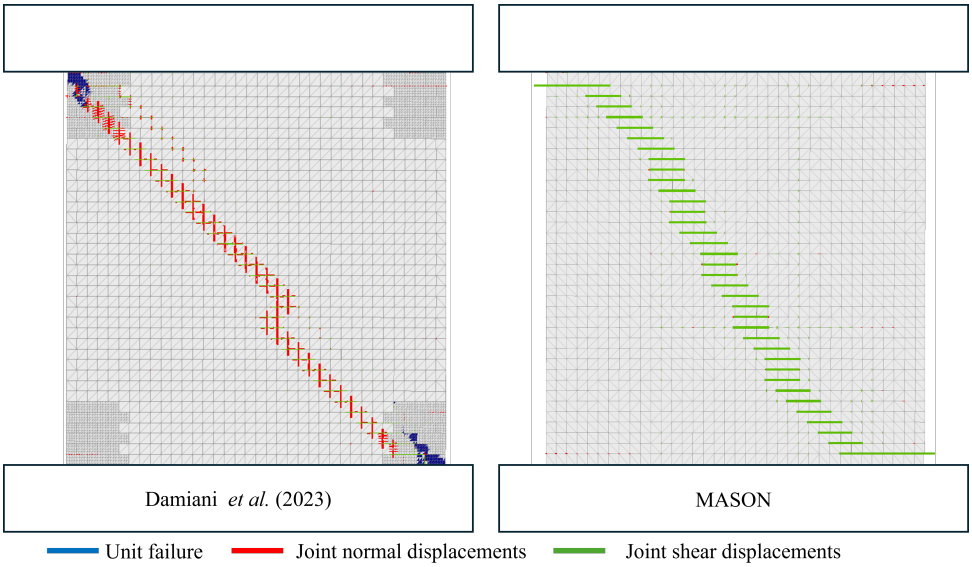


Figure 6.41. In-plane failure mechanism comparison for S-HEA-U at 8 mm displacement

corner. Localised unit-splitting is also observed around the crack path and near the top left corner, indicating stress concentrations and crushing at the compressed toes.

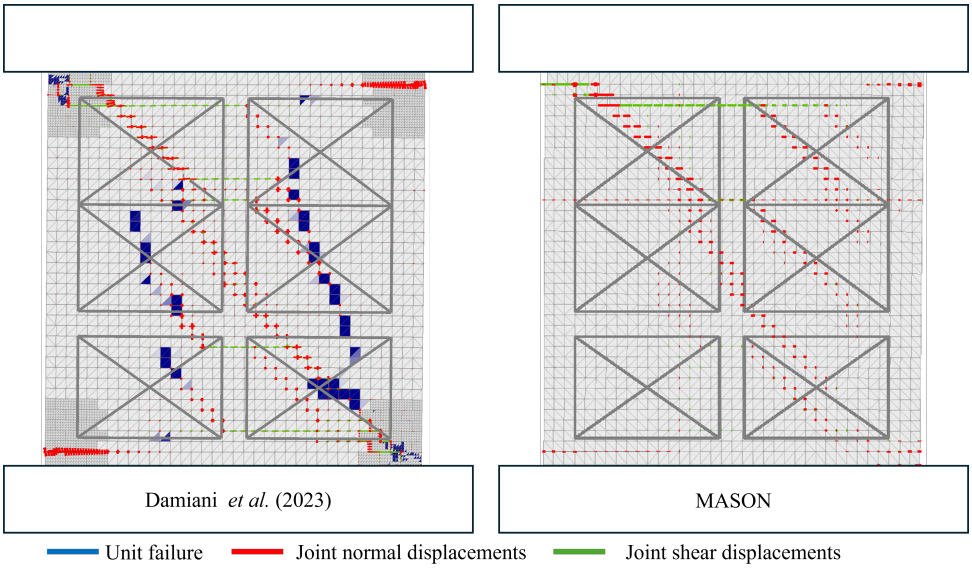


Figure 6.42. In-plane failure mechanism comparison for S-HEA-R at 25 mm displacement

The MASON model (Figure 6.42B) shows a similar failure mechanism. A distinct diagonal crack pattern is observed, followed by sliding on the bed joints close to the top of the wall that branched from this diagonal crack. This indicates the occurrence of a load-transfer mechanism at the transition from diagonal crack to sliding failure. The damage is dominated by shear sliding along the bed joints, with minimal tensile opening at the head joints, which is not visible in the crack pattern. It remains localised to the mortar joints and does not extend to the potential crack plane of the units.

Computational effort

In terms of computational cost, the MASON contact model proved to be substantially more efficient. Using the same *3DEC* output settings on a Windows workstation equipped with a 3.2 GHz Intel Xeon CPU and 512 GB of memory, the MASON model reached 8.0 mm lateral displacement in approximately 1.5 h, whereas the reference model, with the same computational power, required about 19 h to reach the same displacement. This difference motivates the sensitivity analysis presented in the next section, as the MASON model enables systematic parametric analysis within a feasible computational budget and supports a more robust assessment of the model's sensitivity to changes in material parameters.

6.4.4. Sensitivity analysis on the material parameters

In the retrofit benchmark, the remaining mismatch between the MASON simulations and the Resisto 5.9 experimental envelope is less concentrated in the governing mechanism and more in the timing of peak resistance and in how post-peak degradation evolves. To quantify the robustness of the predicted response and to prioritise which material inputs deserve calibration effort, this section introduces a systematic sensitivity analysis of the unreinforced configuration (S-HEA-U). The sensitivity analysis is conducted on the unreinforced specimen to isolate the influence of masonry material variability on the global response. This choice is further supported by the observation that the increase in peak capacity from unreinforced to retrofitted is minimal in both experiments and simulations; the retrofit primarily alters the deformation capacity and the post-peak response, not the peak load. In the retrofitted configuration, the response also reflects the retrofit-specific mechanisms, such as connection failure, making masonry and retrofit parameters non-identifiable. The unreinforced case, therefore, provides a cleaner ranking of the governing masonry parameters, which can then be carried forward as a baseline for targeted variation of retrofit parameters.

The sensitivity analysis considers masonry mechanical properties as either independent random variables or dependent variables deterministically updated from the sampled controls to maintain consistency of the constitutive description [26]. The independent variables were selected to represent the dominant sources of uncertainty governing crack initiation, shear resistance, and stiffness in the unreinforced specimen. Namely, they are the joint cohesion c_0, friction angle ϕ, the unit tensile strength $f_{t,b}$, and the elastic moduli of mortar and brick, E_{mo} and E_b, respectively. Each sampled value is applied uniformly across all interface contacts and unit blocks within a given realisation. Therefore, the analysis captures the inter-realisation variability of the global

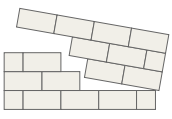
mechanical properties without representing the intra-specimen spatial variability arising from local heterogeneity in mortar quality or unit defects. The remaining interface properties are treated as dependent variables and computed from these controls to preserve the modelling assumptions adopted in Table 6.11. Finally, for a fixed mortar thickness of 10 mm, the interface normal and shear stiffnesses are recomputed using the homogenised equation in Equation (5.1) with $\nu = 0.25$. Table 6.14 summarises the independent random variables, their assumed distributions, and the dependent relationships used throughout the parametric study.

Table 6.14. Summary of the input parameters.

Random variable	**Distribution**	**Mean (μ)**	**COV**	**Bounds**
c (MPa)	Trunc. normal	0.15	—	[0.10, 0.30]
ϕ (°)	Trunc. normal	31.38	—	[30, 35]
$f_{t,b}$ (MPa)	Uniform	—	—	[0.8, 2.0]
E_{mo} (MPa)	Trunc. normal	1259	0.05	—
E_b (MPa)	Trunc. normal	7207.5	0.20	—
Dependent random variables and relationships				
$f_{t,mo}$ (MPa)	$f_{t,mo} = c/3.0$			
G_I (N/m)	$G_I = 0.025\left(2 f_{t,mo}\, 10^{-6}\right)^{0.7}\, 1000$			
G_s (N/m)	$G_s = 15\, G_I$			
$k_{n,j}$ (Pa/m)	$k_{n,j} = \dfrac{E_b E_m}{t_m (E_b - E_m)}$			
$k_{s,j}$ (Pa/m)	$k_{s,j} = \dfrac{k_{n,j}}{2(1+\nu)}$			

$t_m = 10$ mm and $\nu = 0.25$.

Each random variable is assigned a probability distribution consistent with physical admissibility and with the level of dispersion reported in the material characterisation accompanying the Resisto campaign [24]. The joint cohesion c_0 and friction angle ϕ are treated as bounded strength parameters and sampled within $c \in [0.10, 0.30]$MPa and $\phi \in [30°, 35°]$ to avoid non-physical draws and to remain within a plausible, experiment-informed range; they are implemented as truncated normal marginals. The mortar and brick Young's moduli, E_{mo} and E_b, are modelled as truncated normal variables with COV of 5 % and 20 %, respectively, reflecting the comparatively low dispersion observed for mortar stiffness relative to the units. Finally, the unit tensile strength $f_{t,b}$ is sampled uniformly within [0.8, 2.0]MPa as a bounded parameter governing crack initiation at the potential tensile failure plane.



Once the marginal distributions are defined, Latin Hypercube Sampling (LHS) is employed to generate $N = 300$ realisations. LHS partitions each marginal distribution into equiprobable intervals and draws one sample per interval, resulting in a space-filling parametric design that improves coverage of the multi-dimensional parameter space for a limited simulation budget compared to a naïve Monte Carlo sampling [27, 28]. In the present implementation, no additional inter-parameter correlations are enforced. Instead, physically inconsistent stiffness combinations are prevented by recomputing $(k_{n,j}, k_{s,j})$ directly from the sampled (E_{mo}, E_b), ensuring that each realisation remains mechanically compatible with the experimental observation. Figure 6.43 visualises the LHS design used to generate the $N = 300$ realisations.

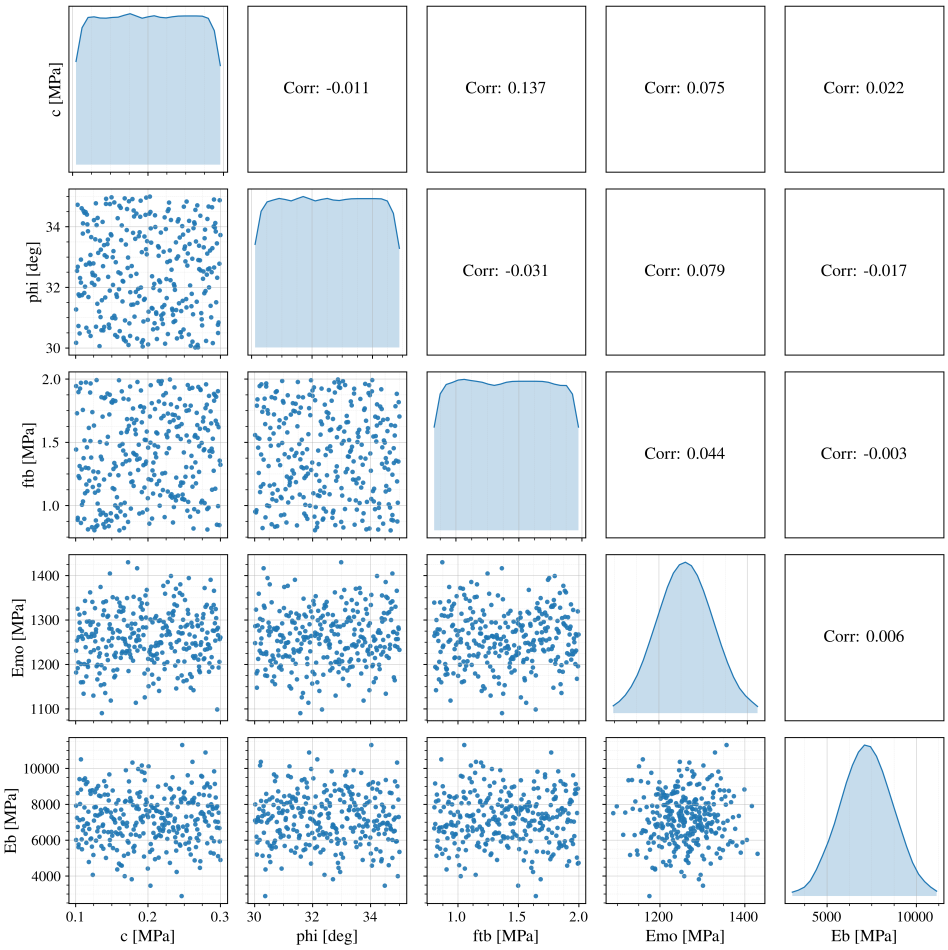


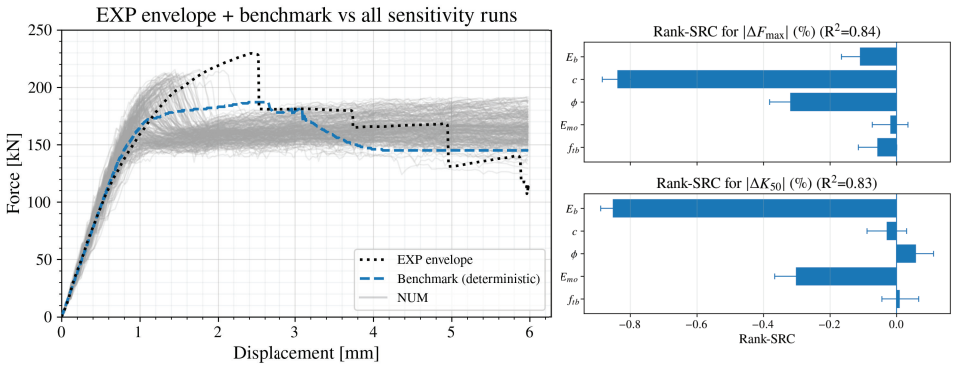
Figure 6.43. Latin Hypercube design for the sensitivity study ($N = 300$): marginal distributions and pairwise correlations

The diagonal panels in Figure 6.43 show the marginal coverage of each input (bounded for $c, \phi, f_{t,b}$, and approximately Gaussian for E_{mo} and E_b), while the lower-triangular scatter plots confirm a space-filling distribution without clustering. The upper-triangular correlation coefficients are close to zero, showing that no spurious linear dependence was introduced by the sampling procedure.

In the present non-spatial sensitivity analysis, parameter variability is modelled at the specimen level. Accordingly, each uncertain material parameter is assigned a single value per simulation that is applied uniformly to all corresponding joints or units throughout the structure. A set of 300 candidate values is generated for each random variable from its prescribed distribution, and each simulation draws one value per variable from this set to define a globally uniform parameter realisation. Thus, the ensemble of simulations represents 300 distinct wall realisations with different but spatially homogeneous material properties, enabling assessment of the influence of specimen-to-specimen variability on the global response without introducing additional uncertainty from spatial random fields.

Force-displacement response

Figure 6.44 summarises the outcomes of the non-spatial sensitivity analysis for the S-HEA-U specimen. In Figure 6.44A, the experimental envelope is compared against the deterministic benchmark simulation and the ensemble of sensitivity realisations generated via LHS. The sampled runs produce a band of responses that captures the dispersion in both the initial branch and the post-peak regime, visualising how plausible material variability propagates to the global force-displacement response. The deterministic benchmark lies within the ensemble, while the spread of runs highlights the range of stiffness and strength trajectories attainable within the prescribed parameter bounds.



(A) Force-displacement (300 realisations)

(B) Ranked-SRC plot for F_{max} and K_{50}

Figure 6.44. (**A**) Force vs displacement curve (**B**) Rank-based standardised regression coefficients (Rank-SRC) plot

Figure 6.44B reports the ranked standardised regression coefficient (rSRC) indices for the absolute percentage errors relative to the experimental targets, i.e.:

$$|\Delta F_{\max}| = 100 \left| \frac{F_{\max}^{\text{num}} - F_{\max}^{\text{exp}}}{F_{\max}^{\text{exp}}} \right| \tag{6.20}$$

$$|\Delta K_{50}| = 100 \left| \frac{K_{50}^{\text{num}} - K_{50}^{\text{exp}}}{K_{50}^{\text{exp}}} \right| \tag{6.21}$$

It is important to note that K_{50} denotes the stiffness obtained by dividing 50 kN by the corresponding displacement at 50 kN. The rSRC magnitude indicates the relative importance of each input, whereas the sign indicates whether increasing a parameter tends to increase or decrease the absolute mismatch to the experiment. Here, rSRC is obtained by fitting a linear regression to rank-transformed inputs and outputs so that the resulting coefficients quantify monotonic sensitivity in a scale-independent manner. For $|\Delta F_{\max}|$, the joint cohesion c_0 is the dominant driver, with secondary contributions from the friction angle ϕ, while the elastic moduli (E_{mo} and E_b) and the unit tensile strength $f_{t,b}$ play a comparatively minor role. In contrast, the error in the stiffness proxy $|\Delta K_{50}|$ is governed primarily by the brick modulus E_b, followed by the mortar modulus E_{mo}, consistent with the strong dependence of the interface normal/shear stiffness on the elastic moduli through the adopted stiffness closure. The high coefficients of determination ($R^2 \approx 0.85$–0.87) indicate that most of the variance in the error metrics can be explained by a monotonic (rank-linear) model, supporting the robustness of the inferred parameter importance ranking.

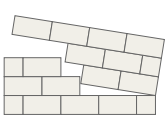
Variations of input parameters to global response

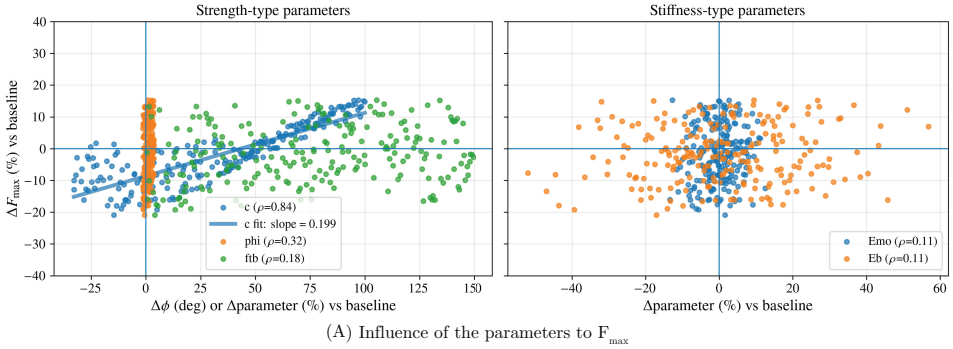
Figure 6.45 visualises the baseline-referenced sensitivity trends for the S-HEA-U specimen using Pearson correlation coefficients (ρ). Figure 6.45A relates the change in peak capacity $\Delta F_{\max}$, to the variations in the strength-type inputs (c, ϕ, and $f_{t,b}$; left) and stiffness-type inputs (E_{mo} and E_b; right). The scatter patterns and the reported ρ reconfirm that $\Delta F_{\max}$ is primarily governed by the joint cohesion c_0 ($\rho \approx 0.87$), with a secondary influence from the friction angle ϕ, while the stiffness parameters show only weak linear association with the peak response.

Figure 6.45B repeats the analysis for the stiffness proxy ΔK_{50}. In this case, the stiffness-type inputs dominate, most notably the brick modulus E_b ($\rho \approx 0.86$) and, to a lesser extent, the mortar modulus E_{mo}, whereas the strength-type inputs exhibit near-zero correlations. Overall, the figure supports the separation of control mechanisms: joint strength parameters primarily drive the peak load response, whereas the elastic moduli (via Equation (5.1)) primarily govern the initial stiffness measure.

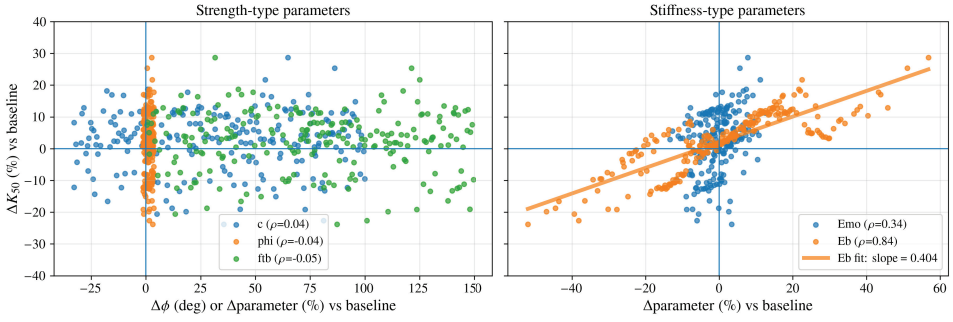
Effect on local mechanism

Figure 6.46 links the global peak response to the evolution of local subcontact failure mechanisms as the joint cohesion c_0 varies across the sensitivity ensemble. The upper panel reports the normalised share of tensile-type (TF), sliding/shear-type (SF), and compressive-type (CF) subcontact failures for each realisation, together with a rolling median to highlight the central trend. Here, the normalisation is performed with respect to the *total number of failed subcontacts* in a given run, i.e. TF + SF + CF = 1, instead





(A) Influence of the parameters to F_{max}



(B) Influence of the parameters to K_{50}

Figure 6.45. Pearson correlations between baseline-referenced input variations and the changes in $F_{\max}$ and K_{50}.

of the total number of active subcontacts in the model. With increasing cohesion, the mechanism composition exhibits a systematic redistribution: the TF share decreases, the SF share increases, and CF remains consistently negligible. This shows that, within the explored range, raising c does not trigger a transition towards compressive crushing failure, but pushes towards a more frictional/sliding-dominated dissipation mode along the joints.

The lower panel shows the corresponding predicted peak force $F_{\max}$ as a function of c, with the rolling median and the experimental peak force as references. The median $F_{\max}$ increases with cohesion, consistent with the enhanced joint shear resistance and the accompanying shift towards SF-dominated subcontact activity. Nevertheless, the simulated peak remains below the experimental reference over $c \in [100, 300]$ kPa, indicating that matching the peak would require cohesion values beyond 300 kPa, or, alternatively, adjustments to other influential parameters such as stiffness and the adopted strength–fracture-energy closure.

The supplementary visualisation of the spatial localisation of damage across the ensemble is given in Figure B.6. The reported fields correspond to the occurrence probability $p_{\mathrm{occ}}(i, j)$, defined in Equation (6.22) as the fraction of N realisations for which at least one damaged subcontact is recorded in grid cell (i, j) (mode-wise for dt, ds, dc,

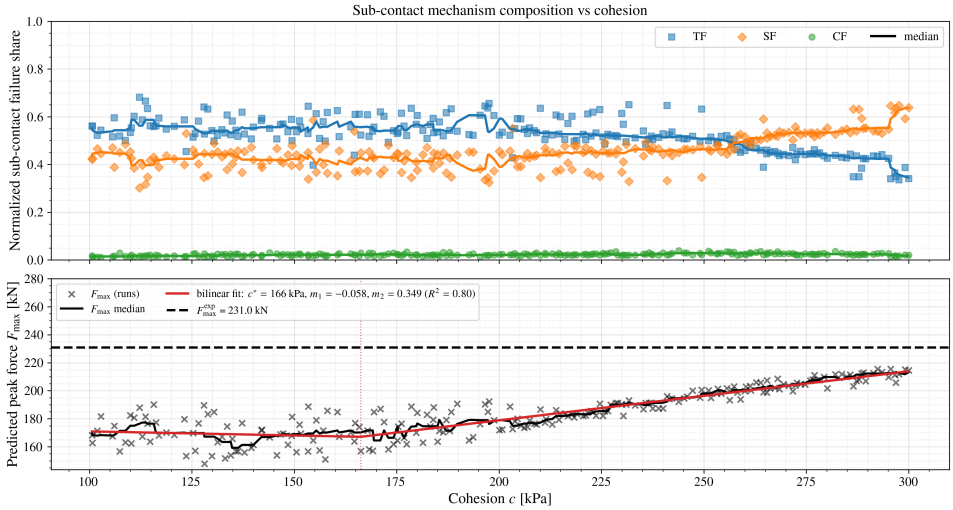


Figure 6.46. subcontact mechanism composition and peak capacity as a function of joint cohesion c_0.

and as a logical OR for the any mode map).

$$p_{\mathrm{occ}}(i,j) = \frac{1}{N}\sum_{r=1}^{N} \mathbb{I}\big[\, d_r(i,j) = 1 \,\big], \tag{6.22}$$

where $p_{\mathrm{occ}}(i,j) \in [0,1]$ is the occurrence probability in grid cell (i,j), N is the number of realisations, $\mathbb{I}[\cdot]$ is the indicator function, and $d_r(i,j)$ is a binary flag equal to 1 if at least one damaged subcontact is recorded in cell (i,j) for realisation r (and 0 otherwise).

Figure B.6A indicates a recurring diagonal localisation band, evidencing a consistent mechanism across all realisations, while Figure B.6B and Figure B.6C decompose this band into opening- and sliding-dominated contributions consistent with mixed-mode joint failure. Figure B.6D shows how localised the compressive crushing damage is, as it is mostly confined to the toe regions, suggesting that compressive failure is secondary relative to joint opening/sliding in this unreinforced configuration.

Best-fit material parameters

Figure 6.47 compares the experimental force–displacement envelope with the deterministic benchmark simulation and the best-fit realisation identified from the sensitivity ensemble. The best-fit run is selected by minimising the composite objective Equation (6.23), which balances agreement in peak capacity and overall curve shape through a weighted sum of the standardised peak-load error and curve-shape error.

$$J = w_F\, z\big(e_F\big) + w_c\, z\big(\mathrm{NRMSE}\big), \qquad z(x) = \frac{x - \mathrm{med}(x)}{\mathrm{IQR}(x)}, \tag{6.23}$$

where $w_F = 0.7$ and $w_c = 0.3$, med and IQR are the median and interquartile range of the respective error measure over the ensemble, and

$$e_F = \frac{\left|F_{\max}^{\text{num}} - F_{\max}^{\text{exp}}\right|}{F_{\max}^{\text{exp}}}, \tag{6.24}$$

$$\text{NRMSE} = \frac{\sqrt{\frac{1}{N}\sum_{i=1}^{N}\left(F_i^{\text{num}} - F_i^{\text{exp}}\right)^2}}{F_{\max}^{\text{exp}} - F_{\min}^{\text{exp}}}. \tag{6.25}$$

The peak-load term is the relative deviation from the experimental peak force (Equation (6.24)) and the curve-shape term is the normalised root-mean-square error between numerical and experimental forces on a common displacement grid (Equation (6.25)). Both measures are standardised over the ensemble before weighting, so the weights express the relative importance of the two criteria independently of their scale, and J is a ranking score rather than an error in physical units. The best-fit cohesion approaches the upper bound of the sampled range (0.282 MPa versus the 0.3 MPa upper limit). A wider sampling range or a follow-up local search would be needed to test whether an interior optimum exists. The analysis here treats 0.3 MPa as the upper bound consistent with experiment-informed plausibility.

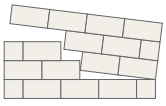
Overall, the overlay illustrates how the best-fit parameter set given in Table 6.15 improves the weighted objective defined in Equations (6.23) to (6.25) relative to the benchmark. This calibrated parameter set is subsequently adopted as the reference material configuration for the cyclic analyses, providing a consistent baseline that preserves the monotonic force–displacement characteristics while enabling the cyclic simulations to focus on the evolution of unloading/reloading stiffness, hysteretic dissipation, and damage accumulation under reversed loading.

Table 6.15. Best-fit parameter set corresponding to Figure 6.47.

Parameter	**Symbol**	**Best-fit value**
Realisation ID	rev	0
Joint cohesion	c	0.282 MPa
Friction angle	ϕ	34.26°
Unit tensile strength	$f_{t,b}$	1.79 MPa
Mortar/masonry modulus	E_{mo}	1271.7 MPa
Brick modulus	E_b	9162.7 MPa
Peak-load absolute error	e_F	8.39%
Stiffness-proxy absolute error	$\lvert\Delta K_{50}\rvert$	55.18%
Curve mismatch (NRMSE)	NRMSE	64.56%

6.4.5. Quasi-static cyclic analysis results

Based on the monotonic sensitivity analysis, the quasi-static assessment is identified as the next verification step to evaluate the model's ability to capture hysteretic energy



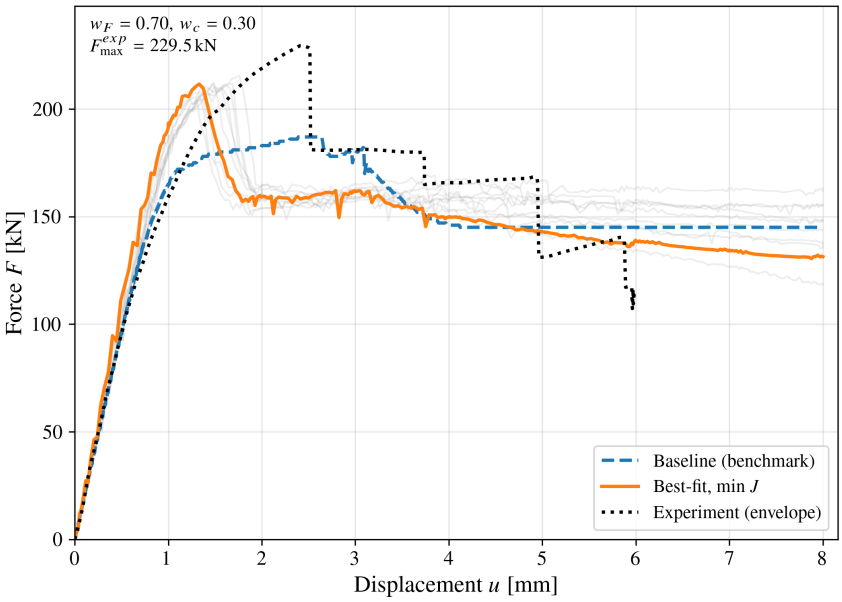


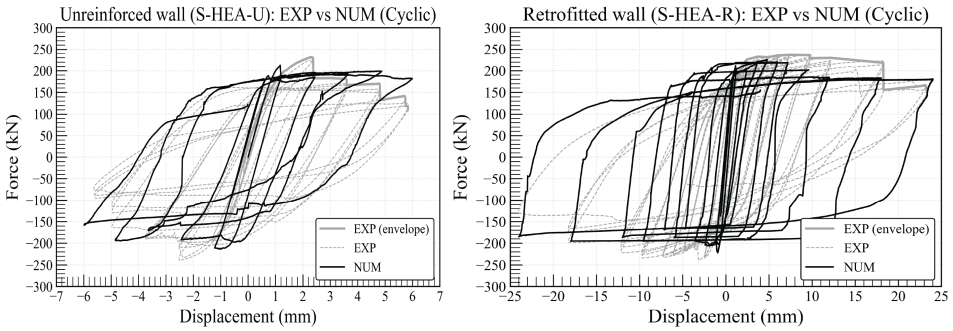
Figure 6.47. Overlay of the experimental envelope, the benchmark simulation, and the best-fit realisation obtained from the weighted optimisation objective. The experimental curve (black dotted) is the envelope of a cyclic test, whereas the benchmark, the best-fit realisation, and the grey curves are all monotonic simulations. The simulated monotonic response is therefore compared against the envelope of the cyclic response, not against an identical loading history. The grey curves are the individual realisations of the parameter sweep, among which the best-fit (orange) minimises the objective J formed with the weights $w_F = 0.70$ and $w_c = 0.30$. The experimental peak force is $F_{\max}^{\text{exp}} = 231.03\,\text{kN}$.

dissipation, stiffness degradation, and ultimate failure. The sensitivity study showed that the uncertainty in the unreinforced response is dominated by a small subset of masonry parameters, and the transition from the unreinforced to the retrofitted configuration yields only a limited increase in peak resistance, instead primarily affecting the deformation capacity and the post-peak trajectory.

The best-fit parameter set identified from the weighted objective in Table 6.15 is therefore carried forward as the reference material configuration. Quasi-static cyclic simulations are performed on both the unreinforced (S-HEA-U) and retrofitted (S-HEA-R) specimens to validate the baseline masonry model and quantify the structural improvements provided by the retrofit under reversed cyclic loading.

The experimental and numerical force-displacement curves for both specimens are compared in Figure 6.48. The numerical model successfully captures the initial stiffness and the general envelope of the experimental results for both configurations, while

underestimating the peak capacity to a degree consistent with the monotonic analysis. The experimental specimen failed at approximately 6 mm, and the numerical analysis was terminated at the same displacement to enable a like-for-like comparison of the cyclic response over the experimentally imposed range. The simulation has not detected a numerically defined failure event up to this point, so the comparison addresses the cyclic envelope and hysteresis shape rather than the model-predicted ultimate capacity. The numerical loops reproduce the overall backbone trend but still underestimate the peak capacity; the model also shows less pronounced pinching than the experiment and a comparatively stiffer reloading branch at larger amplitudes.



(A) Unreinforced wall (S-HEA-U) (B) Retrofitted wall (S-HEA-R)

Figure 6.48. Force-displacement curve of the cyclic analysis for S-HEA-U and S-HEA-R.

For the retrofitted specimen (Figure 6.48B), the numerical force-displacement response reproduces both the strength level and the enlarged deformation capacity. The analysis carried through to displacements exceeding 20 mm in agreement with the experimental observation. The peak resistance is reproduced within a smaller margin than for the unreinforced wall, although the loops exhibit substantially reduced pinching relative to the experiment. A characteristic feature of the simulated loops is the abrupt force drop at approximately 10 mm displacement in the positive loading branch. The drops are not indicative of a sudden loss of global stability of the masonry panel. They reflect rapid reconfigurations of the force-transfer mechanism in the coupled masonry-frame system, triggered by localised interface softening and changes in contact state over narrow displacement intervals. This produces an apparently over-stiff pre-activation sequence followed by a step-like reduction once the frame engages, yielding the rectangular cycle shape that distinguishes the numerical response from the more gradual hysteretic envelope of the experiment.

Figure 6.49 shows the numerical damage patterns at the ultimate displacement for each specimen, at 6.0 mm and 25 mm for S-HEA-U and S-HEA-R, respectively. The unreinforced model (Figure 6.49A) develops a shear-dominated mechanism with a pronounced diagonal localisation band, governed by joint opening and frictional sliding, which is consistent with the experimentally observed crack pattern (Figure 6.36A).

In the retrofitted model (Figure 6.49B), the deformation pattern is governed by a coupled frame–masonry mechanism. Joint shear displacements concentrate along the

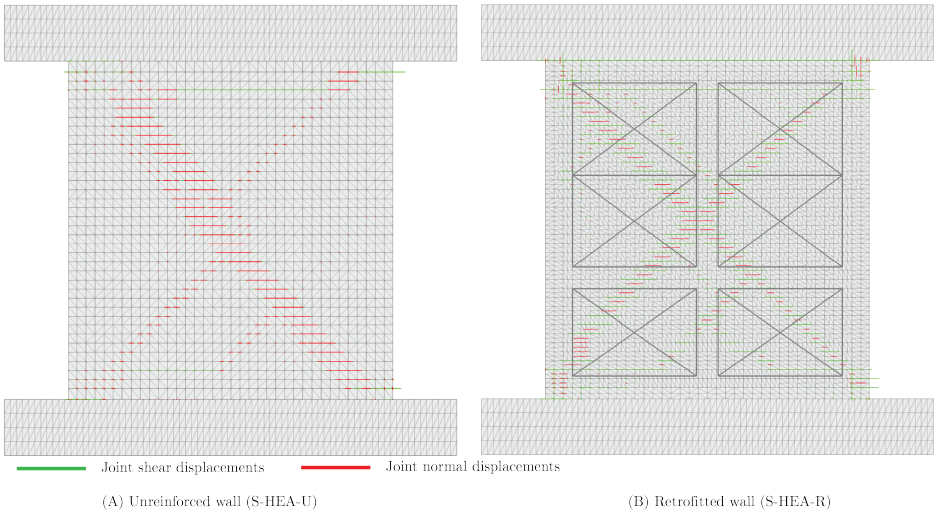


Figure 6.49. Numerical failure mechanisms and joint displacements at ultimate drift

diagonals spanning between the frame corners and the panel centre, while the joint opening localises at the frame anchorage regions close to the toes and the boundary zones where the frame transfers forces into the masonry. Bed joint sliding is also observed at the connection between the loading beam and the masonry at the top course, along with the straight-line crack through the units at each corner of the wall, consistent with the experimental crack pattern in Figure 6.36B.

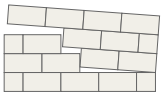
In conclusion, the combined comparison of hysteresis loops and deformation patterns indicates that the adopted material baseline remains transferable from monotonic calibration to cyclic response for both S-HEA-U and S-HEA-R. The model reproduces the governing shear-localisation mechanism and the increase in deformation capacity resulting from the retrofit. The deformable-block configuration remains stable under load reversals, confirming that the MASON contact model can operate consistently when joint nonlinearity is coupled with unit deformation. Remaining discrepancies in peak load and hysteretic pinching are systematic. The peak-load underprediction is present in both the unreinforced and retrofitted models, and its origin lies in the shared material baseline rather than in the retrofit link behaviour. The nonlinear links were therefore not included among the parameters of the sensitivity study, and their explicit characterisation is left to future work. The retrofitting strategy is subsequently carried forward to the building-level assessment in Chapter 8.

6.5. Summary and conclusions

This chapter evaluated the MASON contact constitutive model at the component scale, where structural response emerges from the interaction among many joints, blocks, and boundary conditions rather than from isolated interfaces. Across the selected

benchmarks, the assessment was mechanism-oriented, as the model was evaluated not only on force-displacement agreement but also on its reproduction of the intended governing kinematics, the spatial localisation of damage, and the dissipated energy under monotonic and cyclic loading sequences. This chapter established component-scale evidence that the proposed MASON contact model transfers from material calibration in Chapter 5 to structural response, evaluated against the monotonic solid clay wall experiment by Vermeltfoort *et al.* [1], cyclic calcium silicate (CS) walls by Messali *et al.* [2], and modular steel-frame retrofitted masonry piers by Albanesi *et al.* [3]. Specifically:

- Using a deformable-block configuration for the Vermeltfoort monotonic walls [1], the governing diagonal localisation is reproduced across the tested confinement levels. The comparison with the rigid-block formulation shows that the same governing mechanism and a comparable peak resistance are recovered at substantially reduced computational cost. The rigid-block formulation is therefore adopted for the subsequent analyses in this chapter, except for the retrofitted-wall test campaign, which retains the deformable-block configuration.
- The mesh-size variation, performed with the rigid-block model, indicates effective objectivity of the governing mechanism and the peak resistance across the edge lengths considered, with the initial stiffness contained within ±15 % and showing no systematic trend with discretisation. The post-peak softening and the dissipated energy are more sensitive, since these are path quantities set by the order and location of the discrete cracking and sliding events, with coarser discretisations tending to over-dissipate.
- The timestep variation indicates effective objectivity when $\Delta t \approx \Delta t_{\text{crit}}$. Strongly reduced fixed timesteps mainly perturb the post-peak softening through altered crack opening–closing and stick–slip sequence ordering, but the overall responses remain weakly sensitive to the change in the stable timesteps.
- For the cyclic analysis of CS walls [2], the MASON contact model remains stable over the tested loading protocol and captures the observed transition with increasing drift from rocking-dominated response to frictional sliding, with residual discrepancies concentrated in pinching and stiffness recovery at larger drifts. The loading application approach introduced in this chapter combines a calibrated quasi-static velocity with an energy-balance check on the kinetic-to-strain energy ratio. The approach performs reliably across the cyclic protocol, and the same methodology can be adopted in future quasi-static DEM analyses of masonry walls under reversed cyclic loading.
- The cross-comparisons to other numerical approaches available in the literature indicate that the MASON contact model yields responses consistent with established block-based approaches for both the Vermeltfoort *et al.* [1] and Messali *et al.* [2] tests, while preserving numerical robustness under softening and cyclic mechanisms within the explicit solver.
- In the Resisto 5.9 benchmark, both the MASON approach and the reference DEM model [23] reproduce the diagonal crack pattern. The reference model uses



a softening contact for the mortar combined with a Mohr-Coulomb plasticity model for the deformable units. The principal discrepancy in both models is an underestimation of the peak resistance by about 14 % to 22 %, accompanied by a peak that is mobilised at a smaller displacement than in the experiment. The initial stiffness is reproduced within 7 %, so the gap lies in strength and deformation scale and not in elastic stiffness. The MASON formulation achieves this agreement at substantially lower computational cost, as it operates on linearly elastic deformable blocks with a single internal crack plane, rather than on full block-level plasticity.

- Concentrating nonlinearity at interfaces promotes stronger joint localisation and earlier capacity drop once the diagonal band becomes connected, relative to formulations with distributed unit nonlinearity in the reference DEM model [23].
- The sensitivity study identifies cohesion as the primary control on peak capacity, with the cohesion-to-tensile-strength ratio held at approximately $c/f_t \approx 3.0$ during the parametric analysis, while the stiffness proxy is governed by the elastic moduli of the bricks and mortar joints through the adopted homogenised stiffness equations.
- A best-fit baseline from the weighted objective is fixed and carried forward as subsequent calibration and assessment focus on cyclic response, since the remaining retrofit uncertainties primarily govern the hysteretic degradation and damage evolution under repeated loading protocol.
- The model reproduces the cyclic benchmark for both the unreinforced and retrofitted walls, capturing the force-displacement response and local damage patterns for both configurations. The transition from brittle, low-displacement-capacity behaviour in the unreinforced specimen to ductile, large-displacement-capacity behaviour in the retrofitted specimen is reproduced numerically, thereby supporting the use of the MASON model for predictive cyclic analysis of unreinforced and strengthened masonry walls.

Overall, Chapter 6 shows that the MASON contact model can reproduce component-scale response in a mechanism-consistent manner across monotonic and cyclic, unreinforced and retrofitted configurations, while making clear which parts of the numerical response are robust to numerical settings and which remain governed by post-peak events and assumptions controlling deformation at peak resistance.

Chapter 7 extends this evidence from component behaviour to structural performance under dynamic demand. This chapter assesses whether the calibrated interface law remains stable and predictive under conditions where inertia, higher loading rates, and repeated damage cycles dominate the component's behaviour. Chapter 8 evaluates building-level response, where global kinematic constraints, load-path redistribution, and interaction between in-plane facades and out-of-plane transversal walls control the failure mechanism and the distribution of damage and dissipation of energy at the system level.



Chapter 6

Bibliography of Chapter 6

[1] A. T. Vermeltfoort, T. M. J. Raijmakers and H. J. M. Janssen. 'Shear Tests on Masonry Walls'. In: *Proceedings of the 6th North American Masonry Conference*. Ed. by A. A. Hamid and H. G. Harris. Philadelphia, Pennsylvania, USA: Technomic Publishing Co., June 1993, pp. 1183–1193.

[2] F. Messali, R. Esposito, G. Ravenshorst and J. Rots. 'Experimental investigation of the in-plane cyclic behaviour of calcium silicate brick masonry walls'. In: *Bulletin of Earthquake Engineering* 18.8 (2020), pp. 3963–3994. DOI: 10.1007/s10518-020-00835-x.

[3] L. Albanesi, C. F. Manzini and P. Morandi. 'Experimental In-Plane Seismic Performance of an Innovative Steel Modular Strengthening System for URM Walls'. In: *Journal of Earthquake Engineering* 28.5 (2024), pp. 1331–1357. ISSN: 13632469. DOI: 10.1080/13632469.2023.2231087.

[4] L. Macorini and B. A. Izzuddin. 'A non-linear interface element for 3D mesoscale analysis of brick-masonry structures'. In: *International Journal for Numerical Methods in Engineering* 85.12 (Mar. 2011), pp. 1584–1608. ISSN: 00295981. DOI: 10.1002/nme.3046.

[5] P. B. Lourenço and J. G. Rots. 'Multisurface Interface Model for Analysis of Masonry Structures'. In: *Journal of Engineering Mechanics* 123.7 (July 1997), pp. 660–668. ISSN: 0733-9399. DOI: 10.1061/(ASCE)0733-9399(1997)123:7(660).

[6] B. Pulatsu. 'Coupled elasto-softening contact models in DEM to predict the in-plane response of masonry walls'. In: *Computational Particle Mechanics* 10 (2023), pp. 1759–1770. ISSN: 2196-4378. DOI: 10.1007/s40571-023-00586-x.

[7] E. Minga, L. Macorini and B. A. Izzuddin. 'A 3D mesoscale damage-plasticity approach for masonry structures under cyclic loading'. In: *Meccanica* 53.7 (May 2018), pp. 1591–1611. ISSN: 15729648. DOI: 10.1007/S11012-017-0793-Z/FIGURES/25.

[8] Z. Xie, M. Sousamli, F. Messali and J. G. Rots. 'A sub-stepping iterative constitutive model for cyclic cracking-crushing-shearing in masonry interface elements'. In: *Computers & Structures* 257 (Dec. 2021), p. 106654. ISSN: 0045-7949. DOI: 10.1016/J.COMPSTRUC.2021.106654.

[9] Y. Nie, A. Sheikh, P. Visintin and M. Griffith. 'A robust computational strategy for failure prediction of masonry structures using an improved multi-surface damage-plastic based interface model'. In: *International Journal for Numerical Methods in Engineering* 124.11 (June 2023), pp. 2498–2528. ISSN: 10970207. DOI: 10.1002/NME.7218.

[10] K. Chaimoon and M. M. Attard. 'Modeling of unreinforced masonry walls under shear and compression'. In: *Engineering Structures* 29.9 (Sept. 2007), pp. 2056–2068. ISSN: 0141-0296. DOI: 10.1016/J.ENGSTRUCT.2006.10.019.

[11] S. Jafari. 'Material characterisation of existing masonry: A strategy to determine strength, stiffness and toughness properties for structural analysis'. PhD thesis. Delft: Delft University of Technology, 2021, pp. 1–272. DOI: https://doi.org/10.4233/uuid:3bcbbc72-0212-44e9-ac86-2fdc54ec5987.

[12] B. Pulatsu and K. Tuncay. 'Computational Modeling of Damage Progression in Unreinforced Masonry Walls via DEM'. In: *Turkish Journal of Civil Engineering* (Dec. 2023). ISSN: 2822-6836. DOI: 10.18400/tjce.1323977.

[13] G. Andreotti, F. Graziotti and G. Magenes. 'Detailed micro-modelling of the direct shear tests of brick masonry specimens: The role of dilatancy'. In: *Engineering Structures* 168 (Aug. 2018), pp. 929–949. ISSN: 0141-0296. DOI: 10.1016/J.ENGSTRUCT.2018.05.019.

[14] S. Sharma, F. Graziotti and G. Magenes. 'Torsional shear strength of unreinforced brick masonry bed joints'. In: *Construction and Building Materials* 275 (Mar. 2021), p. 122053. ISSN: 0950-0618. DOI: 10.1016/J.CONBUILDMAT.2020.122053.

[15] P. Lourenco. 'Computational strategies for masonry structures'. PhD thesis. Delft, Netherlands: Delft University of Technology, 1996.

[16] G. van Zijl. 'Modeling Masonry Shear-Compression: Role of Dilatancy Highlighted'. In: *Journal of Engineering Mechanics* 130.11 (Nov. 2004), pp. 1289–1296. ISSN: 0733-9399. DOI: 10.1061/(asce)0733-9399(2004)130:11(1289).

[17] R. Esposito, F. Messali and J. G. Rots. *Tests for the Characterization of Replicated Masonry and Wall Ties*. 2016. URL: http://resolver.tudelft.nl/uuid:a0923cf9-0ccd-48a1-9ce1-082aa66e97af.

[18] S. Jafari, J. G. Rots and R. Esposito. 'A correlation study to support material characterisation of typical Dutch masonry structures'. In: *Journal of Building Engineering* 45 (Jan. 2022). ISSN: 23527102. DOI: 10.1016/j.jobe.2021.103450.

[19] M. Sousamli. 'Orthotropic Cyclic Continuum Constitutive Model for Masonry Structures and Comparative Studies'. Doctoral thesis. Delft, The Netherlands: Delft University of Technology, May 2024, p. 214. ISBN: 978-94-6384-584-7. DOI: 10.4233/uuid:34614723-9a3c-42c8-b70c-e4ac1dca5e8c. URL: https://doi.org/10.4233/uuid:34614723-9a3c-42c8-b70c-e4ac1dca5e8c.

[20] A. M. D'Altri, F. Messali, J. Rots, G. Castellazzi and S. de Miranda. 'A damaging block-based model for the analysis of the cyclic behaviour of full-scale masonry structures'. In: *Engineering Fracture Mechanics* 209 (Mar. 2019), pp. 423–448. ISSN: 00137944. DOI: 10.1016/j.engfracmech.2018.11.046.



[21] B. Pulatsu, R. Wilson, J. V. Lemos and N. Mojsilović. 'Exploring the Cyclic Behaviour of URM Walls with and without Damp-Proof Course (DPC) Membranes through Discrete Element Method'. In: *Infrastructures 2024, Vol. 9, Page 11* 9.1 (Jan. 2024), p. 11. ISSN: 2412-3811. DOI: 10.3390/INFRASTRUCTURES9010011. URL: https://www.mdpi.com/2412-3811/9/1/11/htm%20https://www.mdpi.com/2412-3811/9/1/11.

[22] J. G. Rots. 'Invited Paper: Comparative Study of Crack Models'. In: *Finite Elements in Civil Engineering Applications: Proceedings of the Third DIANA World Conference, Tokyo, Japan, 9–11 October 2002*. Ed. by M. A. N. Hendriks and J. G. Rots. Lisse, The Netherlands: A. A. Balkema, 2002. DOI: 10.1201/9781003211365-4.

[23] N. Damiani, M. J. DeJong, L. Albanesi, A. Penna and P. Morandi. 'Distinct element modeling of the in-plane response of a steel-framed retrofit solution for URM structures'. In: *Earthquake Engineering & Structural Dynamics* 52.10 (2023), pp. 3030–3052. ISSN: 1096-9845. DOI: https://doi.org/10.1002/eqe.3910.

[24] C. F. Manzini, L. Albanesi and P. Morandi. *Studio del comportamento sismico di murature portanti rinforzate con rivestimento esterno modulare in acciaio*. Rapporto sperimentale EUC054/2021E–EUC088/2021U. Pavia, Italy: Fondazione EUCENTRE, 2021.

[25] Itasca Consulting Group Inc. *3DEC - Three Dimensional Distinct Element Code Ver. 9.1*. Minneapolis, 2024.

[26] B. Pulatsu, S. Gonen, F. Parisi, E. Erdogmus, K. Tuncay, M. F. Funari and P. B. Lourenço. 'Probabilistic approach to assess URM walls with openings using discrete rigid block analysis (D-RBA)'. In: *Journal of Building Engineering* 61 (Dec. 2022), p. 105269. ISSN: 2352-7102. DOI: 10.1016/J.JOBE.2022.105269.

[27] M. D. McKay, R. J. Beckman and W. J. Conover. 'A Comparison of Three Methods for Selecting Values of Input Variables in the Analysis of Output from a Computer Code'. In: *Technometrics* 21.2 (1979), pp. 239–245. DOI: 10.1080/00401706.1979.10489755.

[28] R. L. Iman, J. C. Helton and D. K. Campbell. 'An Approach to Sensitivity Analysis of Computer Models: Part I—Introduction, Input Variable Selection and Preliminary Variable Assessment'. In: *Journal of Quality Technology* 13.3 (1981), pp. 174–183. DOI: 10.1080/00224065.1981.11978748.

Chapter 6

7

Dynamic Validation and Damping Sensitivity

Building on the contact constitutive formulation and explicit stress-update strategy introduced in Chapter 4, this chapter explores the dynamic analysis of masonry structures using the Distinct Element Method (DEM). It focuses on simulating the response of masonry gable walls and cross-vaults under dynamic loading conditions, such as those encountered in shake-table tests. The chapter begins with an introduction to the challenges of modelling masonry structures dynamically in Section 7.1. In Section 7.2, a cross-comparison of dynamic in-plane tests on masonry cross-vaults is conducted, examining the difference between the available contact constitutive model for masonry in 3DEC and the proposed constitutive model in this study. The effect of different damping models on the dynamic response of the masonry cross-vault is investigated in Section 7.3, emphasising the importance of an accurate representation of energy dissipation. Section 7.4 presents a detailed case study of a dynamic shake-table test on masonry gable walls, highlighting the model setup, calibration, and validation against experimental data. The chapter concludes with a summary of findings and implications for future research in Section 7.5.

Contents

7.1. Introduction 242
7.2. Contact model comparison on the masonry cross-vault 244
7.2.1. Brief description of the SERA cross-vault shake-table experiment . . 244
7.2.2. Differences between the contact constitutive models 247
7.2.3. Numerical model and input parameters 247
7.2.4. Displacement response comparison 252
7.2.5. Local damage comparison 256

Parts of this chapter have been adapted from the published paper in *Bulletin of Earthquake Engineering*, 10.1007/s10518-026-02379-y and in *International Journal of Architectural Heritage*, 10.1080/15583058.2023.2277328.



7.2.6. Acceleration response comparison . . . 258
7.2.7. Discussion . . . 262
7.3. Damping model comparison on the masonry cross-vault . . . 263
7.3.1. Damping configurations . . . 264
7.3.2. Selection of the target damping ratio . . . 264
7.3.3. Adopted damping parameters . . . 269
7.3.4. Displacement response comparison . . . 271
7.3.5. Damage progression comparison . . . 271
7.3.6. Acceleration response comparison . . . 273
7.3.7. Discussion . . . 276
7.4. Shake-table tests on masonry gable walls . . . 277
7.4.1. Experimental description . . . 277
7.4.2. Numerical modelling setup . . . 283
7.4.3. Numerical results . . . 285
7.4.4. Comparison to mass-proportional damping on the STIFF specimen . 299
7.4.5. Discussion . . . 301
7.5. Summary and conclusions . . . 302

7.1. Introduction

Chapters 5 and 6 validated the MASON contact constitutive model under quasi-static loading. The material-level tests in Chapter 5 showed that the formulation reproduces the strength and fracture energy measured in monotonic characterisation tests on small-scale masonry specimens, together with the stiffness and strength degradation observed under cyclic loading. The component-level study in Chapter 6 extended this to in-plane shear-compression walls and to retrofitted piers under monotonic and cyclic loading. These quasi-static validations do not engage the mechanisms governing the dynamic seismic response. Inertia and viscous dissipation become active only under dynamic excitation, as does the impact generated when contacts separated during closure re-close. The dynamic behaviour of the modelling strategy must therefore be validated against experiment in its own right, and the sensitivity of the predicted response to the modelling decisions quantified. This chapter does so through controlled numerical experiments on well-instrumented shake-table specimens, varying the contact constitutive model and the damping scheme independently and comparing the predictions against the recorded response. This controlled validation lets the seismic response of the building in Chapter 8 be explored without revalidating the dynamic method itself.

Two modelling concepts are examined. The first is the contact constitutive model: does the additional complexity of MASON relative to simpler elasto-softening formulations translate into different dynamic predictions, or does the simpler model suffice? The second concept concerns the viscous damping scheme: does the frequency-dependent bias of mass-proportional damping affect the predicted response in a way that makes the Maxwell damping scheme preferable, and at what computational cost? The Distinct Element Method (DEM), introduced in Chapter 3, provides the common numerical framework for all analyses in this chapter. Its explicit time-marching scheme permits continuous updates to the structural geometry and contact topology, accommodating

finite block displacements and rotations without convergence difficulties often found in implicit solvers. The conditional stability of the explicit scheme, however, requires the timestep to remain below a critical threshold dictated by the stiffness-to-mass ratio of the smallest element (Equation (3.20)). This stable timestep was further tightened when stiffness-proportional damping is considered (Equation (3.31)).

The contact law at the unit-mortar interfaces determines how forces are transmitted between blocks, how cracks initiate and propagate, and how energy is dissipated through inelastic deformation. The MASON model developed in this dissertation was motivated by observed differences in the way existing elasto-softening formulations represent cyclic unloading-reloading behaviour, damage coupling, and energy dissipation, as discussed in Chapter 4. However, whether those differences actually affect the predicted seismic response of a complex structure has not been tested. The TSCLinear model [1], an elasto-softening formulation with linear post-peak degradation and a compression cut-off coupling the shear and compression regimes, has been applied successfully to a range of masonry typologies [2–4] and is available in *3DEC* [5]. Under monotonic loading with moderate damage, both models produce comparable results, as shown in Chapter 6. Under dynamic loading, repeated load reversals activate the unloading-reloading paths and the damage coupling that distinguishes the two formulations. Whether the additional constitutive features of MASON translate into measurably different predictions requires a controlled cross-comparison of the same benchmark. A detailed description of the differences between the two models is given in Section 7.2.

Even with an inelastic contact model, DEM simulations of dynamic problems typically require additional viscous damping to represent dissipation mechanisms not captured by the constitutive law, such as internal material damping and chattering at boundaries. The standard approach is to implement mass-proportional Rayleigh damping, which is computationally feasible but produces a damping ratio that varies inversely with frequency: low-frequency modes are overdamped, and high-frequency modes are underdamped. As damage softens the structure and shifts its dominant frequency downward, the overdamped region may artificially suppress the response [6, 7]. The stiffness-proportional component of Rayleigh damping corrects this frequency bias but reduces the critical timestep by one to two orders of magnitude in an explicit solver (Equation (3.31)), making it impractical for large deformable-block models.

The Maxwell damping scheme (Section 3.2.3) offers a middle ground. Spring-dashpot elements in series are placed in parallel with the joint springs at unit-mortar interfaces. By stacking multiple elements with different relaxation times, the combined damping ratio becomes approximately uniform over a specified frequency band without the severe timestep penalty. The formulation was initially tested for rigid DEM blocks by Lemos *et al.* [8] and applied to masonry arches in Lemos and Sarhosis [9]. In this thesis, the scheme has been extended to a three-dimensional deformable-block cross-vault model with an automatic calibration algorithm based on Levenberg-Marquardt optimisation (Section 3.2.3).

Finally, the first two investigations described above vary the constitutive model and the damping scheme independently on the same cross-vault benchmark, which is primarily loaded in-plane. A further objective is to check whether these two components work together on a different structural typology and loading direction. Masonry



gable walls in Dutch residential buildings are slender, lightly loaded, and laterally restrained only by the roof diaphragm. Their seismic response is typically governed by out-of-plane mechanisms, including horizontal cracking, rocking, and overturning. These mechanisms differ from the in-plane shear failure observed in the cross-vault. The ERIES-SUPREME experimental campaign [10, 11] tested three full-scale solid clay gable walls on a dual shake-table setup at the EUCENTRE 9DLAB facility, applying differential base motions to simulate stiff, semi-flexible, and flexible roof configurations. The tests were run incrementally until complete collapse. This case study uses MASON with Maxwell damping, supplemented by a short cross-comparison against mass-proportional damping to assess whether the latter can adequately predict the collapse of slender out-of-plane components. The full description and results are presented in Section 7.4.

7.2. Contact model comparison on the masonry cross-vault

The SERA blind prediction and post-diction competition provided a well-documented benchmark for evaluating discontinuum-based modelling strategies applied to masonry cross-vaults under seismic loading [12]. The earlier work conducted by Oktiovan *et al.* [2] employed the elasto-softening contact model (TSCLinear) by Pulatsu [1] within a simplified micro-modelling framework implemented in *3DEC* to simulate the unstrengthened and retrofitted cross-vault specimen tested at the LNEC facility in Portugal. The study demonstrated satisfactory agreement with the experimental response at both qualitative and quantitative levels, yet also identified areas where the constitutive representation of post-peak damage and energy dissipation could be improved.

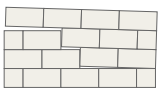
The purpose of this section is to re-analyse the same cross-vault model using the MASON contact constitutive model and to compare the results directly against those obtained with the TSCLinear formulation. The comparison is structured around two aspects: the global response quantities, namely displacement and acceleration time histories at selected monitoring points; and local damage evolution, assessed through the spatial distribution of joint damage scalars.

The numerical model geometry, mesh discretisation, boundary conditions, and loading protocol are identical in both analyses. Both models adopt the post-diction calibrated material parameters, meaning that the contact stiffnesses, strength values, and fracture energies have been adjusted in light of the experimental results from the SERA campaign. This ensures that any observed differences between the two predictions arise from the constitutive formulation itself rather than from differences in calibration quality.

7.2.1. Brief description of the SERA cross-vault shake-table experiment

The experimental benchmark used in this section and in Section 7.3 is the shake-table campaign conducted at LNEC within the SERA project, reported in detail in Bianchini *et al.* [13]. An overview of the results from the associated blind prediction and post-diction competition is given by Calderini *et al.* [12]. Only the aspects relevant to the numerical comparison are summarised here; the reader is referred to the original publications for the full experimental programme.

The specimen, shown in Figure 7.1, is a single-ring masonry cross-vault with a square plan of 3.5×3.5 m^2, a rise of 1.2 m, a net span of 2.9 m, and a thickness of 0.12 m. The



vault was built with clay bricks ($0.045 \times 0.12 \times 0.23\ m^3$, H × W × L) laid in an orthogonal bond pattern with 10 mm mortar joints. It rests on four piers: two are masonry assemblies fixed to the reinforced-concrete shake-table base, and two are steel masses on wheels that can slide in both horizontal directions. The piers are connected by three pairs of ϕ32 mm steel tie bars, except at the fixed-pier connection, which uses steel profiles. Steel UPN profiles are added to the fixed piers to reduce relative displacements between supports. Corner infill masonry extends up to half the vault rise at the four springings.

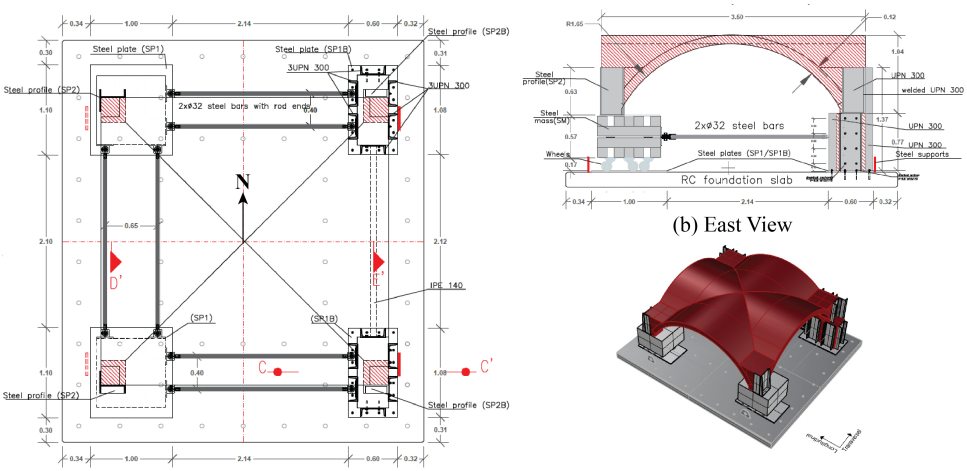


Figure 7.1. The experimental cross-vault detailed specifications (Bianchini *et al.* [13])

The instrumentation layout is presented in Figure 7.2. Four *optical cameras* (OC, i.e., still cameras used for optical displacement tracking) were placed to record the displacement response at the vault's extrados, following the experimental terminology of [13] (OC1–OC4; see Figure 7.2A). Four video cameras (VC) on each elevation of the vault were used to document crack initiation and propagation during the tests.

The seismic input is the 6th April 2009 L'Aquila earthquake record, recorded along the North-South direction at the *Italian Rete Accelerometrica Nazionale* (RAN) Station AQA ([13]). Figure 7.2B illustrates the 75% scaled input (AQA75). The maximum absolute acceleration, velocity, and displacement of the AQA75 earthquake are $4.25\,m\,s^{-2}$,$26.33\,cm\,s^{-1}$, and 37.0 mm, respectively. The first 15 s ($t = 0$–15 s) of the 25 s input segment provided by the experimental campaign is adopted as loading. This truncation contains 97 % of the Arias intensity of the 25 s sample (Figure 7.2B). The effective duration based on the 5 % to 95 % Arias interval is 8.28 s. The seismic load was applied unidirectionally along the longitudinal (North-South) direction of the vault, with four increments of amplitude considered for the UNS specimen: 10 %,25 %,50 %, and 75 %. The shake-table test for the UNS vault specimen was performed up to the damage level at which structural equilibrium is still maintained, thereby allowing strengthening through the TRM grid.

For more details regarding the material characterisation tests, design and construction

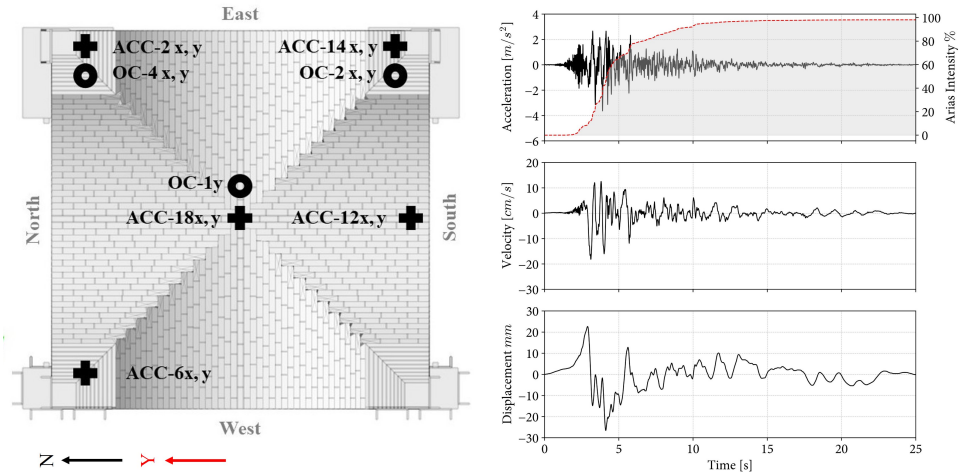


Figure 7.2. Instrumentation setup of the unstrengthened (UNS) cross-vault specimen Bianchini *et al.* [13] and AQA75 input signal

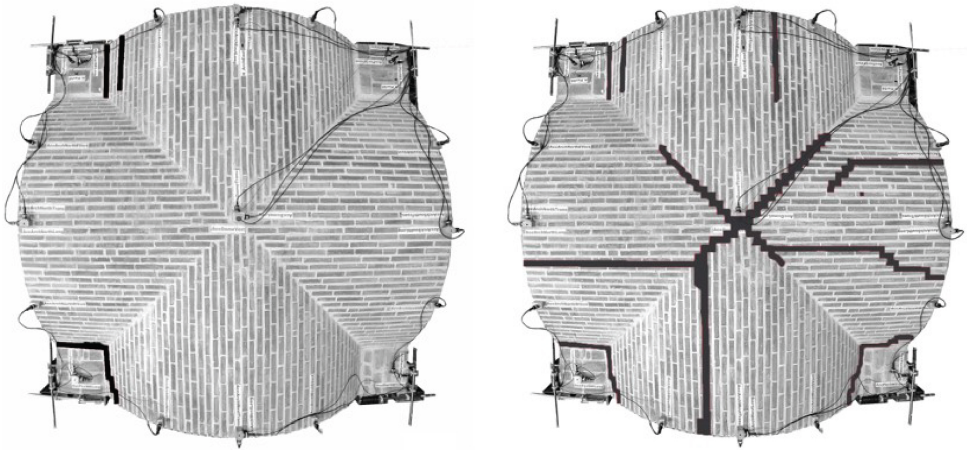


Figure 7.3. Experimental crack patterns at the end of tests for 50 % and 75 % of AQA EQ amplitude [13]

processes, and experimental results, readers are referred to [13]. The experimentally observed crack patterns at the end of tests for 50 % and 75 % maximum amplitude of AQA EQ are presented in Figure 7.3. No visible cracks were observed at the 10 % and 25 % load increments. At the end of 50 % load increment, detachments between the infill masonry and the cross-vault were observed at both the fixed and moving piers in the north section (Figure 7.3A). Significant damage was observed at the 75 % load increment (Figure 7.3B), representing an in-plane shear failure mode. The damage started from the vault crown, propagated towards the groins in all directions, and eventually dispersed to the four

webs of the cross-vault. Since full collapse was out of the scope of the experiment, load increment was stopped at 75 %.

7.2.2. Differences between the contact constitutive models

Both the TSCLinear model and MASON belong to the family of elasto-softening contact formulations that lump the nonlinear behaviour of masonry constituents at zero-thickness interfaces between expanded masonry units. They share the same simplified micro-modelling philosophy described by [14] and employ normal and shear springs at each contact point to relate relative displacements to contact stresses. However, they differ in several respects that become relevant under dynamic loading conditions.

The TSCLinear model, as implemented by Pulatsu [1], defines linear softening branches in tension, shear, and compression, governed by fracture energies G_f^I, G_f^{II}, and G_c. Upon reaching the respective peak strengths, the contact stresses degrade linearly with increasing relative displacement until the residual strength is reached. A compression cut-off is used to define the shear-compression interaction. The unloading-reloading behaviour follows the same elastic stiffness in both normal and shear directions, meaning that no stiffness degradation is accounted for in tension, compression, or shear upon repeated load reversals.

The MASON model, by contrast, introduces several modifications that separate the two formulations once the contacts undergo load reversals (Figure 7.4):

1. A multi-surface plasticity formulation with coupled damage evolution across tension, shear, and compression regimes, governed by independent damage scalars d_t, d_s, and d_c. The tensile and shear modes are coupled through a combined tensile-shear damage scalar d_{ts}.

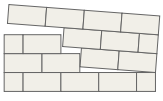
2. Nonlinear softening curves in compression, consisting of a parabolic ascending branch followed by a combined quadratic-exponential descending branch rather than the linear envelope.

3. Stiffness degradation upon unloading in both tension and compression, with a recovery factor that governs the reloading path and the amount of hysteretic energy dissipated during load reversals.

These differences do not matter under monotonic loading at moderate damage levels, where both models produce comparable results. Seismic excitation, however, reverses the loading direction repeatedly, and these reversals activate the unloading-reloading paths and the coupling between damage modes, so the constitutive differences become more pronounced. The following subsections examine the practical consequences of these differences against experimental data.

7.2.3. Numerical model and input parameters

The cross-vault model adopted in this section is taken from Oktiovan *et al.* [2] with identical geometry, mesh discretisation, and boundary conditions. The comparison is restricted to the unstrengthened (UNS) specimen. The unstrengthened configuration



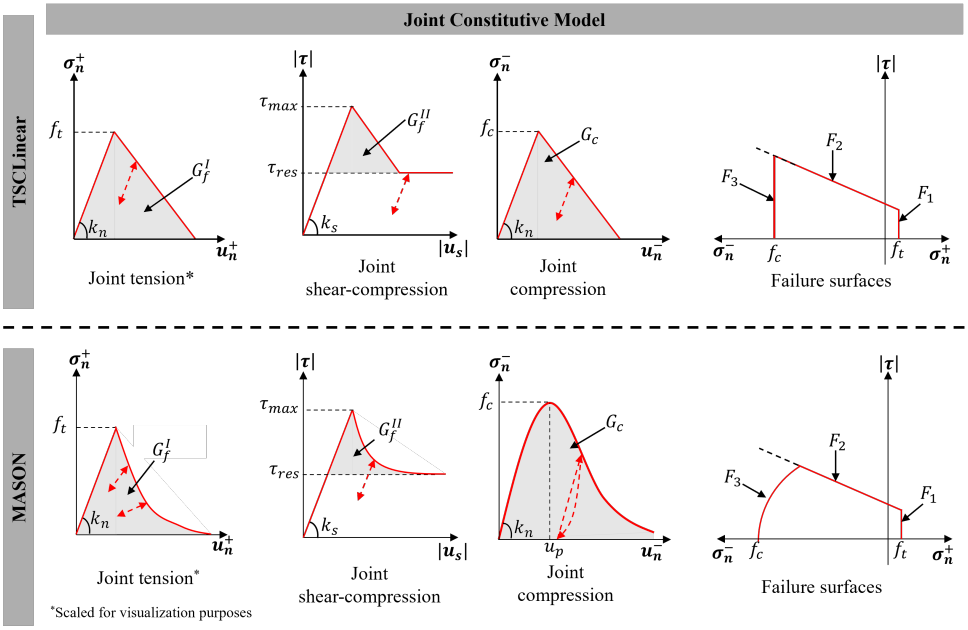
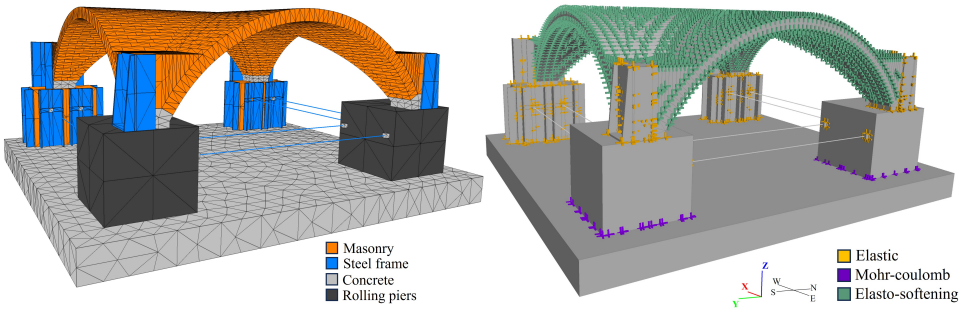


Figure 7.4. Elasto-softening joint constitutive model used for the vault and infill contacts, compared for the TSCLinear (top) and MASON (bottom) formulations. From left to right, the joint tension, shear-compression, and compression responses are shown, followed by the corresponding failure surfaces in the $|\tau|$ versus σ_n plane. Here k_n and k_s are the normal and shear contact stiffnesses, f_t and f_c are the tensile and compressive strengths, τ_{max} and τ_{res} are the peak and residual shear strengths, and G_f^I, G_f^{II}, and G_c are the mode I, mode II, and compressive fracture energies. The failure surface is composed of the tension cut-off F_1, the Coulomb friction surface F_2, and the compression cap F_3. The joint tension response is scaled for visualisation.

isolates the masonry response from the additional modelling assumptions that the strengthening layer would introduce (bond between the cementitious repair and the substrate, composite stiffness), which would add variables beyond the scope of the present constitutive model comparison. The reader is referred to Oktiovan *et al.* [2] for the full description of the model. A brief summary is provided here for completeness.

The mesh discretisation of the cross-vault model is presented in Figure 7.5A. The wheel system on the movable piers (Figure 7.1) is omitted from the numerical model due to its modelling complexity. To allow the movable piers to slide in the horizontal direction, a low shear stiffness and a friction angle are applied at the contact points between the piers and the shake table base. The movable piers and concrete foundation are meshed independently, using different CST element edge lengths to eliminate irregular meshes that could bottleneck the system's critical timestep (Equation (3.20)).

The maximum edge length for the tetrahedral elements of the masonry components is



(A) Mesh discretisation (B) Contact discretisation

Figure 7.5. Mesh discretisation of the cross-vault components

set to 25 cm while the maximum edge length for the steel frame and movable piers is set to 50 cm. The maximum edge length for the concrete elements (vault support, tie anchors, and shake table base) is set to 25 cm. The steel ties were also modelled as trusses, with one degree of freedom at each end and perfect connections to the tie anchors. The cross-section of the steel ties is 8×10^{-4} m^2 and the density is set to 7800 kg m^{-3}. Partial density scaling is applied to distorted steel and tie-anchor elements, increasing the total system mass by 5.92% while permitting a stable timestep of 1.25×10^{-6} s.

The contact discretisation on each component of the cross-vault model is presented in Figure 7.5B, and the corresponding constitutive models are illustrated in Figure 7.6. Potential crack planes are not considered at the brick's mid-length, as no unit splitting was observed in the experimental evidence. Three contact formulations are assigned based on the interface's physical role. The elastic joint model (Figure 7.6A) is defined for the contacts between the steel frame parts and the other components, where a linear transfer of forces without inelastic mechanisms is intended. The Mohr-Coulomb joint model (Figure 7.6B) with zero tensile strength, cohesion, and low friction is implemented on the movable piers to simulate the dry joint connection between them and the shake-table base. The elasto-softening joint model (Figure 7.4) is used for all contacts within the vault and infill components, where the TSCLinear and MASON formulations diverge. The elastic and Mohr-Coulomb contacts are identical in both analyses.

The material properties obtained from the material characterisation test [13] and used as the modelling input parameters are summarised in Table 7.1. The normal and shear stiffnesses needed for the contact constitutive laws are obtained using Equation (5.1) ([14]), where t_m is the thickness of the actual mortar layer. There is no distinction between parallel and perpendicular joints to the web of the vault in the cross-vault model in this study.

For the MASON model, the additional parameters governing the unloading-reloading behaviour and the dilatancy softening are calibrated following the procedure described in Chapter 6. The fracture energies in both models follow the empirical expressions of Equations (7.1) to (7.3) [15].

$$G_f^I = 0.025(2f_t)^{0.7} \tag{7.1}$$

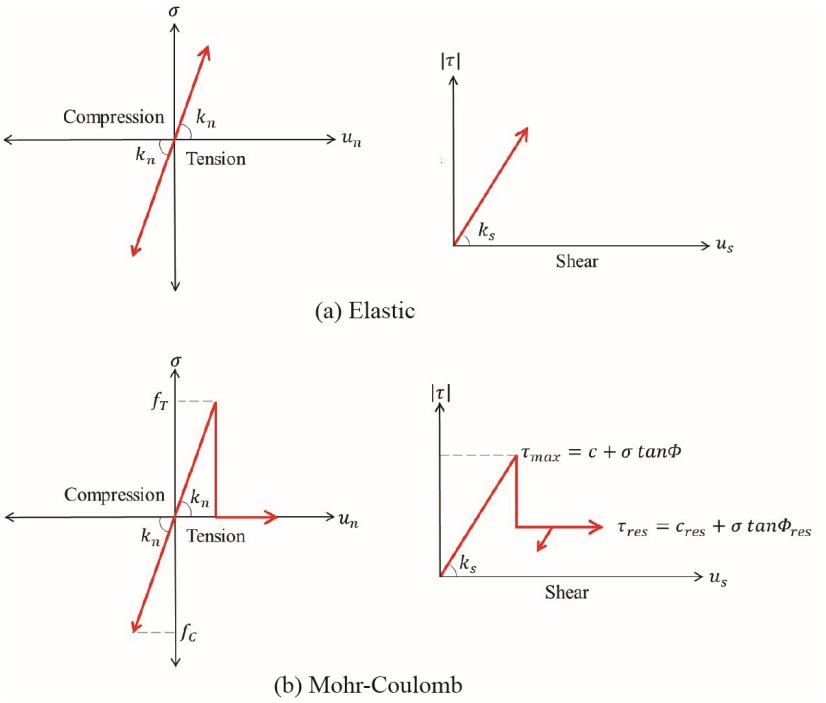


Figure 7.6. Contact constitutive models implemented in the cross-vault simulation: (a) elastic joint and (b) Mohr-Coulomb joint. The normal stress-displacement response (left) and the shear stress-displacement response (right) are shown for each model, after Oktiovan *et al.* [2].

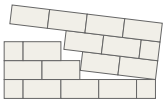
Table 7.1. Material properties used for the modelling input parameters ([13])

Units		Mortar	Interface/joints			
Young's modulus[a]	Poisson ratio	Young's modulus[a]	Tensile strength	Comp. strength	Cohe-sion	Friction angle
E_b	ν	E_m	f_t	f_c	c	ϕ
MPa	-	MPa	MPa	MPa	MPa	deg
6200	0.25	370.05	0.3	9.1	0.3	38

a Modulus of elasticity was obtained from the average slope of the secant line at 50% and 80% compressive strength.

$$G_f^{II} = 10G_f^I \tag{7.2}$$

$$G_c = 15 + 0.43f_c - 0.0036f_c^2 \tag{7.3}$$



The normal and shear stiffnesses defined in Equation (5.1) apply only to the brick-to-brick contacts, i.e., the contact points with the elasto-softening joint constitutive model. For the linear elastic joint model, the normal and shear stiffnesses are set to a relatively high value of 100 GPa m^{-1}. For the Mohr-Coulomb joint model, the normal stiffness is set to 10 GPa m^{-1} to avoid interpenetration of the movable piers to the shake table base. The shear stiffness is equal to 0.01 GPa m^{-1} while the cohesive strength and friction angle are set to 0 MPa and 1°, respectively. The density and Young's modulus of the auxiliary components are also provided in Table 7.2. Since steel parts connect the fixed piers, the back frame density is adjusted so that the numerical prediction error is negligible.

Table 7.2. Density and Young's Modulus of the auxiliary components

Component	Density ρ kg/m^3	Young's modulus E GPa	Poisson ratio ν -
Back Frame Steel	10685	200	0.3
Rolling Piers	5570	200	0.3
Tie Anchors	2000	200	0.3
Concrete	2000	25	0.3

Density scaling is commonly used to enhance the computational efficiency of explicit solvers in the DEM, particularly for large and geometrically complex models. In this approach, the density of certain elements is artificially increased to allow a larger stable timestep, thereby reducing the overall simulation time. However, global density scaling, in which the mass of all elements in the model is uniformly increased, can introduce significant inertial artefacts, rendering it unsuitable for dynamic simulations. A separate, local difficulty remains. Small or highly distorted tetrahedral elements may still form during automatic mesh generation, and because of their high stiffness-to-mass ratios, they control the critical timestep, substantially reducing it to keep the explicit integration scheme stable. To address this, partial density scaling is applied selectively to only the distorted elements. This localised adjustment increases their mass enough to meet a prescribed timestep, without significantly altering the system's total mass. In *3DEC*, the partial density scaling is applied by specifying a target timestep, allowing the program to apply the necessary amount of density scaling to the system to achieve that timestep.

The density scaling factor (dsf) shown in Figure 7.7 is defined as a nodal mass multiplier, $\text{dsf}_i = m_i^{\text{scaled}} / m_i^{\text{real}}$. Hence, dsf = 1.0 indicates no mass scaling, while dsf > 1.0 indicates added mass. Without applying partial density scaling, the critical timestep for the cross-vault model is limited to 5.27×10^{-7} s. By increasing the timestep to 1.25×10^{-6} s through partial density scaling, the total system mass increases by only

5.92 %. Furthermore, as illustrated in Figure 7.7, density scaling is confined to the steel components and tie anchors, which are not expected to influence the structural behaviour of the vault. Consequently, the numerical simulations presented in the following section employ density scaling with the target timestep of 1.25×10^{-6} s.

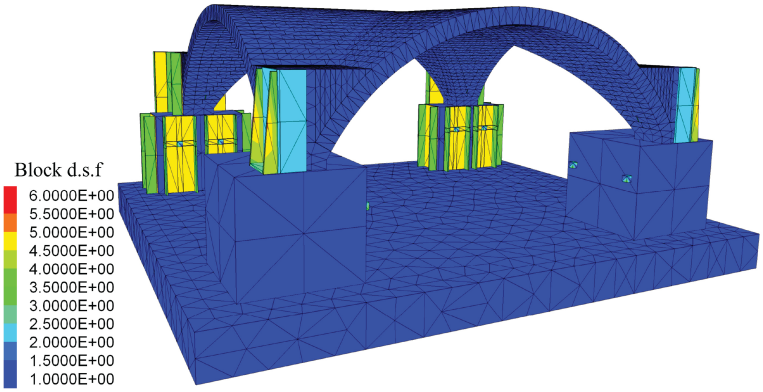


Figure 7.7. Density scaling factor plot of the cross-vault model with the target timestep of 1.25×10^{-6} s.

The damping ratio for the MassProp model is taken at 4 % with a centre frequency of 7.5 Hz. The centre frequency corresponds to the first mode natural frequency of the cross-vault model, which is slightly shifted to account for the reduction of the natural frequency due to damage. The damping ratio is determined based on recommendations from other researchers for masonry structures [3].

7.2.4. Displacement response comparison

At the AQA25 and AQA50 amplitude levels, the TSCLinear and MASON models produce displacement time histories that are nearly indistinguishable from each other and track the experimental recordings closely at all monitoring points. This is expected as at these intensity levels the vault remains in the elastic or near-elastic regime, and the constitutive features that differentiate the two models have not yet been activated. The corresponding time histories are included in Figures C.1 and C.2 for completeness. The AQA75 results, where the constitutive differences become visible, are presented in Figure 7.8. In the longitudinal direction (OC1-y through OC4-y), where the seismic excitation was applied, both models reproduce the experimental phase and amplitude during the strong-motion window ($t \approx 2$–5 s) with comparable accuracy. After the main pulse, the response diverges.

Between $t = 3$ s and $t = 4$ s, the input transitions to a low-frequency, high-amplitude pulse that drives the largest negative displacement of the record. Both TSCLinear and MASON capture this negative peak with similar magnitudes, indicating that constitutive differences have a limited effect on peak response prediction when the same damping scheme is used. After the main pulse ($t > 5$ s), the two models begin to drift apart, where the residual oscillations differ slightly in amplitude and mean offset, with one model settling at a marginally different residual displacement than the other. These differences

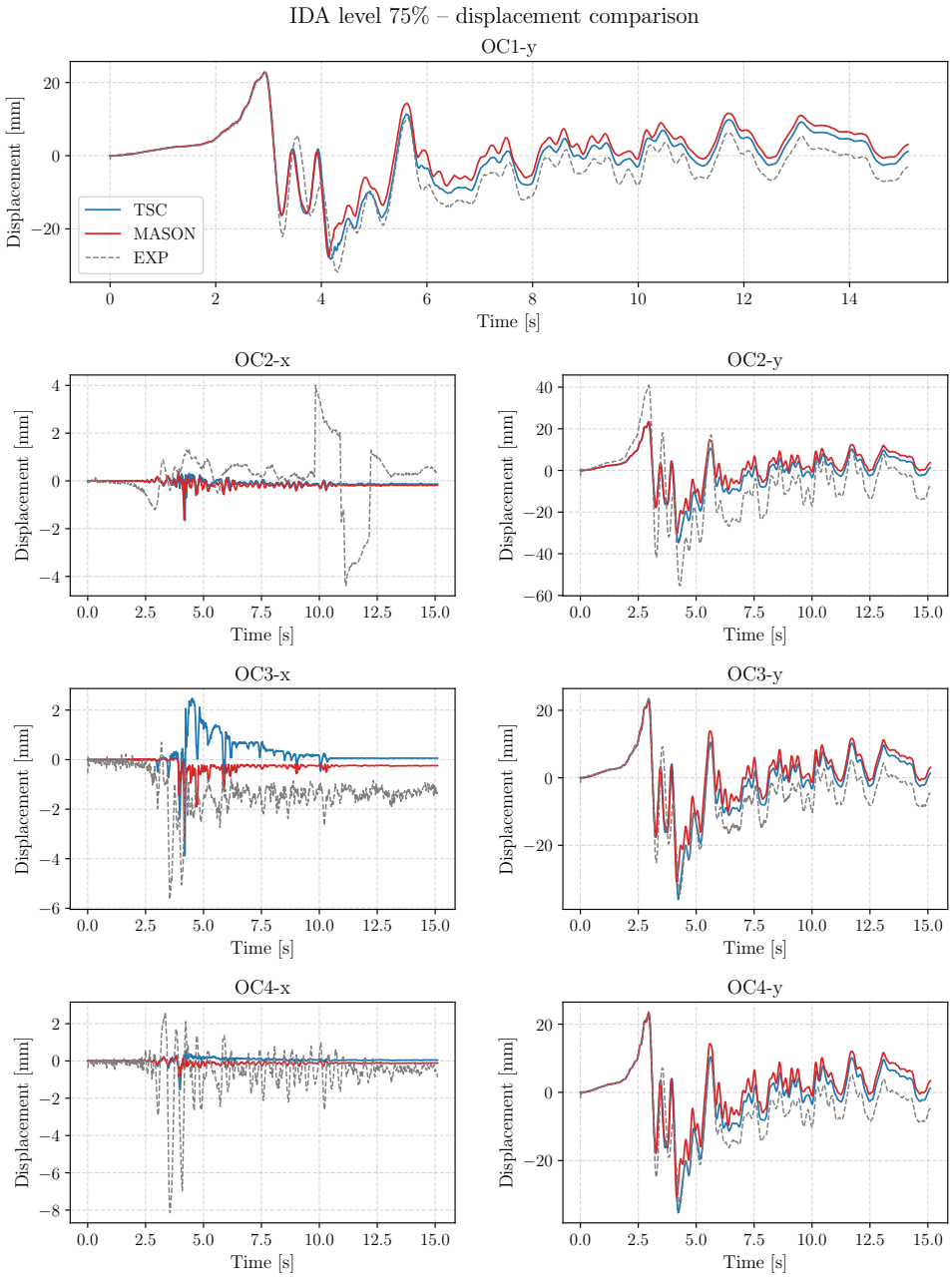


Figure 7.8. Displacement time histories at the four optical camera locations (OC1–OC4) for the AQA75 amplitude level.

remain small relative to the overall displacement range and to the discrepancy between either numerical model and the experimental recording. The close agreement between TSCLinear and MASON at peak suggests that, for this benchmark, the constitutive model is not the governing factor in the peak displacement prediction under the adopted mass-proportional damping scheme.

In the transverse direction (OC2-x, OC3-x, OC4-x), the experimental data show displacement amplitudes of several millimetres that develop after the onset of significant cracking. Neither model captures the full magnitude of these transverse displacements, as expected, given that the loading is applied unidirectionally along the Y-direction and the transverse response arises from the asymmetric redistribution of forces through the damaged vault. At OC3-x and OC4-x, both models predict transverse displacements well below the measured values. At OC3-x, the small offset predicted by TSCLinear is directed opposite to the measured response, whereas MASON follows the direction recorded in the experiment. Because this transverse response is a secondary effect, as noted above, the sign of these small offsets is not taken as a measure of relative accuracy.

Figure 7.9 summarises the global response comparison across all amplitude levels through the absolute peak displacement at each monitoring point as a function of the IDA level. In the longitudinal direction, both models follow the experimental trend and remain close to each other at all intensity levels. MASON predicts slightly lower peaks than TSCLinear at AQA75, most noticeably at OC2-y and OC4-y, where TSCLinear is closer to the experimental value. The difference between the two models is, however, small compared to the gap between either model and the experiment. In the transverse direction, both models underpredict the experimental peaks by a wide margin at all intensity levels. This confirms that the transverse response is governed by the asymmetric redistribution of forces that occurs when damage occurs, which is relatively difficult to capture in numerical simulations.

To assess the deviation of the numerical prediction from the experimental value, the root-mean-square deviation (RMSD) is calculated and compared with the experimental RMSD. Let $d \in \{x, y\}$ be the displacement in the East-West and North-South directions, respectively, $k \in \{1,2,3,4\}$ be the measurement point at OC1, OC2, OC3, and OC4, and $\{t_i\}_{i=1}^{N}$ be the sampled times. For any signal $u^{k,d}(t)$ (both experimental and numerical), the RMSD is calculated as follows:

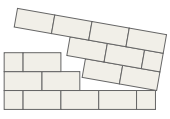
$$\mathrm{RMSD}^{k,d}[u] = \sqrt{\frac{1}{N}\sum_{i=1}^{N}\left(u^{k,d}(t_i)\right)^2} \tag{7.4}$$

Averaged across the selected optical cameras:

$$\overline{\mathrm{RMSD}}^{d}[u] = \frac{1}{4}\sum_{k=1}^{4}\mathrm{RMSD}^{k,d}[u] \tag{7.5}$$

which is then compared to the experimental RMSD to obtain the relative error:

$$\epsilon^{d}_{RMSD} = \frac{\left|\overline{\mathrm{RMSD}}^{d}[u] - \overline{\mathrm{RMSD}}^{d}[u_{exp}]\right|}{\overline{\mathrm{RMSD}}^{d}[u_{exp}]} \times 100\% \tag{7.6}$$



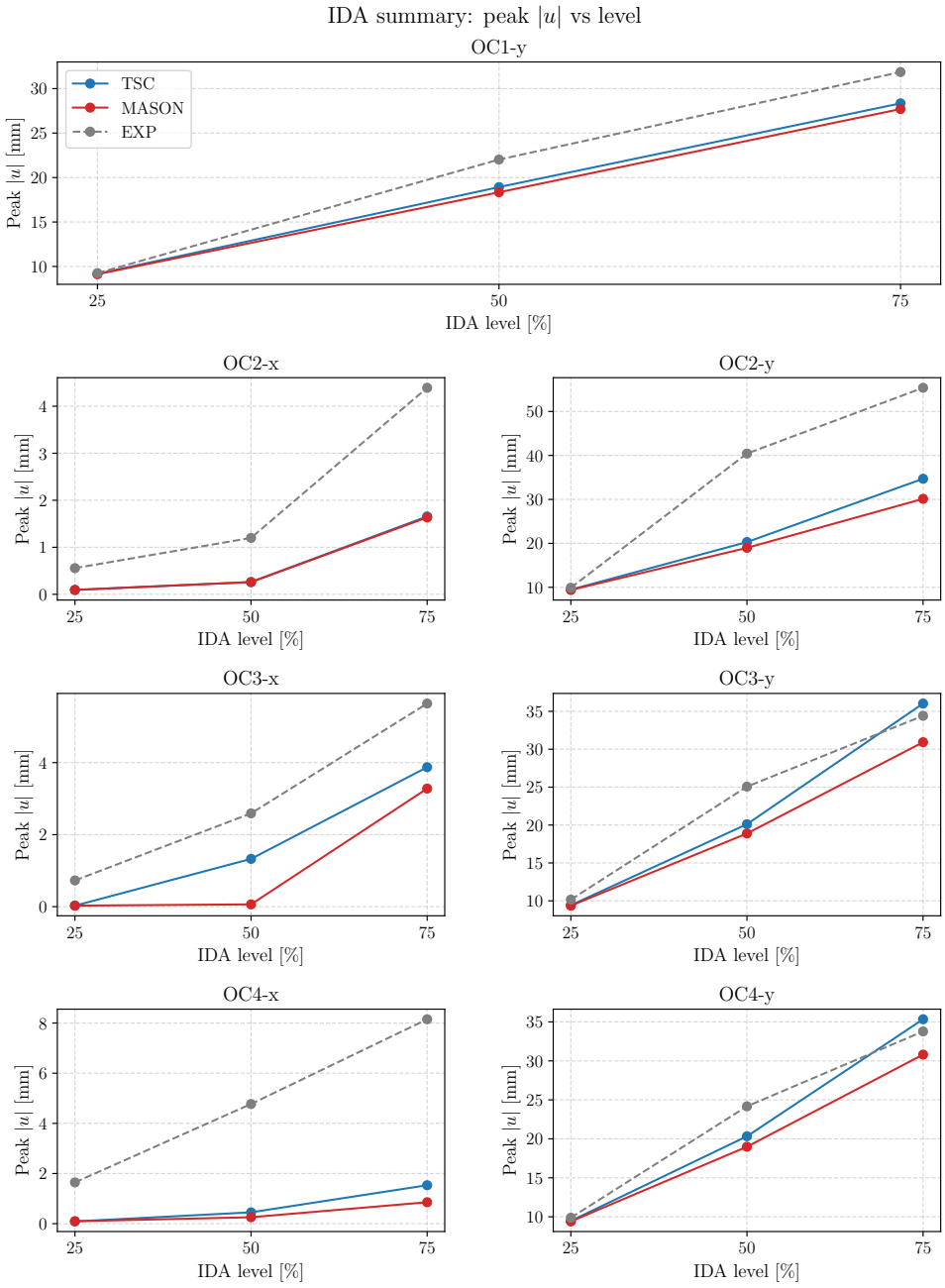


Figure 7.9. Absolute peak displacement at each monitoring point.

Figure 7.10 shows the averaged RMSD relative error (ϵ^d_{RMSD}) against the experimental data for both directions. In the Y-direction, both models maintain errors below 30 % at AQA75, increasing approximately linearly with the intensity level. The two models perform comparably, with neither consistently outperforming the other. In the X-direction, errors exceed 70 % at all intensity levels for both models, reflecting the inability to reproduce the experimentally observed transverse displacements. However, these apparent differences should be interpreted with caution, as the absolute transverse displacements are an order of magnitude smaller than the longitudinal ones, so even small absolute differences produce large relative errors. Both models could be brought closer to the experimental response through case-specific calibration of the mechanical parameters, though this would be unlikely to alter the overall comparison.

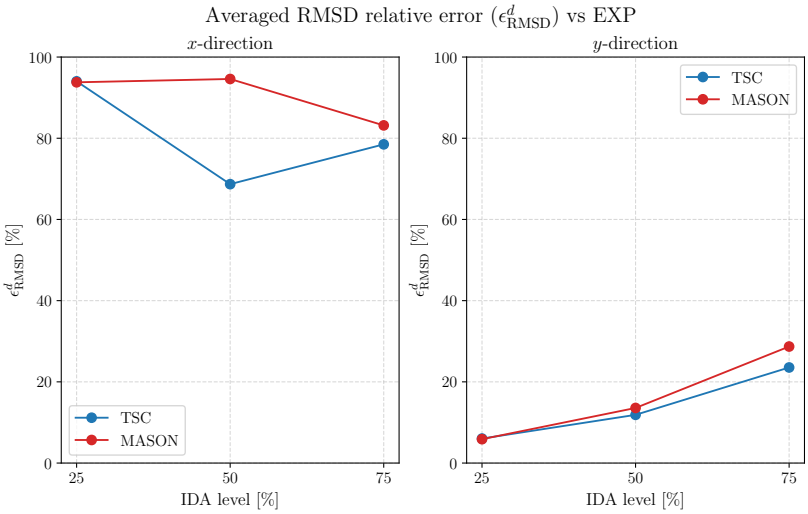


Figure 7.10. Averaged RMSD relative error (ϵ^d_{RMSD}) versus experimental data.

7.2.5. Local damage comparison

Figure 7.11 presents the combined tensile-shear damage scalar d_{ts} at the vault extrados for both models at the end of AQA50 and AQA75, viewed from the top. The experimental crack patterns reported by Bianchini *et al.* [13] are shown in Figure 7.3 for comparison.

At AQA50 (Figure 7.11A), MASON predicts no visible damage at the vault contacts, whereas TSCLinear shows some contact activation at the south-east infill-vault interface (Figure 7.11C). The experimental evidence at this amplitude level reported detachments between the infill and the vault of the north section in Figure 7.3A. A plausible explanation is the different unloading paths. In MASON, the degraded unloading stiffness reduces the stress upon reloading, which may redistribute the forces to neighbouring contacts, hence delaying the visible accumulation of damage at the same location. In TSCLinear, contacts that have exceeded the peak strength unload at the original elastic

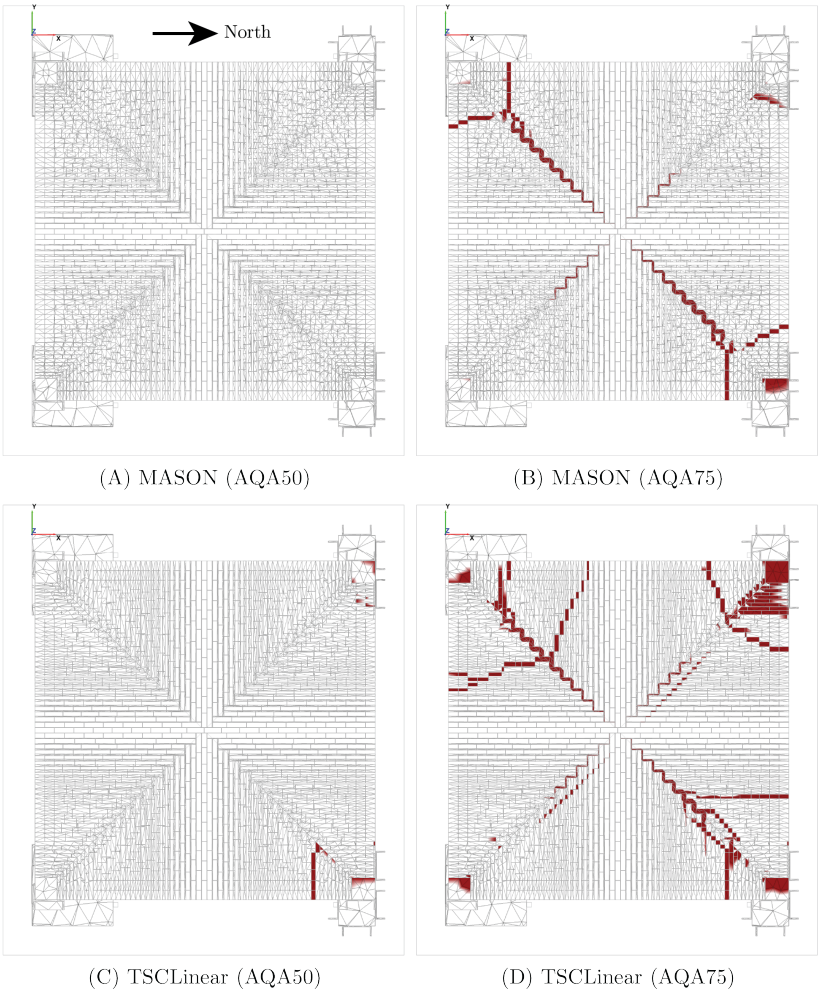


Figure 7.11. Combined tensile-shear damage scalar d_{ts} at the vault extrados at the end of AQA50 (left) and AQA75 (right).

stiffness and are reloaded to the same stress level on subsequent cycles, allowing damage to accumulate progressively.

At AQA75 (Figure 7.11B, D), both models develop a diagonal crack pattern extending from the vault crown towards the groins, consistent with the experimentally observed in-plane shear failure mode (Figure 7.3B). The governing failure mechanism is the same in both models, where cracks initiate at the crown and propagate along the diagonal bands of the vault webs. However, the spatial extent of the damage differs. The MASON model concentrates the damage more tightly along the main diagonal bands (Figure 7.11B), with less damage activation along the vault edges. The TSCLinear model, by contrast, produces more diffused damage at the vault edges and at the corner

infill regions, with additional contact activation observed at both the north-east and south-east corners in Figure 7.11D. Since the tensile-shear coupling mechanism is the same in both formulations, the difference in spatial extent is more likely attributable to different unloading-reloading paths, as observed in AQA50. The stiffness degradation in MASON alters the force redistribution after each load reversal, which may favour concentration along the primary crack path, whereas the elastic unloading in TSCLinear reloads secondary contacts to the same stress level, allowing them to accumulate damage over successive cycles.

7.2.6. Acceleration response comparison

Further comparison of the performance of both models includes analysing the acceleration responses against the experimentally recorded accelerometer data. Acceleration time histories provide a complementary view to the displacement comparison, as they are more sensitive to high-frequency content and to the interaction between the damping scheme and the constitutive model. The experimental acceleration is determined by the accelerometers attached to the vault extrados. However, the acceleration response from the numerical model cannot be directly obtained, as the explicit solution procedure of the blocky system in *3DEC* typically produces excessive noise in the higher frequency range. To circumvent this, the model output is first recorded as translational velocities at the corresponding global X and Y directions at the node closest to the instrument location. Accelerations are then obtained by numerical differentiation of these velocities using a centred finite-difference scheme on a uniform time grid. These accelerations are then immediately compared to the experimental results. This allows an averaged acceleration response over the given time interval to be obtained.

Figure 7.12 presents the acceleration time histories at all five accelerometer locations (Figure 7.2) for the AQA75 amplitude level. The response comparison for AQA25 and AQA50 is presented in Figures C.3 and C.4, respectively. At AQA25, the two models produce nearly identical acceleration responses that track the experimental recordings relatively well at all accelerometer locations. At AQA50, TSCLinear begins to produce noticeably higher acceleration spikes than MASON, particularly in the transverse direction during the strong-motion window ($t \approx 3$–5 s).

The insets zoom into the $t = 3$–6 s window where the largest accelerations occur. In the longitudinal direction, both models reproduce the general waveform during the strong-motion phase, but TSCLinear consistently produces higher peak accelerations than MASON across all accelerometer locations. Both models overpredict the experimental peak acceleration at this intensity level, with TSCLinear overpredicting by a larger margin. In the transverse direction, TSCLinear again shows higher acceleration amplitudes than MASON. The X-direction accelerations at ACC2, ACC6, and ACC12 exhibit high-frequency content that neither model reproduces in detail, though TSCLinear captures a larger share of the transverse acceleration energy.

The difference in peak acceleration between the two models is more pronounced than the difference in peak displacement observed in the preceding subsection. This is expected, as accelerations are governed by the second derivative of the displacement and are more sensitive to local stiffness variations at the contacts. In TSCLinear,

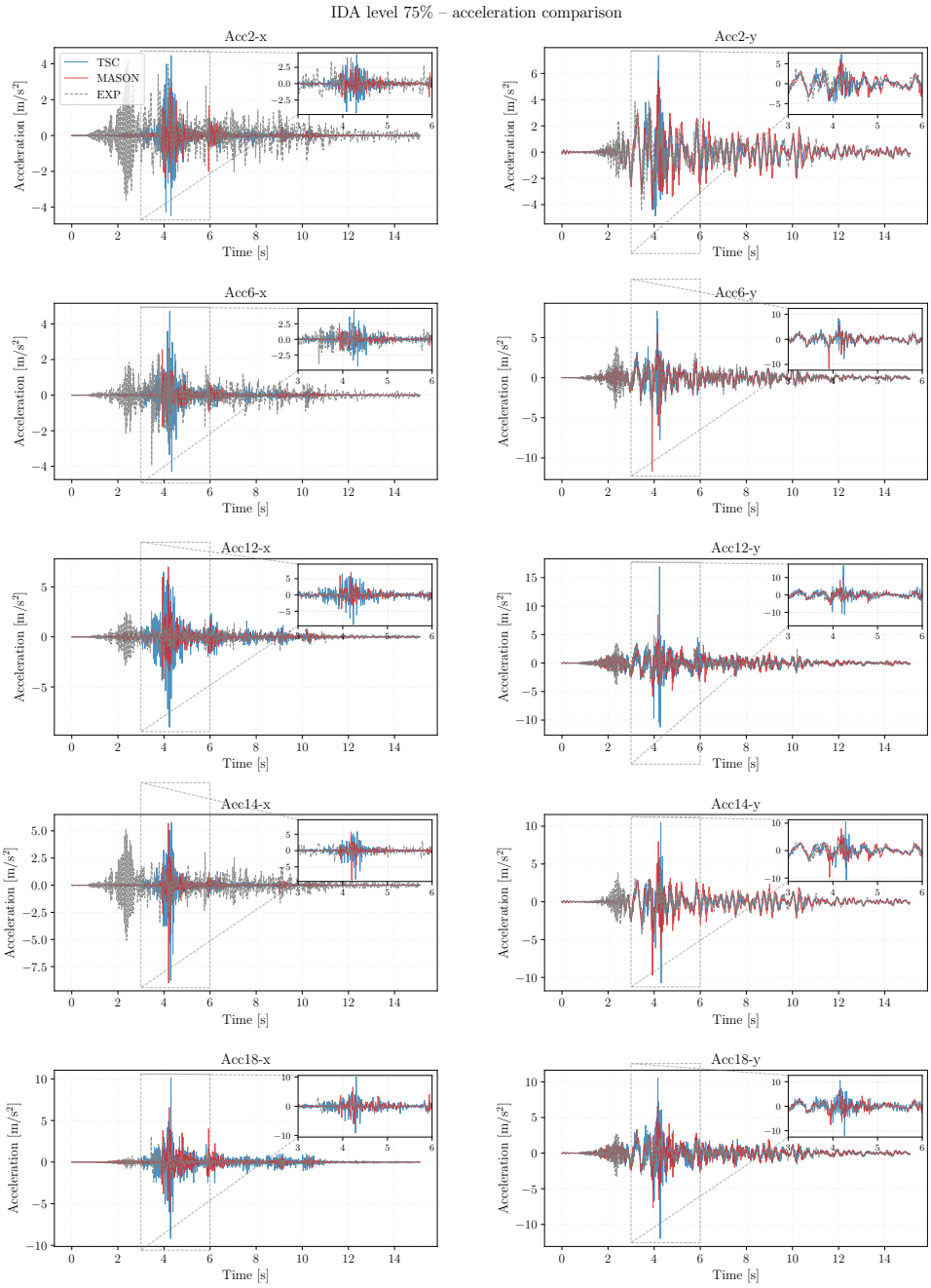


Figure 7.12. Acceleration time histories at five accelerometer locations for AQA75.

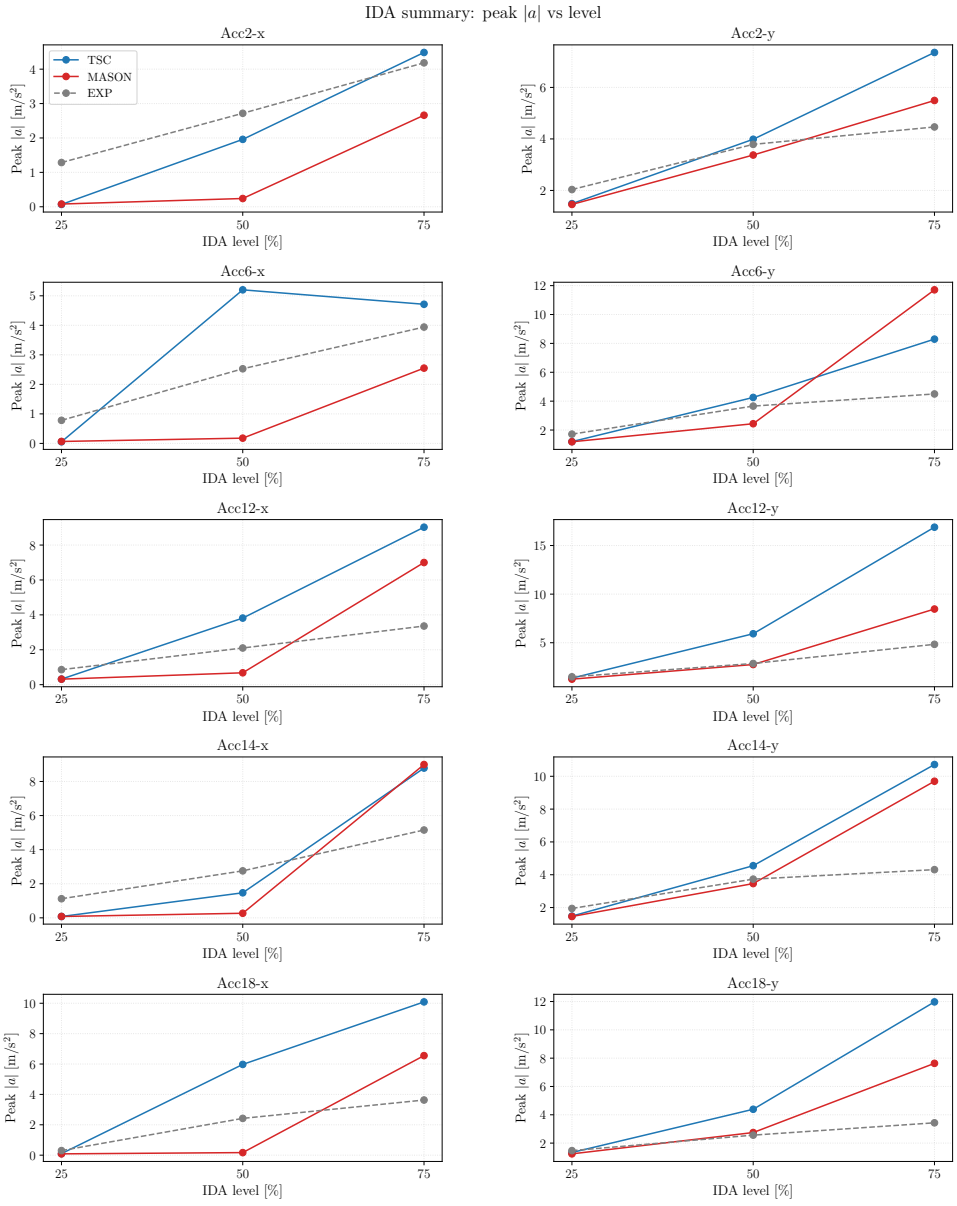


Figure 7.13. Absolute peak acceleration at each accelerometer location.

contacts that crack and re-close return to the original elastic stiffness, producing sharp stress increments upon re-contact that manifest as high-frequency acceleration spikes, which are also consistent with more damage activations in Figure 7.11. In MASON, the unloading stiffness reduces the stress increment upon re-contact, smoothing the

acceleration response.

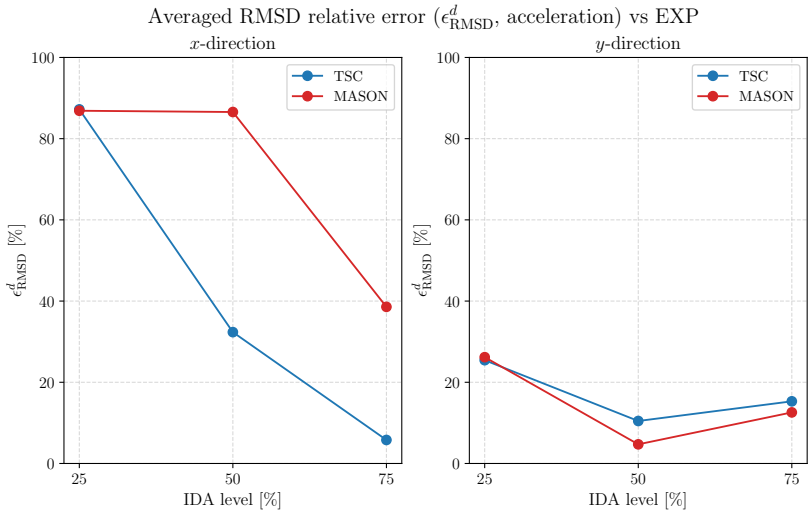


Figure 7.14. Averaged RMSD relative error (ϵ^d_{RMSD}, acceleration) versus the experimental data

Figures 7.13 and 7.14 summarise the acceleration comparison across all amplitude levels. Figure 7.13 shows the absolute peak acceleration at each accelerometer as a function of the IDA level. At AQA25, both models remain close to each other and to the experimental values, at least along the longitudinal direction. At AQA50 and AQA75, both models progressively overpredict the experimental peak accelerations, with TSCLinear exceeding MASON at nearly every location. The overprediction is particularly pronounced at ACC6, ACC12, and ACC18, where TSCLinear reaches peak values roughly twice the experimental ones at AQA75.

Figure 7.14 presents the averaged RMSD relative error for accelerations, with RMSD denoting the root-mean-square amplitude of each signal (Equation (7.6)). In the Y-direction, the error decreases with increasing intensity for both models, falling below 15 % at AQA75. MASON performs slightly better than TSCLinear at AQA50. In the X-direction, the TSCLinear error decreases from approximately 88 % at AQA25 to below 10 % at AQA75, while the MASON error decreases more gradually and remains higher, near 38 % at AQA75. Since this measure compares root-mean-square amplitudes rather than deviations between the histories, the lower X-direction error of TSCLinear at higher intensities indicates that its transverse amplitude approaches the recorded value. Faithful reproduction would force the two amplitudes to agree, but the converse does not hold, because many different acceleration histories share the same root-mean-square amplitude. The TSCLinear and recorded transverse signals differ in timing and peak positions while carrying comparable overall energy, so the agreement is in amplitude alone, and the transverse mechanism itself is reproduced by neither model. As noted for the displacement comparison, the X-direction absolute accelerations at AQA25 are an

order of magnitude smaller than the Y-direction values, so the high relative errors at low intensity levels are amplified by the small denominator and should not be interpreted as a failure of either model at that stage.

7.2.7. Discussion

This section compared the MASON and TSCLinear contact constitutive models on the same cross-vault benchmark, using identical post-diction-calibrated parameters, mesh, boundary conditions, and mass-proportional damping scheme. The comparison constitutes a controlled numerical simulation in which the sole independent variable is the contact constitutive law at the elasto-softening interfaces. Three observations emerged:

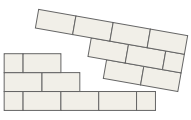
1. In terms of displacement prediction, both TSCLinear and MASON models produce comparable results across all amplitude levels. At AQA25 and AQA50, the displacement time histories are nearly indistinguishable. At AQA75, the models begin to drift apart in the residual oscillations after the main pulse, but the peak displacement predictions remain close to each other, and the inter-model difference is small relative to the discrepancy between either model and the experimental data. The RMSD error in the longitudinal (excited) direction stays below 30 % for both models at AQA75. For the purpose of peak displacement prediction under mass-proportional damping, the choice of constitutive model is not the governing factor for this benchmark.

2. The acceleration response reveals a clearer distinction. TSCLinear consistently produces higher peak acceleration than MASON, and both models overpredict the experimental values at AQA75. The difference is attributed to the unloading-reloading path: TSCLinear returns to its original elastic stiffness upon unloading, whereas MASON degrades stiffness upon unloading. This mechanism also explains the more diffuse damage distribution observed in TSCLinear at AQA75.

3. Despite these differences in acceleration amplitude and damage dispersion, the governing failure mode is identical in both models. Both predict diagonal cracking from the vault crown towards the groins, consistent with the experimentally observed in-plane shear failure. The constitutive model affects the quantitative details of the response (acceleration peaks, spatial extent of damage, residual displacement drift) but does not alter the qualitative failure mechanism for this structure and loading scenario.

A direct comparison of computational cost between the two models is not possible in this work, as the TSCLinear simulations were conducted using a different version of the *3DEC* engine in the earlier work by Oktiovan *et al.* [2], and differences in software version, hardware, and parallelisation would confound the comparison.

The results of this comparison raise a question that the constitutive model alone cannot answer. Both models overpredict the peak accelerations and underpredict the peak displacements relative to the experimental data at AQA75. Part of this discrepancy may originate from the selection of a mass-proportional damping scheme, which overdamps



low-frequency modes and underdamps high-frequency modes as the structure softens. The next section investigates whether changing the damping formulation while keeping the MASON constitutive model fixed can reduce this discrepancy.

7.3. Damping model comparison on the masonry cross-vault

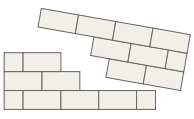
The preceding section showed that, under mass-proportional (MP) damping, the choice of contact constitutive model has a limited effect on peak displacement predictions but a more visible effect on acceleration amplitudes and damage dispersion. Both models, however, overpredicted the peak accelerations and under-predicted the peak displacements at AQA75 relative to the experimental data. A plausible source of this residual discrepancy to explore is the damping scheme itself, which, in the preceding section, was held constant at MP damping for both constitutive models. This section isolates the damping scheme as the independent variable.

In the explicit time-marching integration scheme used by DEM, the equations of motion are solved at each timestep without assembling or inverting a global stiffness matrix. This formulation handles large displacements, contact updates, and block separation without convergence issues, but it is conditionally stable. The so-called stable timestep must remain below a critical value governed by the highest eigenfrequency of the system (Equation (3.20)). Energy dissipation at interfaces via the contact constitutive model (cracking, frictional sliding, compressive failure) accounts for part of the physical energy loss. These mechanisms constitute hysteretic (frequency-independent) damping, as the energy dissipated per cycle depends on the displacement amplitude and the accumulated damage state rather than on the loading rate. However, mechanisms such as impact-induced dissipation at re-closing contacts, propagation into the foundation, and rate-dependent effects in the mortar are not explicitly represented. External viscous damping is therefore introduced to approximate these residual dissipation sources.

The standard choice in DEM practice is MP damping, in which a velocity-proportional force, scaled by the nodal mass, is added to the equation of motion. This formulation does not alter the critical timestep and is straightforward to implement. Its limitation is a frequency-dependent damping ratio that decreases as frequency increases. Modes below the target frequency are overdamped, and modes above it are underdamped. As damage softens the structure and shifts its dominant frequency downward, the overdamped region may artificially suppress the response. Several authors have reported that this can lead to unconservative collapse predictions for rocking and overturning mechanisms [6, 7, 16].

The stiffness-proportional component of Rayleigh damping (SP) addresses the frequency bias by providing a damping ratio that increases linearly with frequency. Combined with the MP component, full Rayleigh damping can be tuned to achieve a target damping ratio at two frequencies. However, as explained in Section 3.2.2, the stiffness-proportional term imposes a severe reduction on the critical timestep in an explicit integration scheme, typically by one or two orders of magnitude [8]. For complex three-dimensional models with deformable blocks and thousands of contacts, this reduction renders the computation impractical.

The Maxwell damping scheme (Section 3.2.3) offers an alternative that approximates



the frequency-selective dissipation of SP damping without a significant penalty on the stable timestep. Spring-dashpot elements placed in series are arranged in parallel with the joint springs at the unit-mortar interfaces and with the internal tetrahedral elements of the deformable blocks. Each Maxwell element is characterised by a stiffness fraction α_M and a relaxation time τ_M, which together define a damping peak at a specific frequency. By stacking multiple elements with different relaxation times, the combined damping ratio can be made approximately uniform over a broad frequency band. The formulation was first introduced for rigid DEM blocks by Lemos *et al.* [8], and applied to masonry arches by Lemos and Sarhosis [9]. In this thesis, the scheme is extended to a three-dimensional deformable-block model of a masonry cross-vault, and the element parameters are calibrated automatically using a Levenberg-Marquardt optimisation algorithm, as explained in Section 3.2.3.

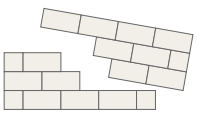
Three damping configurations are compared on the same cross-vault model using the MASON constitutive law: mass-proportional damping, Maxwell damping with three optimised elements, and zero-viscous damping (in which all energy dissipation is provided by the constitutive model). The numerical model, mesh discretisation, boundary conditions, material parameters, and seismic input are identical to those described in Section 7.2. The content of this section follows the methodology presented by Oktiovan *et al.* [17], where the damping evaluation was conducted using the TSCLinear contact model. The present analysis repeats the same evaluation with MASON as the contact constitutive law.

7.3.1. Damping configurations

Due to the small timesteps required by the stiffness-proportional and full Rayleigh damping schemes, even with partial density scaling, the computational cost of performing a complete incremental dynamic analysis of the cross-vault model under these formulations is prohibitively high. Oktiovan *et al.* [17] conducted a trial run with full Rayleigh damping using a mixed rigid-deformable-block configuration and wavelet-based truncation of the input record to reduce the computational burden. Even with these measures, the complete incremental dynamic analysis required approximately 1.5 months of wall-clock time and yielded only a marginal improvement in the peak displacement prediction at OC1-y compared with the mass-proportional and Maxwell cases. The damping evaluation in this section is therefore constrained to three configurations: mass-proportional damping (MP), Maxwell damping (Maxwell), and zero-viscous damping (noDamp). The noDamp configuration does not imply the absence of all damping; the hysteretic dissipation provided by the MASON contact model (cracking, frictional sliding, compressive failure) remains active. What is removed is the external velocity-proportional viscous force.

7.3.2. Selection of the target damping ratio

Both the MP and Maxwell configurations require specifying a target damping ratio $\zeta^\star$. In the MP scheme, this ratio is achieved exactly at one reference frequency and deviates from it at all others. In the Maxwell scheme, the optimisation algorithm distributes the damping approximately uniformly over a prescribed frequency band, so the target ratio is



achieved (within a small tolerance) across that entire band. The choice of $\zeta^\star$ therefore affects both schemes, but in different ways.

To select a suitable value, a parametric sweep is conducted over $\zeta^\star \in \{2,3,4,5\}\%$ for both MP and Maxwell. Each configuration is subjected to the full incremental dynamic analysis (AQA25 through AQA75) on the cross-vault model using the MASON constitutive law. The noDamp case, which has no free parameter, serves as a baseline. Two monitoring points are used for the calibration: OC1-y for the displacement response and ACC18-y for the acceleration response. These are selected because OC1-y and ACC18-y are located at the vault crown in the loading direction, where the sensitivity to damping is expected to be most pronounced.

Figure 7.15 presents the displacement metrics at OC1-y. All configurations underpredict the experimental peak displacement (negative peak errors), consistent with the observation from Section 7.2.7. For the MP scheme, the peak error remains approximately constant across the four ratios, ranging from $-12.8\,\%$ at $2\,\%$ to $-13.7\,\%$ at $5\,\%$. The Maxwell scheme shows a larger spread as the smallest peak error is $-9.6\,\%$ at $2\,\%$, increasing to $-15\,\%$ at $3\,\%$ and remaining around $-15\,\%$ for higher ratios.

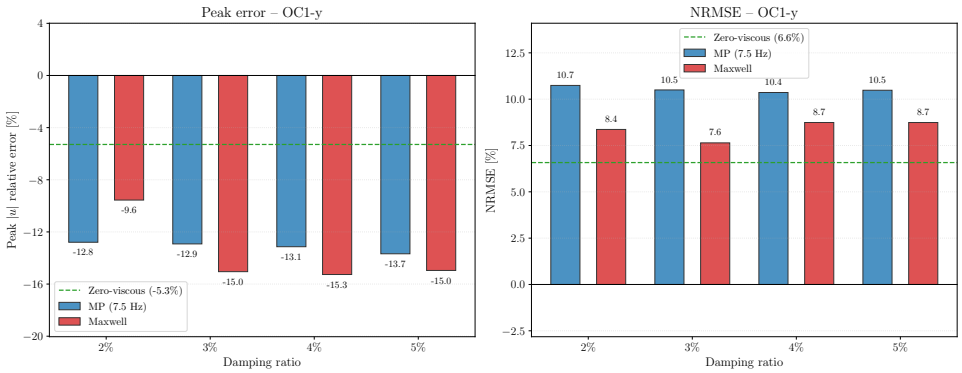


Figure 7.15. Peak displacement error (left) and NRMSE (right) at OC1-y for the MP and Maxwell configurations at AQA75. The dashed green line indicates the noDamp baseline.

The configurations are also compared using the normalised root-mean-square error (NRMSE), which measures the pointwise deviation between the numerical and experimental signals. For a numerical response s_{num} and its experimental counterpart s_{exp} sampled at the instants $\{t_i\}_{i=1}^{N}$,

$$\text{NRMSE} = \frac{\sqrt{\dfrac{1}{N}\sum_{i=1}^{N}\left(s_{\text{num}}(t_i) - s_{\text{exp}}(t_i)\right)^2}}{\max\limits_i s_{\text{exp}}(t_i) - \min\limits_i s_{\text{exp}}(t_i)}, \tag{7.7}$$

where the numerator is the root-mean-square error between the two signals and the denominator is the peak-to-peak range of the experimental signal.

In contrast to the peak error, the NRMSE leads to a different ranking of the two

damping schemes. MP damping errors are stable around 10.5 % regardless of the damping ratio, while Maxwell error decreases from 8.4 % at 2 % to 7.6 % at 3 % before rising again. Maxwell consistently outperforms MP in terms of NRMSE at all ratios. The noDamp baseline sits at −5.3 % peak error and 6.6 % NRMSE, the best values among all configurations, suggesting that for displacements the MASON constitutive hysteresis alone gives sufficient dissipation at this monitoring point.

Figure 7.16 shows the acceleration metrics at Acc18-y. All MP and Maxwell configurations overpredict the experimental peak acceleration. The MP peak error exceeds 100 % at every damping ratio, whereas the Maxwell peak error decreases from 157 % at 2 % damping to 22.6 % at 5 %, falling below 100 % from 3 % onwards. The NRMSE values are more compressed, ranging from 11% to 16% for both schemes across all ratios. The noDamp baseline produces an extreme peak acceleration error of 825% and an NRMSE of 48%, confirming that external viscous damping is necessary to control the acceleration response even though the displacement response is adequately captured by constitutive hysteresis alone.

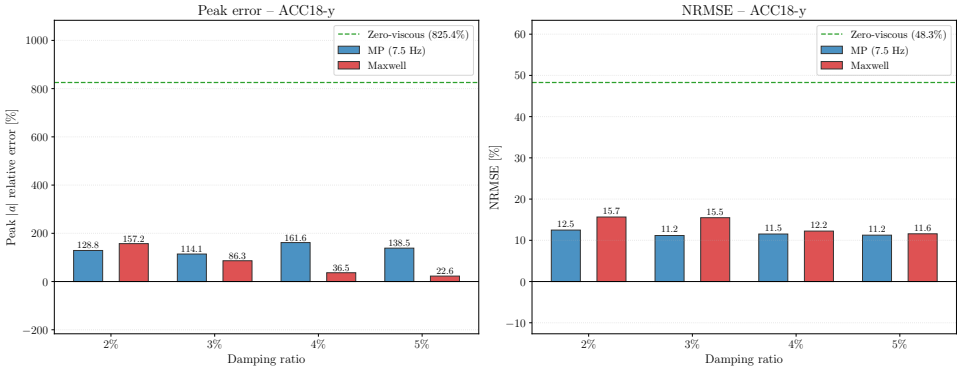


Figure 7.16. Peak acceleration error (left) and NRMSE (right) at Acc18-y for the MP and Maxwell configurations at AQA75. The dashed green line indicates the noDamp baseline.

The peak error and NRMSE metrics evaluate single monitoring points. To assess the overall signal agreement across all channels, the Sprague-Geers metric [18] is computed for each channel and averaged. The Sprague-Geers metric decomposes the signal comparison into a magnitude component M and a phase component P, defined as follows.

$$M = \sqrt{\frac{\Psi_{aa}}{\Psi_{bb}}} - 1, \qquad P = \frac{1}{\pi} \cos^{-1}\left(\frac{\Psi_{ab}}{\sqrt{\Psi_{aa} \cdot \Psi_{bb}}}\right) \tag{7.8}$$

where $a(t)$ and $b(t)$ are the numerical and experimental signals, respectively, and the inner products are the time integrals over the common window $[t_0, t_1]$ in Equation (7.9), evaluated by the trapezoidal rule after interpolating the numerical signal onto the experimental time grid.

$$\Psi_{aa} = \int_{t_0}^{t_1} a^2(t)\,\mathrm{d}t, \qquad \Psi_{bb} = \int_{t_0}^{t_1} b^2(t)\,\mathrm{d}t, \qquad \Psi_{ab} = \int_{t_0}^{t_1} a(t)\,b(t)\,\mathrm{d}t \tag{7.9}$$

The combined metric C is then expressed in Equation (7.10).

$$C = \sqrt{M^2 + P^2} \tag{7.10}$$

where $C = 0$ indicates a perfect match between the two signals. The magnitude component M captures amplitude differences and the phase component P captures timing misalignment, so C penalises both simultaneously. M, P and C are evaluated per channel and then averaged, separately for the displacement and acceleration channels. Since M is signed, its channel average can cancel between channels, whereas C cannot; the mean C is therefore not the composite of the mean M and the mean P. The numerical accelerations are obtained by finite differencing of the velocity histories, and both displacement records are zeroed at the start of the common window. This metric complements the peak error (which is sensitive only to the maximum value) and the NRMSE (which averages over the entire record without distinguishing amplitude from phase).

Figure 7.17 shows the Sprague-Geers components averaged over all OC channels for the displacement response at AQA75. Increasing the damping ratio worsens the magnitude error for both schemes, as expected, since greater damping further suppresses the dynamic response. The phase error P increases with the damping ratio, reflecting a progressive timing misalignment as the damped response lags behind the experimental signal. The composite error is lowest at 2 % for Maxwell (50.4 %) and at 2 % for MP (55.4 %), rising with the damping ratio for both schemes.

The noDamp baseline has a composite error of 101 %, driven primarily by the large magnitude error (42.2 %) combined with phase error (35.1 %). This contrasts with the favourable noDamp performance observed at OC1-y in Figure 7.15. The Sprague-Geers metric, averaged over all OC channels, reveals that the good agreement at OC1-y does not extend to the other monitoring points: the absence of viscous damping allows the response at peripheral locations to deviate from the experimental signal in both amplitude and phase.

Figure 7.18 presents the same metrics averaged over all accelerometer channels. The magnitude error M is small for MP (1.2 % at 2 % to −15.3 % at 5 %) and varies more widely for Maxwell (69.8 % at 2 % to −34.1 % at 5 %). The Maxwell value crosses zero between 3 % and 4 %, so the Maxwell model changes from overprediction to underprediction of the acceleration amplitudes within the swept range. The phase error P lies between 41 % and 45 % for all configurations and ratios, which indicates that the timing misalignment in the acceleration signal is not governed by the damping ratio. The composite error C is lowest for MP at 3 % (51.6 %) and for Maxwell at 4 % (65.0 %). It varies little with the ratio for MP (51.6 % to 54.2 %) but widely for Maxwell (65.0 % to 92.6 %). The noDamp baseline produces a composite error of 389 %, dominated by the extreme magnitude overprediction (380 %).

The effect of the target damping ratio on the predicted damage distribution is examined in Appendix C.3. Figures C.5 and C.6 present the combined tensile-shear damage scalar d_{ts} at the vault extrados at the end of AQA75 for the MP and Maxwell configurations,

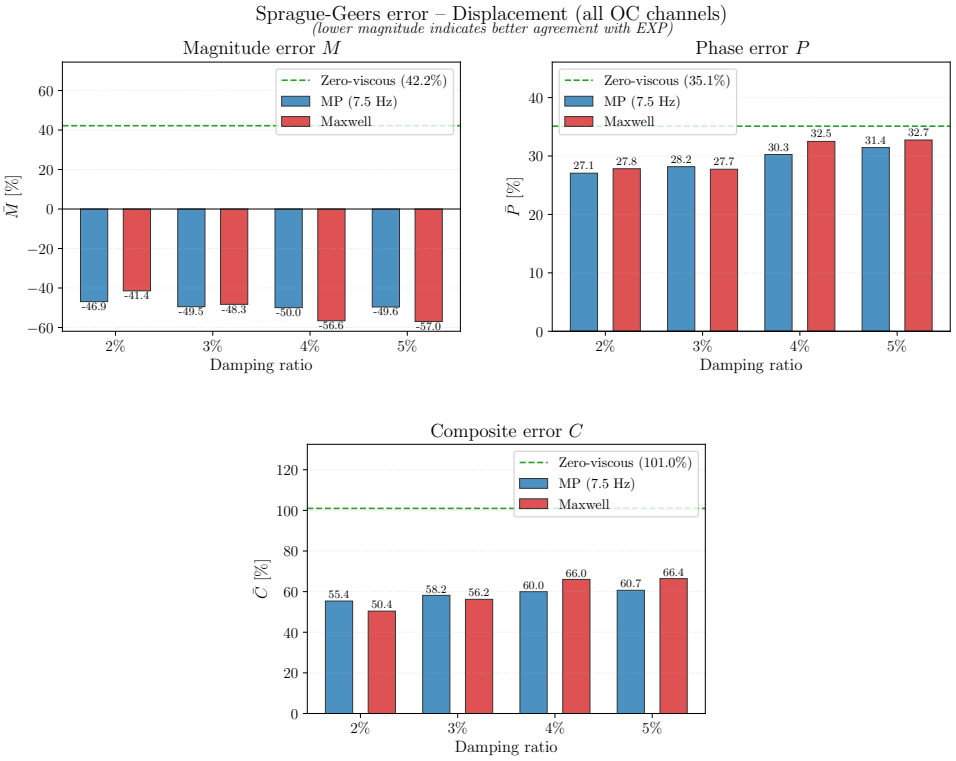


Figure 7.17. Sprague-Geers magnitude error M (left), phase error P (centre), and composite error C (right) averaged over all OC displacement channels at AQA75.

respectively, at each of the four candidate ratios. For the MP configurations (Figure C.5), damage at the groin connections is predicted at all four damping ratios, and the governing failure pattern is consistent across the sweep. The only notable difference among the four cases is the severity of damage to the infill elements at the north-west corner, which decreases with increasing damping ratio. For the Maxwell configurations (Figure C.6), the sensitivity to the damping ratio is more pronounced. Damage at the groin connections fully appears only at the 2.0 % ratio. At 4 % and 5 %, the damage at the vault extrados is nearly absent, suggesting that the system is overdamped at these ratios under the Maxwell scheme.

The displacement and acceleration metrics point in opposite directions. Lower damping ratios produce better displacement agreement (smaller C and NRMSE at OC1-y), while higher ratios improve the acceleration peak prediction for Maxwell (peak error at Acc18-y drops from 157 % at 2 % to 23 % at 5 %). A target ratio of $\zeta^\star = 3\%$ is adopted for the remainder of this section. At this ratio, the Maxwell scheme gives its lowest displacement NRMSE at OC1-y (7.6 %), still reproduces the governing damage pattern albeit at lower intensity than at $\zeta^\star = 2\%$, and nearly halves the acceleration peak

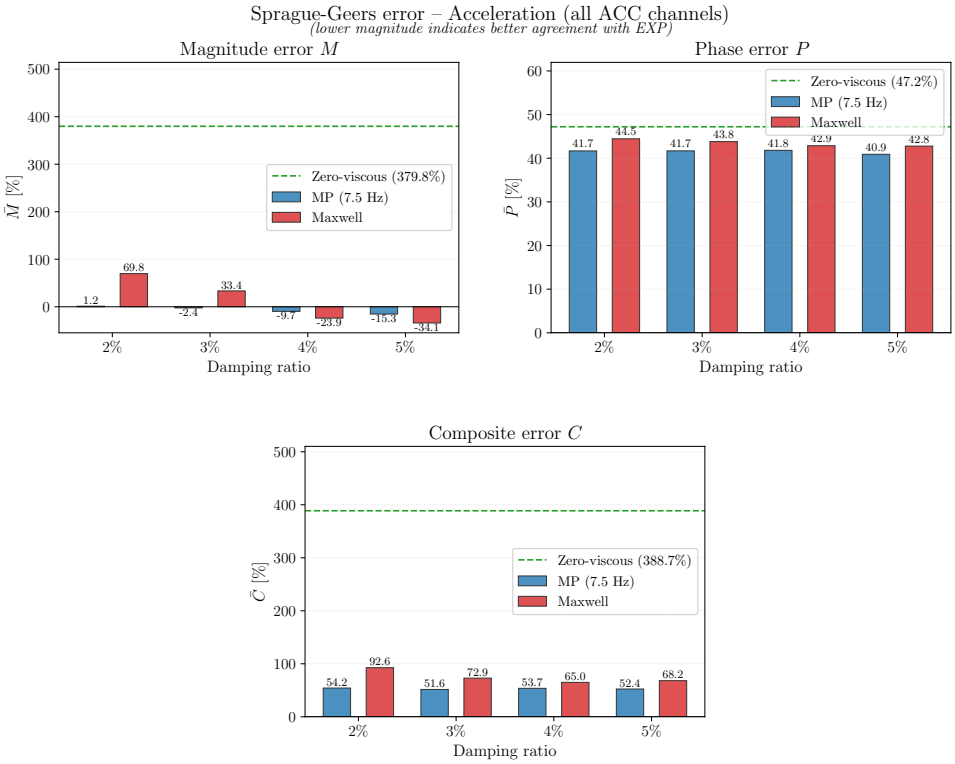


Figure 7.18. Sprague-Geers magnitude error M (left), phase error P (centre), and composite error C (right) averaged over all accelerometer channels at AQA75.

error relative to the 2 % case (157 % to 86 %). Its Sprague-Geers composite error for accelerations (72.9 %) remains above that of MP (51.6 %).

7.3.3. Adopted damping parameters

With the target damping ratio selected, the specific parameters for each configuration are defined as follows. For the MP scheme, the damping coefficient $\alpha_R = 2.82743$ is computed to provide $\zeta^\star = 3\%$ at the fundamental frequency of 7.5 Hz. For the Maxwell scheme, the same target ratio is prescribed over the frequency band from $f_{lb} = 1$ Hz to $f_{ub} = 40$ Hz. The Levenberg-Marquardt optimisation yields the parameters listed in Table 7.3 for the three Maxwell elements. The variation of damping ratio with frequency for the MP and Maxwell configurations at $\zeta^\star = 3\%$ is shown in Figure 7.19.

The resulting combined modulus factor $|\overline{M_T}|_{\max} = 1 + \sum_i \alpha_{M,i}$ is 1.29, which reduces the stable timestep from 1.25×10^{-6} s to approximately 1.10×10^{-6} s (Equation (3.40)). The noDamp configuration uses the same timestep as MP (1.25×10^{-6} s). The MP curve decreases monotonically with frequency, reaching the target ratio at the fundamental mode and overdamping all modes below it. The Maxwell curve remains approximately

Table 7.3. Optimised Maxwell element parameters for the cross-vault model at $\zeta^\star = 3\%$.

Element	$\alpha_{M,i}$ [-]	$\tau_{M,i}$ [s]	ψ_i [-]	f_i [Hz]
1	0.1050	1.513×10^{-1}	0.0250	1.00
2	0.0706	2.057×10^{-2}	0.0170	7.48
3	0.1111	3.775×10^{-3}	0.0263	40.00
$\sum$	0.2867			

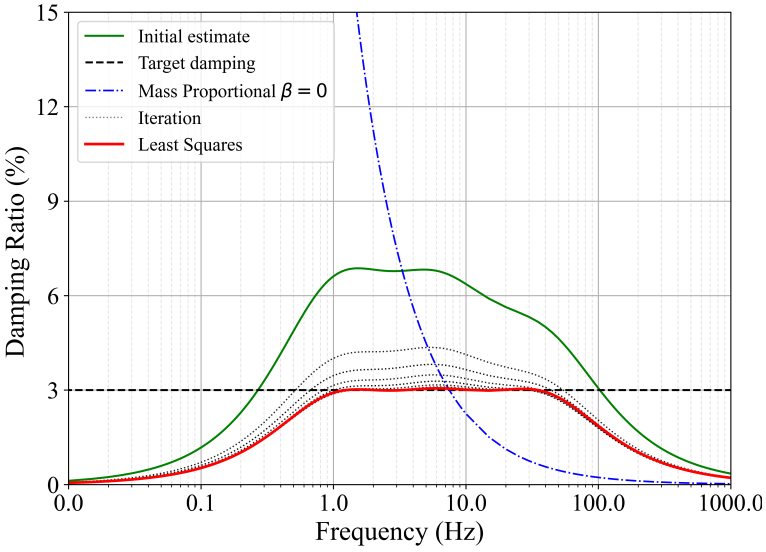


Figure 7.19. Damping ratio as a function of frequency for the MP and Maxwell damping configurations at $\zeta^\star = 3\%$.

uniform within the prescribed band and tapers off outside it. Table 7.4 summarises the three configurations and their associated timestep.

Table 7.4. Summary of the three damping configurations.

	MP	Maxwell	noDamp
Viscous damping type	Mass-proportional	Maxwell (3 elements)	None
Target $\zeta^\star$ [%]		3	–
Frequency band	7.5 Hz	1–40 Hz	–
Stable timestep [s]	1.25×10^{-6}	1.10×10^{-6}	1.25×10^{-6}

7.3.4. Displacement response comparison

The displacement time histories at four optical camera locations for the MP, Maxwell, and noDamp configurations at $\zeta^\star = 3\%$ under the AQA25 and AQA50 amplitude levels are presented in Figures C.7 and C.8, respectively, in Appendix C.4. At AQA25 (Figure C.7), the three configurations overlap almost entirely in the Y-direction and track the experimental record closely. The choice of damping scheme has no discernible effect on the displacement response at this intensity level, consistent with the vault remaining in the near-elastic regime. At AQA50 (Figure C.8), MP and Maxwell still overlap, but noDamp develops a mild positive offset at OC2-y, OC3-y, and OC4-y after $t \approx 6$ s. This deviation marks the onset of the trend discussed herein.

Figure 7.20 shows the displacement time histories at four optical camera locations for the AQA75 amplitude level. In the Y-direction, the MP and Maxwell response overlap during the strong-motion window ($t \approx 2$–5 s). Both underpredict the negative peak at $t \approx 4$ s. After the main pulse, the two responses diverge. MP decays faster and stays above the experimental trace during the residual oscillation phase. Maxwell retains more of the oscillation amplitude and stays closer to the experimental record, which aligns with the lower NRMSE and Sprague-Geers metric from the calibration sweep in the previous subsection.

The noDamp configuration behaves differently. At OC1-y, it tracks the other configurations during the pulse but develops a negative offset afterwards. At OC2-y, OC3-y, and OC4-y, the noDamp response drifts to approximately −40 mm by the end of the record and does not recover. This drift is not a small-amplitude oscillation around the experimental mean, but a sustained displacement away from it. It also explains the 101 % composite error reported for noDamp in the Sprague-Geers analysis (Figure 7.17). The MASON contact model dissipates energy during large-amplitude load reversals, but once the structure enters the residual oscillation phase, the small-amplitude cycles do not activate enough contact hysteresis to keep the response bounded. External viscous damping is still needed to control this drift.

In the X-direction, MP and Maxwell produce displacements that are an order of magnitude smaller than the experimental readings, similar to the comparison in Section 7.2.4. At OC3-x, noDamp drifts to approximately +3 mm and stays there, which is closer in magnitude to the experimental values than MP or Maxwell, but in the wrong direction. The damping scheme does not resolve the transversal displacement gap, and the apparent noDamp match at OC3-x is a coincidence of magnitude rather than a physical agreement. The absolute transverse values remain small (maximum experimental amplitudes on the order of a few millimetres, compared to tens of millimetres in the longitudinal direction), so small absolute differences between configurations can produce disproportionately large relative errors.

7.3.5. Damage progression comparison

Figure 7.21 shows the combined tensile-shear damage scalar d_{ts} at the vault extrados at the end of AQA75 for the three damping configurations. MP and Maxwell reproduce the same governing failure pattern observed in the experiment and in the cross-comparison of Section 7.2.5, where diagonal crack bands propagate from the crown towards the four groins, with additional damage at the infill corners. The two configurations differ

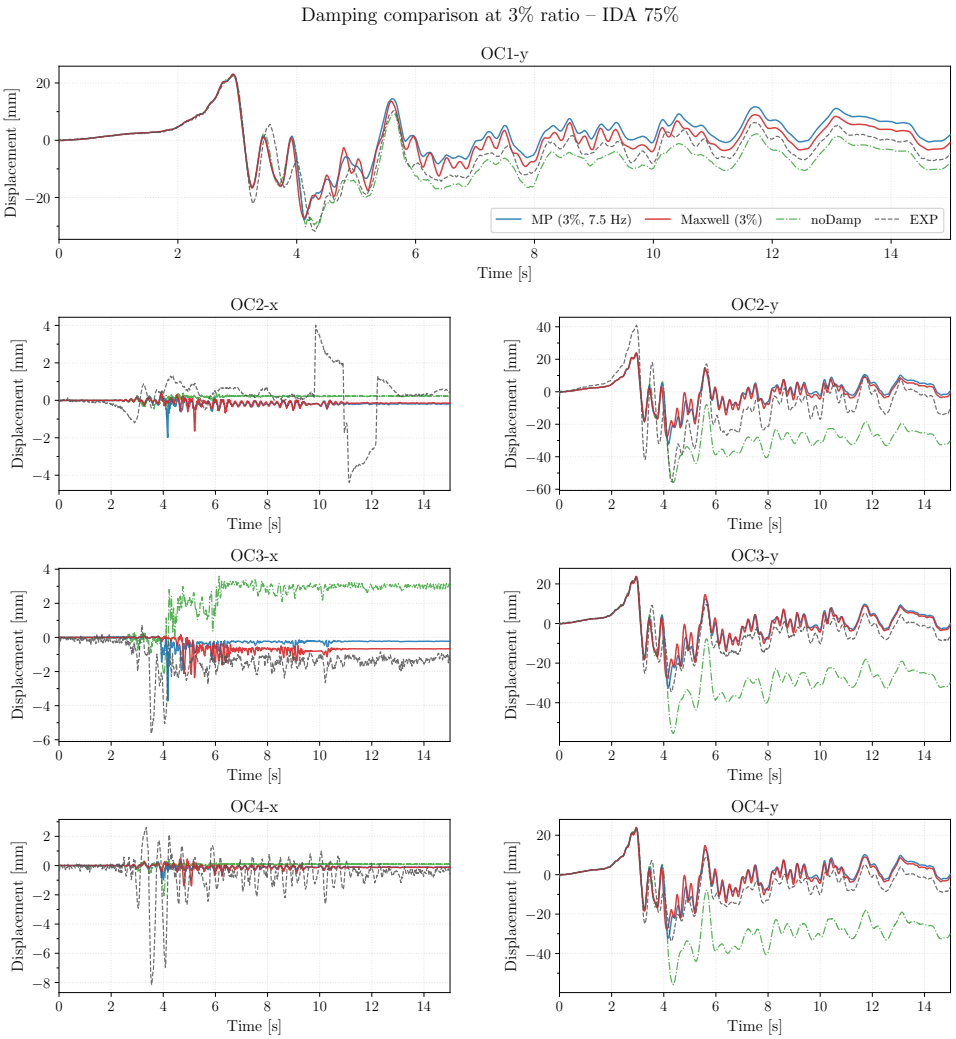


Figure 7.20. Displacement time histories at the four optical camera locations (OC1–OC4) for the AQA75 amplitude level under the three damping configurations at $\zeta^\star = 3\%$.

mainly in the severity of the damage at the groin connections and the infill regions. MP produces more pronounced damage along the diagonal bands and at the north-west and south-east infill corners, while Maxwell shows less extensive diagonal damage at the extrados view.

The noDamp configuration produces the most severe damage of the three. The diagonal crack bands are wider and more intense, and additional damage appears along the vault edges and at locations that remain largely undamaged under MP and

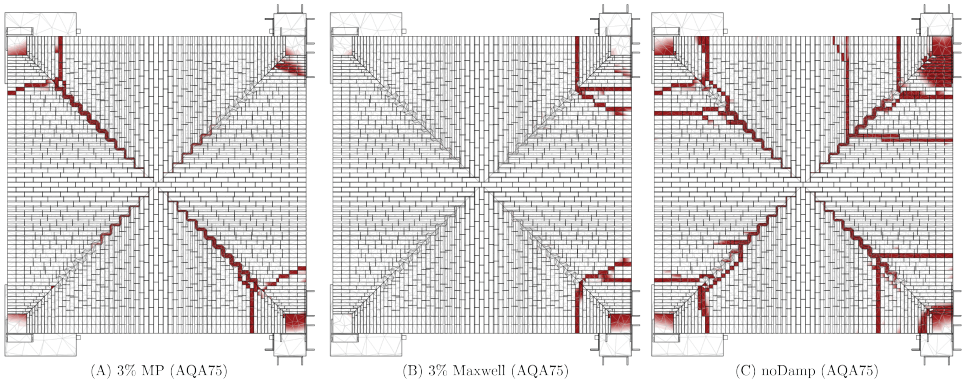


Figure 7.21. Combined tensile-shear damage scalar d_{ts} at the vault extrados at the end of AQA75 for the three damping configurations.

Maxwell. This is consistent with the sustained post-pulse oscillations observed in the displacement and acceleration responses, which drive repeated contact activation and accumulate damage well after the main pulse has passed. The noDamp damage distribution is considered a byproduct of the absence of viscous dissipation and should not be interpreted as a physically meaningful prediction of failure.

The extrados view of the Maxwell configuration shows little damage along the groin connections. This could be read as a challenge to the Maxwell scheme to capture the governing failure mode. Figure 7.22 shows the same model from a different viewing angle and confirms that damage at the groin connections is present. The intensity of the groin damage is lower than the infill corner damage and than that predicted by MP (Figure 7.21A), but the governing failure mode is reproduced.

7.3.6. Acceleration response comparison

The acceleration time histories for the MP, Maxwell, and noDamp configurations at $\zeta^\star = 3\%$ under the AQA25 and AQA50 amplitude levels are presented in Figures C.9 and C.10, respectively, in Appendix C.5. At AQA25 (Figure C.9), the MP and Maxwell track the experimental waveform in the Y-direction at all five accelerometer locations. The noDamp response is close to MP and Maxwell in the Y but already shows elevated amplitudes at Acc18-x, where sustained oscillations are visible throughout the record. At AQA50 (Figure C.10), the MP and Maxwell responses stay close to the experiment in both directions. The noDamp response develops amplified peaks during the strong-motion window at several locations (Acc6-y and Acc14-y in particular, with transient amplitudes of the order of 10–15 m/s^2 at $t \approx 4$–5 s) and sustains oscillations after the pulse.

The contrast between MP/Maxwell and noDamp grows with the intensity level and reaches its maximum at AQA75 in Figure 7.23. The noDamp configuration produces sustained oscillations that persist well beyond the main pulse. The experimental accelerations decay after $t \approx 5$ s, but the noDamp prediction continues to oscillate in a steady-state manner at amplitudes close to those of the strong-motion window. This

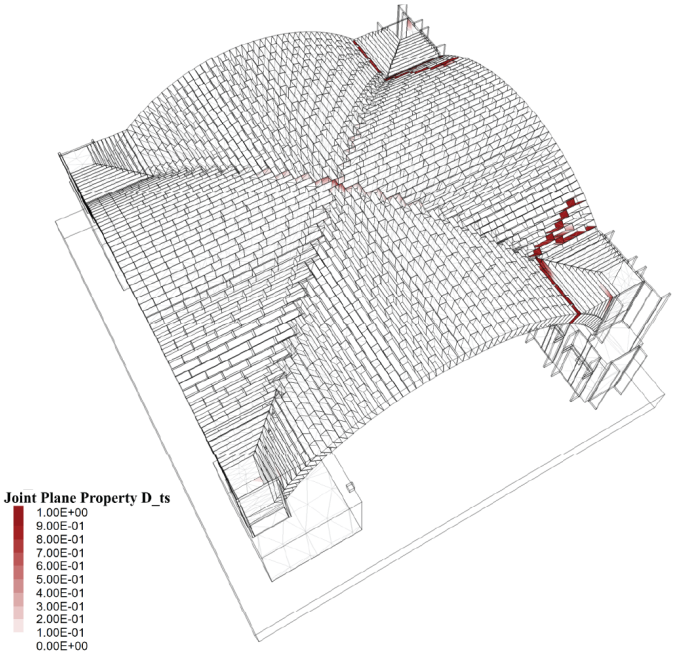


Figure 7.22. Combined tensile-shear damage scalar d_{ts} for the Maxwell configuration at $\zeta^\star = 3\%$ at the end of AQA75, viewed from a different angle.

is the source of the 825% peak error at Acc18-y, as reported in the calibration sweep, and confirms that external viscous damping is needed for the acceleration response. The MASON contact model alone does not dissipate enough energy at the frequencies that drive the acceleration signal, similar to the findings in Oktiovan *et al.* [17] using TSCLinear.

The MP and Maxwell configurations both track the experimental waveform during the strong-motion window and decay afterwards. During the pulse, the two are nearly identical at most accelerometer locations. After $t \approx 5$ s, Maxwell keeps slightly more residual oscillation than MP, which mirrors the pattern seen in the displacement response. MP produces a more damped post-pulse response, consistent with the overdamping of the low-frequency content after the structure has softened. At Acc18, Maxwell shows higher peak accelerations than MP during the strong-motion window, which reflects the more uniform damping distribution of the Maxwell scheme across the 1–40 Hz band compared to the MP scheme that only hits the 3 % damping ratio at 7.5 Hz.

The overall finding from the displacement and acceleration comparisons is that MP and Maxwell produce similar predictions at AQA75 when paired with the MASON contact model, for this specific cross-vault specimen. Maxwell is slightly better in residual displacement amplitude, but MP is slightly better in post-pulse acceleration, and neither is clearly superior across all metrics. The noDamp case confirms that viscous damping is required for both quantities, since it prevents sustained drift in the displacement

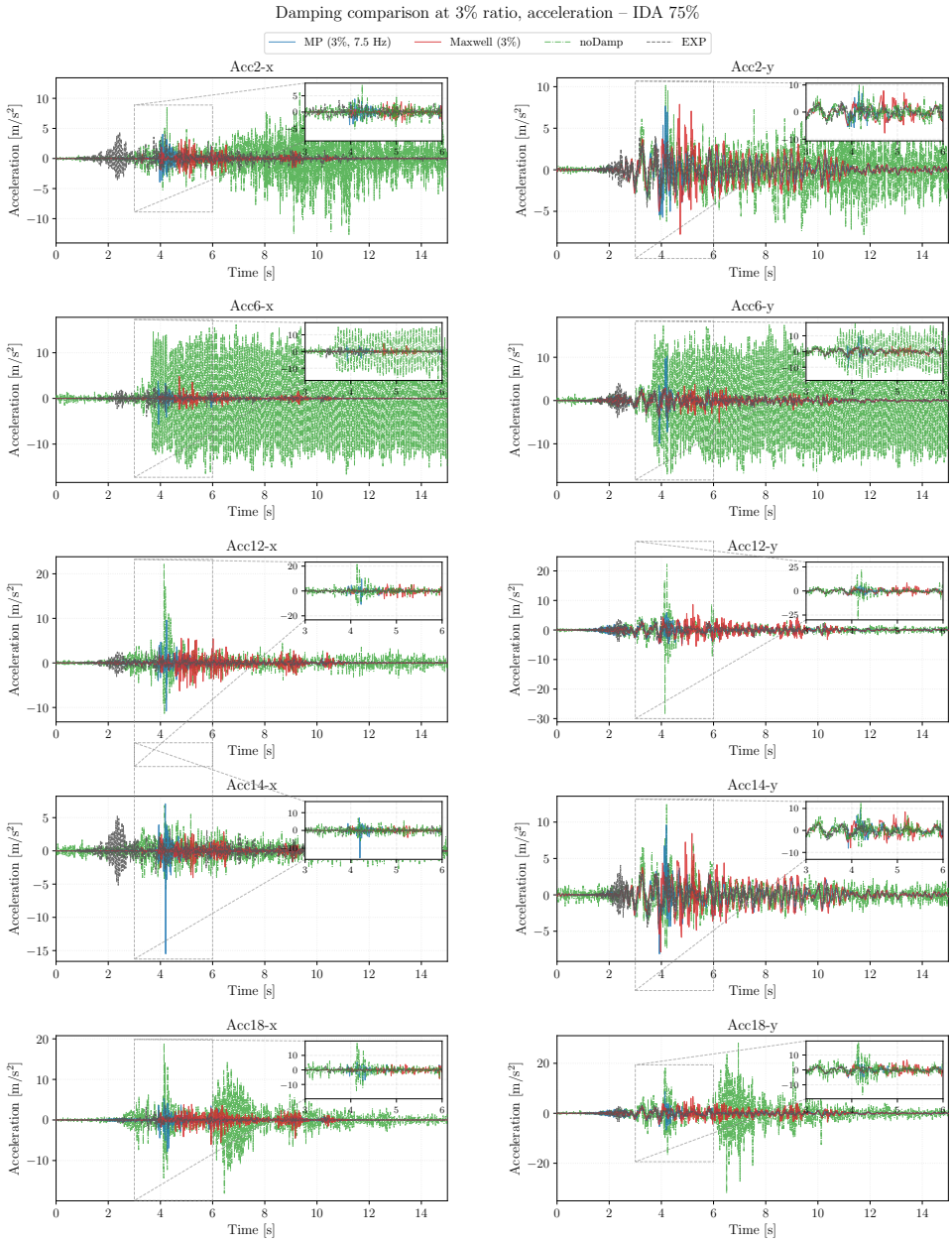


Figure 7.23. Acceleration time histories at five accelerometer locations for the AQA75 amplitude level under the three damping configurations at $\zeta^\star = 3\%$.

response observed by several optical cameras and suppresses the steady-state oscillations

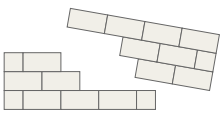
in the acceleration response that persist after the main pulse. The MASON contact model dissipates energy through hysteresis during large-amplitude load reversals, but this dissipation alone is not enough to keep the system bounded once the structure is damaged.

7.3.7. Discussion

A noteworthy point emerges when the findings of this section are compared against the results reported in Oktiovan *et al.* [17] for the same cross-vault benchmark using the TSCLinear contact model. The gap between MP and Maxwell at AQA75 is smaller here than the gap reported in the earlier study. The explanation lies in the frequency content of the response produced by each constitutive model. TSCLinear unloads along the initial stiffness, so a cracked contact that re-closes regains the full undamaged stiffness in a single step. This abrupt jump in stiffness generates high-frequency force impulses that propagate through the block assembly as acceleration spikes, as observed in Section 7.2.6. MASON unloads along the secant stiffness, which is lower than the initial stiffness and decreases further with accumulated damage. The re-contact transition is therefore softer and produces less high-frequency content. MP and Maxwell differ most in how they treat frequencies above the 7.5 Hz reference mode. MP underdamps that range while Maxwell provides approximately uniform damping across the full 1–40 Hz band. When the response is rich in high-frequency energy (TSCLinear), this difference matters. When the high-frequency content is weaker, the two schemes produce similar results.

The computational cost of the three configurations differs substantially. For the full incremental dynamic analysis up to and including AQA75, the Maxwell configuration required 314.99 h of wall-clock time, the MP configuration required 210.34 h, and the noDamp configuration required 153.07 h. All analyses were run on a 3.5 GHz Intel Xeon CPU with 16 cores and 128 GB of memory. Relative to MP, Maxwell incurs a 49.8 % increase in wall-clock time while noDamp runs 27.2 % faster. The Maxwell overhead is due to the added stiffness of the Maxwell elements that reduces the stable timestep from 1.25×10^{-6} s to approximately 1.10×10^{-6} s, which contributes a factor of 1.13 to the cycle count.

At AQA75 the Maxwell scheme gives a modest advantage in displacement, with a displacement NRMSE of 7.6 % against 10.5 % at OC1-y and a displacement composite Sprague–Geers error of 50.4 % against 55.4 %. This advantage does not extend to the accelerations, where MP is slightly better after the pulse. The narrow margin is consistent with the reduced sensitivity to the damping scheme established above, since the MASON contact model limits the high-frequency content through which the two schemes differ. The cross-vault specimen was not tested to collapse, and the AQA75 amplitude represents damage without loss of structural integrity. Under collapse-level loading, where block separations are larger, contact re-closing events are more frequent, and the response frequency content is broader, the difference between MP and Maxwell may increase. The next section addresses this question directly. The MASON contact model is applied with both the MP and Maxwell schemes to a full-scale masonry gable wall tested to collapse on a shake table, providing a setting in which the influence of the damping formulation can be assessed, where it is expected to weigh more heavily.



7.4. Shake-table tests on masonry gable walls

The preceding two sections examined the cross-vault, a curved geometry loaded in-plane primarily. This section turns to the out-of-plane seismic response of unreinforced masonry gable walls, a simpler structural typology and a different loading direction. Gable walls are common in Dutch residential buildings, where they support the timber roof structure and extend above the top floor level without lateral restraint other than that provided by the roof diaphragm. Post-earthquake field surveys [19–22] and building-level shake-table tests [23] have repeatedly identified gable walls as one of the most vulnerable components in these structures, owing to their slenderness, low axial load, and sensitivity to the stiffness of the roof diaphragm.

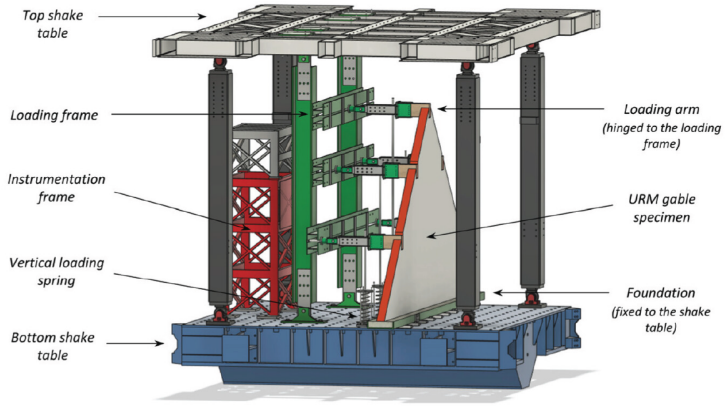
The experimental data used in this section come from the ERIES-SUPREME campaign reported by Damiani *et al.* [10], with the experimental data available in Sharma *et al.* [11]. Three full-scale solid clay gable walls were tested on the dual shake table at the EUCENTRE 9DLAB facility in Pavia, Italy. Instead of constructing a roof, the experimental setup applied differential motion to the top and bottom tables to simulate the interaction between the gable wall and three distinct roof diaphragm configurations. In the first specimen (STIFF), the top and bottom tables received the same motion, simulating a stiff diaphragm. In the second specimen (SEMI-FLEX), the top table motion was linearly amplified relative to the bottom table, simulating a semi-rigid diaphragm. In the third specimen (FLEX), the top-table motion was both amplified and out of phase with the bottom table, representing a flexible diaphragm. Only the STIFF and the FLEX specimens are validated in this case study. Incremental dynamic analysis (IDA) tests were conducted using input signals representative of both induced (Groningen-type) and tectonic earthquake scenarios, with increasing intensity until complete collapse.

This case study serves two purposes within the thesis. First, it validates the MASON contact model under out-of-plane dynamic loading. The failure modes in this regime involve one-way or two-way bending, rocking, and eventual overturning. These differ from the in-plane shear and compression mechanisms that governed the wall and cross-vault analyses in the preceding chapters. Second, it employs the MASON constitutive model and the Maxwell damping scheme simultaneously, combining the two methodological contributions of this thesis in a single application and testing them under collapse-level loading conditions.

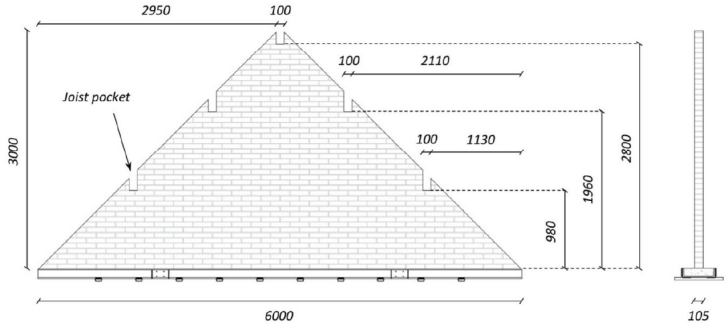
7.4.1. Experimental description

The experimental setup used the 9DLAB dual shake-table facility at the EUCENTRE laboratory in Pavia, Italy, as illustrated in Figure 7.24A, as reported in detail by Sharma *et al.* [11]. A bottom shake table supported the gable foundation, while a top shake table drove a custom steel loading frame that transmitted lateral accelerations to the gable through five horizontal loading arms, each hinged to the frame. Timber beams (purlins) were attached to the steel arms to replicate the behaviour of timber joists found in real roof structures. The loading frame was hinged at the top and bottom to prevent any unintended increase in OOP stiffness and strength.

A rigid instrumentation frame, anchored to the bottom shake table, provided a fixed reference for the displacement measurements. Five springs with stiffness of approximately $50\,\mathrm{N\,mm^{-1}}$ connected to steel bars applied the vertical loads through



(A) 3D Perspective View



(B) Specimen dimensions

Figure 7.24. Test setup and specimen geometry of the ERIES-SUPREME gable wall campaign [11]. Units in mm

the horizontal arms, and their deformations were continuously monitored throughout testing [11]. The two roof diaphragm configurations considered in the present study (STIFF and FLEX) were realised by varying the motion applied to the top shake table.

The tested gable specimens were identical full-scale URM gable walls with a triangular geometry, with a base length of 6000 mm, and a height of 3000 mm (Figure 7.24B). Each gable comprised solid clay bricks with average dimensions of 239 × 105 × 55 mm, and laid in 45 courses with 10 mm thick mortar joints. Five joist pockets were incorporated along the height of the gable to accommodate timber purlins (100 × 200 mm cross-section, $E = 11$ GPa, $\nu = 0.45$). Each purlin was subjected to a vertical load of 4 kN through a spring system, simulating half the weight of a roof diaphragm and producing a total vertical load of 20 kN on the gable. The timber-to-masonry connections relied solely on friction, with the joists placed into the pockets after the masonry had fully cured [11]. Mechanical characterisation of the specimen materials was conducted as part of the experimental campaign, with the measured properties used in this study summarised in Table 7.5.

Each specimen was equipped with accelerometers (Acc), traditional potentiometers (TP), wire potentiometers (WP), and a 3D optical acquisition system (OPT), as shown

Table 7.5. Measured material properties of the gable wall specimens [11].

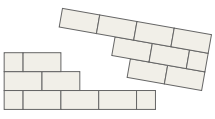
Property	Symbol	Value
Masonry density	ρ	1883 kg/m^3
Brick compressive strength	f_b	42.57 MPa
Masonry compressive strength	f_c	7.44 MPa
Flexural bond strength	f_w	0.27 MPa
Masonry Young's modulus	E_m	4072 MPa
Mortar Young's modulus	E_j	140 MPa

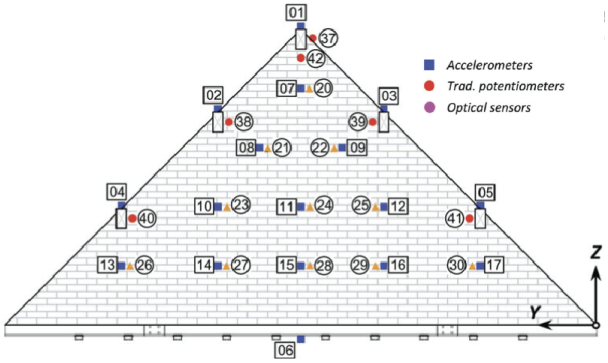
in Figure 7.25. Accelerometers were installed on the gable surface, the loading frame, and the specimen foundation. WPs were used to record OOP displacements at multiple heights on both faces of the gable, while TPs measured spring elongations and relative displacements between the purlins and the masonry. The OPT sensors tracked markers on the gable's free surface and were particularly useful during high-intensity runs, when several contact instruments had to be removed to prevent damage to the equipment. The instrumentation scheme yielded 165 time histories of displacement and acceleration per specimen [11].

Two floor-motion (FM) scenarios were applied: the induced seismicity scenario (FM1) derived from finite element analyses of a typical Groningen URM building, and the tectonic signal (FM2) derived from the 2016 Central Italy earthquake recorded at attic floor level, as described in detail in Mirra *et al.* [24]. Figure 7.26 compares the acceleration time histories and 5 %-damped response spectra at 100 % scaling. For the FLEX configuration, the ridge beam motions exhibit considerably larger spectral accelerations than the bottom table at periods between 0.15 and 0.6 s, while for the STIFF configuration, the two signals are nearly identical.

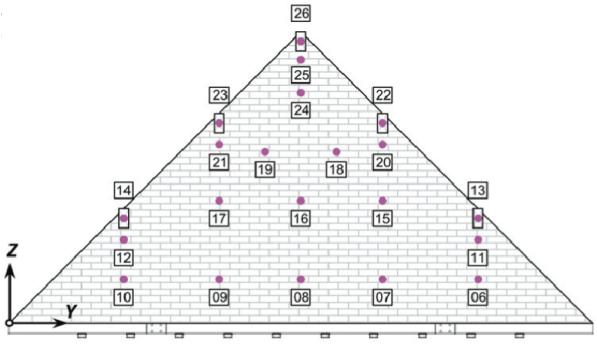
All gables were tested incrementally by linearly scaling both shake-table motions until collapse. Table 7.6 lists the testing sequence along with the peak base acceleration (PBA). Runs 1–6 applied FM1 up to 100 % and runs 7 onward applied FM2 at progressively larger scaling factors. For the FLEX specimen, an additional FM1 100 % run was inserted after run 9 to verify whether the specimen could still withstand the maximum expected induced PBA after sustaining tectonic damage. The STIFF specimen collapsed at run 16 (SF = 3.50, FM2) and the FLEX variant at run 12 (SF = 1.75, FM2).

Figures 7.27 and 7.28 show contour maps of the absolute peak OOP displacement recorded by the optical markers at each run of the testing sequence. This represents the progression of the deformed shape at the end of each IDA run. For the STIFF specimen (Figure 7.27), displacement remained small and symmetric up until run 15, with the maximum consistently located near the gable apex. At run 16 (SF = 3.50, FM2), a sudden change in the deformation pattern was observed. Displacements concentrated in the lower half of the gable reached approximately 85 mm, with a pronounced asymmetry towards the right side of the specimen. This indicates a one-sided rocking mechanism in which a horizontal crack formed between the bottom and middle purlin levels, at approximately one-third of the gable height, and the lower portion displaced outward preferentially to one side [11].





(A) Rear view instrumentation

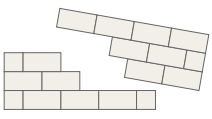


(B) Front view instrumentation

Figure 7.25. Instrumentation layout for each gable specimen [11].

For the FLEX specimen (Figure 7.28), the displacement pattern differed from the early runs onward. Peak displacements were concentrated in the upper triangle and grew rapidly with increasing intensity. By run 9 (FM2 100%), the upper portion of the gable reached approximately 80 mm. After the additional FM1 100% run (run 10), further tectonic loading at run 11 (FM2 125%) produced displacements exceeding 100 mm in the upper half. Collapse occurred at run 12 (FM2 150%), with maximum displacements of approximately 140 mm spread asymmetrically across the upper two-thirds of the gable. The governing mechanism involved the upper portion of the gable rotating outward about a horizontal crack at approximately the mid-upper purlin level [11].

The two configurations thus produced qualitatively different failure modes. The STIFF diaphragm forced failure to develop in the lower, less restrained part of the gable, while the flexible diaphragm concentrated demand on the upper portion, where the amplified ridge motion drove the collapse. This difference in failure mechanisms provides a demanding benchmark for the numerical model, which must capture both behaviours from a single set of constitutive parameters, using only the boundary conditions to distinguish between the two configurations.



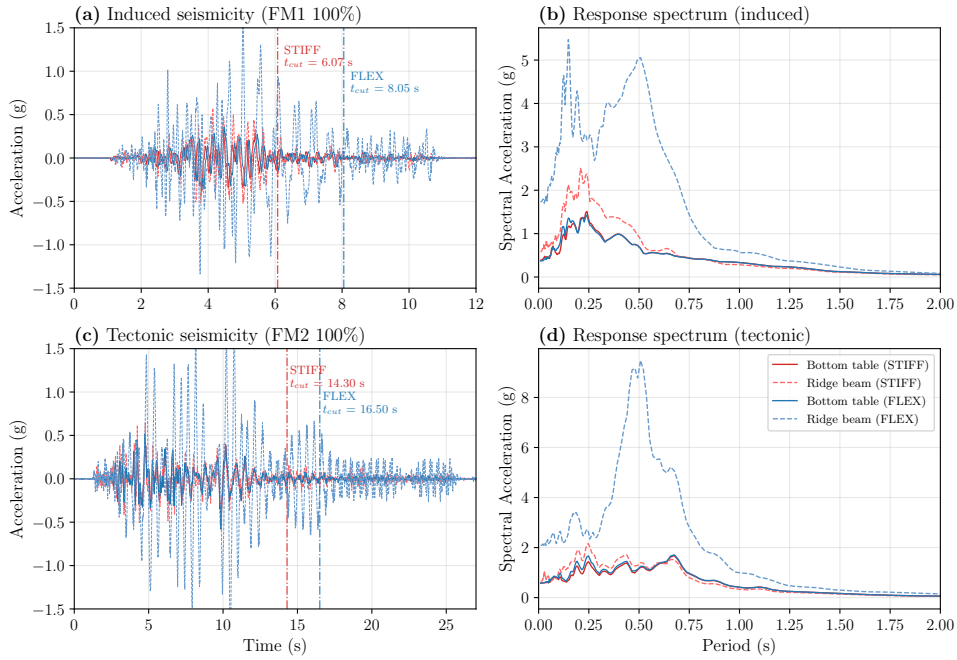


Figure 7.26. Input motions at 100% scaling for the STIFF and FLEX configurations (A, C) acceleration time histories for induced (FM1) and tectonic (FM2) seismicity; (B, D) corresponding 5%-damped response spectra [24].

Table 7.6. Incremental dynamic testing sequence and the peak base acceleration (PBA).

Run	Motion	SF	PBA		Run	Motion	SF	PBA	
			Stiff	Flex				Stiff	Flex
1	FM1	0.10	0.04 g	0.04 g	9	FM2	1.00	0.62 g	0.55 g
2	FM1	0.20	0.07 g	0.08 g	10	FM2	1.25	0.78 g	0.69 g
3	FM1	0.30	0.11 g	0.11 g	11	FM2	1.50	0.93 g	0.83 g
4	FM1	0.50	0.18 g	0.19 g	12	FM2	1.75	1.09 g	0.96 g†
5	FM1	0.75	0.27 g	0.29 g	13	FM2	2.00	1.24 g	—
6	FM1	1.00	0.36 g	0.38 g	14	FM2	2.50	1.55 g	—
7	FM2	0.50	0.31 g	0.28 g	15	FM2	3.00	1.86 g	—
8	FM2	0.75	0.47 g	0.41 g	16	FM2	3.50	2.17 g†	—

† Collapse run.
FLEX: an additional FM1 100% run was inserted between runs 9 and 10.
PBA values are nominal, obtained by linear scaling of the reference table motion with the scale factor (SF) [24]. The recorded bottom-table PBA was lower near collapse [24].

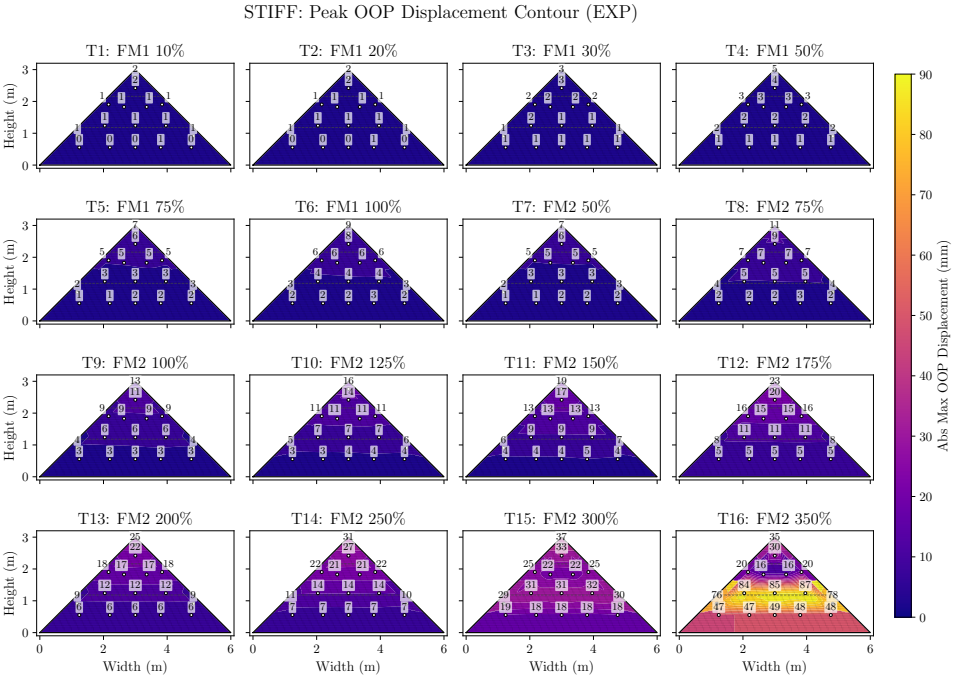


Figure 7.27. STIFF: contour maps of absolute peak OOP displacement (mm) recorded by optical markers at each run of the incremental dynamic testing sequence.

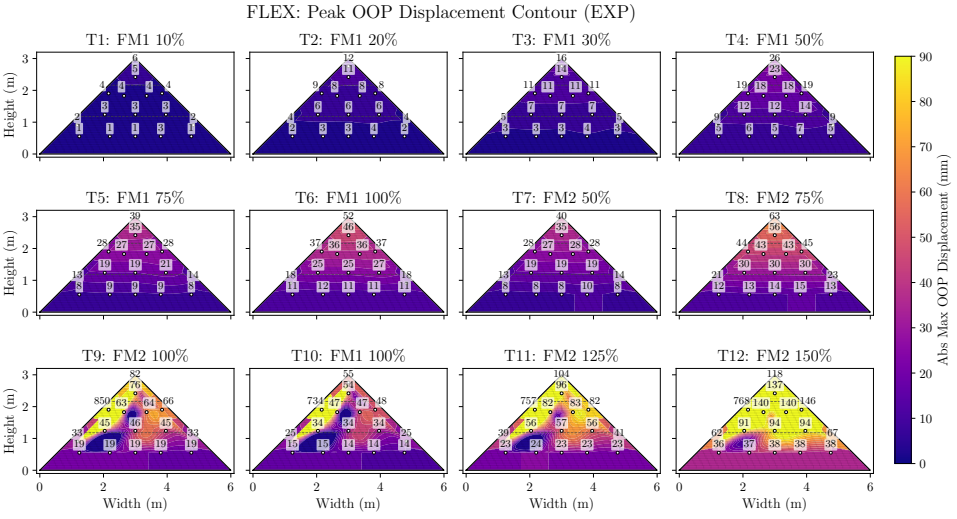


Figure 7.28. FLEX: contour maps of absolute peak OOP displacement (mm) recorded by optical markers at each run of the incremental dynamic testing sequence.

7.4.2. Numerical modelling setup

The gable wall is modelled using the discontinuum modelling strategy adopted throughout this thesis. Bricks are modelled as deformable blocks with expanded dimensions that incorporate the half-thickness of the surrounding mortar layers. The blocks are kept deformable so that the vertical load can be applied through pre-stressed cable elements, which represent the springs and steel bars of the test setup. The cable elements transfer the pre-tension to the masonry through the nodes of the discretised blocks, an attachment that rigid blocks would not provide. Unit-mortar interfaces are governed by the MASON contact constitutive model, and no potential crack plane is considered in this work, as there was no experimental evidence of unit splitting of the gable wall.

The explicit representation of the loading frame, joists, purlins, and vertical loading system is presented in Figure 7.29, following the strategy described in Ghezelbash *et al.* [25]. The HEB300 columns and double HEB180 beams are replaced with solid rectangular blocks having equivalent mass and OOP bending stiffness (Table 7.7). The hinge-to-hinge height of the frame is 3.735 m, with the bottom hinge at the wall base joint. Timber purlins (100 × 200 mm) are modelled as isotropic elastic blocks ($E = 11$ GPa, $\nu = 0.35$).

Table 7.7. Equivalent elastic properties of loading frame components.

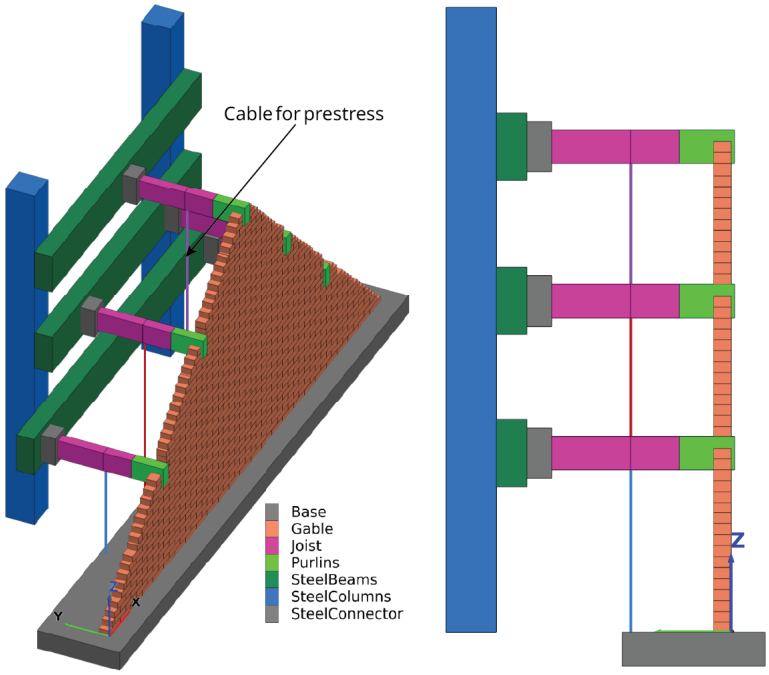
Component	E [GPa]	ν	ρ [kg/m^3]
Columns (HEB300 equiv.)	74.58	0.30	1300
Beams (2×HEB180 equiv.)	78.83	0.30	1422
Connectors (joist–frame)	76.71	0.30	1361
Timber purlins (C24)	11.0	0.35	420

Equivalent values match the mass and OOP bending stiffness of the original steel profiles [25].

The base block receives the bottom-table acceleration and is made rigid through a high Young's modulus. The frame top is driven by the top-table acceleration, transferring lateral loads through the joists and purlins. Both frame ends are hinged. Purlin-to-wall contacts are friction only ($\tan\phi = 0.75$, no cohesion or tensile strength), calibrated against the experimental result at run 1 STIFF (FM1 10%). The wall-to-base connection uses standard MASON mortar-joint properties. The vertical roof load is applied through five prestressed cable elements, one per joist, attached at 47 cm from the joist–frame hinge. Each cable is prestressed to approximately 16.72 kN, computed from moment equilibrium about the hinge as

$$F_{\text{cable}} = \frac{F_{\text{target}} \cdot L_{\text{purlin}}}{L_{\text{spring}}} \cdot \alpha = \frac{4.0 \times 0.9825}{0.47} \times 2.0 \approx 16.72\,\text{kN} \tag{7.11}$$

where $F_{\text{target}} = 4$ kN is the target vertical load at the purlin-wall contact, $L_{\text{purlin}} = 0.9825$ m and $L_{\text{spring}} = 0.47$ m are the moment arms from the hinge to the purlin centreline and to the cable attachment, respectively, and $\alpha = 2.0$ is a geometric correction factor



(A) Perspective view (B) Left-side view

Figure 7.29. 3DEC model of the gable wall: (A) perspective view showing block discretisation, back frame, joists, purlins, and cable elements; (B) left-side view showing boundary conditions and contact groups.

for the joist configuration. Cable stiffness matches the experimental spring stiffness (≈ 50 N/mm).

The input acceleration time histories are truncated at the 95 % Arias intensity threshold (Figure 7.26), filtered with a third-order Butterworth band-pass (0.2–50 Hz), and baseline-corrected [26]. This processing differs from the 48 Hz low-pass filter applied to the experimental output data [11]. For STIFF, the bottom-table signal is applied to both the base and the frame top as velocity input. For FLEX, the bottom and top signals are applied separately.

The MASON contact parameters are listed in Table 7.8. Joint stiffnesses follow Equation (5.1) with $E_b = 12\,772$ MPa, $G_b = 5\,553$ MPa, $E_m = 140$ MPa, $G_m = 60.9$ MPa and $t_m = 10$ mm:

$$k_n = \frac{E_b E_m}{t_m (E_b - E_m)} = 14\,155 \text{ MPa/m}, \qquad k_s = \frac{G_b G_m}{t_m (G_b - G_m)} = 6\,154 \text{ MPa/m} \tag{7.12}$$

The tensile strength is taken as $f_t = f_w/3 = 0.10$ MPa. Fracture energies follow the CEB-FIP expressions of Equations (7.1) to (7.3).

Table 7.8. MASON contact parameters for the gable wall joints.

Parameter	Symbol	Value
Normal stiffness	k_n	14 155 MPa/m
Shear stiffness	k_s	6 154 MPa/m
Tensile strength	f_t	0.10 MPa
Cohesion	c_0	0.15 MPa
Residual cohesion	c_r	0 MPa
Friction angle	φ_{cv}	24.1°
Compressive strength	f_c	7.44 MPa
Residual compressive strength	$f_{c,r}$	1.49 MPa
Mode-I fracture energy	G_f^I	0.0081 N/mm
Mode-II fracture energy	G_f^{II}	0.081 N/mm
Compressive fracture energy	G_c	18.0 N/mm
Peak ratio	n	3.0
Cap parameters	C_n, C_{nn}, C_{ss}	0, 1, 9

Deformable blocks are assigned $\rho = 2000$ kg/m^3, $E = 4072$ MPa, and $\nu = 0.15$. The base block is made rigid by assigning it a Young's modulus three orders of magnitude higher (4072 GPa). Maxwell damping with three elements is calibrated for $\zeta^\star = 5\%$ over 1–40 Hz (Section 7.3.3). A mass-proportional cross-check is conducted for one configuration to test whether the damping-scheme sensitivity observed for the cross-vault (Section 7.3.7) persists under the larger block separations expected near collapse.

The model comprises 648 blocks, 6239 gridpoints, and 7318 zones (≈18 700 DOFs). Mass scaling is applied with a target timestep of 7×10^{-6} s, resulting in an increased mass of 20 % localised at the base block. The model is first solved to equilibrium under a gravity load, then the cable is pre-tensioned. Once the system reaches equilibrium, the incremental dynamic analysis is conducted following the protocol in Table 7.6.

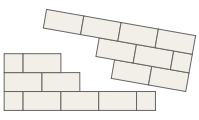
7.4.3. Numerical results

The numerical results are compared against the experimental data for both STIFF and FLEX configurations, organised by response quantity: displacement, acceleration, damage evolution, and hysteretic responses.

Displacement response

Figures 7.30 and 7.31 compare the numerical and experimental OOP displacement time histories at three sensor locations (bottom purlin, OPT-8, $z = 0.55$ m; middle purlin, OPT-16, $z = 1.24$ m; upper wall, OPT-25, $z = 2.76$ m) and three representative IDA levels.

For the STIFF configuration (Figure 7.30), a phase offset between the numerical and experimental signals is visible at run 4 (herein labelled T4 in the figures; FM1 50%), most clearly at OPT-16 and OPT-25. The numerical response is stiffer than the experimental one, with smaller displacement amplitudes and a slight frequency shift. This is attributed to the added stiffness of the Maxwell damping elements before any cracking develops. As the IDA level increases and joints begin to open, the effective stiffness decreases,



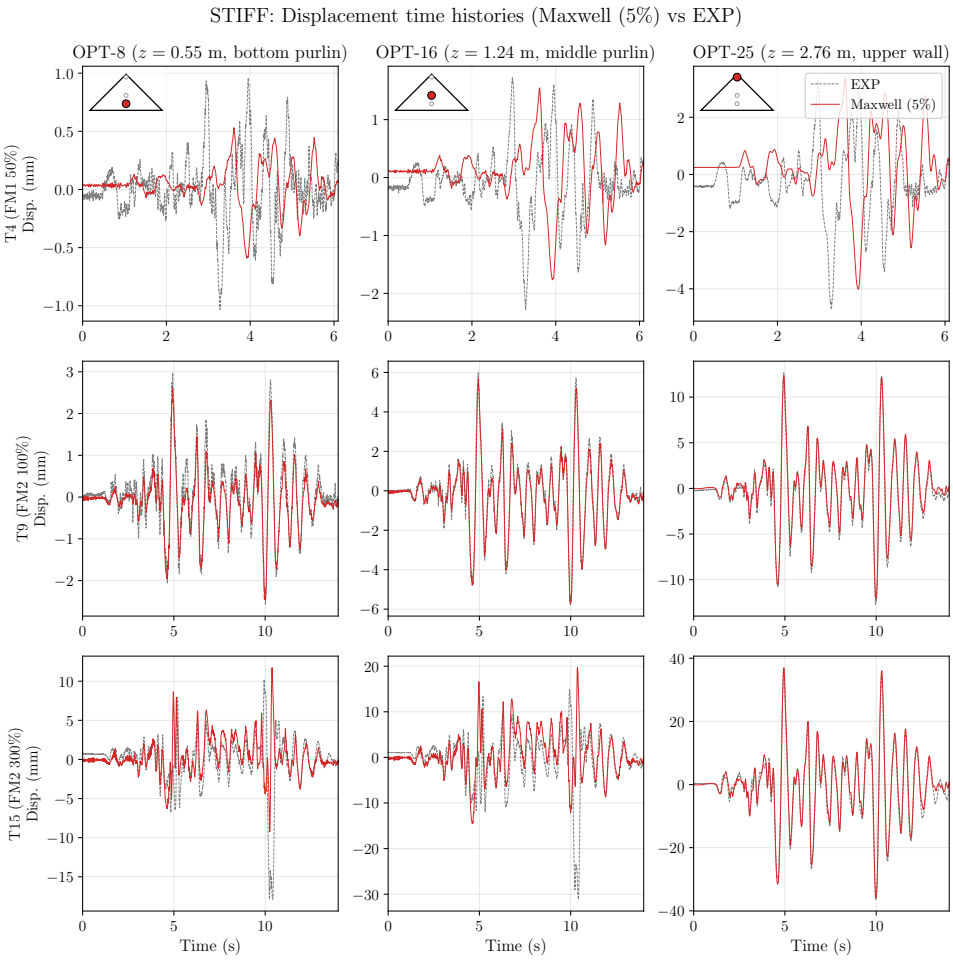


Figure 7.30. STIFF: OOP displacement time histories at three sensor locations (columns) and three IDA levels (rows).

and the phase offset diminishes. By T9 (FM2 100%), the waveforms are well aligned in both phase and amplitude. At T15 (FM2 300%), the model captures the increase in displacement amplitude and the onset of asymmetric rocking, though peak values at OPT-16 are underpredicted by approximately 10 mm.

For the FLEX configuration (Figure 7.31), the same initial stiffness offset appears at T4 but is less pronounced, likely because the amplified ridge motion induces earlier cracking. At T7 (FM2 50%), the time histories at all three sensors show good agreement in both amplitude and phasing. At T11 (FM2 125%, near-collapse), the model overpredicts the peak at OPT-8 by approximately 10 mm, while the match at OPT-16 and OPT-25 remains within 5–10 mm.

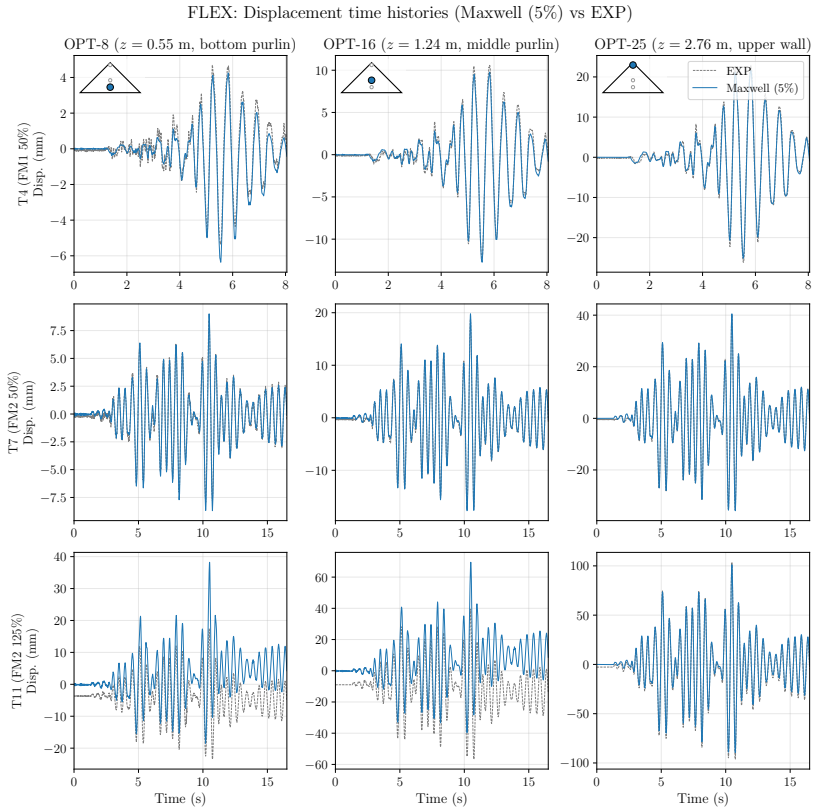


Figure 7.31. FLEX: OOP displacement time histories at three sensor locations (columns) and three IDA levels (rows).

Figures 7.32 and 7.33 present the peak absolute OOP displacement at four representative sensor locations as a function of the peak base acceleration (PBA). A non-monotonic feature is visible in both curves near PBA ≈ 0.36 g, where the transition from the induced seismicity signal (FM1) to the tectonic signal (FM2) produces a temporary drop in PBA despite the increasing scale factor. For STIFF (Figure 7.32), the model tracks the experimental peak displacements well across all 16 runs. At the upper wall sensors (OPT-24 and OPT-25), the numerical and experimental values remain within a few millimetres up to PBA ≈ 1.55 g (T14, FM2 250%). At the lower sensors (OPT-8 and OPT-16), the match remains close until PBA ≈ 1.86 g (T15), after which the experimental displacements increase sharply at PBA ≈ 2.17 g (T16, collapse), whereas the model predicts a more moderate increase. The experimental peak at OPT-8 reaches approximately 50 mm at T16 and OPT-16 approximately 87 mm, whereas the model predicts approximately 17 mm and 25 mm, respectively. The sudden increase is consistent with the damage pattern described in Section 7.4.1, where the experimental collapse mechanism concentrates deformation in the lower half of the gable. The current

model does not fully reproduce this sudden localisation at the final run.

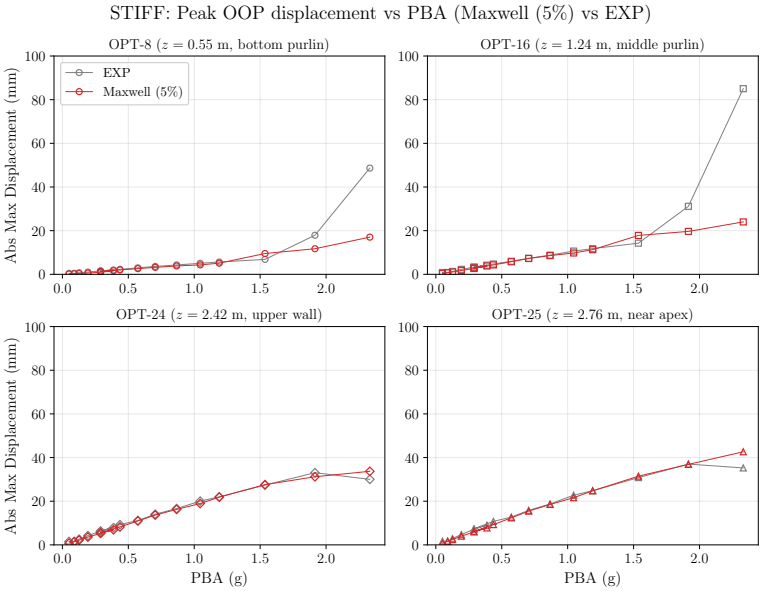


Figure 7.32. STIFF: peak absolute OOP displacement at four sensor locations vs PBA.

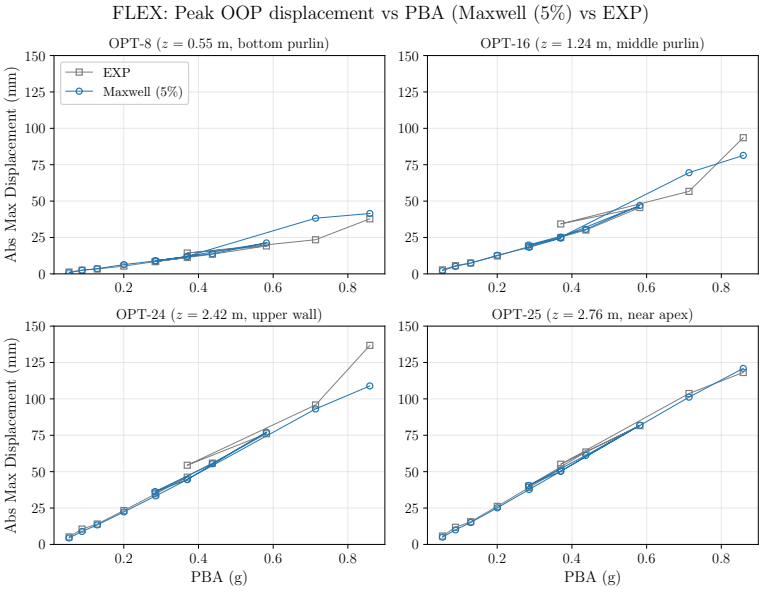


Figure 7.33. FLEX: peak absolute OOP displacement at four sensor locations vs PBA.

For FLEX (Figure 7.33), the peak displacement trends are well reproduced through the full sequence up to PBA ≈ 0.96 g (T12, collapse). The FM1-to-FM2 transition at PBA ≈ 0.38 g produces a similar non-monotonic feature as in the STIFF case. A second drop is visible near PBA ≈ 0.55 g, corresponding to the additional FM1 100% run (T10) inserted after T9 (FM2 100%). When plotted against PBA, this additional run returns to a lower intensity, confirming that its reduced displacement demand is an intensity effect rather than a sign of structural recovery. At OPT-24 ($z = 2.42$ m), the model underpredicts the peak at the collapse run (approximately 110 mm vs 137 mm experimentally). At OPT-25 ($z = 2.76$ m), the numerical and experimental values at T12 are close (approximately 120 mm vs 125 mm). Nevertheless, the overall growth trajectory is well captured at all four sensors.

Acceleration response

Figures 7.34 and 7.35 compare the numerical and experimental acceleration time histories at four representative sensor locations (table, ACC6, $z = -0.15$ m; lower wall, ACC15, $z = 0.55$ m; mid wall, ACC11, $z = 1.20$ m; apex, ACC1, $z = 3.00$ m) for three IDA levels. Numerical accelerations are obtained by frequency-domain differentiation of the velocity output with a 30 Hz cosine taper to suppress high-frequency noise from the differentiation. Overall, the model reproduces the experimental acceleration waveforms reasonably well in the low-to-moderate intensity range but tends to overpredict peak accelerations at the wall sensors near collapse, where re-contact events between separating blocks generate a sharper force impulse than the experimentally observed responses. At the table level, the numerical and experimental accelerations closely match for both configurations across all IDA levels, confirming that the prescribed input motion is correctly applied.

For the STIFF variant (Figure 7.34), the wall sensors show a similar pattern to the displacement comparison. At T4 (FM1 50%), the numerical accelerations at ACC15, ACC11, and ACC1 are smaller than the experimental ones and slightly shifted in phase, again consistent with the added stiffness from the Maxwell elements in the elastic range. By T9 (FM2 100%), the amplitude and phasing at all wall sensors match well. At T13 (FM2 200%), the model reproduces the general waveform shape but generates sharper acceleration peaks at ACC11 and ACC15, which are not present in the experimental record.

For the FLEX configuration (Figure 7.35), the time histories at T4 (FM1 50 %) show good amplitude agreement at all sensors, with the phase offset less visible than in the STIFF case. At T7 (FM2 50 %), the match at all four observed sensors is close. The numerical response slightly overpredicts the experimental acceleration at T11 (FM2 125 %), though the waveform shape remains consistent.

Figures 7.36 and 7.37 show the peak absolute acceleration at the same four sensor locations as a function of PBA. For the STIFF variant (Figure 7.36), the peaks at the table-level (ACC6) are well matched throughout the 16 runs. At ACC1 (apex), the model underpredicts the peak acceleration during the induced FM1 series (PBA < 0.36 g) by a factor of approximately two, most likely due to the increased stiffness caused by the Maxwell elements. From the onset of the FM2 series (PBA ≈ 0.31 g), the apex accelerations converge and track the experimental values within 10–20% up to T14. At ACC15 and

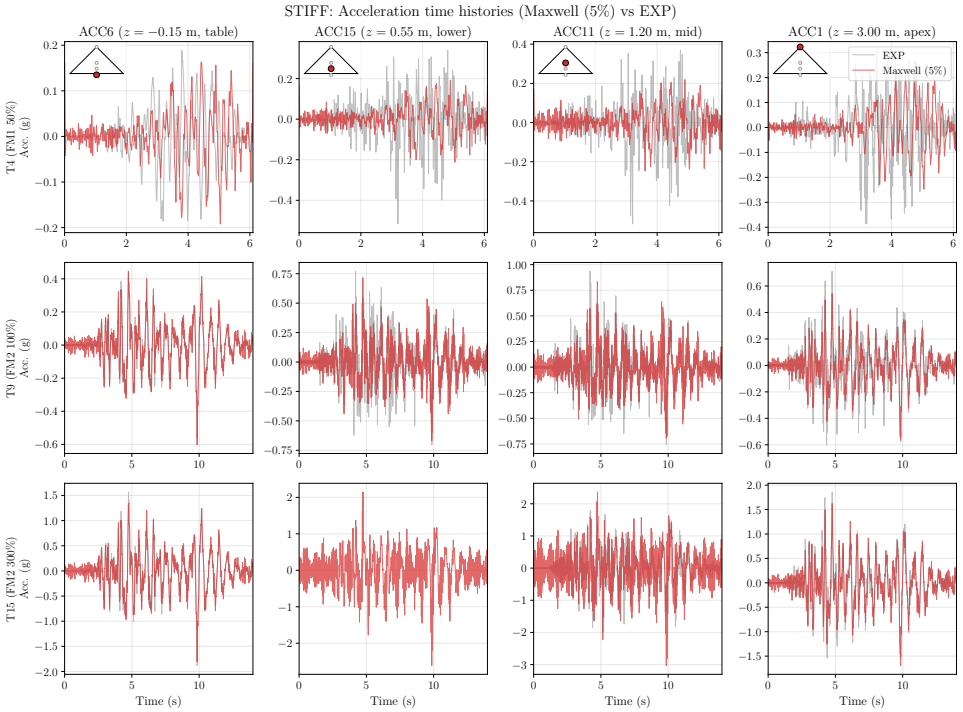


Figure 7.34. STIFF: acceleration time histories at four sensor locations (columns) and three IDA levels (rows).

ACC11, the numerical peaks exceed the experimental ones above PBA ≈ 1.24 g, reaching approximately 2.5 g and 3.0 g at PBA ≈ 1.86–2.17 g compared to experimental values of 0.9 g and 2.0 g. This overprediction at the wall sensors in the near-collapse range is attributed to the sharper re-contact forces at the unit-mortar interfaces. Both the numerical and experimental amplification at the apex remain below 1.5 up to PBA ≈ 1.0 g, then diverge as the model develops more concentrated re-contact forces near collapse.

For the FLEX variant (Figure 7.37), the predicted peak acceleration at the table level (ACC6) closely matches the recorded value, as it does for the STIFF model. At ACC15, the model underpredicts below PBA ≈ 0.29 g and then tracks the experimental trend up to PBA ≈ 0.55 g. Above PBA ≈ 0.69 g (T11, near-collapse), the numerical peak at ACC15 reaches approximately 1.6 g compared to the experimental 0.8 g, an overprediction by a factor of two. A similar pattern is observed at ACC11, where the numerical peak is approximately 2.5 g, compared with the experimental value of 1.4 g. At the apex (ACC1), the match remains closer, with both values reaching approximately 2.3–2.6 g at the collapse PBA. The overprediction at the intermediate wall sensors suggests that the numerical model generates more concentrated inertial forces at the purlin connection levels during near-collapse rocking than the experiment, where the energy may be dissipated more gradually through distributed cracking.

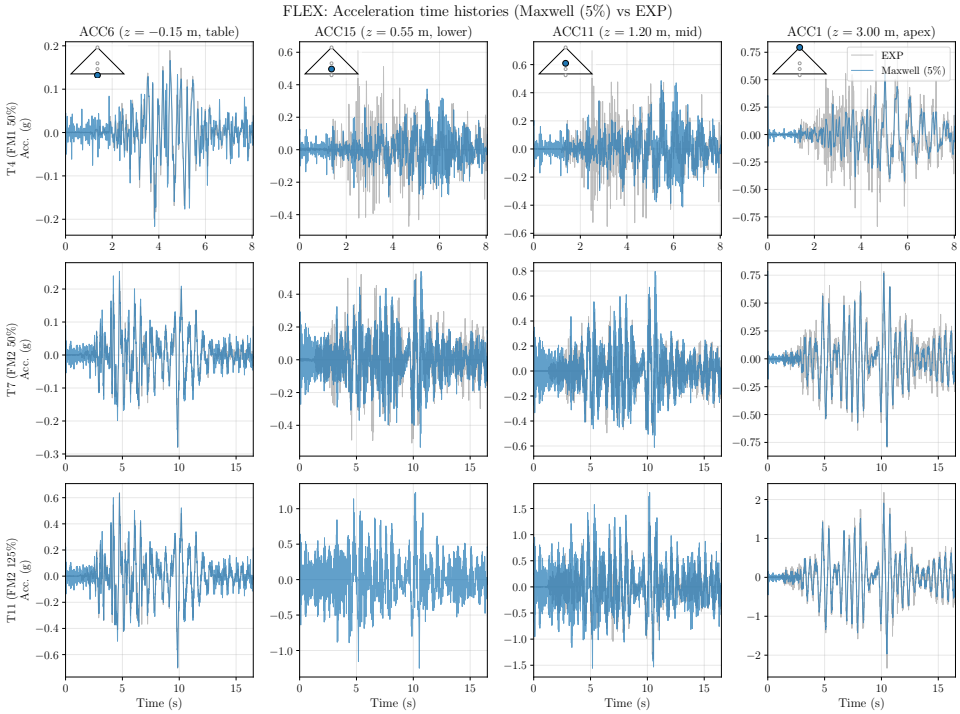


Figure 7.35. FLEX: acceleration time histories at four sensor locations (columns) and three IDA levels (rows).

In summary, the displacement and acceleration comparisons show that the model reproduces the experimental response with good accuracy up to the pre-collapse PBA range for both configurations. The main discrepancies are the overestimation of initial stiffness due to the Maxwell elements at low PBA, and the overprediction of acceleration peaks at the wall sensors near collapse due to sharper numerical re-contact forces. Both configurations collapse during the same loading run as the experiment, at nominal target PBAs of 2.17 g (STIFF) and 0.96 g (FLEX), so the model reproduces the collapse intensity. The achieved table PBA at that run was lower, 1.8 g for STIFF, reflecting reduced table tracking near collapse rather than a modelling error. Plotting the response quantities against PBA reveals a non-monotonic intensity path due to the FM1-to-FM2 signal transition and the additional FM1 run in the FLEX sequence, confirming that displacement and acceleration growth are governed by the input intensity. The following two sections examine the spatial distribution of damage and the global hysteretic response.

Damage evolution

The cumulative damage through the IDA sequence is assessed by comparing the OOP displacement fields obtained from the numerical and experimental records at the

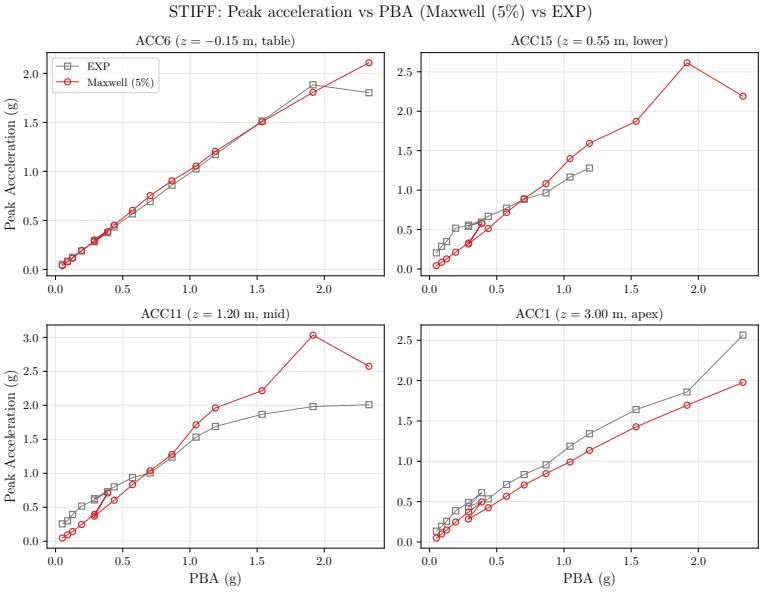


Figure 7.36. STIFF: peak absolute acceleration at four sensor locations vs PBA.

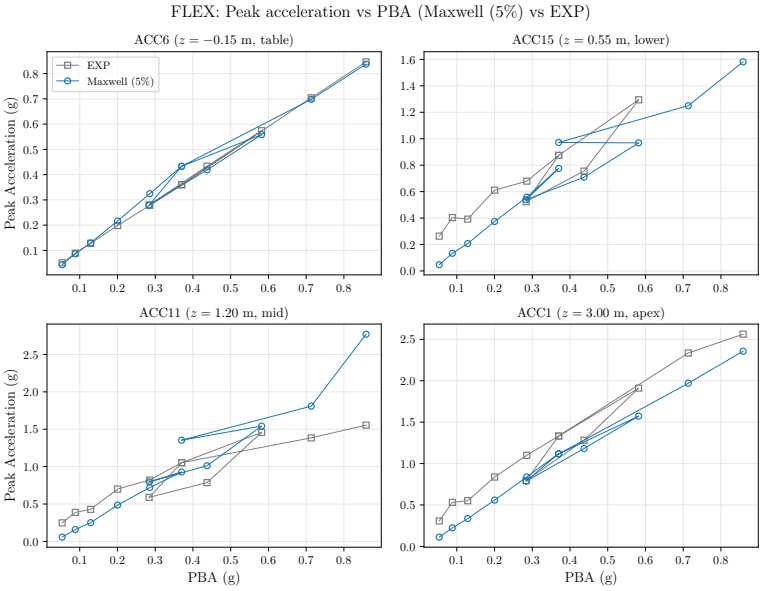


Figure 7.37. FLEX: peak absolute acceleration at four sensor locations vs PBA.

discrete OPT locations on the gable inner face. The experimental displacement envelopes

for the two configurations are reported in Figures 7.27 and 7.28. For every run, the peak OOP displacement is extracted at each OPT position on the wall inner face. Two complementary views are used. The numerical peak displacement fields, interpolated over the wall area, are shown in Figures 7.38 and 7.40 and trace how the deformed shape evolves and where displacement localises as the intensity increases. The residual fields, defined as $\Delta d = d_{\mathrm{NUM}} - d_{\mathrm{EXP}}$ and reconstructed by linear interpolation, are shown in Figures 7.39 and 7.41 and quantify the local mismatch against the experimental envelopes reported in Figures 7.27 and 7.28.

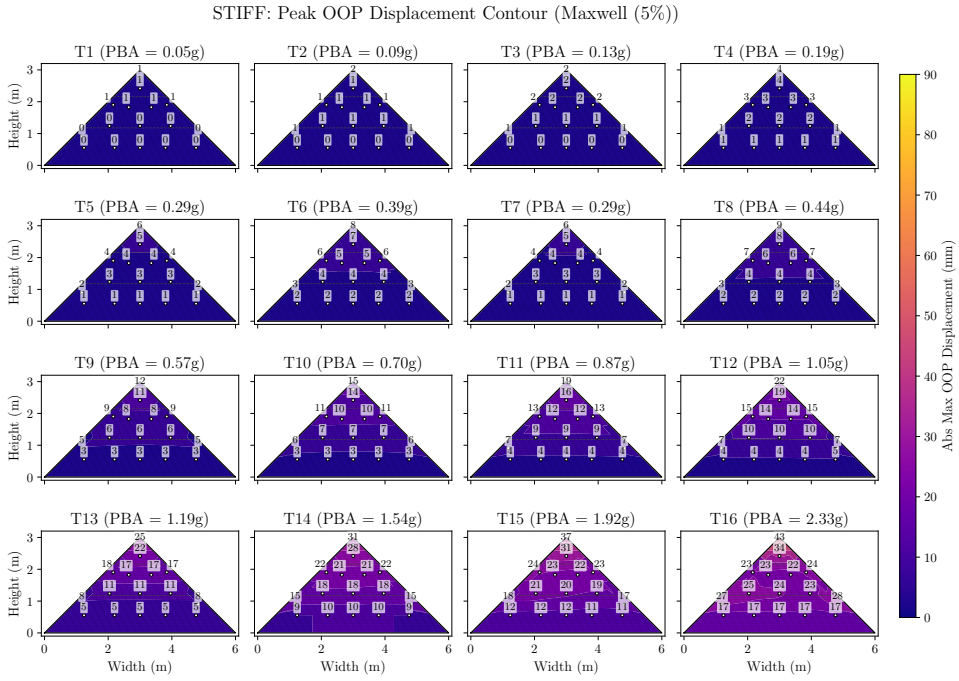


Figure 7.38. Numerical peak OOP displacement field for the STIFF configuration across the IDA sequence. Units in mm.

In the displacement fields, the number printed next to each marker is the local peak displacement in millimetres. In the residual fields, the local residual is used, with positive values denoting overprediction and negative values underestimation relative to the experimental values. The colour field in each case is the interpolation between measurement points and indicates the overall deformed shape at the end of the run.

For the STIFF variant, the numerical displacement field (Figure 7.38) grows with intensity while keeping a smooth distribution over the triangle, with the largest values at the apex, and localises into an apex wedge only at the final runs. The residual field (Figure 7.39) remains within ±1 mm at all OPT locations through T13 (PBA = 1.19 g), consistent with near-rigid response and negligible joint activation up to this intensity. Small positive residuals of +2 to +5 mm develop at T14 (PBA = 1.5 g) across the mid

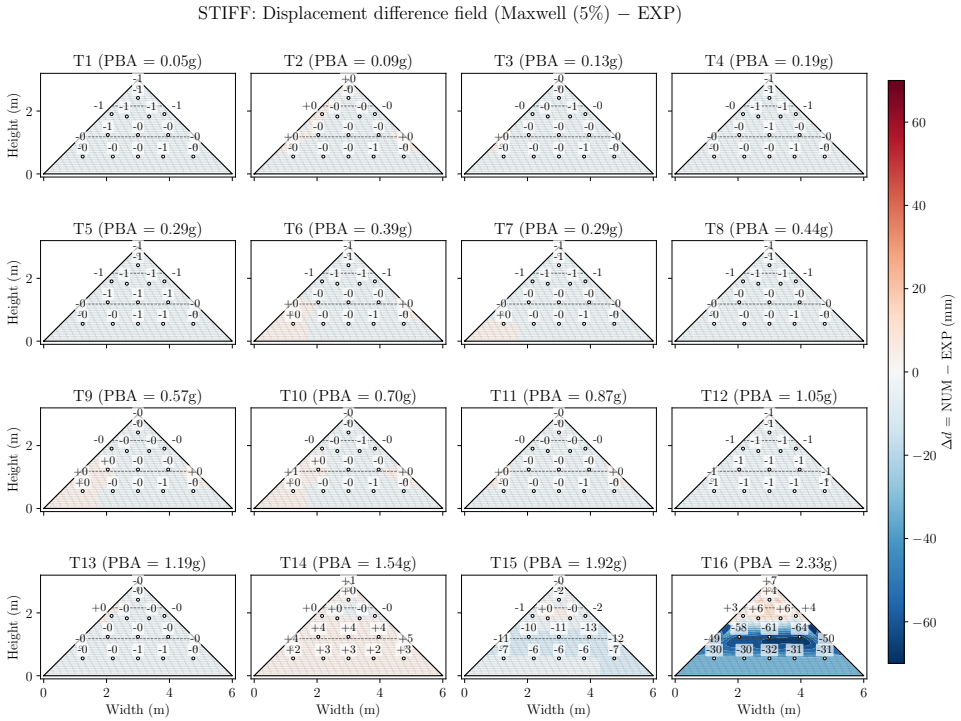


Figure 7.39. Displacement residual field $\Delta d = d_{\mathrm{NUM}} - d_{\mathrm{EXP}}$ for the STIFF configuration across the IDA sequence. Units in mm.

and lower portions of the triangle and reverse to moderate negative residuals of −6 to −13 mm at T15 (PBA=1.92 g). At the collapse run of T16 (PBA = 2.17 g), the residual field distribution becomes strongly bimodal, with positive residuals of +3 to +7 mm at the apex coexisting with large negative residuals of −30 to −64 mm in the lower and mid portions.

This pattern reflects a mismatch in the location of the governing rocking hinge. The numerical model develops a mechanism that pivots near two-thirds of the gable height (Figure 7.42A), whereas the experimental specimen rocks about a lower hinge, located between the bottom and middle purlins at approximately one-third of the gable height. This produces larger measured displacements in the bottom half and correspondingly negative residuals in the contour field. The same mismatch appears in the high-fidelity blind prediction of Ghezelbash *et al.* [25], which also assumes a uniform bond strength. The higher discretisation fidelity, therefore, did not relocate the hinge, so the discrepancy is not specific to the simplified micro-modelling idealisation and is more plausibly tied to the spatial variability of the bond strength, which governs where the horizontal crack forms. Reproducing the experimental hinge location would then require representing this variability, either through specimen-specific calibration of the bond strength at the governing joint or through a stochastic bond-strength field of the kind used in the

bifurcation study (Section 4.8).

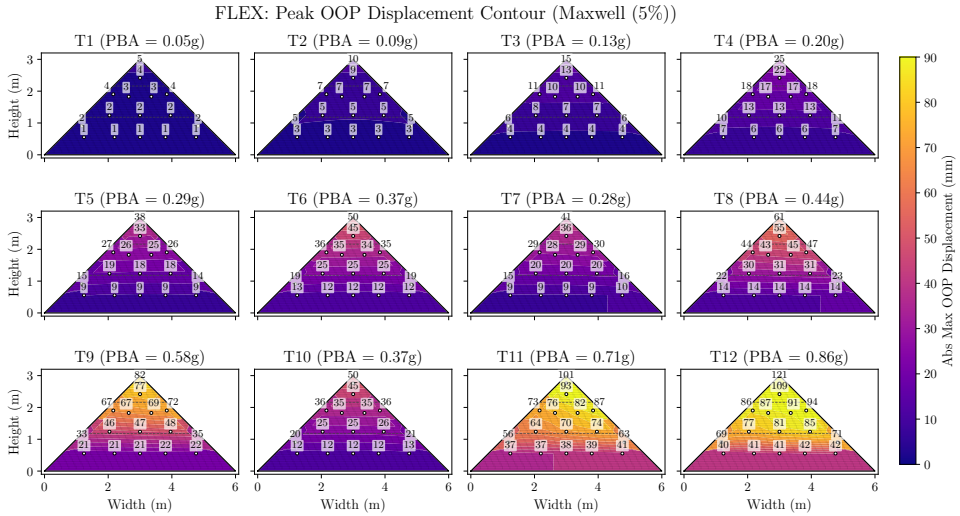


Figure 7.40. Numerical peak OOP displacement field for the FLEX configuration across the IDA sequence. Units in mm.

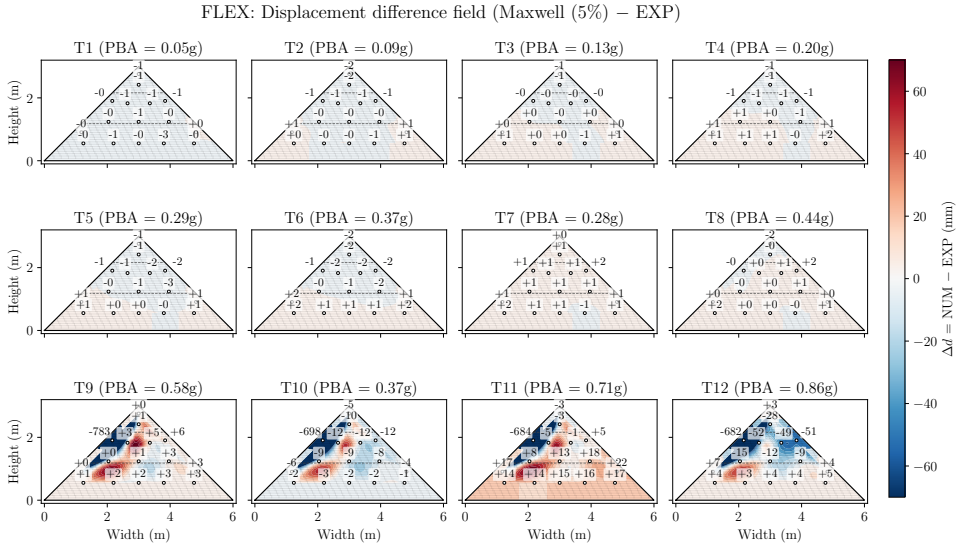
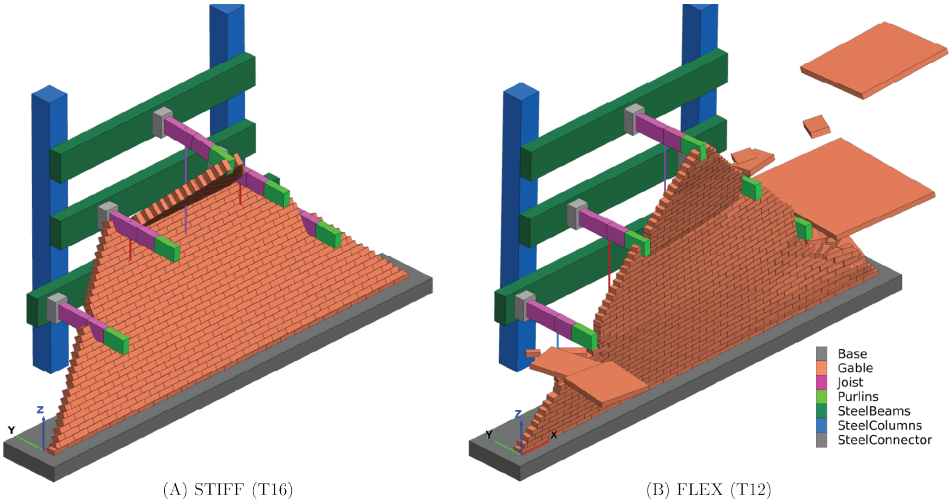


Figure 7.41. Displacement residual field $\Delta d = d_{\text{NUM}} - d_{\text{EXP}}$ for the FLEX configuration across the IDA sequence. Units in mm.

For the FLEX variant, the numerical displacement field (Figure 7.40) localises in the

upper triangle from the intermediate runs onward and grows rapidly towards collapse, reaching roughly 120 mm at the apex at T12. The residual field (Figure 7.41) remains within ±2 mm through T7 (PBA = 0.28 g) and develops positive residuals of up to +14 mm in the upper triangle at T8. From T9 onwards, the contour maps include localised extreme outliers at individual OPT points, with values exceeding −600 mm at OPT-21 (2/3-height, left corner). These magnitudes are inconsistent with the bounded kinematics of the gable triangle and are attributed to loss of optical tracking at specific channels during the high-intensity runs rather than to genuine physical displacement. Discounting these dropouts, the envelope at the final run T12 (PBA = 0.96 g) shows negative residuals of −50 to −53 mm in the upper portion and positive residuals of +5 to +10 mm in the lower band. The large negative residuals in the upper portion and the small residuals in the lower band indicate upper-triangle overturning. The model reproduces this mode, with its horizontal boundary at the middle purlin line rather than at the experimental mid-upper purlin level, and underestimates the displacement of the overturning part by roughly one third. The governing failure mode of the FLEX configuration is therefore reproduced by the model, with a modest hinge offset, in contrast to the hinge-location mismatch observed for the STIFF variant.



(A) STIFF (T16) (B) FLEX (T12)

Figure 7.42. Numerical deformed configurations at the collapse runs for the STIFF specimen at T16 (A) and the FLEX specimen at T12 (B), plotted with a deformation amplification factor of 10.

The terminal configuration of the two collapse runs is shown in Figure 7.42 with a deformation amplification factor of 10. For the STIFF configuration at T16, the gable triangle exhibits a distinct horizontal opening near two-thirds of the wall height, with the apex wedge rotating outward while the remainder of the triangle retains its original geometry. For the FLEX configuration at T12, the deformation concentrates in the upper triangle. The portion above the mid-height purlin line overturns as a coherent body, with unit separation localised at the apex and along the horizontal kinematic boundary. The

deformed geometries are consistent with the failure mode interpretation drawn from the residual fields and the experimental contour in Figure 7.28.

Hysteretic response

The hysteretic behaviour of the two configurations is characterised through the relation between the normalised base shear coefficient V_{base}/W and the OOP displacement at a reference optical target, where V_{base} is the base shear reaction and W is the total weight supported by the gable. The reference target is selected as the location of maximum excitation within each record, which does not coincide across EXP and NUM when the governing mechanism differs. For the STIFF configuration, peak oscillations occur at OPT-16 in the experimental record, consistent with the lower-rocking mechanism of the specimen, and at OPT-25 in the numerical record, consistent with the upper-wedge mechanism reproduced by the model. The total weight used for normalisation is $W_{\text{EXP}} = W_{\text{NUM}} = 17.5\,\text{kN}$, corresponding to the self-weight of the gable triangle plus the applied vertical load at the purlin line. The recorded base shear channel captures the reaction at the shake-table foundation only and excludes the inertial contribution of the steel frame.

Figure 7.43 overlays the hysteresis loops from all runs for each configuration. For the STIFF case, the response clusters around the origin at low to moderate intensities and deviates at collapse. The numerical trajectory at OPT-25 covers a displacement range of approximately ±40 mm with base shear coefficients reaching ±2, while the experimental trajectory at OPT-16 spans a comparable displacement range over the main cluster and exhibits a single excursion extending to approximately −80 mm. A direct comparison of the loop shapes is subject to the caveat that the two trajectories are recorded at different heights on the wall. The FLEX response exhibits the asymmetric, strongly elongated loop geometry associated with the upper-triangle overturning mechanism, with a pronounced drift towards the negative displacement direction at collapse. The numerical trajectory reproduces both the shape of the envelope and the asymmetry of the response, with the loops biased towards the overturning direction rather than centred on zero. At T12, the peak negative displacement reaches −120.9 mm in the model against −118.2 mm in the experiment, a difference of 2.3 %.

Per-run hysteresis loops for both configurations are reported in Figures C.11 and C.12 and are omitted from the main text for brevity. The per-run plots confirm that the close agreement of the superimposed cluster extends to individual runs of comparable intensity, with the deviations noted above localised at the collapse runs.

Figure 7.44 reports the cumulative dissipated energy $W_{\text{dis}} = \int V_{\text{base}}\,\mathrm{d}u$ plotted against PBA. A single reference location at OPT-25 is used for both EXP and NUM in each configuration, enabling a like-for-like comparison of the integrated work at a common height.

For the STIFF variant, the numerical prediction at OPT-25 tracks the experimental curve at OPT-25 closely up to PBA ≈ 1.5 g (run T14), with small divergence at T15 and a pronounced overprediction at T16, where the model accumulates approximately 28 kN·m against 19 kN·m measured experimentally at the same reference, an overprediction of the order of 45%. For FLEX at the common reference OPT-25, the model systematically underpredicts the experimental dissipation across all intensity levels, reaching

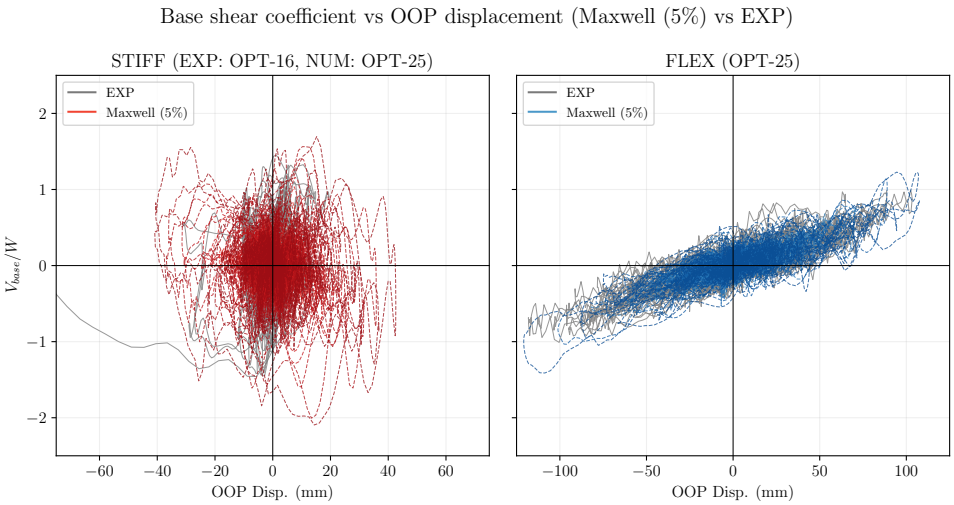


Figure 7.43. Superimposed hysteresis loops of the normalised base shear coefficient V_{base}/W against the OOP displacement, for the STIFF configuration (EXP at OPT-16 $z = 1.24$ m; NUM at OPT-25, $z = 2.76$ m) and the FLEX configuration (OPT-25, $z = 2.76$ m).

approximately 3 kN·m at T12, compared with the experimentally measured 8.5 kN·m.

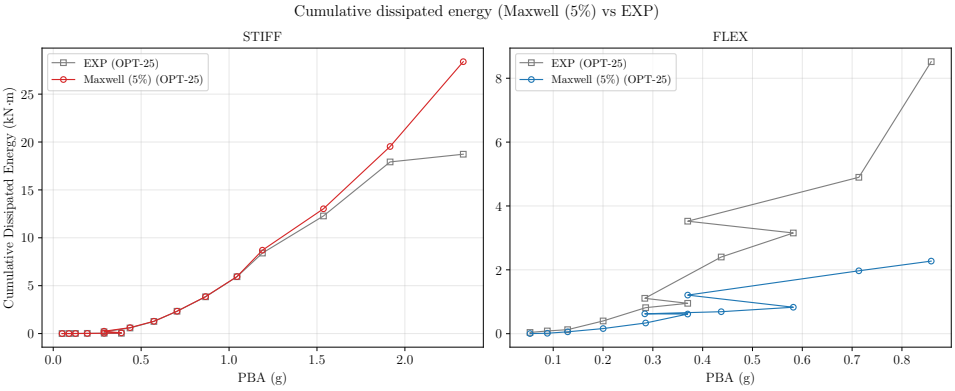


Figure 7.44. Cumulative dissipated energy W_{dis} plotted against PBA for the STIFF and FLEX configurations.

The calculated dissipated energy, given by $\int V_{\text{base}}\,\mathrm{d}u$, depends on the reference point where the displacement u is measured, so a common reference point, OPT-25, is used for both records. The origins of the residual model-experiment gap, including the contribution of the damping scheme and the configuration-dependent hinge location, are examined in Section 7.4.5.

7.4.4. Comparison to mass-proportional damping on the STIFF specimen

A mass-proportional (MP) damping cross-check is performed on the STIFF configuration across the full 16-run IDA sequence, to test the hypothesis raised in Section 7.3.7, which speculated a broader MP-Maxwell gap under larger block separations and more frequent re-contact events expected near collapse. The STIFF configuration is selected over FLEX because its sequence reaches a PBA of 2.33 g and therefore spans the widest intensity range of the campaign. The MP coefficient is calibrated to impose $\zeta = 5\%$ at the fundamental frequency of the specimen (26 Hz), consistent with the procedure adopted for the cross-vault in Section 7.3.3.

Figure 7.45 compares the peak OOP displacement envelopes at the four reference sensors against the experimental record and the Maxwell damping response. The MP prediction reproduces the upper-wall sensors OPT-24 and OPT-25 within 5 mm across the entire IDA sequence. At OPT-8 and OPT-16, the MP envelope tracks the experiment up to PBA ≈ 1.54 g, then underpredicts the sudden experimental increase at T16, reaching approximately 14 mm and 28 mm, compared with experimental values of 48 mm and 85 mm. The MP envelope exhibits the same hinge-location mismatch observed for Maxwell in Figure 7.32. The difference between the two damping schemes at the kinematic envelope is below the experimental measurement margin across the full intensity range.

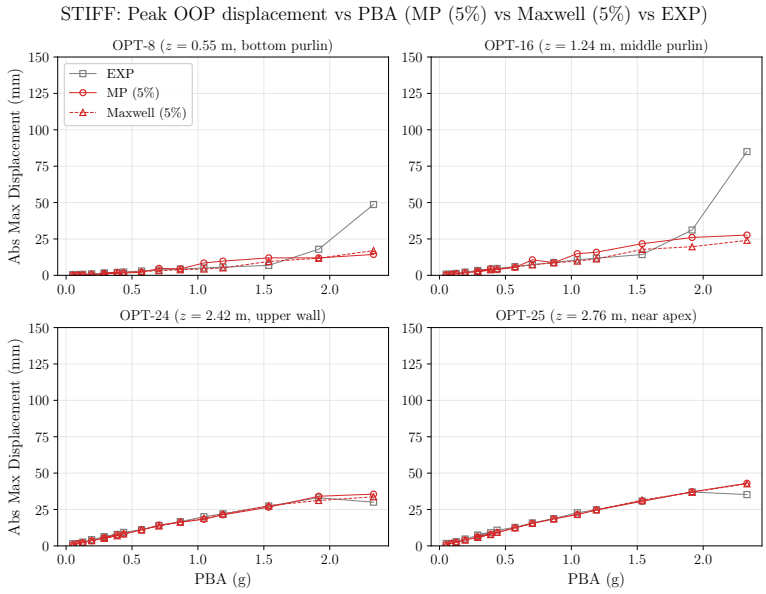


Figure 7.45. STIFF: peak absolute OOP displacement at four sensor locations against PBA (MP vs Maxwell vs EXP).

Figure 7.46 shows the displacement residual field $\Delta d = d_{\mathrm{NUM}} - d_{\mathrm{EXP}}$ obtained under MP damping. Positive residuals of +3 to +5 mm in the lower half of the triangle develop from T10 (PBA = 0.70 g) and grow to +7 to +14 mm across the mid and lower rows at T14.

At T15 the residual field shows a strong positive band of +16 to +17 mm at the mid-height OPT positions together with small negative residuals of −5 to −6 mm near the base. At the collapse run T16, the field exhibits the same bimodal character as Maxwell, with negative residuals of −29 to −66 mm in the lower portion and positive residuals at the apex. A localised outlier of +221 mm appears at a single OPT point in the mid-upper region, together with an adjacent +76 mm value in the same row. These magnitudes are inconsistent with the bounded kinematics of the gable triangle and differ from the Maxwell responses as shown in Figure 7.39.

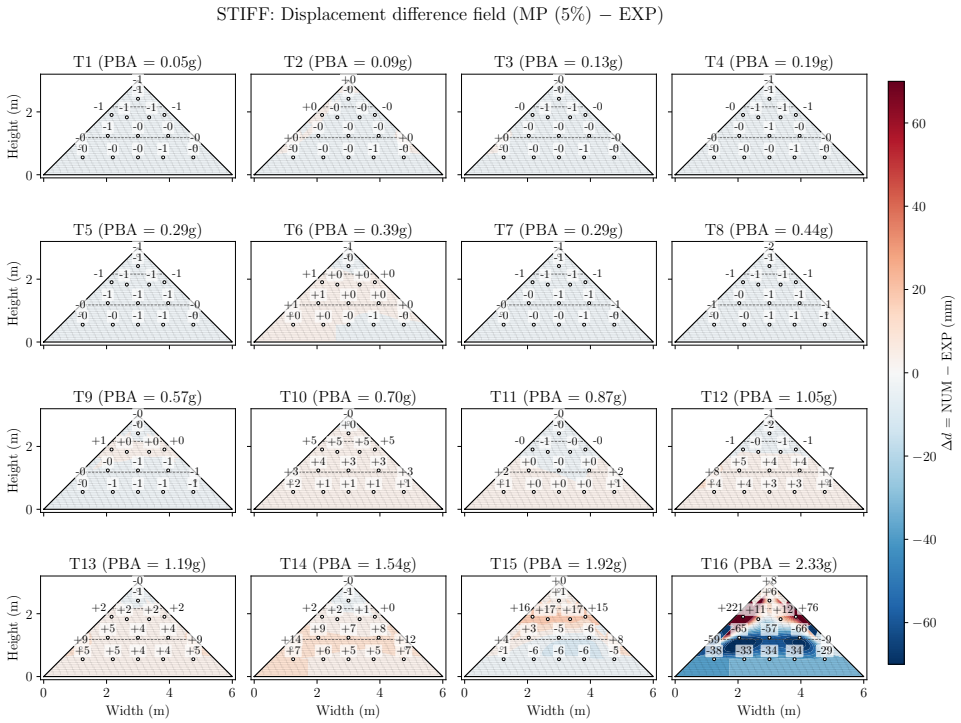


Figure 7.46. STIFF: displacement residual field $\Delta d = d_{\mathrm{NUM}} - d_{\mathrm{EXP}}$ under mass-proportional damping across the IDA sequence.

Figure 7.47 shows the peak acceleration envelopes. At the table sensor ACC6, the MP prediction matches the experimental record across all 16 runs, confirming correct transmission of the input motion. At the apex ACC1, the MP prediction underpredicts the experimental peak by approximately 20% at T16, reaching 2.0 g against 2.6 g measured experimentally. At the intermediate wall sensors, the MP peaks exceed the experimental values by a larger margin than Maxwell near collapse. ACC15 reaches 3.2 g at T16, compared with 1.8 g in the experiment and approximately 2.6 g under Maxwell (Figure 7.36). ACC11 shows a sharp jump from 2.1 g at T15 to 3.8 g at T16, which is absent in both the experimental record and the Maxwell prediction at the same intensity.

The cross-check indicates that the two damping schemes yield comparable peak OOP

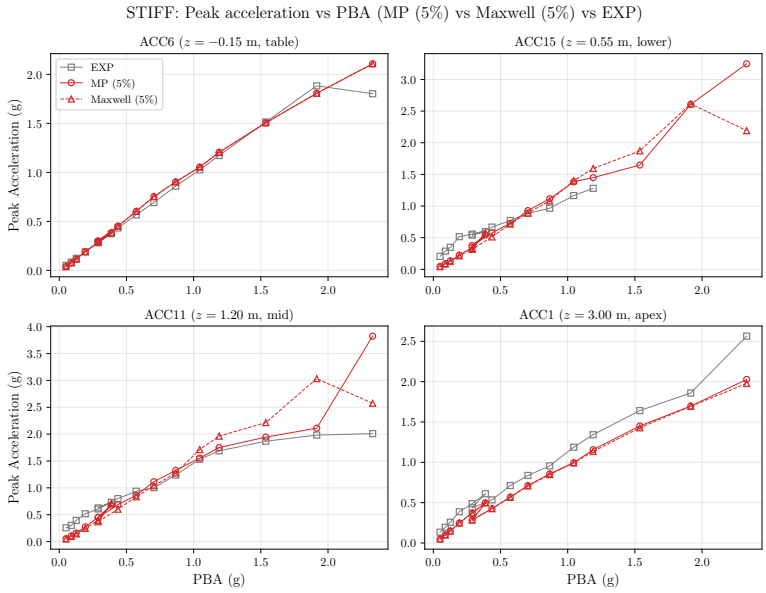


Figure 7.47. STIFF: peak absolute acceleration at four sensor locations against PBA (MP vs Maxwell vs EXP).

displacement envelopes throughout the IDA sequence, showing that the kinematic response of the rocking mechanism is insensitive to the damping formulation in the present configuration. The inertial response at the intermediate wall sensors differs substantially between the two schemes near collapse, with MP generating sharper acceleration peaks and a localised displacement outlier indicative of numerical instability at the highest intensity. The hypothesis raised in Section 7.3.7 is supported, but its influence is largely confined to the local inertial response. The acceleration peaks at the wall sensors near collapse are the quantity most affected by the high-frequency content generated at the re-contacts, whereas the global response shows little sensitivity to it. The collapse intensity, the global displacement magnitudes, and the FLEX failure mode are reproduced with limited sensitivity to this effect. The one global-level discrepancy, the hinge location for the STIFF configuration, originates in the rocking kinematics rather than in the damping treatment, and is addressed through the residual fields and in Section 7.4.5.

7.4.5. Discussion

This validation shows that a single set of MASON contact parameters, derived from standard material-level characterisation and calibrated only with the purlin-wall friction coefficient against the first low-intensity run, reproduces the out-of-plane seismic response of both configurations up to collapse. The FLEX configuration is well represented in both the upper-triangle overturning mechanism and the peak

displacement trend, indicating that sufficiently general contact laws, combined with the differential input motion, are sufficient to distinguish the two failure modes.

The hinge-location mismatch in the STIFF configuration at the collapse run is the main limitation of the validation. The numerical model forms the governing horizontal crack near two-thirds of the gable height, whereas the experimental specimen developed it at approximately one-third of the gable height, between the bottom and middle purlins. Because the same mismatch arises in the high-fidelity blind prediction with uniform bond strength, refining the discretisation is not expected to remove it. The discrepancy is instead tied to the spatial variability of the bond strength that fixes where the crack localises, and capturing the experimental hinge location would require specimen-specific calibration of this variability rather than a finer mesh.

The cross-check with mass-proportional (MP) damping in Section 7.4.4 confirms that the peak OOP displacement envelope is insensitive to the damping formulation across the full IDA sequence, while the inertial response at the intermediate wall sensors degrades measurably under MP near collapse. The damping effect is therefore confined to the local inertial response and does not alter the global failure prediction. Because this discrepancy is driven by high-frequency content, and the MASON contact model attenuates that content (Section 7.2.2), the difference between the two damping schemes is expected to be smaller than it would be for a non-degrading contact model. A direct demonstration would require repeating the damping comparison with such a model, which falls outside the present scope.

Remaining limitations bound the scope of the validation. The purlin-wall friction coefficient is applied unchanged across configurations and intensities and does not account for kinematic changes at the interface during the IDA sequence. The dissipated-energy metric is reference-point dependent, as noted in Section 7.4.3, and the reported 45% STIFF overprediction is contingent on the adoption of OPT-25 as the common reference. However, neither limitation invalidates the main finding that the MASON-Maxwell framework enables prediction of OOP collapse for URM gable walls under differential diaphragm excitation.

7.5. Summary and conclusions

This chapter presented three controlled numerical studies on the dynamic analysis of masonry structures using the Distinct Element Method with the MASON contact model, comprising a cross-comparison of contact constitutive models, an evaluation of viscous damping schemes, and an exploratory validation against shake-table records. Each study varied one modelling decision while the others were held fixed, with the aim of isolating the contribution of the contact constitutive model, the viscous damping formulation, and their combination under out-of-plane collapse-level loading. Section 7.2 compared the MASON contact constitutive model against the elasto-softening TSCLinear [1] formulation on the SERA cross-vault benchmark, using an identical mesh, boundary conditions, and mass-proportional damping scheme. Section 7.3 evaluated three viscous damping formulations (mass-proportional, Maxwell, and zero-viscous damping) on the same cross-vault benchmark with MASON as the contact law. Section 7.4 combined both methodological contributions of this thesis in a single application,



validating MASON with Maxwell damping against the ERIES-SUPREME shake-table tests on full-scale masonry gable walls under differential diaphragm excitation up to collapse. A mass-proportional cross-check on one configuration tested whether the damping-scheme sensitivity observed on the cross-vault persisted at collapse intensity on a simpler typology.

The findings from each section are summarised as follows:

1. On the cross-vault benchmark, the choice between the MASON and TSCLinear contact models leaves the peak displacements and the diagonal failure mode essentially unchanged, but affects the acceleration response. The degraded unloading of MASON softens the re-contact transition and lowers the peak accelerations relative to TSCLinear, which reaches about twice the experimental peaks at ACC6, ACC12 and ACC18 at AQA75. Both models overpredict the experimental peaks, and the difference is attributed to the high-frequency content generated at re-contact.

2. External viscous damping remains necessary even with a dissipative contact model, since the zero-viscosity case fails to bound the acceleration response. Among the schemes tested on the cross-vault, Maxwell and mass-proportional damping give similar predictions at AQA75. Maxwell is slightly better in displacement and mass-proportional damping slightly better in post-pulse acceleration, at a 49.8 % increase in wall-clock time for Maxwell.

3. The gap between mass-proportional and Maxwell damping is smaller under MASON than the gap reported for TSCLinear in Oktiovan et al. [17]. This is attributed to the softer re-contact transition, which reduces the high-frequency content where the two schemes differ most. The comparison is across studies. The mass-proportional cross-check on the gable (Section 7.4.4) is consistent with this explanation but does not test it.

4. A single set of MASON parameters from material-level characterisation, supplemented by a calibrated purlin–wall friction coefficient, reproduces the out-of-plane response of the FLEX configuration through collapse (nominal PBA = 0.96 g) and that of the STIFF configuration up to PBA = 1.86 g. The FLEX upper-triangle overturning mechanism is reproduced with a modest hinge offset. The STIFF lower-rocking mechanism at collapse is not reproduced.

5. At the STIFF collapse (PBA = 1.86 g), the numerical hinge forms at approximately two-thirds of the gable height, whereas the experimental hinge develops at one-third of the gable height. The same mismatch appears in the high-fidelity blind prediction of Ghezelbash *et al.* [25], which also assumes a uniform bond strength, so it is not specific to simplified micro-models. It is more plausibly tied to the spatial variability of the bond strength that governs where the horizontal crack forms, and capturing the experimental location would require specimen-specific calibration of this variability rather than further mesh refinement.

The three investigations together demonstrate that the two methodological contributions of this thesis, the MASON contact constitutive model and the

implementation of the Maxwell damping scheme calibrated by Levenberg-Marquardt optimisation, can be applied jointly to reproduce the collapse-level out-of-plane response of a slender masonry component, a loading direction not addressed in the previous chapters. The remaining quantitative limitation, the hinge-location mismatch in the STIFF specimen during the collapse run, can be addressed by incorporating spatial variability in material properties or by further specimen-specific calibration. This does not undermine the capability of the contact model or the present validation. Whether admitting intra-block cracking would alter the hinge location was not tested here, and the evidence above points to the spatial variability of the bond strength rather than to the discretisation. Future work can broaden this across additional specimens, diaphragm configurations, and ground-motion records, and refine predictions of the near-collapse inertial response and the failure-hinge location, towards a fuller treatment of the out-of-plane seismic response of masonry. Neither benchmark is governed by in-plane wall response. The vault response is driven by differential pier motion with opening and re-contact of the webs, and the gable wall by out-of-plane rocking. The damping conclusions are therefore established for configurations dominated by contact transitions. Dynamic in-plane behaviour of masonry is tested almost exclusively in building-scale shake-table experiments, so its verification is identified in Chapter 9 as a building-scale task.



Bibliography of Chapter 7

[1] B. Pulatsu. 'Coupled elasto-softening contact models in DEM to predict the in-plane response of masonry walls'. In: *Computational Particle Mechanics* 10 (2023), pp. 1759–1770. ISSN: 2196-4378. DOI: 10.1007/s40571-023-00586-x.

[2] Y. P. Oktiovan, L. Davis, R. Wilson, A. Dell'Endice, A. Mehrotra, B. Pulatsu and D. Malomo. 'Simplified Micro-Modeling of a Masonry Cross-Vault for Seismic Assessment Using the Distinct Element Method'. In: *International Journal of Architectural Heritage* (Nov. 2023). ISSN: 15583066. DOI: 10.1080/15583058.2023.2277328.

[3] N. Bianchini, N. Mendes, P. B. Lourenço and C. Calderini. 'Modelling of the Dynamic Response of a Full-Scale Masonry Groin Vault: Unstrengthened and Strengthened with Textile-Reinforced Mortar (TRM)'. In: *International Journal of Architectural Heritage* 18.12 (2024), pp. 2042–2066. DOI: 10.1080/15583058.2024.2320857.

[4] N. Damiani, M. J. DeJong, L. Albanesi, A. Penna and P. Morandi. 'Distinct element modeling of the in-plane response of a steel-framed retrofit solution for URM structures'. In: *Earthquake Engineering & Structural Dynamics* 52.10 (2023), pp. 3030–3052. ISSN: 1096-9845. DOI: https://doi.org/10.1002/eqe.3910.

[5] Itasca Consulting Group Inc. *3DEC - Three Dimensional Distinct Element Code Ver. 9.1*. Software. Minneapolis, 2023.

[6] J. F. Hall. 'Problems encountered from the use (or misuse) of Rayleigh damping'. In: *Earthq Eng Struct Dyn* 35.5 (Apr. 2006), pp. 525–545. ISSN: 1096-9845. DOI: 10.1002/EQE.541.

[7] F. Galvez, L. Sorrentino, D. Dizhur and J. M. Ingham. 'Damping considerations for rocking block dynamics using the discrete element method'. In: *Earthquake Engineering & Structural Dynamics* 51.4 (2022), pp. 935–957. DOI: 10.1002/eqe.3598.

[8] J. V. Lemos, E. Dawson and Z. Cheng. 'Application of Maxwell damping in the dynamic analysis of masonry structures with discrete elements'. In: *International Journal of Masonry Research and Innovation* 7.6 (2022), pp. 663–686. ISSN: 2056-9459. DOI: 10.1504/ijmri.2021.10043266.

[9] J. Lemos and V. Sarhosis. 'Dynamic analysis of masonry arches using Maxwell damping'. In: *Structures* 49 (2023), pp. 583–592. DOI: 10.1016/j.istruc.2023.01.139.

[10] N. Damiani, M. Bertassi, S. Sharma, M. Smerilli, M. Mirra, I. Lanese, E. Rizzo-Parisi, G. J. O'Reilly, F. Messali and F. Graziotti. 'Out-of-Plane Shake-Table Tests on Unreinforced Masonry Gables Considering Different Roof Configurations'. In: *Engineering Research Infrastructures for European Synergies*. Ed. by G. J. O'Reilly and G. M. Calvi. Vol. 718. Lecture Notes in Civil Engineering. Cham: Springer, 2025, pp. 268–279. ISBN: 978-3-031-98893-6. DOI: 10.1007/978-3-031-98893-6_25. URL: https://doi.org/10.1007/978-3-031-98893-6_25.

[11] S. Sharma, N. Damiani, M. Bertassi, M. Smerilli, M. Mirra, I. Lanese, E. R. Parisi, G. J. O'Reilly, F. Messali and F. Graziotti. 'Experimental data from out-of-plane shake-table tests on unreinforced masonry gables'. In: *Earthquake Spectra* 41.5 (2025), pp. 4227–4245. DOI: 10.1177/87552930251378248.

[12] C. Calderini, N. Bianchini, P. B. Lourenço, N. Mendes, P. X. Candeias, O. AlShawa, C. Chácara, M. M. Chávez, G. de Felice, A. Ferrante, P. Fici, R. Gagliardo, P. Kesavan, G. P. Lignola, M. Malena, D. Malomo, D. Pellegrini, F. Peña, M. Petracca, B. Pintucchi, F. P. A. Portioli, B. Pulatsu, G. Ramaglia, D. Rapicavoli and F. Trovatelli. 'Shake-Table Testing of a Brick Masonry Groin Vault: Overview of Blind Predictions and Postdictions and Comparison with Experimental Results'. In: *International Journal of Architectural Heritage* (2024), pp. 1–27. ISSN: 1558-3058. DOI: 10.1080/15583058.2024.2419545. URL: https://doi.org/10.1080/15583058.2024.2419545.

[13] N. Bianchini, N. Mendes, C. Calderini, P. Candeias and P. B. Lourenço. 'Shaking Table Testing of an Unstrengthened and Strengthened with Textile Reinforced Mortar (TRM) Full-Scale Masonry Cross Vault'. In: *Int J Archit Herit* (2024), pp. 1–26. DOI: 10.1080/15583058.2023.2295900.

[14] P. Lourenco. 'Computational strategies for masonry structures'. PhD thesis. Delft, Netherlands: Delft University of Technology, 1996.

[15] P. B. Lourenço. 'Recent advances in masonry modelling: micromodelling and homogenisation'. In: *Multiscale modeling in solid mechanics: computational approaches* (2010), pp. 251–294.

[16] L. De Lorenzis, M. J. DeJong and J. A. Ochsendorf. 'Failure of masonry arches under impulse base motion'. In: *Earthquake Engineering & Structural Dynamics* 36.14 (2007), pp. 2119–2136. DOI: 10.1002/eqe.719.

[17] Y. P. Oktiovan, J. V. Lemos, B. Pulatsu, F. Messali, J. G. Rots and D. Malomo. 'Evaluating damping schemes for the discontinuum seismic analysis of masonry cross-vaults'. In: *Bulletin of Earthquake Engineering* 24 (2026), pp. 2349–2389. DOI: 10.1007/s10518-026-02379-y.

[18] M. A. Sprague and T. L. Geers. 'A spectral-element method for modeling cavitation in transient fluid-structure interaction'. In: *International Journal for Numerical Methods in Engineering* 60.15 (2004), pp. 2467–2499. DOI: 10.1002/nme.1054.

[19] N. Augenti and F. Parisi. 'Learning from Construction Failures due to the 2009 L'Aquila, Italy, Earthquake'. In: *Journal of Performance of Constructed Facilities* 24.6 (2010), pp. 536–555. DOI: 10.1061/(ASCE)CF.1943-5509.0000122.



[20] J. Ingham and M. C. Griffith. 'Performance of Unreinforced Masonry Buildings During the 2010 Darfield (Christchurch, NZ) Earthquake'. In: *Australasian Journal of Disaster and Trauma Studies* 2010.Special Issue (2010). DOI: 10.1080/13287982.2010.11465067.

[21] B. Yön, E. Sayin, Y. Calayir, Z. Ç. Ulucan and M. Karatas. 'Seismic response of buildings during the May 19, 2011 Simav, Turkey earthquake'. In: *Earthquakes and Structures* 5.3 (2013), pp. 343–357. DOI: 10.12989/eas.2013.5.3.343.

[22] A. Penna, C. Calderini, L. Sorrentino, C. F. Carocci, E. Cescatti, R. Sisti, A. Borri, C. Modena and A. Prota. 'Damage to churches in the 2016 central Italy earthquakes'. In: *Bulletin of Earthquake Engineering* 17 (2019), pp. 5763–5790. DOI: 10.1007/s10518-019-00594-4.

[23] M. Miglietta, N. Damiani, G. Guerrini and F. Graziotti. 'Full-scale shake-table tests on two unreinforced masonry cavity-wall buildings: effect of an innovative timber retrofit'. In: *Bulletin of Earthquake Engineering* 19.6 (2021), pp. 2561–2596. ISSN: 15731456. DOI: 10.1007/S10518-021-01057-5/TABLES/6.

[24] M. Mirra, N. Damiani, S. Sharma, F. Graziotti and F. Messali. 'Definition of differential seismic input motions for out-of-plane dynamic testing of unreinforced masonry gable walls considering different roof configurations'. In: *Structures* 79 (2025), p. 109419. DOI: 10.1016/j.istruc.2025.109419.

[25] A. Ghezelbash, A. M. D'Altri, P. B. Lourenço and S. de Miranda. 'Numerical modeling of the out-of-plane dynamic response of masonry gable walls via a high-fidelity block-based finite element modeling approach – part I: Blind prediction'. In: *Bulletin of Earthquake Engineering* (2026). DOI: 10.1007/s10518-025-02328-1.

[26] D. M. Boore and J. J. Bommer. 'Processing of strong-motion accelerograms: needs, options and consequences'. In: *Soil Dynamics and Earthquake Engineering* 25.2 (2005), pp. 93–115. DOI: 10.1016/j.soildyn.2004.10.007.



Chapter 7

8

Application of the Modelling Strategies at the Building Level

Building on the material-level validation in Chapter 5 and the component-level validation in Chapter 6, this chapter extends the MASON contact modelling framework to the building scale, where in-plane and out-of-plane mechanisms, diaphragms, and boundary conditions interact to govern the response. The framework is first validated against a quasi-static cyclic pushover test on a two-storey calcium silicate assemblage (TUD-BUILD-1), which serves as the reference benchmark (Section 8.5). The validated model is then extended to a sequential incremental dynamic analysis of the unreinforced configuration to identify its near-collapse intensity (Section 8.6). Finally, the same framework is applied to the configuration retrofitted with the modular steel frame exoskeleton, quantifying its effect on displacement demand, near-collapse intensity, and the governing failure mechanism (Section 8.7). The main findings and the limitations carried into the present work are summarised in Section 8.8.

Contents

8.1. Introduction 310
8.2. Experimental description 312
8.3. Numerical modelling setup 314
8.4. Monotonic pushover comparison: rigid vs deformable blocks 319
8.5. Quasi-static cyclic analysis with rigid blocks 322
8.5.1. Global responses 322
8.5.2. Local responses 324
8.5.3. Summary of the quasi-static cyclic analysis 326
8.6. Explorative study on the dynamic shake-table performance of the building . 327
8.6.1. Ground-motion input and signal characteristics 327
8.6.2. Peak displacement response evolution 330
8.6.3. Interstorey drift ratio versus intensity measure 332
8.6.4. Damage evolution at each intensity level 340

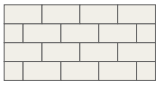
8.6.5. Global hysteretic responses 341
8.6.6. Remarks on the dynamic performance of the unreinforced building . 344
8.7. Explorative retrofit assessment with the modular steel frame exoskeleton . . 345
8.7.1. Retrofit schemes and design rationale 346
8.7.2. Numerical modelling setup for the retrofitted configurations 348
8.7.3. Pushover calibration result 351
8.7.4. Incremental dynamic analysis results 354
8.7.5. Remarks on the performance of the retrofitted building 361
8.8. Summary and conclusions 362

8.1. Introduction

Quasi-static and dynamic experimental testing has been central to establishing the seismic response mechanisms of unreinforced masonry (URM) buildings and to providing benchmarks for numerical validations. Full-scale shake-table tests are informative because they capture the inertia-driven interaction between walls and diaphragms, but they are resource-intensive and therefore relatively scarce. Experimental campaigns are often stopped before reaching collapse due to practical testing constraints. Recent efforts to systematise the available evidence, such as the database compiled by Haindl *et al.* [1], confirm both the limited number of building-scale shake-table campaigns and the variability in boundary conditions, diaphragm details, and test objectives across studies.

Building-level quasi-static cyclic tests impose controlled deformation demands, which makes them well-suited to investigating global load paths, post-peak ductility, and damage localisation. Recent campaigns include half-scale building tests with geometric irregularities performed under quasi-static loading protocols [2]. The TU Delft benchmark used in this chapter similarly employs a quasi-static cyclic pushover protocol with increasing displacement amplitudes and a fixed cycle duration [3]. While these loading protocols provide a controlled reference for stiffness and strength degradation, as well as crack evolution, they idealise inertial effects because lateral actions are imposed through prescribed displacements or force distributions rather than acceleration inputs. This motivates an explicit comparison between the quasi-static and dynamic responses to assess whether the governing mechanism and drift distribution inferred from the cyclic pushover remain representative when inertia-driven interaction is introduced. With the MASON model already developed and validated in the preceding chapters, this chapter applies it at the building scale, the largest structural system considered in the thesis, to demonstrate its ability to predict the structural response under quasi-static cyclic and its extension to dynamic loading.

Within this context, block-based models are well-suited because the governing nonlinearities can be expressed at the interfaces, while failure through the bricks can be represented either through nonlinear unit behaviour [4] or through embedded potential crack planes [5]. In practice, however, applying such models at the building scale is often prohibitive due to the effort required to construct detailed discretisation, the connection details, and the computational cost associated with a large number of degrees of freedom,



the small stable timesteps required by explicit integration, and the need to repeat analyses across multiple loading historeys.

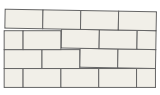
To that end, this chapter evaluates the applicability of the proposed MASON contact model within the DEM framework as it extends from material- and component-level calibrations to building-scale response. Initially, validation is performed using the TU Delft two-storey calcium silicate masonry assemblage subjected to quasi-static cyclic pushover loading. The assessment considers base shear–displacement relationships, interstorey drift demands, and the observed evolution and localisation of cracking and sliding mechanisms during the experiment.

The second part extends the assessment to dynamic behaviour through an incremental dynamic analysis (IDA), driven by the EQ-NPR record, a hazard-consistent ground motion representative of the induced seismicity of the Groningen region and adopted from the shake-table programme documented by Brunesi *et al.* [6]. The single record is scaled to increasing intensity levels to observe changes in dominant kinematics, drift-demand patterns, and the stability of the simulated response mechanism, with the selection and properties of the record given in Section 8.6.1. In this work, each intensity level departs from the damaged state of the preceding run, resembling a numerical shake-table campaign. This differs from the classical IDA defined by Vamvatsikos & Cornell [7], in which each scaled record is applied to the undamaged structure to construct independent IDA curves.

The final part examines the retrofit behaviour of the calibrated building model using the Resisto 5.9 modular steel-frame system [8], applied to the Dutch residential typology represented by TUD-BUILD-1. The system was developed and experimentally characterised in the Italian context. Its application to calcium silicate masonry combined with precast reinforced concrete (RC) floor diaphragms, representative of Dutch terraced houses, has not been experimentally investigated. The retrofit configuration, the available experimental coverage, the untested aspects of the building-scale application, and the corresponding modelling assumptions are presented in Section 8.7.1. The influence of the retrofit on the lateral response and damage development under dynamic input motion is then quantified for the Dutch residential configuration using the same modelling framework adopted for the unreinforced case. The analyses are conducted using consistent modelling assumptions across the unreinforced and retrofitted configurations, so that changes in response can be attributed to the retrofit intervention and not to variations in numerical settings.

The validation and IDA results are interpreted primarily in terms of the dominant deformation mechanism and its localisation along the specimen height. The quasi-static pushover benchmark provides a reference for mechanism development and drift distribution under controlled displacement demand. The subsequent dynamic analyses are then used to assess whether this mechanism is preserved under inertial loading or whether dynamic effects shift the drift profile and the pattern of damage accumulation. The IDA protocol and the associated intensity measure are defined before presenting the results, ensuring that comparisons between the unreinforced and retrofitted cases are traceable.

The chapter is organised as follows. Section 8.2 describes the TUD-BUILD-1 experimental specimen, and Section 8.3 explains the numerical modelling setup.



Section 8.4 compares the rigid and deformable-block idealisations under monotonic pushover, and Section 8.5 reports the quasi-static cyclic validation. Section 8.6 presents the IDA on the unreinforced configuration, including the near-collapse identification against three drift-capacity formulations. Section 8.7 extends the IDA to the retrofitted configuration using a modular steel frame, including pushover calibration of the frame-to-reinforced-concrete anchorage and the resulting IDA results. Section 8.8 summarises the findings and the remaining limitations, with reference to the damping study already presented in Chapter 7.

8.2. Experimental description

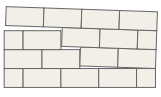
The building-scale benchmark is based on a quasi-static cyclic pushover test complemented by dynamic identification tests performed at the Stevin II laboratory of TU Delft. The test comprises a two-storey assembled masonry structure representing the Groningen terraced-house typology, consisting of calcium silicate masonry walls and RC floor diaphragms [3].

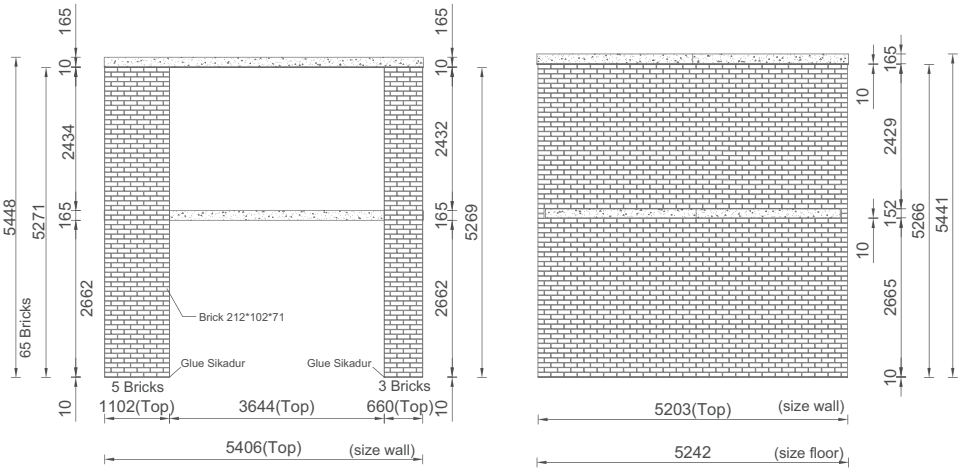
Two calcium silicate building specimens were tested at TU Delft. The first, tested in 2015, was built from traditional calcium silicate bricks (210 × 71 × 102 mm) in stretcher bond, with toothed interlocking at the wall-to-pier corners; this is the specimen modelled in this chapter, designated TUD-BUILD-1. A second assemblage, proposed in 2017 [9], used large calcium silicate elements (CASIELS, 897 × 643 × 120 mm) joined with a thin glue mortar, omitting interlocking at the longwall-to-pier connection, owing to the current Dutch construction practice. The two specimens differ in unit size, joint type, and corner detailing, all of which influence lateral strength and the wall-to-pier interaction. TUD-BUILD-1 is adopted here because it uses the same calcium silicate unit and mortar system calibrated at the material scale in Chapter 5 and verified at the component scale in Chapter 6, giving traceable validation chains from material to building level on one experimental campaign.

The experimental drawing of the building specimen termed TUD-BUILD-1 is shown in Figure 8.1. The assemblage included two longitudinal load-bearing walls at the west and east sides and two pier walls at the north and south sides, each consisting of a wide pier (1100 mm) and a narrow pier (662 mm) (Figure 8.1A). The masonry was built in a stretcher bond, and corner connections between the longitudinal walls and piers were achieved through toothed interlocking. The structure was constructed on a steel substructure, with the first masonry course glued to the steel base to prevent sliding at the steel interface. This boundary condition was intended to shift the initial base damage to the first mortar joint between the first and second brick rows.

The floors comprised two prefabricated reinforced-concrete slabs bearing on the load-bearing walls via a mortar bed joint. Details of the RC to masonry connections at each storey are shown in Figure 8.2. At the first-floor level, the slab was connected horizontally to the façade piers using 6 mm-diameter cast-in anchors embedded in the masonry. At the second-floor level, the slab was first positioned on the load-bearing walls, and the pier-to-slab joint was filled afterwards, indicating limited vertical load transfer from the slab to the façade piers.

The cyclic pushover test was conducted using a braced steel reaction tower and





(A) Facade view facing South (B) Wall view facing East

Figure 8.1. Experimental drawing of TUD-BUILD-1 [3]

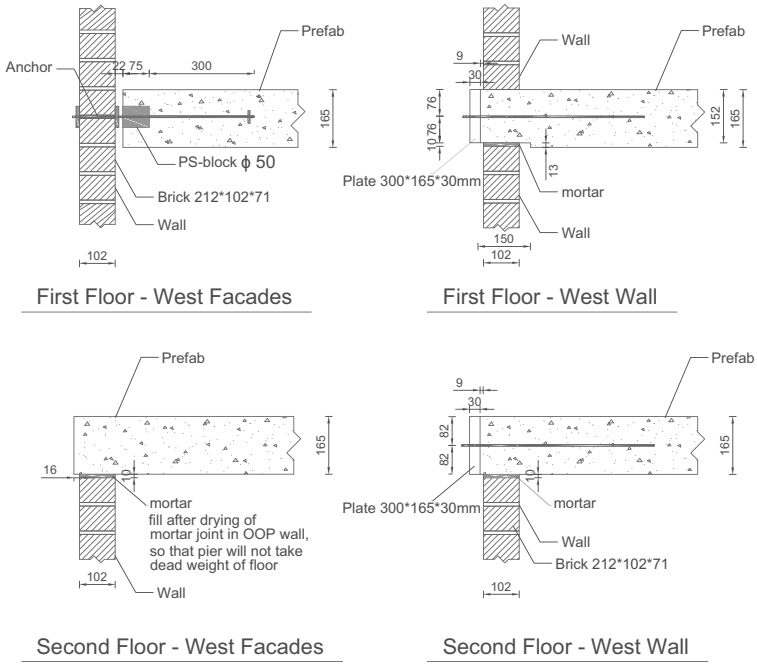
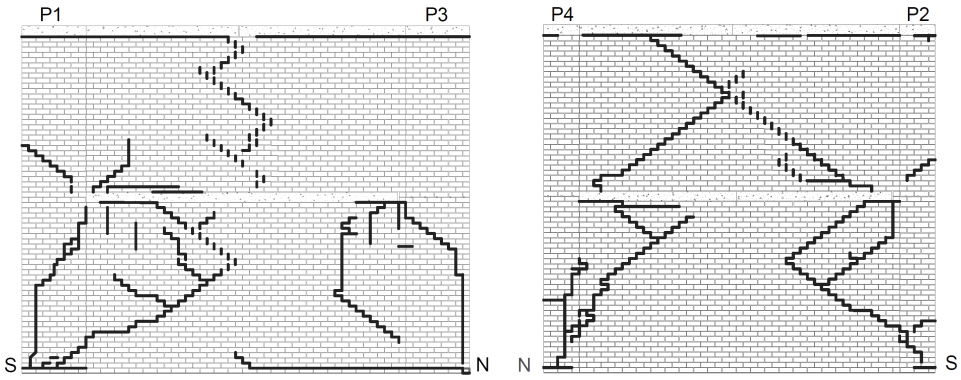


Figure 8.2. Connection details between the prefabricated concrete floors and the transversal walls and piers

actuators mounted at the floor levels. Displacement control was applied at the second-floor level, while a target storey force ratio of 1:1 between the second and first floors was enforced by coupling the actuator forces on each side. The loading protocol comprised an initial, pre-peak, and post-peak phase, with a total of 23 cycles. Target displacements were defined at the second-floor level and reported using the average of the north and south measurements at the loading points.

Dynamic identification tests were performed at three stages by disconnecting the actuators and applying hammer impacts while the structure was free to vibrate. The tests targeted the first global mode in the loading direction (East-West) and the first vertical bending mode of each floor. The identified first natural frequency in the loading direction decreased from 4.05 Hz to 3.74 Hz and then to 2.5 Hz across the three stages, consistent with the observed stiffness degradation during the pushover response.



(A) West-wall + facades (inside view) (B) East-wall + facades (inside view)

Figure 8.3. Unfolded elevations of the final crack pattern recorded by visual inspection at the end of the quasi-static cyclic test: (A) west wall with its connected north and south piers, and (B) east wall with its connected piers. Adapted from [3].

The crack maps in Figure 8.3 record the final damage state of the building after quasi-static cyclic loading. The response is dominated by in-plane shear, with cracking largely following the bed and head joints. In the west wall and piers (Figure 8.3A), stepped diagonal cracking is concentrated in the ground-floor piers, accompanied by local vertical cracks splitting through the brick units in both piers. In the east wall and piers (Figure 8.3B), the upper storey shows a more continuous diagonal crack field, and the ground-storey piers crack diagonally towards the corners. The distribution of cracking across both the piers and the longitudinal walls indicates that they acted as a coupled system in resisting the in-plane deformation demand.

8.3. Numerical modelling setup

Figure 8.4 summarises the numerical set-up adopted for the building-scale simulations. For the monotonic pushover comparison and quasi-static cyclic validation, a rigid-block modelling approach is employed to optimise computational efficiency, consistent with

the rigid-block idealisation validated against the cyclic calcium silicate wall test at the component scale in Section 6.3. Whereas the quasi-static cyclic validation uses rigid blocks, the dynamic analyses adopt a deformable-block configuration. The steel-frame retrofit is represented with beam finite elements that couple only to the nodal points of deformable meshes, so the rigid idealisation cannot accommodate them. The unreinforced configuration is therefore also analysed with deformable blocks under dynamic loading, so that the unreinforced and retrofitted cases share a single modelling basis and any difference in response reflects the retrofit instead of the block idealisation.

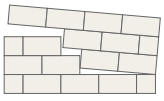
The masonry assemblage is supported on a steel base and coupled to rigid concrete floor diaphragms, which enforce the in-plane compatibility at each storey. Symmetry is imposed on the rear plane by restraining the displacement in the Y direction. This restraint halves the model and reduces the computational cost. It is justified by the symmetric plan of the specimen, the uniaxial input applied along the global X direction, and the absence of mass eccentricity. The condition suppresses any torsional and antisymmetric response by construction.

The pier-to-floor connection at the first-floor level is represented in a simplified manner consistent with the anchorage detail reported in Figure 8.2. The cast-in anchors primarily provide restraint normal to the pier by tying the pier to the floor diaphragm. Accordingly, the connection is idealised so that the normal interaction is transferred along the global Y direction, thereby accounting for the confinement provided by the anchorage. Pull-out restraint is not represented, since the interface carries no tension. In contrast, no shear is transferred across the connection in the in-plane directions of the slab (global X and Z).

The behaviour is implemented using a Mohr-Coulomb contact model assigned to the anchor interface between the first floor and the masonry piers. The contact is configured with a high normal stiffness and a comparatively low shear stiffness to provide stable normal constraint while limiting tangential coupling. The strength parameters (cohesion, friction, and tension) are set to zero, so that the connector acts as a unilateral normal contact that prevents interpenetration and transmits compression only. The shear stiffness is retained for numerical stability, but the zero cohesion and friction cap the transmitted shear force at zero. The properties, along with the assigned densities for each element in the building specimen, are summarised in Table 8.1.

Table 8.2 summarises the constitutive parameters adopted for the masonry in the building-scale simulations, distinguishing between unit properties and joint properties. The unit response is defined by the elastic modulus E_b applied to the blocks, while the strength properties (tensile $f_{t,b}$, cohesion c_b, and friction angle ϕ_b) are applied to the potential crack plane at mid-length. The unit fracture energies G_{ftb} and G_{fsb}, which are not directly measurable at the brick scale, are derived from the tensile strength through Equations (6.18) and (6.19), as at the component scale.

The joint parameters in Table 8.2 define the behaviour of the mortar interfaces where damage and sliding localise. The interface normal and shear stiffnesses k^n and k^s follow from the homogenised equations in Equation (5.1), with the brick modulus E_b, the mortar modulus E_{mo}, and Poisson's ratio ν as inputs. The reported stiffness values correspond to the deformable-block configuration. In the rigid-block configuration, these stiffnesses are reduced by a factor 10. The blocks carry no deformation in this



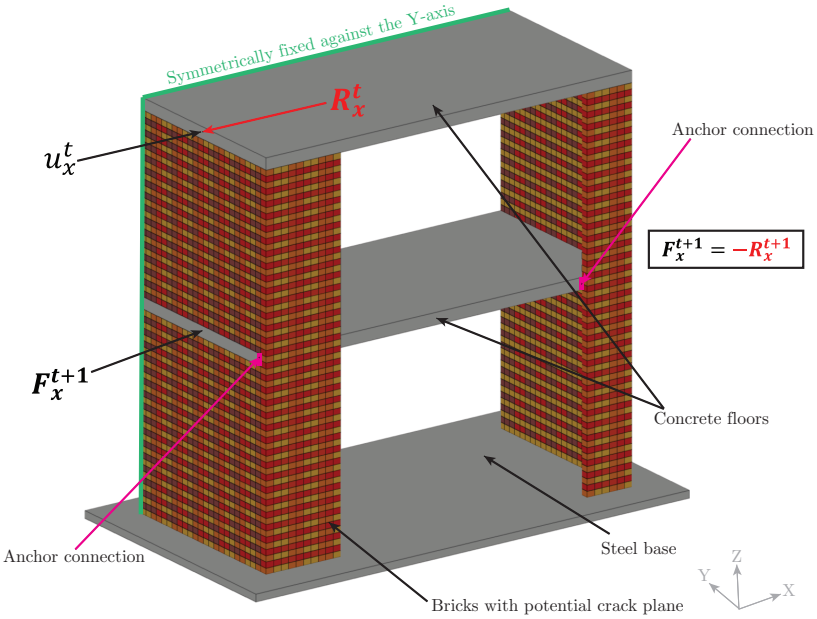


Figure 8.4. Perspective view of the half-symmetry numerical model of TUD-BUILD-1 and the quasi-static loading arrangement. Only one half is modelled, with symmetry restraint (Y-displacement fixed) on the rear plane.

configuration, so the full compliance of one course is represented by the interface alone. Matching the rigid-block interface compliance to the combined brick and mortar compliance of the course gives

$$\frac{1}{k_{n,\mathrm{rig}}} = \frac{h_b}{E_b} + \frac{t_m}{E_m} \quad \text{and} \quad \frac{1}{k_{s,\mathrm{rig}}} = \frac{h_b}{G_b} + \frac{t_m}{G_m}, \tag{8.1}$$

where h_b is the unit height and t_m the mortar thickness. For the adopted parameters the resulting reduction factor is 9.8 in both directions, rounded to 10.

Fracture energies (G_{ft} and G_{fs}), the compression strength parameters (f_c, n, and G_c) and the cap parameters (C_n, C_{nn}, C_{ss}) are listed for completeness, as they affect the post-peak softening and compressive crushing response at building scale without introducing additional degrees of freedom beyond the calibrated MASON formulation.

The building model is first brought to equilibrium under gravity, with the equilibrium out-of-balance ratio limit set to 1×10^{-5}. The quasi-static pushover is then applied in the X direction by prescribing the roof displacement u_x^t at time t, while the corresponding reaction R_x^t is recorded at the loading point (Figure 8.4). At the first-floor level, the lateral action is not prescribed as an independent displacement history. Instead, the applied force is updated from the reaction forces at the roof using the equilibrium equation:

Table 8.1. Densities and anchorage parameters adopted for the building-scale simulations.

Properties	Symbol	Unit	Value
Steel base			
Density	ρ_{St}	$\mathrm{kg\,m^{-3}}$	7780
Young's modulus	E_{St}	GPa	200
Concrete floors			
Density	ρ_{c}	$\mathrm{kg\,m^{-3}}$	2300
Young's modulus	E_{c}	GPa	37.3
Masonry units			
Density	ρ	$\mathrm{kg\,m^{-3}}$	1800
Pier-to-slab anchors			
Normal stiffness	k^n	$\mathrm{GPa\,m^{-1}}$	100
Shear stiffness	k^s	$\mathrm{GPa\,m^{-1}}$	34.783

$$F_x^{t+1} = -R_x^t \tag{8.2}$$

The minus sign reflects Newton's third law: R_x^t is the reaction force exerted by the structure on the roof actuator, while F_x^{t+1} is the force applied to the structure at the first floor. The equality enforces equal-magnitude actuator forces at the two storeys, consistent with the experimentally imposed 1:1 force ratio. This exploits a practical feature of the explicit time-marching integration scheme: at each timestep, internal and contact forces are assembled, and the resulting nodal reactions are directly available. This allows the force-controlled action to be imposed through a step-wise update without solving a coupled implicit equilibrium problem. Because the adopted stable timestep is small relative to the assemblage's characteristic response period, the one-step delay between extracting the roof reaction and applying the corresponding first-floor force update is negligible for the quasi-static loading rates considered.

For the pushover analysis, the second floor is subjected to a velocity of $5\,\mathrm{mm\,s^{-1}}$ until the target displacement of 80 mm is reached. The velocity is applied to the block centroid for the rigid-block configuration, while it is applied to the nodal points for the deformable-block configuration. For the quasi-static cyclic analysis, only the rigid-block configuration is considered to limit computational cost, as the experiment exhibited joint-dominated behaviour. The cyclic analysis is conducted using the velocity-plateau implementation defined in Equation (6.2), with target displacement amplitudes set to the experimentally applied values listed in Table 8.3.

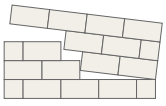


Table 8.2. Masonry unit and joint parameters adopted for the building-scale simulations.

Properties	Symbol	Unit	Value
Masonry units			
Young's modulus	E_b	MPa	4800
Tensile strength	$f_{t,b}$	MPa	1.0
Cohesion	c_b	MPa	2.0
Friction angle	ϕ_b	°	35
Mode-I fracture energy[a]	G_{ftb}	$\mathrm{N\,m^{-1}}$	40.61
Mode-II fracture energy[a]	G_{fsb}	$\mathrm{N\,m^{-1}}$	406.13
Masonry joints			
Masonry modulus[b]	E_m	MPa	3174.6
Mortar modulus[b]	E_{mo}	MPa	2500
Unit height	t_b	mm	71
Mortar thickness	t_{mo}	mm	10
Poisson's ratio	ν	[-]	0.16
Normal stiffness[b]	k^n	$\mathrm{GPa\,m^{-1}}$	521.8
Shear stiffness[b]	k^s	$\mathrm{GPa\,m^{-1}}$	225
Tensile strength	f_t	MPa	0.05
Cohesion	c	MPa	0.14
Residual cohesion	c_{res}	MPa	0.014
Friction angle	ϕ	°	25
Mode-I fracture energy[a]	G_{ft}	$\mathrm{N\,m^{-1}}$	4.99
Mode-II fracture energy[a]	G_{fs}	$\mathrm{N\,m^{-1}}$	49.88
Compressive strength	f_c	MPa	5.93
Compressive fracture energy	G_c	$\mathrm{N\,m^{-1}}$	31 500
Cap parameters	C_n, C_{nn}, C_{ss}	[-]	0.0, 1.0, 12.0
Peak ratio	n	[-]	7.5

[a] Fracture energies computed using the empirical expressions (Equations (6.18) and (6.19)).
[b] Derived quantities based on the adopted homogenised composite-stiffness relationships and joint thickness.

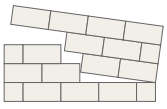


Table 8.3. Target displacement amplitudes adopted for the quasi-static cyclic analysis (applied symmetrically as $\pm d_{2,\max}$).

Initial phase		**Pre-peak phase**		**Post-peak phase**	
Cycle	$d_{2,\max}$ (mm)	Cycle	$d_{2,\max}$ (mm)	Cycle	$d_{2,\max}$ (mm)
1	0.31	9	3.40	15	22.16
2	0.70	10	4.38	16	27.91
3	1.14	11	6.01	17	39.13
4	1.57	12	9.07	18	50.62
5	2.01	13	12.24	19	61.82
6	2.45	14	15.49	20	73.04
7	2.89			21	82.31
8	3.36			22	84.23
				23	92.30

Final cycle executed as a half-run in the experiment.

8.4. Monotonic pushover comparison: rigid vs deformable blocks

Figure 8.5 compares the building-level lateral force–displacement response obtained from the numerical pushover analyses with the experimental pushover envelope, overlaid on the experimental cyclic loops for context. Both numerical idealisations attain a similar peak lateral capacity, close to the experimental envelope, indicating that global strength is governed primarily by joint parameters rather than the deformability of the blocks. Differences primarily emerge in the pre-peak response and post-peak degradation. The rigid-block model is initially stiffer, with an initial secant stiffness about 24 % above the experiment (Table 8.4), but it reaches peak more gradually and sustains a short plateau before a more pronounced step-like softening, with intermittent force drops and partial recoveries consistent with frictional strength regains and abrupt load-path redistribution once sliding localises.

In contrast, the deformable-block model exhibits a smoother, earlier post-peak decay and a lower residual plateau, reflecting additional compliance and stress redistribution within the units, thereby reducing the severity of sudden capacity drops. Both configurations use the same contact parameters, calibrated for the rigid-block idealisation rather than re-tuned for the deformable mesh. Under this common parameter set, the deformable-block response degrades somewhat earlier and settles below the experimental plateau, while the rigid-block response tracks the experimental peak and residual strength more closely. The earlier decay of the deformable model is therefore attributable in part to the transfer of rigid-calibrated parameters; a configuration-specific calibration of the unit and joint properties would be expected to improve the agreement. For the quasi-static validation, the rigid-block idealisation is retained because it reproduces the envelope without additional tuning and at

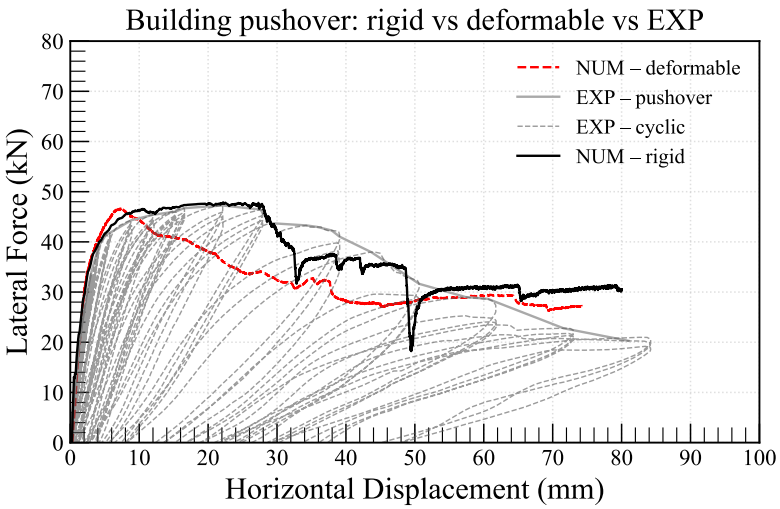


Figure 8.5. Comparison of the monotonic rigid- and deformable-block pushover curves with the experimental envelope in the positive loading direction (west to east). The experimental cyclic loops are shown in the background.

substantially lower computational cost.

A quantitative comparison of peak strength (F_{peak}), initial secant stiffness (K_{init}), displacement at a 20 % post-peak strength drop (d_{ult}), and dissipated work up to 80 mm ($W_{0\to80}$) is reported in Table 8.4. Overall, the rigid-block idealisation provides a closer match to the experimental envelope in peak strength and work, and reduces the error in post-peak deformation capacity relative to the deformable-block configuration. Using the same computational resource (3.2 GHz Intel Xeon E5-2667 with 16 cores and 512 GB of memory), the rigid model reaches a displacement of 80 mm in 5 hours, whereas the deformable model reaches the same target in 3 days.

Table 8.4. Pushover metrics for NUM (rigid/deformable) and EXP envelope.

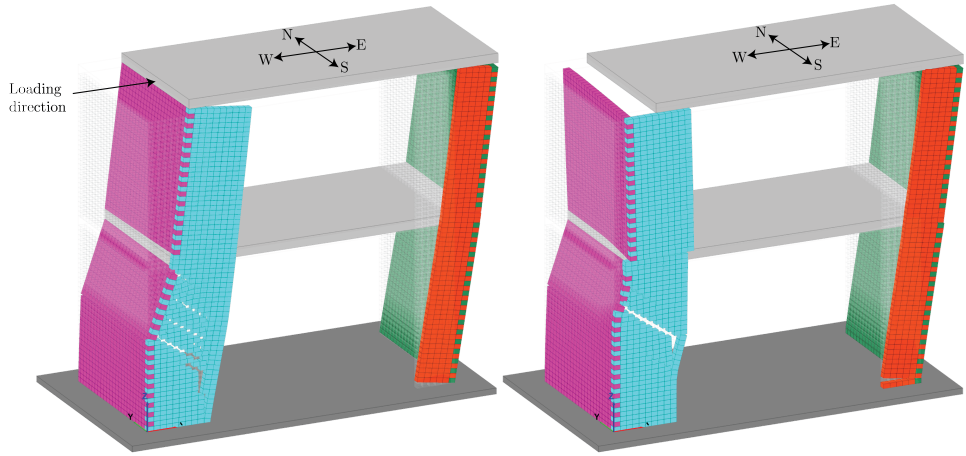
Curve	F_{peak} (kN)	K_{init} (kN/mm)	d_{ult} (mm)	$W_{0\to80}$ (kN·m)
NUM – deformable	46.605	14.670	21.262	2.400
	(−1.39%)	(−2.04%)	(−51.49%)	(−16.45%)
NUM – rigid	47.882	18.634	32.378	2.925
	(+1.32%)	(+24.43%)	(−26.13%)	(+1.85%)
EXP – (envelope)	47.260	14.976	43.828	2.872

Relative errors with respect to the experimental envelope are reported in parentheses on the line below for numerical cases.

Figure 8.6 shows the deformed configuration and dominant failure mechanisms at

the end of the building pushover analysis (80 mm) for the two numerical idealisations, magnified by a factor of 10. In both numerical cases, the response is governed by a progressive redistribution of lateral load between the façades, consistent with the damage localisation in the experimental crack pattern (Figure 8.3). The west pier acts as the primary lateral force-resisting mechanism in the early stage of loading. On the west pier, flexural cracking develops first at the base and top of the pier, followed by the in-plane diagonal strut, evidenced by the inclined compression-shear load path and the associated diagonal cracking and unit splitting near the toe regions. With increasing displacement demand, this in-plane mechanism degrades (toe crushing develops in the toe regions of the pier), and the response transitions towards out-of-plane behaviour of the west wall, where overturning becomes the dominant mode as the wall rotates.

In contrast, the east pier exhibits a distinct mechanism in both the rigid and deformable models. Instead of developing a pronounced in-plane strut, the east wall response is dominated by global rocking, with the wall rotating largely as a rigid body and limited internal deformation.



(A) Rigid blocks (B) Deformable blocks

Figure 8.6. Deformed shape of the rigid and deformable model at 80 mm (Magnified: 10x)

In conclusion, the comparison shows that rigid blocks reproduce the experimental envelope in peak strength (1.3 %) and dissipated work (1.9 %), but overestimate the initial stiffness by 24.4 % and underestimate the displacement at a 20 % post-peak strength drop by 26.1 %. The deformable configuration reproduces the initial stiffness (−2.0 %) but underestimates this displacement by 51.5 % and the dissipated work by 16.5 %. The rigid model reaches 80 mm in five hours against three days for the deformable model, about 7 % of the computational cost. Deformable blocks are nonetheless retained for the dynamic and retrofit analyses that follow (Sections 8.6 and 8.7), because the retrofit's structural elements and their connections couple only to deformable blocks in *3DEC*, and applying them to both the unreinforced and retrofitted cases keeps the comparison

on a single modelling basis. The quasi-static cyclic validation in Section 8.5 is exempt from this requirement and uses rigid blocks for the reasons given in Section 8.3.

8.5. Quasi-static cyclic analysis with rigid blocks

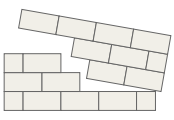
In this section, the quasi-static cyclic response is evaluated using a rigid-block configuration. This choice is informed by the cyclic component-level benchmark in Section 6.3, where the rigid-block idealisation yielded a stable and consistent reproduction of the experimental hysteretic response once the contact parameters were calibrated. For the building-scale pushover, adopting rigid blocks similarly allows the response to be governed by the joint constitutive law and by the imposed boundary conditions, while keeping the computational cost reasonable for the full cyclic protocol. The use of rigid blocks is therefore treated as the baseline configuration for interpreting the global force-displacement response and the damage localisation patterns, before introducing additional modelling complexities through dynamic excitations and retrofit strategies.

8.5.1. Global responses

The global force–displacement responses in the rigid-block simulation closely reproduce the experimental trends in terms of overall backbone shape and the onset of strength degradation, as shown in Figure 8.7A. The numerical loops recover the pronounced stiffness reduction after the initial cycles and reproduce the progressive shift towards larger residual displacements as the amplitude increases. Compared with the experimental cyclic loops, the numerical loops are narrower and flag-shaped, with more pronounced pinching, while reaching a higher peak force. The representative cycle at 51 mm (Figure 8.7B) shows this directly. The experimental loop encloses a larger area than the numerical loop, 1.03 kN m against 0.63 kN m, so the numerical model dissipates less energy in this cycle. The positive loading branch is also systematically higher than the negative branch at large displacements, consistent with the asymmetry observed in the experimental response, although the magnitude of this asymmetry is amplified in the numerical loops at the largest cycles.

A local feature of the last cycle is a short force drop during unloading from the positive loading branch, visible as a step-like decline before the capacity is abruptly recovered in Figure 8.7. This feature is consistent with a reversal of the loading direction, during which joints that opened under the positive branch are expected to close again and the set of active compressive contacts changes in the model. The momentary force reduction and its recovery follow from the discrete re-engagement of these contacts in the explicit solution, sharpened by the rigid-block idealisation, which concentrates the interface compliance at the joints. The step-like decline is therefore a numerical signature of a physical reversal event and not a measured force drop, since the experimental response in Figure 8.7A shows no comparable discontinuity.

The cumulative dissipated energy across cycles in Figure 8.8 shows the same behaviour as the loops. Up to the peak displacement, near 28 mm, the numerical and experimental cumulative curves coincide, indicating that the model reproduces the energy dissipated as the lateral capacity is mobilised. Beyond the peak, the experimental median exceeds



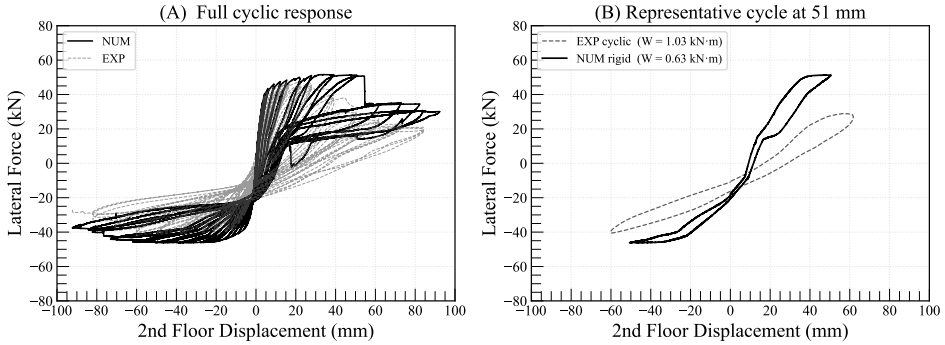


Figure 8.7. Quasi-static cyclic force-displacement response of the building, numerical rigid-block model and experiment. (A) Full response over all cycles, showing the lateral force against the second-floor displacement for the numerical model (solid line) and the experiment (dashed line). (B) A single representative cycle at a displacement amplitude of 51 mm, each loop bounded by consecutive zero up-crossings of the displacement. The experimental loop is the stabilised second cycle at that amplitude, and the numerical loop is the single cycle of the analysis. The value W annotated on each loop is the enclosed area, equal to the energy dissipated in that cycle.

the numerical curve, and the difference widens with amplitude, consistent with the smaller single-cycle area of the numerical loop in Figure 8.7B. The model therefore accumulates less hysteretic energy than the test through the post-peak range, which follows from the narrower and more pinched numerical loops in Figure 8.7. The two curves converge again only at the largest amplitude, where the numerical analysis continues to 92.3 mm past the end of the experimental record near 84 mm, so the final point is not a matched comparison.

Figure 8.9 evaluates whether the stepwise force-control applied at the first-floor level reproduces the intended distribution of lateral deformation between storeys. The figure reports the displacement ratio d_1/d_2 where d_1 and d_2 denote the first- and second-floor in-plane displacements, respectively, shown separately for the positive and negative loading directions. Over most of the loading history, the numerical ratios remain close to the experimental trend and stabilise around a nearly constant value, indicating that the semi-force-control strategy yields a realistic drift partitioning and does not introduce spurious soft-storey behaviour.

The main discrepancy occurs during the early loading cycles, where the experimental ratios vary rapidly while the numerical response approaches the stable ratio more gradually. This deviation is consistent with the initial settling stage of the test, in which small-amplitude cycles are sensitive to gap closure, seating of connections, and the onset of first cracking, so that these differences in stiffness distribution and contact engagement can produce a disproportionate change in interstorey deformation partitioning.

In the numerical model, the initial contact state is more idealised, and the

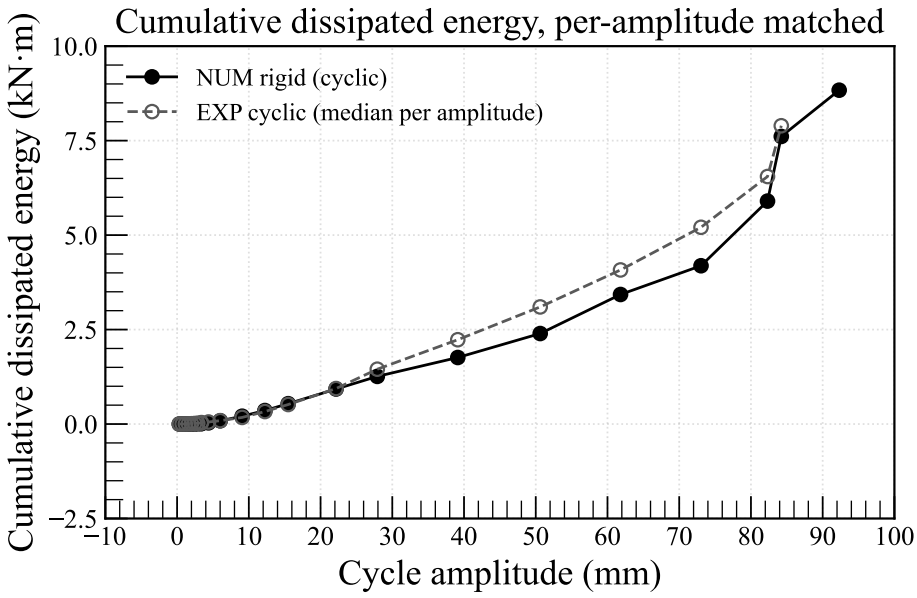
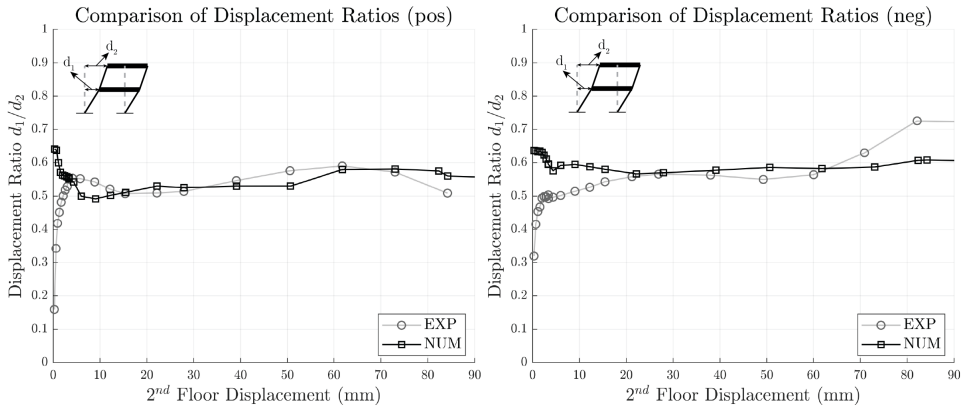


Figure 8.8. Cumulative dissipated energy against cycle amplitude for the rigid-block numerical model and the experiment. Each point is the running sum of the per-cycle dissipated energy, taken as the area enclosed by one force-displacement loop bounded by consecutive zero up-crossings of the second-floor displacement. The numerical curve (solid line, filled markers) uses the single cycle available at each amplitude. The experimental curve (dashed line, open markers) uses the median of the three repeated cycles at each amplitude, so the two series are compared on a one-cycle-per-amplitude basis. The experimental record ends near 84 mm, beyond which only the numerical analysis continues.

force-control update is applied stepwise, which tends to regularise the early response and delay the emergence of the experimentally observed changes in the ratio. As the deformation demand increases and the damaged joint network becomes established, the displacement ratio converges and remains consistent with the experimental trend in both loading directions.

8.5.2. Local responses

As illustrated in Figure 8.10, the local response in the rigid-block quasi-static simulation is dominated by a coupled in-plane and out-of-plane mechanism that initiates at the west pier (in-plane) and subsequently involves the adjacent transverse wall (out-of-plane). Within the piers, the simulated in-plane crack sequence is consistent with the experimental crack maps in Figure 8.3: horizontal flexural cracks form first



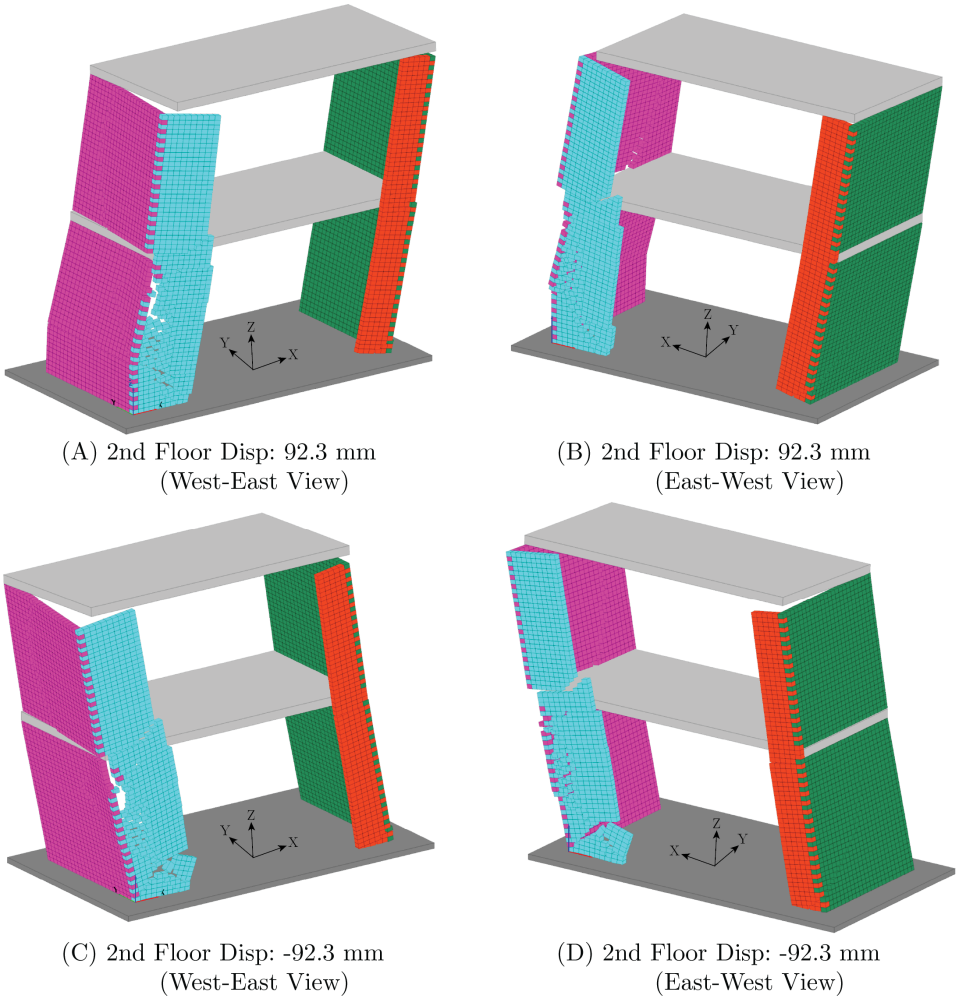
(A) Positive loading cycles (B) Negative loading cycles

Figure 8.9. Displacement ratio d_1/d_2 between the first- and second-floor in-plane displacements over the loading history, numerical rigid-block model against experiment, shown separately for the positive and negative loading directions.

at the base and top of the piers, the diagonal crack develops only at a later stage, and the top flexural crack, together with the diagonal crack, permits the overturning of the pier. However, the timing of the transverse wall engagement differs. In the test, diagonal stepwise cracks developed on the transverse walls already in the pre-peak phase, as extensions of the pier corner cracks running around the corner, well before the diagonal and vertical pier cracks that governed the capacity loss in the post-peak phase [3]. In the simulation, the out-of-plane response develops only after the in-plane discontinuity is established. A plausible explanation for this delay lies in the rigid-block idealisation. With the compliance concentrated entirely at the joints, the transverse walls cannot develop the flexural curvature that precedes out-of-plane cracking, and the initially intact, fully bonded wall junctions provide stronger corner restraint than the as-built connections of the specimen. The transverse-wall engagement is therefore postponed until the in-plane discontinuity releases the corner.

At large displacement demand, a pronounced in-plane diagonal cracking pattern develops in the west pier, expressed by an opening along a stepped diagonal crack band. Local splitting through the brick units, visible as straighter crack traces, also occurs and coincides with the abrupt reduction in lateral resistance observed at approximately 50 mm. With continued cycling, the established in-plane discontinuity reduces lateral restraint at the west corner and activates an out-of-plane response in the connected transverse west wall, which progressively rotates away from the diaphragm planes.

The resulting deformation field is therefore consistent with an overturning-type mechanism, in which diagonal crack opening in the west pier releases the corner restraint of the connected transverse wall, which then rotates out-of-plane away from the



(A) 2nd Floor Disp: 92.3 mm (West-East View)

(B) 2nd Floor Disp: 92.3 mm (East-West View)

(C) 2nd Floor Disp: -92.3 mm (West-East View)

(D) 2nd Floor Disp: -92.3 mm (East-West View)

Figure 8.10. Deformed shape of the cyclic analysis at the maximum displacement in positive and negative loading directions (Magnified 10x)

diaphragm planes. The directional plots indicate that the same mechanism is activated in both loading directions, but with different localisation between the piers depending on whether west-to-east or east-to-west drift is imposed. In each case, the diagonal crack opening remains the governing in-plane failure mechanism.

8.5.3. Summary of the quasi-static cyclic analysis

In summary, the rigid-block quasi-static simulations reproduce the main features of the TU Delft cyclic pushover experimental response at both global and local levels.

The force-displacement loops capture the overall degradation trend and the storey drifts, while the energy metrics confirm that the model activates comparable dissipative mechanisms in the early and intermediate cycles.

At the local scale, the predicted damage localisation and the coupled in-plane-to-out-of-plane mechanism at the west corner are consistent with the experimentally documented crack propagation. The remaining discrepancies are the lower post-peak dissipation, the step-like force drop at load reversal arising from discrete contact re-engagement, and the delayed activation of the out-of-plane mechanism. The delayed out-of-plane activation is revisited under dynamic loading, where the transverse walls are excited directly by inertia and engage earlier. This motivates the next phase of the study, in which the same modelling framework is assessed under dynamic excitation using shake-table-type loading within an IDA setting.

8.6. Explorative study on the dynamic shake-table performance of the building

The dynamic behaviour of the TUD-BUILD-1 structure is explored through an incremental dynamic analysis that applies the calibrated quasi-static MASON model under seismic loading. The aim is to examine how the inertial demand, absent from quasi-static analyses and growing with increasing intensity, affects the response, and, in particular, whether a coupled in-plane and out-of-plane mechanism develops alongside the predominantly in-plane behaviour. No dynamic test of the building is available, so the simulations cannot be validated against a measured response. They instead track how the dominant kinematics, the drift demands, and the stability of the mechanism evolve as the intensity increases.

The dynamic analyses in this section adopt the deformable-block configuration. The choice is required by the retrofit study in Section 8.7, where the structural elements representing the retrofit and their connections can be coupled only to deformable blocks in *3DEC*. The deformable configuration is used for both the unreinforced and retrofitted cases, so that differences in response can be attributed to the retrofit rather than to a change in block idealisation. This is acceptable on the evidence of the pushover comparison in Section 8.4, where the rigid and deformable idealisations gave comparable peak strength and the same governing mechanism, the quantities on which the dynamic assessment rests. The pushover comparison constrains capacity and the governing mechanism, not the damage sequence. The implications for the activation order of the failure mechanisms are assessed in Section 8.6.6. The deformable model degrades earlier in the post-peak range and underestimates the deformation capacity, which biases the near-collapse identification towards lower intensity, a conservative direction for the assessment.

8.6.1. Ground-motion input and signal characteristics

The ground-motion input, termed EQ-NPR [6], was selected for compatibility with the uniform hazard spectrum at a 2475-year return period for the Ten Boer region of the Netherlands, in accordance with the Groningen probabilistic seismic hazard

assessment [10] available at the time of the test. The record has a peak ground acceleration of 0.31 g and the 5–75% significant duration $D_{s,5-75}$ of 1.65 s [11, 12]. The signal has previously been used in the incremental dynamic shake-table test of a full-scale URM cavity-wall building [13], which shares the Groningen terraced-house typology and the same seismic-hazard context, making it a suitable reference record for the TUD-BUILD-1 specimen. Relative to the cavity-wall building tested by Miglietta *et al.* [13], TUD-BUILD-1 is structurally simpler: among other features, it lacks a gable wall, uses single-leaf rather than cavity-wall construction, and incorporates prefabricated reinforced-concrete floor slabs in place of timber diaphragms. This makes TUD-BUILD-1 a controlled reference case for isolating the dynamic response mechanisms most relevant to the seismic risk assessment of the existing Dutch residential building stock in the Groningen region.

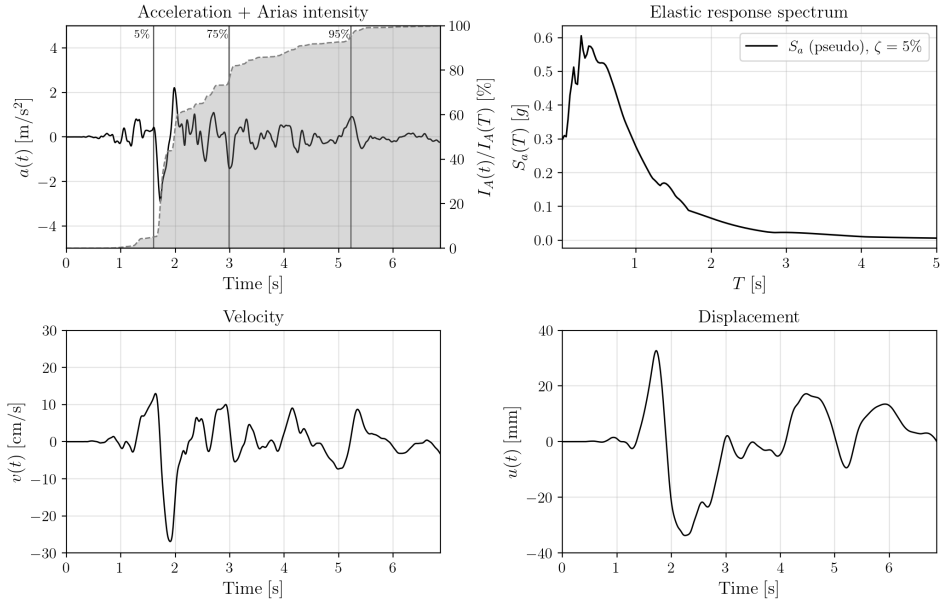


Figure 8.11. Truncated EQ-NPR [6] input record scaled at 100 % and corresponding 5 %-damped elastic response spectrum

The original record of 30 s total duration was truncated at 6.17 s with additional zero-acceleration tails for 0.7 s. This corresponds to 95 % of the Arias intensity, retaining the seismically significant portion of the excitation while substantially reducing the computational cost of the dynamic analyses. The truncated EQ-NPR record and its 5 %-damped elastic response spectrum are shown in Figure 8.11. The spectral content is concentrated at periods below 0.25 s, corresponding to frequencies above 4 Hz. The first identified natural frequency of the TUD-BUILD-1 specimen in the loading direction was 4.05 Hz ($T = 0.247$ s) at the undamaged state, which places it at the lower edge of this range and is consistent with a short-period structure. This period range

coincides with the high-acceleration region of the response spectrum, in line with the short-duration, high-frequency character of induced seismicity in the Groningen region. During the pushover test, the identified frequency decreased to 3.74 Hz and then to 2.5 Hz (Section 8.2), which moves the structure out of this range as damage accumulates.

The incremental dynamic shake-table simulation is conducted by scaling the record incrementally from 20 % to 300 % of its reference amplitude. The corresponding peak ground acceleration (PGA) and peak ground velocity (PGV) values at each intensity level are listed in Table 8.5. All intensity measures are derived through linear scaling from 100 % reference level (Figure 8.11), which corresponds to a PGA of 0.31 g, and a PGV of 0.24 $\mathrm{m\,s^{-1}}$. The lower intensity levels up to 100 % are consistent with the nominal scale factors applied in the experimental shake-table campaign of Miglietta *et al.* [13]. Beyond this level, the record is scaled up to 300 %, reaching a PGA of 0.93 g, to drive the structure into the post-peak damage range and assess the stability of the simulated response mechanism at increasing seismic demand. It is important to note that linear scaling assumes a proportionality between the scale factor and all ground-motion intensity measures, a standard assumption in IDA, but it may introduce non-physical spectral shapes at the highest intensity levels.

Table 8.5. IDA intensity levels and corresponding ground-motion intensity measures

Scale factor (SF)	PGA (g)	PGV (m/s)	Scale factor (SF)	PGA (g)	PGV (m/s)
20%	0.06	0.05	150%	0.47	0.36
33%	0.10	0.08	175%	0.54	0.42
50%	0.16	0.12	200%	0.62	0.48
66%	0.21	0.16	225%	0.70	0.54
85%	0.26	0.20	250%	0.78	0.60
100%	0.31	0.24	275%	0.85	0.66
125%	0.39	0.30	300%	0.93	0.72

All dynamic analyses in this section adopt 3 % mass-proportional damping with a centre frequency of 4.0 Hz, corresponding to the first identified natural frequency of the undamaged specimen. This choice is motivated primarily by computational cost, since mass-proportional damping requires only a diagonal scaling of the mass matrix at each timestep and does not reduce the critical timestep, whereas stiffness-proportional or Rayleigh formulations require evaluating the tangent stiffness at every contact and impose a more restrictive stability limit on the explicit scheme. For a building-scale model subjected to multiple sequential intensity levels, this difference translates to a substantial reduction in total runtime.

The trade-off, however, is that mass-proportional damping applies forces proportional to absolute velocity, which means it damps rigid-body motion following the base input. In a base-excited system, this can limit the dynamic response in an unphysical way, particularly at higher intensity levels, where the structure has softened and the dominant frequencies have shifted well below the initial target. Furthermore, as the

structure degrades and its natural frequencies decrease, the effective damping ratio at the governing modes increases beyond the intended 3 %, introducing bias on the displacement demand. This choice is supported by the damping evaluation in Chapter 7. There, the gap between mass-proportional and Maxwell damping was small when paired with the MASON model. The degraded unloading of MASON suppresses the high-frequency content where the two schemes differ most. The displacement error under mass-proportional damping was also stable across target damping ratios. The same finding was also observed on the gable walls tested to collapse, where the peak displacement envelope and the failure mode were insensitive to the damping formulation. The penalty of the mass-proportional scheme was confined to the local inertial response near collapse. The present assessment rests on displacement-based demand parameters, so these findings support the adopted scheme. Its transfer to the building scale has not been verified, and the identified near-collapse intensity remains conditional on the damping configuration.

8.6.2. Peak displacement response evolution

The incremental dynamic analysis subjects the unreinforced TUD-BUILD-1 model to the truncated EQ-NPR record (Figure 8.11) scaled from 20 % to 300 % of the reference intensity until collapse is imminent. The analysis follows a sequential protocol where each intensity level starts from the damaged state produced by the preceding run, so the IDA curves reflect the cumulative effect of progressive degradation across the entire loading sequence. Peak relative displacements are extracted at each floor level for the west and east longitudinal walls, resolved into in-plane (IP, global X) and out-of-plane (OOP, global Y) components relative to the base of each storey. Figure 8.12 presents the resulting relationships as a function of the peak ground acceleration (PGA) of the scaled input record.

The in-plane response carries the greater demand at all intensities. Below 0.20 g (66 % SF), all monitored locations grow moderately, with displacements below 25 mm, and the second-floor locations lead the first floor by a factor of roughly 1.5 to 2, consistent with the drift partitioning from the quasi-static analysis in Figure 8.9. The first-floor in-plane displacements remain in a consistent ratio up to 125 % SF, beyond which the first-floor west wall departs from this pattern, as described next. Beyond 0.20 g, the in-plane displacements grow progressively. The second-floor east wall reaches the largest of these gradual responses, approximately 130 mm at 0.54 g (175 % SF), with the second-floor west and first-floor east walls following at approximately 86 mm and 80 mm. The first-floor west wall instead changes abruptly. It stays near 19 mm up to 125 % SF (0.39 g), then jumps to approximately 119 mm at 150 % SF (0.47 g) and continues past 170 mm at 175 % SF, the largest in-plane displacement recorded. This sudden change marks the activation of a soft-storey mechanism in the first-floor west piers.

The out-of-plane response shows a similar trend at lower intensities. All monitored locations grow moderately and approximately proportionally up to 0.20 g, with peaks below 20 mm. Although the structure has sustained damage in the preceding lower-intensity runs, the cumulative degradation at the pier-to-wall corners has not yet progressed to the point where nonlinear displacement amplification appears at the global level. Beyond 0.20 g, the out-of-plane displacements rise progressively, with the

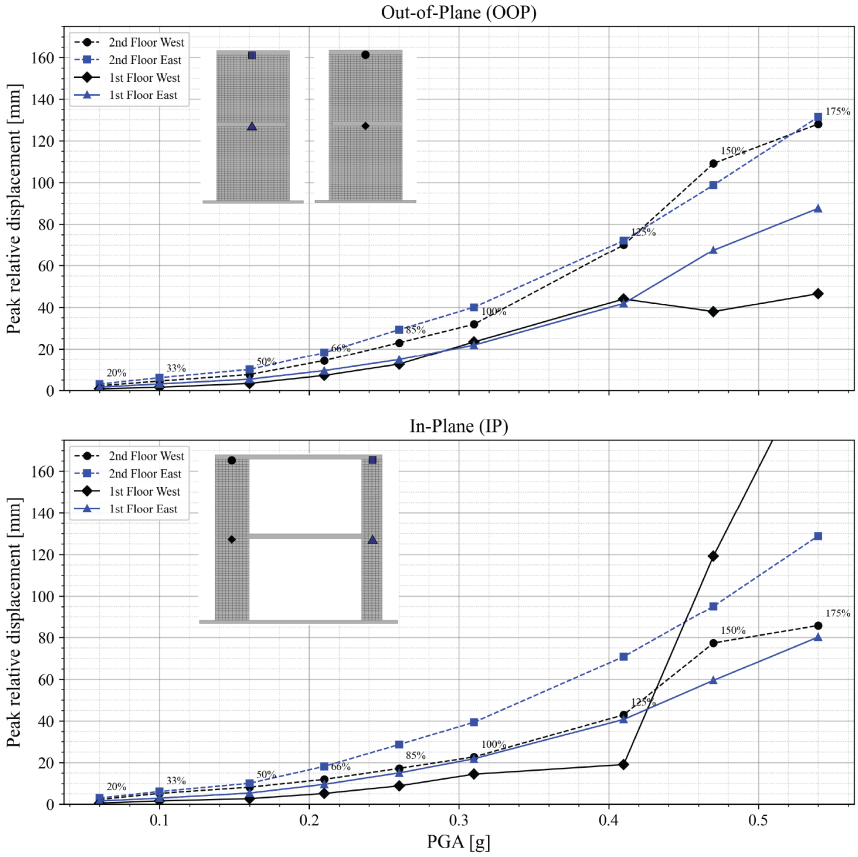


Figure 8.12. Peak relative displacement vs peak ground acceleration (PGA) for the unreinforced TUD-BUILD-1 model under sequential IDA using the EQ-NPR record.

growth rate increasing smoothly and no abrupt change in slope. The second-floor west and east walls reach the largest peaks, approximately 110 mm at 0.47 g (150 % SF) and 130 mm at 0.54 g (175 % SF). The first-floor displacements remain below those of the second floor across all intensities, giving a clear gradient between the two levels.

At the highest PGA of 0.54 g (175 % SF), the IP demand (≈ 170 mm on the west wall) exceeds the corresponding OOP demand (≈ 130 mm), confirming that the in-plane mechanism governs the peak structural demand. The OOP growth rate accelerates in the same PGA range (0.20 g to 0.30 g) as the IP response, consistent with the failure sequence established in the quasi-static analysis that the OOP demand is not driven independently but is triggered by the in-plane damage at the pier-to-wall corners. A first-floor OOP asymmetry is also apparent, with the east wall reaching ≈ 88 mm at 0.54 g compared to 45 mm for the west wall. This difference is attributable to the narrower east pier, which provides less in-plane restraint at the corner and allows the adjacent transverse wall to

develop larger OOP rotations.

A notable feature in the IP response is the sharp increase in displacement demand between PGA 0.31 g and 0.39 g (100 % and 125 % SF), where the second-floor curves transition from moderate growth to a steeper trajectory. This acceleration is consistent with the formation of a coherent ground-storey mechanism, as documented by the damage scalar progression in Figure D.1 (Appendix D) where the damage scalar fields show the gradual formation of diagonal crack bands in the ground-storey pier between 0.20 g and 0.30 g. Whether it marks the onset of the near-collapse regime is examined in the following section using formal drift-capacity thresholds.

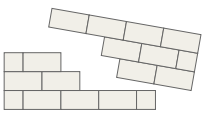
8.6.3. Interstorey drift ratio versus intensity measure

Defining collapse for a masonry structure analysed using the DEM differs from the implicit finite-element case. In an implicit non-linear solution procedure, collapse coincides with the loss of numerical convergence, through failure of the Newton-Raphson iteration to meet the equilibrium tolerance, loss of positive-definiteness of the tangent stiffness, or excessive displacement increments within a load step. The solver then cannot advance, so it signals that equilibrium can no longer be found, but does not represent the collapse itself.

The explicit DEM behaves in the opposite way. The central-difference integration advances the solution unconditionally at each step, provided the step stays below the Courant-Friedrichs-Lewy stability limit (Equation (3.20)), so the solver follows the blocks as they separate, slide, and overturn, and represents the collapse kinematics that the implicit solver cannot. This is the property commonly cited as an advantage of the DEM over the implicit-based finite element method. The same property removes any automatic collapse flag. A structure that has collapsed by any engineering definition continues to produce a valid displacement field, and the analysis can be carried past any physically meaningful limit state. The numerical output, therefore, cannot be relied on without expert interpretation.

When no collapse develops, as is the case here, two explanations are possible. The structure may not collapse at the applied intensities, or the model may not capture a collapse that the structure would otherwise undergo, for example, because of the damping treatment. The limit states introduced in the following sections serve as reference thresholds against which the simulated drift demands are judged, providing the basis for separating the two readings. A more direct indicator would be the out-of-plane collapse of part of the structure, which the DEM can represent explicitly; however, no such collapse occurs in the present analyses, so the assessment rests on the limit-state thresholds.

This characteristic of explicit integration means that collapse cannot be inferred from solver failure; instead, it must be defined by an engineering demand parameter (EDP) exceeding a justifiable capacity threshold. The EDP selected here is the peak absolute interstorey drift ratio (IDR), defined per storey as the maximum over the time history of the relative displacement between consecutive floor levels, normalised by the corresponding storey height, as shown in Equation (8.3).



$$\mathrm{IDR}_{i,\max} = \max_t \left| \frac{u_i(t) - u_{i-1}(t)}{H_i} \right| \tag{8.3}$$

where $u_i(t)$ and $u_{i-1}(t)$ denote the horizontal displacement historeys at the top and bottom of storey i, respectively, and H_i is the storey height. For the TUD-BUILD-1 specimen, $H_1 = 2.66\,\mathrm{m}$ for the ground storey (base to first floor) and $H_2 = 2.56\,\mathrm{m}$ for the upper storey (first floor to roof).

Definition of the cap for near-collapse limit

IDR is preferred over global drift ratio because the governing out-of-plane and in-plane mechanisms in this building typology are storey-localised, and a global metric would obscure the concentration of damage at a single level. A further choice concerns the direction in which the IDR is evaluated since both in-plane and out-of-plane drift demands are present in the TUD-BUILD-1 response, as shown by the peak displacement trends in the preceding section (Figure 8.12). The adoption of in-plane near-collapse drift limits as the governing criterion is justified by the governing role of the in-plane mechanism across both the quasi-static and dynamic analyses. In each case, in-plane shear in the ground-storey piers controls the loss of lateral capacity, with overturning-type out-of-plane kinematics of the transverse walls developing as the in-plane corners degrade. Out-of-plane cracking of the walls may appear earlier under dynamic excitation, in part because the piers are restrained out-of-plane only by floor-level anchors (Figure 8.2), but it is the exhaustion of in-plane capacity that controls collapse rather than an out-of-plane failure mode.

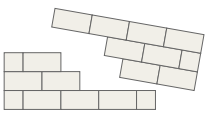
The capacity thresholds against which the in-plane IDR demand is compared are derived from three complementary formulations. Alternative drift-capacity frameworks exist in the international literature, notably ASCE 41 [14] and the NZSEE guidelines [15], but are not adopted here because the TUD-BUILD-1 specimen falls within the Dutch regulatory context, where the Eurocode and the NPR-9998 national annex govern the seismic assessment of existing masonry structures.

The first formulation follows the 2005 version of the Eurocode 8 Part 3 [16] for piers failing in flexure, as expressed in Equation (8.4)

$$\delta_{u,\mathrm{EC8-OLD}} = \frac{4}{3} 0.8\% \frac{H_0}{L} \tag{8.4}$$

where the ultimate drift is expressed as a function of wall slenderness (or shear ratio H_0/L). H_0 is taken as the relevant storey height and L is the corresponding pier length. The second cap is the updated formulation of the code [17], in which the shear span ratio has been removed entirely, and the drift capacity is governed solely by the normalised axial load $\nu = N/(Lt f_c)$, where the code denotes this quantity by ν. Here N is the axial force on the pier, L its length and t its thickness. The formulation is given in Equation (8.5).

$$\delta_{u,\mathrm{EC8-NEW}} = \frac{4}{3} 0.01\,(1 - n_{\mathrm{ax}}), \qquad n_{\mathrm{ax}} = \frac{\sigma_0}{f_c} \tag{8.5}$$



However, both expressions were derived from experimental databases dominated by clay brick and stone masonry from Southern European construction practice, and they were not specifically calibrated for calcium silicate masonry. They are nonetheless included here as the normative references within the European regulatory framework.

The third formulation follows Messali and Rots [18], derived from a dataset of 38 quasi-static tests on calcium silicate and clay brick masonry piers characterised by low axial compressive loads and limited thickness, consistent with Dutch terraced-house construction. The drift limit is expressed in Equation (8.6).

$$\delta_u = A\left(1 - 2.6\,\frac{\sigma_0}{f_c}\right)\left(\frac{H_0}{L}\right)\left(\frac{H_{\text{ref}}}{H}\right) \tag{8.6}$$

with $H_{ref} = 2.4\,\text{m}$. The coefficient A is taken as the mean (best-estimate) value of 1.6 %. In Equation (8.6), H denotes the storey height and is used as a proxy for the shear span H_0 when the boundary condition matches the test database (cantilever piers). For partially restrained boundary conditions, $H_0 < H$ may be substituted, in which case Equation (8.4) and Equation (8.6) employ the same shear-span argument.

All three formulations were calibrated against quasi-static cyclic test databases. Their application to predicting the near-collapse limit under dynamic analysis implicitly assumes that the drift capacity of masonry piers is rate-independent. For the loading rates encountered in these simulations, which remain well below impact-type loading regimes, this assumption is considered reasonable.

Calculation of the storey-dependent axial load ratio

The evaluation of both the code-based and empirical drift capacities requires storey-specific values of the normalised axial load, taken here from the gravity load path. For the TUD-BUILD-1 specimen, the axial stress ratio σ_0/f_c differs between the two storeys because the vertical load path is asymmetric, i.e., no RC slab is directly connected at the first-floor level. Therefore, the piers at the ground storey carry only the tributary roof slab mass plus the self-weight of the masonry above, while the upper storey piers carry only the roof slab contribution.

The roof slab is assumed to distribute the gravity load in two-way action to the surrounding perimeter walls. Using outside-to-outside plan dimensions L_x and L_y (Figure 8.1), the tributary area assigned to the south-side piers is defined in Equation (8.7).

$$A_S = \frac{L_y\left(2L_x - L_y\right)}{4}, \qquad (L_x \geq L_y). \tag{8.7}$$

This tributary area is then distributed among the piers proportionally to their bearing lengths along the wall line. For the west pier, the slab tributary area is obtained by Equation (8.8).

$$A_{\text{slab}}(\text{WF}) = A_S\,\frac{L_{\text{WF}}}{L_{\text{WF}} + L_{\text{EF}}} \tag{8.8}$$

where $L_{\text{WF}} = 1.1\,\text{m}$ and $L_{\text{EF}} = 0.662\,\text{m}$ are the west and east pier lengths, respectively.

Let the roof slab thickness be t_{slab} and density ρ_{rc}. The slab tributary mass is defined in Equation (8.9).

$$m_{\text{slab}} = A_{\text{slab}}\, t_{\text{slab}}\, \rho_{\text{rc}}. \tag{8.9}$$

The corresponding axial force contribution is $N_{\text{slab}} = m_{\text{slab}} g$. The masonry mass of the wall segment above the first storey is estimated as in Equation (8.10)

$$m_{\text{mas}} = \eta_{\text{open}}\, (t_{\text{wall}}\, L\, H_2)\, \rho_{\text{mas}}, \tag{8.10}$$

where t_{wall} is wall thickness, L is the pier length (S-WP-FF), H_2 is the upper-storey height, ρ_{mas} is masonry density, and η_{open} is an opening reduction factor, set to 1.0 since there are no openings within the piers.

The compressed area is approximated as $A = t_{\text{wall}}\, L$. The storey-dependent axial load ratios then follow as:

$$\left(\frac{\sigma_0}{f_c}\right)_2 = \frac{N_{\text{slab}}}{A\, f_c}, \tag{8.11}$$

$$\left(\frac{\sigma_0}{f_c}\right)_1 = \frac{N_{\text{slab}} + m_{\text{mas}}\, g}{A\, f_c}, \tag{8.12}$$

where the subscripts 1 and 2 refer to the ground storey and upper storey, respectively. The resulting ratios are inserted into Equations (8.5) and (8.6) to obtain the near-collapse drift capacities for each storey. Because these ratios are derived from the gravity load path, they describe the axial state before shaking. During the dynamic analysis, the axial load on each pier varies in time as the global overturning response and the rocking of the piers redistribute the vertical force across the section and between the piers, so the instantaneous axial load ratio departs from the static value used here. The drift capacities computed from these ratios are therefore an initial, gravity-based estimate, and the thresholds are held constant in the comparison that follows. The numerical inputs and derived ratios are summarised in Table 8.6.

Table 8.6. Storey-dependent axial load components, compressed area, and derived axial stress ratios for the piers.

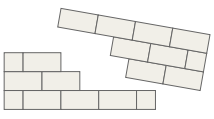
Pier	L [m]	m_{slab} [kg]	m_{mas} [kg]	A [m^2]	$(\sigma_0/f_c)_2$ [%]	$(\sigma_0/f_c)_1$ [%]
S_{EF}	0.662	1091.5	311.2	0.0675	2.67	3.44
S_{WF}	1.10	1813.6	517.0	0.1122	2.67	3.44

$m_{\text{slab,1F}} = 0$ (no RC slab directly connected at the first-floor level).
Masonry mass above computed with $H_2 = 2.56$ m and $\eta_{\text{open}} = 1.00$.
S_{EF} and S_{WF} denote the south-east and south-west piers (the loaded piers in the X-direction; the corresponding north-side piers are identical by symmetry due to the Y-axis restraint).

For completeness, the shear ratios used in the code-type slenderness/shear-based expressions are:

$$\text{Shear ratio (2nd floor)}: \quad 2.327\ (S_{WF}),\ 3.867\ (S_{EF}), \tag{8.13}$$

$$\text{Shear ratio (1st floor)}: \quad 2.418\ (S_{WF}),\ 4.018\ (S_{EF}). \tag{8.14}$$



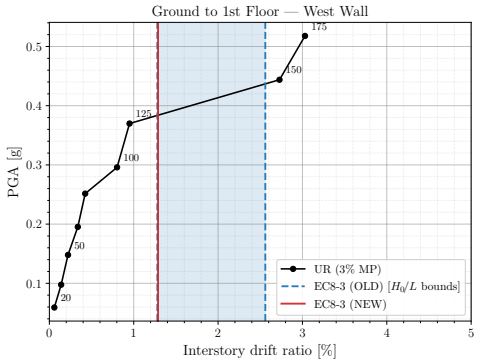
Comparison results

A practical difficulty arises in evaluating the H_0/L-dependent formulations at the first storey. The boundary condition at the top of the first-storey façade pier is intermediate between fixed-fixed ($H_0 = H/2$) and cantilever ($H_0 = H$) because the rotational restraint does not originate from the slab clamping the pier directly. Instead, it is provided indirectly by the continuity of the masonry above the floor level and by the interlocking with the transversal walls at the corners (Figure 8.2). This partial restraint is weaker than full fixity but stronger than a free end, placing the effective shear span somewhere between the two idealised limits. To reflect this epistemic uncertainty, the drift capacities from Equation (8.4) and Equation (8.6) are computed for both bounding assumptions and presented as shaded bands on the EDP–SF curves. At the second storey, the limited vertical load transfer to the façade piers and the absence of structural continuity above the roof slab justify assuming a cantilever, yielding a single capacity value. The updated formulation (Equation (8.5)) is insensitive to this boundary condition uncertainty, as it contains no shear span parameter.

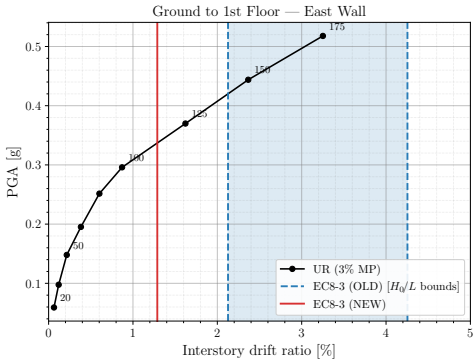
EC8 thresholds Figure 8.13A and Figure 8.13B show the ground-storey IDR against PGA for the west and east piers, with the EC8-3 (2005, OLD) [16] and EC8-3 (2023, NEW) [17] thresholds; the upper-storey results are in Figure D.2. The east-wall IDR grows monotonically, reaching 1.7 %, 2.3 %, and 3.4 % at 125 %, 150 %, and 175 % SF, respectively. It crosses the NEW threshold before 125 % SF and the fixed-fixed lower bound of the OLD band near 150 % SF, while the cantilever upper bound is not reached within the analysed range. The west-wall IDR reaches 1.3 % at 125 % SF, at the 2023 threshold, and continues to about 2.6 % at 150 % SF and 3.0 % at 175 % SF. It enters the OLD band between 125 % and 150 % SF, reaches the cantilever bound (2.6 %) at 150 % SF, and exceeds it at 175 % SF.

In the upper-storey west wall (1st floor to roof, Figure D.2A), the interstorey drift ratio snaps back at 150 % SF, falling from about 1.7 % at 125 % SF to 1.0 % before rising sharply at 175 %. This reflects a transient shift in the governing deformation mode. At this intensity, the cumulative in-plane damage in the west pier has progressed to the point where the deformation demand is no longer accommodated by localised storey-level drift but instead by a combination of rigid-body translation of the pier and out-of-plane rotation of the adjacent transverse wall. The IDR metric, defined from in-plane floor relative displacements, does not capture this out-of-plane component and therefore registers an apparent decrease. The east wall does not develop a comparable diagonal crack band. Consistent with the mechanism identified in the monotonic pushover (Section 8.4), its response is dominated by global rocking, with the wall rotating largely as a rigid body and limited internal deformation. No equivalent change in the governing deformation mode therefore occurs, and the east-wall IDR grows monotonically throughout the intensity range.

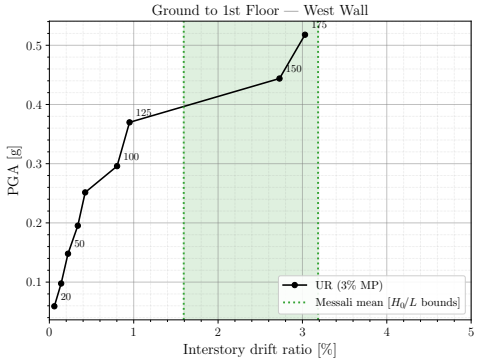
The coincidence between the EC8-3 (NEW) value and the fixed-fixed lower bound of the EC8-3 (OLD) band has practical implications. For the low axial load ratios typical of Dutch calcium silicate masonry piers, the updated code resolves the ambiguity in boundary conditions by converging on the conservative interpretation of the old code. In their conservative interpretation, both formulations identify the near-collapse onset at approximately 125 % SF: the ground-storey IDR reaches the EC8-3 (NEW) threshold, and



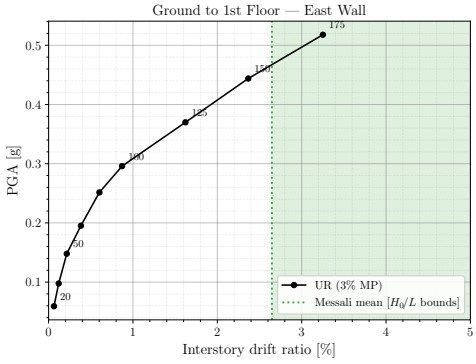
(A) West wall – EC8 thresholds



(B) East wall – EC8 thresholds



(C) West wall – Messali and Rots thresholds



(D) East wall – Messali and Rots thresholds

Figure 8.13. Ground-storey EDP vs IM results for the west and east piers.

equivalently the fixed-fixed bound of EC8-3 (OLD), at this intensity on the governing west pier, and earlier on the more slender east pier, consistent with the deformed configuration at this intensity (Figure 8.14).

Comparing with the peak displacement response in Figure 8.12, the 125 % SF flagged by the EC8 formulations corresponds to the nonlinear displacement growth phase, where the IP and OOP demands begin to diverge from their initial proportional trend. At this intensity, the second-floor IP displacements remain below 75 mm, indicating that the structure still possesses residual deformation capacity beyond the code-identified near-collapse point. The EC8 formulations, therefore, identify the near-collapse state at an intensity level where the structure still possesses residual deformation capacity, suggesting a conservative prediction relative to the observed evolution of displacement demand. Whether this conservatism is appropriate or excessive depends on the assumed boundary condition. The fixed-fixed interpretation and the NEW expression provide the conservative identification at 125 % SF. The cantilever interpretation of the OLD expression is more permissive, extending the admissible range towards 150 % SF, where

the displacement response has already entered its accelerating regime and the deformed configuration (Figure 8.14B) shows a state approaching collapse.

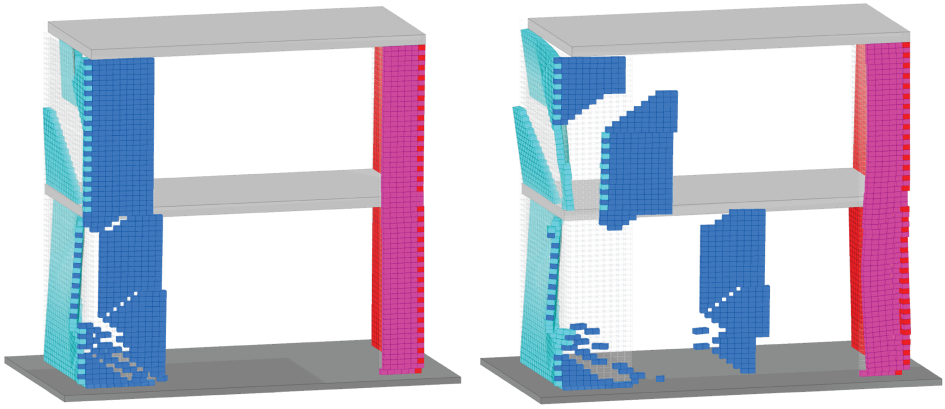
Messali and Rots thresholds Figure 8.13C and Figure 8.13D present the same EDP–IM curves overlaid with the Messali and Rots mean band (Equation (8.6)) for the ground storey. The corresponding upper-storey results are provided in Figure D.2. The Messali mean band spans a wider intensity range than the EC8 thresholds, and for the east wall, it sits farther to the right than for the west. The east pier is the more slender of the two piers, with an in-plane length of 0.66 m against 1.1 m for the west pier, so its larger shear-span ratio raises every drift capacity that scales with H_0/L. Its fixed-fixed lower bound, near 2.7 %, is therefore not crossed until between 150 % and 175 % SF, and its cantilever upper bound, near 5.4 %, is not reached within the analysed range. This is consistent with the mean calibration representing the central tendency of the 38-pier dataset, intended to capture the most probable drift capacity and not a safe lower bound. At 150 % SF, the intensity at which the structure reaches its collapse state through the west pier, the east-wall interstorey drift ratio is approximately 2.4 % and remains below its own fixed-fixed bound. Even though the building has collapsed at this intensity, the east pier is still below its own drift bound. A drift check on the east pier alone would not detect it, which confirms that the governing element is the west pier.

Referring back to the peak displacement response (Figure 8.12), the 150 % to 175 % SF range over which the east-wall band is crossed corresponds to the regime where both IP and OOP displacements have undergone their steepest escalation and the structure is already in an advanced state of damage. The Messali and Rots mean band, for both piers, therefore places the near-collapse limit well beyond the point at which the deformed configuration and the damage scalar field indicate that the ground-storey mechanism is fully mobilised.

The deformed configuration at 125 % SF (Figure 8.14A), corresponding to a PGA of 0.39 g, shows that the ground-storey mechanism is already fully formed at an intensity below the Messali band crossing. The fully developed diagonal crack band in the ground-storey west pier, the block separation at the base, and the out-of-plane rotation of the transverse wall at the corner are all consistent with the west pier having exhausted its in-plane capacity. The visible damage matches the failure mode described by the drift capacity formulations. The governing diagonal mechanism in the west pier has fully formed, and its residual resistance now comes from friction and mechanical interlocking. The global interstorey drift at this intensity, however, has not yet reached the calibrated capacity values.

At 150 % (Figure 8.14B), corresponding to a PGA of 0.47 g, the damage state exceeds the admissible range of any of the adopted capacity formulations. The ground-storey west pier has largely detached, the upper-storey west wall has separated from the pier, and outward deformation is visible at the east pier ground storey. This configuration constitutes a collapse in physical terms and confirms that the 125 % SF identification, coincident with the conservative EC8-3 crossing on the governing pier and conservative with respect to the remaining thresholds, reflects a genuine structural limit state and not an arbitrary choice.

In conclusion, the near-collapse state of the unreinforced configuration is identified at



(A) Deformed shape at the end of 125% SF (B) Deformed shape at the end of 150% SF

Figure 8.14. Dynamic response at the end of (A) 125% (PGA = 0.39 g) and (B) 150 % (PGA = 0.47 g) intensity (Def factor: 10)

125 % SF, on the basis of the physical damage evidence and a conservative treatment of the single ground motion. At this intensity, the deformed configuration (Figure 8.14A), corresponding to a PGA of 0.39 g, shows a fully developed diagonal crack band in the ground-storey west pier with block separation and corner detachments, which indicates that the governing in-plane mechanism has formed. The west wall snap-back at 150 % SF, where the deformed state (Figure 8.14B) would be recognisable as collapse, confirms that the stable deformation capacity has already been exhausted at the preceding intensity.

The drift thresholds bound this identification from both sides. In their conservative interpretation, the EC8-3 (NEW) value and the coincident fixed-fixed bound of EC8-3 (OLD) are reached at 125 % SF on the governing west pier and earlier on the east pier. The permissive interpretations show later: the cantilever bound of EC8-3 (OLD) is reached near 150 % SF, the intensity already identified as collapse, and the Messali and Rots mean band is crossed only between 150 % and 175 % SF for the east pier. The conservative code thresholds therefore corroborate the 125 % SF identification, the permissive ones corroborate the 150 % SF collapse, and the spread between them follows from the assumed boundary condition. Because the assessment uses a single ground motion, the record-to-record variability is not captured, so a lower-bound near-collapse estimate is the sounder choice. The 125 % SF level is the intensity at which the governing west pier reaches the conservative thresholds. It precedes the permissive thresholds and the collapse at 150 % SF, and it is supported by the physical simulation evidence. The east pier crosses the EC8-3 (NEW) threshold earlier, but it does not govern the collapse, so 125 % SF is adopted as a lower-bound near-collapse estimate for the governing mechanism, not as the first exceedance of every threshold on every pier. For the subsequent retrofit assessment, 125 % SF is taken as the near-collapse reference for the unreinforced configuration, against which the retrofitted case in Section 8.7 is compared.

8.6.4. Damage evolution at each intensity level

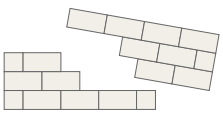
The full progression of the combined damage scalar d_{ts} from 20 % to 175 % SF is presented in Figure D.1 in Appendix D. The deformed configuration at the instant of peak response was not recorded during the simulations; only the residual state at the end of each run is available. The damage scalar, however, is not subject to this limitation, as it records the maximum irreversible damage at each contact point over the entire time history and does not recover upon unloading. It therefore provides a representative spatial record of progressive degradation through the sequential IDA protocol, even when the residual deformed shape under-represents the peak response.

At 20 % to 33 % SF (Figure D.1A–B), damage is confined to the floor-slab interfaces, consistent with the stress localisations introduced by the stiffness contrast between the RC slabs and the masonry. At 50 % SF (Figure D.1C), initial diagonal traces appear at the ground-storey pier corners and on the transverse walls, marking the onset of shear-driven joint degradation. Between 66 % and 85 % SF (Figure D.1D–E), these diagonal patterns develop into coherent stepped crack bands in the ground-storey piers, while the transverse walls show corresponding diagonal damage. At this stage, the peak displacement response (Figure 8.12) still grows approximately linearly with intensity, showing that the local joint degradation has not yet accumulated sufficiently to alter the global stiffness.

The transition to nonlinear displacement growth occurs at approximately 100 % SF (Figure D.1F), coinciding with the development of a coherent diagonal damage band in the ground-storey pier. The near-collapse drift thresholds established in the preceding section are crossed at approximately 125 % SF, one increment beyond this transition point. Between 125 % and 150 % SF (Figure D.1G–H), the damage intensifies substantially, with denser cracking through both mortar joints and potential crack planes in the units (shown by straight vertical cracks in the pier), and the transverse walls show pronounced damage at the pier-to-wall connections. The deformed configurations at these intensities (Figure 8.14) confirm the physical progression from a heavily damaged but stable structure at 125 % SF to effective collapse at 150 % SF.

At 175 % SF (Figure D.1I), the damage is extensive throughout the ground storey, with the joint damage scalar approaching saturation along multiple crack bands. The upper storey shows comparatively limited damage growth, consistent with the drift plateau observed in the upper-storey EDP–IM curves (Figure D.2).

The damage progression confirms the failure sequence inferred from the peak displacement and IDR analyses. Damage on the transverse walls appears early, but the in-plane mechanism in the ground-storey piers governs: stepped diagonal cracking progressively degrades the corner connections and converts the transverse-wall response into overturning. The transition from local joint damage to a coherent ground-storey mechanism occurs at approximately 100 %–125 % SF, consistent with the near-collapse identification at 125 % SF established in the preceding section. Beyond 150 % SF, the damage at the ground storey diffuses while the upper storey remains comparatively intact, providing a mechanistic explanation for both the upper-storey drift plateau and the west-wall snap-back in the EDP–IM curves.



8.6.5. Global hysteretic responses

Figure 8.15 presents the base shear versus global drift ratio response of the dynamic IDA, with one panel per scaling factor, overlaid on the experimental quasi-static backbone from the TUD-BUILD-1 specimen [3]. The global drift ratio is defined as the average second-floor in-plane displacement of four channels (two per pier wall) relative to the base motion, divided by the total height of 5.22 m. The base shear coefficient $C_s = V/W$ is obtained by dividing the total horizontal reaction at the foundation by the system weight of 334.54 kN. The dynamic loops are truncated at 125 % SF, the near-collapse intensity. The 150 % SF run is excluded, since the near-simultaneous failure of several components produces a noisy signal that reflects post-collapse kinematics and not meaningful structural response. Since no experimental dynamic reference is available for the TUD-BUILD-1 specimen, the quasi-static cyclic results serve as the closest benchmark. The numerical backbone, shown in the 125 % SF panel, is defined by extracting, for each IDA run, the point of maximum base shear and its corresponding drift in each loading direction.

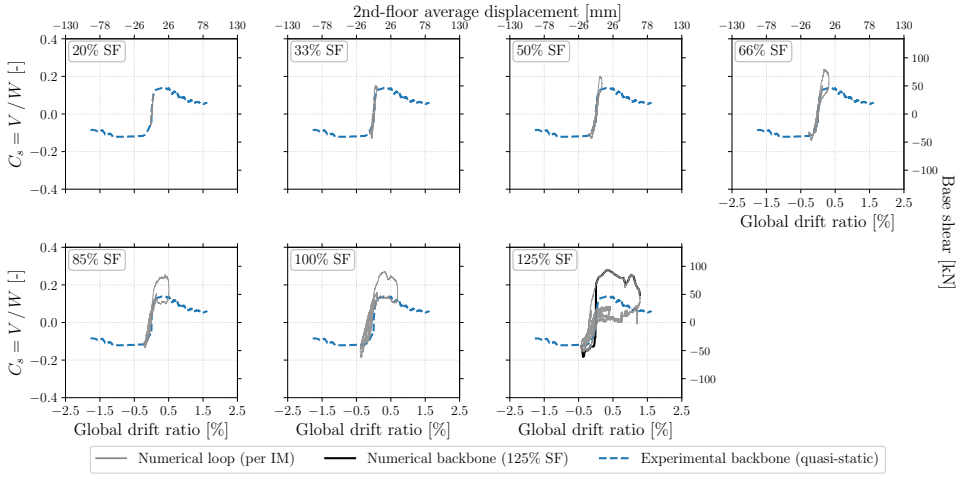


Figure 8.15. Base shear coefficient versus global drift ratio per scaling factor, compared with the experimental quasi-static backbone. The numerical backbone is shown in the 125 % SF panel.

The panels trace the hysteretic progression with intensity. Up to 50 % SF, the response remains essentially elastic. The loops are narrow, the drift excursions stay below approximately 0.1 %, and the response follows the initial branch of the experimental backbone. At 66 % and 85 % SF, the loops begin to widen, and the peak base shear climbs above the experimental envelope, marking the onset of joint damage and stiffness degradation. At 100 % SF, the hysteresis becomes pronounced, with drift excursions approaching 0.8 % and a visible asymmetry between the two loading directions. The 125 % SF run produces wide, pinched loops with excursions beyond 1 % drift, a shape characteristic of frictional sliding and re-contact at the joints as the structure

approaches collapse. The transition from quasi-elastic behaviour to full hysteretic response is therefore concentrated between 85 % and 100 % SF, consistent with the damage progression reported in Figure D.1.

In the positive loading direction (West-East), the numerical backbone reaches a peak base shear coefficient of approximately 0.27, compared to the experimental peak of approximately 0.14. Part of this difference reflects a measurement inconsistency. The quasi-static base shear is the sum of actuator forces at the floor levels, excluding the distributed wall mass inertia, while the dynamic base shear is the total foundation reaction including all inertial contributions. The remaining difference is attributed to the transient mobilisation of distributed inertial forces, which allows the structure to sustain higher instantaneous resistance before damage localisation occurs. In the negative direction (East-West), the numerical peak C_s is approximately 0.15, more closely aligned with the experimental envelope. The directional asymmetry reflects the geometric irregularity of the piers and is consistent with the quasi-static cyclic results in Section 8.5.

A further factor shaping the loops is the timing with which the transverse walls engage. In the test, diagonal cracking of the transverse walls developed in the pre-peak phase as an extension of the pier corner cracks, after the in-plane flexural cracking of the piers and well before the diagonal pier failure that governed the capacity loss [3]. Under dynamic loading, the transverse walls engage even earlier. The joint damage progression in Figure D.1 and the deformed configuration at 125 % SF (Figure 8.14A) show diffuse OOP damage on the transverse walls from 50 % SF upward, preceding the full mobilisation of the pier in-plane mechanism, while the in-plane capacity remains the mechanism that governs collapse. The quasi-static cyclic analysis (Section 8.5) engages them last, only after the in-plane discontinuity is established. The three responses therefore share the same governing in-plane mechanism and differ in when the transverse walls participate, with the test lying between the two simulations. The candidate explanations for this ordering are assessed in Section 8.6.6. At intermediate drift levels, part of the input energy is therefore dissipated through OOP mechanisms in the transverse walls, in the test and in the dynamic model alike. Since the loops in Figure 8.15 are defined from in-plane base shear and in-plane drift, this contribution does not appear in the hysteresis.

A direct comparison of dissipated energy between the two regimes would confound the cycle-by-cycle dissipation with the number and amplitude of reversals applied, which differ between the IDA records and the fixed quasi-static protocol. Dissipation is therefore examined per hysteresis loop using the equivalent viscous damping ratio. For a single loop [19, 20],

$$\xi_{eq} = \frac{E_D}{4\pi E_{So}}, \qquad E_{So} = \tfrac{1}{2} F_{sec}\, u_{amp}, \tag{8.15}$$

where E_D is the area enclosed by the loop, E_{So} is the secant strain energy at the displacement peak, F_{sec} is the restoring force at that peak, and u_{amp} is the loop amplitude. The ratio normalises the dissipated energy to the energy stored at the same amplitude, thereby isolating cycle-by-cycle damping and removing the cycle-count dependence of the cumulative measure.

Figure 8.16 shows ξ_{eq} against drift amplitude. The grey circles are the individual loops extracted from each dynamic run via reversal detection, representing the full per-cycle

population. Their scatter at small amplitudes reflects the sensitivity of Equation (8.15) when the loop and its stored energy are small. The black curve connects the largest loop of each IDA run, labelled by the scaling factor, and the blue curve gives the experimental median per target drift amplitude. The red dashed curve is the imposed mass-proportional Rayleigh damping expressed on the same axis,

$$\xi_\alpha(\delta) = \frac{\alpha}{2\,\omega_{sec}(\delta)}, \qquad \omega_{sec}(\delta) = \sqrt{\frac{g\,C_s(\delta)}{u(\delta)}}, \tag{8.16}$$

where α is the mass-proportional coefficient and ω_{sec} is the secant circular frequency of the building at drift δ, obtained from the secant stiffness $K_{sec} = V_b(\delta)/u(\delta)$ and the seismic mass W/g. Here $C_s(\delta) = V_b(\delta)/W$ is the base shear coefficient read from the backbone at drift δ, W the seismic weight, g the gravitational acceleration, and $u(\delta) = \delta H$ the lateral displacement corresponding to that drift over the reference height H. Because ξ_α scales with $1/\omega_{sec}$, the imposed damping rises as the structure softens and its secant frequency falls.

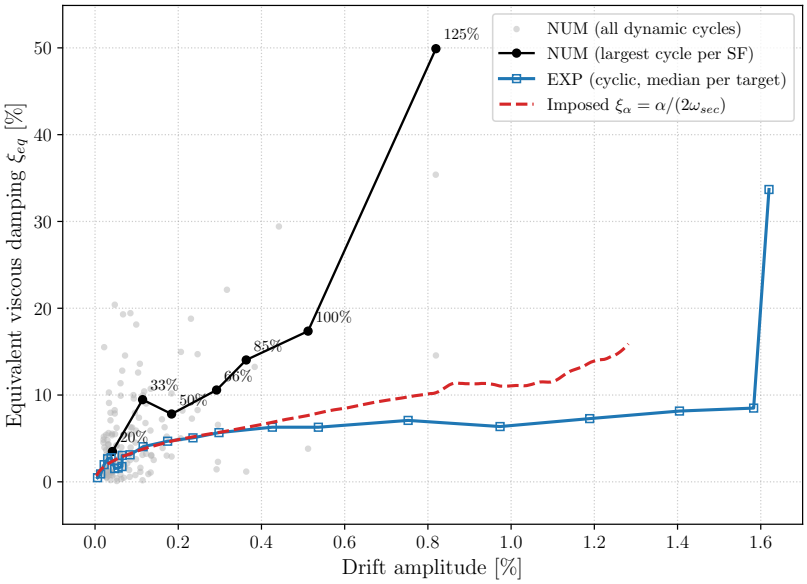


Figure 8.16. Equivalent viscous damping per hysteresis loop against drift amplitude. Grey circles: all individual loops extracted from the dynamic runs up to 125 % SF. Black: the largest loop of each IDA run, labelled by scaling factor. Blue: experimental median per target amplitude. Red dashed: the imposed mass-proportional Rayleigh damping, $\xi_\alpha = \alpha/(2\omega_{sec})$.

Figure 8.16 must be read keeping in mind that the experiment is quasi-static. A quasi-static cyclic test has negligible velocity, so the experimental curve (blue) represents material hysteretic damping only, with no viscous contribution. The imposed ξ_α (red,

Equation (8.16)) is the model's mass-proportional viscous damping, which acts only in the dynamic analysis. The numerical curve (black) is the total per-cycle dissipation of the dynamic model, combining material hysteresis, the imposed viscous damping, and the contact response. Up to 0.5 % drift, the imposed viscous damping is of similar magnitude to the experimental material damping, both near 5 % to 6 %. The dynamic total is about twice this level, near 10 % to 17 % between 66 % and 100 % SF, consistent with a viscous term of comparable size acting on top of the hysteresis. The further rise with drift comes from the contact response under dynamic loading, the frictional sliding and re-contact at the joints mobilised by the early out-of-plane activation described above.

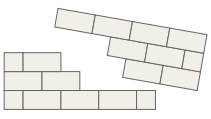
The two endpoints, at 125 % SF for the dynamic analysis and near 1.6 % drift for the quasi-static test, are unreliable. Once the strength degrades, the secant force in Equation (8.15) drops and inflates ξ_{eq}, so the comparison is only meaningful up to about 0.5 % drift. The 3 % target ratio used for the viscous damping is a conventional, low value for masonry. It is not validated by the quasi-static test, which contains no viscous dissipation, and no dynamic reference exists for the specimen, so only the material part of the dynamic damping is constrained here.

The decomposition nonetheless shows that the elevated cycle-by-cycle dissipation of the dynamic model is attributable to identifiable mechanisms, namely the material hysteresis, a conventional viscous term, and the contact sliding that grows with drift, and not to an unexplained numerical energy loss. The analysis does not rule out that the dynamic model dissipates more per cycle than the real structure would, because the imposed viscous damping cannot be validated against the quasi-static test. Its effect on the reported results is nonetheless bounded. The retrofit assessment in Section 8.7 rests on the ratio of the retrofitted to the unreinforced near-collapse intensity, both obtained with the same model and the same damping scheme, so the systematic effect of the damping ratio and scheme largely cancels.

8.6.6. Remarks on the dynamic performance of the unreinforced building

The comparison shows that the two loading regimes agree on the governing in-plane mechanism, which the quasi-static simulation reproduces well, and on the concentration of damage at the ground storey. They differ in when the transverse walls engage. In the test, diagonal cracking of the transverse walls developed in the pre-peak phase as an extension of the pier corner cracks, after the in-plane flexural cracking of the piers and well before the diagonal pier failure that governed collapse, even though the quasi-static protocol imposes no inertial demand on the transverse walls and their damage develops through compatibility with the in-plane deformation alone [3]. The quasi-static simulation reproduces this order but engages the transverse walls later, only once the in-plane discontinuity is established, a delay attributed to the rigid-block idealisation (Section 8.5). The dynamic analysis engages them earlier than the test, with diffuse transverse-wall damage from 50 % SF upward (Figure D.1).

The early engagement under dynamic loading is plausibly inertial, since the record loads the transverse walls directly, whereas in the test, their damage develops through compatibility with the in-plane deformation. The adopted 3 % mass-proportional damping acts on absolute velocity, so its damping ratio decreases with frequency and rigid-body motion is damped more than high-frequency deformation. It therefore affects



the in-plane and out-of-plane responses differently, and the direction of its influence on the early transverse-wall damage is not established here. The insensitivity of the rocking-dominated displacement kinematics to the damping formulation in Chapter 7 limits this concern for global displacements, but not for the local inertial response, which was the quantity most affected there. The block idealisation changes together with the loading regime and confounds the comparison with the quasi-static simulation. Settling the attribution would require a deformable-block rerun of the quasi-static analysis, a building-scale damping-sensitivity study, and a dynamic experimental benchmark for the specimen, none of which was available here. The early out-of-plane engagement is therefore retained as a model observation. In all cases, however, the collapse state is ultimately triggered by the exhaustion of the piers' in-plane drift capacity, which governs the loss of lateral load-carrying capacity regardless of when the transverse walls engage. The MASON contact model produces the governing in-plane mechanism under both regimes without recalibrating the strength parameters, demonstrating its applicability across loading regimes.

Two sources of uncertainty remain unaddressed. The dynamic shake-table simulation was conducted using a single ground-motion record (EQ-NPR), so the identified near-collapse range of 125 % to 150 % SF is specific to this signal and does not capture record-to-record variability. A multi-record campaign would be needed to establish a statistically robust fragility estimate. Additionally, the analyses used a single damping configuration (3 % mass-proportional). The sensitivity of the near-collapse identification to damping ratio and damping model was not explored at the building scale due to the computational cost of repeating the full IDA protocol under alternative damping formulations. The influence of damping model selection on dynamic response was examined in Chapter 7 on smaller benchmark structures. A building-scale counterpart remains an extension of the present work.

The near-collapse range established here for the unreinforced configuration gives the baseline against which the effectiveness of retrofit interventions can be quantified. The ground-storey localisation of damage, the coupled in-plane/out-of-plane failure sequence, and the identified intensity thresholds define the performance targets that a retrofit strategy must address. The following section applies the same modelling framework and sequential IDA protocol to the retrofitted configuration, allowing the comparison to isolate the structural effect of the intervention from differences in modelling assumptions and loading procedure.

8.7. Explorative retrofit assessment with the modular steel frame exoskeleton

The preceding analysis established that the unreinforced TUD-BUILD-1 assemblage reaches the near-collapse state with peak ground acceleration between 0.39 g and 0.47 g (corresponding to 125 % to 150 % scale factor), governed by the progressive localisation of in-plane damage at the ground-storey piers and the subsequent activation of out-of-plane overturning of the transverse walls. This failure sequence identifies two structural deficiencies that a retrofit intervention must address, namely the limited in-plane drift capacity of the ground-storey pier and the insufficient lateral restraint at the

pier-to-wall connections, which together permit the coupled in-plane and out-of-plane mechanism.

The retrofit strategy examined in this section is the Resisto 5.9 modular steel-frame system, representative of current practice for the seismic upgrade of masonry residential buildings in the Italian context. This system was already modelled at the single-wall scale in Section 6.4, and the present analysis applies that component model at the building scale. The system is mounted on the exterior faces of the west pier and the west wall and is modelled using the same deformable-block configuration and sequential IDA protocol as in the unreinforced case, so that differences in response can be attributed to the retrofit intervention rather than to changes in the modelling assumptions. The retrofit scheme and its numerical idealisation are presented in the following sections.

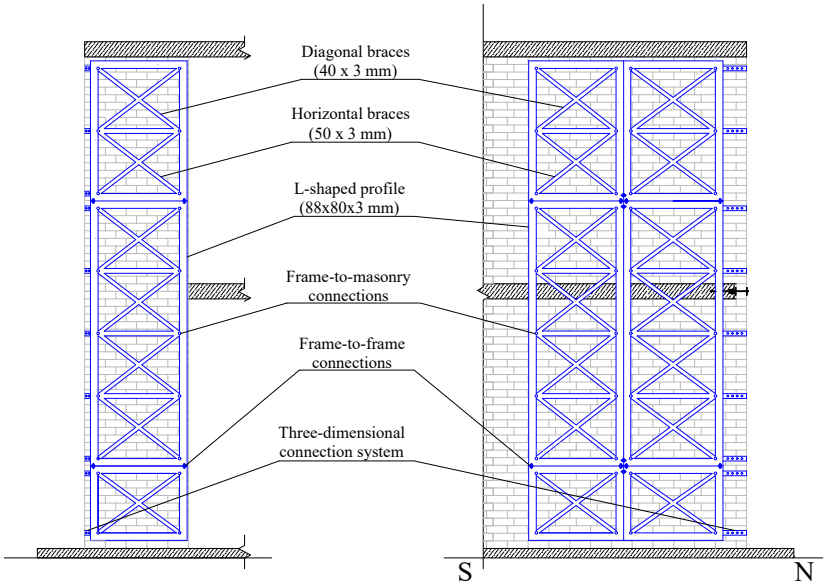
8.7.1. Retrofit schemes and design rationale

A modular steel-frame exoskeleton offers a minimally invasive retrofit strategy for URM buildings, in which prefabricated steel modules are mounted on the exterior surfaces of existing walls and interconnected to form a continuous bracing system. The Resisto 5.9 system, developed by Progetto Sisma s.r.l., consists of galvanised steel modules with L-shaped border members and plate-section diagonal bracing, connected to one another with class 8.8 bolts and fastened to the masonry components using chemical anchors and threaded bars. The system integrates seismic and energy retrofit functions within a single intervention.

Damiani *et al.* [21] investigated the in-plane lateral performance of this system using DEM, calibrated against quasi-static cyclic tests [8] conducted at the EUCENTRE laboratory on full-scale piers of two masonry typologies representative of Italian residential construction, namely solid clay brick with lime mortar in a header bond pattern and hollow clay units with cement-lime mortar in a Flemish bond pattern. The in-plane response of the system has been reproduced at the component scale using the MASON contact model in Section 6.4, confirming that the modelling framework adopted in this thesis captures the pier-level lateral capacity and failure mode of the retrofitted masonry. Both the original experimental campaigns and the component-scale validation focused exclusively on isolated in-plane pier behaviour on clay-based masonry typologies, and the connections between the steel frame, the RC floors, and the orthogonal walls were not included in the tested configurations.

The configuration adopted for TUD-BUILD-1, shown in Figure 8.17, extends the system to a full-façade layout with three-dimensional wall-intersection connections and multi-storey frame continuity. The Resisto 5.9 system specification requires a clearance of 100 mm to 150 mm between the masonry surface and the steel frame, consistent with the configuration adopted in the pier-scale tests reproduced in Section 6.4. The façade dimensions of TUD-BUILD-1 do not accommodate this clearance at either the west or the east piers. The frame stand-off from the masonry is therefore reduced, as illustrated in Figure 8.17A, and the three-dimensional connection at each wall corner is realised through two class 8.8 M12 bolts that transfer force between the in-plane and the out-of-plane frames at the available offset. The nominal frame plan dimension is retained on the west façade, whereas the frame length on the east façade is reduced by half to fit within the narrower pier of 662 mm. The west wall view in Figure 8.17B displays a reduced

layout in which the symmetry-side frame is omitted, which produces an apparent offset of the out-of-plane frame relative to the wall centreline. The configuration comprises five modular frames distributed along the 5.2 m span of the west wall.



(A) West façade retrofit scheme (Resisto) (B) West wall view (facing East) (Resisto)

Figure 8.17. Resisto 5.9 modular steel-frame retrofit layout for the exterior of the west façade and west wall of TUD-BUILD-1

Within this configuration, the frames are connected to the surrounding structure through four distinct interface types, each associated with a different level of experimental evidence. The frame-to-masonry connection is made with chemical anchors using 14 mm class 8.8 threaded bars. Its behaviour was characterised in the EUCENTRE campaign [22] through monotonic pull-out and shear tests on solid clay brick and hollow clay unit components, and these results were used to determine the properties adopted in the model. No equivalent anchor characterisation is available for calcium silicate masonry, the unit type modelled in TUD-BUILD-1. The anchor capacity in calcium silicate may differ from that in solid clay due to differences in unit tensile strength and bond behaviour, so the clay-derived characterisation is adopted as a proxy for the calcium silicate interface in the model and treated as a modelling assumption.

The vertical elements of the Resisto frame are designed as continuous members across the full height of a building's pier. They remain uninterrupted even as they pass through the first-floor slab band, adhering to the in-plane flexural-resistance criterion detailed in the EUCENTRE numerical report [23]. This criterion allows designers to account for an increase in flexural strength ($\Delta M_{u,r}$) at intermediate floors, provided there is vertical continuity of reinforcement between levels. This strength increment can be claimed even without a direct mechanical connection to the floor band itself. However, if the

reinforcement is not continuous between floors and lacks a direct connection to the floor band, the increment must be taken as zero ($\Delta M_{u,r} = 0$) [23].

The physical logic for this relies on the transmission of axial forces along these continuous vertical frames. These forces are anchored in the masonry above and below the flexural cracks that typically form at pier ends. This continuity allows the gravity load and reaction from the upper storeys to act as a stabilising force, countering the "rocking" motion at the base of the pier on the floor below. Cutting the vertical members at the slab level would disrupt this load path, violating the performance standards defined in the report. Furthermore, this design aligns with practical building-scale installations, where bolted splices are placed away from floor level to avoid the highest flexural stress area.

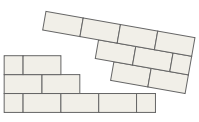
The frame-to-RC anchorage at the floor levels and foundation draws on the design concept proposed in the EUCENTRE report [22] (Figures 2.5 and 2.6 therein) and was tested at the pier scale on specimens RCBPS01 and RCBPS02, in which the steel modules were connected to both the RC foundation and to the top loading beam. These tests demonstrated that the foundation-connected configuration modified the pier response relative to the variant without reinforced concrete anchorage, particularly in terms of the rocking restraint at the pier base. At the building scale, the Resisto 5.9 configuration adopted for TUD-BUILD-1 requires anchorage at both the RC foundation and the precast RC floor slabs. Only the foundation connection has a direct experimental counterpart in the tested specimens. The frame-to-precast-slab anchorage is outside the scope of the EUCENTRE cyclic campaign, and its load-transfer behaviour depends on the grouted joint between adjacent slabs and on the mortar bed joint at the slab-to-wall interface.

The two-bolt three-dimensional connection at each wall corner, shown in Figure 8.17 and derived from the schematics in Figure 2.4 of the EUCENTRE report [22], was not included in any of the cyclic pier tests, which were all conducted on isolated piers. Its role in restraining the out-of-plane overturning of the transverse walls is therefore based on the design intent of the system and not on experimental force-displacement behaviour.

The differences in masonry typology, specimen scale, and the untested frame-to-floor-slab anchorage define the knowledge gap addressed by the present assessment. In the absence of direct experimental backing for the frame-to-floor-slab interface, the building model is calibrated through a pushover sensitivity study, in which the anchored and unanchored variants bound the response and the yield plastic moment at the frame-to-reinforced-concrete interface is reduced relative to the nominal design value to reflect the absence of a cyclic test reference for this connection detail. The calibration results are reported in Section 8.7.3.

8.7.2. Numerical modelling setup for the retrofitted configurations

The retrofit elements are introduced into the TUD-BUILD-1 deformable-block model as additional structural components, leaving the masonry discretisation, joint constitutive parameters, and damping configuration unchanged. All masonry properties follow the values in Table 8.2. The same gravity equilibrium procedure and sequential IDA protocol adopted for the unreinforced case are retained. Therefore, any observed differences in the dynamic response are attributable to the retrofit intervention. The retrofit system is represented using the structural element library in 3DEC, which provides beam finite-element types that couple to the faces and nodal points of deformable blocks. This



coupling requirement is the reason for adopting the deformable-block configuration throughout the dynamic analyses, as established in Section 8.6.

The numerical idealisation of the Resisto 5.9 system is shown in Figure 8.18. Individual steel frame modules are assigned distinct colours to distinguish their spatial extent across the building elevation. The modules are applied to external faces of the pier walls and the transverse walls across both storeys, providing lateral resistance in the loading direction while restraining out-of-plane overturning of the transverse walls.

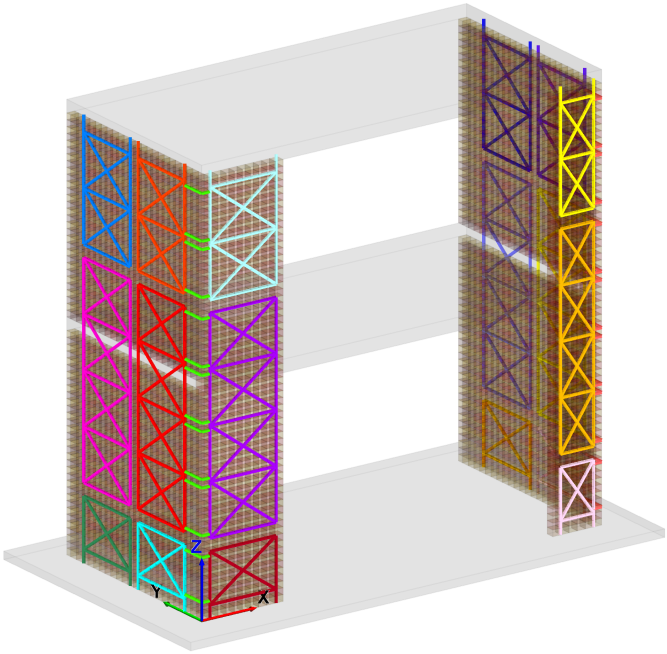


Figure 8.18. Discontinuum model of TUD-BUILD-1 retrofitted with the Resisto 5.9 system. Individual steel frame modules are distinguished by colour.

Similar to the wall-level validation in Section 6.4, the steel frame members are modelled as one-dimensional beam elements with linear elastic material behaviour ($E = 210\,\text{GPa}$, $\nu = 0.3$, $\rho = 7850\,\text{kg m}^{-3}$). The diagonal and horizontal braces are thin plate sections susceptible to buckling under compression. To capture this behaviour, sinusoidal geometric imperfections of 1 mm amplitude are pre-imposed at mid-length of each brace prior to the dynamic analyses, following the approach adopted by Damiani *et al.* [21].

A representative single-bay strip on the wider west pier is shown in Figure 8.19, which maps the four connection types of the Resisto 5.9 system to their corresponding numerical idealisation. The four types are: (1) the frame-to-masonry chemical anchors, (2) the frame-to-frame bolted shear connections at module corners, (3) the three-dimensional corner connections at slab elevations where the pier frame meets the orthogonal wall frame, and (4) the frame-to-RC anchorages at the foundation. Types 2

and 3 share the same rigid-link treatment in the model and are therefore presented together with a single description below.

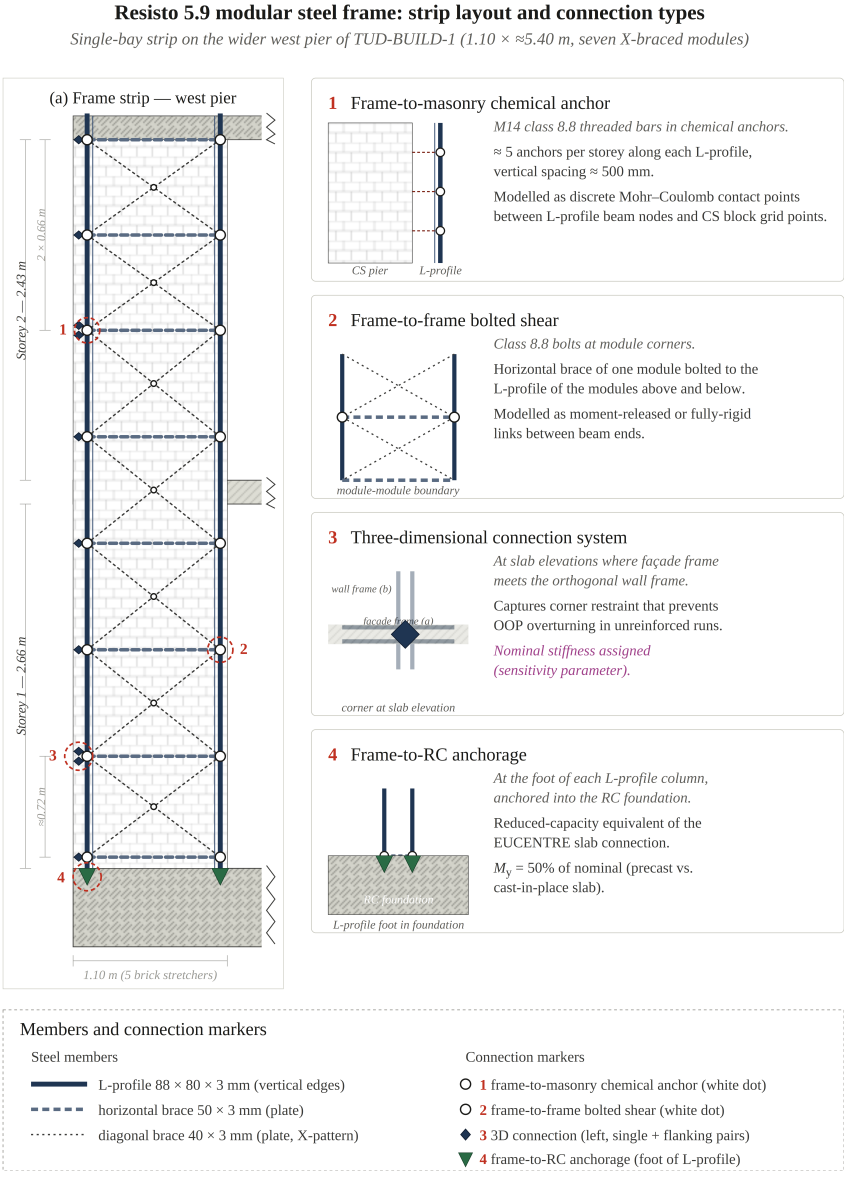


Figure 8.19. Resisto 5.9 strip layout and connection types on the wider west pier of TUD-BUILD-1.

The material properties and connection parameters are summarised in Table 8.7. The

mechanical interaction between the steel frames, the masonry, and the RC floor slabs is represented by nonlinear structural links placed at the actual anchor and bolt locations. Four link types are employed, labelled 1–4 in Figure 8.19. The frame-to-masonry links (type 1) are assigned a shear-yield constitutive law defined by the multi-linear force-displacement path comprising an initial elastic branch, a yield plateau, and a softening phase [21] (Figure 6.37). The input parameters are fitted to the median curve from the EUCENTRE pull-out and shear test data in Manzini *et al.* [22]. The frame-to-frame bolted connections (type 2) and the three-dimensional corner links (type 3) are both modelled as rigid node-to-node links, with high initial stiffness to enforce kinematic compatibility between adjacent modules without introducing artificial flexibility at the inter-module interfaces.

The frame-to-RC floor connections (type 4) require a more detailed representation to capture the rocking behaviour of the steel frame base relative to the RC foundation. At each anchor location, it is built from two links in series, connected by an intermediate node coincident with the frame base node. The first link, a node-to-node link between the frame base node and the intermediate node, represents the bolted base plate. It enforces translational compatibility rigidly but permits rocking through a normal-yield law on the rotational degree of freedom, with the yield moment set to half of the nominal design resistance of the base plate. The second link, a node-to-zone link from the intermediate node to the underlying RC zones, represents the anchorage into the slab, with a normal-yield law in the axial direction and a shear-yield law in the lateral directions. Arranging the two in series, instead of combining them in a single link, keeps the rocking and the anchorage independent and prevents the artificial strength enhancement that parallel load paths would produce.

The retrofit elements introduce additional degrees of freedom that reduce the critical timestep for explicit integration by approximately 15 % relative to the unreinforced model. As noted in Section 8.7.1, the frame-to-masonry connection parameters were characterised on solid clay brick and hollow clay unit substrates; no equivalent data exist for calcium silicate masonry. Furthermore, the frame-to-RC-slab connection topology and the three-dimensional corner links have not been subjected to cyclic testing in configurations directly comparable to the TUD-BUILD-1 geometry. The building-scale predictions for this configuration are therefore interpreted as indicative of the system's potential instead of as validated performance estimates.

8.7.3. Pushover calibration result

The numerical setup described in Section 8.7.2 involves uncertainties in calibrating the frame-to-RC connections at both the foundation and the second-floor precast RC slab. The adopted two-stage series topology has been validated against EUCENTRE component-scale tests on cast-in-place RC loading beams [22]. However, at the building scale, the bond-anchor performance of these connections for calcium silicate masonry remains unverified.

To address this, a monotonic pushover study is conducted prior to the incremental dynamic analysis. First, the sensitivity of the global force-displacement response to connection assumptions is evaluated by comparing two limiting retrofit configurations. Next, the pushover envelope is benchmarked against the quasi-static cyclic envelope

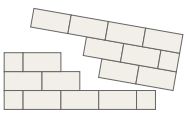
Table 8.7. Material and connection parameters adopted for the Resisto 5.9 modular steel frame based on numerical calibration.

Category	Parameter	Symbol	Value
Steel material	Young's modulus	E_s	210 GPa
	Poisson's ratio	ν_s	0.30
	Density	ρ_s	7850 kg m^{-3}
	Yield strength	f_y	350 MPa
	Brace imperfection amplitude[d]	δ_{imp}	1.0 mm
Frame-to-masonry links[a]	Shear stiffness	k_s	7.5×10^6 N m^{-1}
	Cohesion (Yield force)	F_y	11.0 kN
	Normal stiffness	k_n	25.0×10^6 N m^{-1}
	Ultimate tension	$F_{t,u}$	11.0 kN
	Ultimate compression	$F_{c,u}$	110.0 kN
RC boundary links[b]	Shear stiffness	$k_{s,RC}$	7.5×10^6 N m^{-1}
	Cohesion (Yield)	$F_{y,RC}$	11.0 kN
	Normal stiffness	$k_{n,RC}$	50.0×10^6 N m^{-1}
	Ultimate tension	$F_{t,RC}$	11.0 kN
	Ultimate compression	$F_{c,RC}$	110.0 kN
Frame base: rocking link	Yield moment[c]	M_y	217.5 N m
	Translational DOF	–	Rigid
Frame-to-frame / corner links	Idealisation	–	Rigid

[a] Based on median EUCENTRE pull-out and shear test data [22].
[b] Specific parameters for anchors connected to reinforced concrete elements, characterised by increased normal stiffness ($k_{n,RC}$).
[c] Half of the nominal design resistance of the base plate, adopted for the anchored variant.
[d] Sinusoidal geometric imperfection imposed at the mid-length of the diagonal and horizontal braces, following Damiani et al. [21].

of the unreinforced specimen. This comparison provides a reference for assessing retrofit-induced improvements in lateral capacity and post-peak softening. The monotonic protocol isolates the connection's effect, eliminating the influence of rate-dependent and inertial factors that complicate seismic response. Two configurations were compared against the quasi-static cyclic experimental envelope of the unreinforced specimen, as presented in Figure 8.20.

The variant without RC anchors excludes the frame-to-foundation and frame-to-



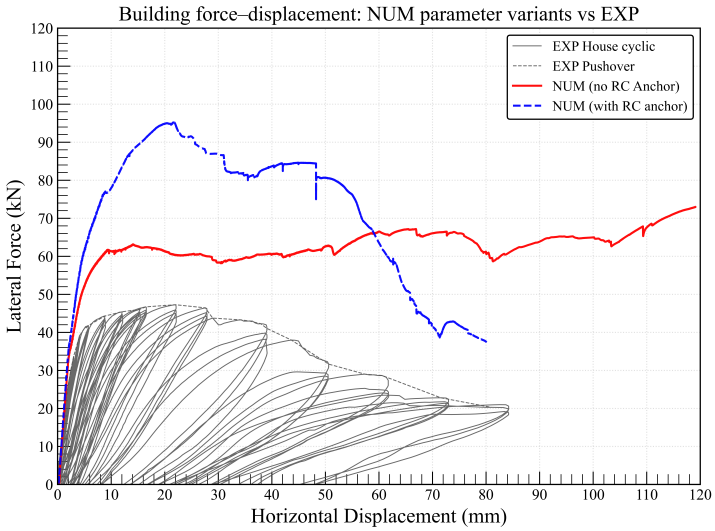


Figure 8.20. Force-displacement comparison of the pushover analysis of TUD-BUILD-1 retrofitted with the Resisto 5.9 modular steel frame

second-floor-slab connections entirely, in line with the retrofitted pier tests validated in Section 6.4, so the exoskeleton transfers force to the building only through the chemical anchors to the masonry walls. The frame has no base fixity. The variant with RC anchors retains both connections but reduces the yield plastic moment at these interfaces to half of the nominal design value [22]. This reduction is an assumed engineering penalty, as it reflects the expected lower capacity when anchoring to RC foundation and precast RC slabs, for which no cyclic test reference exists, compared with the cast-in-place loading beams tested in the EUCENTRE campaign. The factor of one-half is not calibrated against test data; hence, its effect on the identified near-collapse intensity has not been quantified.

The comparison highlights critical aspects of the system's structural behaviour. Both model variants exceed the experimental unreinforced envelope at peak capacity. The variant with RC anchors reaches a higher peak strength because the anchors provide base fixity, but the failure of these connections produces a brittle post-peak transition. The variant without RC anchors has no base fixity and behaves as a rocking system, close to the unreinforced building, in which the capacity gain over the unreinforced case comes from the larger mass mobilised in the rocking mechanism. Its peak strength is lower, but it sustains a stable plateau, so its main improvement over the unreinforced building is the very high, effectively unlimited, deformation capacity rather than strength. Together, the two curves bracket the possible physical response. The real building, with partial and degrading engagement of the RC connections, would peak between 62 and 95 kN and then settle towards the unanchored rocking plateau as the connections degrade.

The deformed shapes at the end of the pushover (Figure 8.21) further illustrate the difference. In the anchored variant (Figure 8.21A), the frame base is restrained and the

beam displacement field grows progressively from the foundation upward. In contrast, the unanchored variant (Figure 8.21B) allows the frame base to displace freely; this loss of restraint is accompanied by more pronounced out-of-plane (OOP) movement of the transverse wall. These results show that the frame-to-RC connections restrain the frame base. With the connections, the walls deform in a mode anchored to the foundation, whereas without them, they tilt in a near-rigid rocking mode at the base. Neither variant reaches out-of-plane overturning, so the connections reduce the rocking at the base without being required to prevent out-of-plane collapse in this case.

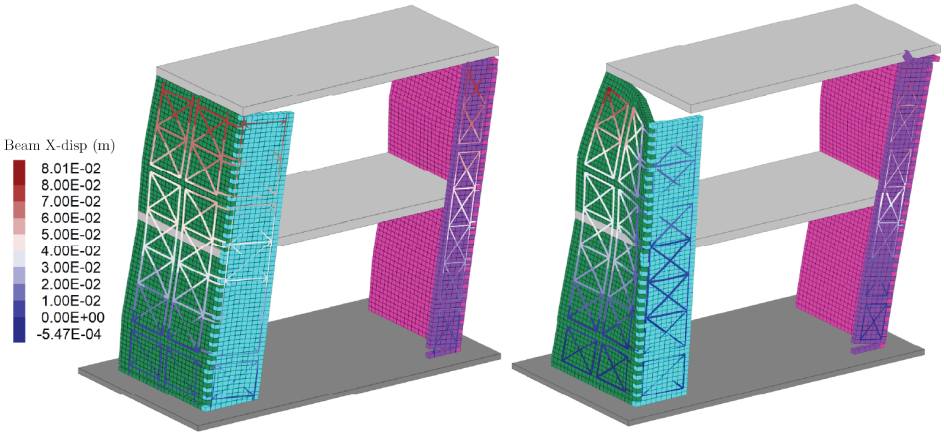


Figure 8.21. Deformed shape of the pushover analysis of TUD-BUILD-1 retrofitted with Resisto 5.9 (Def factor: 10)

The anchored variant is adopted for the dynamic analysis. This variant represents the fully designed system, with both reinforced-concrete connections active, and the halved yield moment at these interfaces carries the penalty for the untested precast-slab detail. The unanchored variant omits a load path that the design intends to engage, so it understates the system as built. The selection fixes the upper bound of the bracket for the dynamic assessment. The near-collapse intensity reported in Section 8.7.4 and the retrofit gain derived from it are therefore upper-bound estimates with respect to the connection assumption. The unanchored response remains the lower bound, towards which the real system would migrate as the connections degrade.

8.7.4. Incremental dynamic analysis results

This subsection presents the dynamic response of the Resisto-5.9 retrofitted model under the sequential IDA protocol. The calibrated configuration identified in Section 8.7.3 is retained, with the frame-to-RC connections preserved at the foundation and at the second-floor slab and with the reduced yield plastic moment adopted at these links. The protocol mirrors the one applied to the unreinforced specimen in Section 8.6, so that response differences are attributable to the retrofit intervention.

Peak relative displacement vs PGA

The IDA used the same ground motion record and scaling protocol as the unreinforced model in Table 8.5. The comparison is shown to the near-collapse intensity of each model, 125 % SF (PGA 0.39 g) for the unreinforced model (UR), one increment below its collapse at 150 % SF, and 225 % SF (PGA 0.70 g) for the Resisto-retrofitted model (hereafter Resisto-R), whose collapse at 250 % SF is examined in the failure mechanism discussion below. Peak relative displacements were extracted at eight sensor locations (first-floor and second-floor slabs, east and west walls, in-plane and out-of-plane directions), positioned identically in both models. The results are compared in Figure 8.22.

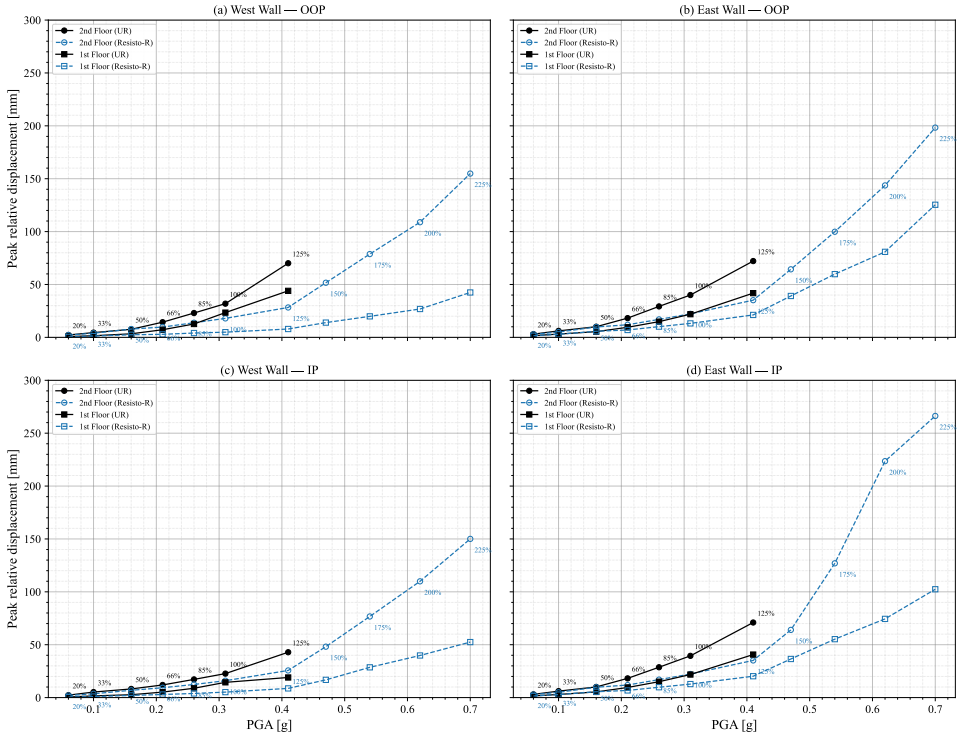


Figure 8.22. Peak displacement comparison between the unreinforced and Resisto-retrofitted TUD-BUILD-1 against PGA.

Below 0.3 g (100 % SF), the UR and Resisto-R response overlap in all four panels, consistent with the negligible elastic-stiffness contribution of the modular frame established in Section 8.7.3. Above this threshold, the UR response steepens as the ground-storey diagonal crack band develops, whereas the Resisto-R response continues with a smaller slope governed by the rocking-controlled in-plane mode.

At the unreinforced near-collapse intensity (125 % SF, PGA ≈ 0.39 g), the in-plane second-floor displacement is reduced from approximately 42 mm to 26 mm on the west wall and from approximately 71 mm to 36 mm on the east wall. The out-of-plane

reductions at the same intensity are of comparable or larger magnitude, reflecting the out-of-plane bracing provided by the modular frame.

The second-floor demand exceeds the first-floor demand in all four panels and both configurations. The east-wall in-plane second-floor demand exceeds the west-wall in-plane demand above 0.3 g, attributable to the narrower east pier. The retrofit attenuates the demand while preserving these spatial patterns, so the modular frame scales the deformation field without redistributing it across the elevation.

The Resisto-R model remains stable through the unreinforced collapse range and up to its own near-collapse intensity of 225 % SF (PGA ≈ 0.70 g). At this intensity, the east-wall in-plane second-floor sensor reaches approximately 265 mm, marking the onset of block detachment at the wall-to-slab interfaces in the second storey. Whether the stability beyond the unreinforced near-collapse intensity reflects a physical reserve or an artefact of the unmodelled anchor degradation cannot be confirmed without experimental data.

Interstorey drift ratio versus PGA (IDA curves)

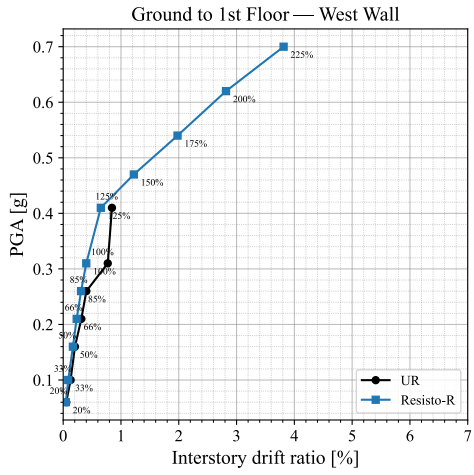
The in-plane interstorey drift ratio is computed at each intensity level as the peak absolute value of the relative horizontal displacement between two consecutive floor levels, normalised by the clear interstorey height (Equation (8.3)). Figure 8.23 reports the resulting IDR-PGA relationships for the west and east piers at the ground-to-first-floor and first-to-second-floor levels.

The empirical drift caps adopted in Figures D.2 and 8.13 for the unreinforced case, comprising the EC8-3 (2005) band, the prEN 1998-3 (2023) threshold, and the Messali and Rots [18] mean band, are not reported in Figure 8.23. These formulations were derived from cyclic compression-shear testing of unreinforced masonry piers and have not been recalibrated for piers strengthened with externally applied modular steel frames. Component-scale results [23] indicated that the in-plane drift capacity of retrofitted piers exceeds that of unreinforced piers, so the unreinforced caps would represent a conservative reference instead of a calibrated retrofit-specific limit.

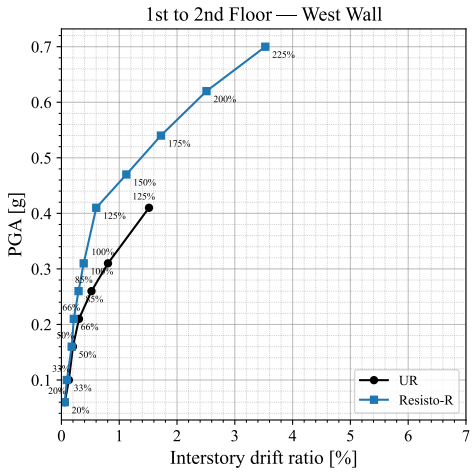
Three of the four panels exhibit the same qualitative pattern. Below 0.3 g (100 % SF), the UR and Resisto-R curves overlap, consistent with the negligible elastic-stiffness contribution of the modular frame. Above this intensity, the two curves diverge as the masonry enters the nonlinear range, with the Resisto-R curve reaching each PGA at lower drift than the UR curve and extending to higher PGA without the steepening of the unreinforced response.

The UR curve steepens towards a near-vertical slope as it reaches its near-collapse intensity at 125 % SF (0.39 g), beyond which the unreinforced model loses stability at 150 % SF, as reported in Section 8.6. The Resisto-R curve shows no comparable steepening within the range examined and continues with a finite slope to 225 % SF at 0.70 g. The in-plane lateral capacity of the retrofitted pier is therefore not exhausted at the unreinforced near-collapse intensity, which the failure mechanism later explains.

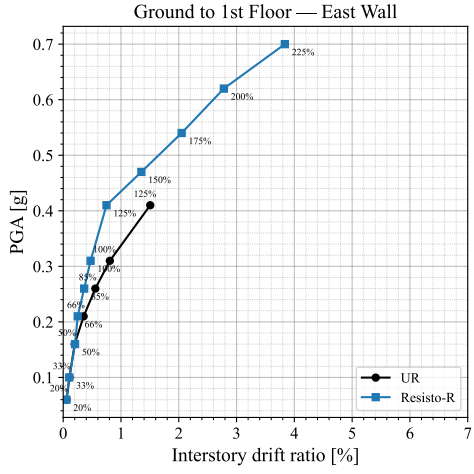
The east-wall first-to-second-floor panel (Figure 8.23D) departs from this pattern above 125 % SF, where the Resisto-R curve turns nearly horizontal, and the drift grows at almost constant PGA. The masonry block carrying the second-floor East sensor displaces substantially at this stage, associated with block detachment at the wall-to-slab interface, so the readings at that location are a local artefact and do not represent the storey-level



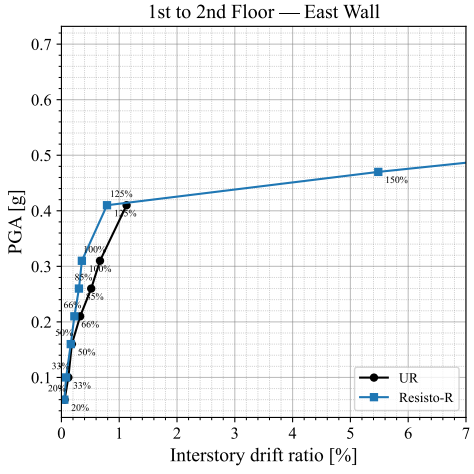
(A) West wall – Ground to 1st floor



(B) West wall – 1st floor to 2nd floor



(C) East wall – Ground to 1st floor



(D) East wall – 1st floor to 2nd floor

Figure 8.23. EDP vs IM results for the west and east piers (Unreinforced vs Resisto-R).

drift.

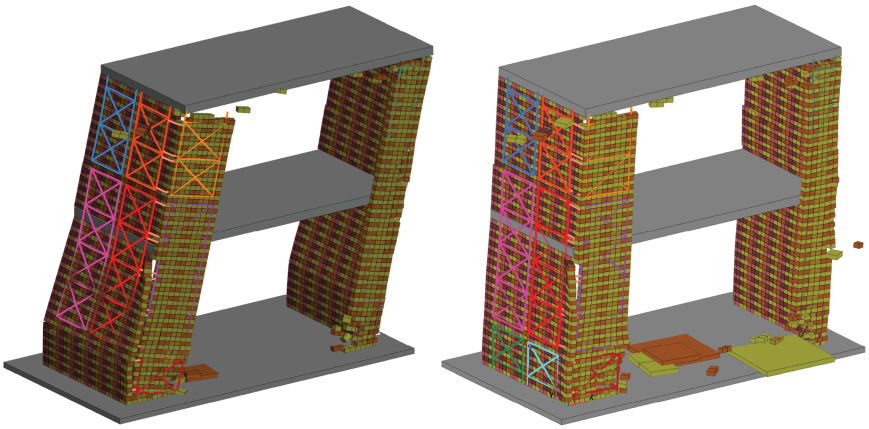
The storey partition is wall-dependent. In the east wall, the ground storey carries the larger drift in both configurations, with an upper-to-ground ratio near 0.75 at matched intensity, so the frame leaves the east partition unchanged. On the west wall, the two storeys exhibit comparable drift up to 100 % SF in both models. The unreinforced west wall then localises in the upper storey at its near-collapse intensity, a concentration that the retrofitted model does not develop. The upper-storey curves above the unreinforced near-collapse intensity are governed by the block-detachment artefact and are not

interpreted.

Failure mechanism evolution

The deformed configuration of the retrofitted TUD-BUILD-1 specimen at the end of the 225 % and 250 % intensity levels, corresponding to the PGA of 0.7 g and 0.78 g, respectively, is reported in Figure 8.24 with a magnification factor of 10 applied to the displacement field. At these intensities, several joints have opened, and individual units have lost contact, so the apparent large fragments are detached units shown at their true size but ten times farther from their origin than they have moved, while the deformable blocks still in contact are drawn stretched. The steel frame is likewise locally hidden when the amplified block surfaces move in front of it. Neither effect alters the analysis.

The corresponding deformed configuration of the unreinforced specimen at 125 % and 150 % intensity, reported in Figure 8.14 of Section 8.6, serves as the reference state. The comparison establishes the qualitative assessment of the collapse mode induced by the Resisto retrofit and provides the interpretive framework for the IDA results presented in the following subsections.



(A) Deformed shape at the end of 225%IM (B) Deformed shape at the end of 250%IM

Figure 8.24. Deformed configuration of the retrofitted TUD-BUILD-1 specimen at the end of 225 % and 250 % intensity. A magnification factor of 10 is applied to the displacement field. Detached units and distorted blocks are amplified accordingly, and the steel frame is locally hidden where the amplified block surfaces occlude it; neither effect alters the analysis.

At 225 % SF (PGA=0.7 g, Figure 8.24A), the modular frame retains structural integrity over the full elevation of the west pier. The continuous frame configuration couples the ground-storey and upper-storey portions of the pier into a single slender pier from the foundation to the second-floor slab. No coherent stepped diagonal crack band is observed in the ground-storey piers. Masonry damage at the pier base is flexural, with horizontal bed-joint opening on the tension side and crushing at the compressed toes of the west pier. The continuous pier rotates as a rigid body about the foundation

interface, so the dominant in-plane mode is flexural and rocking-controlled rather than shear-controlled. Damage at the pier-to-transverse-wall corner is evident, with brick separation along the upper portion of the ground-storey corner indicating that the eventual collapse trigger has been activated.

At 250 % SF (PGA=0.78 g, Figure 8.24B), the coupled in-plane and out-of-plane failure mechanism of the retrofitted pier is fully developed. The modular frame delays in-plane damage progression but does not suppress it, consistent with experimental observations at the component level for the retrofitted piers in Section 6.4. The longitudinal piers continue to develop rocking and toe crushing at the base, with localised block detachment at the compressed toes, which remains confined by the modular grid. The progressive pier-base damage reduces the lateral and corner restraint provided to the adjacent transverse walls, causing them to overturn as near-rigid panels rather than through one-way or two-way out-of-plane bending. Stability is lost due to the combined effect of rocking-induced toe crushing of the pier and rigid-panel overturning of the transverse walls, which can no longer provide lateral resistance once the corner restraint is exhausted. The qualitative assessment of the failure mechanism indicates that the indicative near-collapse limit occurs at 225 % SF, with a PGA of 0.7 g.

Comparison with the unreinforced configuration in Figure 8.14 shows that the collapse region remains localised at the compressed regions of the ground-storey pier and the corner zone between the pier and the transverse walls. Furthermore, the transverse-wall overturning remains a secondary consequence of in-plane damage at the ground-storey pier base, not an independent failure mode. The retrofitted configuration improved the responses as follows. The diagonal stepped cracking that defines the unreinforced ground-storey response, fully developed at 125 % intensity in Figure 8.14A, is suppressed in the retrofitted configuration at all intensities up to 225 %. The transverse wall overturning that follows the loss of corner restraint in the unreinforced case manifests as near-rigid-panel rotation in the retrofitted case. The energy dissipation pathway is reconfigured from cumulative damage along the diagonal crack network to mechanisms distributed across the retrofit system and the connection between the masonry, frame, and the RC foundation. The approximate doubling of the intensity required to reach comparable damage states reflects the global capacity gain provided by the retrofit. The detailed quantitative response is examined in the following subsections.

Hysteretic response

The base shear versus second-floor average displacement loops for the unreinforced and Resisto-R configurations are compared in Figure 8.25. The base shear is taken as the sum of the horizontal reactions at the foundation interface, the second-floor displacement is the average of the four corner readings at roof level, and the global drift ratio is normalised by the total pier height $H = H_1 + H_2 = 5.22\,\text{m}$.

The unreinforced loops remain bounded within ±0.4 % drift up to 100 % SF, with peak base shear of approximately 95 kN. The 125 % run extends the positive branch to 1.3 % drift at reduced reaction force, exhibiting the elongated tail that precedes the snap-back observed at 150 % SF and reported in the IDR versus PGA section.

The Resisto-R configuration attains a peak base shear of approximately 120 kN at 150 % SF, an increase of about 25 % over the unreinforced peak. The positive and negative

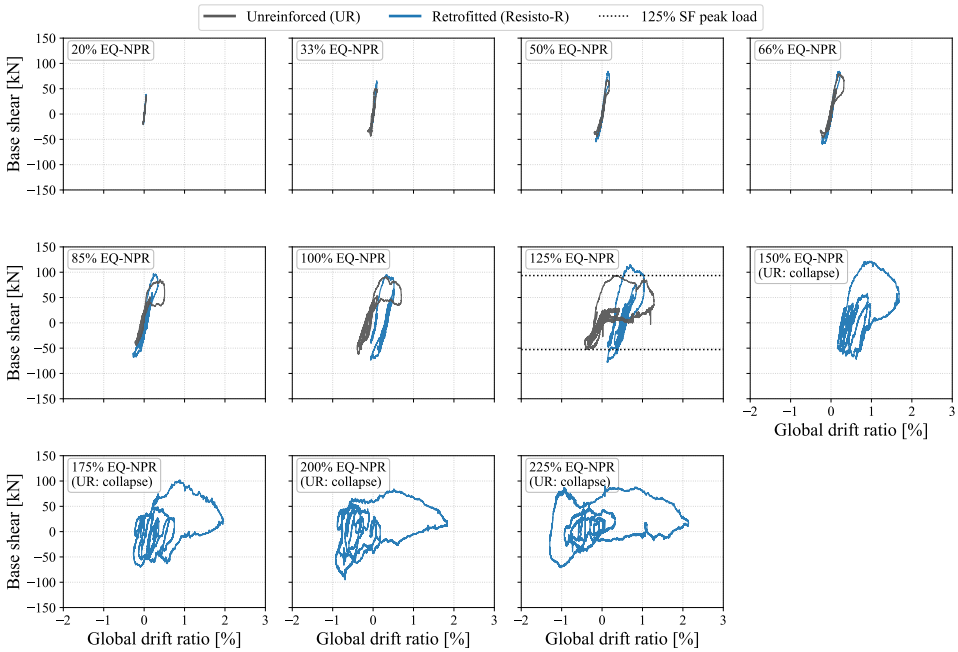


Figure 8.25. Base shear versus second-floor average displacement under the EQ-NPR record, arranged as a grid of intensity levels with the unreinforced (grey) and Resisto-R (blue) configurations overlaid in each cell. Each cell corresponds to a single scale factor, indicated by its label as a percentage of the reference amplitude, so that colour encodes the configuration rather than the intensity; intensity is instead given by the cell position. The base shear is the sum of the horizontal reactions at the foundation interface; the second-floor displacement is the average of the four corner readings at roof level, and the lower axis reports the corresponding global drift ratio, obtained by normalising the roof displacement by the total pier height $H = 5.22\,\mathrm{m}$. Each loop is one complete dynamic run at the stated scale factor. The unreinforced model is shown up to 125 %, beyond which it collapses; cells labelled "UR: collapse" therefore show the Resisto-R loop alone. The Resisto-R model is shown up to 225 %, and the absence of an unreinforced counterpart at higher intensities indicates the collapse margin gained by the retrofit.

drifts at this intensity reach 1.7 % and 1.0 %, respectively, against 1.3 % and 0.4 % for the unreinforced model at its last stable intensity. Both force and displacement capacities are therefore extended by the modular frame, with the relative displacement gain exceeding the relative force gain.

Beyond 150 % SF, the peak base shear of the retrofitted model decreases progressively to approximately 85 kN at 225 % SF, while the displacement variation grows to 2.1 % positive and −1.5 % negative. The reduction of about 30 % in peak resistance over the

150 %-225 % interval places the retrofitted pier on its post-peak softening branch within the examined intensity range.

The cumulative dissipated energy as a function of the maximum global drift achieved at each intensity level is reported in Figure 8.26. The 125 % SF intensity is taken as the assumed collapse limit of the unreinforced configuration, consistent with the loss of stability documented in the IDR versus PGA section.

Up to this collapse limit, the UR and Resisto-R trajectories overlap and reach approximately 20 kN m at 1.3 % maximum drift, indicating that the modular frame does not alter the dissipative response of the pier across the intensity range over which the bare structure remains stable. Between 175 % and 200 % SF, the Resisto-R energy rises from 33 kN m to 50 kN m with negligible advancement of the maximum drift, which remains close to 1.95 %. This near-vertical segment indicates that energy accumulates through repeated cycling at a saturated drift level, not through monotonically increasing deformation, which is the kinematic feature of progressive strength degradation. The subsequent 225 % SF run extends the drift to 2.15 % with a further energy increment of approximately 20 kN m, after which the analysis is terminated.

The near-collapse intensity for the Resisto-R configuration is taken as 225 % SF, the highest scale factor at which the dynamic analysis remained stable (Section 8.7.4). The hysteretic and energy evidence indicates that this stopping point reflects physical degradation instead of a numerical limit. The loops exhibit post-peak strength reduction from 150 % SF upward, and the energy trajectory rises steeply between 175 % and 200 % SF while the maximum drift remains close to 1.95 %, indicating that energy is dissipated through repeated cycling at a saturated drift rather than through increasing deformation. By 225 % SF the configuration is on its post-peak softening branch, consistent with a structure approaching collapse.

8.7.5. Remarks on the performance of the retrofitted building

Given the exploratory scope of this study, it is important to summarise the work conducted, the limitations encountered, and the main conclusions. The TUD-BUILD-1 model was enhanced to include the Resisto 5.9 modular steel frame, represented as a continuous grid across both storeys according to the in-plane flexural-resistance criterion introduced in Damiani *et al.* [23]. The pushover analysis focused the uncertainty in the frame-to-RC connection with two limiting variants, and the anchored variant, which gives the upper bound of the response, was carried forward to the incremental dynamic analysis. Relative to the unreinforced model, the retrofit reduced the displacement demand, preserved the spatial pattern of the deformation field, and raised the near-collapse intensity from 125 % to 225 % SF, a factor of 1.8 that is an upper bound with respect to the connection assumption, while the failure mode remained a coupled in-plane and out-of-plane mechanism.

Several limitations should be addressed in future studies. The current model does not account for cumulative degradation of frame-to-masonry and frame-to-RC anchors under repeated loading, so the observed stability of the retrofitted system beyond near-collapse may be a modelling artefact. Using only a single ground motion also prevents assessment of variability between different seismic events. Additionally, existing drift capacity formulations have not been recalibrated for piers retrofitted with modular

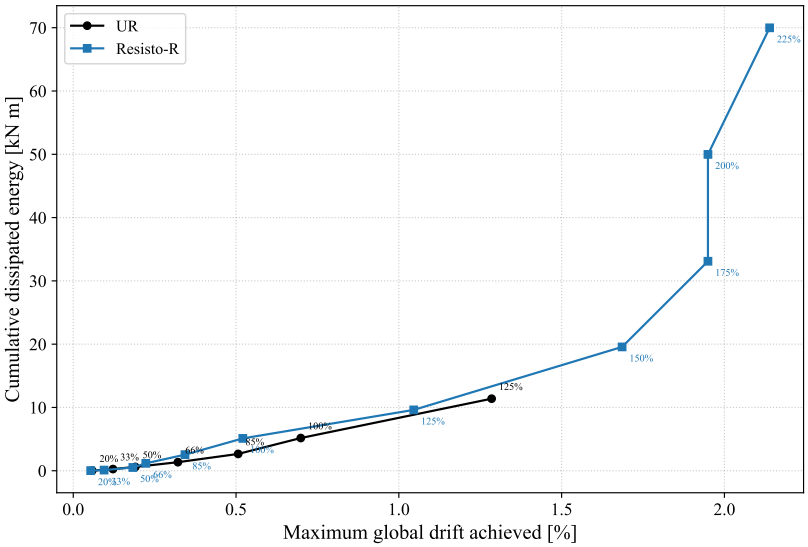


Figure 8.26. Cumulative dissipated energy versus maximum global drift for the unreinforced and Resisto-R configurations.

steel frames; component-scale recalibration is needed before applying these criteria at the building scale.

Finally, these findings are based solely on numerical simulations. While the model has been validated against quasi-static cyclic in-plane loading of the retrofitted piers, there is currently no shake-table data for the retrofitted piers tested out of plane or for the retrofitted building. Therefore, the capacity gain reported here should be regarded as a hypothesis pending experimental confirmation and further validation for other structural types or loading scenarios. These limitations are summarised together with those of the unreinforced analysis in Section 8.8. The damping sensitivity question raised here and in Section 8.6 was addressed in Chapter 7 on smaller benchmark cases. Its conclusions have not been verified at the building scale.

8.8. Summary and conclusions

This chapter extended the proposed MASON contact constitutive model from the material- and component-level validations of Chapters 5 and 6 to the building scale, using the TUD-BUILD-1 specimen as the reference benchmark. Three sequential assessments were conducted, comprising a monotonic pushover that compared rigid and deformable-block idealisations against the experimental envelope, a quasi-static cyclic analysis using the rigid-block configuration that reproduced the full loading protocol, and an incremental dynamic analysis (IDA) using the EQ-NPR record applied to both the unreinforced and the retrofitted configuration equipped with the modular steel exoskeleton.

In the monotonic pushover, both rigid and deformable-block idealisations reproduced the experimental peak capacity within ±1.4 %. This finding indicates that the global strength of TUD-BUILD-1 is governed more by the joint constitutive response than by the deformability of the blocks. The rigid-block configuration provided a closer match to the experimental envelope in terms of peak strength and cumulative work, and reduced the wall-clock runtime from three days to five hours on identical computational resources. Nevertheless, deformable blocks were retained for the dynamic and retrofit analyses because the structural elements representing the steel frame can only be coupled to deformable meshes in the adopted DEM platform.

The quasi-static cyclic simulation reproduced the main features of the TUD-BUILD-1 hysteretic response. The numerical loops captured the post-peak degradation, the asymmetry between the positive and negative loading directions, and the storey drift partitioning observed during the experiment. The local damage field reproduced the coupled in-plane to out-of-plane mechanism documented at the west pier-to-wall corner. The remaining discrepancies were confined to lower post-peak dissipation in the numerical loops, a step-like force drop at load reversal due to discrete contact re-engagement, and later engagement of the transverse walls than observed in the test.

The IDA of the unreinforced configuration identified the near-collapse intensity at 125 %SF, corresponding to a PGA of 0.39 g. The identification was supported by the exceedance of the EC8-3 (2023) drift threshold at 125 % SF, with the more permissive cantilever bound and the Messali and Rots mean band reached between 150 % SF and 175 % SF, together with visual evidence of fully developed diagonal cracking with corner detachment in the deformed configuration. Under dynamic loading, out-of-plane damage in the transverse walls developed earlier and more diffusely than in the test, where the transverse walls engaged in the pre-peak phase through extensions of the pier corner cracks, and earlier than in the quasi-static simulation, which engages them only after the in-plane discontinuity forms. As assessed in Section 8.6.6, the contributions of inertial loading, the block idealisation, and the mass-proportional damping to this early engagement cannot be separated with the available evidence, so it is reported as a model observation. Both regimes nevertheless converged to the same final damage state, with collapse triggered by exhaustion of in-plane drift capacity in the ground-storey piers.

The retrofit assessment using the Resisto 5.9 modular steel-frame system extended the near-collapse intensity to approximately 225 % SF (PGA 0.7 g), consistent with the in-plane capacity gain reported at the component scale in Section 6.4. The retrofit did not change the collapse sequence, in which damage at the ground-storey pier base removed the corner restraint and the transverse walls overturned as rigid panels. It changed the in-plane mode of the piers from diagonal shear cracking to flexural rocking with toe crushing. The retrofit also reduced the peak displacement demand and delayed the onset of collapse. In both configurations, it combined in-plane rocking with toe crushing in the ground-storey piers and out-of-plane rigid-panel overturning of the transverse walls. The retrofit reduced the peak displacement response and delayed the onset of this mechanism without changing its type.

Across these three assessments, the MASON contact model simulated the full range of building-scale responses with a single parameter set, calibrated at the material and component scales in Chapters 5 and 6 and transferred to the building scale without

recalibrating the strength parameters. The same constitutive formulation reproduced the hysteretic loops, the pinching, and the damage localisation under quasi-static cyclic loading, followed the joint-governed degradation into the collapse kinematics under dynamic excitation, and remained stable when coupled with the beam elements and nonlinear links of the retrofit system. It also captured the coupled in-plane and out-of-plane interaction at the pier-to-wall corners in both loading regimes, the feature that governs the failure of this typology. This consistency across loading regimes, block idealisations, and structural configurations supports the applicability of the MASON formulation to the seismic assessment of URM buildings.

Several limitations are acknowledged. The dynamic analyses adopted a single ground-motion record and a single damping configuration (3 % mass-proportional), so the identified near-collapse intensities are conditional on these choices and do not reflect record-to-record variability. The mass-proportional formulation, selected on computational grounds given the cost of repeated dynamic runs at building scale, damps absolute velocity and is therefore expected to interact differently with rigid-body-dominated out-of-plane kinematics than with shear-controlled in-plane modes. Whether the early out-of-plane activation observed under dynamic loading reflects the inertial demand or is partly an artefact of the damping formulation cannot be resolved without a damping-sensitivity study at the building scale, which was not undertaken in the present work. The damping study in Chapter 7 constrains this uncertainty but does not eliminate it. Displacement-based predictions on benchmark components were insensitive to the damping scheme, yet a building-scale verification remains open. The frame-to-RC-slab anchorage and the three-dimensional corner connections of the Resisto 5.9 system have not been experimentally characterised on calcium silicate masonry, so the retrofit performance reported here is interpreted as indicative, pending experimental characterisation. The drift-capacity formulations adopted as near-collapse thresholds were calibrated on unreinforced piers under quasi-static cyclic protocols and have not been recalibrated for retrofitted configurations or for dynamic loading rates.

Bibliography of Chapter 8

[1] M. Haindl, I. F. C. Smith and K. Beyer. 'A database of shake-table tests conducted on unreinforced masonry buildings'. In: *Earthquake Spectra* 41.1 (2025), pp. 931–954. DOI: 10.1177/87552930241268214. URL: https://doi.org/10.1177/87552930241268214.

[2] A. Aşıkoğlu, G. Vasconcelos, A. Barontini and P. B. Lourenço. 'Quasi-static test on half-scale modern unreinforced masonry building with plan irregularity'. In: *Bulletin of Earthquake Engineering* 23 (Nov. 2025), pp. 6393–6435. DOI: 10.1007/s10518-025-02275-x. URL: https://doi.org/10.1007/s10518-025-02275-x.

[3] G. Ravenshorst, R. Esposito, R. Schipper, A. Tsouvalas and E.-M. Lourens. *Quasi-static Cyclic Pushover Test and Dynamic Identification Test on the Assembled Masonry Structure at TU Delft*. Final report. Project number C31B60, Version 3, Status: Final. Client: Nederlandse Aardolie Maatschappij B.V. Delft, The Netherlands: Delft University of Technology, Faculty of Civil Engineering and Geosciences, 10th June 2016.

[4] A. M. D'Altri, F. Messali, J. Rots, G. Castellazzi and S. de Miranda. 'A damaging block-based model for the analysis of the cyclic behaviour of full-scale masonry structures'. In: *Engineering Fracture Mechanics* 209 (Mar. 2019), pp. 423–448. ISSN: 00137944. DOI: 10.1016/j.engfracmech.2018.11.046.

[5] P. B. Lourenço and J. G. Rots. 'Multisurface Interface Model for Analysis of Masonry Structures'. In: *Journal of Engineering Mechanics* 123.7 (July 1997), pp. 660–668. ISSN: 0733-9399. DOI: 10.1061/(ASCE)0733-9399(1997)123:7(660).

[6] E. Brunesi, S. Peloso, R. Pinho and R. Nascimbene. 'Shake-table testing of a full-scale two-story precast wall-slab-wall structure'. In: *Earthquake Spectra* 35.4 (2019), pp. 1583–1609. DOI: 10.1193/072518EQS184M.

[7] D. Vamvatsikos and C. A. Cornell. 'Incremental dynamic analysis'. In: *Earthquake Engineering & Structural Dynamics* 31.3 (2002), pp. 491–514. DOI: 10.1002/eqe.141.

[8] L. Albanesi, C. F. Manzini and P. Morandi. 'Experimental In-Plane Seismic Performance of an Innovative Steel Modular Strengthening System for URM Walls'. In: *Journal of Earthquake Engineering* 28.5 (2024), pp. 1331–1357. ISSN: 13632469. DOI: 10.1080/13632469.2023.2231087.

[9] H. R. Schipper, P. Ham and G. Ravenshorst. *Proposal of Quasi-Static Cyclic Pushover Test on an Assembled Structure in CS Elements*. Technical Report C31B67-WP5-1. Version 2, Final Draft. TU Delft Large-scale testing campaign 2016, WP5; NAM Structural Upgrading project. Delft, The Netherlands: Delft University of Technology, Feb. 2017.

[10] S. J. Bourne, S. J. Oates, J. J. Bommer, B. Dost, J. van Elk and D. Doornhof. 'A Monte Carlo Method for Probabilistic Hazard Assessment of Induced Seismicity due to Conventional Natural Gas Production'. In: *Bulletin of the Seismological Society of America* 105.3 (2015), pp. 1721–1738. DOI: 10.1785/0120140302.

[11] J. J. Bommer and A. Martínez-Pereira. 'The Effective Duration of Earthquake Strong Motion'. In: *Journal of Earthquake Engineering* 3.2 (1999), pp. 127–172. ISSN: 1363-2469. DOI: 10.1080/13632469909350343.

[12] J. J. Kempton and J. P. Stewart. 'Prediction Equations for Significant Duration of Earthquake Ground Motions Considering Site and Near-Source Effects'. In: *Earthquake Spectra* 22.4 (2006), pp. 985–1013. DOI: 10.1193/1.2358175.

[13] M. Miglietta, N. Damiani, G. Guerrini and F. Graziotti. 'Full-scale shake-table tests on two unreinforced masonry cavity-wall buildings: effect of an innovative timber retrofit'. In: *Bulletin of Earthquake Engineering* 19.6 (2021), pp. 2561–2596. ISSN: 15731456. DOI: 10.1007/S10518-021-01057-5/TABLES/6.

[14] American Society of Civil Engineers (ASCE). *Seismic Evaluation and Retrofit of Existing Buildings (ASCE/SEI 41-13)*. Tech. rep. Reston, VA: American Society of Civil Engineers, 2014.

[15] New Zealand Society for Earthquake Engineering (NZSEE). *The Seismic Assessment of Existing Buildings, Part C8: Seismic Assessment of Unreinforced Masonry Buildings*. Tech. rep. Wellington, New Zealand: MBIE, EQC, SESOC, NZSEE and NZGS, 2017.

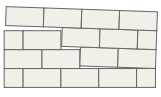
[16] European Committee for Standardization (CEN). *Eurocode 8: Design of Structures for Earthquake Resistance – Part 3: Assessment and Retrofitting of Buildings*. Tech. rep. EN 1998-3:2005. Brussels: European Committee for Standardization (CEN), 2005.

[17] European Committee for Standardization (CEN). *Eurocode 8: Design of Structures for Earthquake Resistance – Part 3: Assessment and Retrofitting of Buildings and Bridges (Draft)*. Tech. rep. prEN 1998-3. Draft for CEN enquiry, September 2023. Brussels: European Committee for Standardization (CEN), 2023.

[18] F. Messali and J. Rots. 'In-plane drift capacity at near collapse of rocking unreinforced calcium silicate and clay masonry piers'. In: *Engineering Structures* 164 (2018), pp. 183–194. DOI: 10.1016/j.engstruct.2018.02.050.

[19] L. S. Jacobsen. 'Steady Forced Vibration as Influenced by Damping'. In: *Transactions of the ASME* 52 (1930), pp. 169–181.

[20] A. K. Chopra. *Dynamics of Structures: Theory and Applications to Earthquake Engineering*. 5th. Pearson, 2017.



[21] N. Damiani, M. J. DeJong, L. Albanesi, A. Penna and P. Morandi. 'Distinct element modeling of the in-plane response of a steel-framed retrofit solution for URM structures'. In: *Earthquake Engineering & Structural Dynamics* 52.10 (2023), pp. 3030–3052. ISSN: 1096-9845. DOI: https://doi.org/10.1002/eqe.3910.

[22] C. F. Manzini, L. Albanesi and P. Morandi. *Studio del comportamento sismico di murature portanti rinforzate con rivestimento esterno modulare in acciaio*. Rapporto sperimentale EUC054/2021E–EUC088/2021U. Pavia, Italy: Fondazione EUCENTRE, 2021.

[23] N. Damiani, L. Albanesi, C. F. Manzini and P. Morandi. *Studio del comportamento sismico di murature portanti rinforzate con sistemi modulari esterni innovativi: II fase sperimentale – Rapporto numerico*. Tech. rep. Rapporto numerico, Prot. N. EUC105/2022E, in Italian. Pavia, Italy: Fondazione EUCENTRE, Feb. 2026.

Chapter 8



9

Conclusion

Above all, don't lie to yourself. The man who lies to himself and listens to his own lie comes to a point where he cannot distinguish the truth within him or around him, and so loses all respect for himself and for others. And having no respect, he ceases to love.

Fyodor Dostoevsky, The Brothers Karamazov (Russia)

This dissertation developed, implemented, and validated a contact constitutive model for the analysis of masonry structures with the Distinct Element Method (DEM), the Masonry Advanced Softening cONtact (MASON) model. The MASON model captures the tensile, shear, and compressive response of masonry joints, including post-peak softening, mixed-mode interaction, and cyclic degradation, and was implemented in 3DEC for both rigid- and deformable-block representations. The MASON model was then validated against experimental benchmarks at the material (couplets, triplets, or prisms), component (walls and piers), and building scales under monotonic, cyclic, and dynamic loading. A second methodological contribution concerns the damping of explicit dynamic analyses. The Maxwell damping formulation in DEM, implemented by Lemos *et al.* [1], was adopted in place of, and compared with classical Rayleigh damping, and its parameters are calibrated automatically through a Levenberg-Marquardt optimisation routine, which yields an approximately uniform damping ratio over a prescribed frequency band without the timestep restriction imposed by stiffness-proportional damping.

This chapter draws together the outcome of that work. Section 9.1 revisits the research objectives and states the contribution of each sub-project. Section 9.2 consolidates the conclusions by validation scale. Section 9.3 and Section 9.4 separate the limitations intrinsic to the model from those arising from the analyses conducted in this work, and Section 9.5 identifies directions for further study.

9.1. Revisiting the research objectives

The principal objective of the dissertation was operationalised through five sub-projects, each addressing a specific aspect of the development and validation of the MASON contact constitutive model. The objectives are restated below, and the scientific contributions of each sub-project are summarised. Cross-references to the sub-project descriptions in Section 1.3.2 are appended to each entry.

1. **Objective:** *To review the state of the art in distinct element modelling of masonry structures and joint constitutive formulations, and to identify the strengths and limitations of existing interface models and damping strategies* (SP1).

   Motivation. Available reviews and appraisals of computational masonry modelling strategies [2, 3] organise discontinuum methods into broad taxonomic categories but do not identify the specific constitutive deficiencies that remain within joint-level DEM formulations, namely the absence of exponential mixed-mode softening, pressure-dependent compressive failure, and robust cyclic degradation laws, nor do they evaluate damping parameter identification strategies against dynamic experimental benchmarks.

   Scientific Contribution. Chapter 2 surveys the mechanical behaviour and computational modelling of masonry, compares block-based discontinuum strategies with continuum, macroelement, NSCD, and AEM approaches, and

Chapter-opening illustration: Johannes Vermeer, *The Little Street* (*Het Straatje*), c. 1658, oil on canvas, Rijksmuseum, Amsterdam. Public domain.

identifies five knowledge gaps that motivate the developments of this thesis. Chapter 3 outlines the formulation of DEM for masonry and adopts the Maxwell damping formulation of Lemos *et al.* [1] as an alternative to classical Rayleigh damping and contributes an automatic parameter-identification routine.

2. **Objective:** *To formulate and implement a contact constitutive model for masonry interfaces in DEM, capturing tensile, shear, and compressive responses with post-peak softening and cyclic degradation within a strictly local stress-update scheme* (SP2).

   Motivation. None of the existing constitutive laws available in the adopted commercial DEM platform supports simultaneous tensile, shear, and compressive softening with dilatancy degradation and a strictly local update.

   Scientific Contribution. Chapter 4 presents the formulation of the MASON contact constitutive model, a multi-surface plasticity framework with three yield surfaces (a tension cut-off, a frictional shear surface with dilatancy, and an elliptical compression cap adopted from Lourenço and Rots [4]) coupled to damage scalars, with an exponential dilatancy decay and an unloading-reloading rule differentiated by failure mode. The model is implemented in *3DEC*, a commercial DEM software, using a strictly local stress update as a user-defined joint constitutive model. The model supports both rigid- and deformable-block configurations. The implementation is provided as a user-defined dynamic-link library (.dll) for Windows and as a shared object (.so) for Linux, enabling deployment on high-performance computing clusters.

3. **Objective:** *To calibrate the MASON model against experimental data at the joint and component levels and to validate its performance under monotonic and cyclic loading across selected masonry typologies* (SP3).

   Motivation. Validation of a contact constitutive model for masonry requires experimental evidence across multiple scales and loading scenarios; the observed responses at the joint level do not transfer directly to the component or structural scales without verifying that the calibrated parameters preserve the failure mode.

   Scientific Contribution. Chapter 5 validates the MASON model at the material scale against shear-compression tests on couplets and triplets, four-point bending tests on wallets, and monotonic and cyclic uniaxial compression tests on wallets. Chapter 6 extends the validation to the component scale on three benchmarks, comprising the monotonic shear-compression walls by Vermeltfoort *et al.* [5], the cyclic calcium silicate shear walls by Messali *et al.* [6], and the modular steel frame retrofitted piers by Albanesi *et al.* [7].

4. **Objective:** *To investigate viscous and alternative damping formulations within DEM and to evaluate their influence on the dynamic response of masonry assemblies governed by the MASON model, with attention to the prediction quality in local and global responses, and the computational effort* (SP4).

   Motivation. Dynamic analysis using DEM relies on a damping formulation that controls the numerical dissipation to represent the physical energy losses that



the joint constitutive law does not capture explicitly. The explicit time integration scheme provides no algorithmic damping of its own, and the hysteresis at the contacts dissipates energy only where damage has developed at the joints.

Scientific Contribution. Chapter 3 presents the Maxwell damping formulation adopted in this work as an alternative to classical Rayleigh damping, and contributes an automatic parameter-identification routine based on Levenberg-Marquardt optimisation. Chapter 7 provides the dynamic evaluation. It compares the MASON model against an alternative constitutive law on the SERA cross-vault [8, 9], evaluates the damping schemes on the same benchmark in terms of local and global response and computational effort, and validates the MASON-Maxwell combination against the ERIES-SUPREME gable wall shake-table tests [10]. The wall-scale observation in Chapter 6, that hysteretic dissipation dominates the cyclic energy balance under quasi-static loading and local numerical damping is secondary, frames the question addressed dynamically in Chapter 7, whether constitutive hysteresis alone suffices once inertial and high-frequency effects are present.

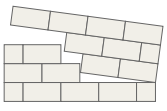
5. **Objective:** *To apply the calibrated MASON model to a representative masonry building subjected to quasi-static and dynamic seismic loading, and to assess the predictive capability and numerical stability for a practical seismic assessment scenario* (SP5).

   Motivation. Having established the predictive capability of the MASON model at the material and component scales, the building scale represents the *final and most demanding validation stage*, in which in-plane façades, out-of-plane transverse walls, floor diaphragms, and load-path redistribution interact simultaneously. Full-scale experimental campaigns at this level are resource-intensive, and dynamic shake-table evidence for this building typology and retrofit configuration remains unavailable.

   Scientific Contribution. Chapter 8 applies the DEM strategy with the MASON contact model to the TUD-BUILD-1 full-scale calcium silicate masonry building [11], addressing whether the joint- and wall-level calibrations of Chapters 5 and 6 carry over to the global response under the combined action of in-plane façades, transverse walls, and floor diaphragms. The chapter conducts a monotonic pushover comparing rigid-block and deformable-block idealisations against the experimental envelope, a quasi-static cyclic analysis under the full loading protocol, and an exploratory incremental dynamic analysis using the EQ-NPR record [12] applied to both the unreinforced configuration and a retrofit application with the Resisto 5.9 modular steel-frame exoskeleton system [7].

9.2. Conclusions

This section consolidates the substantive findings of the dissertation. The conclusions are grouped by validation scale (material, component, building) and by the dynamic study, with the synthesis claims that emerge from looking across the scales combined into the relevant groups.



Material-scale validation. The main conclusions from the studies of Chapter 5 are summarised as follows.

1. The MASON model reproduces the monotonic response of masonry joints. It captures the initial stiffness and the peak strength, as well as post-peak softening governed by the mode-I and mode-II fracture energies. Under mixed-mode loading, it also reproduces the transition between tensile cracking, frictional sliding and compressive crushing. In the bonded-block extension, the units are subdivided into sub-blocks connected by internal MASON contacts. This extension reproduces composite compressive failure as unit splitting and spalling without recalibrating the contact parameters.

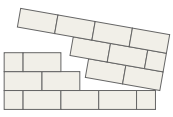
2. Under cyclic loading, the model captures stiffness degradation, residual offsets and the evolution of dissipated energy, and remains stable in the explicit update. The unloading rule differs by failure mode: elastic in shear, secant in tension, and nonlinear with a plastic offset in compression [13]. With this rule, the model reproduces dissipated energy and residual displacements across the considered loading protocols.

3. The joint strength and fracture parameters of MASON were obtained from material characterisation tests or empirical correlations, with calibration limited to a few parameters identified in Table 9.1. The joint stiffnesses and the hardening factor n depend on the block idealisation. For deformable blocks, they are derived from the moduli of the constituents. For rigid blocks, the joint must also carry the deformation of the units, and its stiffness is reduced accordingly: by compliance matching at building scale, by a fixed factor for the clay walls, and by calibration to the measured initial stiffness for the cyclic material tests (Table 9.1). Because the law is defined locally at the contact points, it introduces no parameter that depends on the scale of the model.

Component-scale validation. The main conclusions from Chapter 6 are summarised as follows.

4. The material-scale accuracy of the MASON model carries over to the component scale. The joint parameters were taken from the respective characterisation tests or the literature, and recalibration was confined to the hardening ratio and the boundary conditions. With these parameters, the governing diagonal failure mode is reproduced across the tested pre-compression levels in both block idealisations. The rigid-block formulation gives a comparable peak strength at a much lower computational cost. Pre-peak response metrics are objective with respect to mesh and timestep within the stable range, whereas post-peak softening remains sensitive to the mesh.

5. The model reproduces the cyclic response of the unreinforced calcium silicate walls, including the transition from rocking to sliding with increasing drift. The remaining discrepancies concern pinching and stiffness recovery at large drifts.



6. For the piers retrofitted with modular steel frames tested by Albanesi *et al.* [7], the model captures the initial stiffness within 5 % and the strengthening effect of the retrofit at small displacements. It underestimates the peak capacity by 14 % to 16 % and recovers only part of the gain in deformation capacity.

7. A Latin Hypercube sensitivity study with 300 realisations of the unreinforced pier identifies joint cohesion as the main control on peak capacity at a fixed cohesion-to-tensile-strength ratio. The friction angle, the brick tensile strength and the elastic moduli of mortar and brick act as secondary controls.

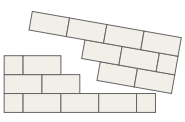
8. Quasi-static loading was applied at a calibrated velocity, with an energy check on the ratio of kinetic to strain energy. This procedure performed reliably across the cyclic protocols and was adopted for the quasi-static analyses at building scale.

Dynamic analysis and damping. The main conclusions from Chapter 7 are as follows.

9. Under mass-proportional damping, the choice of contact model has little effect on the peak displacements of the SERA cross-vault [9]. Its effect on the acceleration amplitudes and on the spatial spread of damage is larger. At AQA75, the MASON model gives lower peak accelerations than the TSCLinear formulation [14], which reaches about twice the experimental peaks at three accelerometers, because its secant unloading softens re-contact and is expected to attenuate high-frequency content.

10. On the cross-vault benchmark, Maxwell damping [1], with parameters identified by least-squares optimisation, lowers the displacement error relative to mass-proportional damping. At $\zeta^\star = 3\,\%$, the displacement NRMSE at the vault crown falls from 10.5 % to 7.6 % and the Sprague–Geers composite error averaged over the optical channels from 58.2 % to 56.2 %, at a 49.8 % increase in wall-clock time. For accelerations the result is mixed: the Maxwell peak error decreases with the damping ratio to 22.6 % at 5 %, whereas the mass-proportional error stays between 114 % and 162 %, but the composite error averaged over the accelerometer channels is higher for Maxwell at all ratios. Without any viscous damping, peak accelerations are in error by more than 800 %. External viscous damping is therefore needed to control the acceleration response, even where constitutive hysteresis alone captures the displacements adequately.

11. The damping formulation and the joint constitutive law are coupled through the unloading rule at re-contact. The gap between mass-proportional and Maxwell damping is smaller under MASON than under TSCLinear, because MASON unloads along the secant stiffness and generates less high-frequency content at re-contact, which is the band in which the two damping schemes differ most. The damping scheme is therefore not independent of the constitutive law, and the two should be specified together when inertial quantities are the target. On the cross-vault benchmark, the MASON–Maxwell combination gave comparable agreement with the experimental accelerations and the damage localisation, with a small advantage in displacement. This finding rests on the cross-vault and gable-wall benchmarks,



neither of which is governed by in-plane wall response; its extension to dynamic in-plane wall behaviour and to building scale remains to be verified.

12. The MASON–Maxwell combination reproduces the collapse of the full-scale gable walls [10, 15]. It uses one material-level parameter set and a single calibrated purlin–wall friction coefficient. In the STIFF configuration, equal top and bottom table motions represent a rigid diaphragm; in the FLEX configuration, differential motions represent a flexible one. The model reaches collapse at the experimental intensities, with a peak base acceleration (PBA) of 2.17 g for STIFF and 0.96 g for FLEX. The upper-triangle overturning of FLEX is reproduced, with the hinge only marginally shifted from its experimental position. In STIFF, however, the model rocks about a hinge near two-thirds of the wall height, whereas the specimen rocked about a hinge near one-third. The high-fidelity blind prediction of Ghezelbash *et al.* [16], which also assumes a uniform bond strength, shows the same mismatch. The mismatch is therefore not caused by the simplified micro-modelling idealisation and is more plausibly attributed to the spatial variability of the bond strength. Reproducing the experimental hinge location would require representing that variability rather than refining the discretisation.

Building-scale application. The main conclusions from Chapter 8 are summarised as follows.

13. The model reproduces the experimental peak capacity of TUD-BUILD-1 within ±1.4 % under both block idealisations. The unit crack-plane parameters were adjusted to the global response (Table 9.1), so this agreement reflects partial calibration. That both idealisations reach the same peak indicates that the lateral strength of this building is governed by the joints rather than by the deformability of the units. The rigid-block model matches the experimental envelope more closely in peak strength and cumulative dissipated work, and reduces the runtime from three days to five hours on the same hardware. Deformable blocks are still required for the dynamic and retrofit analyses because, in the adopted DEM platform, the structural elements representing the steel frames couple only to deformable meshes.

14. The quasi-static cyclic analysis reproduces the main features of the hysteretic response. These include the post-peak degradation, the asymmetry between the loading directions and the distribution of drift between storeys. Locally, it identifies the coupled in-plane and out-of-plane mechanism at the west pier-to-wall corner. The remaining discrepancies are a higher post-peak dissipation and a step-like force drop, caused by the sequential activation of the potential crack planes in the units.

15. The incremental dynamic analysis places the near-collapse intensity of the unreinforced TUD-BUILD-1 configuration between 125 % and 150 % of the EQ-NPR record [12], corresponding to a PGA between 0.41 g and 0.47 g. Three indicators support this range: the EC8-3 (2023) drift limit is exceeded, the drift at the west wall reaches the lower bound of the band of Messali and Rots [17], and a full diagonal

crack band forms with corner detachment. The dynamic and quasi-static analyses end in the same damage state, with collapse triggered when the ground-storey façade piers exhaust their in-plane drift capacity. They differ in the order in which the in-plane and out-of-plane mechanisms activate (Section 8.6.6).

16. With the Resisto 5.9 modular steel-frame retrofit, the near-collapse intensity rises from 125 % to 225 % of the record (PGA 0.70 g), a factor of 1.8. The retrofit does not change the collapse sequence, in which damage at the ground-storey pier base removes the corner restraint and the transverse walls overturn. It changes the in-plane mode of the piers from diagonal shear cracking to flexural rocking with toe crushing. It also reduces the peak displacement demand and delays the onset of collapse. In both configurations, collapse combines in-plane rocking with toe crushing in the ground-storey piers and out-of-plane rigid-panel overturning of the transverse walls. The retrofit reduces the peak displacement demand and delays the onset of this mechanism. These intensities depend on the single EQ-NPR record, the sequential IDA protocol and the provisional idealisation of the frame connections (Section 9.4). They mark the current limit of what the framework can predict at building scale, pending experimental dynamic evidence.

Table 9.1 summarises the origin of every input parameter used in Chapters 5 to 8. Each parameter is classified as measured (T) in the same experimental campaign, taken from the literature (L) or standard correlation, derived (D) from such values by a stated relationship, calibrated (C) against the benchmark response, or assumed (A). Most strength and fracture parameters belong to the first two classes. At the material scale, calibration is confined to the joint stiffness and hardening ratio n of the rigid-block models and to the cohesion of the monotonic tests. At larger scales, it is confined to the unit crack-plane values of the building and to parameters of specific boundary conditions and connections, namely the purlin–wall friction in Chapter 7 and the anchor and retrofit links in Chapter 8. The MASON joint parameters themselves are not recalibrated between scales. The table therefore makes explicit the basis for the transfer of one parameter set from the material to the building level, which the preceding sections have relied on.

9.3. Intrinsic limitations of the MASON model

The following limitations are intrinsic to the MASON constitutive model and its current implementation and qualify its use in assessment practice, independent of the analyses conducted in this thesis.

- **Contact history not preserved under contact regeneration.** In 3DEC, contacts are created and deleted as blocks separate and re-engage during large-displacement motion. When a contact is recreated upon re-engagement, the history variables stored at that contact, namely the tensile, shear, and compressive damage scalars, the cap projection state, and the accumulated plastic and dilatant displacements, are not preserved. The new contact starts from a default undamaged state. The MASON model is therefore reliable when contacts persist throughout the loading history, and its representations become uncertain at large-displacement modes where contact regeneration occurs frequently.

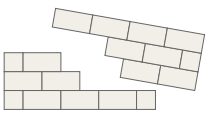


Table 9.1. Origin of the input parameters across the validation and application scales. T: measured; L: literature or standard correlation; D: derived; C: calibrated; A: assumed. Values are in the chapter tables listed in the last row.

		Material	Component (Ch. 6)			Dynamic (Ch. 7)		Building
Parameter group	Symbols	(Ch. 5)	TUE clay	TUD-COMP	S-HEA-U/R	Vault	Gable	(Ch. 8)
Unit density and elasticity	ρ, E_b, ν	T	T	T	T	T	A[4], T	T
Unit crack plane	$f_{t,b}$, c_b, φ_b, $G_{f,b}$	T	T, L	–	T, L	–	–	T/C[1], L
Joint stiffness	k_n, k_s	D, C[2]	D, A[5]	D	D	D	D	D
Joint strength	f_t, c_0, ϕ_{cv}	T, C, D[3]	L	T	T	T	T, D	T
Joint fracture energies	G_f^I, G_f^{II}	T	L	T	L	L	L	L
Joint compression	f_c, G_c, n	T, C	L	T, C	T, L, C	T, L	T, L	T, C
Boundaries and connections	plates; purlin; anchors; links	A	–	–	T/C	L	C, D	A, T/C
Damping	$\zeta^\star$, scheme	–	–	–	–	A	A	A
Source tables		5.1, 5.3, 5.4	6.1, 6.4	6.8, 6.10	6.11, 6.14	7.1–7.3	7.5, 7.7, 7.8	8.1, 8.2, 8.7

Cap shape C_n, C_{nn}, C_{ss} and the compressive unloading rule γ_{un}, γ_{pl}, e are literature values (L) in all analyses. Dilatancy is measured (T) for the triplet test only and set to zero (A) elsewhere. The bonded-block prism (Table 5.3) uses numerical unit and mortar moduli (A). Rigid-block stiffness factors (Chapters 6 and 8) are derived (D).

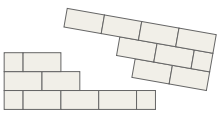
[1] Measured in the Esposito et al. [18] tests and adjusted to match the global building response.

[2] For the shear-compression and bending couplets the mortar modulus E_m was calibrated to the global response (Table 5.1, note b).

[3] Cohesion calibrated in the monotonic analyses (Table 5.1) and taken as $2.0 f_t$ in the cyclic analyses (Table 5.4); friction angle measured in the monotonic analyses and inactive in uniaxial compression. Cyclic compression: f_t and n from the recommendations of Jafari et al. [19] (Table 5.4, note 4). [4] Gable wall density rounded to 2000 kg/m^3 from the measured 1883 kg/m^3 (Table 7.5). [5] Reduced by a factor of 0.7 in the rigid-block configuration to lump the block deformability into the interface (Section 6.2.4).

- **Empirical compressive unloading parameters.** The nonlinear unloading branch in compression follows the functional form proposed by Facconi *et al.* [13], with three parameters (γ_{un}, γ_{pl}, e) used in this work taken from the suggested values by the authors, adjusted to compensate for the strain-to-displacement conversion required by the DEM contact formulation. The parameter values themselves were not refitted to the cyclic compression data used in Chapter 5, and the validation of the functional form across qualitatively different masonry typologies (lime mortar, stone, multi-leaf, hollow brick) has not been performed.

- **Limited application to historical masonry structures.** The material characterisation and component- and building-scale validation campaigns cover only engineered masonry typologies, namely solid clay brick and calcium silicate. The cross-vault benchmark in Chapter 7 demonstrates the applicability of the framework to a historical structural form, but its parameter identification relies on literature values rather than a dedicated material characterisation campaign. Historical and heritage masonry more broadly, including stone masonry, lime-mortar joints, multi-leaf walls with poorly consolidated rubble cores, and irregular bond patterns, requires calibration against material characterisation of the relevant typology, followed by component- and structural-level validation, before the MASON model can be applied with confidence to such structures.



9.4. Limitations of the analyses in this work

The limitations below do not arise from the constitutive model but from decisions taken in this study and are therefore amenable to resolution in future work without modifying MASON.

- **Spatially homogeneous material properties.** All analyses use uniform material parameters throughout the specimen, without specimen-specific spatial variability. The sensitivity study in Chapter 6 quantifies the influence of parameter scatter at the component scale, but a full stochastic implementation with spatially distributed parameter fields has not been pursued.

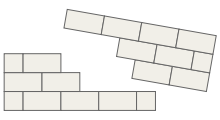
- **Single ground-motion record at the building scale.** The exploratory incremental dynamic analysis on TUD-BUILD-1 uses a single record (EQ-NPR). The intensities reported in Chapter 8 are therefore record-specific. A hazard-consistent suite of records would be required to quantify record-to-record variability and to support fragility analysis suitable for performance-based assessment of the building.

- **Mass-proportional damping at the building scale.** Mass-proportional damping applies forces proportional to the absolute velocity, thereby damping rigid-body motion following the base input and causing the effective damping ratio to exceed the intended target as the structure softens and its natural frequencies decrease. Maxwell damping would avoid both defects, but a building-scale comparison between the two schemes was not conducted, as the cost of repeating the full sequential IDA protocol under an alternative damping formulation was prohibitive at this model size. The damping sensitivity findings from Chapter 7 are established on cross-vault and gable-wall benchmarks. Whether the same shortfall affects the building-scale IDA outcomes has not been verified, since the deformable-block mesh size and timestep restrictions at that scale make a direct damping-scheme comparison computationally expensive.

- **Retrofit connection idealisation.** The Resisto 5.9 retrofit assessment in Chapter 8 uses a provisional idealisation of the frame-to-RC-slab anchorage and of the three-dimensional corner-to-corner connections, which have not been experimentally characterised on calcium silicate masonry. The retrofit performance reported at the building scale is therefore interpreted as indicative pending experimental characterisation of these connections.

9.5. Recommendations for further study

During the development of the MASON contact constitutive model, the validation campaigns at material, component, and building scales, and the comparative dynamic analyses with alternative constitutive models and damping schemes, several modelling aspects arose that would be worth further investigation, but could not be pursued within the time available for the present work. The following topics are identified to address the limitations of Section 9.3 and Section 9.4 and to extend the applicability of the modelling strategy beyond the typologies and loading scenarios examined in this work.



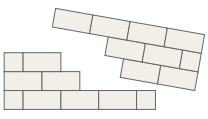
- **Contact history under contact regeneration.** When *3DEC* deletes and recreates a contact during large-displacement motion, the history stored at that contact is lost. This history comprises the damage scalars, the cap projection state and the accumulated plastic and dilatant displacements. A strategy is needed that preserves these variables over the life of a contact. One option is a persistent identity for each block pair, independent of the current contact state. Another is to map the history to a recreated contact by its proximity to the original location. A third is to port MASON to a DEM framework with persistent contact identity by design. Each option should be weighed for implementation effort and runtime overhead on a building-scale benchmark.

- **Calibration of the compressive unloading rule.** The compressive unloading branch follows the functional form of Facconi *et al.* [13]. Its three parameters (γ_{un}, γ_{pl}, e) were taken from the values suggested by the authors, adjusted for the conversion from strain to displacement. These parameters could first be refitted to the cyclic compression data of Esposito *et al.* [18], to quantify how much direct fitting improves on the published values. A review of cyclic compression data on other typologies, such as lime-mortar, stone and hollow-brick masonry, would then show whether the functional form holds beyond solid brick. Where the literature lacks such data, targeted tests could follow. Finally, the bonded-block extension of Chapter 5 reproduces compressive failure as unit splitting and spalling without any prescribed unloading rule. Applying it to the same cyclic tests [18] would show whether compressive unloading can emerge from contact-level mechanisms, and where it departs from the empirical rule [13].

- **Multi-record incremental dynamic analysis.** Repeating the IDA of TUD-BUILD-1 with a hazard-consistent suite of records would quantify the record-to-record variability of the near-collapse intensity. It would also show whether the governing collapse mechanism is sensitive to the record. Combined with spatially variable material properties, the same suite would support fragility analysis of both the unreinforced and the retrofitted building.

- **Retrofit connections on calcium silicate masonry.** The Resisto 5.9 assessment in Chapter 8 relies on a provisional idealisation of the frame-to-slab anchors and the corner connections. Testing these connections under quasi-static cyclic and dynamic loading would allow the retrofit assessment to be revisited on a validated basis.

- **Historical and heritage masonry.** MASON was validated on brick masonry with regular bond patterns, including the coursed brickwork of the cross-vault in Chapter 7. The harder case is irregular masonry, such as rubble stone, multi-leaf walls with loose cores, and lime-mortar joints of variable thickness. For such masonry, the regular unit geometry assumed in the simplified micro-model no longer holds. The bonded-block extension of Chapter 5 is a candidate path, since MASON contacts can be assigned along irregular internal interfaces without prescribing a periodic unit geometry. Material characterisation of the relevant typology, followed by component- and structural-level validation, is a prerequisite.



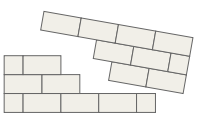
- **Mortar healing and time-dependent behaviour.** Mortar continues to cure during service life, and self-healing mortars can restore some of the crack-bridging capacity of masonry joints after damage [20]. MASON treats damage as monotonically accumulating and represents no recovery. A healing law parameterised by rest duration, environmental conditions and accumulated damage would extend the model to repeated loading with rest periods and to masonry repaired with such mortars.

- **Spatial variability of material properties.** The bifurcation study in Section 4.8 showed that a Weibull-distributed tensile strength lets the crack nucleate where the random field dictates, without a prescribed defect. The sensitivity study in Section 6.4.4 identified joint cohesion as the main control on peak capacity, at a fixed ratio of cohesion to tensile strength. A full stochastic implementation would extend such fields to all strength and dilatancy parameters, with distributions informed by that sensitivity ranking. Its first step should be a study of the Weibull shape parameter m, which bounds the effect of variability between wide scatter at low m and the deterministic limit at high m. The same tool would address the hinge-location mismatch of the STIFF gable wall in Chapter 7.

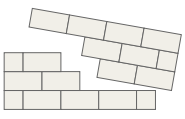
- **Intra-block cracking.** Each unit is split into two half-bricks by a single potential crack plane at mid-length, which fixes where intra-unit fracture can occur. Two consequences were observed. The shear-compression walls of Section 6.2 show a stepwise post-peak decline, because cracks are forced through the mid-length plane rather than along the observed paths. The cyclic analysis of TUD-BUILD-1 in Chapter 8 shows the same step-like force drop, caused by the sequential activation of the crack planes. Three remedies are possible, in order of increasing flexibility: more potential crack planes per unit, the bonded-block approach at component and building scale, or a contact-based intra-block cracking criterion. Each adds computational cost that must be weighed against the gain in fidelity.

- **Computational cost and building-scale damping comparison.** The shared-object build of MASON already runs on Linux clusters. Parallel contact updates, GPU implementation or domain decomposition would reduce the runtime of building-scale models further. Coupling DEM with macro-element or continuum models would restrict the detailed DEM description to regions where joint mechanisms govern, extending the strategy to building portfolios and urban-scale studies. A shorter runtime would also make the building-scale comparison of Maxwell and mass-proportional damping, deferred in Section 9.4, feasible. Since dynamic in-plane wall response is tested almost exclusively on complete buildings, the shake-table test of a full-scale terraced house with calcium silicate walls by Graziotti *et al.* [21] is the natural benchmark for this comparison.

The MASON contact constitutive model and its implementation are made openly available at `https://github.com/yopi1838/mason_constitutive_model`, in the hope that the framework developed in this dissertation will find application beyond the typologies and loading scenarios examined here, including the historical and heritage structures identified in the outlook. Masonry is among the oldest and most widespread



building materials in the world, and a significant share of the structures that remain standing were built without the seismic provisions that govern modern construction. The author hopes the tools developed here will help improve understanding and reduce vulnerability.



Chapter 9

Bibliography of Chapter 9

[1] J. V. Lemos, E. Dawson and Z. Cheng. 'Application of Maxwell damping in the dynamic analysis of masonry structures with discrete elements'. In: *International Journal of Masonry Research and Innovation* 7.6 (2022), pp. 663–686. ISSN: 2056-9459. DOI: 10.1504/ijmri.2021.10043266.

[2] A. M. D'Altri, V. Sarhosis, G. Milani, J. Rots, S. Cattari, S. Lagomarsino, E. Sacco, A. Tralli, G. Castellazzi and S. de Miranda. 'Modeling Strategies for the Computational Analysis of Unreinforced Masonry Structures: Review and Classification'. In: *Archives of Computational Methods in Engineering* 27.4 (2020), pp. 1153–1185. ISSN: 1134-3060. DOI: 10.1007/s11831-019-09351-x.

[3] D. Malomo and B. Pulatsu. 'Discontinuum models for the structural and seismic assessment of unreinforced masonry structures: a critical appraisal'. In: *Structures* 62 (Apr. 2024), p. 106108. ISSN: 2352-0124. DOI: 10.1016/J.ISTRUC.2024.106108.

[4] P. B. Lourenço and J. G. Rots. 'Multisurface Interface Model for Analysis of Masonry Structures'. In: *Journal of Engineering Mechanics* 123.7 (July 1997), pp. 660–668. ISSN: 0733-9399. DOI: 10.1061/(ASCE)0733-9399(1997)123:7(660).

[5] A. T. Vermeltfoort, T. M. J. Raijmakers and H. J. M. Janssen. 'Shear Tests on Masonry Walls'. In: *Proceedings of the 6th North American Masonry Conference*. Ed. by A. A. Hamid and H. G. Harris. Philadelphia, Pennsylvania, USA: Technomic Publishing Co., June 1993, pp. 1183–1193.

[6] F. Messali, R. Esposito, G. Ravenshorst and J. Rots. 'Experimental investigation of the in-plane cyclic behaviour of calcium silicate brick masonry walls'. In: *Bulletin of Earthquake Engineering* 18.8 (2020), pp. 3963–3994. DOI: 10.1007/s10518-020-00835-x.

[7] L. Albanesi, C. F. Manzini and P. Morandi. 'Experimental In-Plane Seismic Performance of an Innovative Steel Modular Strengthening System for URM Walls'. In: *Journal of Earthquake Engineering* 28.5 (2024), pp. 1331–1357. ISSN: 13632469. DOI: 10.1080/13632469.2023.2231087.

[8] C. Calderini, N. Bianchini, P. B. Lourenço, N. Mendes, P. X. Candeias, O. AlShawa, C. Chácara, M. M. Chávez, G. de Felice, A. Ferrante, P. Fici, R. Gagliardo, P. Kesavan, G. P. Lignola, M. Malena, D. Malomo, D. Pellegrini, F. Peña, M. Petracca, B. Pintucchi, F. P. A. Portioli, B. Pulatsu, G. Ramaglia, D. Rapicavoli and F. Trovatelli. 'Shake-Table Testing of a Brick Masonry Groin Vault: Overview of Blind Predictions and Postdictions and Comparison with Experimental Results'. In: *International Journal of Architectural Heritage* (2024),

pp. 1–27. ISSN: 1558-3058. DOI: 10.1080/15583058.2024.2419545. URL: https://doi.org/10.1080/15583058.2024.2419545.

[9] N. Bianchini, N. Mendes, P. B. Lourenço and C. Calderini. 'Modelling of the Dynamic Response of a Full-Scale Masonry Groin Vault: Unstrengthened and Strengthened with Textile-Reinforced Mortar (TRM)'. In: *International Journal of Architectural Heritage Conservation, Analysis, and Restoration* (2024). DOI: 10.1080/15583058.2024.2320857. URL: https://www.tandfonline.com/action/journalInformation?journalCode=uarc20.

[10] S. Sharma, N. Damiani, M. Bertassi, M. Smerilli, M. Mirra, I. Lanese, E. R. Parisi, G. J. O'Reilly, F. Messali and F. Graziotti. 'Experimental data from out-of-plane shake-table tests on unreinforced masonry gables'. In: *Earthquake Spectra* 41.5 (2025), pp. 4227–4245. DOI: 10.1177/87552930251378248.

[11] G. Ravenshorst, R. Esposito, R. Schipper, A. Tsouvalas and E.-M. Lourens. *Quasi-static Cyclic Pushover Test and Dynamic Identification Test on the Assembled Masonry Structure at TU Delft*. Final report. Project number C31B60, Version 3, Status: Final. Client: Nederlandse Aardolie Maatschappij B.V. Delft, The Netherlands: Delft University of Technology, Faculty of Civil Engineering and Geosciences, 10th June 2016.

[12] E. Brunesi, S. Peloso, R. Pinho and R. Nascimbene. 'Shake-table testing of a full-scale two-story precast wall-slab-wall structure'. In: *Earthquake Spectra* 35.4 (2019), pp. 1583–1609. DOI: 10.1193/072518EQS184M.

[13] L. Facconi, F. Minelli and F. J. Vecchio. 'Predicting Uniaxial Cyclic Compressive Behavior of Brick Masonry: New Analytical Model'. In: *Journal of Structural Engineering* 144.2 (Feb. 2018). ISSN: 0733-9445. DOI: 10.1061/(asce)st.1943-541x.0001961.

[14] B. Pulatsu. 'Coupled elasto-softening contact models in DEM to predict the in-plane response of masonry walls'. In: *Computational Particle Mechanics* 10 (2023), pp. 1759–1770. ISSN: 2196-4378. DOI: 10.1007/s40571-023-00586-x.

[15] M. Mirra, N. Damiani, S. Sharma, F. Graziotti and F. Messali. 'Definition of differential seismic input motions for out-of-plane dynamic testing of unreinforced masonry gable walls considering different roof configurations'. In: *Structures* 79 (2025), p. 109419. DOI: 10.1016/j.istruc.2025.109419.

[16] A. Ghezelbash, A. M. D'Altri, P. B. Lourenço and S. de Miranda. 'Numerical modeling of the out-of-plane dynamic response of masonry gable walls via a high-fidelity block-based finite element modeling approach – part I: Blind prediction'. In: *Bulletin of Earthquake Engineering* (2026). DOI: 10.1007/s10518-025-02328-1.

[17] F. Messali and J. Rots. 'In-plane drift capacity at near collapse of rocking unreinforced calcium silicate and clay masonry piers'. In: *Engineering Structures* 164 (2018), pp. 183–194. DOI: 10.1016/j.engstruct.2018.02.050.

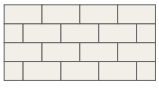
[18] R. Esposito, F. Messali and J. G. Rots. *Tests for the Characterization of Replicated Masonry and Wall Ties*. 2016. URL: http://resolver.tudelft.nl/uuid:a0923cf9-0ccd-48a1-9ce1-082aa66e97af.



[19] S. Jafari, J. G. Rots and R. Esposito. 'A correlation study to support material characterisation of typical Dutch masonry structures'. In: *Journal of Building Engineering* 45 (Jan. 2022). ISSN: 23527102. DOI: 10.1016/j.jobe.2021.103450.

[20] M. B. Gaggero. 'Autonomous masonry repair with a bacteria-based self-healing mortar: Research framework and multi-level experimental validation tailored to historical constructions'. PhD thesis. Delft University of Technology, 2026. DOI: 10.4233/uuid:1bf71164-26a0-411c-80d3-7d67bad34fe7.

[21] F. Graziotti, U. Tomassetti, S. Kallioras, A. Penna and G. Magenes. 'Shaking table test on a full scale URM cavity wall building'. In: *Bulletin of Earthquake Engineering* 15.12 (2017), pp. 5329–5364. DOI: 10.1007/s10518-017-0185-8.



Chapter 9

A

Normal Force Evaluation in a Nonlinear Interface

Closure is taken as positive: $u_n \geq 0$ in compression and $u_n < 0$ in tension. $u_{\text{hist,ten}}$ and $u_{\text{hist,comp}}$ are the largest tensile opening and the largest closure reached, f_{peak} the stress at the last unloading point, $(u_{n_{ro}}, f_{m_{ro}})$ the end point of the last unloading branch, and $(u_{\text{rev}}, f_{\text{rev}})$ the anchor of an inner loop opened by a reversal from a reloading line. Algorithm 1 selects the branch, Algorithm 2 and Algorithm 3 give the compressive unloading and reloading, and the shear and strength corrections follow in Section 4.6.

Algorithm 1 Normal force update: branch selection, tension, backbone loading and compressive damage.

Require: u_n, Δu_n, F_n^{old}, A_c, parameters, history variables
Ensure: F_n, d_c, updated history variables

$u_n^{\text{new}} \leftarrow u_n + \Delta u_n$
if $u_n < 0$ **then** ▷ tension
  if $\Delta u_n < 0$ **and** $u_n \le u_{\text{hist,ten}}$ **then**
    $u_{\text{hist,ten}} \leftarrow u_n$ ▷ drives d_t and $k_n(d_{ts})$
  end if
  if $u_n^{\text{new}} \ge 0$ **then**
    $F_n \leftarrow k_{n,0}\, A_c\, u_n^{\text{new}}$ ▷ gap closes within the step
  else
    $F_n \leftarrow \min\big(k_n(d_{ts})\, A_c\, u_n^{\text{new}}, 0\big)$ ▷ secant form
  end if
  return
end if
virgin $\leftarrow (\Delta u_n \ge 0)$ **and** $(u_n \ge u_{\text{hist,comp}})$ **and** (reloadFlag = 0)
if virgin **then** ▷ loading on the backbone
  $u_{\text{hist,comp}} \leftarrow u_n$; $\quad (u_{\text{rev}}, f_{\text{rev}}) \leftarrow (0,0)$
  $F_n^{\text{trial}} \leftarrow F_n^{\text{old}} + k_n A_c \Delta u_n$
  if $u_n \le u_{n_{el}}$ **then**
    $F_n \leftarrow F_n^{\text{trial}}$
  else
    $F_n \leftarrow \min\big(F_n^{\text{trial}},\, \sigma_{\text{env}}(u_n)\, A_c\big)$ ▷ Equation (4.10) or Equation (4.12)
  end if
  $f_{\text{peak}} \leftarrow F_n / A_c$
else if $\Delta u_n < 0$ **and** $u_{\text{hist,comp}} > u_{n_{el}}$ **then**
  Algorithm 2 ▷ unloading
else
  Algorithm 3 ▷ reloading
end if
if $u_{\text{hist,comp}} > u_{n_{el}} + u_{cp}$ **then** ▷ compressive damage
  $d_c \leftarrow 1 - \sigma_{\text{env}}(u_{\text{hist,comp}}) / f_c$
else
  $d_c \leftarrow 0$
end if

Algorithm 2 Compressive unloading ($\Delta u_n < 0$ after plastic closure).

if previous point lies off the current unloading curve **then** ▷ reversal from a reloading line
  $(u_{\text{rev}}, f_{\text{rev}}) \leftarrow (u_n - \Delta u_n,\ \sigma_n)$
  if $u_{\text{rev}} > u_{\text{hist,comp}}$ **then** $u_{\text{hist,comp}} \leftarrow u_{\text{rev}}$; $f_{\text{peak}} \leftarrow f_{\text{rev}}$
  end if
end if
$u_{n_{pl}} \leftarrow$ Equation (4.18)
$b \leftarrow \min\left(0.015\,u_{\text{hist,comp}},\ 0.10\,(u_{\text{hist,comp}} - u_{n_{pl}})\right)$ ▷ near-peak band
if $u_n > u_{\text{hist,comp}} - b$ **and** no inner loop **then**
  $F_n \leftarrow F_n^{\text{old}} + k_n A_c \Delta u_n$; reloadFlag $\leftarrow 0$ ▷ elastic
  $(u_{n_{ro}}, f_{m_{ro}}) \leftarrow (u_n, F_n / A_c)$
else if $\sigma_n + \Delta\sigma_n \le 0$ **then**
  $F_n \leftarrow 0$; $f_{m_{ro}} \leftarrow 0$; reloadFlag $\leftarrow 1$ ▷ complete unloading
else
  $\sigma_n \leftarrow$ Equation (4.19), χ from $(u_{\text{hist,comp}}, f_{\text{peak}})$ to $u_{n_{pl}}$
  if inner loop **then** offset the curve through $(u_{\text{rev}}, f_{\text{rev}})$
  $\sigma_n \leftarrow \min(\sigma_n,\ F_n^{\text{old}}/A_c)$; $F_n \leftarrow \sigma_n A_c$; reloadFlag $\leftarrow 1$
  if outer loop **then** $(u_{n_{ro}}, f_{m_{ro}}) \leftarrow (u_n, \sigma_n)$
end if

Algorithm 3 Compressive reloading ($\Delta u_n \ge 0$ inside the envelope).

if $u_n < u_{n_{ro}}$ **then**
  $F_n \leftarrow F_n^{\text{old}}$ ▷ below the unloading end point: hold
else if reloadFlag = 1 **then**
  if inner loop **and** $u_n < u_{\text{rev}}$ **then**
    $\sigma_n \leftarrow$ linear interpolation to $(u_{\text{rev}}, f_{\text{rev}})$
    $F_n \leftarrow \sigma_n A_c$
  else
    $u'_{\text{rec}} \leftarrow (u_{\text{hist,comp}} - u_{n_{ro}})/u_{cp}$; $\beta \leftarrow$ Equation (4.24)
    $k_{re} \leftarrow (\beta f_{\text{peak}} - f_{m_{ro}})/(u_{\text{hist,comp}} - u_{n_{ro}})$
    $\sigma_n \leftarrow f_{m_{ro}} + k_{re}\,(u_n - u_{n_{ro}})$ ▷ Equation (4.22)
    $\sigma_{\text{bound}} \leftarrow f_{\text{peak}}$ **if** $u_n \le u_{\text{hist,comp}}$ **else** $\sigma_{\text{env}}(u_n)$
    if $\sigma_n < \sigma_{\text{bound}}$ **then**
      $F_n \leftarrow \sigma_n A_c$
    else
      $F_n \leftarrow \sigma_{\text{bound}} A_c$; reloadFlag $\leftarrow 0$ ▷ rejoin the backbone
      if $u_n > u_{\text{hist,comp}}$ **then** $u_{\text{hist,comp}} \leftarrow u_n$; $f_{\text{peak}} \leftarrow \sigma_{\text{bound}}$
      end if
    end if
  end if
else
  $F_n \leftarrow F_n^{\text{old}} + k_n A_c \Delta u_n$; reloadFlag $\leftarrow 0$ ▷ elastic
end if

Algorithm 4 Partial unloading and reloading in compression

Require: closure u_n, increment Δu_n, stress σ_n at the start of the step; stored bottom (u_{ro}, σ_{ro}), reversal point (u_{rev}, σ_{rev}), line start (u_s, σ_s), plastic displacement u_{pl}

Reversal from a reload line

if $\Delta u_n < 0$ **and** reloading **and** $u_n^{prev} > u_{pl}$ **and** $|\sigma_n - \sigma_{act}(u_n^{prev})| > 10^{-6} f_c$ **then**
  if no reversal point stored **or** $u_n^{prev} \geq u_{rev}$ **then**
    if a reversal point is stored **and** $u_n^{prev} > u_{rev}$ **then**
      $(u_s, \sigma_s) \leftarrow (u_{rev}, \sigma_{rev})$
    else
      $(u_s, \sigma_s) \leftarrow (u_{ro}, \sigma_{ro})$
    end if
    $(u_{rev}, \sigma_{rev}) \leftarrow (u_n^{prev}, \sigma_n)$
  end if
end if

Active unloading curve

function $\sigma_{act}(u)$
  if no reversal point stored **then**
    return $\sigma_{out}(u)$ ▷ outer curve, Equation (4.19)
  end if
  $\delta_s \leftarrow \sigma_s - \sigma_{out}(u_s)$ if $u_s > u_{pl}$, else 0
  $\delta_r \leftarrow \sigma_{rev} - \sigma_{out}(u_{rev})$
  if $u \geq \max(u_s, u_{pl})$ **then**
    $\delta \leftarrow \delta_s + (\delta_r - \delta_s) \min\left(\frac{u - u_s}{u_{rev} - u_s}, 1\right)$
  else if $u > u_{pl}$ **then**
    $\delta \leftarrow \delta_s \frac{u - u_{pl}}{u_s - u_{pl}}$
  else
    $\delta \leftarrow 0$
  end if
  return $\min(\sigma_{out}(u) + \delta,\ \sigma_{rev})$
end function

Reloading

if $\Delta u_n \geq 0$ **and** a reversal point is stored **then**
  if $u_n < u_{rev}$ **then**
    $\sigma_n \leftarrow \sigma_{ro} + (\sigma_{rev} - \sigma_{ro}) \frac{u_n - u_{ro}}{u_{rev} - u_{ro}}$ ▷ back to the reversal point
  else
    $\sigma_n \leftarrow \sigma_{rev} + \frac{\sigma_{rev} - \sigma_s}{u_{rev} - u_s} (u_n - u_{rev})$ ▷ same reload line
  end if
  if $\sigma_n \geq$ envelope bound **then**
    return to the envelope; clear the reversal point
  end if
end if

B

Appendix B

B.1. Dilatancy sensitivity: TU Eindhoven wall, HIGH pre-compression

This appendix reports the parametric study of the dilatancy angle ψ for the TU Eindhoven (TUE) wall specimen under HIGH pre-compression ($\sigma_n = 2.12\,\text{MPa}$), complementing the LOW pre-compression analysis presented in Section 6.2.5. The two bounding assumptions, the parameter range, and the relationships between ϕ and ψ are identical to those of the main analysis and are not repeated here (Table 6.6 and Figure 6.10).

The HIGH configuration is reported despite the boundary-amplified contribution addressed in Section 6.2.4, where the kinematic interaction between rigid-block rocking and the clamped top boundary was shown to influence the post-peak response. The results presented here therefore reflect the combined effect of the constitutive dilatancy contribution and the boundary-amplified contribution rather than the constitutive contribution in isolation, and the trends should be interpreted accordingly.

The HIGH analysis is reported as a complement to the LOW analysis because it characterises the dilatancy sensitivity under the boundary-amplified kinematic conditions intrinsic to the rigid-block configuration with a clamped top boundary. These conditions are representative of the lower-storey conditions encountered in low-rise masonry buildings, and the comparison with the LOW response under identical constitutive parameters provides indirect access to the magnitude of the boundary-amplified contribution.

Figure B.1 compares the force-displacement responses obtained from the parameter variation against the experimental envelope. The qualitative trends mirror those observed at LOW pre-compression and are not re-described here for brevity. The peak resistance under the lower-bound formulation is only weakly sensitive to ψ, with the peak force remaining within a narrow band across the parameter range. The pre-compression-driven frictional capacity dominates the peak when σ_n is high, and the compensating reduction of ϕ as ψ increases offsets the additional dilatant contribution at peak. Under the upper-bound formulation, by contrast, the peak resistance increases monotonically with ψ, since ϕ is held constant and the dilatant contribution is added to the peak shear capacity.

Furthermore, the magnitude of the post-peak variation across ψ is amplified relative to the LOW analysis. Under the lower-bound formulation, simulations with $\psi \geq 20°$ exhibit a markedly reduced residual capacity and a pronounced post-peak strength loss relative to

the $\psi < 20°$ group, in line with the brittleness threshold identified at the LOW specimen but with a larger absolute drop. The upper-bound formulation retains the step-like post-peak drops across the parameter range. These drops are characteristic of the HIGH configuration and reflect the discrete release of accumulated bed-joint shear capacity. Increasing ψ does not soften this stepwise pattern but shifts the post-peak envelope upwards, so that the residual branch is systematically higher for $\psi \geq 20°$.

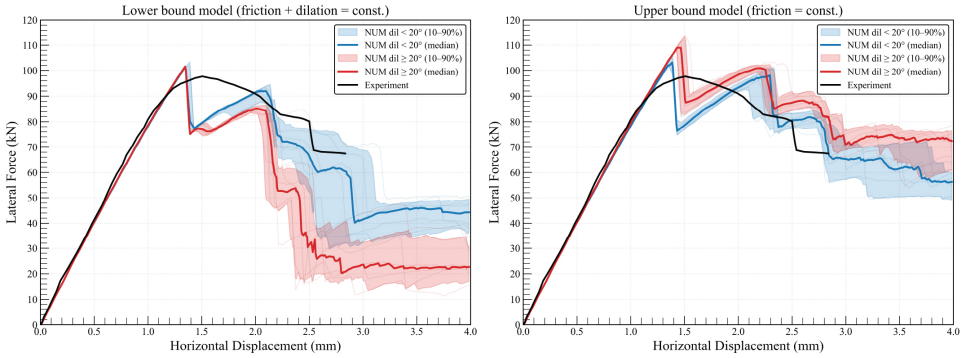


Figure B.1. Force-displacement response of the lower-bound (A) and upper-bound (B) dilation angle parameter variation at HIGH pre-compression.

The damage fields at the end of the analysis are reported in Figures B.2 and B.3 for lower-bound and upper-bound formulations, respectively. In both formulations, the damage localises along a diagonal load path connecting the loaded top corner to the opposite support, with vertical cracks at several locations that pass through the unit's potential crack plane. The dilatancy treatment governs the magnitude of diagonal force redistribution without altering the spatial distribution of damage, which is also consistent with the LOW analysis. The boundary-amplified kinematic over-constraining at HIGH pre-compression is reflected in the post-peak force-displacement evolution rather than in the joint damage field, suggesting that the boundary constraint operates through the global wall kinematics and the bed-joint sliding at the rocking interfaces, instead of through a localised redistribution of the damage pattern.

The candlestick summary in Figure B.4 reports the peak force, displacement at peak, and dissipated work for both formulations across the parameter range. The peak force at HIGH pre-compression is only weakly sensitive to ψ, with the upper-bound branch consistently slightly higher than the lower-bound branch and limited scatter within each bound. The displacement at peak shows a systematic bias relative to the experimental value, with both bound states reaching peak at smaller displacements than the experiment and only a modest upward shift at larger ψ. The dissipated work diverges substantially between the two formulations, with the upper-bound branch increasing monotonically with ψ and remaining above the experimental baseline across the range, while the lower-bound branch decreases with ψ and falls below the experimental baseline at higher ψ. The magnitude of this divergence is greater than that in the corresponding LOW analysis,

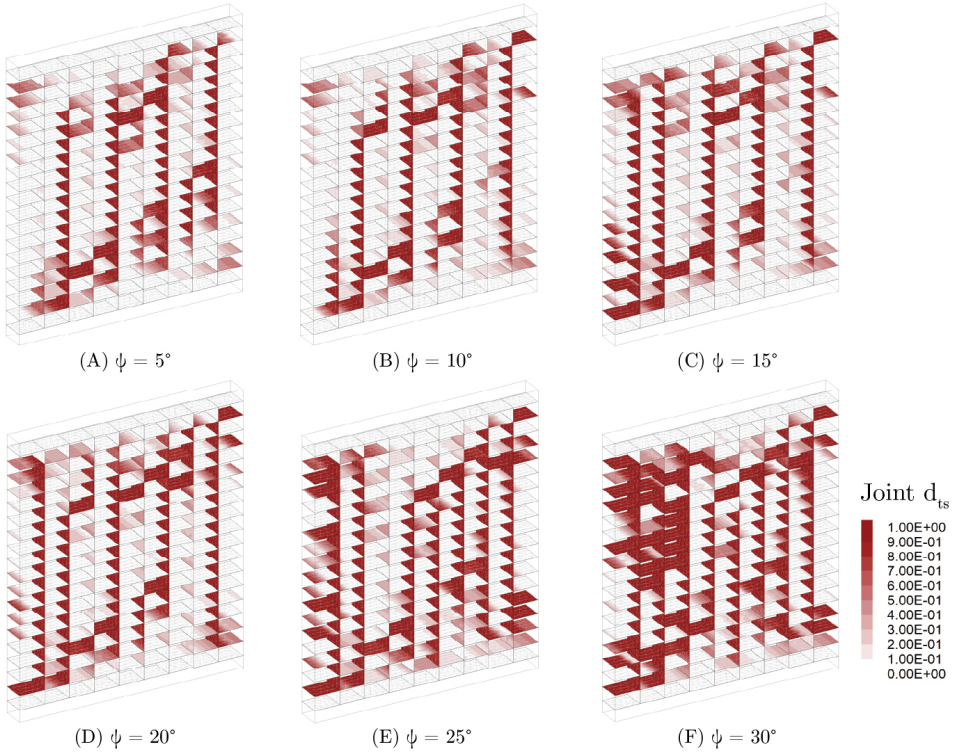


Figure B.2. Combined shear-tension damage field d_{ts} at the end of the analysis for the HIGH case under the lower-bound parameter variation ($\phi + \psi = 35°$).

supporting the interpretation that the boundary-amplified contribution scales with both the confinement level and the dilation magnitude.

The qualitative trends observed at HIGH pre-compression are similar to those reported in the LOW specimen analysis. The two formulations produce coupled but not identical sensitivities in the FD response; the lower-bound formulation develops brittle post-peak behaviour at large ψ, and the upper-bound formulation overshoots the experimental envelope at moderate to large ψ due to increased shear resistance. The recommendation regarding calibration practice when direct shear data report only peak strength, made at the end of Section 6.2.5, applies to the HIGH regime as well, with the additional consideration that calibration against HIGH pre-compression benchmarks performed under the same boundary conditions inherits the boundary-amplified contribution and may produce ψ values that are not transferable to lower confinement levels or to differently constrained boundary conditions without verification.

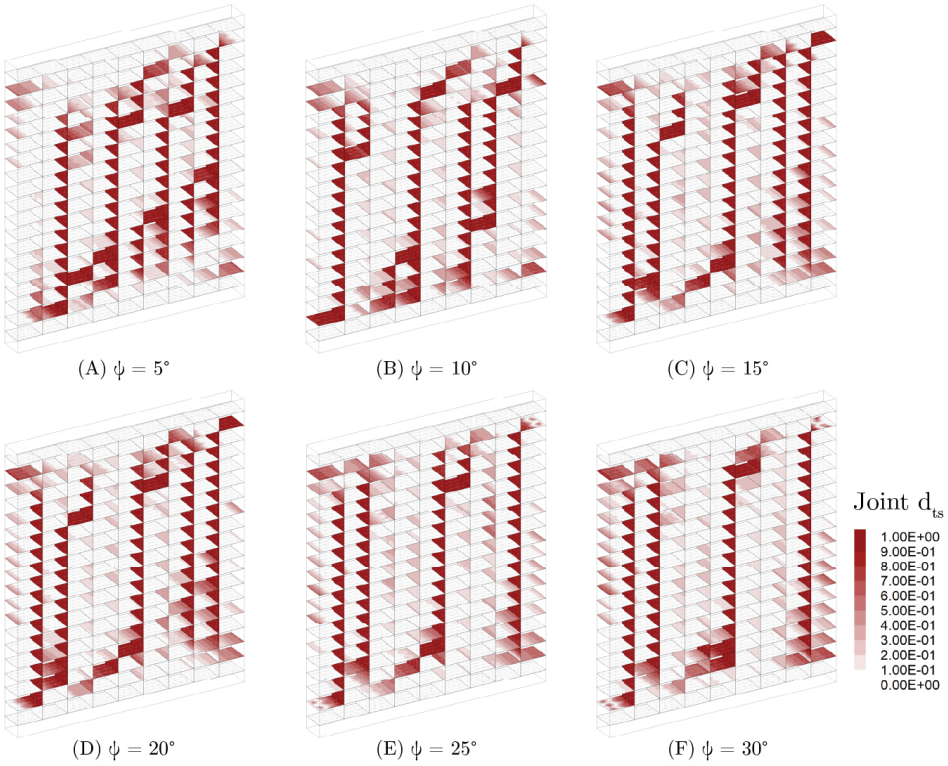


Figure B.3. Combined shear-tension damage field d_{ts} at the end of the analysis for the HIGH case under the upper-bound parameter variation ($\phi = 35°$).

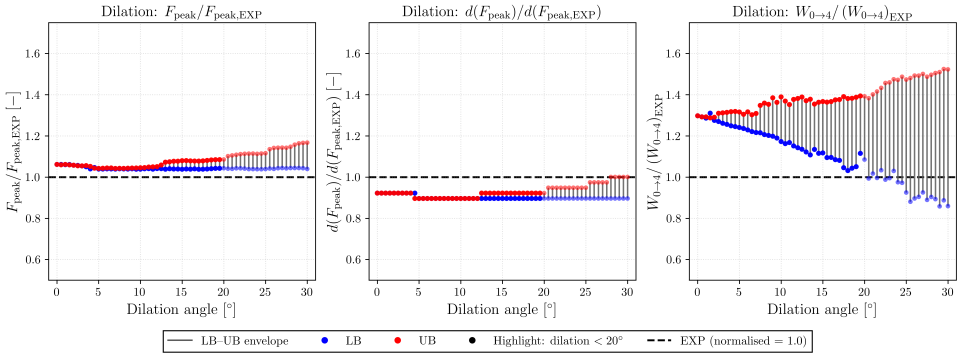
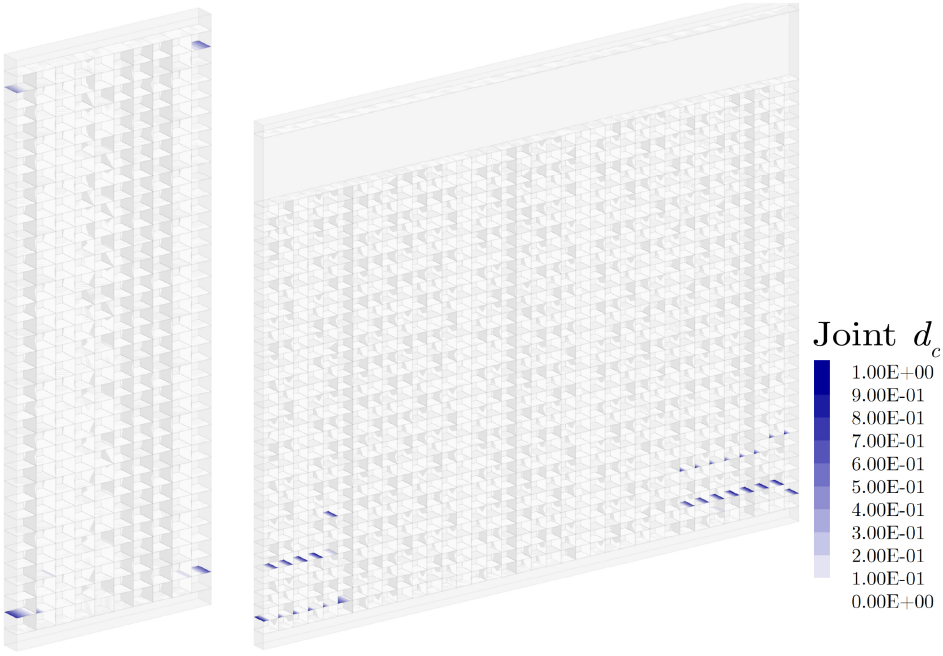


Figure B.4. Candlestick summary of the HIGH pre-compression dilatancy parameter variation comparing the lower-bound (LB) and upper-bound (UB) formulations.

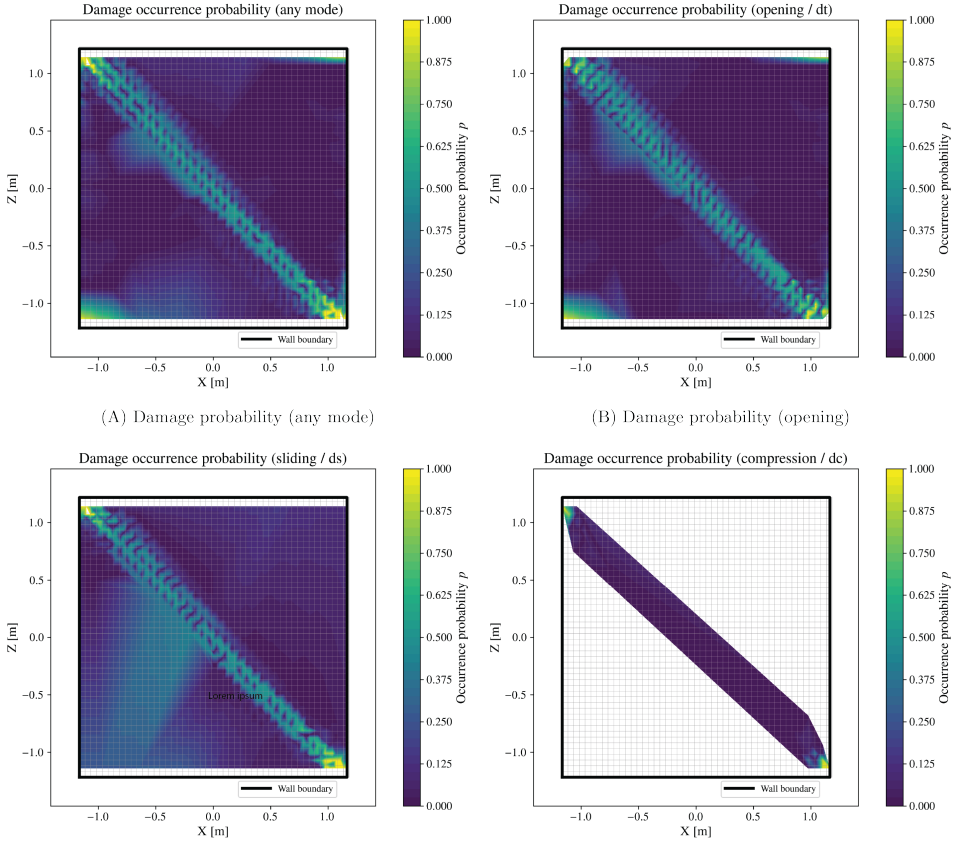
B.2. Joint compression damage scalar plot at the end of analysis



(A) TUD-COMP-0a (B) TUD-COMP-6

Figure B.5. Joint compression damage scalar plot at the end of analysis

B.3. Spatial maps of damage occurrence probability over all realisations of S-HEA-U wall



(A) Damage probability (any mode)

(B) Damage probability (opening)

(C) Damage probability (sliding)

(D) Damage probability (crushing)

Figure B.6. Spatial maps of damage occurrence probability across the S-HEA-U wall over all realisations

C

Appendix C

This appendix collects the supplementary time-history comparisons and damage distributions that support the analyses presented in Chapter 7. Appendices C.1 and C.2 present the displacement and acceleration comparisons between the TSCLinear and MASON contact models at the AQA25 and AQA50 amplitude levels, where the two models produce nearly identical responses. These are included for completeness and to substantiate the statement in Section 7.2.4 that the constitutive differences have not yet been activated at these intensity levels. Appendix C.3 presents the damage scalar distributions from the damping ratio parametric sweep discussed in Section 7.3.2. Appendices C.4 and C.5 report the displacement and acceleration time histories for the damping model variations (mass-proportional, Maxwell, and undamped) at the AQA25 and AQA50 amplitude levels, complementing the AQA75 comparisons discussed in Sections 7.3.4 and 7.3.6, where the responses of the three configurations have not yet diverged appreciably. Finally, Appendix C.6 presents the per-run hysteresis loops of the normalised base shear coefficient against the OOP displacement for the STIFF and FLEX gable wall specimens, complementing the superimposed representation reported in Section 7.4.3.

C.1. Displacement comparison between TSCLinear and MASON

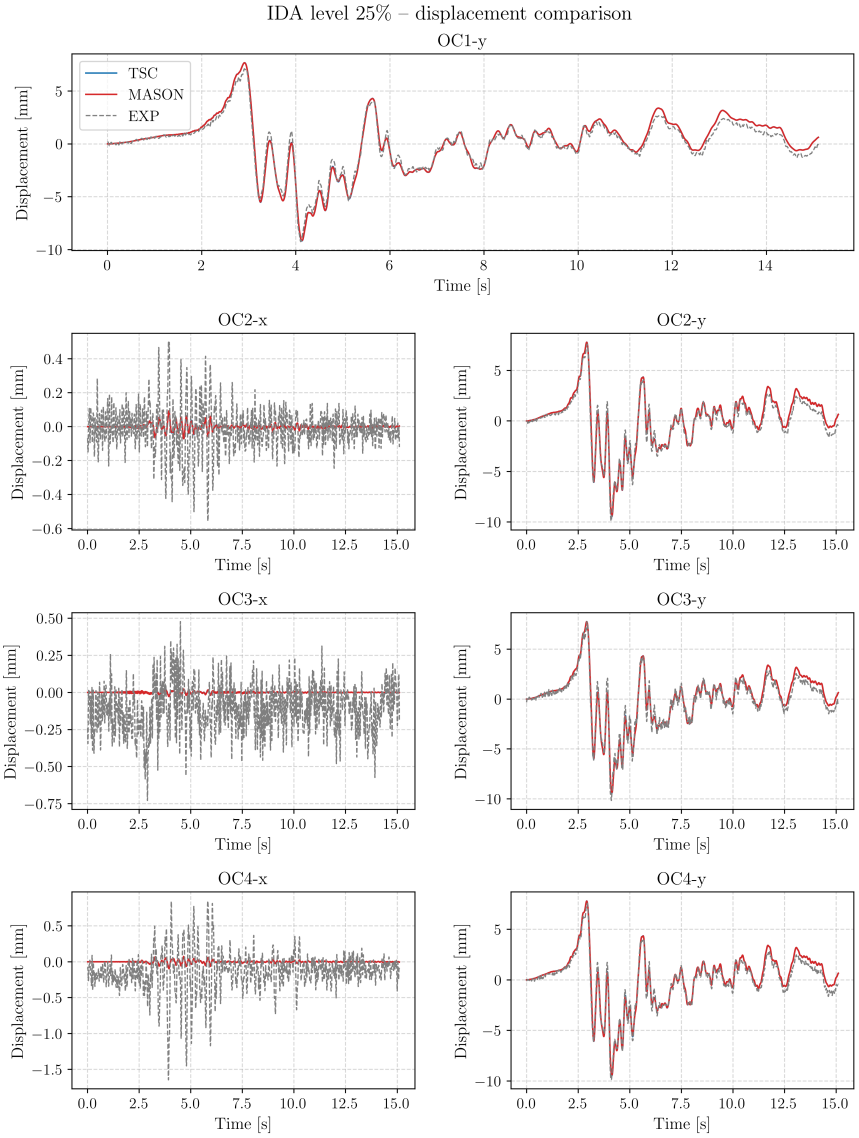


Figure C.1. Displacement comparison between EXP, TSCLinear, and MASON at AQA25

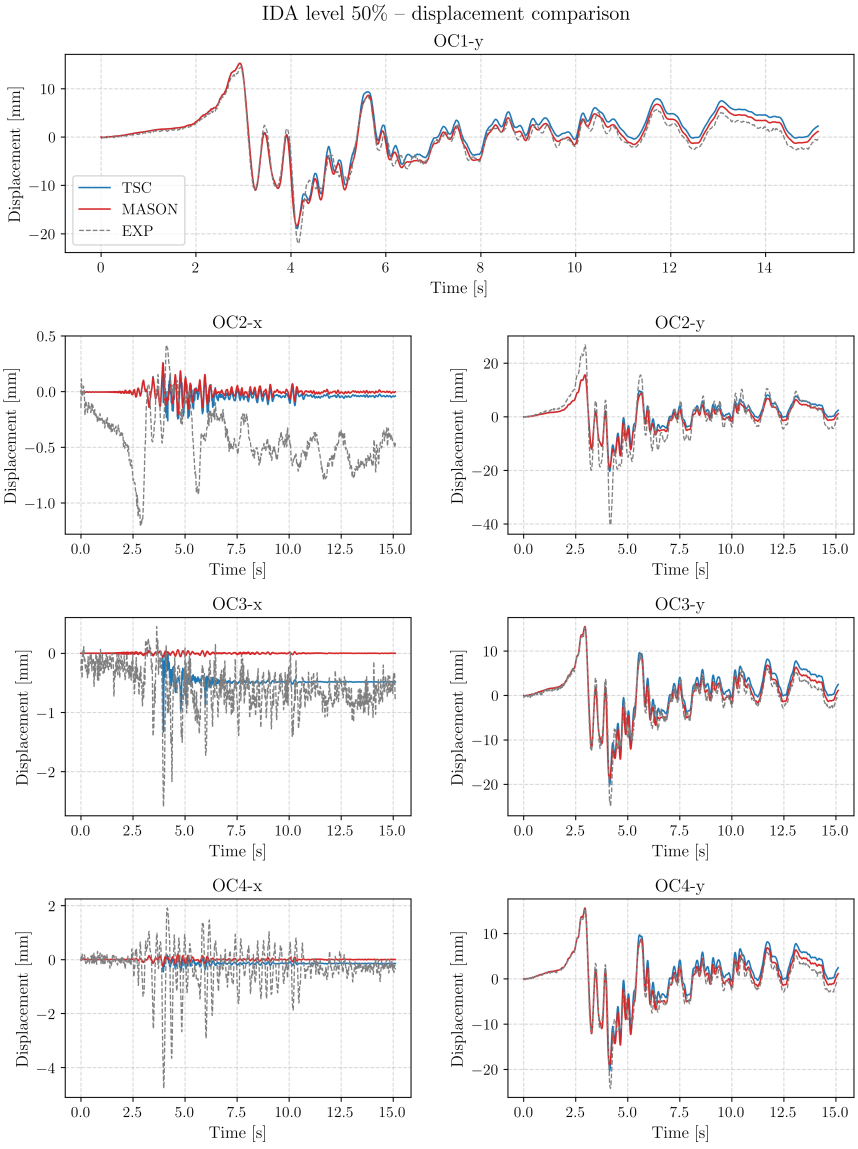


Figure C.2. Displacement comparison between EXP, TSCLinear, and MASON at AQA50

C.2. Acceleration comparison between TSCLinear and MASON

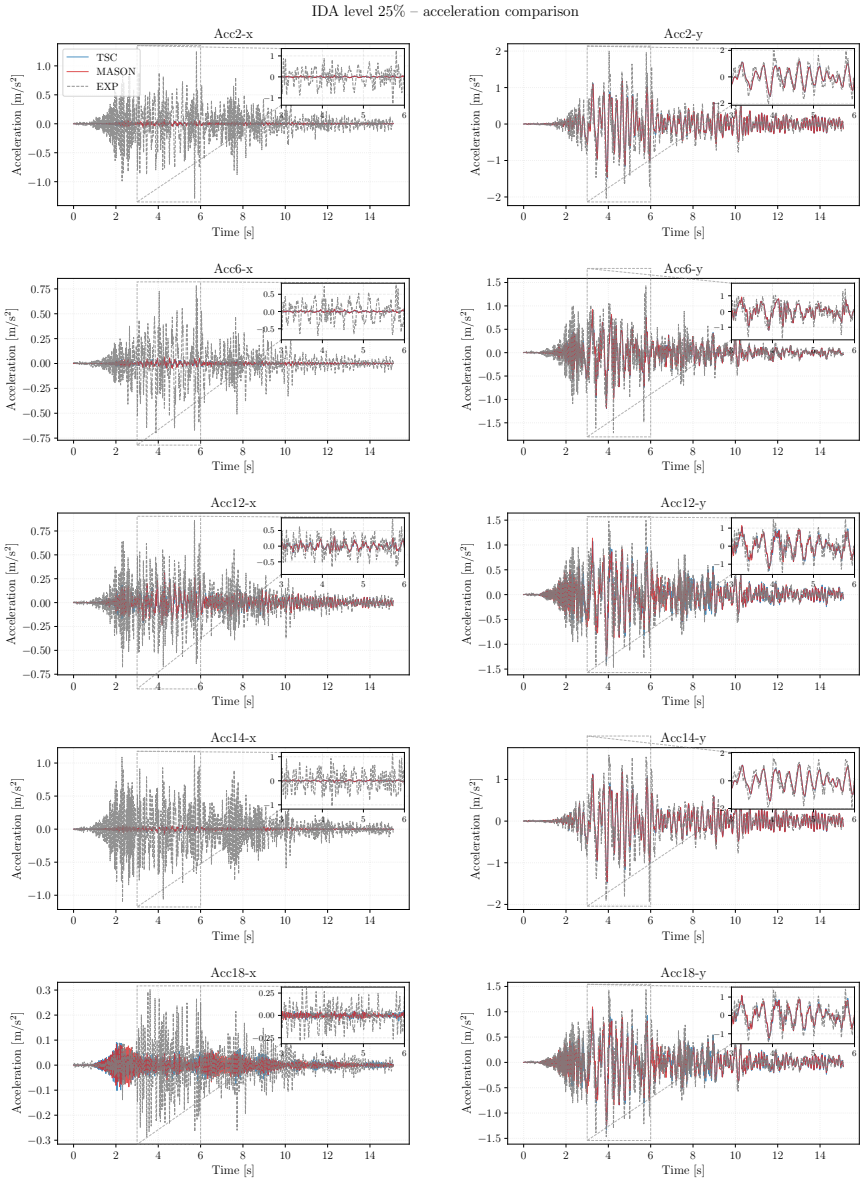


Figure C.3. Acceleration comparison between EXP, TSCLinear, and MASON at AQA25

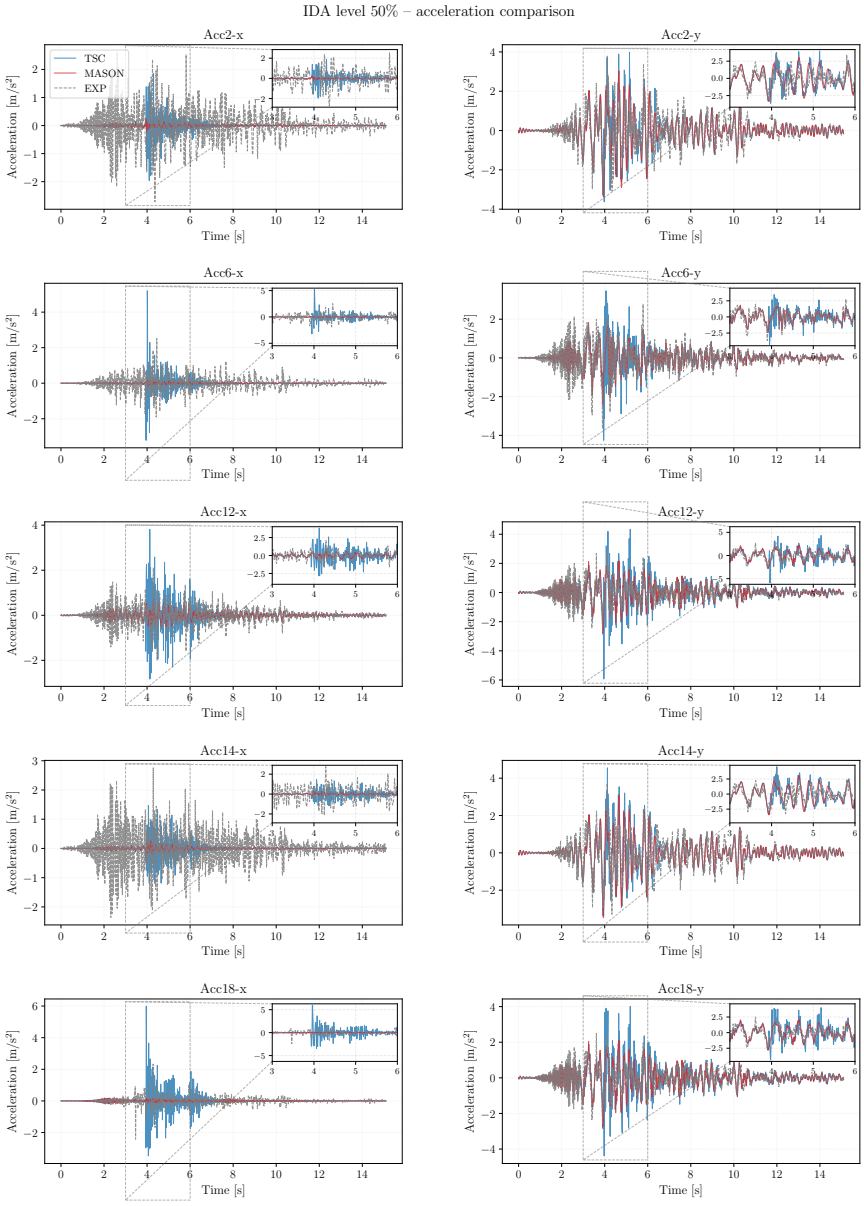


Figure C.4. Acceleration comparison between EXP, TSCLinear, and MASON at AQA50

C.3. Damage distributions for the damping ratio parametric sweep

This appendix presents the combined tensile-shear damage scalar d_{ts} at the vault extrados at the end of AQA75 for the mass-proportional (MP) and Maxwell damping configurations at each of the four candidate target damping ratios ($\zeta^\star \in \{2,3,4,5\}\%$) considered in Section 7.3.2.

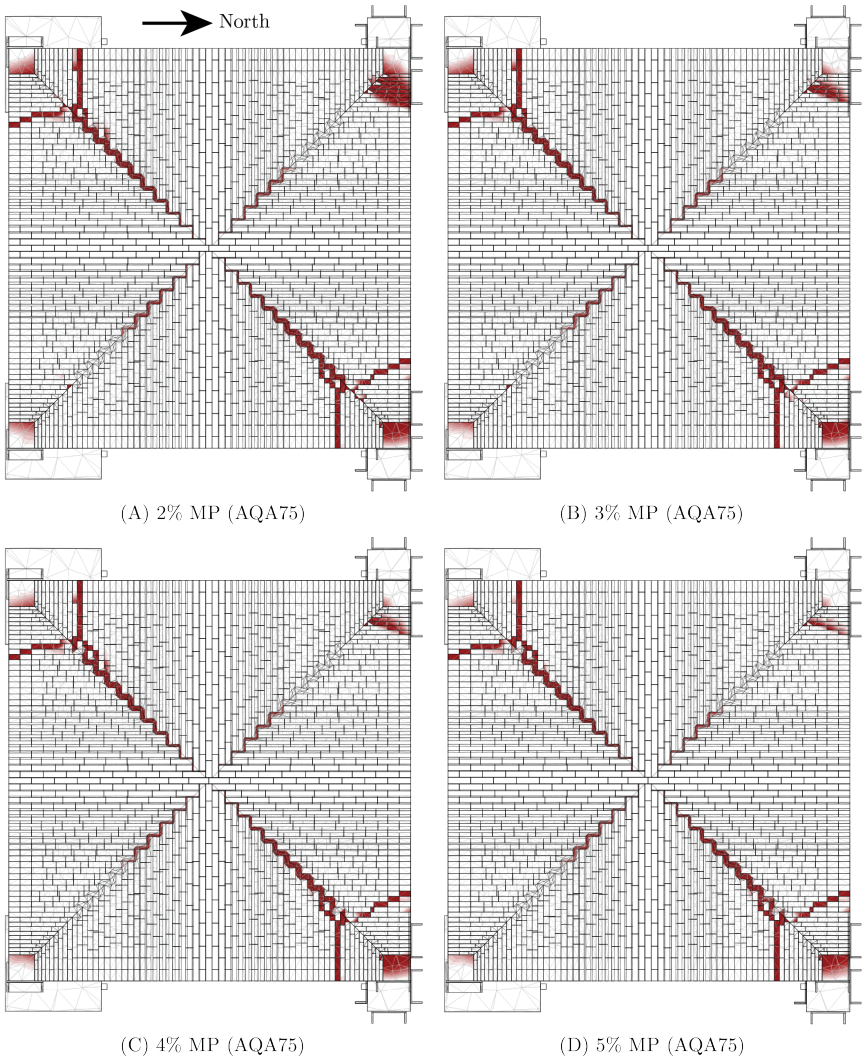
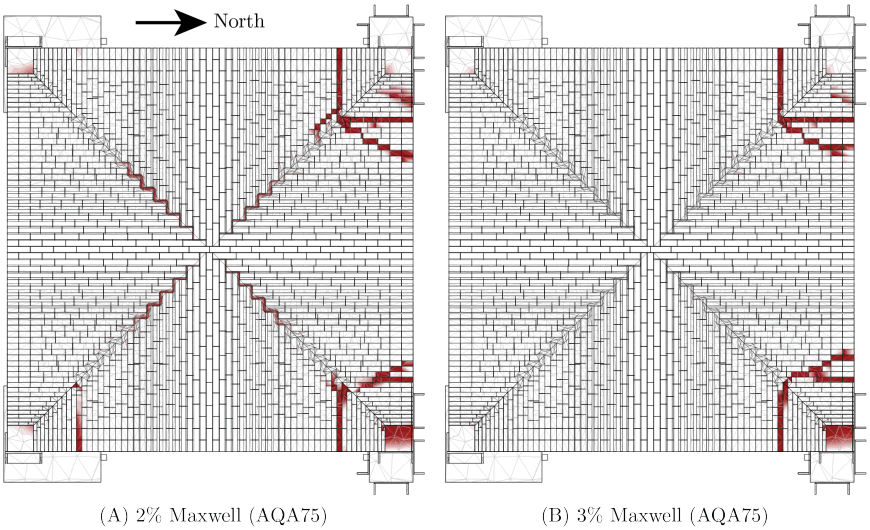


Figure C.5. Combined tensile-shear damage scalar d_{ts} at the vault extrados at the end of AQA75 for the mass-proportional (MP) damping configuration.



(A) 2% Maxwell (AQA75) (B) 3% Maxwell (AQA75)

(C) 4% Maxwell (AQA75) (D) 5% Maxwell (AQA75)

Figure C.6. Combined tensile-shear damage scalar d_{ts} at the vault extrados at the end of AQA75 for the Maxwell damping configuration.

C.4. Displacement comparison for the damping model variations

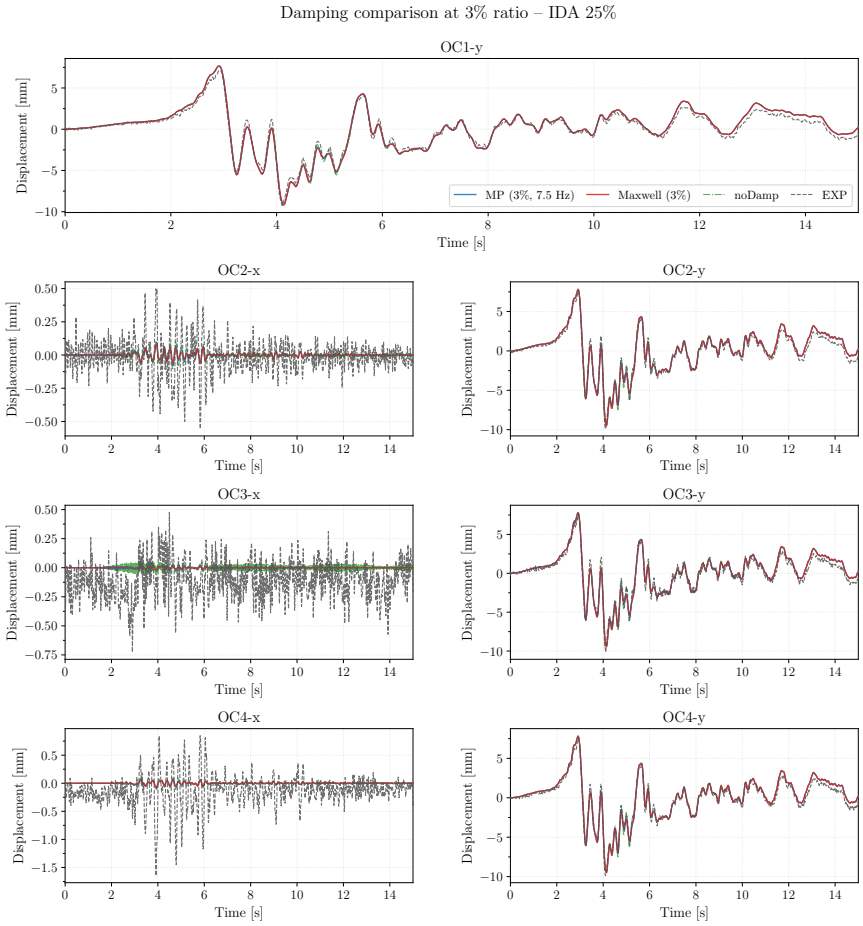


Figure C.7. Displacement time histories at the four optical camera locations (OC1–OC4) for the AQA25 amplitude level under the three damping configurations at $\zeta^{\star} = 3\%$.

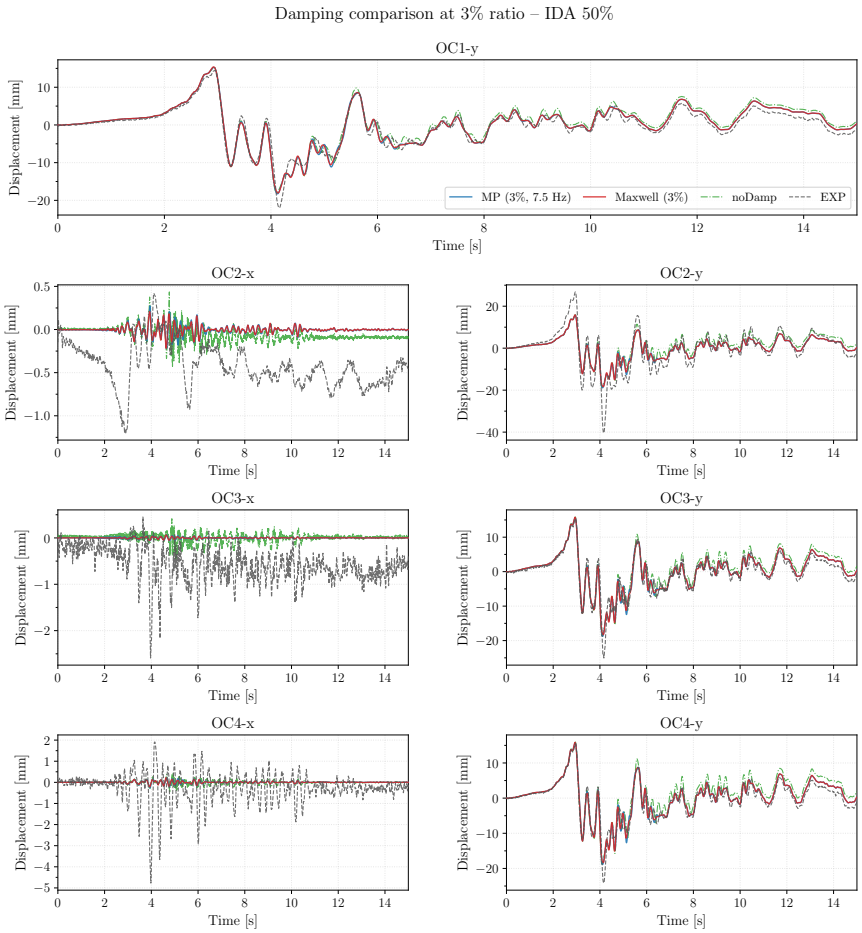


Figure C.8. Displacement time histories at the four optical camera locations (OC1–OC4) for the AQA50 amplitude level under the three damping configurations at $\zeta^{\star} = 3\%$.

C.5. Acceleration comparison for the damping model variations

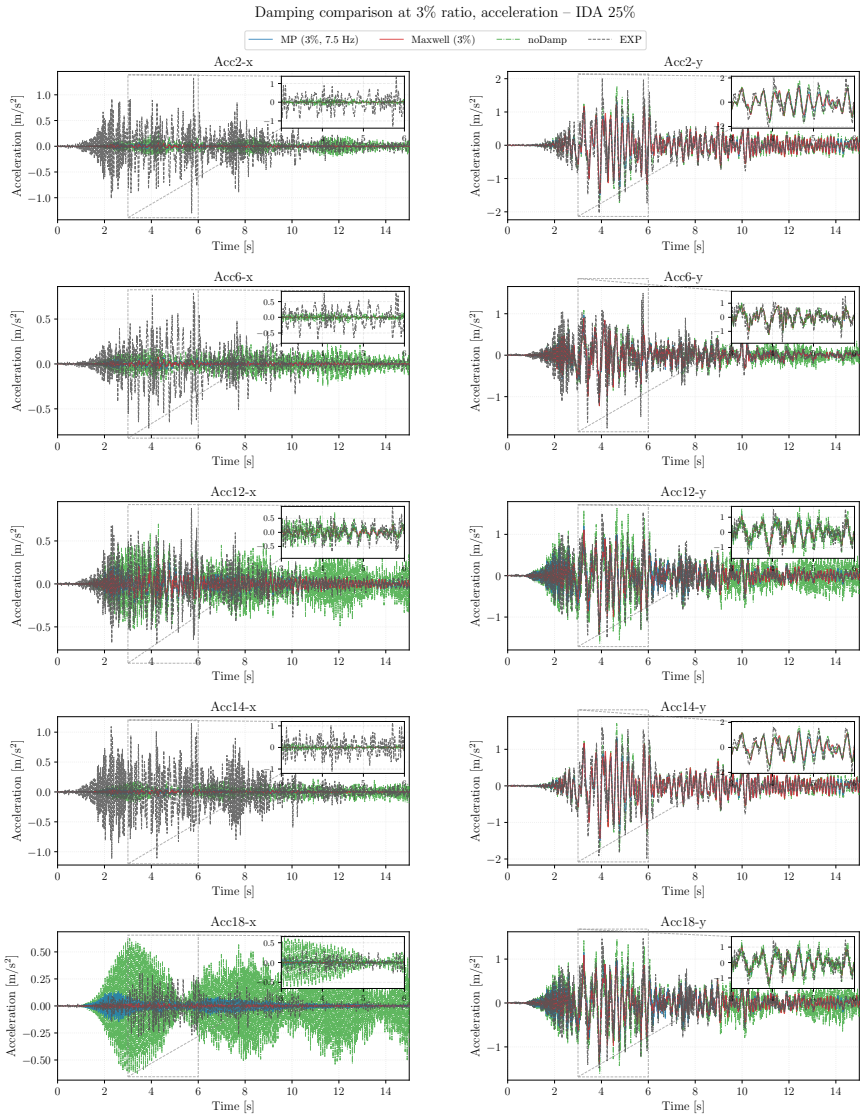


Figure C.9. Acceleration time histories at five accelerometer locations for the AQA25 amplitude level under the three damping configurations at $\zeta^{\star} = 3\%$.

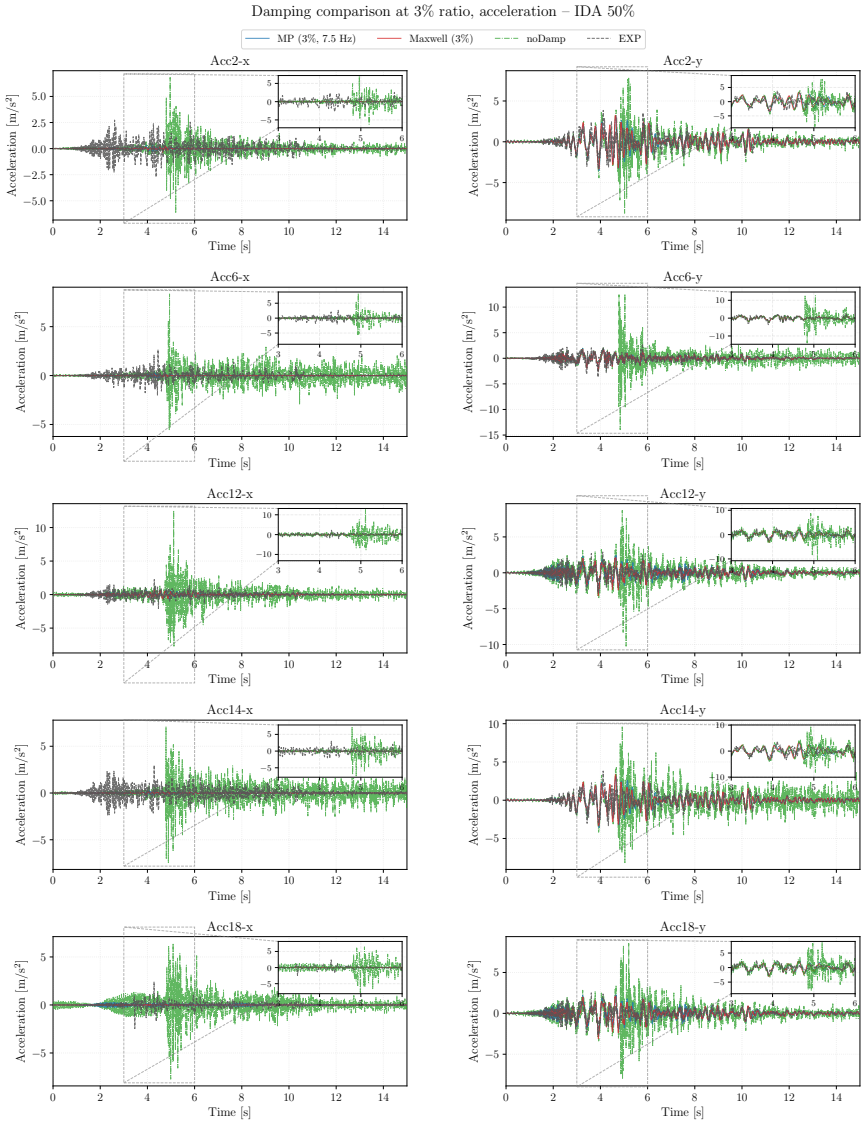


Figure C.10. Acceleration time histories at five accelerometer locations for the AQA50 amplitude level under the three damping configurations at $\zeta^{\star} = 3\%$.

C.6. Per-run hysteretic response of the gable wall specimens

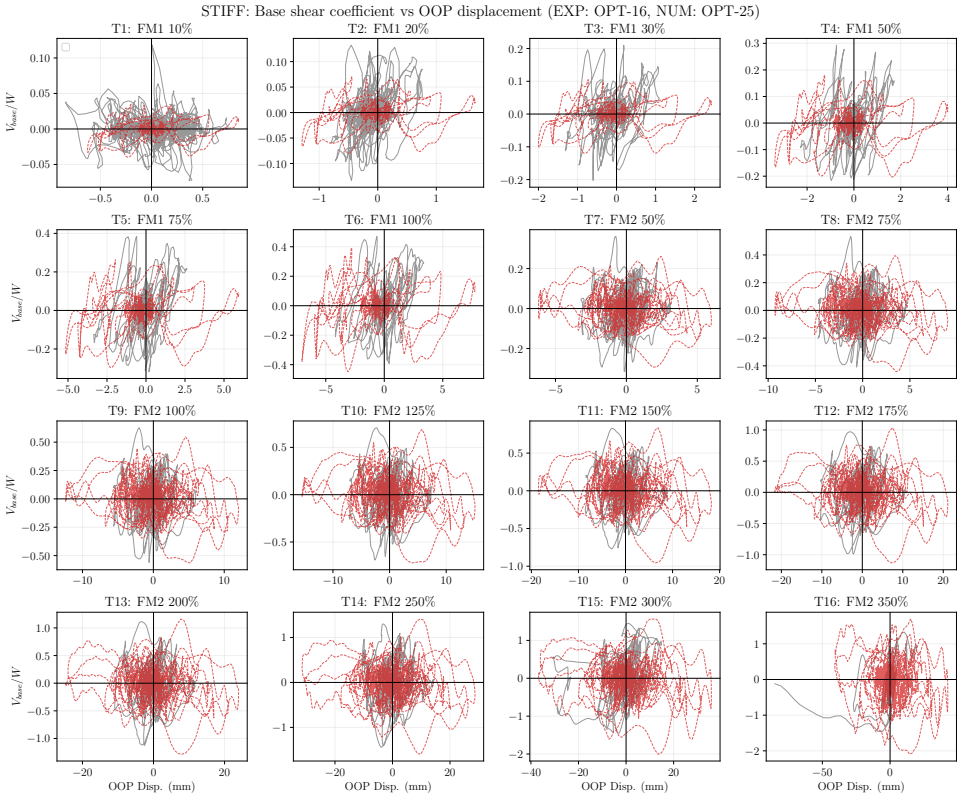


Figure C.11. STIFF: Per-run hysteresis loops of the normalised base shear coefficient V_{base}/W against the OOP displacement at OPT-25 at NUM and OPT-16 at EXP.

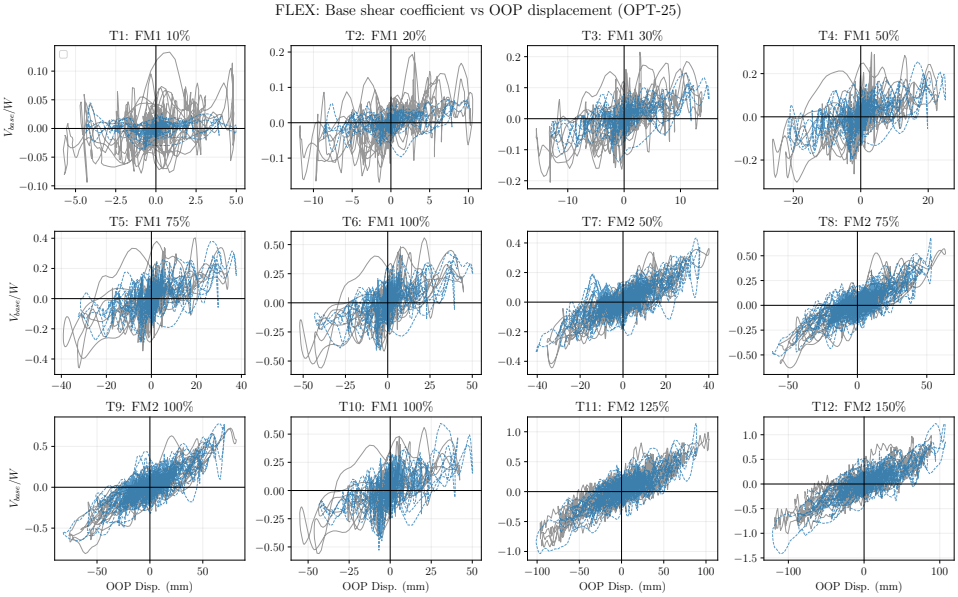


Figure C.12. FLEX: per-run base shear coefficient (V_{base}/W) against the OOP displacement at OPT-25.

Appendix C

D

Appendix D

This appendix complements the discussion of the unreinforced TUD-BUILD-1 model in Chapter 8. It presents the evolution of the contact damage scalar across the full set of scaled EQ-NPR analyses and the corresponding inter-storey drift demands, which together explain how the governing failure mechanism develops and at which intensity the structure loses its load-bearing capacity. The main text reports only the damage states at selected intensities. Here, the complete progression is shown so that the onset, growth, and localisation of damage can be traced from one intensity step to the next.

D.1. Damage state of the unreinforced TUD-BUILD-1 test

Figure D.1 shows the joint damage scalar d_{ts} at the end of each analysis, for input motions scaled from 20% to 175% of the EQ-NPR record. The scalar combines the tensile and shear damage accumulated at each contact and ranges from 0 (undamaged) to 1 (fully damaged joint, with only frictional resistance remaining). Reading the nine panels in sequence reveals three distinct phases of behaviour.

At low intensities (panels a–c, 20% to 50%), damage remains confined to the connections. The wall-to-diaphragm interfaces at the attic level and the bed joints at the base of the ground-storey piers are the first to open. Cracking at these locations reflects the low tensile capacity of the joints and the concentration of demand where the stiff diaphragms restrain the walls. The piers themselves remain essentially intact, and the deformation pattern is still close to that of the uncracked structure. From 50% onwards, a horizontal crack also develops at mid-height of the west facade, marking the start of the rocking response of the upper pier.

At intermediate intensities (panels d–f, 66% to 100%), the damage migrates from the connections into the piers. Diagonal stepped cracks form in the ground-storey piers of the west facade and propagate towards the corners, while horizontal cracks at the first-floor level extend across the full pier width. The combination of diagonal shear cracks in the squat ground-storey piers and flexural cracks at the storey interfaces indicates a mixed rocking-and-shear response, with the west facade bearing most of the demand. The east facade shows the same crack pattern at a visibly lower level of damage, consistent with the asymmetry of the openings and the resulting difference in pier geometry between the two facades.

At high intensities (panels g–i, 133% to 175%), the damage is no longer localised in discrete cracks but spreads over large portions of both facades and into the transverse walls. The ground storey is heavily fragmented, with multiple intersecting diagonal bands and near-complete loss of joint integrity along the base. At 150% of EQ-NPR, the west facade collapses, and the patterns shown for the two highest intensities therefore represent a structure that has already exceeded its near-collapse limit state. The concentration of damage in the ground storey, with the second storey remaining comparatively intact, confirms the soft-storey character of the governing mechanism discussed in Section 8.6.4.

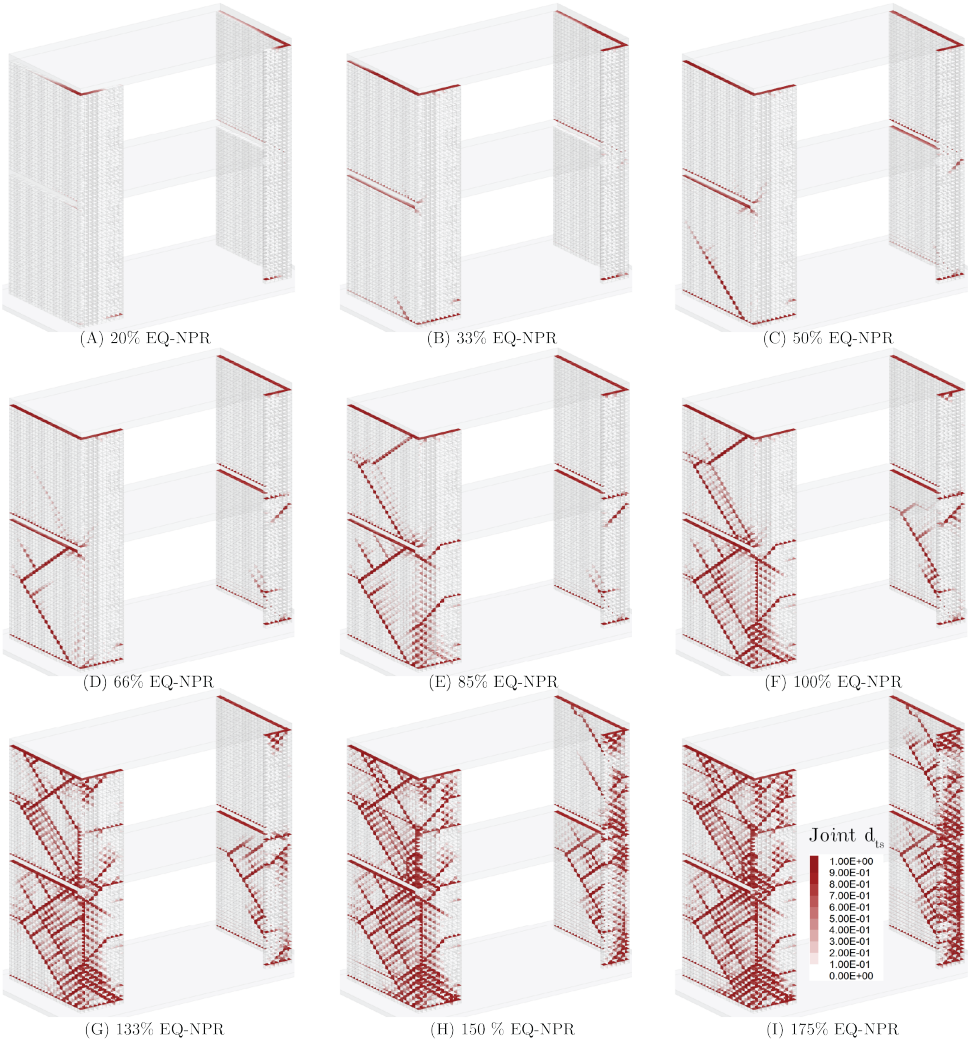


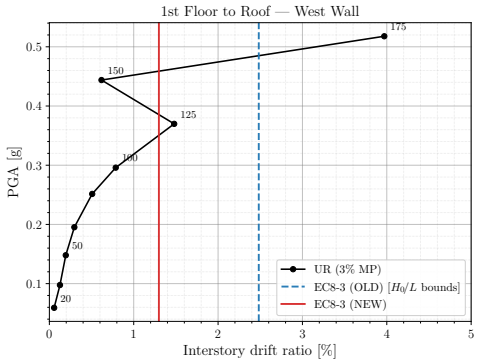
Figure D.1. Final damage state of the unreinforced TUD-BUILD-1 model in terms of the joint damage scalar d_{ts}, for input motions scaled from 20% to 175% of the EQ-NPR record (panels a–i). The scalar ranges from 0 (undamaged, white) to 1 (fully damaged contact with only frictional resistance, dark red). At low intensities, damage is confined to the wall-to-diaphragm connections and the base bed joints. With increasing intensity, diagonal stepped cracks develop in the ground-storey piers of the west facade, and the damage progressively localises in the ground storey. The west facade collapses at 150% of EQ-NPR, so panels (h) and (i) show post-collapse states.

D.2. Interstorey drift versus intensity measure, unreinforced

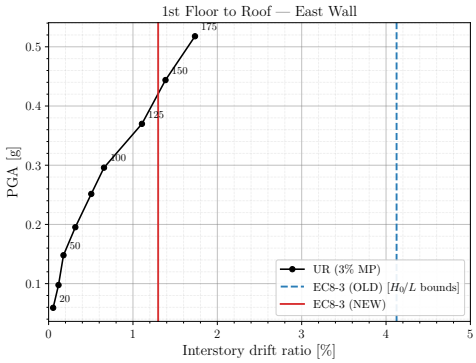
The damage states described above are quantified in Figure D.2, which relates the peak interstorey drift ratio of the second storey (first floor to roof) to the peak ground acceleration of each scaled record, separately for the west and east facade piers. Each marker corresponds to one analysis, labelled with its scaling percentage. The resulting curves are compared against two sets of drift limits. Panels (a) and (b) use the near-collapse thresholds of EC8-3, in both the previous and the revised formulation, evaluated for the H_0/L bounds of the piers. Panels (c) and (d) use the empirical drift capacities proposed by Messali and Rots for calcium silicate masonry piers.

The two facades respond very differently. The east wall (panels b and d) follows a stable, monotonically increasing curve. Drift demand increases gradually up to 100% of EQ-NPR and accelerates beyond it, reaching approximately 1.8% drift at 175% intensity while remaining below the EC8-3 (OLD) and Messali and Rots limits over most of the intensity range. The west wall (panels a and c) shows the same gradual trend up to 125%, but at 150% the curve reverses. The reversal does not indicate an improved response. At that intensity, the west facade collapses, and the peak drift extracted from the analysis no longer describes a stable configuration. The apparent drift reduction at 150%, followed by the large jump at 175%, should therefore be read as the signature of collapse, and the points beyond 125% as post-capacity states rather than meaningful demand values.

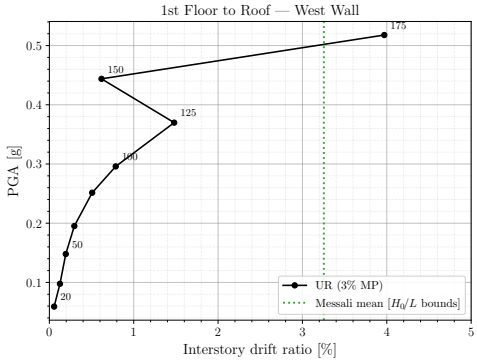
The comparison with the thresholds supports the same conclusion from a code assessment perspective. The west pier crosses the NEW EC8-3 limit between 125% and 150% of EQ-NPR, which is consistent with the intensity at which the damage scalar in Figure D.1 shows the transition from localised cracking to a ground-storey mechanism. The OLD EC8-3 formulation and the Messali and Rots mean capacity place the near-collapse point at higher drifts, illustrating the considerable scatter between codified and empirically derived limits for unreinforced masonry. For this structure, the NEW EC8-3 threshold gives the most conservative, and in view of the observed collapse at 150%, the most realistic estimate of the near-collapse intensity.



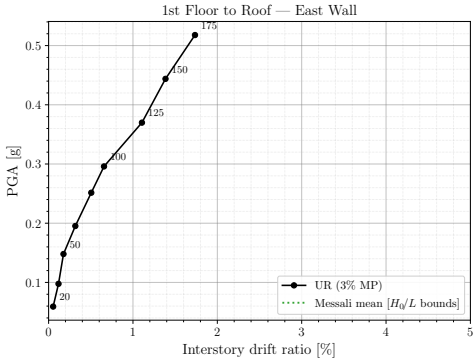
(A) West wall – EC8 thresholds



(B) East wall – EC8 thresholds



(C) West wall – Messali and Rots thresholds



(D) East wall – Messali and Rots thresholds

Figure D.2. First-storey to second-storey EDP vs IM results for the west and east facade piers.

Acknowledgements

I had always assumed that the acknowledgements would be the easiest part of this dissertation to write, which is exactly why I *strategically postponed* them until the very last moment. I imagined a short list of names and a few sentences of thanks would suffice. Turns out I was wrong. Once I began, I realised how many people had shaped this work, often in ways I had not noticed at the time. The difficulty turned out to lie not in finding people to thank but in doing justice to all of them.

This journey began long before Delft. I left Indonesia for Japan, and later moved to an entirely different continent, and each move meant learning a new language, culture, and a new sense of what counts as normal. It is in the Netherlands, however, that I have built the life I have today. I arrived as a rather socially awkward stranger, and over the years the people I met here patiently made room for me, until this country became home.

This dissertation owes a great deal to my supervisors. To **Francesco**, thank you for so generously sharing your expertise in the numerical modelling of masonry structures, and for helping me find the direction that this research eventually took. I am also deeply grateful that you took on supervising my PhD after Anjali's departure, which allowed this work to continue without *losing its way*.

To **Anjali**, this project would not have existed without you. Thank you for setting it in motion and for believing in me. You made my first six months here wonderfully welcoming, and that warmth stayed with me long after.

To **Jan**, your vast experience in masonry mechanics, together with your perspective on implicit methods, showed me my work from the other side. Beyond your knowledge, it has been an honour to have you as my promotor. You have always been remarkably down to earth, and I was always struck by how you came to every progress meeting with a folder of my work and notes from our previous discussions, which showed how much you cared about this research. I could not have asked for a better "boss".

I am also grateful to the committee members, Dr. **Bora Pulatsu**, Prof. **Andrea Penna**, Prof. **Vasilis Sarhosis**, Prof. **İhsan E. Bal**, and Prof. **Max Hendriks**, for agreeing to take part in this defence. Thank you for reading this dissertation and for the thoughtful comments that helped refine it. It is a privilege to have this work examined by researchers whose contributions to masonry I have cited throughout these pages.

Research is rarely solitary, and this work owes much to close collaboration. I am particularly indebted to Dr. **José Lemos**, who guided me through the low-level implementation of the constitutive model in DEM at the very start of my PhD, and whose insight shaped many of the discussions that followed. My first real understanding of how DEM behaves came from the post-diction of the SERA cross-vault, and for this I thank Prof. **Daniele Malomo**, together with **Lucy Davis** and **Rhea Wilson**.

To Dr. **Nicolò Damiani**, thank you for stress-testing both the MASON model and me. The model has become what it is today largely through your input and scrutiny, and I

look forward to the collaborations still to come. I am also thankful to **Alessia Furiosi** and **Marta Bertassi** for adopting the constitutive model in their own research. Seeing it applied beyond this dissertation has been one of the most rewarding parts of this journey.

Beyond Nicolò, Alessia and Marta, I am grateful to the wider group in Pavia, whom I have had the pleasure of meeting at conference after conference: the *Maestro* **Gabriele Guerrini**, **Christian Salvatori**, **Marco Smerilli**, **Simone Reale**, **Margherita Buttazzoni**, **Elena Sara Saeed**, **Luigi Greco**, **Alessandro Damiani** and the honorary *pavese* **Madalena Ponte**. You made every one of those trips something to look forward to, and proved that a conference dinner can be as productive as any session.

To my colleagues in the Structural Mechanics chair, thank you for the four years we shared. Somewhere between long lunches and PSOR beers, you turned what could have been a solitary PhD into something I actually looked forward to showing up for. Thank you, **Paul**, **Rita**, **Michele**, **Ziwei**, **Abide**, **Navid**, **Amir**, **Pedro**, **Uday**, **Giovanna**, and **Abridhi**, for the good company along the way. The same goes for **Mani** and **Marianthi**, who have since moved on from the group but remain very much part of these memories. I will miss our coffee breaks and group meetings more than I will miss writing this dissertation, which says a lot.

I am also indebted to **Iris**, **Sandra**, **Jacqueline**, and **Jaap**, who always seemed to know which form I needed before I did. Thank you for your patience with every administrative question, and for insisting that I ask them in Dutch. My Dutch is still a work in progress, but it is far better because of you, so *hartelijk bedankt*!

A special mention goes to **Satyadhrik Sharma**, my partner in crime through four years in Delft. Our conversations ranged from work to life, usually over more beers than either of us would care to count, and they made this journey far more colourful. I am especially grateful for the evenings before my interview at Hanze, when, drink in hand, he taught me more about the ways of academia than any career workshop ever could.

Speaking of PSOR beers, that small bar gave me far more than a place to unwind after work. It is where I found a tight-knit Italian community that welcomed me as one of their own, and I thank **Desa**, **Manu**, **Emanuele**, **Stefano**, **Pier**, **Vlad**, both **Nicola** (**Franciuli** and **Meggiato**), and many others for every evening we spent there. My Italian listening skills have improved a lot thanks to you, mostly because I could rarely get a word in.

Beyond Delft, I am deeply grateful to my church community. To **Brother Mattheus**, thank you for your spiritual guidance and for the advice you have given me over the years. **Henny**, **Romanita**, and **Aryo** welcomed Jessica and me into the church and showed us how to make a life in Den Haag. I treasure the weekends and evenings spent at the home of **Lily**, **Ruben**, **Virtu**, and **Santiago**, who always made us feel like family. And to **Rieza**, **Geby**, **Tessa**, and **Cato**, thank you for giving us countless reasons to celebrate and for showing us what it means to build a married life in the Netherlands.

To my close friends **Vanessa** and **Galaad**, thank you for being the first friendly faces I met in the Netherlands. That warm welcome grew into many evenings together, and I am grateful you have been part of this journey from day one.

No acknowledgement would be complete without the emotional support animals I have borrowed over the past four years: **Mek**, **Xiaoluobo**, **Prenses**, **Mowgli**, **Bart** the cat, and **Bart** the dog. You asked for nothing but snacks and attention, and gave far more in return. My thanks also go to your owners for their generous lending policy.

Finally, to my paranymphs, the friends I hold dearest. I first met Dr. **Sebastian Tommi Tandar** during our first year in Bandung, before he left for Osaka and I later followed to Tokyo. We spent years in the same country without ever crossing paths, until he moved to Leiden and I to Delft, and our roads finally converged in the Netherlands. Sebastian, to you and **Danica** (and **Mek**), thank you for the countless dinners and wine bars, and for the late-night *curhat* sessions that made life here so much richer for Jessica and me.

And to my other paranymph, Dr. **Maria Belén Gaggero**. It still amuses me how long it took us to get to know each other. We crossed paths in the Structural Mechanics chair for quite some time before realising how much we had in common, but once we did, you became one of my closest friends. Through the toughest times of writing this dissertation, you were a steady and cheerful presence. Your countless “how are you?” messages had a way of arriving at exactly the right moment, and they carried me through more than you know. It means a great deal to me that we get to stand beside each other at both of our defences.

Last but certainly not least, to my family. **Mom** and **Dad**, thank you for your unconditional support from the other side of the world. The distance never once made your love feel smaller, and every call home reminded me where I come from. To my sisters, **Shania** and **Sharen**, together with **Denis** and **Ella**, thank you for cheering me on from afar and for keeping me in the loop on everything I missed back home. And to my sister-in-law, **Roselina Nadia**, thank you for your radiant energy, which somehow reaches us all the way from Berlin.

Most of all, to **Jessica**. Our marriage began at almost the same time as this PhD, and I often joke that you signed up for two commitments at once without knowing what the second would involve. Thank you for bearing with my indecisiveness; more often than not, you knew the answer long before I did. When things got rough, you stood next to me, steady and patient, and reminded me why I started. On the days I doubted myself, your belief in me was enough for both of us. I am proud of how much we have grown since the day we said "I do," and even more excited about the chapters we still have to write together.

And to my younger self, who packed up his life in Japan and boarded a plane to a country he barely knew: thank you for not looking back. It was worth it. On to the next one.

Yopi Prabowo Oktiovan
October 2026, Delft.

Curriculum Vitæ

Yopi Prabowo OKTIOVAN

13-10-1996	Born in Medan, Indonesia.
2013–2017	Bachelor of Science in Civil Engineering Bandung Institute of Technology, Indonesia
2017–2019	Master of Engineering in Civil Engineering Institute of Science Tokyo (formerly Tokyo Institute of Technology), Japan
2017–2021	Civil Engineer Commonwealth Engineers Co., Ltd., Japan
2021–2022	Civil Engineer Tokyo Electric Power Services Co., Ltd., Japan
2022–2026	Doctor of Philosophy Delft University of Technology, the Netherlands *Thesis:* Advancing the Distinct Element Modelling of Masonry Structures *Promotor:* Em. prof. dr. ir. J. G. Rots *Copromotor:* Dr. F. Messali
2026–present	Researcher and Lecturer Research Centre NoorderRuimte, Hanze University of Applied Sciences, Groningen, the Netherlands
2025–present	Reviewer Archives of Computational Methods in Engineering; Earthquake Engineering and Engineering Vibration; Engineering Science and Technology, an International Journal; International Journal of Architectural Heritage; Meccanica; Reliability Engineering & System Safety; Structures.

List of Publications

Journal articles

1. **Y. P. Oktiovan**, L. Davis, R. Wilson, A. Dell'Endice, A. Mehrotra, B. Pulatsu and D. Malomo. 'Simplified Micro-Modeling of a Masonry Cross-Vault for Seismic Assessment Using the Distinct Element Method'. In: *International Journal of Architectural Heritage* (Nov. 2023). ISSN: 15583066. DOI: 10.1080/15583058.2023.2277328

2. **Y. P. Oktiovan**, F. Messali, B. Pulatsu, J. V. Lemos and J. G. Rots. 'A contact-based constitutive model for the numerical analysis of masonry structures using the distinct element method'. In: *Computers & Structures* 303 (2024), p. 107499. ISSN: 0045-7949. DOI: 10.1016/J.COMPSTRUC.2024.107499

3. **Y. P. Oktiovan**, F. Messali, B. Pulatsu, S. Sharma, J. V. Lemos and J. G. Rots. 'Cyclic constitutive model for masonry joint damage and energy dissipation using the distinct element method'. In: *Computers & Structures* 321 (Jan. 2026), p. 108094. ISSN: 00457949. DOI: 10.1016/j.compstruc.2025.108094

4. **Y. P. Oktiovan**, J. V. Lemos, B. Pulatsu, F. Messali, J. G. Rots and D. Malomo. 'Evaluating damping schemes for the discontinuum seismic analysis of masonry cross-vaults'. In: *Bulletin of Earthquake Engineering* 24 (2026), pp. 2349–2389. DOI: 10.1007/s10518-026-02379-y

5. A. Furiosi, N. Damiani, **Y. P. Oktiovan**, M. Rota and A. Penna. 'Benchmarking substructural discrete-element models for masonry arch bridges'. Submitted to *Earthquake Engineering & Structural Dynamics*, under review. 2026

Conference contributions

1. **Y. P. Oktiovan**, F. Messali and J. Rots. 'Detailed distinct element modeling of a Utrecht wharf cellar for the assessment of the load-bearing capacity and failure mechanism'. In: *Proceedings of the Seventeenth International Conference on Civil, Structural and Environmental Engineering Computing*. Ed. by P. Ivanyi, J. Kruis and B. H. V. Topping. Vol. 6. Civil-Comp Conferences Paper 6.2. Edinburgh, UK: Civil-Comp Press, 2023. DOI: 10.4203/ccc.6.6.2

2. **Y. Oktiovan**, A. Mehrotra, F. Messali and J. Rots. 'Investigation of the Structural Performance of Masonry Wharf Cellars in Utrecht Using the Distinct Element Method'. In: *Structural Analysis of Historical Constructions*. Ed. by Y. Endo and T. Hanazato. Vol. 46. RILEM Bookseries. Cham: Springer Nature Switzerland, 2024, pp. 287–300. ISBN: 978-3-031-39450-8. DOI: 10.1007/978-3-031-39450-8_24

3. **Y. P. Oktiovan**, F. Messali, J. Lemos, B. Pulatsu and J. Rots. 'Prediction of the In-Plane Response of Masonry Walls Using a Piecewise Softening Contact Model Within the Distinct Element Method'. In: *18th International Brick and Block Masonry Conference*. Ed. by G. Milani and B. Ghiassi. Vol. 613. Lecture Notes in Civil Engineering. Cham: Springer Nature Switzerland, 2025, pp. 76–92. ISBN: 978-3-031-73314-7. DOI: 10.1007/978-3-031-73314-7_6

4. **Y. P. Oktiovan**, N. Damiani, F. Messali and J. Rots. 'Comparison of Distinct Element Modeling Strategies on the In-Plane Response of Retrofitted URM Structures'. In: *Structural Analysis of Historical Constructions*. Ed. by S. Saloustros and K. Beyer. RILEM Bookseries. Cham: Springer Nature Switzerland, 2026, pp. 1231–1244. ISBN: 978-3-032-13469-1. DOI: 10.1007/978-3-032-13469-1_97

5. **Y. P. Oktiovan**, N. Damiani, A. Ghezelbash and F. Messali. 'Dynamic analysis and seismic retrofit assessment of a Dutch calcium silicate terraced house using the distinct element method'. In: *Proceedings of the 18th European Conference on Earthquake Engineering (ECEE 2026)*. Berlin, Germany, 2026

6. **Y. P. Oktiovan**, N. Damiani and F. Messali. 'A Distinct Element Method Comparison of Retrofit Systems for a Two-storey Unreinforced Masonry Building'. In: *International Masonry Conference 2026: State of the Art in Masonry Research. Proceedings of the 11th International Masonry Conference (IMC 2026)* (Lübeck, Germany, 12th–15th July 2026). Ed. by International Masonry Society. Stuttgart: Fraunhofer IRB Verlag, 2026, pp. 1199–1200. DOI: 10.60628/9783738810400-1199

7. **Y. P. Oktiovan**, B. Pulatsu, E. Smyrou and I. E. Bal. 'Spectrum-matched sinusoidal excitation for out-of-plane seismic assessment of masonry walls using DEM'. In: *International Masonry Conference 2026: State of the Art in Masonry Research. Proceedings of the 11th International Masonry Conference (IMC 2026)* (Lübeck, Germany, 12th–15th July 2026). Ed. by International Masonry Society. Stuttgart: Fraunhofer IRB Verlag, 2026

TU Delft

